MECHANISMS AND CONDITIONS OF DEFORMATION IN QUARTZITES FROM THE CANTABRIAN AND WEST ASTURIAN-LEONESE ZONES, NORTH SPAIN

VOLUME II

T.G. Blenkinsop

A Thesis submitted for the degree of Doctor of Philosophy

University of Keele

1987

VOLUME II

CHAPTER 5

BERNESGA VALLEY, CREMENES, LUNA LAKE

5.1 STRATIGRAPHY AND LITHOLOGY

The stratigraphy and lithology of the S.W. Cantabrian zone has been summarised by Wallace (1972) and aspects are also referred to in Baldwin (1977). There are highly significant regional variations over the whole Cantabrian zone reflecting tectonic controls on sedimentation referred to in Chapter 1, but within the confines of the southwest area, the lower Palaeozoic stratigraphy consisting of up to 4km of shallow water sediments described below for the Bernesga Valley applies over the whole area. The area is located in Figure 1.3, and a summary of the stratigraphy given in Figure 5.1. The structural analysis on the meso and microscopic scales (5.3 and 5.4) and all the sampling with the exception of the illite crystallinity samples, has been confined to two formations: the Oville and Barrios.

The lowest unit exposed is the Láncarra Formation, consisting of 150m of white/yellow dolomite, with ooliths, limestone microbreccias, quartz grains, stromatolites and bird's eye texture. The top third of the formation is a distinctive red nodular griotte with broken brachiopods and intertidal stromatolites. The formation is clearly shallow marine, probably intertidal and shallow sub-tidal.

The Láncarra Formation is followed by approximately 250m of interbedded shales and thin sandstones, the latter becoming thicker (up to 1m) and more abundant up-section. The Oville Formation shows load casting, slumping, cross-bedding and ripples with browsing trace fossils and interbedded dolomites and tuffs. Glauconite is reported in the sands. The environment is shallow water marine, with rapid sedimentation in a subsiding basin. Trace fossils in the Oville Formation indicate that the base is Middle Cambrian; the presence of Cruziana furcifera in the top of the Oville gives it a maximum Upper Tremadoc age by comparison with Great

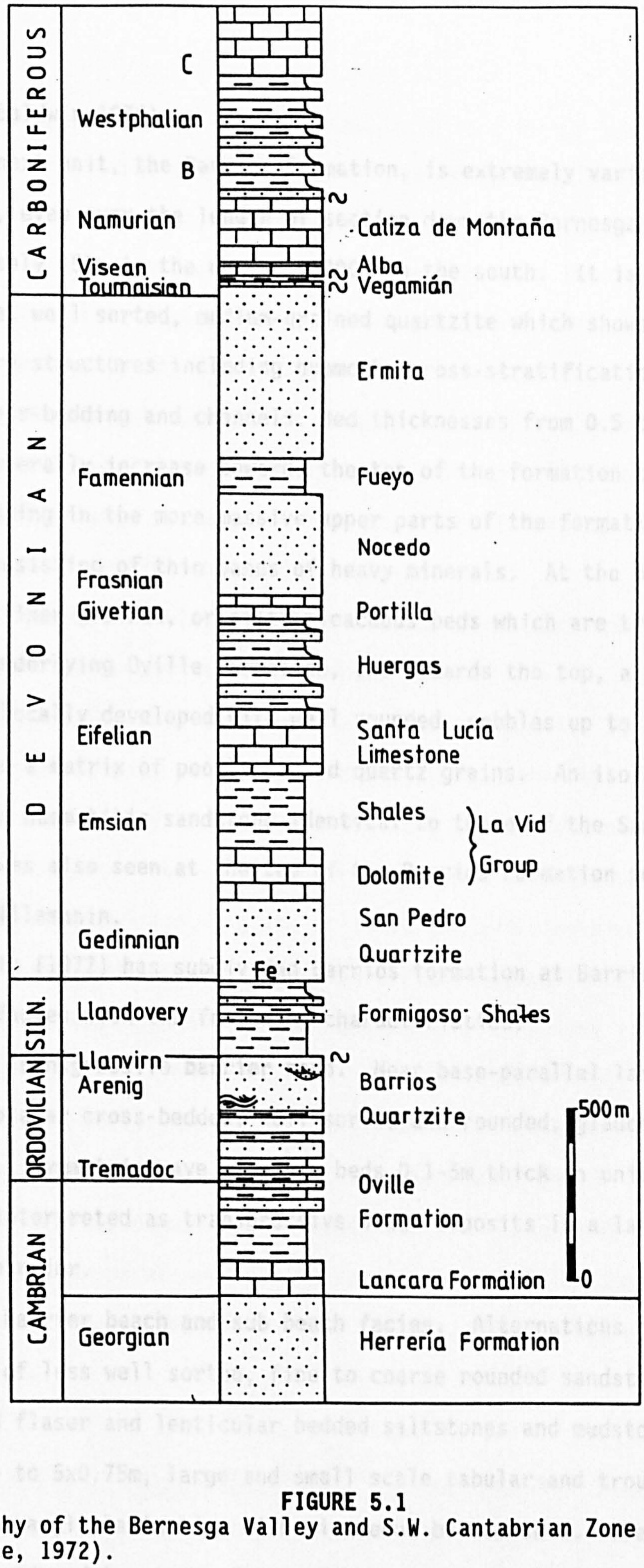

FIGURE 5.1
Stratigraphy of the Bernesga Valley and S.W. Cantabrian Zone (This study and Wallace, 1972).

Britain (Baldwin 1976).

The next unit, the Barrios Formation, is extremely variable in thickness, even over the length of section down the Bernesga Valley, from approximately 150m in the north to 300m in the south. It is dominated by a pure white, well sorted, medium-grained quartzite which shows a variety of sedimentary structures including hummocky cross-stratification, planar and trough cross-bedding and channels. Bed thicknesses from 0.5 to several metres, generally increase towards the top of the formation throughout the area. Bedding in the more massive upper parts of the formation is hard to define, consisting of thin bands of heavy minerals. At the base are a number of finer grained, or silty micaceous beds which are transitional from the underlying Oville Formation, and towards the top, a conglomeratic facies is locally developed with well rounded, pebbles up to 10mm in diameter in a matrix of poorly sorted quartz grains. An isolated outcrop of dull red haematitic sandstone identical to those of the San Pedro Formation was also seen at the top of the Barrios Formation immediately south of Villamanin.

Baldwin (1977) has subdivided Barrios formation at Barrios de Luna into five facies with the following characteristics:

Member A. Transgressive barrier sand. Near base-parallel laminated and low angle planar cross-bedded, well sorted and rounded, glauconitic sandstones. Symmetric wave ripples, beds 0.1-5m thick in units up to 35m. These are interpreted as transgressive beach deposits in a landward migrating barrier.

Member B. Barrier beach and sub beach facies. Alternations of Member A with units of less well sorted, fine to coarse rounded sandstones with interbedded flaser and lenticular bedded siltstones and mudstones. Channels up to 5x0.75m, large and small scale tabular and trough-cross bedding, low angle lamination with micaceous bottom sets. The interbedded siltstones and mudstones are due to local regressive sedimentation controlled by variations in sand supply.

Member C. Tidal flat facies. Well to poorly sorted, locally glauconitic, sub-angular to sub-rounded medium sandstones, interbedded with flaser and lenticular-bedded mudstones and siltstones with beds 1mm-0.5m thick. Large scale current structures are rare; herringbone sets, current ripples and clay pebbles are found, indicating a tidal environment.

Member D. High tidal flat facies. Well to poorly sorted sandstones, silty shales and mudstones in beds 1mm-1.5m thick, with 1m fining-upwards sequences, and large scale cross beds in channelled units. A tidal influence with ebb-directed sand bars is indicated.

Member E. Lagoonal facies. Bioturbated mudstones with current-rippled lenses of siltstone and fine sandstone.

At Barrios de Luna, Baldwin interpreted the section as indicating two transgressive littoral and littoral/deltaic sequences separated by a regressive tidal delta-fluvial deposit; i.e. a tidal dominated shallow marine environment. The overall coarsening upwards sequence observed in the Bernesga Valley also suggests at least one transgressive sequence there. The presence of hummocky cross-stratification (H.C.S.), only gaining widespread recognition as a sedimentary structure since Baldwin's publication, however, indicates that storm influences were present (Walker 1979, Brenchley pers.comm.). H.C.S. is generated between the fair-weather and storm-wave bases by oscillatory storm-generated waves, probably following sand emplacement by turbidity current. The storm influence is confirmed by the overall coarsening up sequence: tidally dominated shallow marine sequences are expected to fine upwards, whether transgressive or not (Walker 1979).

Trace fossils in the Barrios Formation include Cruziana, Rusphycous, Skolithos, Diplocraterion, Planolites, Diplichnites and Teichinus. At Barrios de Luna itself, the presence of C.semiplicata in the lower two-thirds of the section, gives it a likely Tremadoc age (Baldwin 1977).

At Cabo de Peñas, the upper part of the quartzite there exposed is Arenig to possibly Llanvirn (Crimes and Marcos 1976); by inference, the Barrios quartzite at Barrios de Luna and the Bernesga valley is Tremadoc to Llanvirn in age.

The top of the Barrios quartzite has a knife sharp, undulating contact with the overlying Formigoso Formation (220m) in which the initial lithology is a black, fissile, homogeneous graptolitic shale with visible mica flakes, but towards the top, thin sandstones are increasingly intercalated, containing trace fossils, burrows and load casts. A quiet stagnant basin is indicated, with occasional clastic input. The fauna give basal Upper Llandoverian age. Thus, although the contact between the Barrios and Formigoso Formations is usually interpreted as an unconformity, no very large time interval can be represented.

The San Pedro Formation (220m) follows conformably and gradationally with thick red sandstones with haematite ooliths indicating a change to well oxygenated, turbulent, shallow marine conditions. An interval of red and green sandstones with chamosite ooliths, ripples, burrows and thin shales follows as energy input reduces, leading to black shales with lenses of pure white quartzite, 50-100m along strike, identical to the Barrios quartzite, but entirely isolated within the shales. Where contacts between shales or sandstones and these quartzites lenses can be seen, they are definitely not tectonic, and therefore represent a channel or bar sand deposit in otherwise quiet water conditions. The San Pedro Formation is Gedinnian. Both it and the Formigoso appear to thicken slightly to the south.

Conformably overlying the San Pedro is a well-bedded dolomite (150m), weathering a pale buff colour with algal stromatolites, similar to the Láncarra Formation. This intertidal deposit is the first member of the La Vid Group, which is followed by thinly bedded shales, sandstones and sparry limestones, comprising the second member, in which there are burrowed horizons rich in spiriferids and rhynconellids. The third member which combines with the underlying member to give a thickness of 200m, consists of tobacco brown and black fissile shales with lenses of nodular marl rich in brachiopods, bryozoans and crinoids, indicating a normally marine environment. The La Vid Group spans the interval from Gedinnian to Emsian.

The shales of the La Vid Group contrast with the succeeding limestones of the Santa Lucía Formation (at least 400m): a highly fossiliferous grey micrite with thick beds containing brachiopods, corals, stromatoporoids, algal stromatolites, bird's eye texture and dessication cracks, clearly a shelf biostrome, possibly in the back reef area. Reef facies are very well developed further west along the Sabero-Gordon line on the shores of Luna Lake to the north of Mirantes (Figure 5.3). The Santa Lucía Formation is Eiefelian.

The remainder of the Devonian, comprising the Huergas, Portilla, Nocedo and Ermita Formations, is not seen in the section studied at Bernesga. The lithologies continue to be varied shales, sandstones and limestones with a combined maximum thickness of 700m. The Ermita Formation is unconformable, increasingly so to the north, and succeeded by black shales and cherts of the Vegamian on an erosion surface representing an early Carboniferous regression (Higgins and Wagner-Gentis 1982), which also represents an increasingly large time interval to the north. Locally, however, the shales are absent and replaced by crystalline limestones along the Sabero-Gordon line (the Baleas Formation). A widespread transgression at the top of the Tournasian led to the deposition of the red nodular limestones (Griotte) which are the basal member of the Genicera (or Alba) Formation, the Gorgera. This deposit continues, although with an incomplete conodont zone, into the Viséan where it changes to cherts in red shales, the Lavander member. Immediately above the cherts is another widespread missing conodont zone which may extend throughout much of N.W. Europe (Holdsworth pers.comm.). Above this, the Canalon member continues as a griotte into the Namurian.

An important contrast between the early Namurian deposits is observed between the northeast and southwest of the area. In the former, the Genicera Formation is followed by the carbonate platforms limestones of the Barcaliente Limestone, the first appearance of the massive 'Caliza de Montaña' which extends over much of the Cantabrian zone to the north of the area studied. In the south the Olaja beds are laterally equivalent to the Canalon member, and these are a condensed mudstone sequence, forming the base of a thick turbidite sequence, the Olleros Formation. A northerly advance of the terrigenous basin with the retreat of the shallow shelf conditions of the Genicera and Barcaliente Formations, evidently begun in the lowest Namurian. The shallow shelf area has been referred to as the Cantabrian Block (Higgins and Wagner-Gentis 1982). Certain difficulties with this interpretation are now emerging. The depth of both limestone and turbidite deposition is highly problematic: what were formerly considered as evaporitic breccias in the Caliza de Montaña may be turbiditic, and limestones of similar appearance to the Caliza de Montaña interfinger with turbidites in the syncline north of Villamanin (Mart, pers.comm.).

5.2 MACROSTRUCTURES

The three sampling localities of this chapter all belong to the Somiedo-Correcilla nappe unit, the most interior of the major tectonic units in the Cantabrian zone. To the south are exposed the pre-Cambrian rocks of the Narcea antiform, while the Sobia-Gordon nappe unit and Central Coal basin lie to the north (Figure 1.2).

5.2.1 The Bernesga Valley

The Somiedo-Correcilla nappe unit is divided into four thrust sheets along the Bernesga Valley (from south to north, the Correcilla, Rozo, Pozo and Bregon sheets). The Correcilla sheet may be subdivided into two smaller sheets by a second thrust, and a small imbricate has been mapped in the Rozo sheet. The basal thrust to each sheet takes the name of that sheet. Within each sheet, the same lower Palaeozoic stratigraphy is repeated, with a general younging direction towards the south. The decollement level for each is the Láncarra Formation, but the highest stratigraphic level preserved increases from the San Pedro (Gedinnian) in the Correcilla sheet to the La Vid (Emsian) in the Rozo and Pozo sheets to the Santa Lucía (Eifelean) in the Bregon sheet (Figure 5.2). The thrust planes and parallel beds dip steeply towards the north and northeast, with the consequence that the whole section is overturned.

Figure 5.2 also shows that there are major tight folds within the thrust sheet bedforms,which do not affect the thrust, including a SW plunging synform in the Correcilla sheet, a synform plunging at 33^0 to 333^0 in the Rozo sheet, an antiform in the hangingwall of the Pozo thrust, plunging to the west at 40^0, some smaller scale folding in the Santa Lucía Formation below the Bregon thrust, and a west-plunging hangingwall antiform in the Bregon thrust sheet. The parallelism of these fold axial planes to the E-W to NW-SE strike would class them as arched folds in the terminology of Julivert and Marcos (1973). In addition to this major group of folds, the effects of cross-strike folding ('radial folds' of Julivert and Marcos) can be seen in the NE corner of Figure 5.2 and in Figure 5.3, where NS open folds affect both thrusts and thrust sheet bed forms.

5.2.2 Cremenes

The frontal thrust of the Somiedo-Correcilla nappe unit is covered by Mesozoic sediments to the east of Bernesga Valley, but it is quite probably the same feature which forms the base of the Esla nappe (Figure 1.3), making the two nappe units laterally equivalent. The decollement is again on the Láncarra Formation throughout the nappe until a ramp cuts up

FIGURE 5.2

Geology of the Bernesga Valley. Sample locations, structural data and field sketches of fracture orientation and appearance.

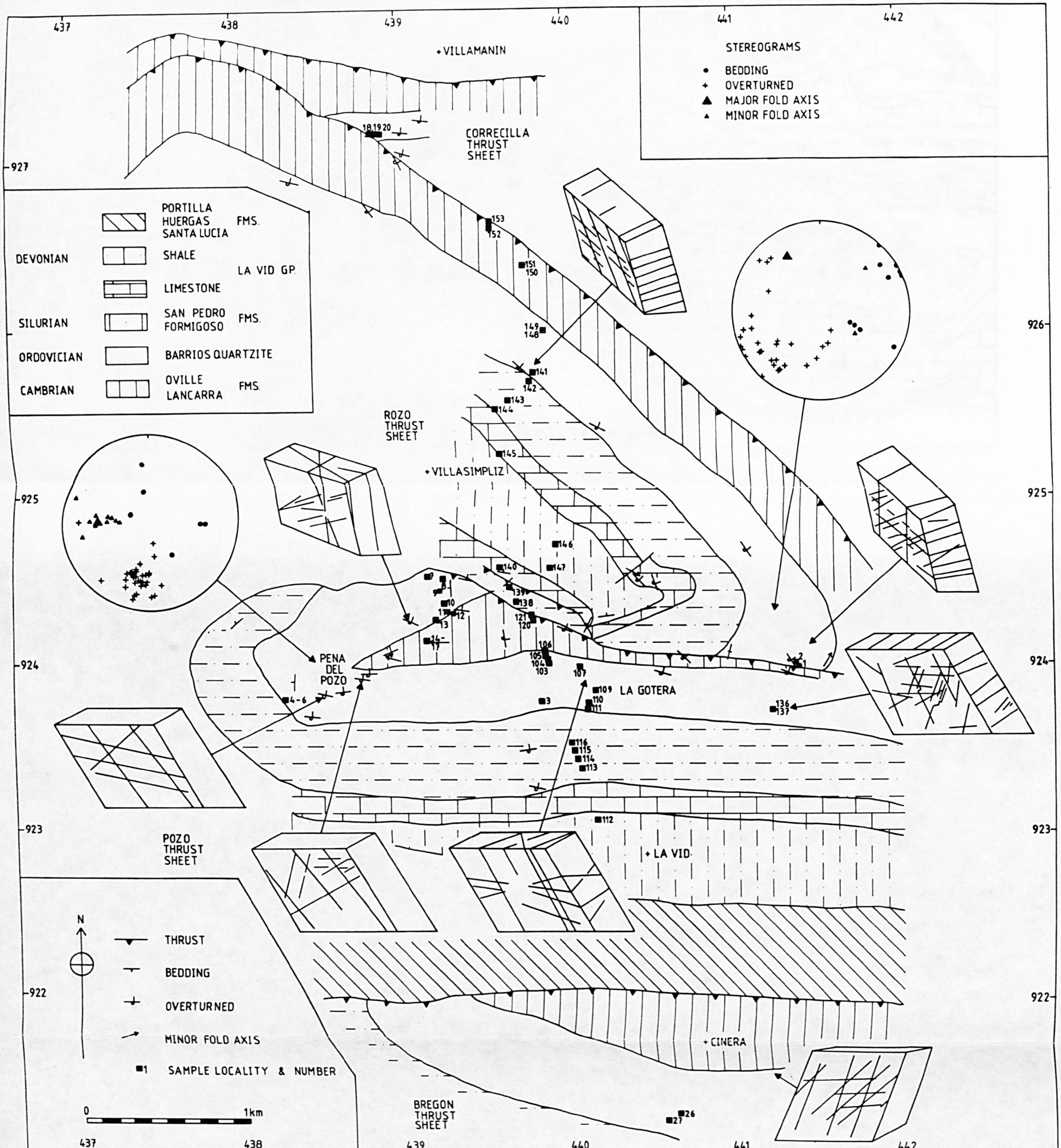

STEREOGRAMS
BEDDING
OVERTURNED
MAJOR FOLD AXIS
MINOR FOLD AXIS
VILLAMANIN
CORRECILLA THRUST SHEET
DEVONIAN
PORTILLA HUERGAS SANTA LUCIA FMS.
SHALE
LIMESTONE
LA VID GP.
SILURIAN
SAN PEDRO FORMIGOSO FMS.
ORDOVICIAN
BARRIOS QUARTZITE
CAMBRIAN
OVILLE LANCARRA FMS.
ROZO THRUST SHEET
VILLASIMPLIZ
PENA DEL POZO
LA GOTERA
POZO THRUST SHEET
LA VID
CINERA
BREGON THRUST SHEET
N
THRUST
BEDDING
OVERTURNED
MINOR FOLD AXIS
SAMPLE LOCALITY & NUMBER
0
1km
437
438
439
440
441
442
927
926
925
924
923
922

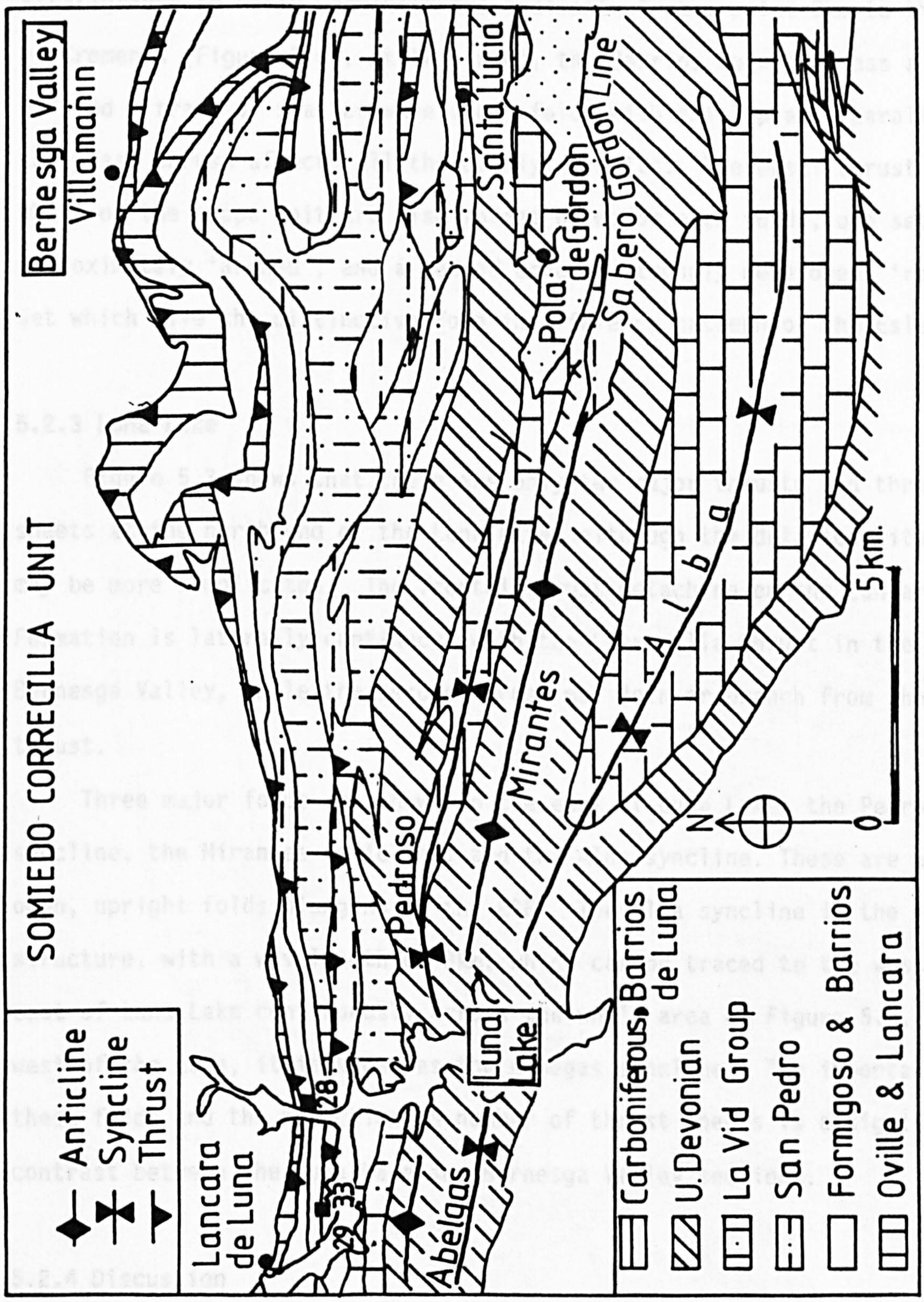

FIGURE 5.3
Sketch map of the relationship between the Luna Lake and Bernesga Valley (After Wallace, 1972).

stratigraphy to early Carboniferous sediments from a point 2km to the ENE of Cremenes (Figure 5.4). At this ramp, the Barrios quartzite has a bend of 90^0 and a train of smaller wavelength folds with axial planes parallel to the basal thrust affects all the overlying units. The basal thrust and the whole of the nappe unit are also folded by major open folds, one set approximately 'arched', and a second equally strongly developed, 'radial' set which give the distinctive fold interference pattern of the Esla nappe.

5.2.3 Luna Lake

Figure 5.3 shows that there are only two major thrusts and thrust sheets at the north end of the Luna Lake, although the detailed situation may be more complicated. The frontal thrust detaching on the Láncarra Formation is laterally continuous with the Correcilla thrust in the Bernesga Valley, while the second thrust may join or branch from the Bregon thrust.

Three major folds are shown to the east of Luna Lake: the Pedrosso syncline, the Mirantes anticline, and the Alba syncline. These are all open, upright folds plunging to the ESE. The Alba syncline is the largest structure, with a wavelength of 8km, which can be traced to the west and east of Luna Lake continuously across the whole area of Figure 5.3. To the west of the Lake, it is known as the Albegas syncline. The importance of these folds and the reduction in number of thrust sheets is a significant contrast between the Luna Lake and Bernesga Valley sections.

5.2.4 Discussion

Four important questions are posed by the macroscale structures described above:

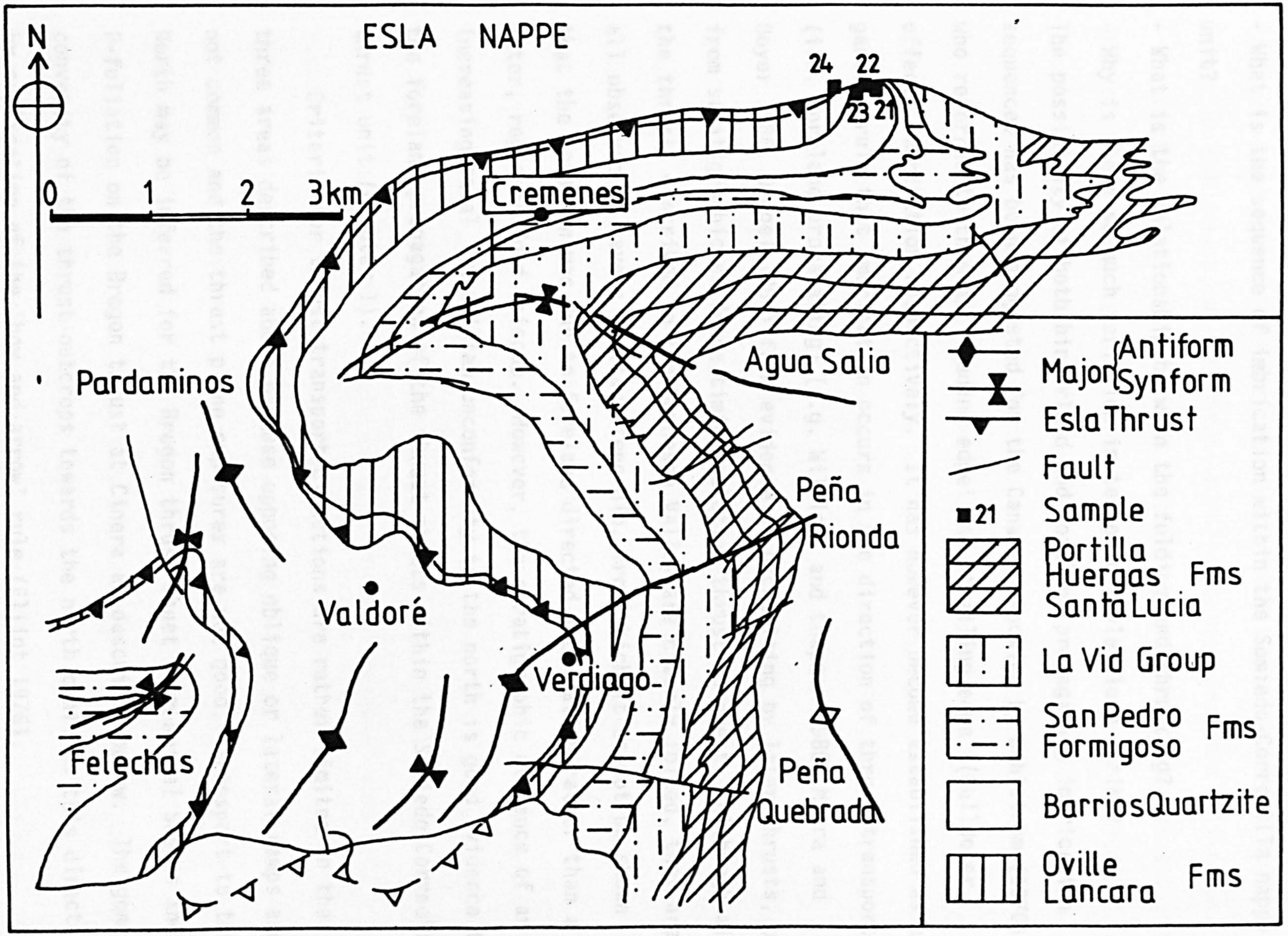

FIGURE 5.4

Geology of the Esla Nappe (After Rupke 1965, Alonso 1987).

- What is the transport direction and displacement?
- What is the sequence of imbrication within the Somiedo-Correcilla nappe unit?
- What is the relationship between the folding and thrusting?
- Why is there so much variation in tectonic style along strike?

The possibility of both hinterland and foreland propagating imbrication sequences has been suggested for the Canadian Rockies by Dahlstrom (1970), who referred to them as 'leading edge' and 'trailing edge' (bulldozer effect) imbrication respectively. It has however become established as a general rule that imbrication occurs in the direction of thrust transport (i.e. foreland propagating) (e.g. Williams and Chapman 1986, Mitra and Boyer 1986, Diegel 1986) from evidence of backtilting by later thrusts, or from stratigraphic evidence timing relative thrust movement. Although all the thrusts described in the Bernesga Valley are clearly folded, they are all observed to have a similar steep dip, from which it cannot be shown that the rotation was due to foreland directed imbrication rather than a later, regional fold episode. However, the stratigraphic evidence of an increasing basal Tournaisian unconformity to the north is good evidence for the foreland propagation of the thrust sheets within the Somiedo-Correcilla thrust unit (Chapter 1).

Criteria for thrust transport directions are rather limited in the three areas described above because opposing oblique or lateral ramps are not common and the thrust plane exposures are not good. Transport to the North may be inferred for the Bregon thrust sheet from Reidel Shears and P-foliation on the Bregon thrust at Cinera as described below. The general convexity of the thrust outcrops towards the north confirms this direction by application of the 'bow and arrow' rule (Elliot 1976).

There is one area (at Fuentas de Sancenas) along the Somiedo-Corecilla basal thrust where oblique ramps from the Láncarra Formation through to the Santa Lucía define a good direction of transport locally (Map C in Julivert and Arboloya, 1984): this is to the NNE. Julivert and Arboleya (1986) use similar evidence from Rodiezmo (2km east of Villamanin, Figure 5.2) to deduce an ENE direction, and obtain a NNE direction from the Esla nappe.

Thrust displacements are more difficult to estimate. Figure 5.3 shows that the Rozo thrust has approximately 1km displacement in the section plane. Restoring the thrust to horizontal by a strike parallel rotation would give 1km displacement resolved towards the North, or $1x(\sin45)^{-1}$=1.4km total displacement towards the northeast. Similar amounts can probably be inferred for the other imbricates of the Bernesga Valley, but there is not evidence for the amount of the basal thrust of the Somiedo-Correcilla unit.

It is likely, at least with in the Rozo and Pozo thrust sheets, that the fold component of shortening is more important than the thrust component. The relation between thrusting and folding is therefore of some interest. Three alternative models have recently been widely discussed from thrust and fold belts (Figure 5.5).

a) Structurally Necessary Folds. These are formed to accommodate geometrically necessary shape changes due to thrust plane topography (Figure 5.5a). The hangingwall anticlines of Rich's (1934) staircase thrust geometry are the classic examples. Lack of footwall strain is diagnostic of this simplest case. Boyer (1986) refers to this type of fold as a 'trailing edge fold' and points out that there are two separate folds after significant thrust displacement: one is the hangingwall above the ramp itself, and a second due to the cut-off in the hangingwall units against the thrust. Such folds have also been called 'fault bend folds' by Higgs et al. (1986), and Jamison (1987).

A second example of structurally necessary folding is found in duplexes. In this case, identical folds in both the footwall and hangingwall are formed: the former due to rotation of individual horses by successive imbricates and the latter as ramp generated folds (Figure 5.5).

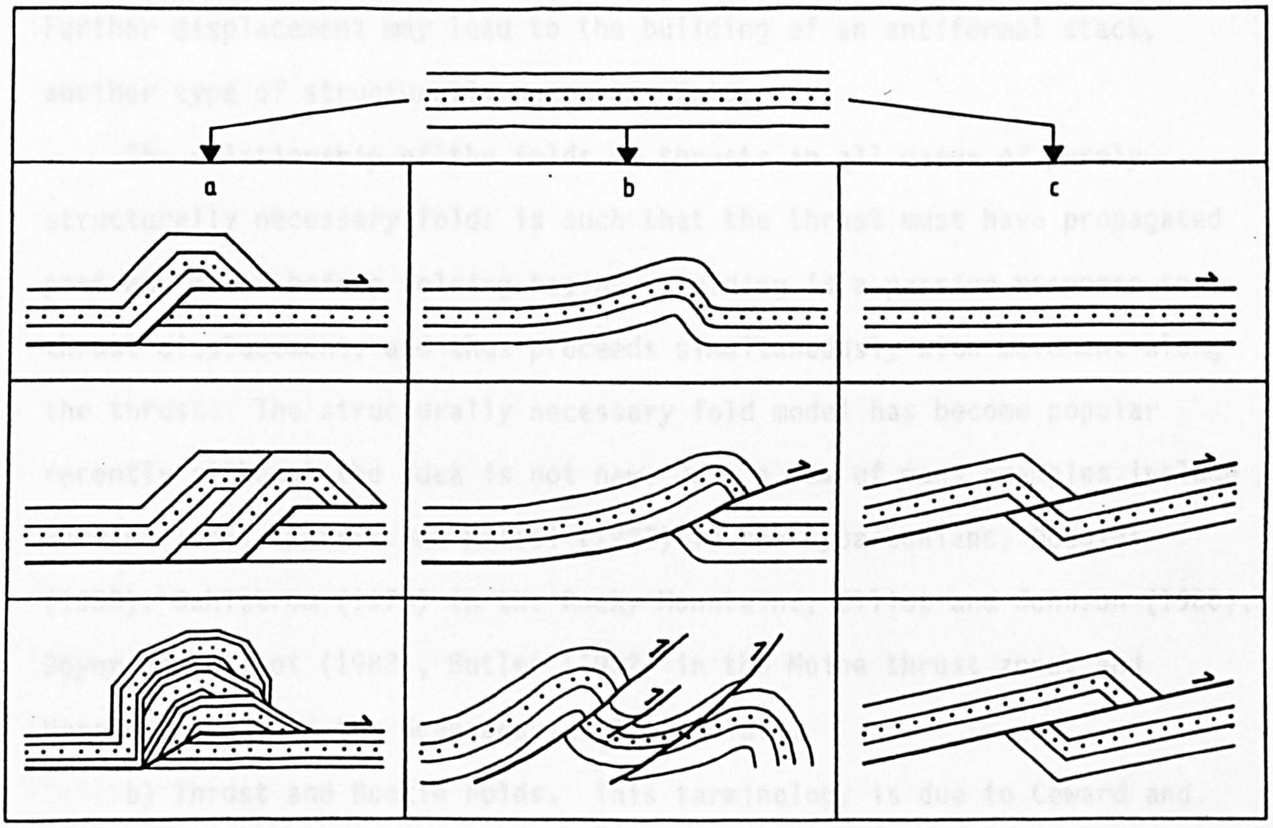

FIGURE 5.5

A simple classification of relationships between folds and thrusts.

a) Structurally necessary folds. Folding follows thrust displacement, due to thrust plane topography. The third box (lower left corner) shows a structurally necessary folds in an antiformal stack (Boyer and Elliot 1982).

b) Thrust and Buckle Folds. Folding precedes thrusting. The third box (lower centre) shows Forelimb, Out of Syncline, and Backlimb Thrusts (after Dahlstrom 1970) respectively from left to right.

c) Buckling between two thrusts. Folding follows thrusting between two parallel thrusts which join to form a single thrust (after Casey 1982).

This is the classic duplex model of Boyer and Elliott (1982), which can be recognised by symmetry in footwall and hangingwall strain in conjunction with the usual criterion for duplexes as summarised in Boyer and Elliott. Further displacement may lead to the building of an antiformal stack, another type of structurally necessary fold.

The relationship of the folds to thrusts in all cases of purely structurally necessary folds is such that the thrust must have propagated past any point before folding begins. Folding is a passive response to thrust displacement, and thus proceeds simultaneously with movement along the thrust. The structurally necessary fold model has become popular recently although the idea is not new. Just a few of many examples include Harris (1976), Harris and Milici (1977) in the Appalachians, Douglas (1950), Dahlstrom (1970) in the Rocky Mountains, Elliot and Johnson (1980), Boyer and Elliot (1982), Butler (1982) in the Moine thrust zone, and Hossack (1983) in the Scandanavian Caledonides.

b) Thrust and Buckle Folds. This terminology is due to Coward and Potts (1983), and includes fold nappes, 'ductile bead' folds, 'tip line' folds (Hossack 1983), fault propagation folds (Higgs et al. 1986, Jamison 1987) and folds in association with 'smooth trajectory' thrusts (Cooper and Trayner 1986) (Figure 5.5b). A ductile bead is the volume surrounding the edge of a slipped area defined by a tip or branch line in which there is ductile strain. Boyer's 'Intraplate' and 'Leading Edge' folds and the 'fault propagation folds' of Suppe and Medwedeff (1984) are all geometrically of this type, in which the fold initiation and amplification occurs in advance of or above the thrust propagation at any point. It therefore also includes Jamison's (1987) category of 'detachment folds', which he distinguished from fault propagation folds by the fact that they initiated over a part of the thrust which had not formed a ramp.

A characteristic of the relation between thrusting and folding is thus that both hanging- and foot-wall will have experienced some folding, although the amount can be variable depending on where the thrust cuts the early formed fold: Dahlstrom identified this position as 'forelimb', 'out-of-syncline', or 'backlimb' (Figure 5.5b). Coward and Potts proposed five criteria for the identification of thrust and buckle folds:

High strains on steep, inverted limbs.

Tight interlimb angles

Folds in the footwall.

Presence of parasitic folds

Layer parallel shortening on the bedding surface.

These are not individually diagnostic of thrust and buckle folds; the only necessary feature is that all parts of the footwall and hangingwall must show evidence of shortening corresponding to the movement of the ductile bead through the medium, as emphasized by Cooper and Trayner (1986), who make the further points that restored sections of smooth trajectory thrusts do not indicate their true geometry at the time of thrust emplacement, and that ductile strains may also be important in restoring sections with thrust and buckle folds. They suggest that the footwall space problem may be solved by a blind thrust, folding with decreasing amplitude at depth, or by ductile deformation, all of which could prove useful criteria for the recognition of thrust and buckle folds. A further feature that can demonstrate the pre-existence of folds is the truncation of fold axes by the thrust.

Because of the popularity of the structurally necessary fold model, examples of thrust and buckle folds are less common, but they have been reported by Dahlstrom (1970) and Brown and Spang (1978) from the Canadian Rocky Mountains, Coward and Potts (1983) from the Moine thrust zone, Hossack (1983) from the Scandanavian Caledonides, and Cooper and Trayner (1986) from the Irish Variscides. It is probable that many other thrust associated folds are of this type, even if not specifically diagnosed as such.

c) Buckling between two thrusts. A third model has been proposed by Casey (1982). In this case, a buckle initiates in the zone of compression between two vertically separated thrusts (Figure 5.5c). As the buckle amplifies, the two thrust planes are rotated into line and linked. This model combines features of both previous types. Where the buckle forms, folding will have occurred before thrust propagation, but points on the initial thrust surfaces will show no evidence of folding. The model could thus be recognised by the footwall/hangingwall symmetry, but no field examples have yet been quoted.

Geometric consequences of models a) and b) have been examined with specific reference to the Cantabrian zone by Julivert and Arboleya (1984). They state "as a general rule, the origin of the ramps as thrusts cutting across undeformed flat-lying beds, rather than as thrusts cutting across limbs of isolated folds, is postulated for the Cantabrian nappes," giving the lack of footwall synforms as the principal reason. They analyse the hangingwall antiform at Cremenes in detail, and show that with the constraint of area conservation, it is possible to calculate a theoretical ramp angle of 25^o from the observed cut-off angle of the hangingwall antiform, which agrees with the ramp angle from field data. The bend of the Barrios quartzite is considered to be initially a structurally necessary fold formed by the hangingwall after travelling up a ramp. The train of smaller wavelength folds, and the increase of the bend in the Barrios quartzite to 90^o, are due to simple shear during nappe emplacement, which would be anticipated to shorten the beds in the toe of the hangingwall since they are oblique to the shear direction. The authors calculate the amount of simple shear involved from the orientation of the bedding in the toe before shear (33^o to the thrust) and the orientation of the fold enveloping source after shear (70^o to the thrust) using the formula $\gamma = \cot\alpha^1 - \cot\alpha$ (α and α^1 being the orientations of material lines relative to the shear direction before and after shear respectively). The value of γ so calculated (1.16) gives a shortening of -0.4, in agreement with the observed shortening in the train of small wavelength folds above the Barrios quartzite.

There are two potential weaknesses in this argument. Firstly, the assumption that the fold enveloping surface acts as a material line in simple shear is unproven. More seriously, the model of structurally necessary folding modified by simple shear calls for extra shortening in the beds above the Barrios quartzite which constrains the ramp angle of the Esla thrust such that it must provide a corresponding deficit in these beds in the footwall. This model is equivalent to the mode I fault-bend fold of Jamison (1987), followed by fault parallel shearing in which shortening of the toe is accommodated not by simple shear and forelimb thickening, but by forelimb buckling. Jamison shows that there is a single unique ramp angle predicted for any given interlimb angle in the toe. For the 123^{o} value given by Julivert and Arboleya, this is 30^{o}. Unfortunately the footwall of the Esla thrust is nowhere exposed (Alonso (in prep.) argues that is must be to the west of the area in Figure 5.3 under the Mesozoic cover); this hypothesis cannot therefore be tested.

Julivert and Arboleya also present geometrical models for the formation of thrust and buckle folds forming before thrust propagation with concentric, chevron and box geometries. These are various cases of detachment or fault propagation folds (Jamison 1987); simple transport of these up a ramp leads to a residual fold giving extra bed length in the upper beds of the hangingwall. The 'stability' of the models is judged by the amount of shortening produced in beds above the basal thrust. In the first case, the shortening decreases upwards; in the second, the amount of shortening increases upwards and only in the case of box folds with equal bed thicknesses is the model stable. From these simple models, it can be deduced that extra bed length in the upper beds of the hangingwall could be provided by an initial concentric buckle fold. The train of small wavelength folds could then be produced by further shortening of the upper beds to bring them into compatibility with the Barrios quartzite, without any constraints on the ramp angle.

An alternative not considered by the authors is that both the folding of the Barrios quartzite and the overlying beds occurred before thrusting to give them essentially the present geometry, allowing for the structurally necessary component of folding following movement up the ramp. This model also has the attraction of preserving bed lengths at every stage through the evolution of the fold and thrust system, and is further suggested by the slight truncation of fold axial planes by the thrust in the train of smaller wavelength folds. An apparent lack of footwall strain is allowed for in this model if the thrust ramps through the synform, as an 'out of syncline' thrust (Figure 5.5). Either of the more likely models for the folds in the Esla Nappe thus involve a component of folding before thrusting, classing them as thrust and buckle folds in the above terminology.

This is even more clearly the case for the major folds in the Bernesga Valley. The diagnostic feature of thrust and buckle folds, the footwall syncline, is present in the Rozo sheet. Of Coward and Potts' four other criteria for thrust and buckle folds, the high strain, steep, inverted limb and tight interlimb angles are also present. It is pertinent that the fold axial traces in both the hangingwall and footwall are slightly oblique to the thrust. However, the general inversion of beds and thrusts in the Bernesga Valley also demands a later phase of strike-parallel folding, which creates the possibility that the footwall syncline in the Rozo sheet is not related to a phase of folding before thrusting. This interpretation is implicit in the section drawn by Ortega (1977) who shows the Rozo thrust folded by almost the same amount as the Rozo syncline. The composite map of Wallace (1972) shows that the Rozo thrust is only slightly folded with the syncline of the Rozo sheet, strengthening the case for pre-thrust buckling. The complex folding of the Correcilla thrust sheet, also independent of the Correcilla thrust itself, and the similarity of the hangingwall in the Bregon thrust sheet, suggest that this applies to the whole sequence in the Bernesga Valley, although details of the footwall in those cases are unknown.

The presence of five separate thrust sheets in addition to the Alba syncline in the Bernesga Valley indicates that this section is shortened considerably more perpendicular to strike than either the Luna Lake or Esla region. If, during the closure of the Cantabrian zone, a constant displacement was required along strike, more shortening would have been necessary in the Bernesga section if it was originally wider than the other areas. This is certainly suggested by the narrowing outcrop of the Somiedo-Correcilla Unit towards the Luna Lake and Narcea antiform. It is also possible that displacement exchange occurred along strike between the Somiedo-Correcilla and Sobia-Gordon units, with the former accounting for more shortening in the Bernesga Valley, and the latter in front of the Luna Lake and Esla nappe, although there are no more thrusts in those areas of the Sobia-Gordon unit.

5.3 MESOSTRUCTURES

5.3.1 Fractures

The most striking feature of the Barrios quartzite in the field is a ubiquitous dense network of fractures, 0.1-several metres long, a few millimetres wide, with both flat and curved irregular profiles (Plate 5.1a, b). Shear displacements of bedding vary between negligible and ten millimetres. The surfaces may be planar or quite irregular when intersected by other fractures. Slickenside surfaces with lineations are common, consisting of fine grooves less than 1mm wide and 10mm long.

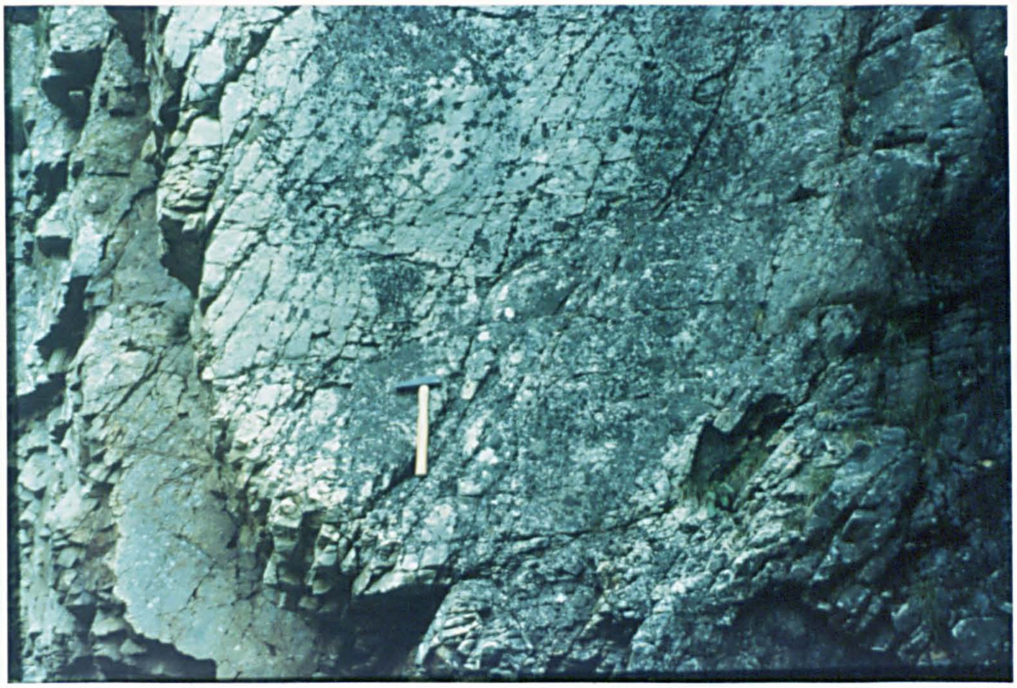

PLATE 5.1a

Multiple Fracture Sets in the Barrios Quartzite, El Tueiro. Fracture Density $39m^{-1}$. Bedding plane view.

PLATE 5.1b

Bedding profile view, vertical section. All fracture sets are perpendicular to bedding.

Several directions of lineation, varying by up to 30^0, are usually seen on one surface, some clearly overprinting others. No surface markings such as plume structure or ribs are seen. The main variation in fracture character, apart from fracture density (see below) is in length and flatness. Short, curved fractures in great density give the quartzite an almost penetrative fabric on Peña del Pozo (Figure 5.2) which contrasts with long, straight, systematic fractures observed at most other localities and shown in Plate 5.1. Some of this variation is illustrated by the field sketches shown in Figure 5.2. It is emphasised that in spite of these detailed variations in character, no clear subdivision of fractures is possible: they all appear to have a common origin.

Most outcrops are characterised by three sets of fractures. This is shown clearly in Figure 5.6, where in all diagrams a minimum of three concentrations of poles to fractures is evident: up to five sets may be distinguished in some cases. The sets are well defined, the concentration being a function mainly of sample size and measurement technique: increasing sample size, and the A measurement technique (see 3.1.2) both increasing the dispersion.

Fracture orientations have a quite distinctive and consistent pattern throughout the whole area, consisting always of poles to fractures lying within a great circle normal to the pole to bedding (Figure 5.6). Within this circle, there are between two and five sets which thus form a 'necklace' around the bedding plane normal that rotates with the bedding around the fold hinge. One set is sub-horizontal, and there are one or two vertical sets perpendicular to bedding in every pattern (Figures 5.2, 5.6). In spite of this division into identifiable sets, in no case could a relative chronology of formation or movement be established unambiguously, and clearly 'conjugate' sets of fractures are not seen. In addition to the 'necklace', four of the stereograms show another set of fractures sub-parallel to bedding and to the adjacent thrust plane: these are in the

FIGURE 5.6

Fracture Orientations in the Bernesga Valley. **N** - number of fractures A,B Method of measurement (see 3.2).

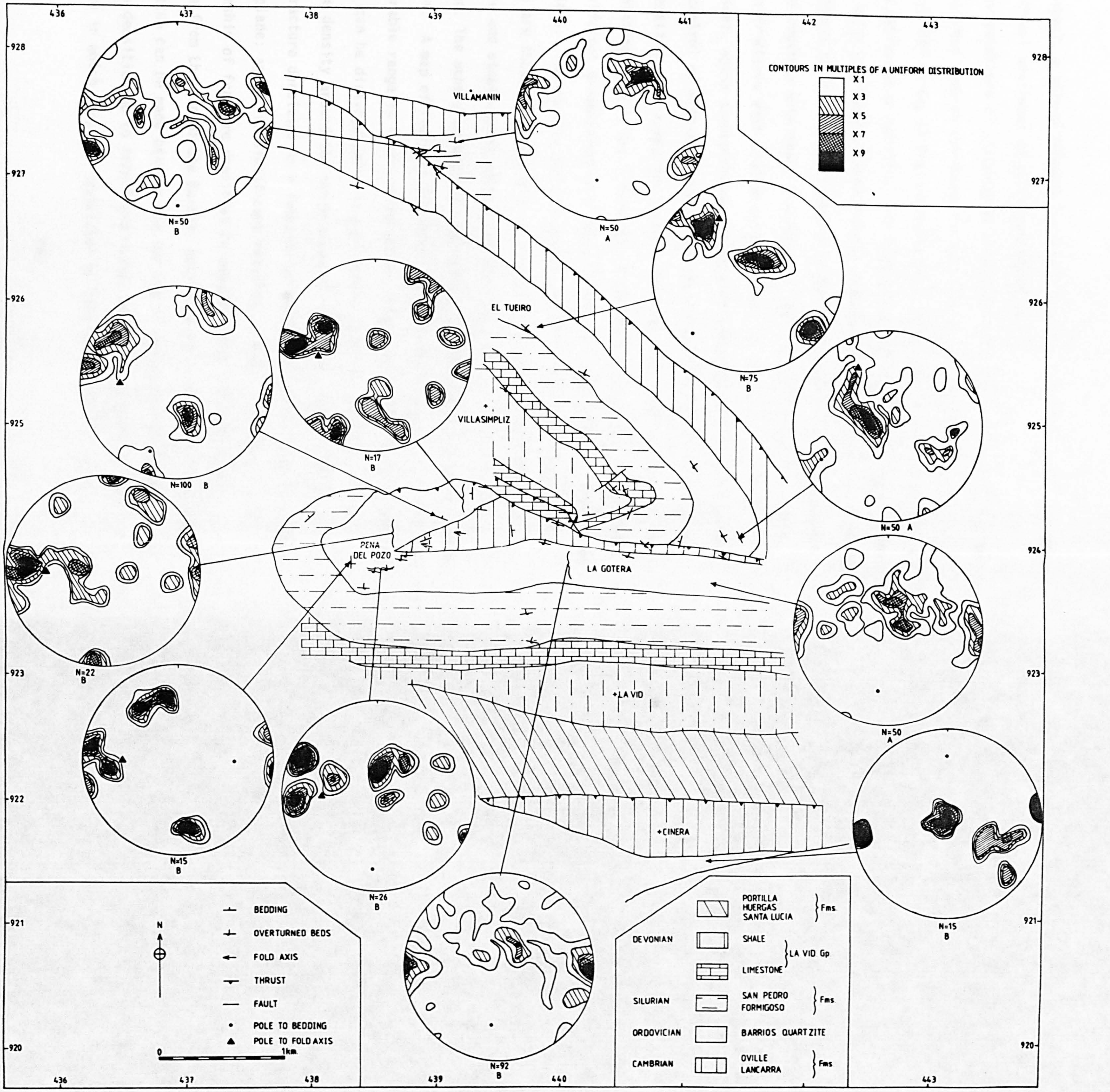

CONTOURS IN MULTIPLES OF A UNIFORM DISTRIBUTION
X 1
X 3
X 5
X 7
X 9
VILLAMANIN
EL TUEIRO
VILLASIMPLIZ
PENA DEL POZO
LA GOTERA
+ LA VID
+ CINERA
N=50 B
N=50 A
N=75 B
N=100 B
N=17 B
N=50 A
N=22 B
N=50 A
N=15 B
N=26 B
N=92 B
N=15 B
BEDDING
OVERTURNED BEDS
FOLD AXIS
THRUST
FAULT
POLE TO BEDDING
POLE TO FOLD AXIS
N
0
1km.
DEVONIAN
PORTILLA
HUERGAS
SANTA LUCIA
Fms.
SHALE
LA VID Gp.
LIMESTONE
SILURIAN
SAN PEDRO
FORMIGOSO
Fms.
ORDOVICIAN
BARRIOS QUARTZITE
CAMBRIAN
OVILLE
LANCARRA
Fms.
436
437
438
439
440
441
442
443
928
927
926
925
924
923
922
921
920

hangingwall antiform/footwall synform fold limbs and the footwall to the Rozo thrust southwest of Villamanin (Figure 5.6).

Orientations of slickenside lineations measured in the field and on reorientated samples are shown in Figure 5.7. No regional pattern is visible, nor do any of the sub-areas with an adequate sample size give a strong preferred orientation. In Figure 5.8, pairs or groups of fracture planes with very similar orientations from the hangingwall antiform in the Pozo thrust sheet, and the footwall of the Rozo sheet at Villamanin, are plotted together with their lineations. The lineations from each area, even on fractures with similar orientations, are in quite different directions, again demonstrating the lack of a regional pattern and more local control of slip directions. Detailed orientations of all fractures and lineations were taken for samples 105, 106, 107, 109, 111 and 112 by reorientating them in the laboratory. A minimum of six planes in at least four different orientations was measured for each sample with a variety of lineations. The results for the sample (106) with the most lineations visible are shown in Figure 5.9, which again emphasises the dispersed fracture and displacement pattern even on the scale of a single hand specimen. The others showed the same features though fewer lineations were recorded. A map of fracture densities is shown in Figure 5.10. There is a considerable range in fracture densities, from 7 to $267m^{-1}$, but no regional pattern can be distinguished; in particular, there is no increase in fracture density around the hinge areas of the major folds. Figure 5.11 shows fracture densities as a function of perpendicular distance from the thrust plane: again, no significant relation is seen. In Figure 5.12, relationship of fracture densities to perpendicular (stratigraphic) distance from the top of the Barrios quartzite is shown. In this case, a distinction can be made between the top 50m of the quartzite in which fracture densities up to $267m^{-1}$ are found, and the remainder of the quartzite in which they are restricted to less than $100m^{-1}$.

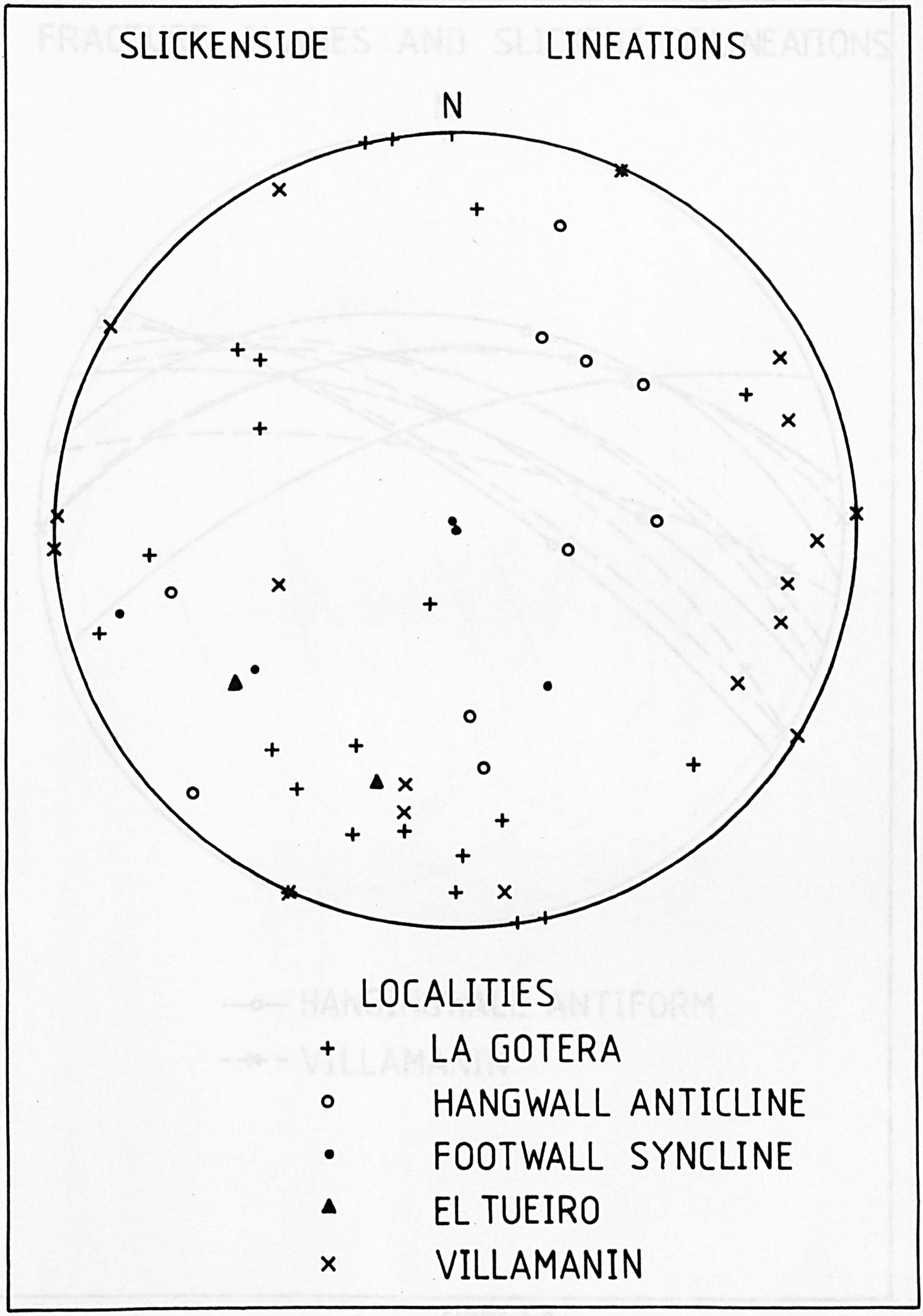

FIGURE 5.7
Slickenside Lineations in the Bernesga Valley. The pattern of combined lineations does not reflect a single regional displacement direction, but the accommodation of local strains.

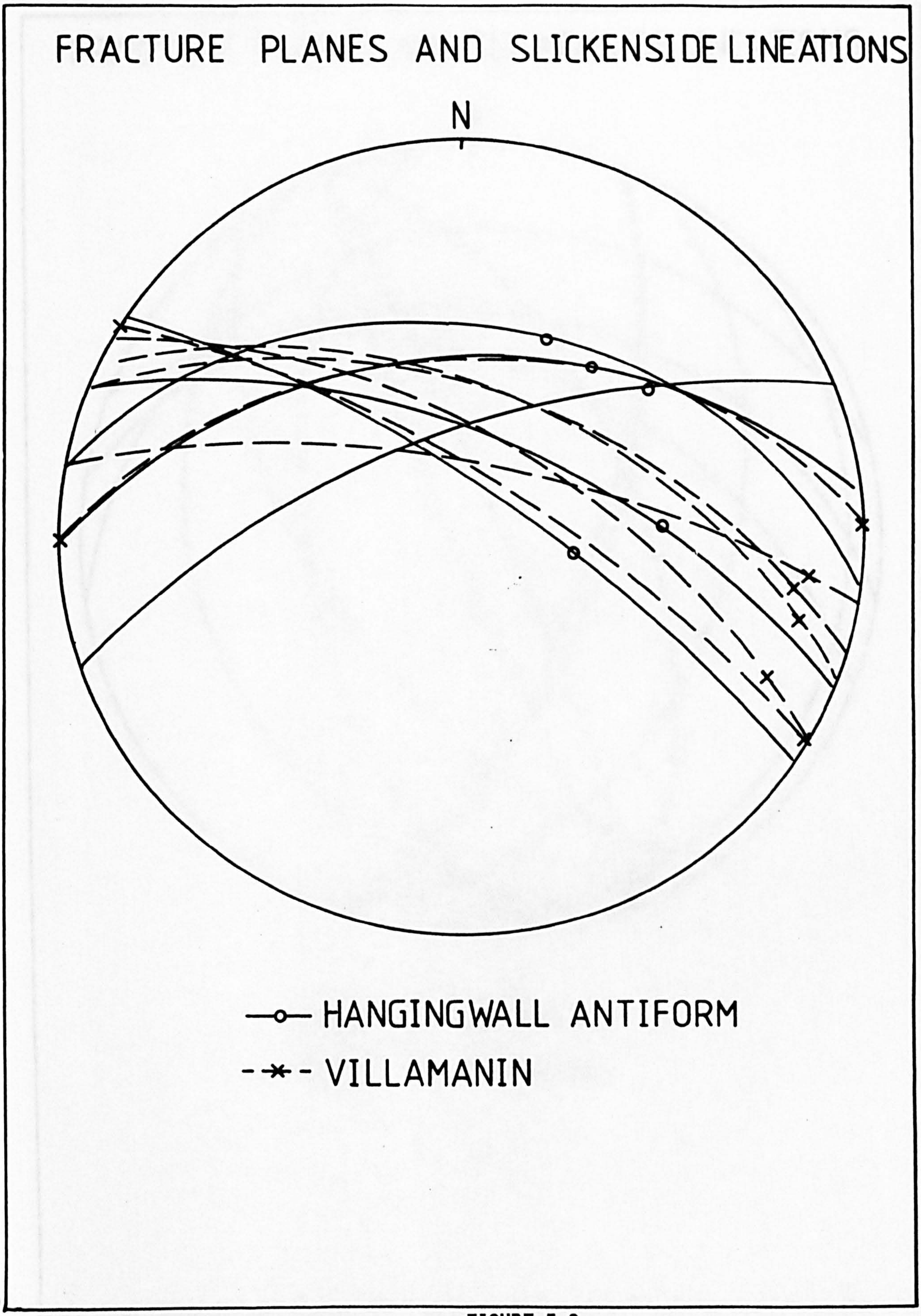

FIGURE 5.8

Fracture planes and slickenside lineations from the hangingwall antiform in the Pozo thrust sheet and the footwall to the Rozo thrust southwest of Villamanin. Fracture Planes with similar orientations have been chosen from both localities, but the lineations on similar fracture planes have different plunges, illustrating the fact that fractures are slip systems accommodating local strains, in support of the Reches model for accommodating three-dimensional strain on a fault network.

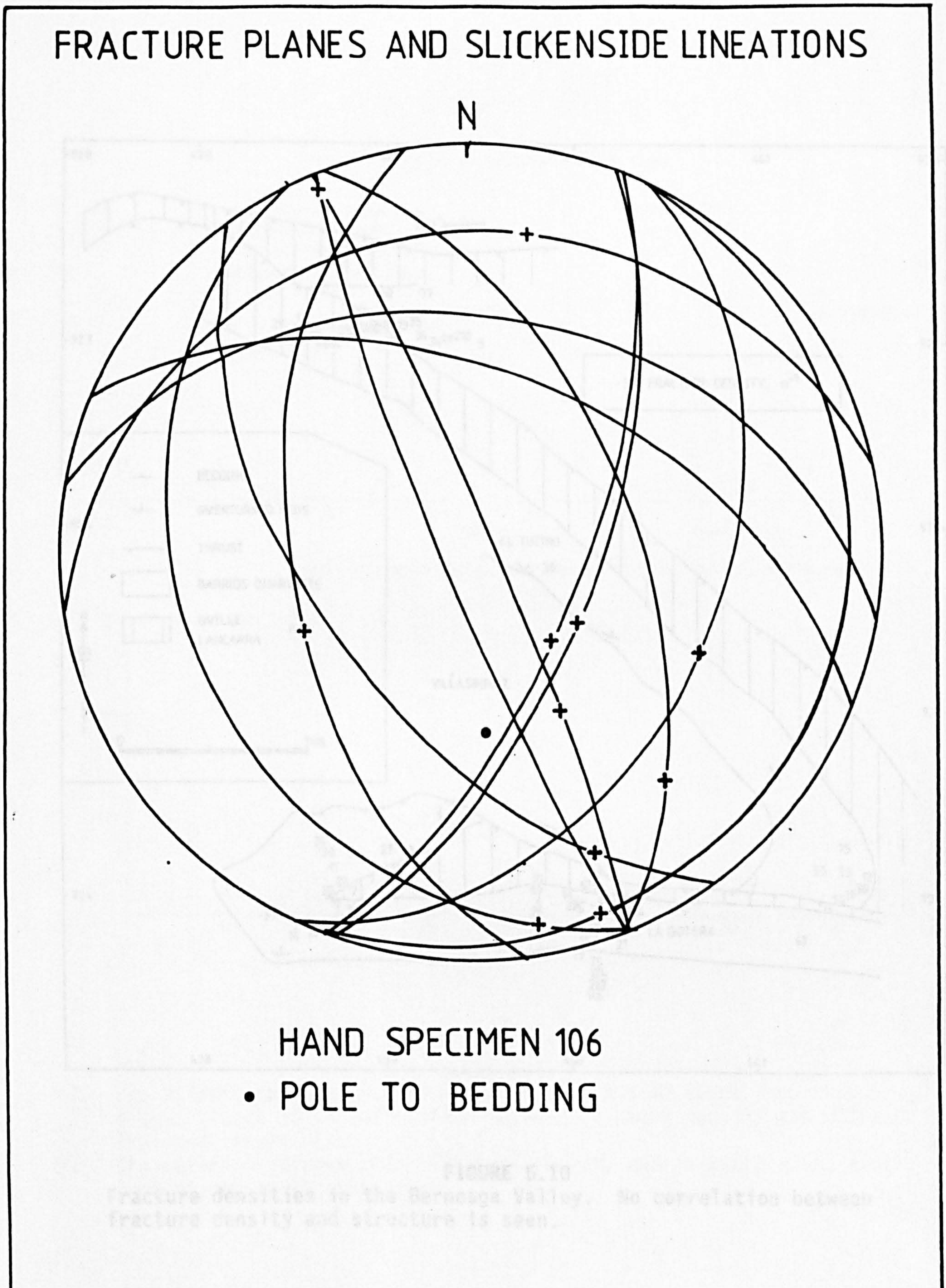

FIGURE 5.9

Fracture and slickenside lineations from a single hand specimen, sample 106. Even on the scale of a hand specimen, a variety of fracture and lineations occurrs, indicating the accommodation of a three-dimensional strain.

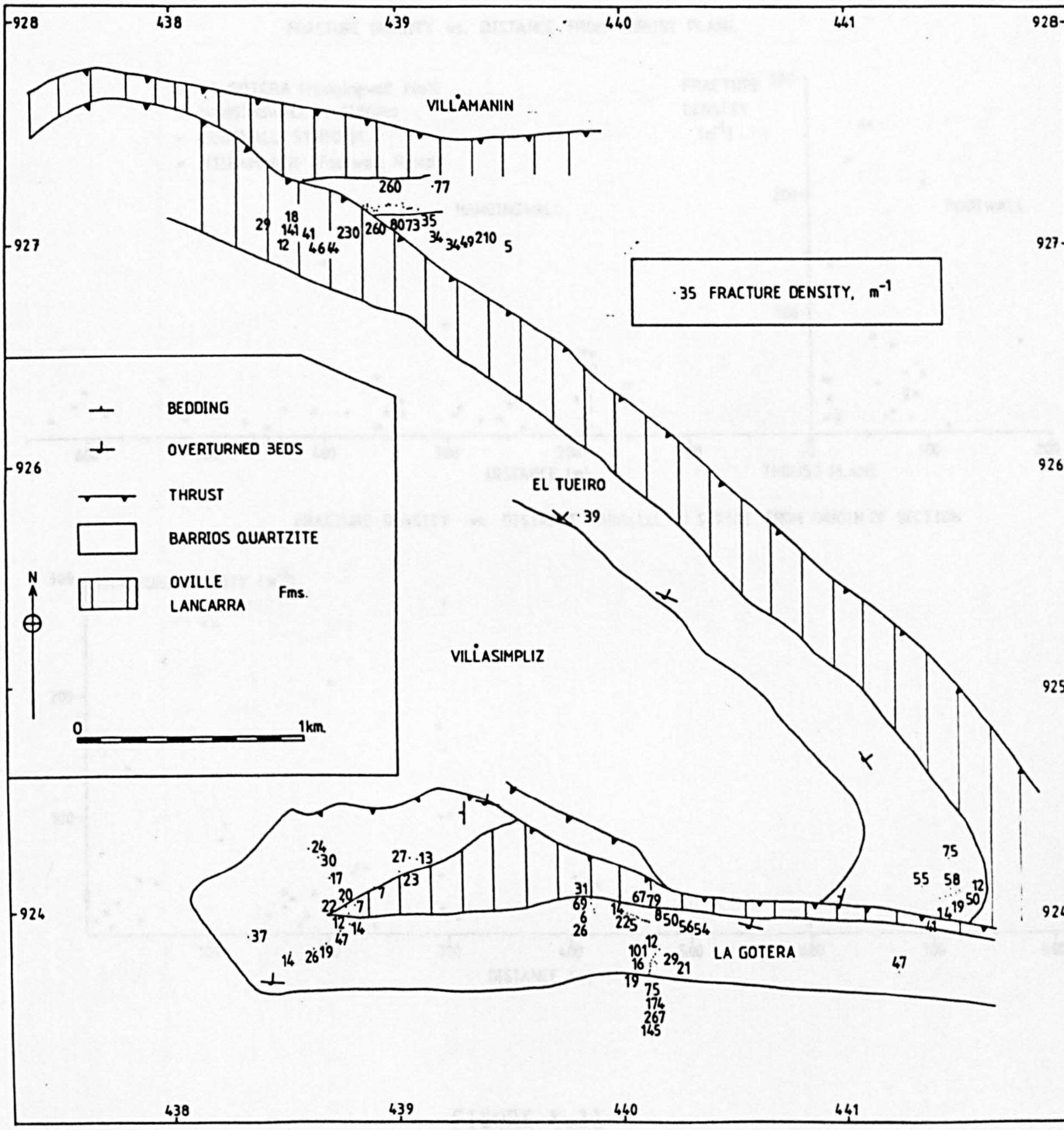

FIGURE 5.10
Fracture densities in the Bernesga Valley. No correlation between fracture density and structure is seen.

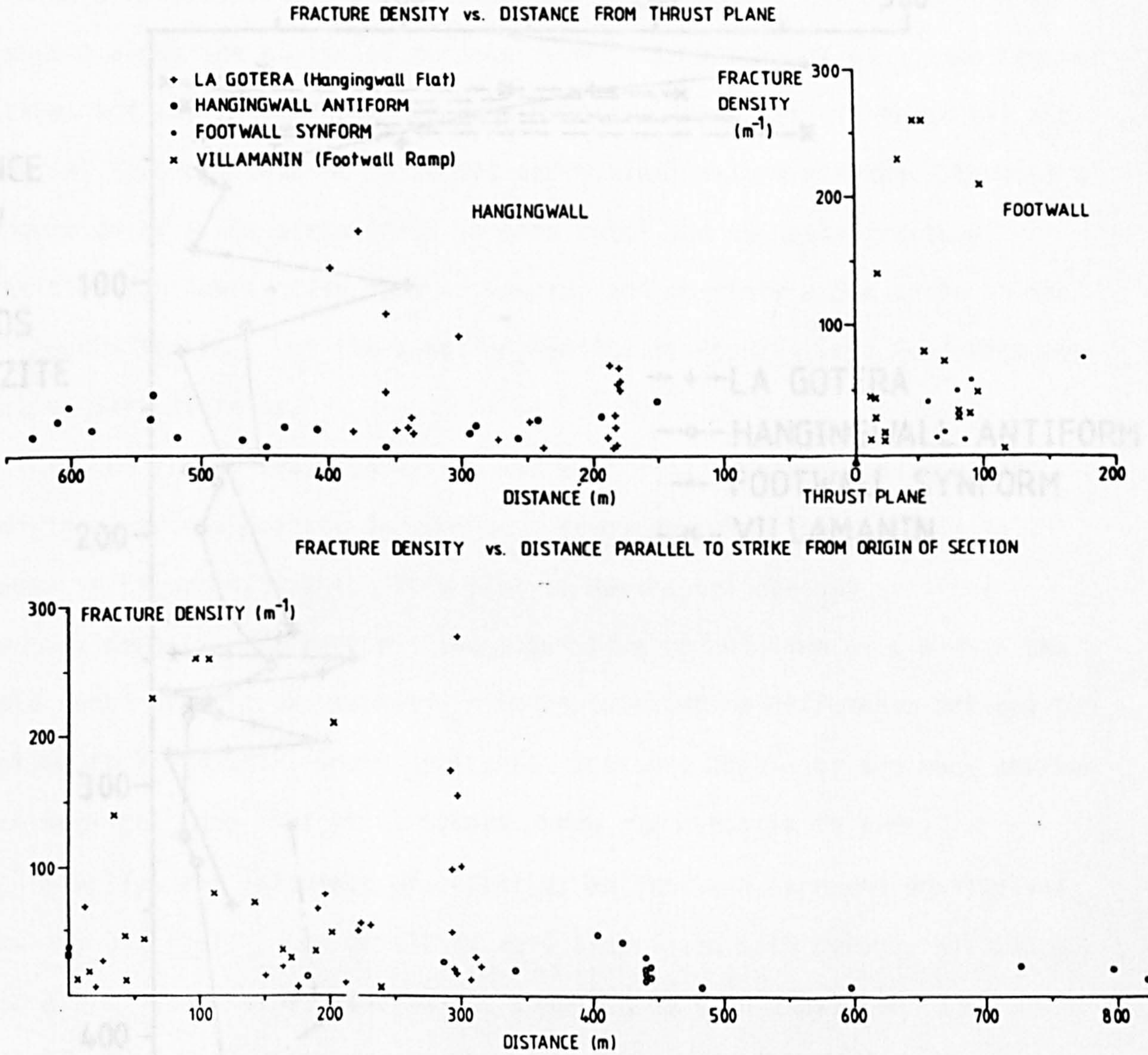

FIGURE 5.11

a) The Relationship between Fracture Density and distance from thrust plane. There is no correlation between fracture density and distance from the thrust plane.

b) The relation between total fracture density and distance along strike from an arbitrary origin.

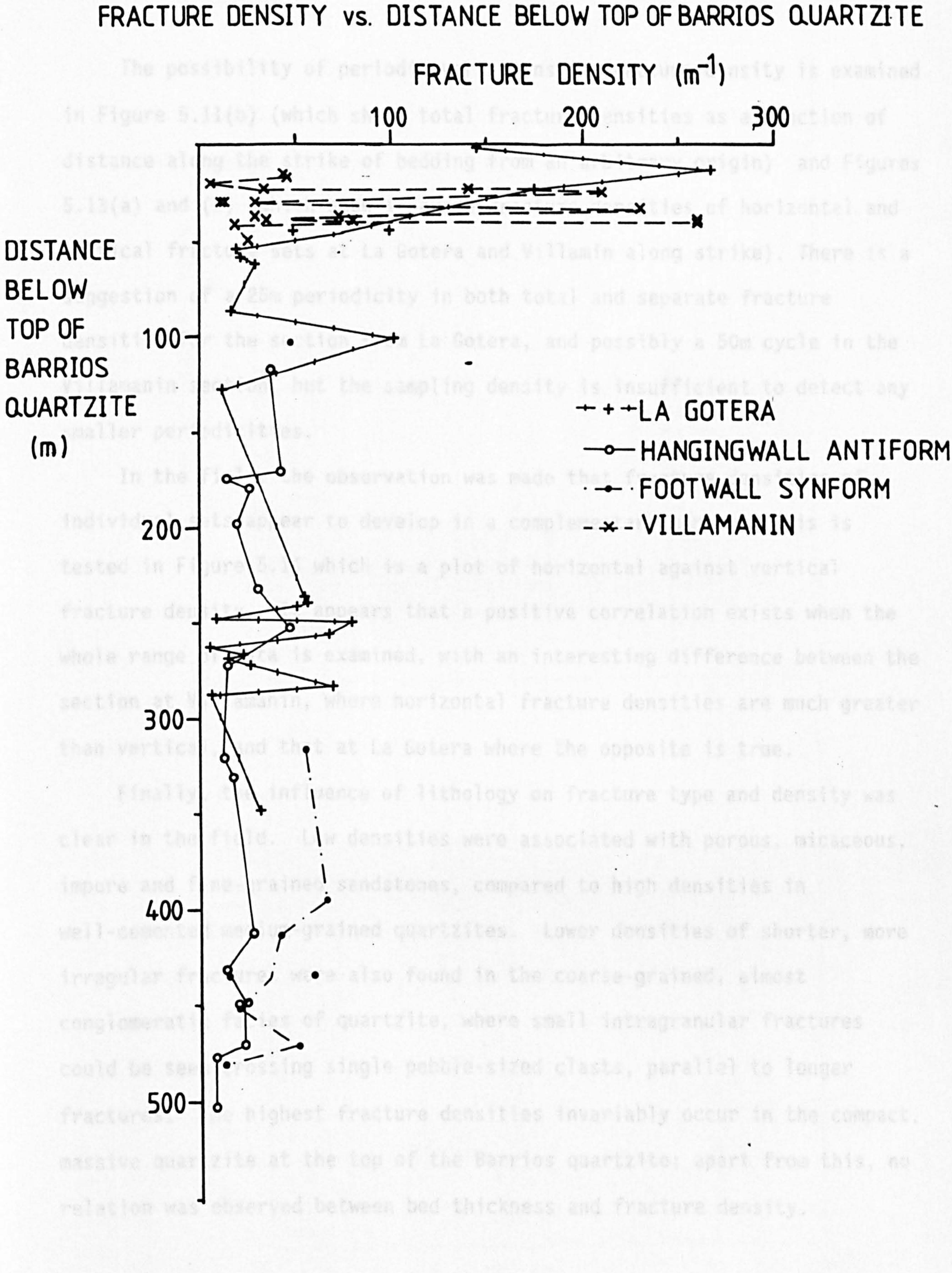

FIGURE 5.12

The Relationship between Fracture Density and distance below the top of the Barrios Quartzite. Densities higher than $100m^{-1}$ occur only in the top 50m of the quartzite, but the largest variations are due to clustering of fractures in deformation zones.

The possibility of periodic variations in fracture density is examined in Figure 5.11(b) (which shows total fracture densities as a function of distance along the strike of bedding from an arbitrary origin) and Figures 5.13(a) and (b) (which show separate fracture densities of horizontal and vertical fracture sets at La Gotera and Villamin along strike). There is a suggestion of a 25m periodicity in both total and separate fracture densities for the section from La Gotera, and possibly a 50m cycle in the Villamanin section, but the sampling density is insufficient to detect any smaller periodicities.

In the field, the observation was made that fracture densities of individual sets appear to develop in a complementary manner. This is tested in Figure 5.14 which is a plot of horizontal against vertical fracture density. It appears that a positive correlation exists when the whole range of data is examined, with an interesting difference between the section at Villamanin, where horizontal fracture densities are much greater than vertical, and that at La Gotera where the opposite is true.

Finally, the influence of lithology on fracture type and density was clear in the field. Low densities were associated with porous, micaceous, impure and fine-grained sandstones, compared to high densities in well-cemented medium-grained quartzites. Lower densities of shorter, more irregular fractures were also found in the coarse-grained, almost conglomeratic facies of quartzite, where small intragranular fractures could be seen crossing single pebble-sized clasts, parallel to longer fractures. The highest fracture densities invariably occur in the compact, massive quartzite at the top of the Barrios quartzite; apart from this, no relation was observed between bed thickness and fracture density.

5.3.2 Deformation and Breccia Zones, Fault Plane, Thrust Planes

When fractures cluster together to reach a density of over $50m^{-1}$, a deformation zone may form, up to 0.8m wide, consisting of highly fractured

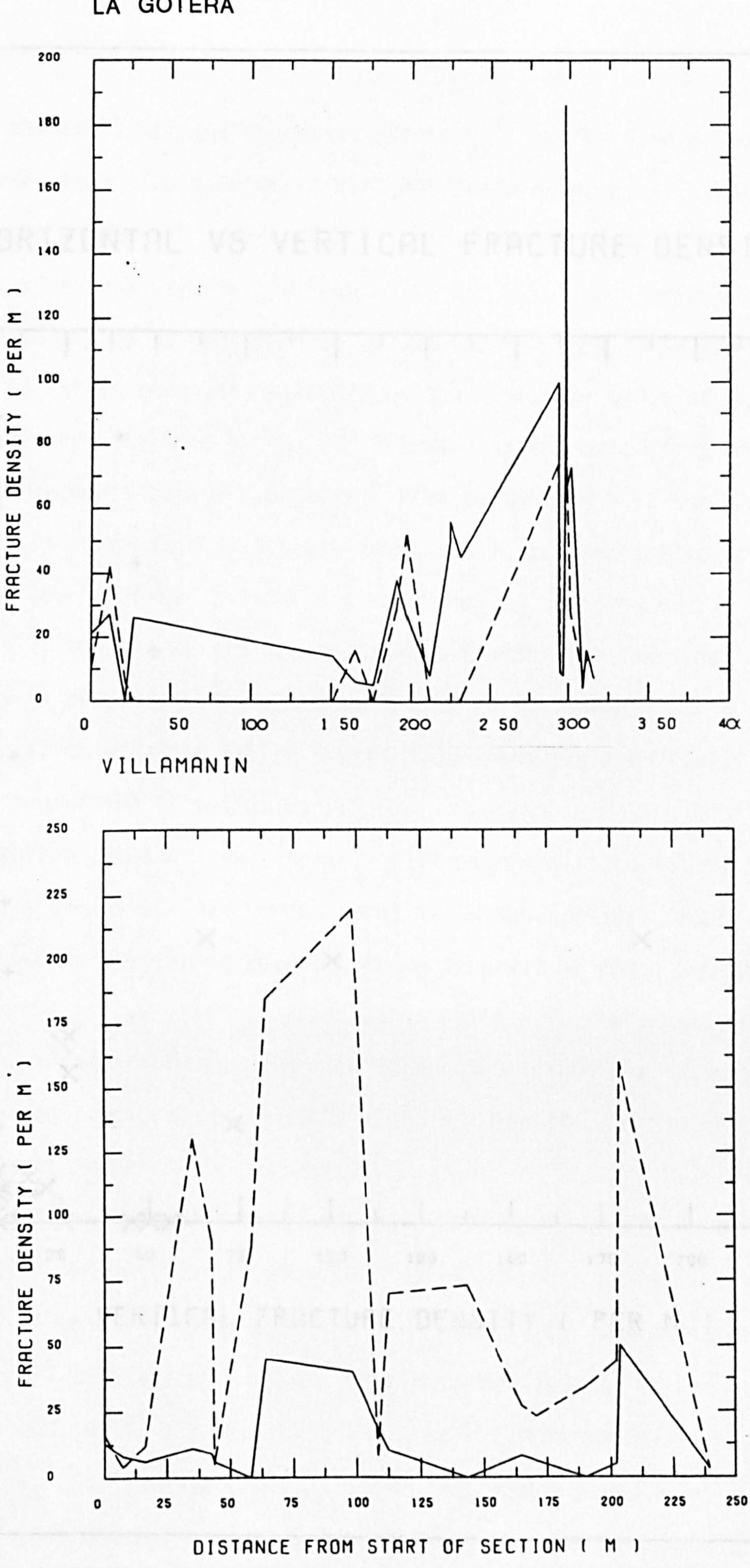

FIGURE 5.13

The Relationship between Fracture Density and distance along strike from an arbitrary origin. Horizontal Fractures - dashed line, Vertical Fractures - solid line.

a) La Gotera. There is a suggestion of a 25m periodicity.

b) Villamanin. A 50m periodicity is apparent.

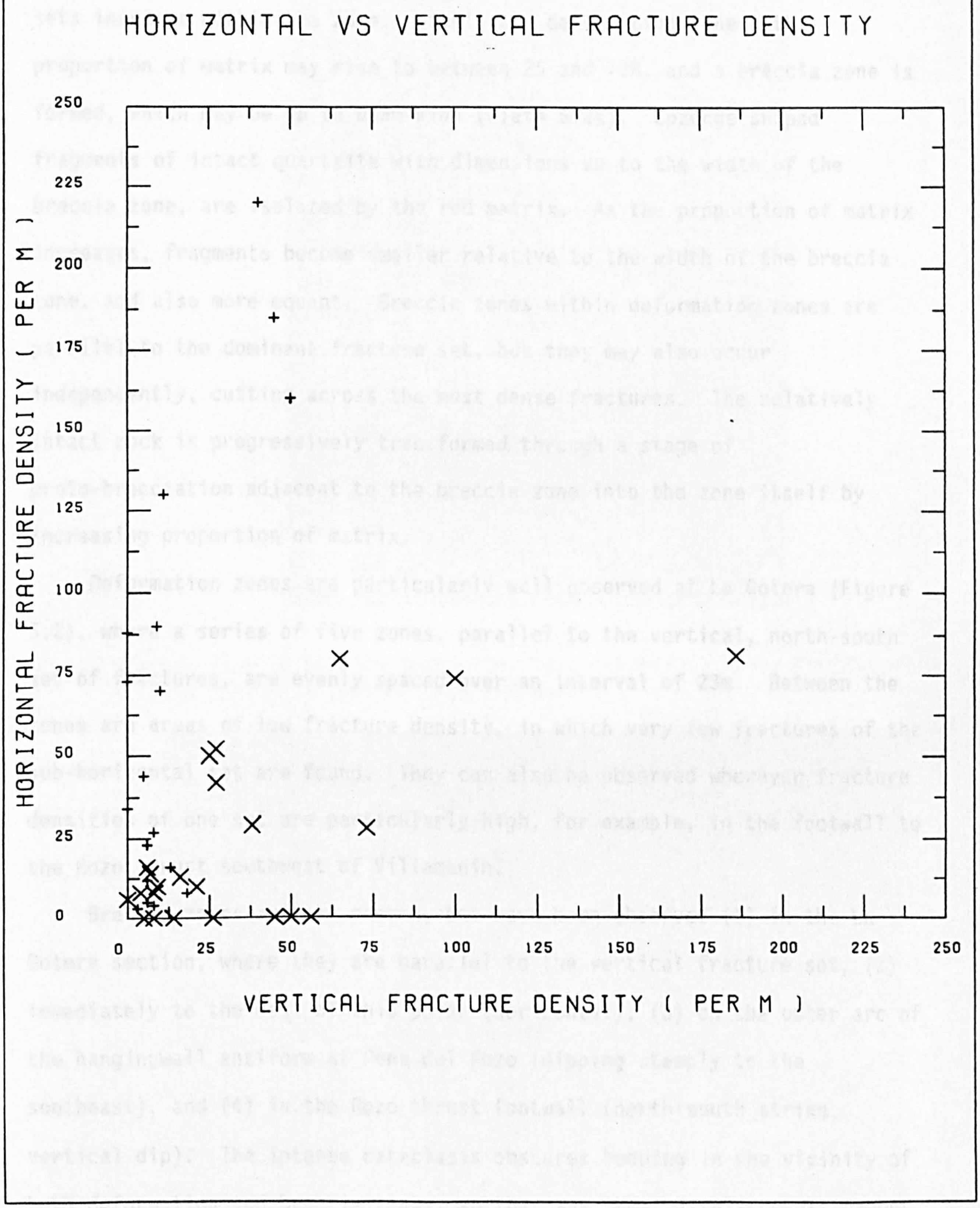

FIGURE 5.14
The Relationship between horizontal and vertical fracture density. There is a positive correlation at both La Gotera (crosses) and Villamanin (plus signs).

quartzite veined by haematite-bearing quartz matrix. The deformation zones form parallel to a single fracture set, but frequencies of all fracture sets increase within the zone. Within the deformation zones, the proportion of matrix may rise to between 25 and 75%, and a breccia zone is formed, which may be up to 0.5m wide (Plate 5.2a). Lozenge shaped fragments of intact quartzite with dimensions up to the width of the breccia zone, are isolated by the red matrix. As the proportion of matrix increases, fragments become smaller relative to the width of the breccia zone, and also more equant. Breccia zones within deformation zones are parallel to the dominant fracture set, but they may also occur independently, cutting across the most dense fractures. The relatively intact rock is progressively transformed through a stage of proto-brecciation adjacent to the breccia zone into the zone itself by increasing proportion of matrix.

Deformation zones are particularly well observed at La Gotera (Figure 5.2), where a series of five zones, parallel to the vertical, north-south set of fractures, are evenly spaced over an interval of 23m. Between the zones are areas of low fracture density, in which very few fractures of the sub-horizontal set are found. They can also be observed wherever fracture densities of one set are particularly high, for example, in the footwall to the Rozo thrust southwest of Villamanin.

Breccia zones are not common, but have been observed (1) in the La Gotera section, where they are parallel to the vertical fracture set, (2) immediately to the west of this point (horizontal), (3) on the outer arc of the hangingwall antiform at Pena del Pozo (dipping steeply to the southeast), and (4) in the Rozo thrust footwall (north-south strike, vertical dip). The intense cataclasis obscures bedding in the vicinity of both deformation and breccia zones, so that any shear displacements cannot be determined, but they cannot be greater than a few metres since they are not detected at map scale.

PLATE 5.2a

Breccia Zone in Barrios Quartzite, Pena del Pozo. Heavy concentration of iron oxides is typical of breccia zones.

PLATE 5.2b

Minor Folds, Oville Formation, Pena del Pozo in core of hangingwall antiform. This style of deformation contrasts with the multiple fracture sets in the Barrios Quartzite, Plate 5.1.

Large slickensided fault planes can be distinguished from deformation and breccia zones by their discrete nature. They are referred to as fault planes to distinguish them from individual fractures, from which they differ only in size. They may be flat or subdivided into small blocks by intersecting fractures. Sinusoidal, cylindrical lineations are common, with wavelengths of up to 100mm, and amplitudes of 5mm. They are seen in La Gotera, El Tueiro and the footwall syncline of the Pozo thrust. Displacements again cannot be greater than a few metres.

Only one thrust plane is well exposed in the whole section, at the base of the Bregon Sheet beside Cinera (Figure 5.16). Here a well developed thrust gouge several metres wide shows two characteristic gouge features: a P-foliation in shales, dipping less steeply to the north than the thrust plane, and Reidel (R1) shears, dipping more steeply to the north. Both these features confirm an approximately northwards transport direction if the thrust plane is rotated clockwise to horizontal. Minor folds with axial planes parallel to the thrust and boudinage of sandstone blocks along Reidel shears are also observed in the gouge.

5.3.3 Minor Folds

Minor folds were observed in the Barrios quartzite in the Bregon thrust sheet in the Bernesga Valley, and in the Oville Formation in the cores of the major fold pair separated by the Rozo thrust, extensively developed above the Bregon thrust, and at the Barrios quartzite/Oville Formation junction at Cremenes.

At this latter locality, isoclinal folding with wavelengths of less than one metre and similar style is seen in the transitional beds between the two formations. Vertical axial planes strike approximately parallel to the Esla thrust. These are fine grained, porous sandstones with a concentration of iron oxides giving them a brown colour. No evidence of cataclasis is seen in these fold hinges. Angular, similar folds of wavelengths up to several metres are also seen in the core of the hangingwall antiform and footwall synform of the Pozo and Rozo thrust sheets (Plate 5.2b). Samples 14 to 17 were collected from the hinge and limbs of one such isoclinal fold in the hangingwall antiform, and their positions are marked on T' and t'/α plots in Figure 5.15 (Ramsay 1967), which shows that the fold is class III (divergent dip isogons). The minor fold axes measured here are parallel to the axis of the major fold, moderately plunging at 30^0 to 60^0 due west, with upright or north dipping axial planes (Figure 5.2). 'M' symmetries are observed in the core of the fold. Folds in thinner, sandy beds have a very low fracture density, but in other beds, shear displacements of several tens of millimetres are distributed on fractures around both the hinge and limbs of the minor folds. The Oville Formation in the footwall synform is very poorly exposed; only two minor folds were seen with axes moderately plunging to the northeast and northwest, quite distinct directions from the major fold axis (Figure 5.2).

A section of approximately 900m of angular chevron and box folding in the Oville Formation can be observed to the south of the Bregon thrust in the Bernesga Valley, structurally in the same position between the Barrios quartzite and a major thrust as the folds described above. A field sketch and some inferred structures are shown in Figure 5.16. The important features of this section are the overall younging direction to the south, and sub-horizontal or gently north-dipping axial planes, and a well defined south vergence on assymmetrical structure. Typical features of multilayer deformation in beds of variable competence and thickness are observed, such as curved inner arc thrusts, small interbed thrusts, flowage of shales into triangular zones at fold hinges, carinate fold hinges, and fanning fractures on outer arcs. The stratigraphy is insufficiently detailed to establish a complete large scale structure linking all exposures, but some extrapolated structures from the section are shown in Figure 5.16. The

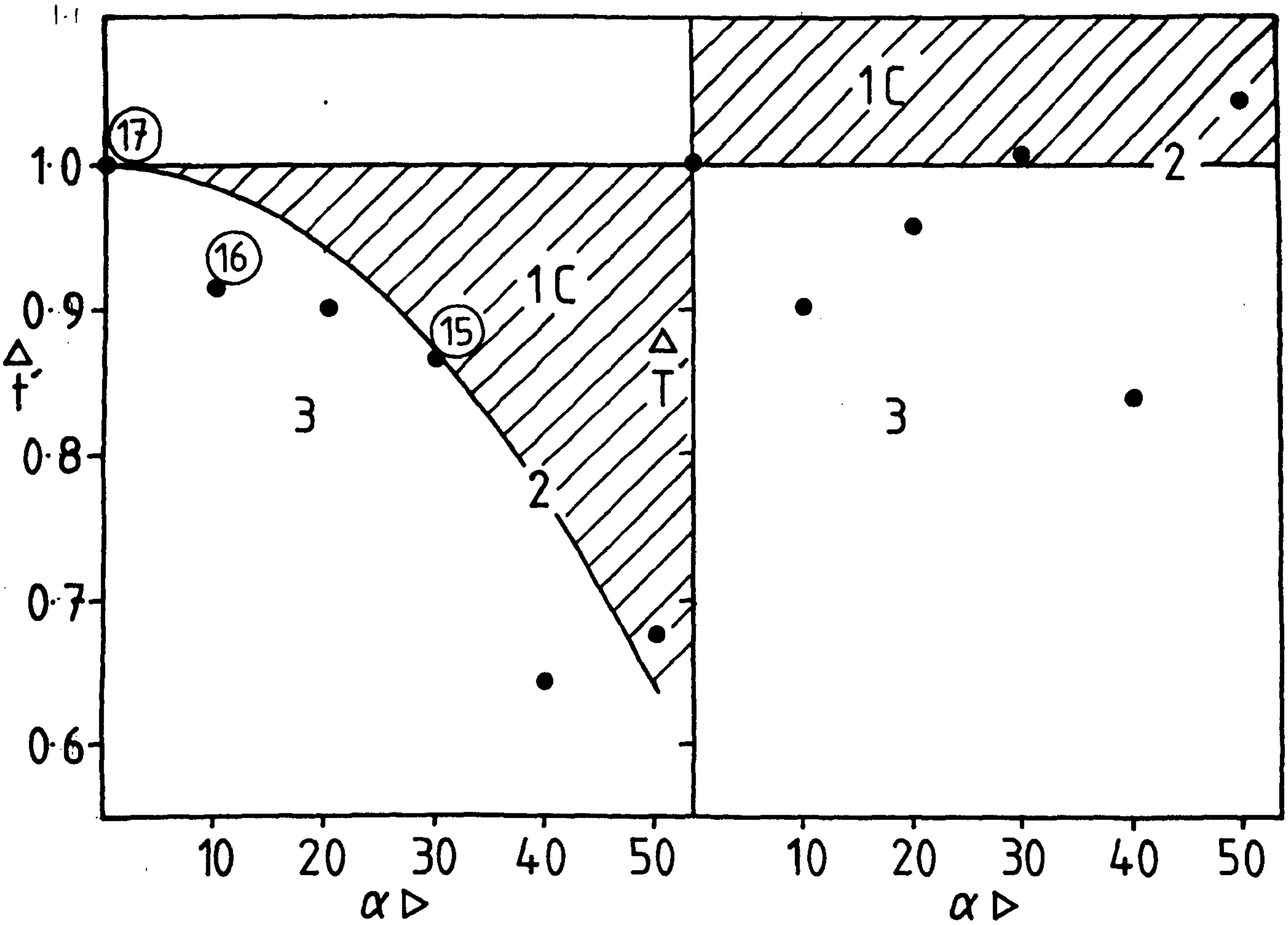

FIGURE 5.15
t' and T'vsα plots of a minor fold in the hangingwall antiform of the Pozo thrust sheet, with positions of samples 15-17 indicated.

horizontal south-vergence of these structures is apparently incompatible with the approximately vertical sense of shear on the Bregon thrust itself: this anomaly is discussed in the next section.

The minor folding in the Oville Formation of this section also occurs in the Barrios quartzite, but with larger wavelengths and less angular fold hinges. Many more fractures are observed in the quartzite. Some of these, in hinges of smaller folds, are also shown in Figure 5.16. Fractures are short and irregular, and in some cases clearly folded. In fold profile, they can be subdivided into those at a low angle to bedding and those approximately perpendicular to bedding. The first group are often folded and may have contractional senses of movement. The second group generally fan around the fold axis, but are not orthogonal to the bedding: they are not genuinely radial. Both sets have mutually cross-cutting relationships.

5.3.4 Discussion

It is proposed that a network of bedding-normal and some bedding-parallel fractures formed early in the stress history of the Barrios quartzite. A minimum of three sets were formed in response to a three dimensional imposed strain at constant volume. The clear and crucial evidence for this is the rotation of the 'necklace' fracture pattern with the bedding plane around the fold axis. The folding of one sub-horizontal fracture set is a widespread feature over much of the Cantabrian zone (Marcos pers.comm.). Although Price (1966) has pointed out that stress refraction and post fold fracture could account for this effect in open folds, the progressive rotation of the fractures through the obtuse angles of the hangingwall-footwall fold pair could not be due to refraction. The localised occurrence of a bedding sub-parallel fracture set in the hinge regions of the fold suggests that at least this set relates to the same stress field as the folding, but neither this nor any other evidence gives an absolute timing for the fracture initiation, which could have occurred

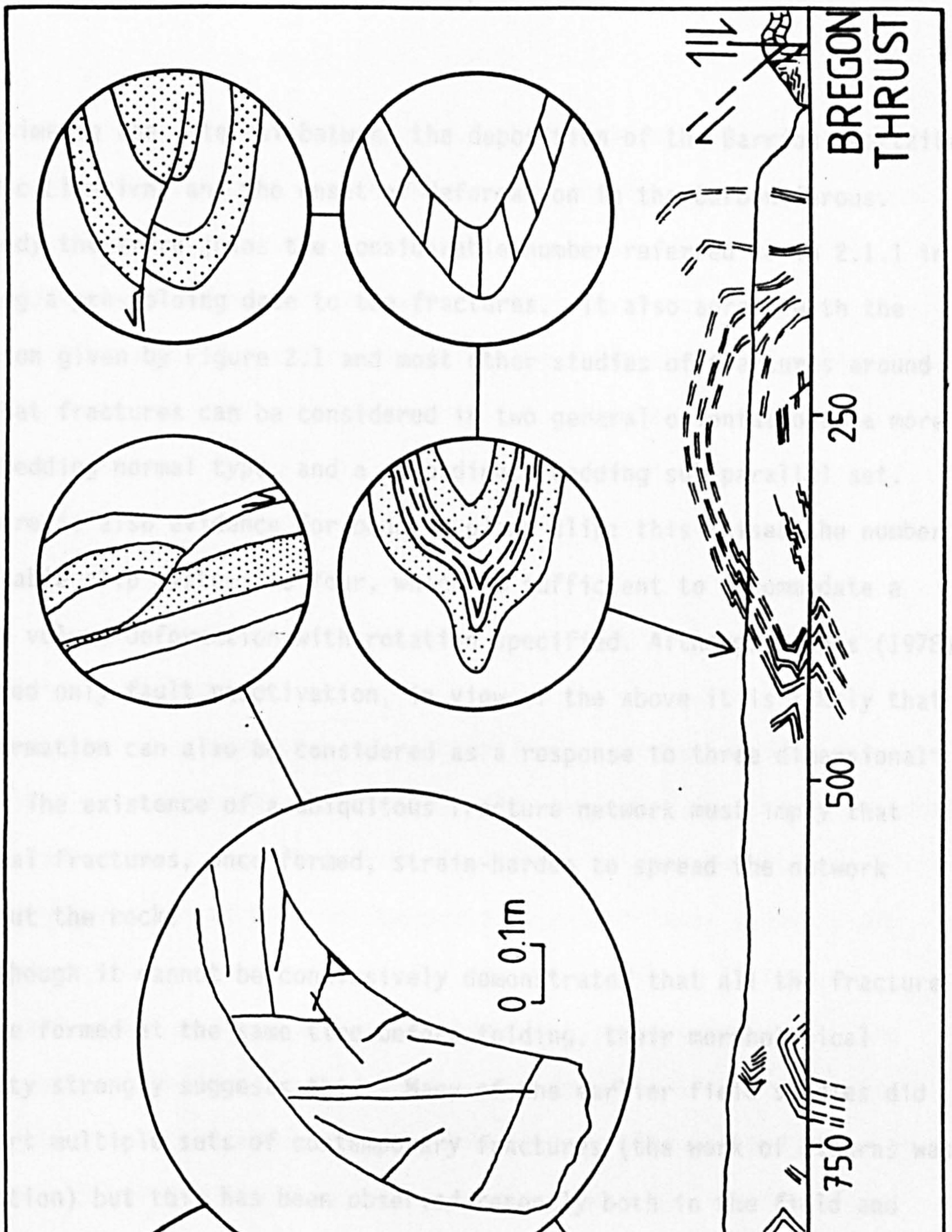

FIGURE 5.16
Minor folding in the Oville and Barrios formations from field sketches

at any time in the interval between the deposition of the Barrios quartzite (Tremadoc-Llanvirn) and the onset of deformation in the Carboniferous. This study therefore joins the considerable number referred to in 2.1.1 in ascribing a pre-folding date to the fractures. It also agrees with the impression given by Figure 2.1 and most other studies of fractures around folds that fractures can be considered in two general orientations: a more common bedding normal type, and a subordinate bedding sub-parallel set.

There is also evidence for bedding plane slip: this raises the number of available slip systems to four, which is sufficient to accommodate a constant volume deformation with rotation specified. Although Reches (1978) considered only fault **reactivation**, in view of the above it is likely that fault **formation** can also be considered as a response to three dimensional strain. The existence of a ubiquitous fracture network must imply that individual fractures, once formed, strain-harden to spread the network throughout the rock.

Although it cannot be conclusively demonstrated that all the fracture sets were formed at the same time before folding, their morphological similarity strongly suggests this. Many of the earlier field studies did not report multiple sets of contemporary fractures (the work of Stearns was an exception) but this has been observed recently both in the field and experimentally (2.1.1). Reches (1978) has shown that the minimum number of faults required to accommodate a three-dimensional strain at constant volume is three (without specifying a rotation): this condition is fulfilled by the fracture network wherever observed (Figure 5.6).

It is further suggested that continued activation of the fracture network, accompanied by bedding plane slip, allowed the cataclastic accommodation of the major fold pair. It has been shown above that sufficient slip systems already exist to accommodate any folding strains. Since these fractures are inherited from pre-fold orientations, they will not be in the ideal theoretical orientation throughout folding to minimise both the shear strain and stress terms of the strain energy, which would predict four sets of faults with orthorhombic symmetry about the principal strain axes. However it is suggested that the strain energy term is nevertheless minimised because the shear stress for reactivation (τ_r) is less than that required for formation of a new fault (τ_i). Therefore the condition for minimising strain energy (W), to accommodate a given strain on n fault sets is

$$W = \sum_1^n \tau_r \gamma_r < \sum_1^n \tau_i \gamma_i$$

where $\gamma_{r,i}$ are the geometrically necessary shear strains on a reactivated and ideal fault respectively.

Small shear displacements and slickenside lineations on fracturesshow that they have accommodated shear strain, in some cases in several episodes and different directions. No useful distinction between shear, hybrid and tensile fractures can be made on the basis of either their geometry or displacements, which vary continuously from negligible up to ten millimetres, since variable amounts of reactivation have occurred. The combined pattern of lineations is dispersed (Figure 5.7) indicating that there is no single regional movement direction over the whole mapping area or at the scale of individual localities. Even hand specimens contain fractures and lineations of several widely differing orientations (Figure 5.9). Furthermore, similar orientations of fracture planes have been shown to provide different slip directions in areas of contrasting strain (Figure 5.8). All these characteristics would be predicted by continu al reactivation of a pre-existing fracture network to accommodate the folding; a small scale analogue is seen on the field sketches of the bedding and profile plane of a minor fold in the Barrios quartzite shown in Figure 5.16.

Observations on the distribution of fracture densities are also in accordance with the hypothesis of a pre-fold fracture network. The fracture density was sufficient at fold inception to allow accommodation of the fold without further fracturing; this explains the apparent contradictions between those studies (e.g. Harris et al. (1960), Stearns (1968a)) indicating higher fracture densities around fold hinges, and this study and that of McQuillan (1973) in which no relation between structure and fracture density was observed. The most important influence on fracture density appears to be an inherent clustering phenomenon which culminates in the formation of deformation zones, moderated by the influence of lithology.

The characteristics of minor folding in the sandstone-shale sequence of the Oville Formation are similar to the kink band geometry predicted at inception for media with high intrinsic anisotropies by Latham (1985b). High intrinsic anisotropies are created by, for example, large competence contrasts between layers such as exist between sandstone and shale layers. The theory accounts well for the style of folding, but the anomalous vergence of the kinks remains a problem.

One simple and elegant solution to this is suggested, derived from Lloyd and Walley's models for the modification of chevron folds by simple shear (1986). An interesting feature of some of these is the inclination of axial planes to the shear direction and the fact that in some cases, isolated fold hinges may have vergence in the opposite direction to the shear sense. Lloyd and Whalley suggest three possible constraints on the deformation of chevron folds in simple shear, leading to three models, two of which can generate axial planes inclined to the shear direction with opposite vergence. In model 1, the interlimb angle (I.L.A.) remains 60^0, with five possible accommodation faults on either axial planes or limbs. Only the latter preserve fold hinges: anticlockwise vergence in a clockwise shear is generated by model '1d', in which faulting on the 60^0 limb controls the rotation rate. Model 2 allows I.L.A. variations with faults: in model 2a, the senses of shear and vergence are opposite, when again faulting on the 60^0 limb controls the rotation rate. The third model permits only folding, accommodating necessary shortening by further folding to create assymmetric box folds, which do not show the observed contradiction between shear sense and fold vergence. It therefore appears that limb faulting, with the 60^0 limb controlling the deformation rate, at either constant or variable I.L.A., can generate some of the structures observed. A necessary consequence of these models is extension in the shear direction.

Fold hinges are not greater than 60^0. Extensional faults at acute angles to the shear direction are implied by the much greater outcrop of both the Barrios quartzite and Oville Formations perpendicular to strike in the Bregon thrust sheet shown in Figure 5.2. A model showing the evolution of the contradictory vergence as the thrust sheet is deformed is shown in Figure 5.17 incorporating these extension faults and model 1d with fixed I.L.A. of 60^0. It explains the dominant features observed in the section.

5.4 MICROSTRUCTURES

5.4.1 Grain Size and Shape

The geometric mean of linear intercept measurements (G.M.L.) for all sections ranges between 0.0728 and 0.249mm (Appendix A1) with a remarkably constant geometric standard deviation. The average of G.M.L. measurements from two perpendicular directions on each of three mutually perpendicular slides shows a much more restricted range, from 0.1055-0.1910mm (Appendix A2). As discussed in 3.2.3, the G.M.L. is the most relatively accurate and useful grain size parameter, but is likely to slightly underestimate the true grain size, given more accurately by the arithmetic mean of linear intercepts. This varies between 0.1219 and 0.2056mm, so that the measured samples can be described as having a fine grain size. Although not represented in the measurements, a much coarser facies was also noticed in

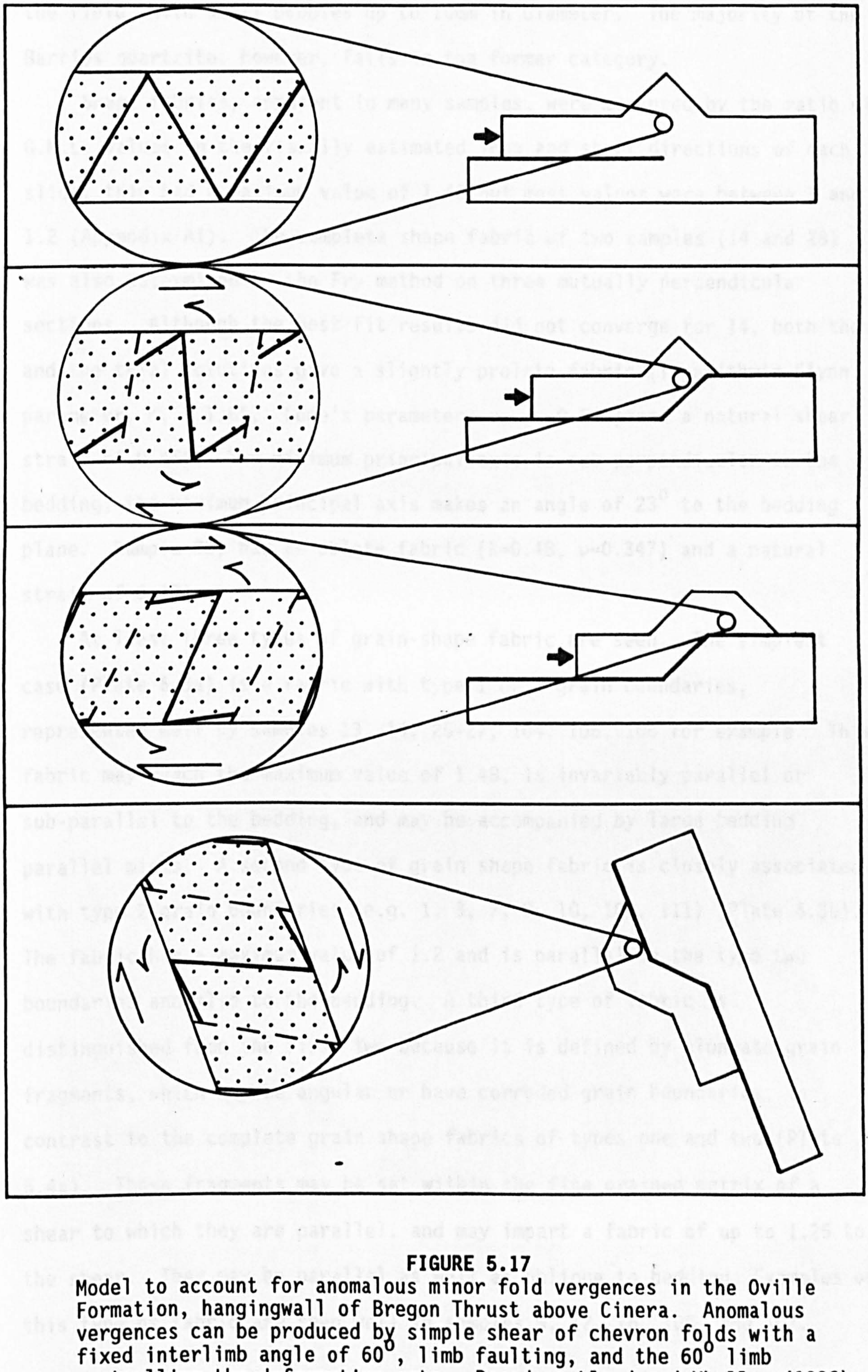

FIGURE 5.17
Model to account for anomalous minor fold vergences in the Oville Formation, hangingwall of Bregon Thrust above Cinera. Anomalous vergences can be produced by simple shear of chevron folds with a fixed interlimb angle of 60^{o}, limb faulting, and the 60^{o} limb controlling the deformation rate. Based on Lloyd and Whalley (1986).

the field, with small pebbles up to 10mm in diameter. The majority of the Barrios quartzite, however, falls in the former category.

Shape fabrics, apparent in many samples, were measured by the ratio of G.M.L. values in the visually estimated long and short directions of each slide; this had a maximum value of 1.48 but most values were between 1 and 1.2 (Appendix A1). The complete shape fabric of two samples (14 and 28) was also determined by the Fry method on three mutually perpendicular sections. Although the best fit results did not converge for 14, both them and the trial solutions gave a slightly prolate fabric (logarithmic Flynn parameter, K, = 1.65, Lode's parameter, ν, = -0.247) and a natural shear strain of 0.466. The minimum principal axis is sub-perpendicular to the bedding; the maximum principal axis makes an angle of 23^o to the bedding plane. Sample 28, had an oblate fabric (k=0.48, ν=0.347) and a natural strain of 0.181.

At least three types of grain-shape fabric are seen. The simplest case (Plate 5.3a) is a fabric with type 1 or 4 grain boundaries, represented well by samples 13, 14, 25-27, 104, 105, 106 for example. This fabric may reach the maximum value of 1.48, is invariably parallel or sub-parallel to the bedding, and may be accompanied by large bedding parallel micas. A second type of grain shape fabric is closely associated with type 2 grain boundaries (e.g. 1, 3, 7, 8, 10, 109, 111) (Plate 5.3b). The fabric has a maximum value of 1.2 and is parallel to the type two boundaries and also to the bedding. A third type of fabric is distinguished from the first two because it is defined by elongate grain fragments, which may be angular or have corroded grain boundaries, in contrast to the complete grain shape fabrics of types one and two (Plate 5.4a). These fragments may be set within the fine grained matrix of a shear to which they are parallel, and may impart a fabric of up to 1.25 to the shear. They may be parallel as well as oblique to bedding. Examples of this type of fabric are seen well in samples 9, 12, 16, 106, and 107.

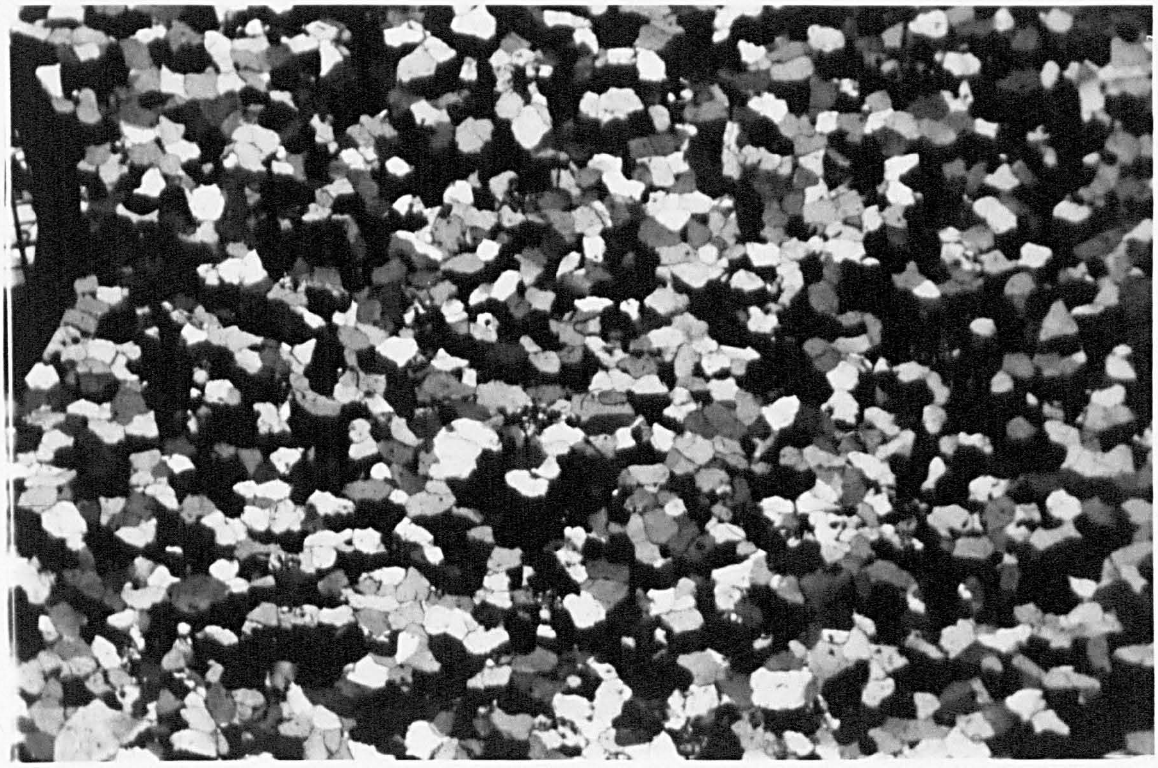

500μ

PLATE 5.3a

Bedding parallel fabric with type 1 grain boundaries. This is interpreted as a primary depositional/compaction fabric. Sample 105, Crossed Polars (X.P.)

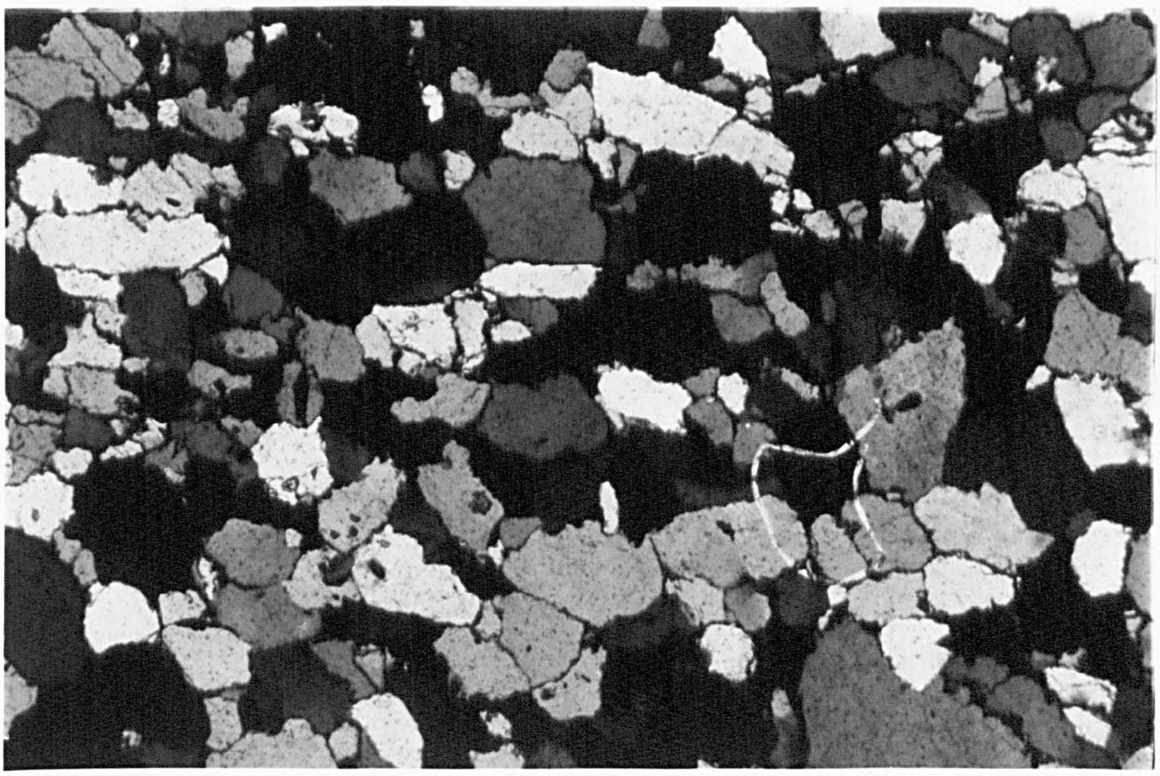

200μ

PLATE 5.3b

Bedding parallel fabric with type 2 grain boundaries. Between grains of equal radius of curvature, contacts are planar or slightly curved (type 2a), but between grains of differing curvatures, the boundaries are highly indented and convex towards the larger grain (type 2b). Such a boundary between one large and several small grains is seen near the center of the photograph. Sample 1, Plane Polarised Light (P.P.L.)

500μ

PLATE 5.4a

Cataclastic and Primary Fabrics. The cataclastic fabric, running north-south, is created by sub-parallel microfracturing. It cross-cuts a weak east-west, bedding parallel fabric which is primary. Sample 106, P.P.L.

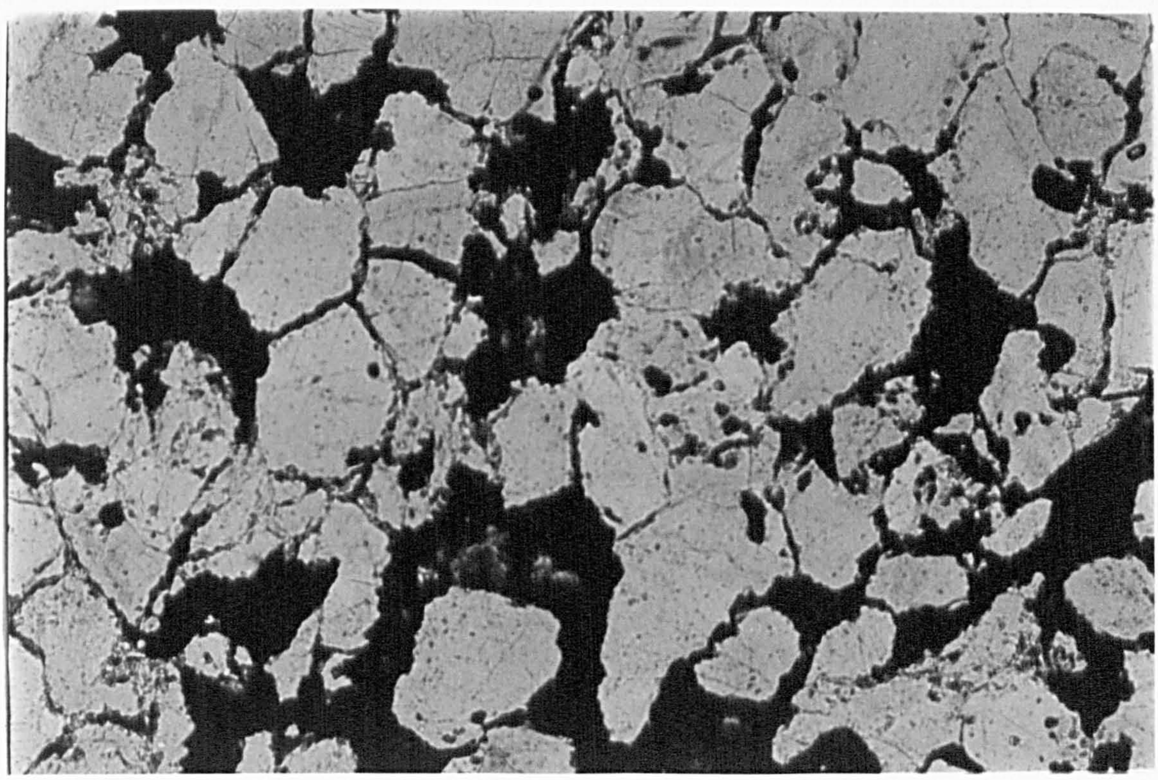

200μ

PLATE 5.4b

Type 4 grain boundaries. These are open or oxide filled, often with evidence of secondary solution. Sample 16, P.P.L.

Sample 106 is particularly instructive because it contains both a simple fabric parallel to bedding and a separate fabric of the third type parallel to shear faults which cut across the bedding (Plate 5.4a).

The three types of fabric are inferred to have three separate origins. The simple bedding parallel/sub-parallel fabric with type 1 grain boundaries is a primary fabric, since the type 1 boundaries indicate that no significant strain after growth of a quartz cement into pore spaces (see below). Further evidence for the original nature of this fabric is the lack of features indicating any form of solution (original grains with overgrowths in all directions can be seen in type 1a grain boundaries), and the very low value of the geometrical means of extinction angles (G.M.A.) which, together with the lack of kink bands, deformation lamellae, sub-grains or grain boundary bulging, indicate that no crystal plasticity has operated (see 5.3.6).

This fabric itself probably forms in two ways. Depositional fabrics in ellipsoidal clasts are a primary feature of even unconsolidated aggregates, commonly formed at a small angle to bedding. The strain data from sample 14 show an angle of 20^{o} between the ellipsoid long axis and bedding which could be interpreted as such an imbricate angle. However, the experiments of Borg and Maxwell (1956) and Borg et al. (1960) also show that a fabric can develop simply by packing of loose sand although the minimum fabric axis is perpendicular to bedding in this case. The operation of this process to some extent during burial compaction seems quite likely.

The second type of fabric differs in being parallel to type 2 grain boundaries, as well as parallel to bedding. Since these grain boundaries are due to solution transfer (see 5.3.2), this fabric is clearly a solution fabric, though it may be enhancing an earlier, primary, bedding fabric; the two components can be partly distinguished from evidence of solution of overgrowth. It therefore appears to be contemporary or later than the cementation.

The third type of fabric is a cataclastic fabric due to microfracturing in a preferred direction creating elongate grain fragments. The production of this fabric by microcracking can be clearly seen in Plate 5.4a and recalls the experimental work on loose St. Peter sand by Borg et al. (1960), in which cataclastic fabrics were produced by grain rotation and fracturing.

5.4.2 Grain Boundaries

Grain boundaries of only types 1, 2 and 4 are represented in the samples from Bernesga Valley, Cremenes and Luna Lake. Generally types 2 and 4 are mutually exclusive, and type 1 occurs with both 2 and 4. Two common varieties of type 2 grain boundaries are shown in plate 5.3b from sample 1. The almost planar contact between two equal-sized grains can be seen, and also a highly indented contact between one large and several smaller grains. The predominant grain boundary types in each sample are summarised in Appendix A2.

The interpretation of type one boundaries is straightforward: they are formed by free growth of a quartz cement between grains into pore space and record no subsequent strain (good planar contacts exist between the overgrowths, and with any adjacent pore space). The identification of an original rounded grain entirely within the overgrowth distinguishes types 1a and 1b; in the absence of this feature, type 1b boundaries admit the possibility of a limited amount of diffusive mass transfer or even crystal plasticity. However, their association and identical geometry to type 1a imply a common origin; the only difference being that the original grains are not clearly visible in type 1b.

Type 2 grain boundaries clearly indicate solution transfer. This can be inferred from the truncation of overgrowths and original grain boundaries in type 2b. The distinction between the two types is one of curvature; higher curvatures, always convex towards the smaller radius grain, occur where there is a greater difference in curvature between the two grains. This effect can be explained from the stress distribution of a Hertzian indent, which predicts that higher stresses will exist within the planar body: solution will thus occur in the grain with the larger radius of curvature (McEwen 1981).

Type 4 boundaries (Plate 5.4b) also indicate solution where cross-cutting of original grain boundaries and overgrowths are seen. However, these boundaries are distinguished by their width and openness, indicating an aggregate of grains loosely supported at few points. This texture could be the product of isotropic solution under low effective confining pressures, or simply lack of cement.

5.4.3 Porosity

All types of porosity figured in 3.8 are visible in the samples from Bernesga Valley, but certain associations are common, notably that between polygonal grain junction porosity (type 1a) with isolated circular (type 2) pores, and the association of irregular grain junction porosity (type 1b) with grain boundary porosity (type 3) and, if they occur, irregular edges on type 2 pores. Type 1a and type 3 porosities tend to be mutually exclusive. There is an obvious association of type 3 porosity with type 4 grain boundaries, since they are both defined by irregular porosity along grain boundaries, and between type 1 porosity with grain boundaries of type 1 (and 2), since this porosity is defined as existing between grains with type 1 boundaries. Porosity types for each sample are also summarised in Appendix A2.

Values of open porosity determined by point counting show a large variation between 0.2 and 11.7% (Appendix A3). These figures, however, give only the existing porosity sensu strictu; the value of microstructural interest is the porosity immediately before and during deformation. To preempt the conclusions of this chapter slightly, it appears that only three processes have affected porosity significantly: solution, cementation and cataclasis. The collection of the point counting data has been made in such a manner as to allow corrections to be made for each of these changes, and hence to estimate a value of porosity before cataclasis. As mentioned in 3.2.2, all types of pores may be filled with iron oxides or clay matrix, which can be demonstrated in several cases as syn- or post-cataclasis. The original porosity is therefore calculated as existing porosity (category 7 of the point count classification) combined with iron oxides and clay matrix (5 and 6). This cementation correction was applied to all samples. The major change induced by cataclasis is the production of non-porous shear matrix along fractures. This comprises categories 3 and 4 of the point count classification. The porosity exclusive of shear matrix can be calculated as

$$\frac{5+6+7}{1+2+5+6+7} \times 100\%$$

Additional cataclastic porosity was introduced by microcracking and grain boundary sliding; however, these effects were much smaller. The cataclasis correction above was applied to all samples with shear matrix. Post-cataclastic solution was evident in samples 14, 15, 16, 17, 18, 31, 33, 104, 106, and 107. This was allowed for by assuming that all existing open porosity was due to later solution: in these cases, the pre-cataclastic porosity was calculated excluding category 7 as

$$\frac{5+6}{1+2+5+6+7} \times 100\%$$

The results indicate in every case but one that the porosity before cataclasis (B.C.) was considerably greater than the present porosity (sensu strictu), by factors of between two and ten (compare columns 7 and 8 of Appendix A3). The range of this porosity is between 4 and 27.2%, with a weak correlation between the B.C. and present porosities (shown in Figure 5.18), in spite of the fact that late porosity has been excluded from the calculation of B.C. porosity of those samples listed above. There is also

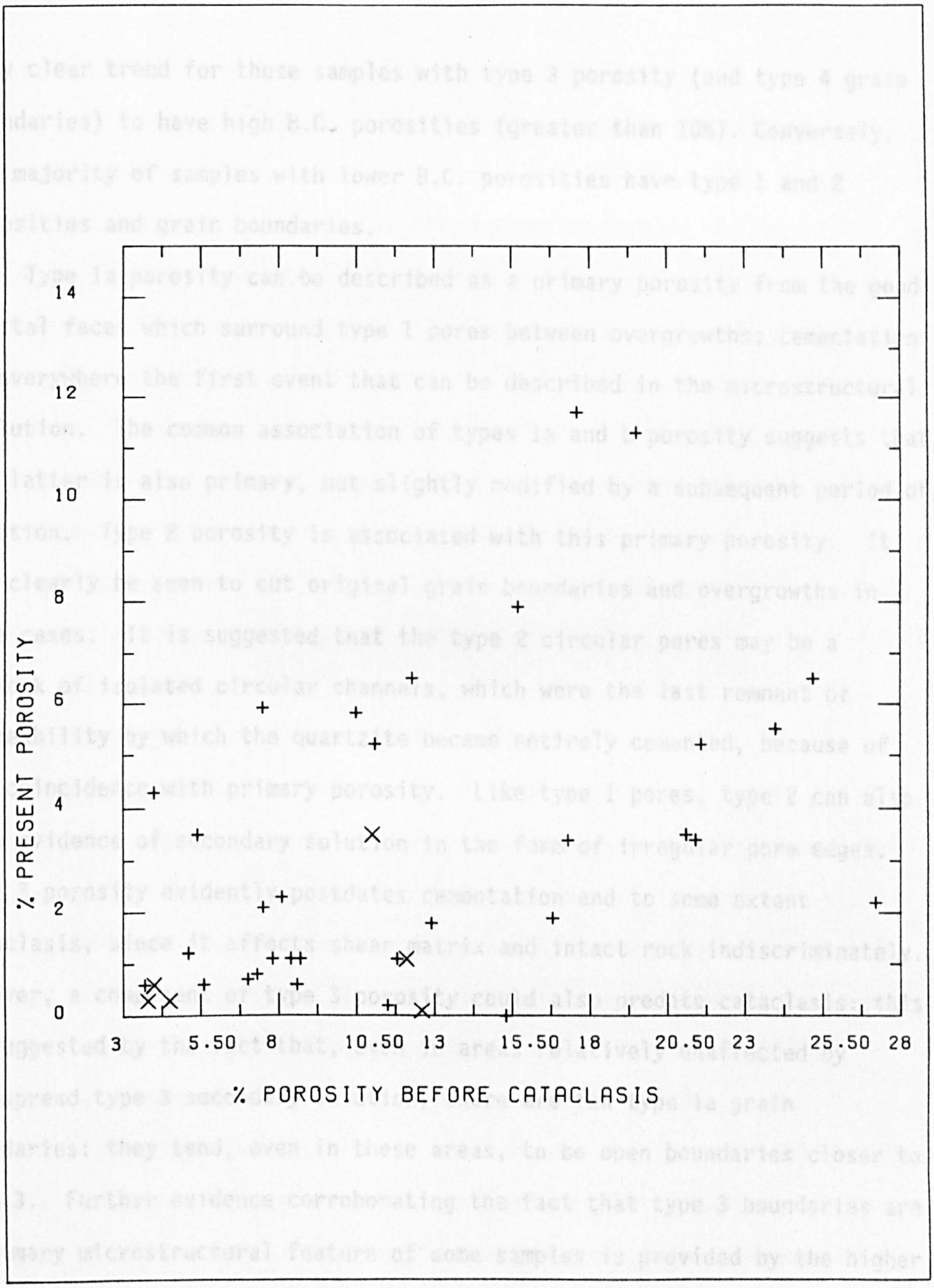

FIGURE 5.18

The relation between existing porosity (7) and estimated porosity before cataclasis (8) (B.C. Porosity). In Figure captions for Figures 5.20 to 5.28, the numbers in brackets refer to the columns of data in Appendices A3 and A4; these are the point count categories. A weak positive correlation is observed between 7 and 8. Bernesga Valley - plus signs, Punta Vidrias - crosses.

very clear trend for those samples with type 3 porosity (and type 4 grain boundaries) to have high B.C. porosities (greater than 10%). Conversely, the majority of samples with lower B.C. porosities have type 1 and 2 porosities and grain boundaries.

Type 1a porosity can be described as a primary porosity from the good crystal faces which surround type 1 pores between overgrowths; cementation is everywhere the first event that can be described in the microstructural evolution. The common association of types 1a and b porosity suggests that the latter is also primary, but slightly modified by a subsequent period of solution. Type 2 porosity is associated with this primary porosity. It can clearly be seen to cut original grain boundaries and overgrowths in some cases. It is suggested that the type 2 circular pores may be a network of isolated circular channels, which were the last remnant of permeability by which the quartzite became entirely cemented, because of the coincidence with primary porosity. Like type 1 pores, type 2 can also show evidence of secondary solution in the form of irregular pore edges. Type 3 porosity evidently postdates cementation and to some extent cataclasis, since it affects shear matrix and intact rock indiscriminately. However, a component of type 3 porosity could also predate cataclasis: this is suggested by the fact that, even in areas relatively unaffected by widespread type 3 secondary solution, there are few type 1a grain boundaries: they tend, even in these areas, to be open boundaries closer to type 3. Further evidence corroborating the fact that type 3 boundaries are a primary microstructural feature of some samples is provided by the higher B.C. porosity of these samples, calculated from the above formula. This indicates that the present porous samples were originally more porous (see correlation between present and B.C. porosity, Figure 5.18) as well as experiencing a substantial post-cataclastic episode of solution. The restriction of this late solution to these samples would be a natural consequence of their higher primary porosity.

5.4.4 Fractures

A wide variety of fractures are visible microscopically, and a very clear distinction can be made between cracks and faults. The former can be subdivided into intra-, trans- or circumgranular cracks, following the classification suggestion in 2.5.1.

a) Intragranular Cracks (Plate 5.5a). These are visible only with difficulty in the optical microscope, where they may appear as lines of bubbles or inclusions, or rarely filled by iron oxides. In C.L., they are readily apparent in brightly luminescing grains as bands of non-luminescing quartz cement. They have typical widths of 1/10 of a grain diameter, although larger proportions (e.g. 1/3) of a grain may consist of a single intragranular crack. Widths are commonly extremely variable both within a single grain and even along a single crack. Intragranular cracks may extend across the whole grain but more commonly have shorter lengths linking with other short cracks. Mode I displacements are by far the most abundant. A highly distinctive feature of some is their irregular crack path, usually consisting of short, angular segments with variable widths. Little preferred orientation is seen in purely intragranular cracks. A type of intragranular crack of particular interest is shown in Plate 5.5b, in which the arrowed crack follows the grain edge but spalls off a crescentic sliver of the grain with the overgrowth along a line sub-parallel to the grain edge. In other cases, the fracture follows the boundary between the original grain and the overgrowth exactly, but several examples where the grain-edge crack occurs entirely within the mantle of the original grain have been observed. It is probable that such grain-edge cracks may be exploiting the grain overgrowth boundary in parts, and also existing within the original grain in other areas.

Of the microcrack mechanisms described in 2.2.1, at least four may apply to the development of the intragranular cracks. The majority are probably impingement induced, showing the same geometries as in the

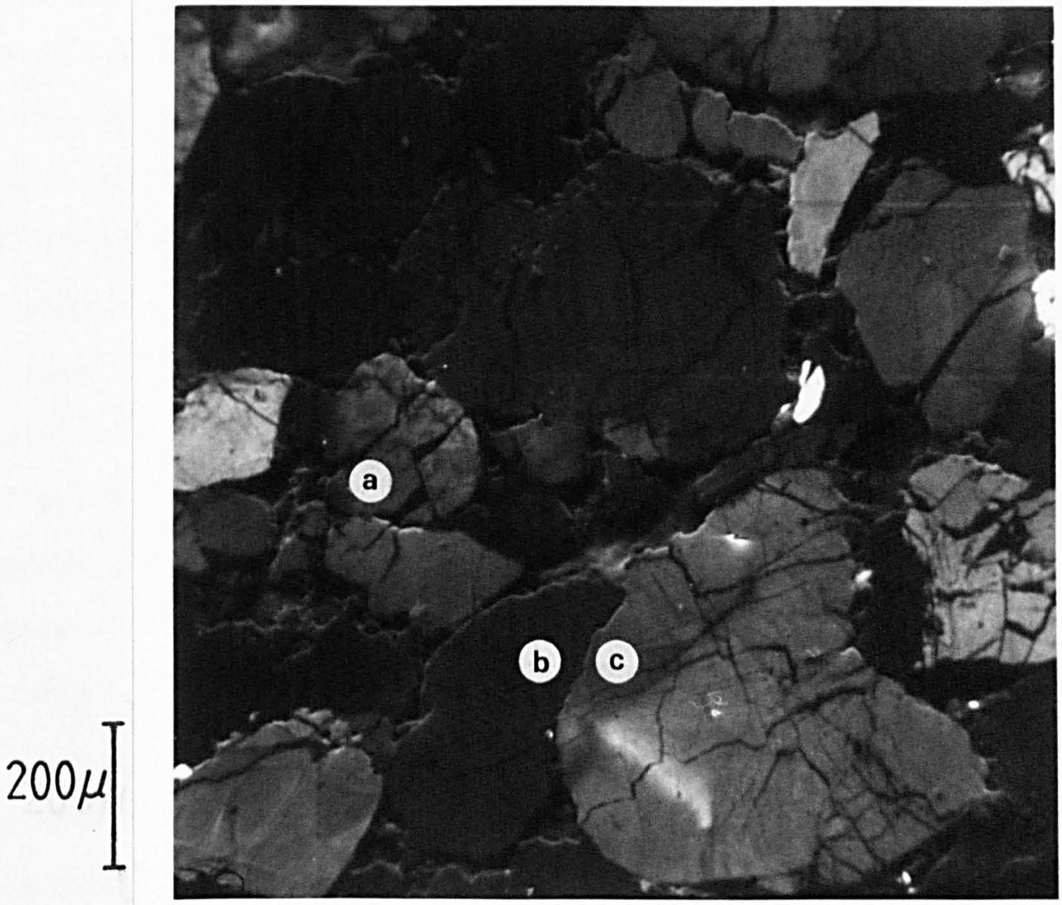

PLATE 5.5a

Intragranular Microfractures. The characteristic short length, variable width, irregular, angular paths and lack of preferred orientation can be seen. A fine example of flaw induced microcracking can be seen in grain a: shear along a thin vertical crack links two wedge shaped tensile cracks opening at either end. Type 2a boundaries can be seen between grains b and c. Sample 8, Cathodoluminescence (C.L.).

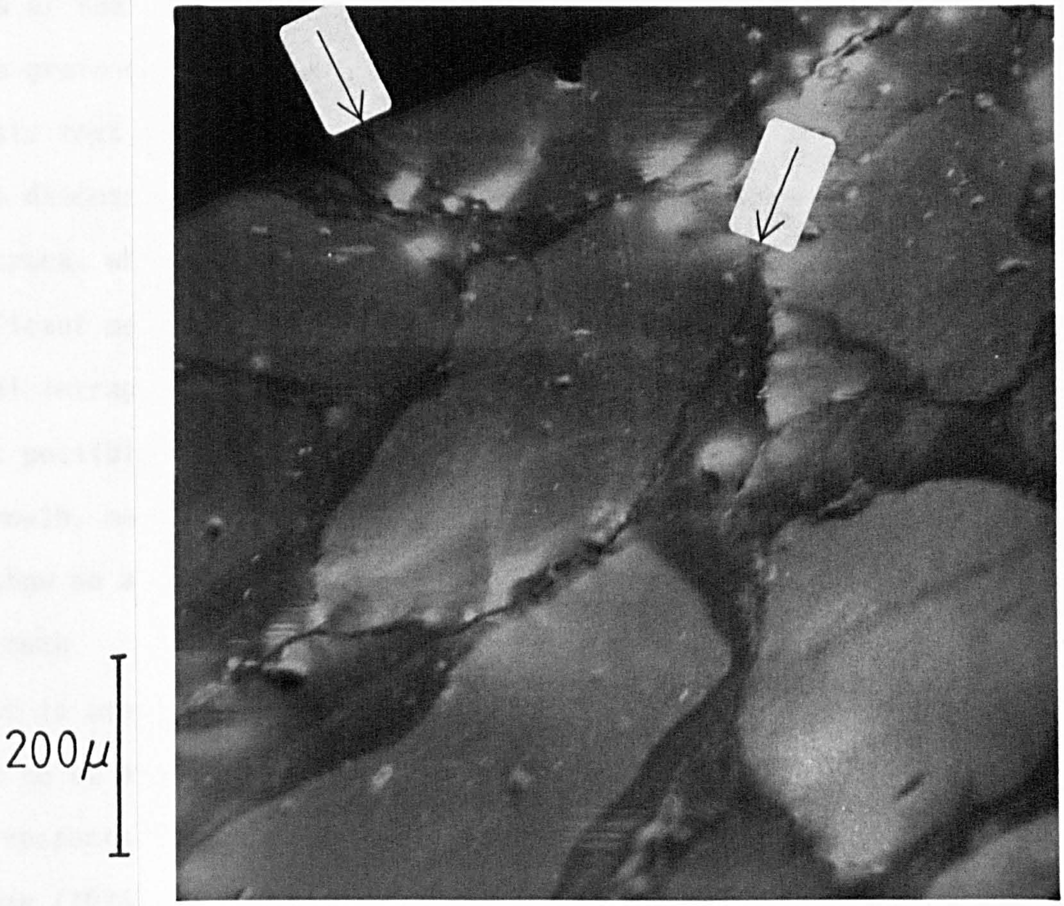

PLATE 5.5b

Intragranular Grain Edge cracks (arrowed). These are parallel to the original uncemented grain boundary, and separate a sliver of the original grain with overgrowth. Sample 6, C.L.

experiments of Gallagher et al. and McEwen. However, the observations on the irregular widths and paths, and lack of preferred orientations suggest that other mechanisms are important. Some of these may be following pre-existing intragranular flaws or planes of weakness (e.g. inherited cracks or features due to crystal plasticity). A particular case of this is the grain-edge cracking in Plate 5.5b. Linearity of many cracks suggests that cleavage induced cracking may indeed be important as implied by the discussion in 2.2.1. Finally, Plate 5.5a shows a pair of microcracks which have a perfect flaw-induced geometry; this may be a significant mechanism in grains with inherited strain features and after initial intragranular microfracture by the mechanisms above. Although it is not possible to see intragranular cracks in the non-luminescing overgrowth, many of them can be inferred to cross-cut overgrowths because they show no attenuation on passing from the original grain to the overgrowth.

It is useful to record that shear fault-induced microcracking does not appear to be a significant mechanism, although shear faults are observed in other respects comparable to the experimental pre-cuts of Conrad and Friedman (1976), Friedman and Logan (1970), and Teuf el (1981) in which such microscopic feather fractures were detected. The evidence for this statement is the fact that microfracture densities do not show any increase in the zone of several grains adjacent to the shear fault. All three studies reported an increase in such fracture densities with confining pressure in the range 0-300MPa. One possibility, therefore, for the lack of shear-fault induced microcracking, would be that the effective confining pressure during cataclasis was at the lower end of this range (i.e. 100MPa or less).

No examples of elastic mismatch-induced microfracture adjacent to large mica flakes were observed. The possibility of microfracturing due to plastic mismatch remains open because plastic strain fractures are not generally visible in C.L., in which the microfractures were best observed.

ii) Transgranular Cracks (Plates 5.6a,b). The same difficulties of observation attend transgranular cracks in the optical microscope, but wider cracks may be visible as discontinuous bands of very slightly misorientated crack filling, which have a similar appearance to elongate sub-grains. Strings or even continuous fillings of iron oxides are seen, and rarely the transgranulars may be open. They are clearly seen in C.L., where they form the most noticeable cataclastic feature, as continuous lines of non-luminescing quartz, with similar widths to the intragranular cracks, but lengths up to several tens of grain diameters. Most have pure mode I displacements. Their geometry contrasts with the intragranular cracks in being more planar. They may terminate or transfer to adjacent en-echelon fractures entirely within single grains, or terminate at grain boundaries. They frequently bifurcate and often the branching crack rejoins the main crack to isolate slivers of grains. The central parts of transgranulars may have an adjacent zone of densely developed short transgranulars and intragranulars, typically no longer than two grain diameters, for similar widths either side of the main crack, but this zone of proximal cracking disappears at either end of the crack (Plate 5.6a). All the cracks, both main and subordinate, have purely Mode I opening in this situation; the central parts are open or oxide filled, while the ends are cemented. A very similar type of short, curved intragranular crack can be found surrounding the circular holes of type 2 pores. A dense pattern of arc shaped cracks, concentric around the pore with oxide fillings, is seen in sample 104 for example.

Transgranular cracks have a good preferred orientation across a thin section, and often occur in sub-parallel sets which may intersect but not offset each other. They have a tendency to form in parallel pairs or even cluster together in zones.

Both trans- and intragranular cracks are only visible in C.L. where

200μ

PLATE 5.6a

Transgranular Microfractures. A wide transgranular is rendered visible in P.P.L. from its iron oxide filling. There is a dense development of short cracks adjacent to the central part of the main crack. Squares of grid are 100μ wide. Sample 106, P.P.L.

200μ

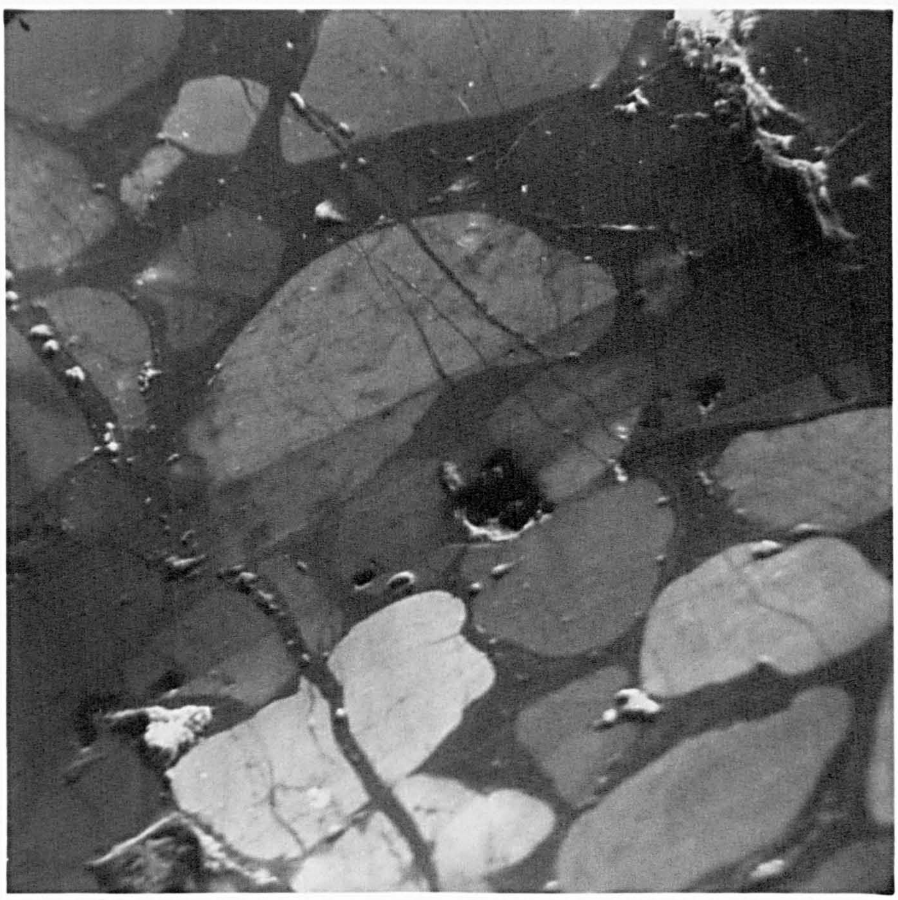

PLATE 5.6b

Transgranular Microfractures. Straight, sub-parallel transgranular cracks can be seen by their contrast in luminescence with brightly luminescing grains. They clearly cut across intervening cement, although there is no contrast between the luminescence of the crack fill and cement. Sample 5a, C.L.

the cracked grain has a brighter luminescence than the non-luminescing crack fill. For this reason it is not possible to observe cracks directly within the non-luminescing quartz cement, and the question of whether the cracks cut cement is difficult to resolve. However, Plate 5.6b does show some excellent examples of trangranular cracks which clearly do cross cement since they are recognisably the same crack in adjacent grains that are not in contact. Nevertheless, it is also evident that there are more cracks in areas where grains are directly in contact. Examples of crack/pore relationships show both cracks crossing pores where the porosity is clearly later and a later crack that cuts an earlier pore filling of clay matrix. Transgranular cracks also truncate and are truncated by faults, but always seem to crosscut intragranular cracks except those of the sort that are adjacent to the central areas of the cracks.

The long transgranular fractures are an unusual feature with no good experimental analogue in triaxial compression. Two possible mechanisms can be suggested for the transgranular microfracture. The first is that they are simple extension failure microfractures similar to those developed in uniaxial compression experiments leading to macroscopic axial fracture, or slabbing. The Mode I character of their displacements and parallel development in zones would support such an origin and suggest very low effective confining pressures. A dense concentration of shorter fractures at the centres of the transgranulars may represent an area of fracturing from which the main fracture eventually propagated in the unstable manner shown by the stress analysis of Hori and Nemat-Nasser, once achieving a critical length. This origin demands a negative effective least principal stress over the length of the crack.

An alternative possibility is that the transgranular fractures originated by linkage of a number of shorter parallel and aligned intragranular fractures developed by impingement stresses. This process can be inferred from four observations illustrated in Plate 5.7a, in which

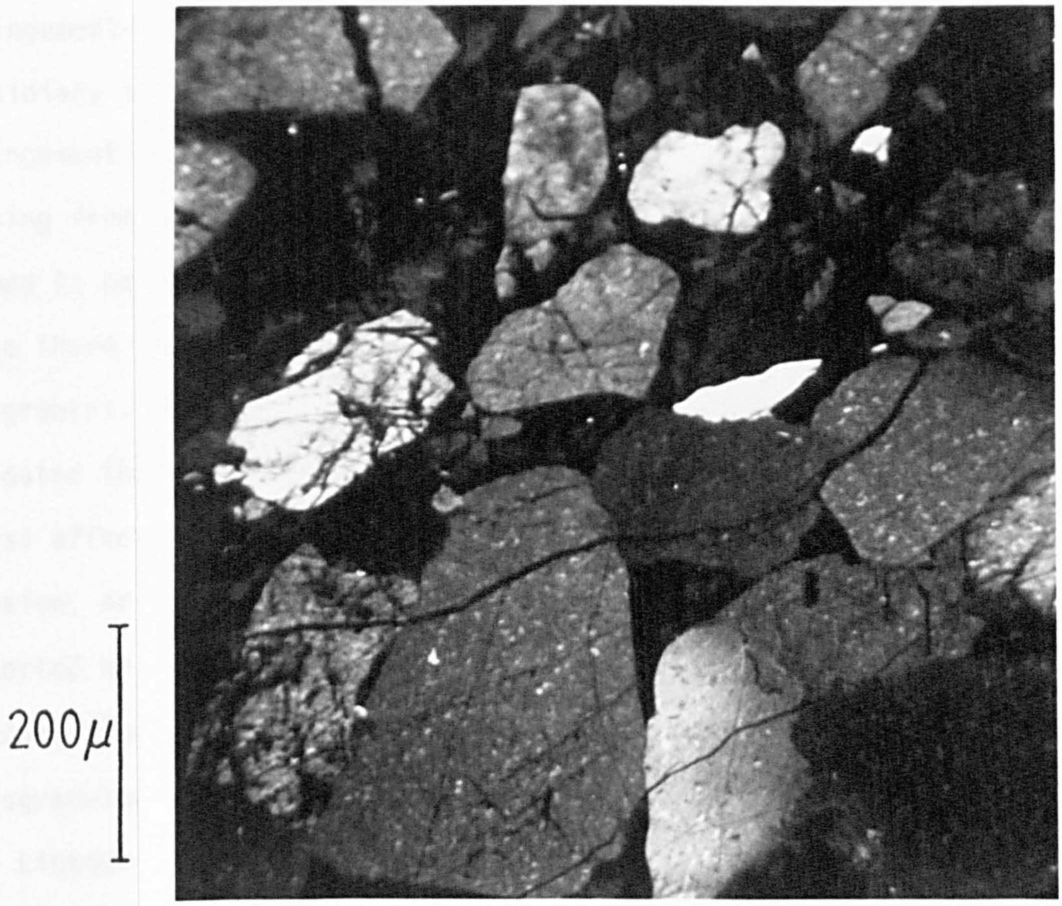

PLATE 5.7a

Transgranular Microfracture probably formed by linking of intragranular impingement induced microcracks. This is suggested by the observations that the transgranular microcrack clearly links points of contact between grains, shows slight changes of trajectory at grain boundaries, and has a variable width in passing from grain to grain. Subsidiary intragranular microcracks with impingement geometries can be seen sub-parallel to the transgranular. Sample 109, C.L.

the central transgranular crack clearly links points of impingement between neighbouring grains in preference to crossing the cement between them, and also shows slight changes in direction at the grain boundaries as if following local stress trajectories. The role of intragranular, impingement-induced microfractures is also indicated by the presence of subsidiary intragranular microfractures adjacent to the main fracture with impingement geometries, and the variations in width of the main fracture passing from grain to grain. It was observed that overgrowths generally seemed to have a lower transgranular fracture density than original grains, while there were nevertheless examples of transgranular fractures which cut overgrowths. Although a possible interpretation is that some transgranulars pre-dated the cement, it is suggested that most were later, yet impingement stress effects could operate to some extent because overgrowth - grain adhesion, or the overgrowth itself, was weaker than intact grains. This is supported by the relative chronology of cement, intra- and transgranular fracture: the intragranular fractures post-dated cementation, and transgranular fractures everywhere post-date intragranulars.

Linkage of such intragranular cracks might occur sequentially in front of the growing transgranular, or sporadically at different positions along its length. The former process would seem more likely since the crack tip creates an additional tensile stress field at each grain boundary. In this case it is possible to imagine a combination of the two mechanisms above, in which the transgranular propagates under a negative or very low effective confining pressure, but influenced within each grain by impingement stresses. This process is illustrated in Figure 5.19.

iii) Circumgranular Cracks. These are almost impossible to identify under either optical or C.L. conditions because they do not displace grain boundaries and exist within the non-luminescing quartz cement. However, they can be inferred from oxide fillings along relatively narrow continuous zones. Segments of transgranular cracks may be circumgranular: some of the

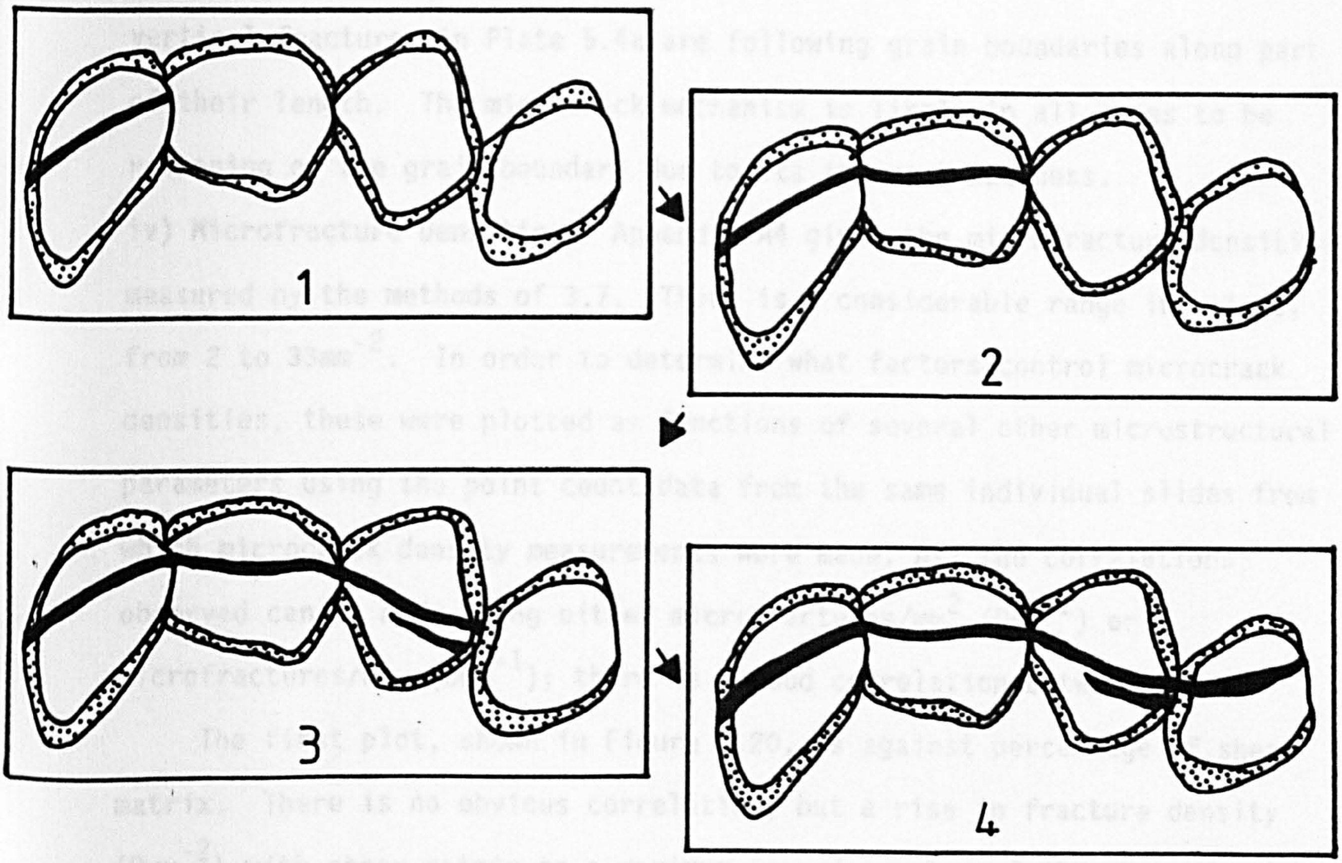

FIGURE 5.19
Formation of a transgranular fracture by sequential intragranular, impingement-induced fractures ahead of the main fracture.

vertical fractures in Plate 5.4a are following grain boundaries along part of their length. The microcrack mechanism is likely in all cases to be reopening of the grain boundary due to its inherent weakness.

iv) Microfracture Densities. Appendix A4 gives the microfracture densities measured by the methods of 3.7. There is a considerable range in values, from 2 to 33mm^{-2}. In order to determine what factors control microcrack densities, these were plotted as functions of several other microstructural parameters using the point count data from the same individual slides from which microcrack density measurements were made. All the correlations observed can be made using either microfractures/mm^2 (Dmm^{-2}) or microfractures/mm, (Dmm^{-1}); there is a good correlation between them.

The first plot, shown in Figure 5.20, is against percentage of shear matrix. There is no obvious correlation, but a rise in fracture density (Dmm^{-2}) with shear matrix to a maximum around a value of 25% shear matrix, followed by a decrease. The same is seen in the fracture densities per grain (DG^{-1}).

In Figures 5.21 and 5.22, Dmm^{-2} is plotted against the existing open porosity and the estimated porosity before cataclasis. There is discernible negative correlation. Both can be separated into a high porosity, low fracture density group of results (14, 16, 17) and a low porosity group with variable densities (the remainder). Again, similar trends can be observed in fracture densities per grain. Several other correlations have been tested although they are not figured. There is a positive correlation between both Dmm^{-2} and DG^{-1} and grain size (G.M.L.), and a negative correlation with the number of grains per unit area. A weak negative correlation exists with the total content of iron oxides, but no relationship is observed to percentage of clay minerals.

The increase in microfracture densities with proportion of shear matrix is reminiscent of the relationship reported in the pre-cut sliding experiments between density and displacement; however, it has been shown

FIGURE 5.20

The relation between microfracture density (Dmm^{-2}) and percentage of shear matrix (3+4). A maximum value of D occurs at 25-30% shear matrix.

FIGURE 5.21

The relation between microfracture density (Dmm^{-2}) and existing porosity (7).

FIGURE 5.22

The relation between microfracture density (Dmm^{-2}) and precataclastic porosity (8). A weak negative correlation is seen in both figures, with samples 14, 16 and 17 forming a separate high porosity, low fracture density group.

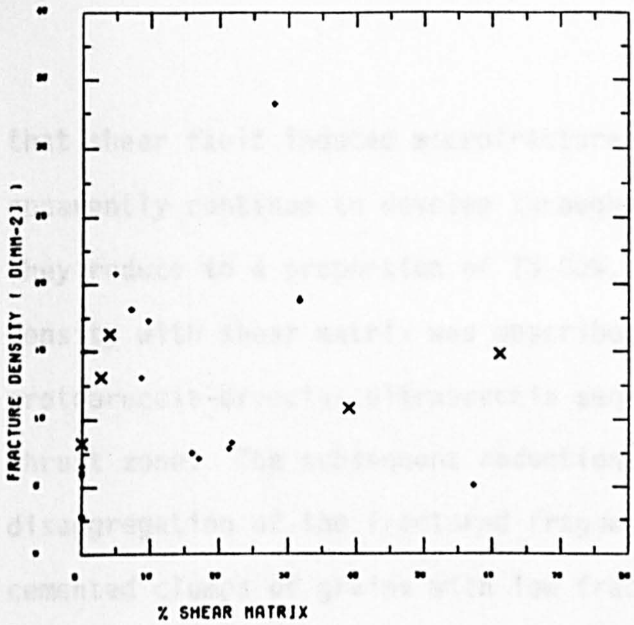
FRACTURE DENSITY (DEMM-2)
% SHEAR MATRIX

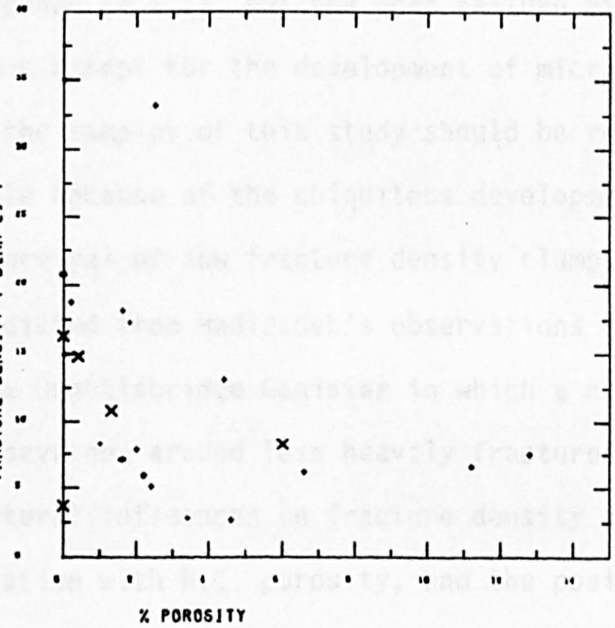
FRACTURE DENSITY (DEMM-2)
% POROSITY

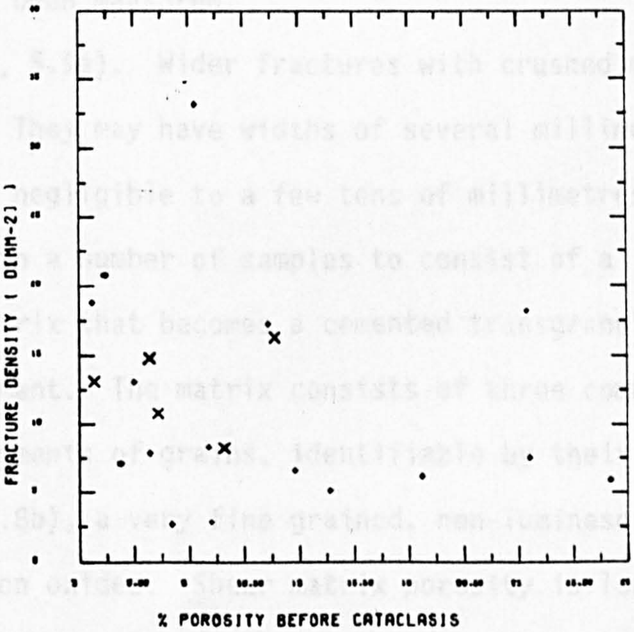
FRACTURE DENSITY (DEMM-2)
% POROSITY BEFORE CATACLASIS

that shear fault induced microfractures are not responsible: microfractures apparently continue to develop throughout the unsheared fragments until they reduce to a proportion of 75-80%. A similar increase in microfracture density with shear matrix was described by Blenkinsop (1982) in the protobreccia-breccia- ultrabreccia sequence in quartzites from the Moine thrust zone. The subsequent reduction in fracture density is due to the disaggregation of the fractured fragments, to leave only exceptionally well cemented clumps of grains with low fracture densities. Experimental increases in microfracture density in the pre-failure region are universally recorded (2.2.1), but the post failure microfracture evolution is not well known except for the development of microscopic feather fractures. All the samples of this study should be regarded as post failure on the meso scale because of the ubiquitous development of the fracture network. The survival of low fracture density clumps of grains would, however, be predicted from Hadizadeh's observations on the microstructural evolution of the Oughtisbridge Ganister in which a cellular network of microfractures develops around less heavily fractured areas (Figure 2.8).

Microstructural influences on fracture density are evident from the negative correlation with B.C. porosity, and the positive correlation with grain size. The latter is good evidence that original grain size, rather than fragmented grains, have been measured.

iv) Faults (Plates 5.7b, 5.8, 5.9a). Wider fractures with crushed matrix are common in many samples. They may have widths of several millimetres and shear displacements from negligible to a few tens of millimetres. Fault terminations are seen in a number of samples to consist of a narrowing zone of crushed matrix that becomes a cemented transgranular crack with no shear displacement. The matrix consists of three components in variable proportions: fragments of grains, identifiable by their bright luminescence (Plates 5.7b, 5.8b), a very fine grained, non-luminescing cement and fine grains of iron oxides. Shear matrix porosity is lower than

200μ

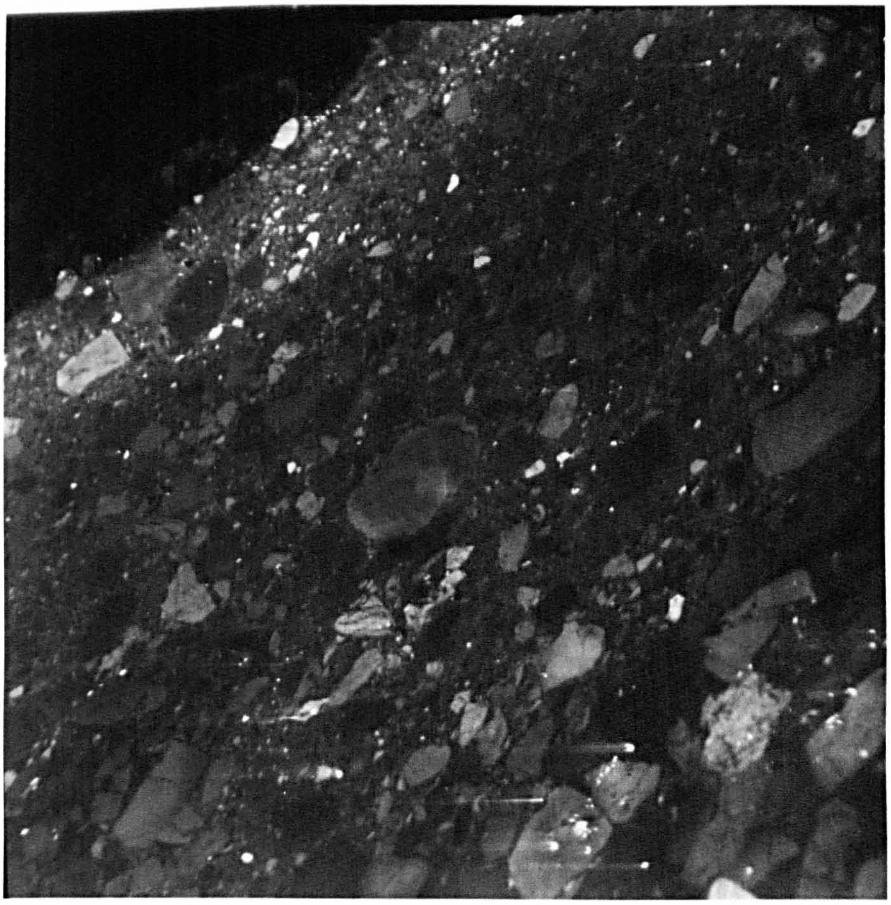

PLATE 5.7b

Compact Fault. Grain fragments can be identified from their bright luminescence within the non-luminescing matrix of the fault. Sample 7, C.L.

200μ

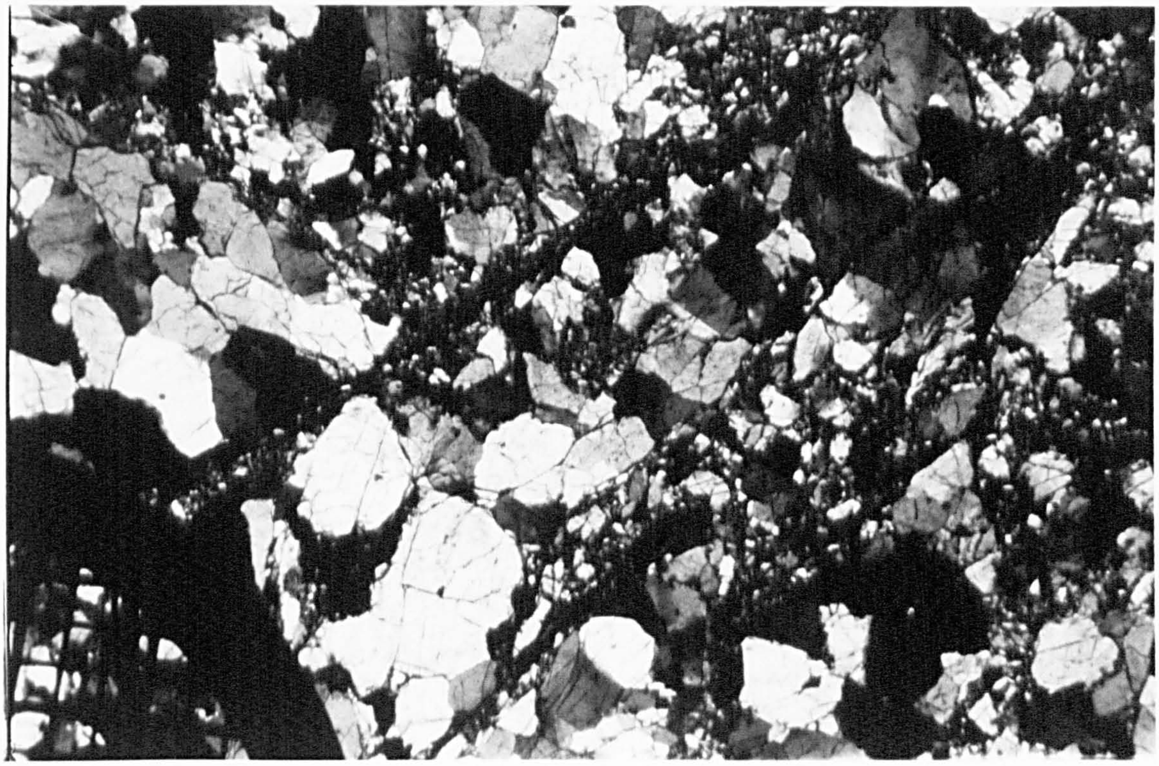

PLATE 5.8a

Compact Fault. The characteristics of compact faults - high proportions of matrix to fragments, sharp planar walls, and low porosity are evident, as is the importance of trangranular microcracking in the evolution of the fault. Sample 107, X.P.

200μ

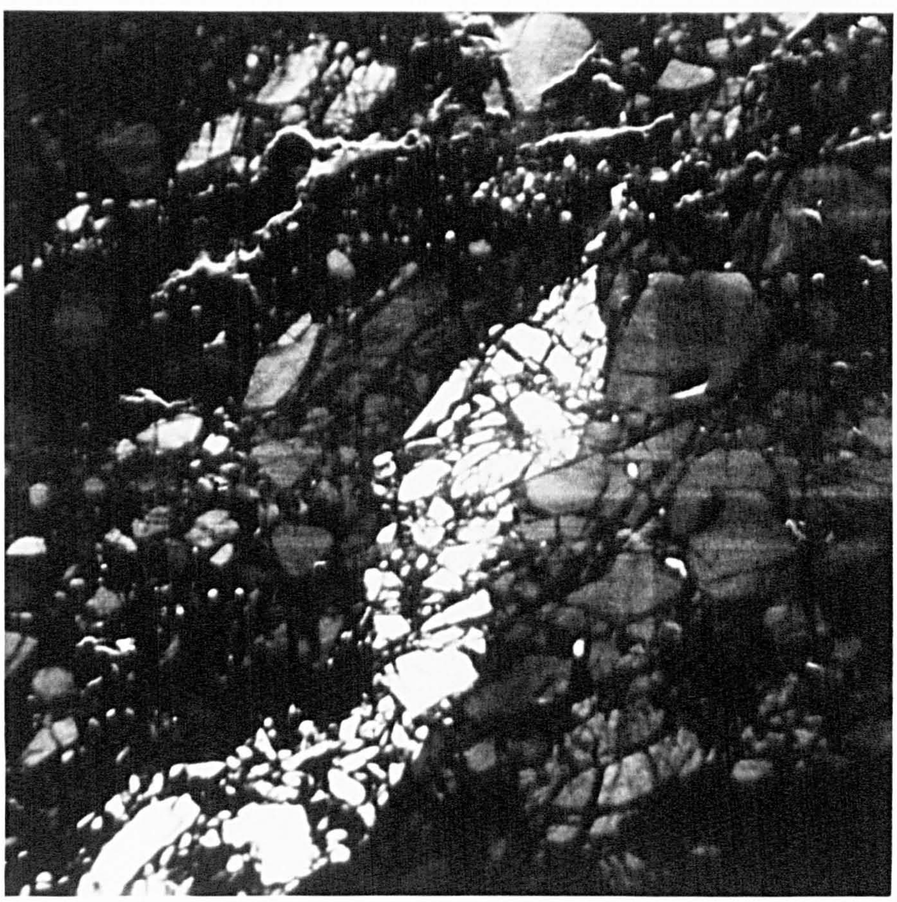

PLATE 5.8b

Compact Fault Matrix. A high magnification image shows highly shattered, luminescing grain fragments in the non-luminescing matrix. Sample 107 (as above), C.L.

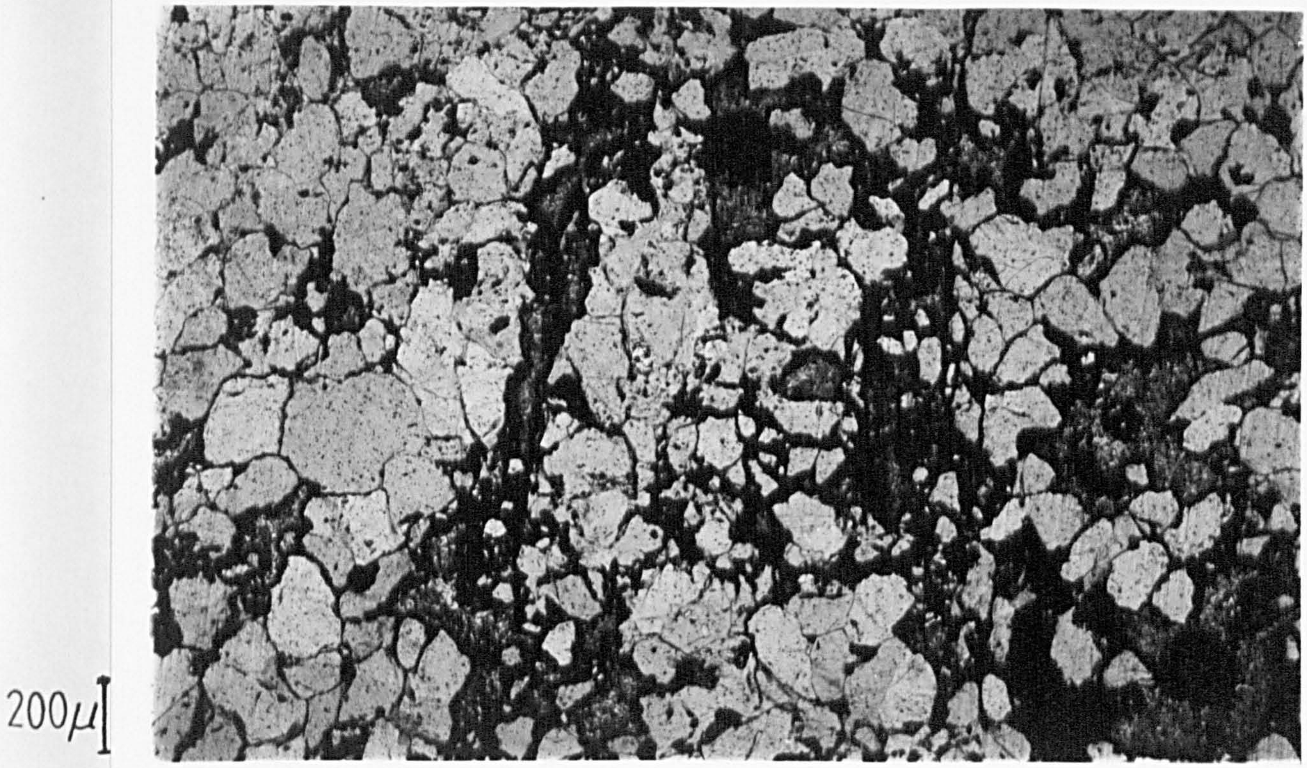

PLATE 5.9a

Porous Fault. Porous faults have low proportion of matrix to fragments, irregular diffuse walls, large fragments which may be intact grains, and high porosities. Sample 16, P.P.L.

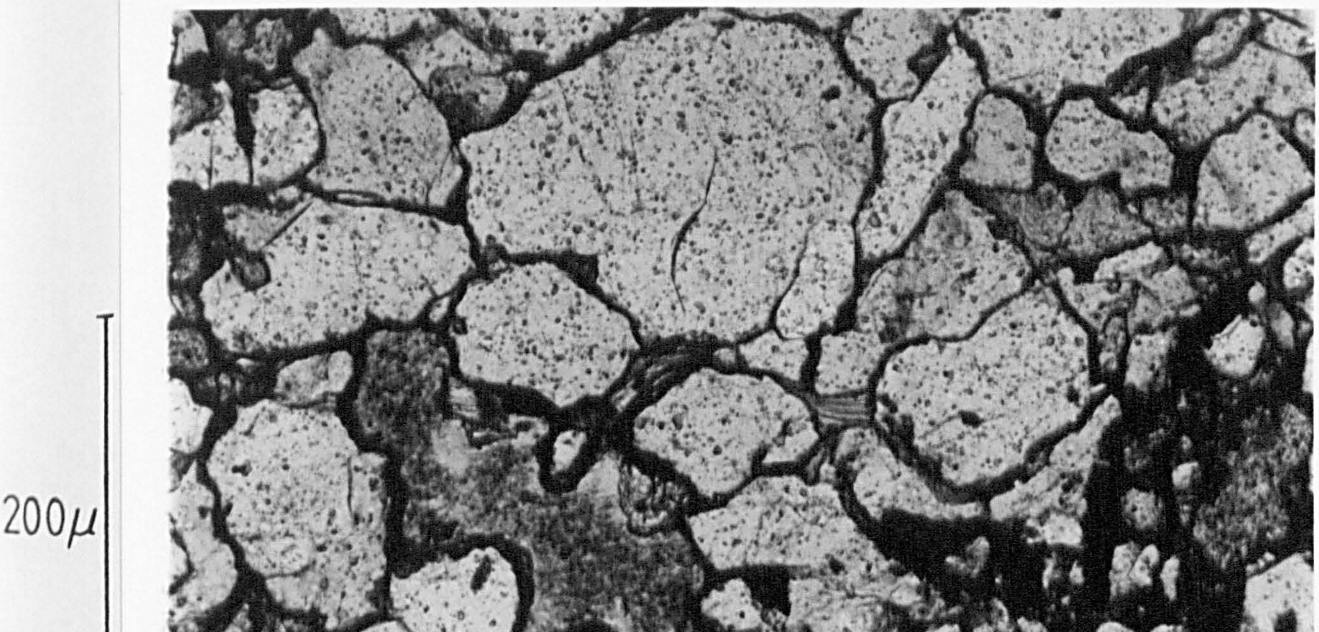

PLATE 5.9b

Sheared detrital phyllosilicate grain. The large mica grain in the center of the photomicrograph has been sheared between two adjacent quartz grains. This provides valuable evidence of the importance of grain boundary sliding. Sample 17, X.P.

intact rock in most samples. Grain fragments may be very angular and inequant, imparting a weak foliation to the matrix, but more rounded fragments are also seen with increasing proportion of fine grained matrix. The relative proportion of fragments to cement is hard to evaluate because the two cannot be distinguished on a fine scale. For this reason, the fault filling is referred to simply as shear matrix with the implication that at least part bears evidence of displacement. Iron oxides are noticeably more abundant in shear matrix than intact rock as disseminated grains, large, amorphous patches and veins. Column 9 of Appendix A3 gives the enrichment of oxides in the shear matrix, calculated as

$$\text{Iron Oxide Enrichment in Shear Matrix} = \frac{4/(3+4)}{5/(2+5+6+7)} \times 100\%$$

This formula assumes that all clays and porosity are within the intact rock, leading to a slight overestimate of the enrichment; however, assuming an equal distribution of porosity over matrix and intact rock makes a negligible difference. The table shows that an enrichment of as much as eight times, occurs in all but four samples, with typical values of 2 to 3.

There appear to be two contrasting types of fault, referred to here as compact (C) or porous (P). Compact faults (Plates 5.7b, 5.8) have negligible matrix porosity, a high proportion of matrix to fragments, and usually sharp, planar walls. They occur in low-porosity rocks with types 1 or 2 grain boundaries and porosity. They contrast with porous faults which may have considerable matrix porosity (Plate 5.9a), cutting both matrix and intact rock, a lower proportion of matrix to fragments and diffuse irregular walls. Fragments in the matrix have a much more distributed range of grain size in faults. The width of both types of fault may vary irregularly, more so in P than C faults, and transgranulars may cut across faults without any deviation or discrimination between fragments and matrix.

Microstructural controls on faulting were evaluated by making correlations between the proportion of shear matrix averaged for all three perpendicular sections in each sample and other microstructural parameters. There is a negative correlation with both existing and pre-cataclastic porosity (Figures 5.23, 5.24). Figure 5.25 shows that there is an excellent positive correlation between the percentage of shear matrix and geometric mean of linear intercepts (G.M.L.). Also tested were relationships with total iron oxide, proportion of clay matrix, and geometric mean of extinction angles, but no correlations could be identified.

Microfractures clearly play an essential role in the formation of faults. However, close observation of fault terminations and the character of microfracture suggests that the simple model of Blenkinsop and Rutter (1986), in which faults form by linking of a network of intragranular, impingement-induced microcracks, is not applicable. Many faults terminate in pure mode 1, transgranular cracks similar to other such fractures throughout the unsheared body of the rock. It would appear that these longer, single microfractures may form before faulting and subsequently localise shear displacement. Not only are such transgranulars clearly truncated by faults, but the narrowest faults have very planar geometries identical to the transgranulars, and perhaps most convincingly of all the evidence, intragranular microcrack densities in the body of intact rock, even immediately adjacent to faults, are far too low to allow the linking of these to form a continuous shear fracture. Fault formation by shear along pre-existing transgranular microcracks is a significantly different mechanism to linking of short axial and grain boundary cracks observed in experiments (e.g. Peng and Johnson 1972, Hallbauer, Wagner and Cook 1973).

The continuous development of microfractures with shear matrix must mean that work hardening is occurring. At least four possible mechanisms have been suggested:

i) Mutual interference of slip systems (Oertel 1965).

ii) Interlocking of asperities on either side of a fault, or fragments

FIGURE 5.23

The relation between percentage of shear matrix (3+4) and existing porosity (7). A negative correlation is observed due to the generally cemented nature of the shear matrix.

FIGURE 5.24

The relation between percentage of shear matrix (3+4) and pre-cataclastic porosity (8). A negative correlation is observed.

FIGURE 5.25

The relation between percentage of shear matrix (3+4) and Geometric Mean of Linear Intercepts (G.M.L.). An excellent positive correlation is observed.

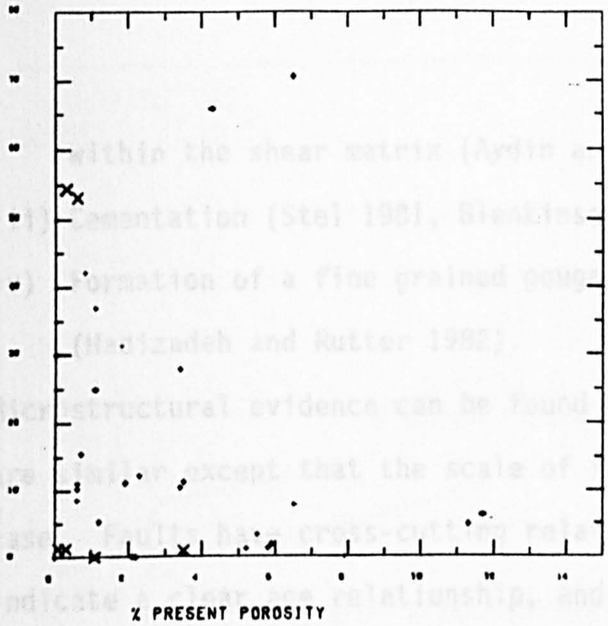
% SHEAR MATRIX
% PRESENT POROSITY

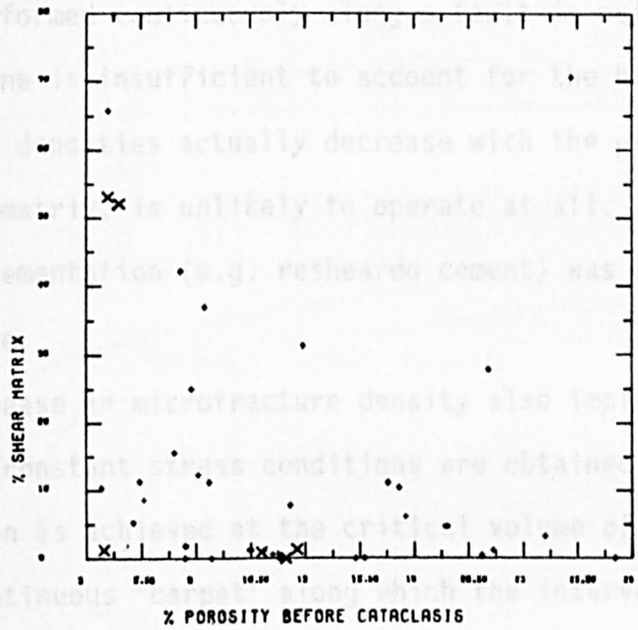
% SHEAR MATRIX
% POROSITY BEFORE CATACLASIS

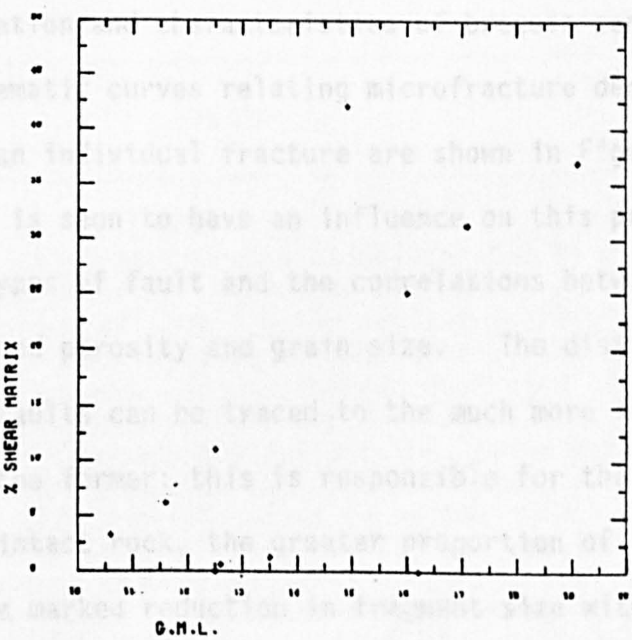
% SHEAR MATRIX
G.M.L.

within the shear matrix (Aydin and Johnson, 1983).

iii) Cementation (Stel 1981, Blenkinsop and Rutter 1986).

iv) Formation of a fine grained gouge with a high coefficient of friction (Hadizadeh and Rutter 1982).

Microstructural evidence can be found for the first two mechanisms, which are similar except that the scale of interlocking is smaller in the second case. Faults have cross-cutting relationships in section which do not indicate a clear age relationship, and also have variable widths of shear matrix suggesting considerable asperities. The fact that a fine-grained gouge is not formed continuously along a fault is evidence that this mechanism alone is insufficient to account for the hardening, and because microfracture densities actually decrease with the production of more than 25-30% shear matrix, is unlikely to operate at all. No clear evidence for the role of cementation (e.g. resheared cement) was seen, but it may have been operative.

The decrease in microfracture density also implies that strain softening or constant stress conditions are obtained. It is possible that this condition is achieved at the critical volume of shear matrix (25-30%) to form a continuous 'carpet' along which the intervening intact blocks can flow, and which can surround any fragments within the fault. This criterion explains the formation and characteristics of breccia zones rather satisfactorily. Schematic curves relating microfracture density to shear matrix and stress on an individual fracture are shown in Figure 5.26.

Initial microstructure is seen to have an influence on this process from the existence of two types of fault and the correlations between the proportion of shear matrix and porosity and grain size. The distinction between compact and porous faults can be traced to the much more important role of microfracturing in the former: this is responsible for the sharp boundary between fault and intact rock, the greater proportion of fine-grained matrix, and the marked reduction in fragment size within the

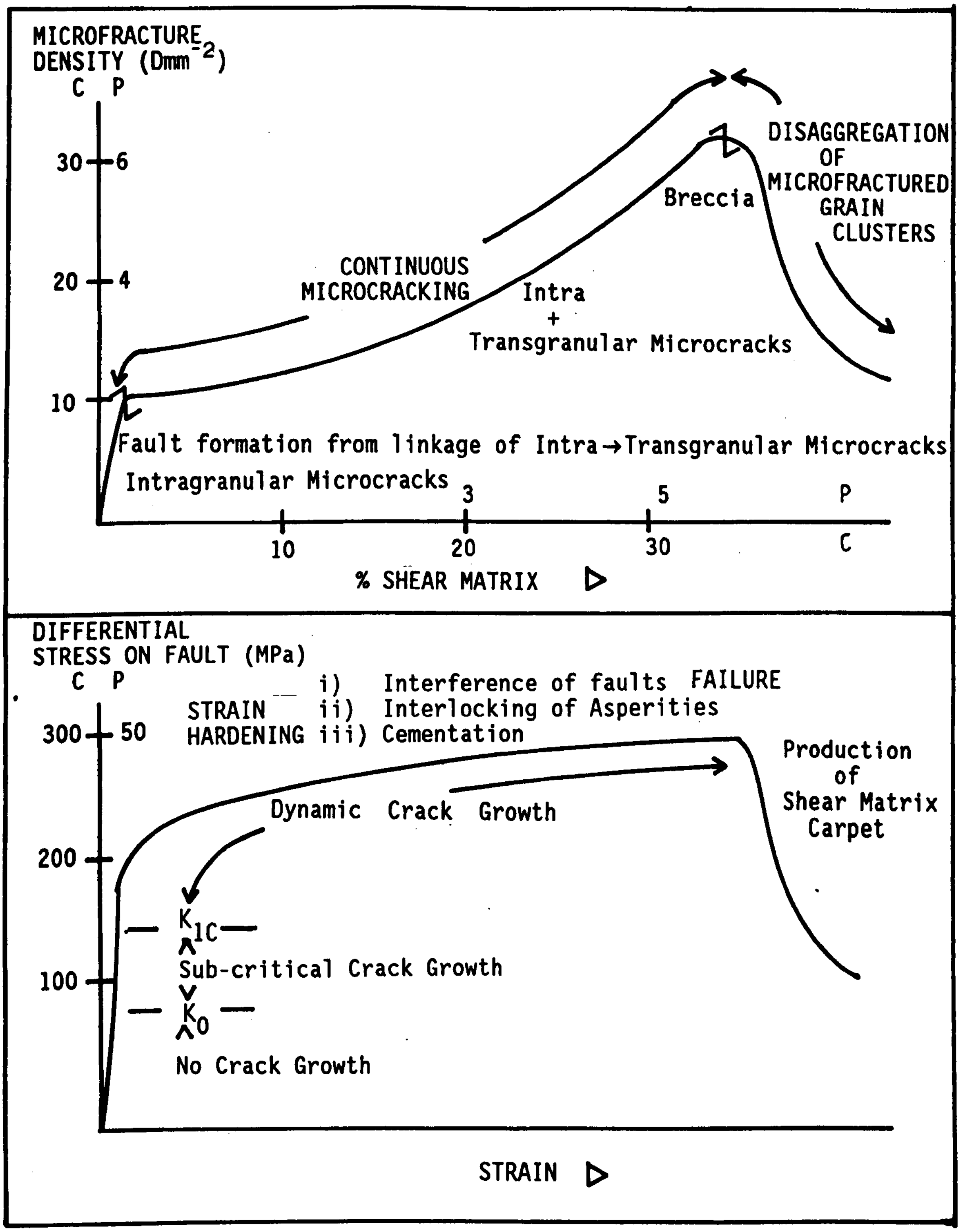

FIGURE 5.26

a) Schematic evolution of microfracture density (Dmm^{-2}) with proportion of shear matrix. Microfracture densities continue to increase to a maximum of 30mm^{-2} after fault formation until the proportion of shear matrix rises to 30%, after which they decrease as microfractured aggregates are destroyed in a breccia and a continuous carpet of shear matrix is formed. The figures given above are for compact (C) faults; the equivalent values for porous (P) faults are shown on the ordinate abscissa.

b) Suggested stress-strain relationship on an individual fault shown at s me stages as (a). Continuous microcrack formation implies the strain hardening; the formation of a breccia zone may occur at the peak stress. The stress-strain relationship for the whole fold can be envisaged as the sum of many such individual fault stress histories.

matrix. Porous faults, on the other hand, do not have such clear distinctions between shear matrix and intact rock because of their lower fracture densities, and they never develop very high proportions of shear matrix. The negative correlation between proportion of shear matrix and present porosity is expected due to the lower porosity of the shear matrix; the same trend with B.C. porosity is due to this lack of high proportions of shear matrix in the rocks with porous faults and initial microstructure. The grain size correlations also reflect the fact that porous faults develop in rocks with low grain size.

5.4.5 Minor Components

a) Iron Oxides/Hydroxides. Iron oxides are a ubiquitous component of the quartzites and sandstones, reaching proportions as high as 22% (columns 4 and 5, Appendix A3). At least two phases are present: one light brown and semi-opaque, the other dark red/brown to opaque. They occur in amorphous patches, in all types of porosity, as discrete rounded grains within intact rock, and concentrated in all types of microfracture and in fault matrix. Their distribution even on the scale of a thin section, is highly irregular where not obviously fracture controlled. In sample 105, an oval anulus of width 2-3mm and outside diameter 10mm could be identified by a complete lack of oxides. This was interpreted as evidence that burrowing activity had affected the oxide distribution. To investigate their distribution in more detail, Figures 5.27 and 5.28 show the relationship between the percentage total iron oxide content (4 and 5) and existing porosity (7) and porosity estimated before cataclasis (B.C.) (8) respectively. No correlation can be said to exist with present porosity; however there is a very clear correlation with B.C. porosity. There is no correlation between the total oxide content and the proportion of shear matrix.

FIGURE 5.27

The relation between total iron oxide content (4+5) and existing porosity (7). No correlation exists.

FIGURE 5.28

The relation between total iron oxide content (4+5) and pre-cataclastic porosity (8). In contrast to Figure 5.27, there is a clear correlation with pre-cataclastic porosity.

FIGURE 5.29

The relation between Geometric Mean of Extinction Angles (G.M.A.) and Fracture Density (Dmm^{-1}). A reasonable positive correlation exists.

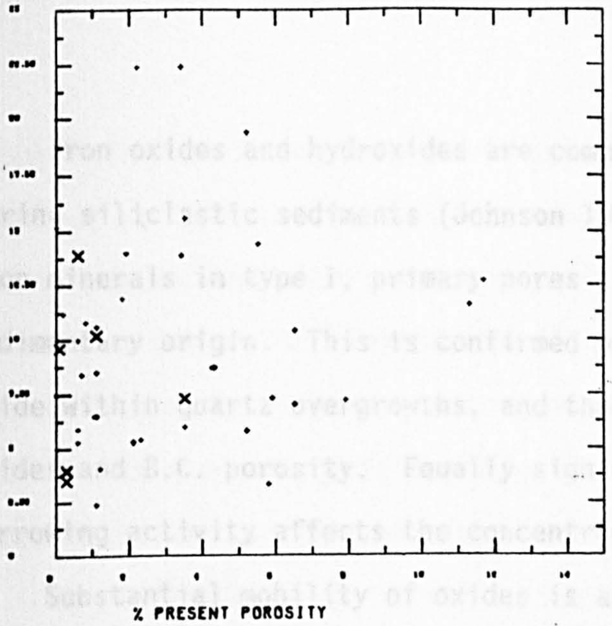

Iron oxides and hydroxides are common authigenic minerals in shallow marine siliclastic sediments (Johnson 1978), and the distribution of the iron minerals in type 1, primary pores is clear evidence for its sedimentary origin. This is confirmed by the inclusion of small patches of oxide within quartz overgrowths, and the good correlation between iron oxide and B.C. porosity. Equally significant is the observation that burrowing activity affects the concentration of oxides.

Substantial mobility of oxides is apparent during all stages of cataclasis from the oxide filling of microfractures and the concentration of oxides in shear matrix, [illegible] from its presence even in porosity cutting shear matrix. A possible secondary source for this oxide is the nearby highly ferruginous San Pedro Formation, but the lack of correlation between the total oxide content and either existing porosity, or the enriched shear matrix, indicates that the majority of the oxide is merely redistributed within the quartzite. This is also evidence for the importance of a fluid phase during cataclasis, although it does not give any information about fluid pressure.

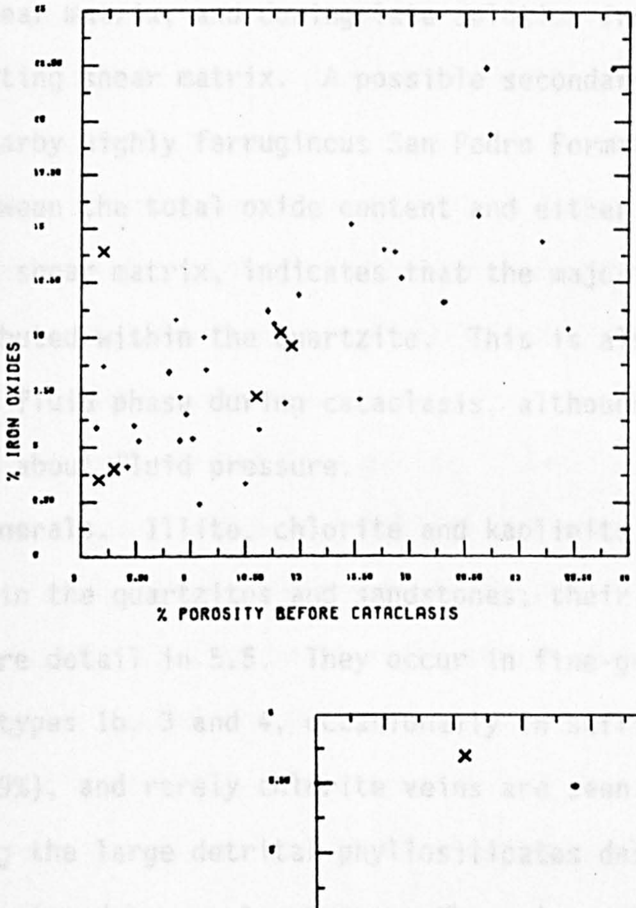

b) Clay Minerals. Illite, chlorite and kaolinite have all been identified within the quartzites and sandstones; their clay mineralogy is discussed in more detail in 5.5. They occur in fine-grained aggregates in pore spaces of types 1b, 3 and 4, occasionally in sufficient quantity to form a cement (9%), and rarely kaolinite veins are seen. They can also be seen surrounding the large detrital phyllosilicates described below, where these are not enclosed by quartz grains. There is good positive correlation between proportion of clays (5) and both present and B.C. porosity (7, 8), but no correlation with total iron oxide content. The distribution of clay minerals is more restricted than oxides: they occur mainly within the larger pores having some evidence of solution (types 1b, 3, 4). This together with the correlation between existing porosity and clay content suggests that a substantial component of the clays has been

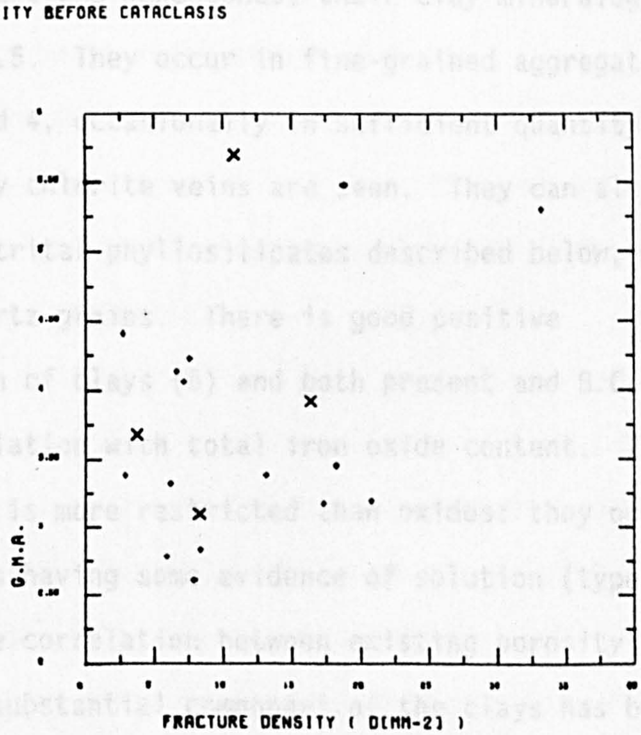

Iron oxides and hydroxides are common authigenic minerals in shallow marine siliclastic sediments (Johnson 1978), and the distribution of the iron minerals in type 1, primary pores is clear evidence for its sedimentary origin. This is confirmed by the inclusion of small patches of oxide within quartz overgrowths, and the good correlation between iron oxides and B.C. porosity. Equally significant is the observation that burrowing activity affects the concentration of oxides.

Substantial mobility of oxides is apparent during all stages of cataclasis from the oxide filling of microfractures and the concentration of oxides in shear matrix, and during late solution from its presence even in porosity cutting shear matrix. A possible secondary source for this oxide is the nearby highly ferruginous San Pedro Formation, but the lack of correlation between the total oxide content and either existing porosity, or the enriched shear matrix, indicates that the majority of the oxide is merely redistributed within the quartzite. This is also evidence for the importance of a fluid phase during cataclasis, although it does not give any information about fluid pressure.

b) Clay Minerals. Illite, chlorite and kaolinite have all been identified within the quartzites and sandstones; their clay mineralogy is discussed in more detail in 5.5. They occur in fine-grained aggregates in pore spaces of types 1b, 3 and 4, occasionally in sufficient quantity to form a cement (9%), and rarely chlorite veins are seen. They can also be seen surrounding the large detrital phyllosilicates described below, where these are not enclosed by quartz grains. There is good positive correlation between proportion of clays (6) and both present and B.C. porosity (7, 8), but no correlation with total iron oxide content. The distribution of clay minerals is more restricted than oxides: they occur mainly within the larger pores having some evidence of solution (types 1b, 3, 4). This together with the correlation between existing porosity and clay content suggests that a substantial component of the clays has been deposited after the oxides, and after cataclasis. Clays can also be observed as fillings of microfractures, and generally where both clays and oxides are present within the same pore, they form a rim around a clay core. The texture of large phyllosilicates surrounded by fine-grained clays is taken to indicate a retrogressive reaction which could provide the source. However, there is probably also a component of authigenic clay, revealed by the correlation between clay content and B.C. porosity.

c) Phyllosilicates. Large grains of white phyllosilicates are a common constituent of the sandstones. These are up to 0.2mm long, have an aspect ratio of about 0.1 and are parallel to bedding. An interesting feature of most grains is their strained or kinked appearance; they may be bent around adjacent quartz grains or crushed in pores between grains. Even more dramatic deformation is seen in Plate 5.9b, where a single grain is shown sheared into two parts connected by a very thin strand between adjacent quartz grains. The bedding parallel fabric of these phyllosilicates, together with the evidence for retrogression leaves no doubt that they are primary detrital grains. Their most significant aspect is their strained texture which is excellent evidence for the action of grain boundary sliding between adjacent quartz grains, that cannot be detected otherwise for lack of small scale strain markers.

d) Accessories. There are negligible amounts of other components in the quartzites and even in the sandstones: a very few grains of heavy minerals, very rare feldspars, and lithic fragments. These all have similar grain size and shapes to the quartz grains.

5.4.6 Optical Strain Features

The most noticeable optical strain feature is a very small amount of distributed undulatory extinction (G.M.A.). The geometric mean of extinction angles (G.M.A.) from all samples at Cremenes in the Bernesga Valley and Luna Lake fall within a very small range of low values from 2.6°

to 5.9^0, with average of 2.787, 3.696 and 3.367^0 respectively. The results of the measurements are given in Appendix A7, and histograms of all the sample measurements are shown in Appendix A10. The histograms show absolutely consistent features, including a strong positive skew and virtually no grains with A greater than 25^0. There is no relationship between G.M.A. and structural position in the Bernesga Valley, nor any systematic difference between the G.M.A. values at the three places. There is quite a reasonable correlation between G.M.A. and fracture density (Dmm^{-1}) (Figure 5.29) and fracture density (DG^{-1}), but no correlation between G.M.A. and percentage of shear matrix (3+4).

Between 5 and 50% of grains show localised strain features, either kink bands or large subgrains. The proportion of such grains correlates with G.M.A. to the same degree as fracture density. Of the four factors that may affect the extinction angle of an individual grain and G.M.A. of a sample (intracrystalline plasticity, rotation of grain parts by microfracturing, cementation and inherited strain features from the source (3.8)), the lack of relation between G.M.A. and structural position (e.g. distance from thrust plane or position around fold axis) would indicate that crystal plasticity is not important as a deformation mechanism; this is confirmed by the lack of any evidence for crystal plasticity contributing towards a shape fabric, and indeed by the lack of any relation between the shape fabric and structural position. Nevertheless, small amounts of crystal plasticity cannot be completely ruled out as a cause of variation in G.M.A.

The role of microfractures in determining G.M.A. is strongly suggested by the correlation between G.M.A. and microfracture density (Figure 5.29). Rotations of several degrees occur between adjacent fragments of grains cut by fractures in C.L. Perhaps even more important are quartz crack fills which are slightly misorientated to the host grain. Undulatory extinction induced by microfracture has also been noted by Jamison and Stearns (1982).

Although care was taken to exclude obviously cracked grains, many are not easily distinguished optically from kink bands or elongate sub-grains.

Variations in inherited strain features undoubtedly adds scatter to this relationship. This is indicated by the variation in luminescence between grains within individual samples, due to a variety of quartz types in the source rock of the Barrios quartzite. The weak correlation between percentage of grains with sub-grains or kink bands and G.M.A. can be interpreted by any of the four factors above, but again the lack of relation between these grains and structural position implies that most sub-grains and kink bands are inherited, providing further evidence for this source of variation.

5.4.7 Discussion

It is suggested that the considerable variation in microstructural parameters shown in sections 5.3.1 to 5.3.6 can best be summarised as variations between two end-member microstructures, called compact (C) and porous (P) respectively. Those samples with compact microstructure have medium grain size, types 1 and 2 grain boundaries, types 1a and 2 porosity, present porosities of less than 7%, pre-cataclastic (B.C.) porosities of less than 15%, and clay contents of less than 1%. They may have any amount of shear matrix from 0 to 70% but faults are of the compact (C) type, and any fracture density (Dmm^{-2}) in the observed range from 2-33mm^{-2}. The porous microstructure, on the other hand, have fine grain sizes (less than 0.13 G.M.L.), type 4 grain boundaries, types 3 and 1b porosity, present and B.C. porosities of greater than 7 and 15% respectively, and clay contents of greater than 1%. The following additional limitations apply to the porous microstructures: the proportion of shear matrix is less than 10% in faults of porous type, and fracture densities do not exceed 8mm^{-2}. All the samples in Appendix A2 can be classified into one of the two groups, and they can also be distinguished in most of the correlations in Figures 5.20

to 5.28 based on the point count measurements. Their designation as porous or compact is indicated in Appendix A2.

Five deformation mechanisms have been identified: grain boundary solution transfer, microfracturing, faulting, grain boundary sliding, and kinking or plastic deformation of phyllosilicates. Observed intragranular microfracture mechanisms can be subdivided into impingement-induced microcracking, pre-existing flaw-induced microcracking, including 'grain-edge cracking', possibly cleavage-induced microcracking, and flaw induced microcracking. Transgranular microcracks may form both as unstable extension microcracks, and by linking of intragranular impingement induced microcracks. Grain boundary cracks fall into the pre-existing flaw-induced mechanism.

The suggestion in 5.3.4 that lack of shear fault-induced microcracks is evidence for low confining pressures during cataclasis only underlines the problem of the development of transgranular microcracks from an experimental point of view, since it was shown in 2.2 that high confining pressures promote transgranular microcracks. The other pertinent observation from that review, however, is the enhancement of 'T/I' ratios by dynamic crack growth observed by Swanson. This naturally leads to the suggestion that the transgranular microcracks involved dynamic crack growth, either episodically in a grain-by-grain fashion as depicted in Figure 5.19, or in a single incident in which the crack trajectory was influenced by local impingement geometries.

Two types of faulting occur: compact faults, in which microfracturing is an important process, and porous faults in which the converse is true. There is good evidence that neither crystal plasticity in quartz, nor cleavage formation in phyllosilicates, occurred. The evidence presented here suggests that variations in deformation mechanism are determined primarily by initial microstructure. Grain boundary solution transfer is seen only in the compact microstructure. Large areas of grain to grain contacts are not seen in the porous microstructure: it has been argued that this is a primary feature, and therefore pressure solution probably did not operate to the same extent, if at all. Microcracking occurs in both microstructures but reaches a maximum density of 8mm^{-2} in the porous type. Compact faulting with extensive microcracking, is found in the C type of microstructure, while porous faulting is seen in the other. Good evidence for grain boundary sliding can be found in the porous microstructure, where kinking is also observed in the phyllosilicates. It is proposed here that the action of grain boundary sliding is a crucial difference between the deformation mechanisms of the two microstructures. Microfracture densities never rose to high values in porous microstructures because of stress relief by grain boundary sliding, and faulting occurred by a combination of a limited amount of microfracture in conjunction with grain boundary sliding: thus porous faults have diffuse edges where grains have become detached and shear matrix consisting of whole grains as much as grain fragments.

The distinction between compact and porous microstructures is similar to Hadizadeh's classification into Types 1 and 2 microstructures. Hadizadeh (1980) and Blenkinsop & Rutter (1986) considered that the significance of the distinction was in the relative timing and roles of grain boundary and intragranular, impingement-induced microcracking, with the low porosity well cemented type 1 microstructure suppressing impingement-induced microcracking until after grain boundary cracking had loosened the microstructure, compared to early axial cracking in type 2 microstructures. This study extends this approach to consider that the accommodation of large amounts of strain by grain boundary sliding is the essential distinction between compact and porous microstructures, and furthermore, the distinction persists in the character of the faulting developed: grain boundary sliding remains important during shear faulting of porous microstructures, giving the characteristics of the porous microfaults.

A very important question to answer is why such different microstructures and mechanisms could exist and persist in a similar environment. The major difference is clearly the complete cementation of the compact microstructure. Lack of cementation in the porous microstructure implies lack of access of fluids, which may have been excluded by shale permeability barriers within these generally interbedded sequences. Another interesting contrast between the microstructures is the grain size. It is also possible that with the finer grain size of the porous microstructure, the initial cementation of just a few smaller pores cut off further fluid access, but in the cemented microstructure, permeability was ensured until almost total cementation: the last fluid access occurring by the circular type 2 pores. Subsequent cementation was prevented by continuous grain boundary sliding. In this case, the grain size becomes ultimately the most important microstructural parameter.

A relative chronology can be given for some aspects of the microscopic deformation. After compaction and production of the primary bedding parallel fabric (by either or both compaction and deposition), cementation almost to completion must have been the first stage in the compact microstructure and possibly to a limited extent in the porous type. Intragranular microcracking, together with mobilisation of iron oxides, followed in both cases. Transgranular microcracking began subsequently and persisted with intragranular cracking while faults formed. Grain boundary sliding accompanied all these processes in the porous microstructure. In most cases, only a limited amount of shear matrix formed, but exceptionally in breccia zones proportions greater than 25-30% were reached, at which point microcracking decreased and microcracked aggregates were broken up. Substantial fluid flow occurred, redepositing iron oxides from intact rock into shear matrix. Cementation of shear matrix accompanied or followed in compact microstructures. A few transgranulars continued to cut the cemented faults. Pervasive solution followed in the porous microstructure, across both relatively intact rock and shear matrix, continuing to redistribute oxides and clay minerals; retrogression of phyllosilicates, where the fluids had access, may have provided some source material, and the solution of the porous microstructure may have provided the source for later cement of the compact rocks.

5.5 ILLITE CRYSTALLINITY AND CLAY MINERALOGY

5.5.1 Results

a) Illite Crystallinity. The results of all the illite crystallinity determinations are given in Appendix A8 as Kubler and Weaver Indices with errors. With the exception of a single anchizone result, the values from Cremenes, Bernesga Valley and Luna Lake are all within the diagenetic zone as defined in Chapter 4; there is a large spread of values over the entire diagenetic zone ranging from 0.4 to $1^{o}2\theta$ (Kubler Index), and no systematic regional variation. The distribution of crystallinity on a map shown in Figure 5.30, and the same data is presented on a N-S cross-section in Figure 5.31, in which the sample points have been projected, along the plunge of the major folds onto the line of section. In many of the following diagrams, the results have been subdivided into two broad lithological types: quartzites plus sandstones, and shales. Where not otherwise distinguished, the 0.45-2μ fraction has been used. The map and section show that no clear change of crystallinity can be associated with the hinges of the major folds. The distribution on the map and section is not easy to interpret, so the data has been plotted on a 'stratigraphic log' through the Rozo and Pozo thrust sheets in Figure 5.32 and 5.33, and these are compared in Figure 5.34. These logs are prepared by measuring the thickness of each formation and plotting the sample at the correct height with respect to the horizontal formation boundaries, irrespective of structure. They show firstly that there are profound differences between

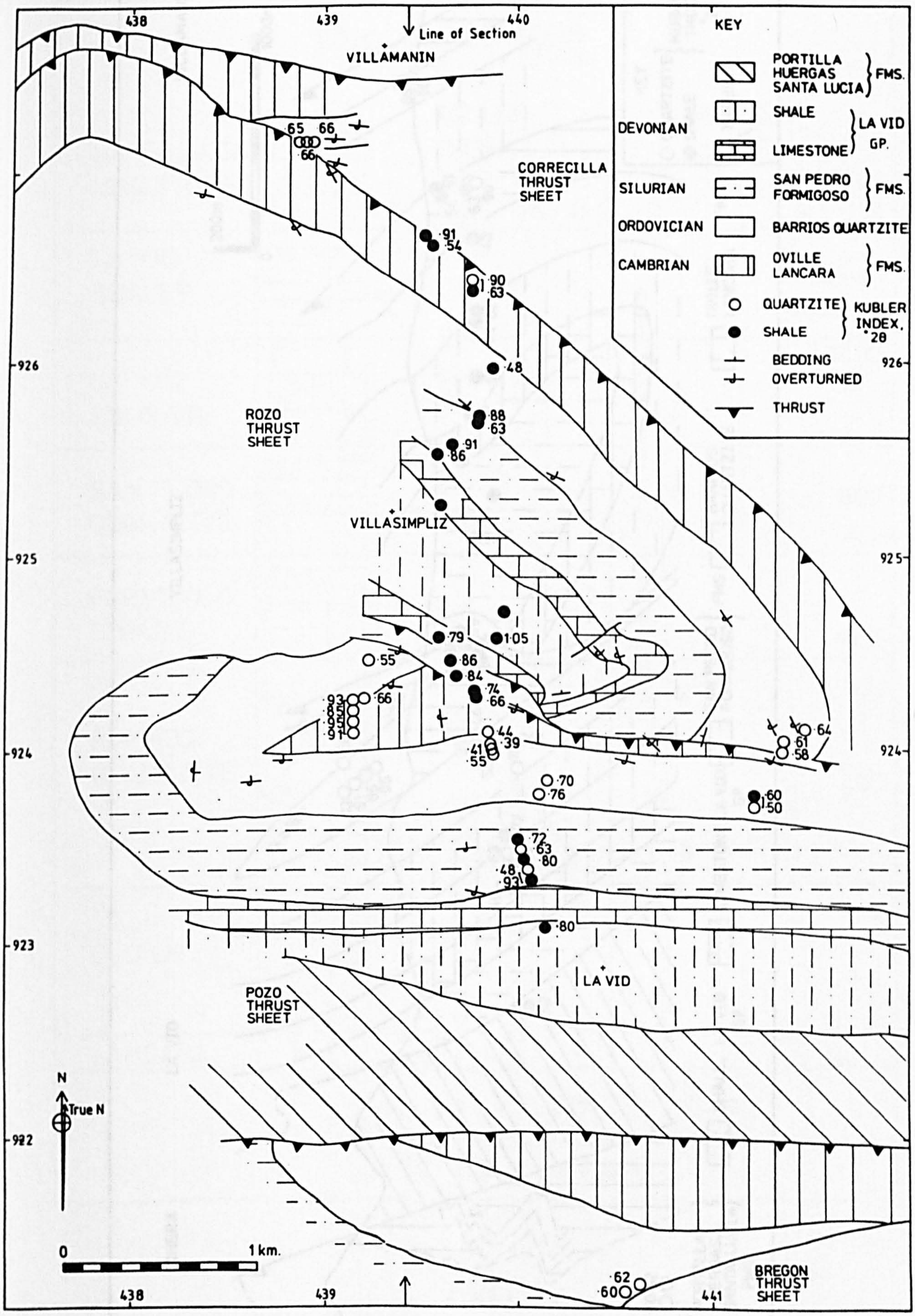

FIGURE 5.30
Illite crystallinity in the Bernesga Valley.

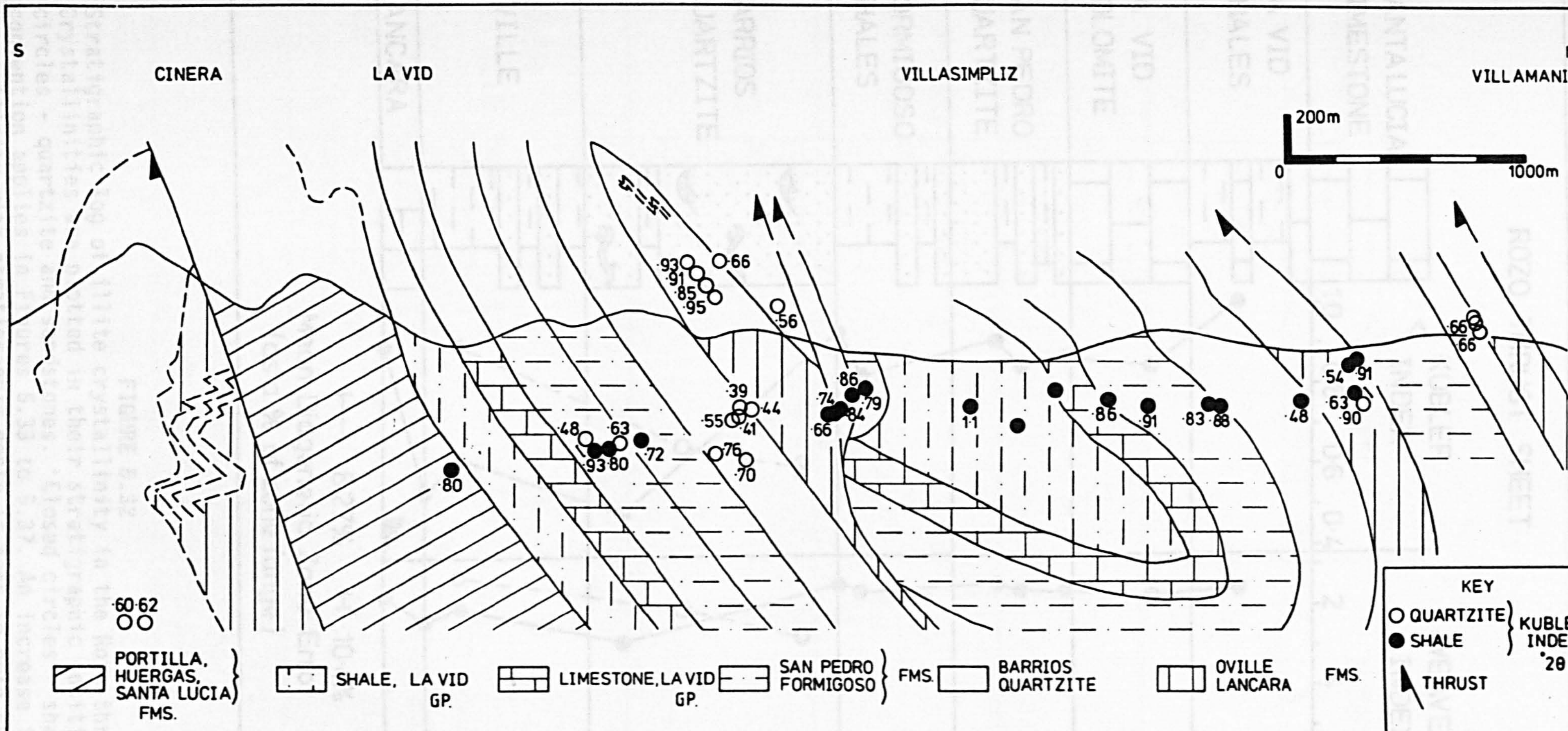

FIGURE 5.31

Illite crystallinity on cross-section of the Bernesga Valley. Sampling points have been projected along plunge onto line of section.

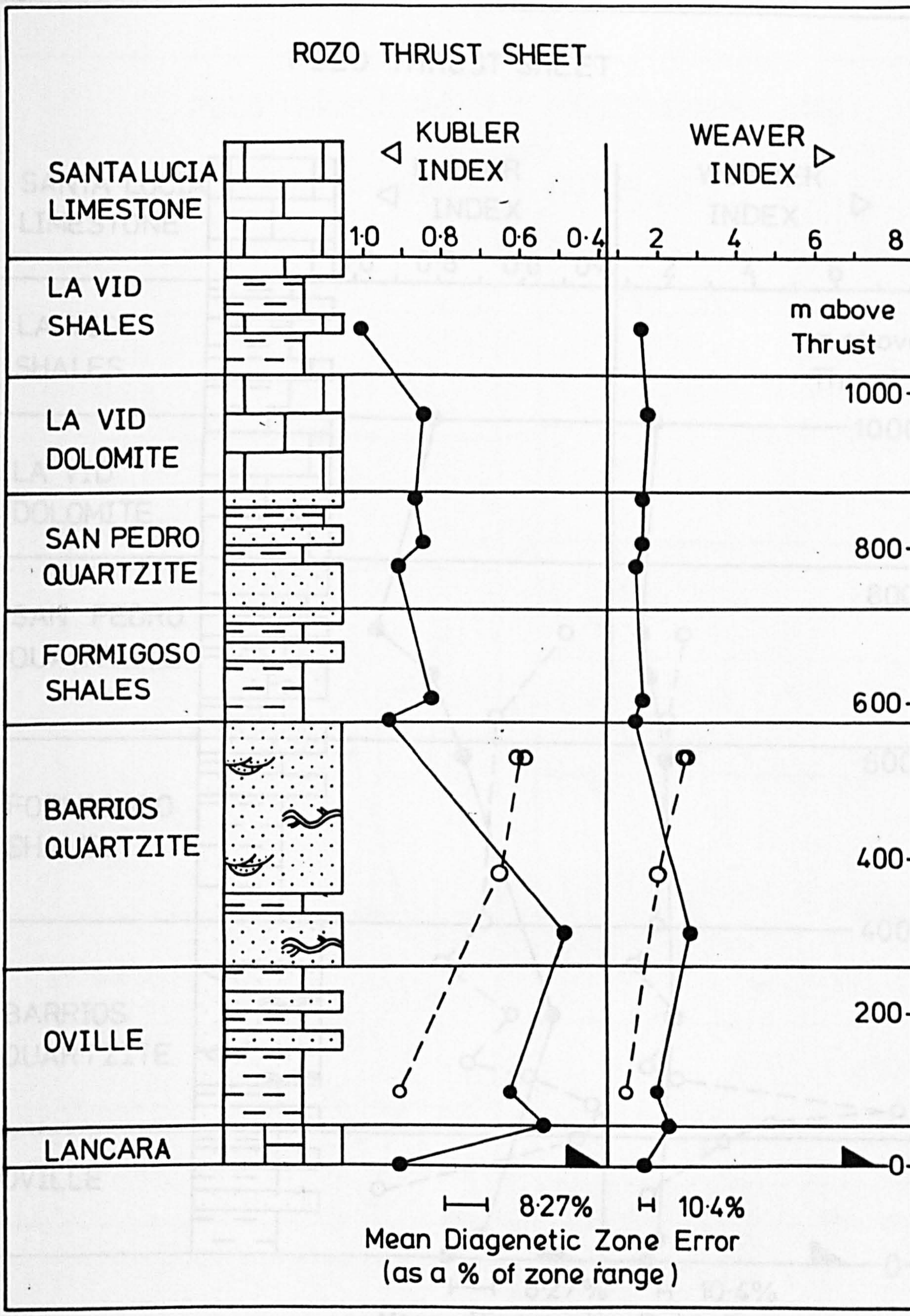

FIGURE 5.32
Stratigraphic log of illite crystallinity in the Rozo thrust sheet. Crystallinities are plotted in their stratigraphic position. Open circles - quartzite and sandstones. Closed circles - shales. This convention applies in Figures 5.33 to 5.37. An increase in shale crystallinity with stratigraphic depth is seen in both Kubler and Weaver Indices.

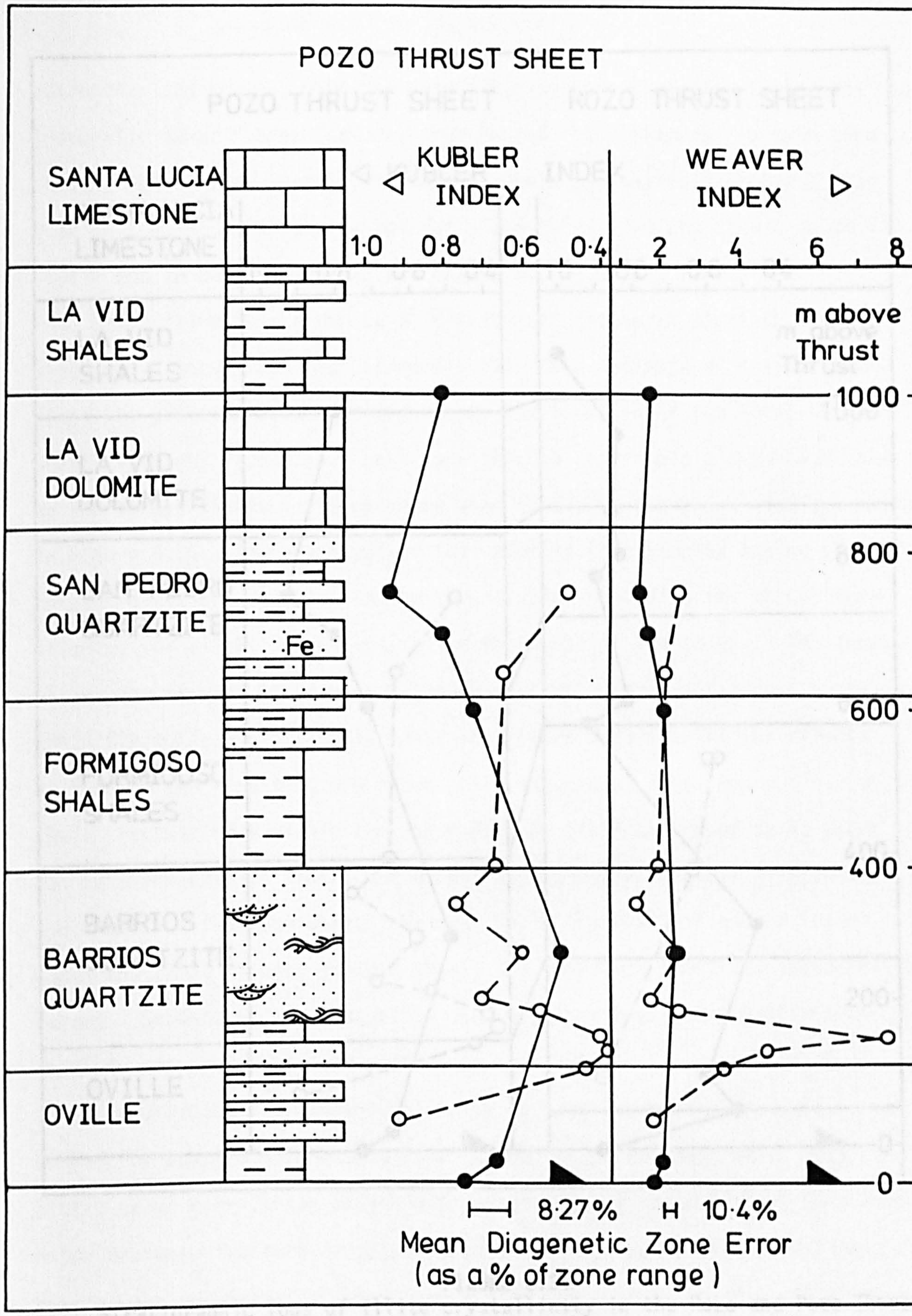

FIGURE 5.33

Stratigraphic log of illite crystallinity in the Pozo Thrust Sheet. Crystallinities are plotted in their stratigraphic position. There is an increase in shale crystallinity with stratigraphic depth.

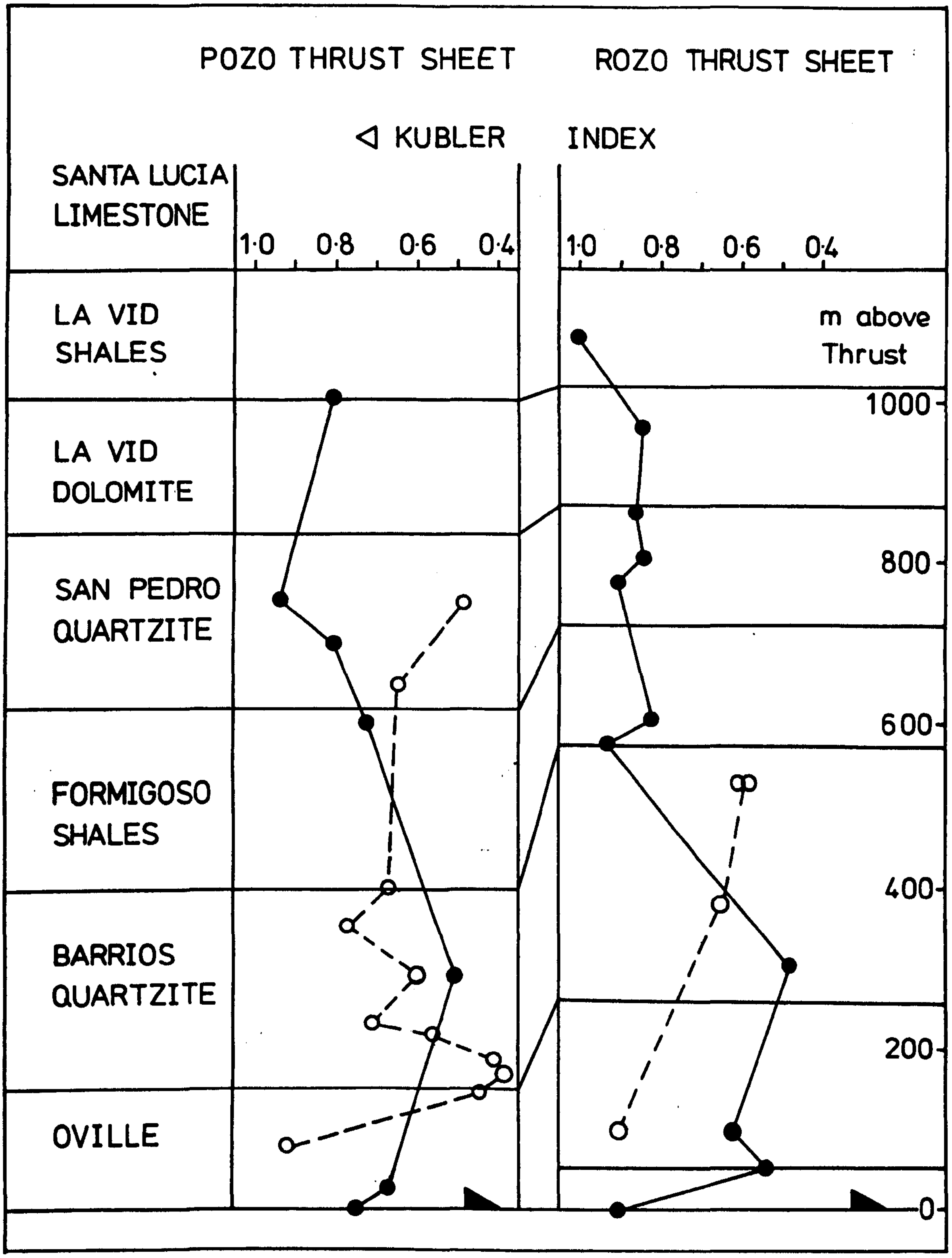

FIGURE 5.34

Stratigraphic logs of illite crystallinity in the Rozo and Pozo Thrust Sheets compared. Both thrust sheets show an increase in shale crystallinity with stratigraphic depth over the same range of Kubler indices in the diagenetic zone. This is interpreted as a preserved burial diagenetic gradient.

quartzites and shales, with the former having more variable crystallinities (generally lower Kubler Indices) than shales. Furthermore, in both thrust sheets, there is an overall increase in shale crystallinity towards the base of the thrust sheet, except for a low value from the thrust gouge itself and in both sandstones and shales of the Oville Formation.

Crystallinity is shown as a function of structural position by plotting a 'structural log' (Figure 5.35). The ordinate of this diagram, R, is the position of a sample given by its fraction of the total thrust sheet thickness from 0 to 1 on a line through the sample and perpendicular to the thrust sheets. The geometry used to derive the value of R is shown in Figure 5.36. The advantage of this plot is that samples can be shown in correct positions relative to the thrust planes bounding the thrust sheet, allowing for slight variations in the thickness of the sheets. The thrust planes are assumed to be planar with a constant dip of 70^0 to the north. The differencefrom the stratigraphic log, therefore, is that the effects of folding and thrusting are shown. The structural logs show a minimum in shale crystallinity within the upper part of the Rozo thrust sheet where the syncline axis is found, and a decrease in shale crystallinity towards the centre of the Pozo sheet. Maximum shale crystallinities are found above the basal thrusts in each sheet: the imbricate sheet has intermediate values. Sandstones and quartzites have highly variable crystallinities, which do not show a similar pattern to the shales.

Correlations between crystallinity and microstructural parameters were tested for quartzites and sandstones using the point count data. Very little or no correlation exists with percentage of shear matrix, total iron oxide content, fracture density or G.M.A. A fair positive correlation exists with proportion of clay, and a good correlation exists with present porosity, but not with B.C. porosity.

Finally, the effect of size fraction on crystallinity was measured for the two lithologies (Figure 5.37). For quartzites and sandstones very

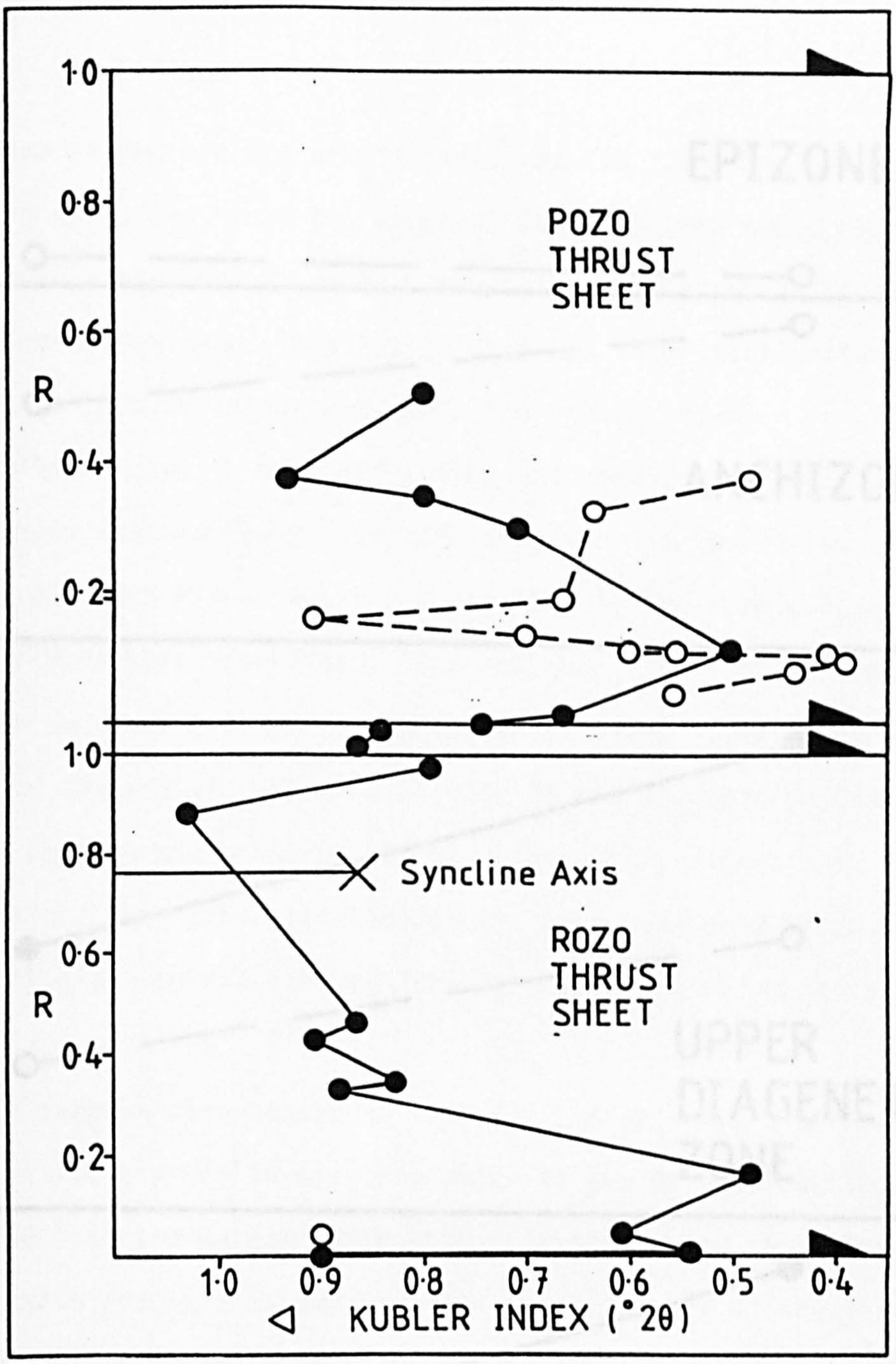

FIGURE 5.35
Structural logs of illite crystallinity in the Rozo and Pozo thrust sheets. Crystallinities are plotted in their structural position relative to the thrust plane, minimum shale crystallinity in the Rozo thrust sheet coincides with the highest stratigraphical level and the syncline axis.

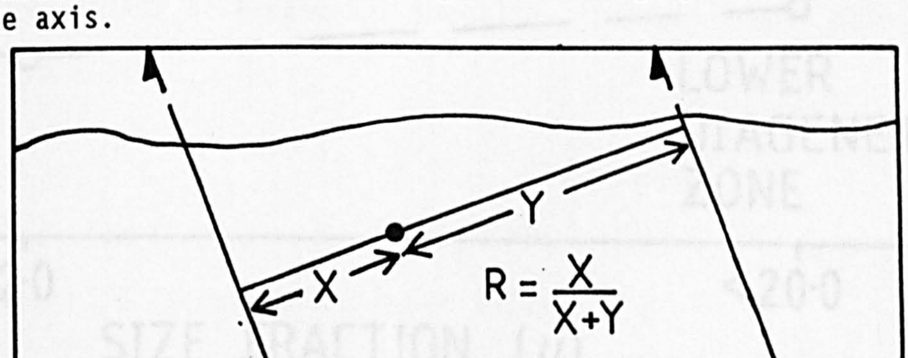

FIGURE 5.36
R, the ordinate of the structural log, is the distance of the sample above basal thrust normalised by the thickness of the thrust sheet perpendicular to strike at the sampling locality. Thrusts are assumed to be planar and dip to the north at 70°.

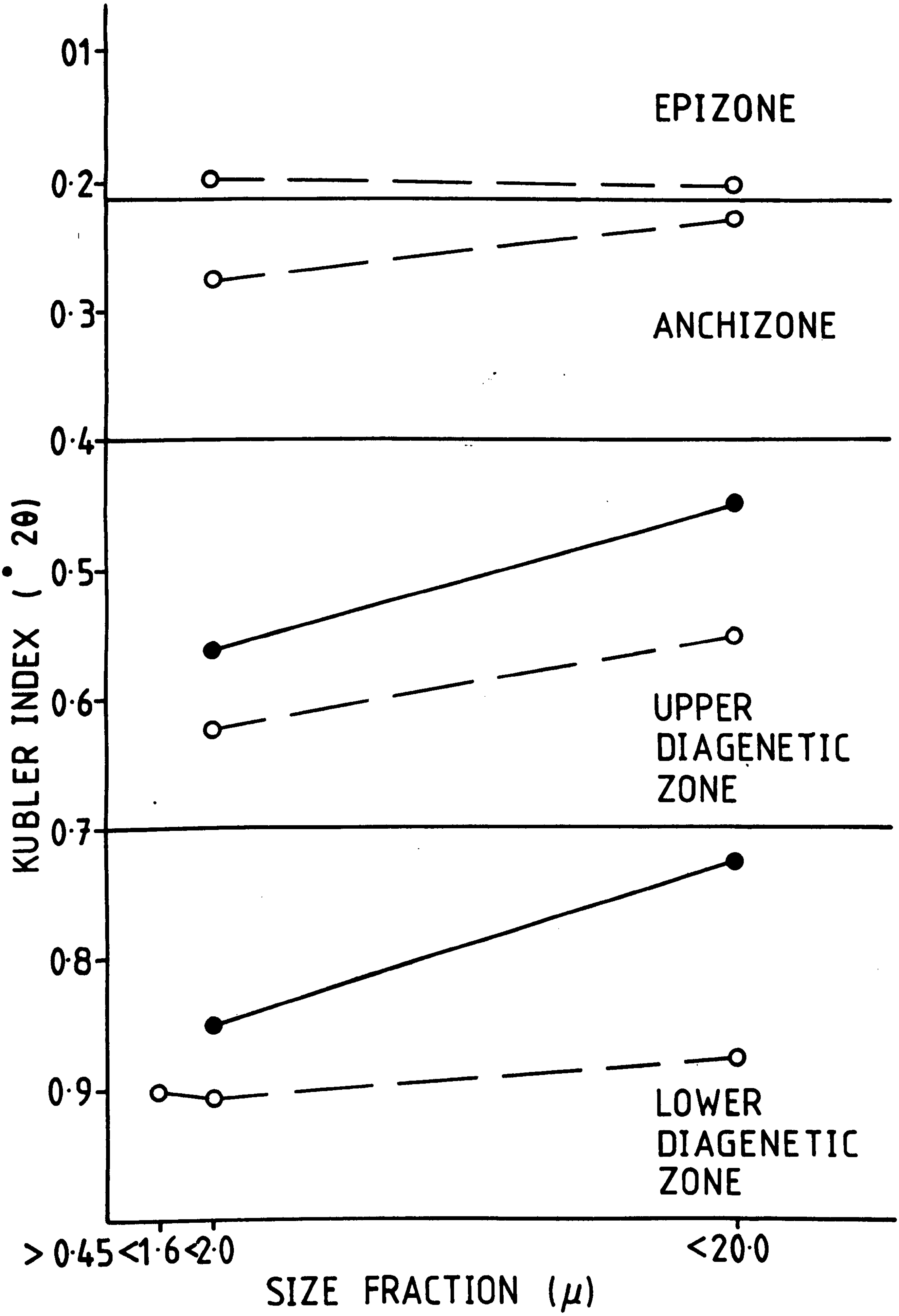

FIGURE 5.37

Effect of Size Fraction on average illite crystallinity in shales (solid circles) and quartzites (open circles). Shales have a significantly greater crystallinity in larger size fractions; a very small increase in crystallinity with size is seen for sandstones and quartzites.

small increases in the average crystallinity as the size fraction increased from less than 2μ to less than 20μ occur in the anchizone and upper and lower diagenetic zones, and an equally small increase occur in the epizone. The shales showed much more significant increases in crystallinity with size fraction in both the upper and lower diagenetic zones.

b) Clay Mineralogy. X-Ray diffraction was used to analyse a small number of samples qualitatively. Illite, chlorite and kaolinite, illite-smectite random mixed layers and possibly illite-vermiculite random-mixed layers were identified. Barrios quartzite samples consist only of illite and kaolinite +/- chlorite, while mixed layers occur additionally in the shales. Samples 22, 23, 28 and 32, 33 from Cremenes and Luna Lake confirm the presence of these three clay minerals in the Barrios quartzite. The rather limited results have been used to deduce the distribution of clay minerals through the stratigraphic column as shown in Figure 5.38.

The shale samples were chosen to test for the presence of mixed layers by their low illite crystallinity, from which it can be inferred that mixed layers would be detected in any shale with a crystallinity lower than 0.900. It is also possible to say from the shapes of the illite peaks in samples with higher crystallinities that mixed layers are likely to be a very minor phase if present at all.

The well defined 17Å peak after glycolation in sample 147 was used to estimate the proportion of expandable smectite. Estimates were obtained from the four methods:

METHOD	% EXPANDABLE
$(001)_{10}$ Peak Position (Reynolds and Hower 1970)	10
$(002)_{10}$ Peak Position (Reynolds and Hower 1970)	0
$\Delta(002)_{10}-(001)_{10}$ (Reynolds and Hower 1970)	20
Saddle-I_{17} Intensity Ratio (Rettke 1981)	57

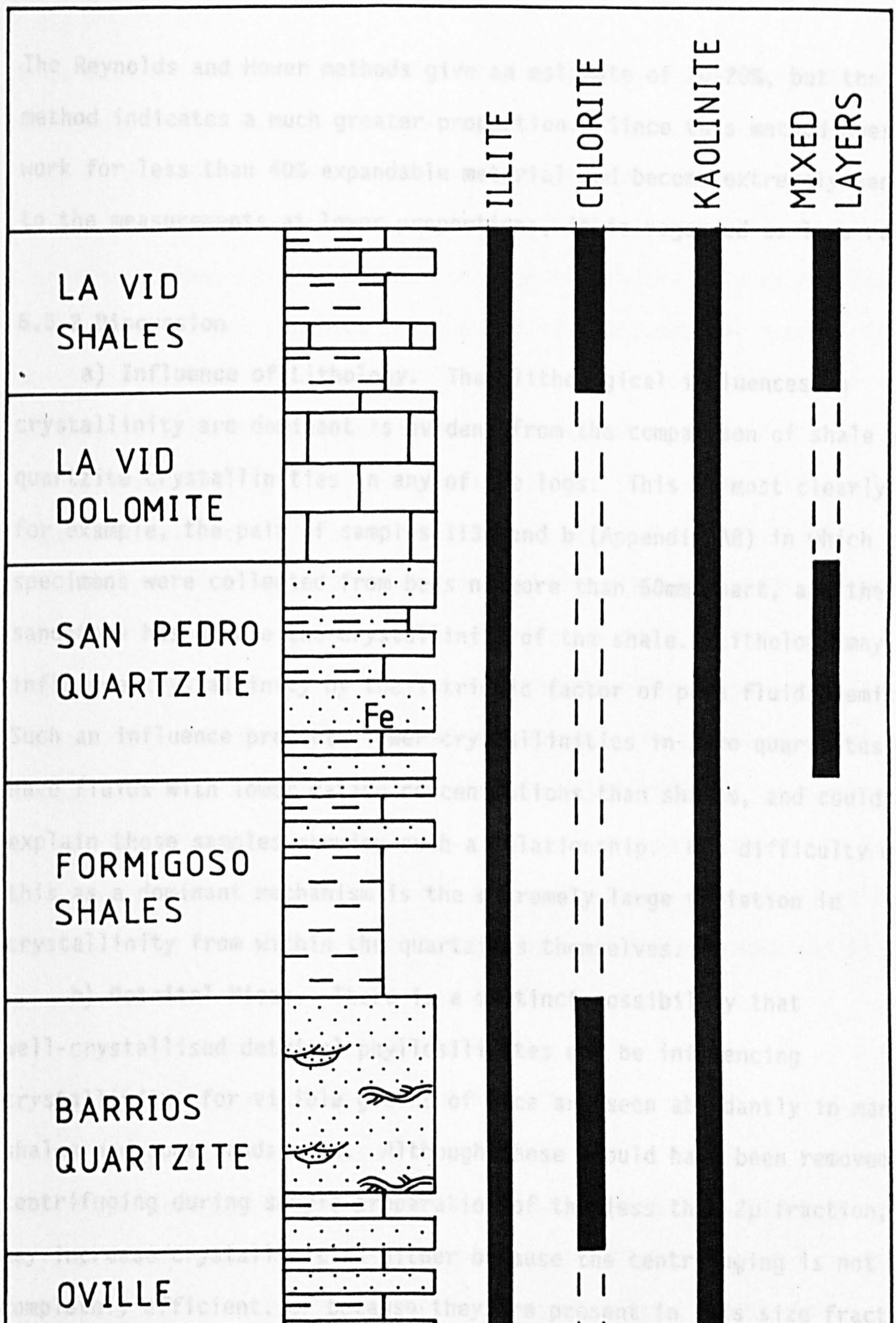

FIGURE 5.38
Distribution of Clay Minerals in the stratigraphic column for Cremenes, Bernesga Valley and Luna Lake.

The Reynolds and Hower methods give an estimate of 10-20%, but the Rettke method indicates a much greater proportion. Since this method does not work for less than 40% expandable material and become extremely sensitive to the measurements at lower proportions, it is regarded as less reliable.

5.5.2 Discussion

a) Influence of Lithology. That lithological influences on crystallinity are dominant is evident from the comparison of shale and quartzite crystallinities in any of the logs. This is most clearly seen in for example, the pair of samples 113a and b (Appendix A8) in which the two specimens were collected from beds no more than 50mm apart, and the sandstone has double the crystallinity of the shale. Lithology may influence crystallinity by the intrinsic factor of pore fluid chemistry. Such an influence predicts lower crystallinities in pure quartzites which have fluids with lower cation concentrations than shales, and could also explain those samples showing such a relationship. One difficulty with this as a dominant mechanism is the extremely large variation in crystallinity from within the quartzites themselves.

b) Detrital Micas. There is a distinct possibility that well-crystallised detrital phyllosilicates may be influencing crystallinity, for visible grains of mica are seen abundantly in many shales and some sandstones. Although these should have been removed by centrifuging during sample preparation of the less than 2μ fraction, they may increase crystallinities either because the centrifuging is not completely efficient, or because they are present in this size fraction following ultrasonic treatment. Analysis of the effect of size fraction does show that increasing the fraction from 2 to 20μ can increase the crystallinity by $0.1^{o}2\theta$, presumably due to this effect (Figure 5.37). It also shows that the effect is greater for shales, and that the average shale crystallinity is higher than sandstone plus quartzite. This mechanism could therefore explain some of the shale/quartzite discrepancies where the former have higher crystallinities. However, two arguments suggest that the mechanism is of minor importance. Firstly, the magnitude of the increase in crystallinity is too small to account for some of the large variations (although this could be attributed to very inefficient centrifuging), and secondly, in the specific instance of samples from the Oville Formation, shale crystallinities remain consistently higher than sandstones although there are abundant micas in the latter.

c) Permeability. The third possibility, that permeability exerts a major control over access of fluids in a relatively large scale circulation, is suggested by the very contrast between shale and quartzite, and confirmed by the good negative correlation that exists between crystallinity and porosity measured in the sandstones and quartzites. This relationship has been tested with present porosity (7), pre-cataclastic (B.C.) porosity, and an intermediate porosity calculated by summing categories 5, 6 and 7 of the point count measurements, which can be taken as porosity after cataclasis but before deposition of iron oxides and clay cements. The correlation coefficients between Kubler Index and these three porosities are:

Pre-cataclastic Porosity	$R = 0.316$
Intermediate Porosity	$R = 0.448$
Present Porosity	$R = 0.568$

This relationship can be interpreted by suggesting that retrogression of crystallinity occurred to an extent controlled by the present porosity, and by inference, permeability. This is strongly supported by the microstructural evidence for retrogression of detrital micas in the porous sandstones. Such a permeability control can explain the major lithological contrasts: the considerable variation in quartzite/sandstone crystallinities, and the contrast between quartzite/sandstone and shales. Anomalies are still found where much higher quartzite/sandstone crystallinities are observed: these imply that at least one other mechanism must be operative.

d) Other 10A Minerals. The fourth extrinsic factor, other 10A minerals, can be discounted as a source of variation in crystallinity since none were detected.

e) Models for the Illite Crystallinity Pattern in the Bernesga Valley. The influence of the four extrinsic variables can be filtered out by examining only the more consistent shale crystallinities. Within both thrust sheets, there is an overall increase in crystallinity towards the basal thrust plane (Figures 5.32 and 5.35). Four possible models for the interaction between deformation and metamorphism can be envisaged.

i) Strain Induced Recrystallisation. Strain induced crystallisation would preferentially occur in high strain areas: along thrust planes or in fold hinges. These two places in fact show some of the lowest crystallinities in both quartzite and shale, for example samples 14-17, and 146 from the antiform and synform hinge areas of the large scale isoclinal fold, and samples 153 and 121 from the thrust planes. There is no regional increase of crystallinity towards the hinges of the fold, and no evidence of fabric development in hand-specimen or thin section.

Samples 14-17 were collected from the limb and hinge of an isoclinal minor fold in a single sandstone bed 100mm thick of the Oville Formation to test for the possibility of strain-induced recrystallisation. The variation in crystallinity from 0.865 to 0.91 is within the average error limits of the Kubler Index determinations, and unsystematic around the fold axis (Figure 5.30). This is conclusive evidence that crystallinity is unrelated to strain.

ii) Shear Heating. Thermal perturbations due to shear heating or access of hot fluids from thrusts might induce recrystallisation along thrust planes. The structural profile (Figure 5.35) was constructed to test for this effect, which would be manifest from an increase in crystallinity towards the thrusts, with a minimum value half way between thrusts, given the reasonable assumption that each thrust would have similar and symmetrical effects in the hanging and footwalls. Figure 5.35 indicates that the minimum shale crystallinity in the Pozo thrust sheet may occur in the centre, but there is only one sample above this position. However the minimum is clearly displaced towards the top of the Rozo thrust sheet. Since maximum shale and quartzite crystallinities in both sheets occur only 200m above the thrust planes, and furthermore the thrust sheet in between the two larger sheets has an intermediate low value of shale crystallinity, shear heating effects can be clearly rejected unless later retrogression has occurred. This model would predict isocrysts parallel to the thrust planes, but these are insufficient samples throughout the mapped area to draw contours.

iii) Thermal Re-equilibriation. The hypothesis of a regional thermal re-equilibrium following stacking of thrust sheets is possibly the easiest to test and reject. A simple pattern of isocrysts, showing a regional decrease in crystallinity towards the south (allowing for lithological variations) would be predicted, shown on the structural profile as a constant upward decrease in crystallinity. Crystallinity variations in either the shales or quartzites cannot support this interpretation (Figure 5.35). This is most evident from the similar range in crystallinity in both thrust sheets, and the sawtooth pattern of crystallinities.

iv) Passive Deformation of preserved burial-diagenetic isograds. The evidence most clearly suggests that isocrysts, established by burial diagenesis, have been passively deformed by folding and thrusting. Identical stratigraphic crystallinity profiles would be anticipated in both thrust sheets with an overall increase in crystallinity with depth. This is observed for the shales (Figure 5.32-34). A rather more complex pattern is predicted for the structural profile due to the effects of folding; the minimum crystallinity should coincide with the syncline axis in the Rozo thrust sheet, with intermediate to low crystallinities in the two samples from the small thrust sheet. Although there are only 2 samples from the latter position, the shales of the Rozo thrust sheet show clearly a minimum crystallinity close to the position of the syncline axis, and the intermediate-low crystallinities typical of the San Pedro Formation shales in the small imbricate thrust sheet. Quartzites do not show systematic variations with either depth or structural position, but crystallinities from each formation have a similar range in both thrust sheets.

The evidence of clay mineralogy shown in Figure 5.38 supports the model of a preserved burial diagenesis well: mixed layers are confined to the top of the stratigraphic column in each thrust sheet, giving a similar distribution to that observed at present in the undeformed sediments of the Gulf coast (e.g. Burst 1969, Hower et al. 1976, Perry and Hower 1977). Lithological controls cannot be eliminated as a possible reason for the lack of mixed layers in the quartzite samples.

Both the illite crystallinities and clay mineralogy reported here correspond remarkably well to the similar study by Brime (1981) in two thrust sheets of the Somiedo-Correcilla Unit at the north end of Luna Lake. Shale samples in both sheets show an overall increase in crystallinity towards the basal thrust. At the junction between the two thrust sheets, there is a similar step to that in Figure 5.32, and it is even possible to match the slightly reduced crystallinities of the Oville Formation samples with those of Figure 5.32. The crystallinities measured in autochthonous shales (San Emiliano Formation) of the foreland at Luna Lake are considerably lower than those of the thrust sheets (which do not preserve this stratigraphic level). Clay minerals are analysed in more detail, to reveal the presence of chlorite only in the very lowest formation (Láncarra Limestone) and the autochthon. Kaolinite is restricted to the formations above the Barrios quartzite, and mixed-layer illite-montmorillorites occur in small quantities throughout the section. The existence of chlorite at both extremes of the stratigraphy, and the distribution of kaolinite, are consistent with the distribution deduced in Figure 5.38, but the presence of mixed layers in the whole column does not agree with the conclusion reached above for the Bernesga Valley. One possible reason for this is the small quantity reported.

5.6 SYNTHESIS

5.6.1 Timing of Deformation

Evidence for the progression of deformation across the whole Cantabrian zone from the Westphallian A in the west to the top of Westphallian in the east was presented in 1.2.1. This also allows the possibility that deformation began even earlier in the Somiedo-Correcilla unit, and evidence for this, and a northwards propagation direction of thrusting, can be deduced from the stratigraphic details given in 5.1. The very earliest interruption to the pre-orogenic Palaeozoic shelf sedimentation is the unconformity at the base of the Ermita formation (Fammenian). Not only is this good evidence for the onset of deformation in the late Devonian, but the increasing size of the unconformity towards the north (Higgins and Wagner-Gentis 1982) can be interpreted rather well as the northward retreat of a peripheral bulge ahead of a foredeep. A second pulse of south-to-north deformation is recorded in another unconformity and transgression at the top of the Ermita Formation, in the early Tournaisian. The Sabero-Gordon line was active at this time, producing the contrast between the generally-deposited black shales of the Vegamian and the crystalline limestones of the Baleas Formation over the line of the discontinuity. The important intra-Viséan unconformity (above the Lavandera Formation) probably does not have any local tectonic significance, since it may be a feature found over a much wider region (N.W. Europe). However the contrast between early Namurian sedimentation from southwest to northeast within the Somiedo-Correcilla unit can be interpreted using the same concept of a foredeep basin, where the Olaja and Olleros Formations were deposited, between the hinterland to the southwest and the carbonate platform to the northeast ('Cantabrian Block', Higgins and Wagner-Gentis 1982).

The tectonic story of the S.W. part of the Somiedo-Correcilla unit can therefore be summarised as two pulses of north travelling transgression in the Fannemian and early Tournaisian, with the establishment of a more permanent basin in the southwest of the area by early Namurian. A significantly new conclusion from this review is that thrusting could have begun as early as late Devonian, and lasted until upper Westphallian.

5.6.2 Deformation Modes and Mechanisms

On a macroscopic scale, it is suggested that the major hangingwall antiform at Cremenes, and the major fold pair in the Rozo and Pozo thrust sheets, both have an element of pre-thrust buckling. There is clearly a variety of hangingwall and footwall geometries in the Cantabrian zone: in many cases there are no associated folds, in some there are hangingwall folds but no apparent footwall folding, and in some there are both hanging- and footwall folds, though this is not generally the case. It is suggested that the exceptional folding in the Rozo and Pozo thrust sheets may be due to a pre-thrusting buckling instability created by one anomalous feature of the Barrios quartzite at this place: it is exceptionally thick. There is no evidence that the thickening is tectonic: a primary thickness variation could trigger an instability leading to buckling during the initial regional compression.

At a mesoscopic scale, deformation modes of the quartzite (exclusively discontinuous and localised fracturing) are contrasted with those of the sandstones (continuous, pervasive kinking). The characteristics of the quartzite fracture network, a bedding normal necklace of at least three sets of simultaneously active faults, are shown to agree well with theoretical models for faulting in response to a three-dimensional strain. Fold accommodation in the quartzite has occurred by the operation of multiple sets of pre-existing fractures and bedding-plane slip(Fig.5.39).This contrasts with sandstones in which pervasive minor kinking has been the fold accommodation mechanism.

Microscopically, five deformation mechanisms have been identified: grain boundary solution transfer, microfracturing, faulting, grain boundary sliding and kinking in phyllosilicates. An important new feature revealed by the microscopic studies is the importance of transgranular microcracks in shear faulting. The quartzites and sandstones have quite different microstructures: compact, microfracture-dominated shear faulting characterises the quartzites, while porous faulting in sandstones is due to large amounts of grain boundary sliding. This contrast can be attributed to variations in the initial microstructure.

Possibly the most significant conclusion of this chapter is that the mesoscopic deformation features can be very closely linked with the microscopic mechanisms and are controlled by them and therefore by the initial microstructure. Quartzites with a compact microstructure deform by microfracture-dominated faulting, while sandstones with a porous microstructure deform by grain boundary sliding and kinking. These observations provide a physical interpretation for the properties required in localisation theories to explain the fracturing/folding distinction. Both types of deformation mechanism are cataclastic, but the difference between them determines the strain distribution and continuity, and is itself ultimately determined by the initial microstructure. Thus the compact/porous microstructural distinction has great significance on both the microscopic and mesoscopic scales.

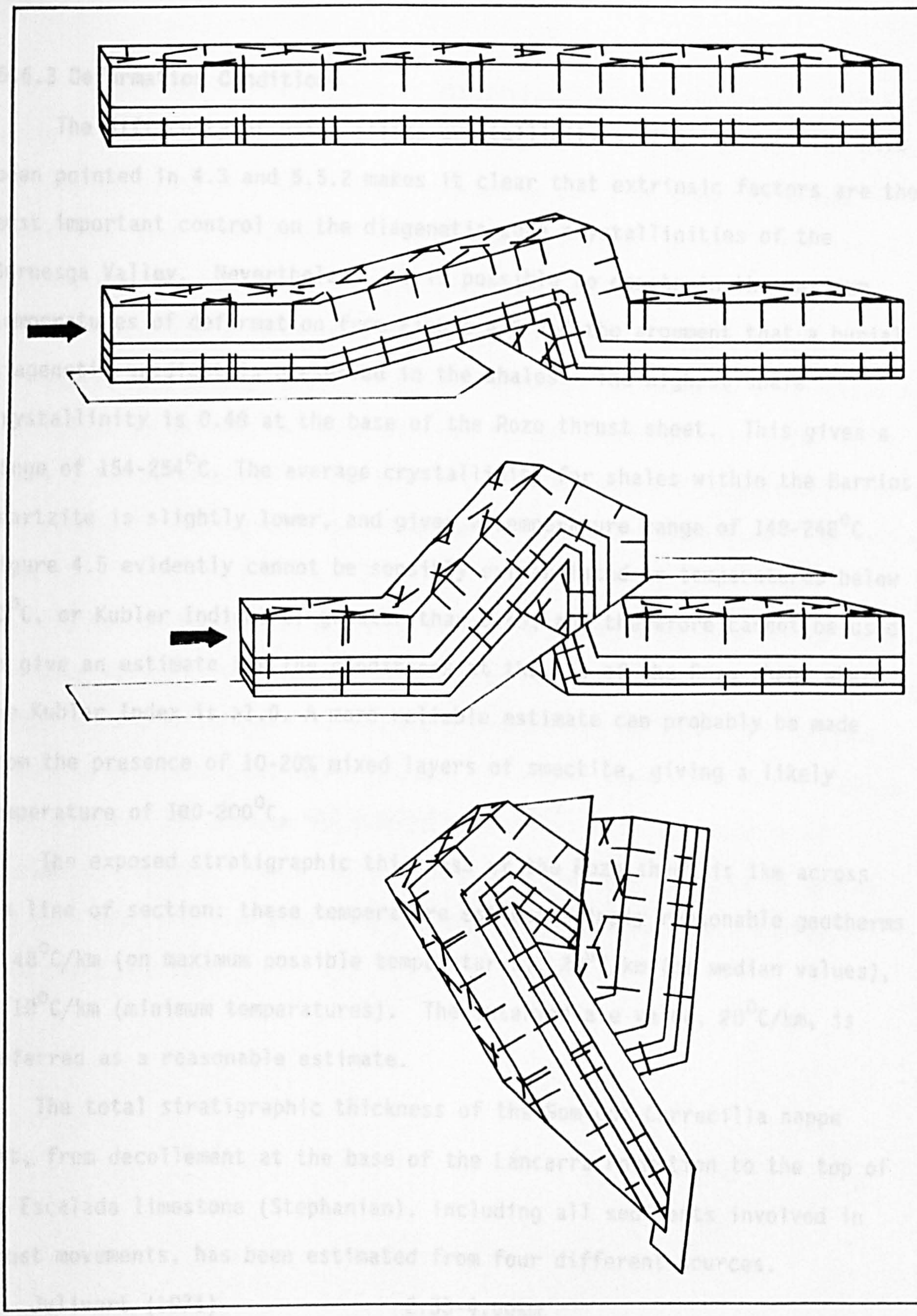

FIGURE 5.39

Model for folding and thrusting in the Rozo and Pozo thrust sheets. In the first stage, a network of bedding normal fractures is formed; these accommodate a 'thrust and buckle' fold in advance of the thrust in the second stage. As this climbs a ramp, it is tightened and, in the final stage, overturned.

5.6.3 Deformation Conditions

The difficulty of using illite crystallinity as a geothermometer have been pointed in 4.3 and 5.5.2 makes it clear that extrinsic factors are the most important control on the diagenetic zone crystallinities of the Bernesga Valley. Nevertheless, it is possible to constrain the maximum temperatures of deformation from Figure 4.5 and the argument that a burial diagenetic gradient is preserved in the shales. The highest shale crystallinity is 0.48 at the base of the Rozo thrust sheet. This gives a range of 154-254°C. The average crystallinity for shales within the Barrios quartzite is slightly lower, and gives a temperature range of 148-248°C. Figure 4.5 evidently cannot be sensibly extrapolated to temperatures below 50°C, or Kubler Indices of greater than 0.65, and therefore cannot be used to give an estimate for the conditions at the top of the Rozo sheet where the Kubler Index is >1.0. A more reliable estimate can probably be made from the presence of 10-20% mixed layers of smectite, giving a likely temperature of 160-200°C.

The exposed stratigraphic thickness of the Rozo sheet is 1km across the line of section: these temperature estimates imply reasonable geotherms of 48°C/km (on maximum possible temperatures), 20°C/km (on median values), or 12°C/km (minimum temperatures). The intermediate value, 20°C/km, is preferred as a reasonable estimate.

The total stratigraphic thickness of the Somiedo-Correcilla nappe unit, from decollement at the base of the Lángcarra Formation to the top of the Escalada limestone (Stephanian), including all sediments involved in thrust movements, has been estimated from four different sources.

Julivert (1971)	2.53-4.66km
Wallace (1972)	3.6 -3.8km
Julivert et al. (1981)	2.23-4.28km
Marcos and Pulgar (1982)	3.5km

These ranges express variations in stratigraphy across the nappe, with a general trend to reduced thickness in the north and east, but all indicate an average value of 3.5km. This is close to but less than the values calculated from a geotherm of $20^{o}C/km$ and a range of $154-254^{o}C$ for the temperature at the base of the thrust sheets, giving depths of 7.7 to 12.7km. The difference between the estimates may be due to tectonic thickening by folding before thrusting, although there is no distinction in crystallinity between the Rozo and Pozo thrust sheets as this model would imply. The uncertainty of the crystallinity/temperature relationship and variations of stratigraphy do not allow the analysis to be made in any more detail.

It is concluded that the temperature at the time of deformation in the Bernesga Valley were $154-254^{o}C$ at the base of the thrust sheets which had a stratigraphic thickness of 3.5km and a geotherm of $20^{o}C/km$. The minimum confining presures (from stratigraphic thickness) were 80MPa (with a range of 63-114MPa) and maximum value (from the upper geotherm estimate of thickness) 318 MPa. These imply values of 48 (with a range of 19-68MPa) and 191 MPa effective confining pressure respectively with a hydrostatic pore fluid pressure.

CHAPTER 6

PUNTA VIDRIAS AND CABO DE PEÑAS

6.1 STRATIGRAPHY AND LITHOLOGY

6.2 MACROSTRUCTURES

6.3 MESOSTRUCTURES

6.4 MICROSTRUCTURES

6.5 ILLITE CRYSTALLINITY

6.6 SYNTHESIS

6.1 STRATIGRAPHY AND LITHOLOGY

There are important differences between the stratigraphic section at Punta Vidrias and that described in the previous chapter for the Bernesga Valley, although both areas lie along strike and form the basal part of the Somiedo-Correcilla nappe unit. The section at Punta Vidrias is described in the I.G.M.E. 1:25,000 map of Aviles (Hoja 13, 12-3) and the geology of the Cabo de Peñas by Julivert (1976), Crimes and Marcos (1976), and Brime and Pérez-Estaún (1980) amongst others. The two areas are separated by 15km parallel to strike (Figure 6.1) and can be treated together.

The lowest formation exposed in the study area is the Herrería Sandstone, which outcrops in the west of the map (Figure 6.2). Here it consists of a fine grained green sandstone in irregular beds of 0.3m thickness, and some shale intercalations. Trace fossils at the top of the formation establish a date of earliest lower Cambrian (Julivert et al. 1973). The Herrería sandstone has a total thickness of 2,300m and is followed by the Vegadeo limestone (100m) and the shales and sandstones of the Los Cabos series (5000m to the west of the area) which together represent the middle and upper Cambrian, but are not exposed in the study area.

The next and most important formation in this study is the Barrios quartzite (500m), with many of the same characteristics as described in 5.1. Large-scale cross-bedding, ripples, hummocky cross-stratification, channels, and mud cracks indicate periods of high- and low-energy processes, which, together with a marine ichnofauna, establish a shallow water marine environment with similarities to that described by Baldwin (1976) for the Los Cabos series at Luarca and the Barrios quartzite at Barrios de Luna and the Bernesga Valley. Both environments are shallow marine, but the influence of massive sand bodies, interpreted by Baldwin as barrier sands, is much smaller in the West Asturian-Leonese zone than in

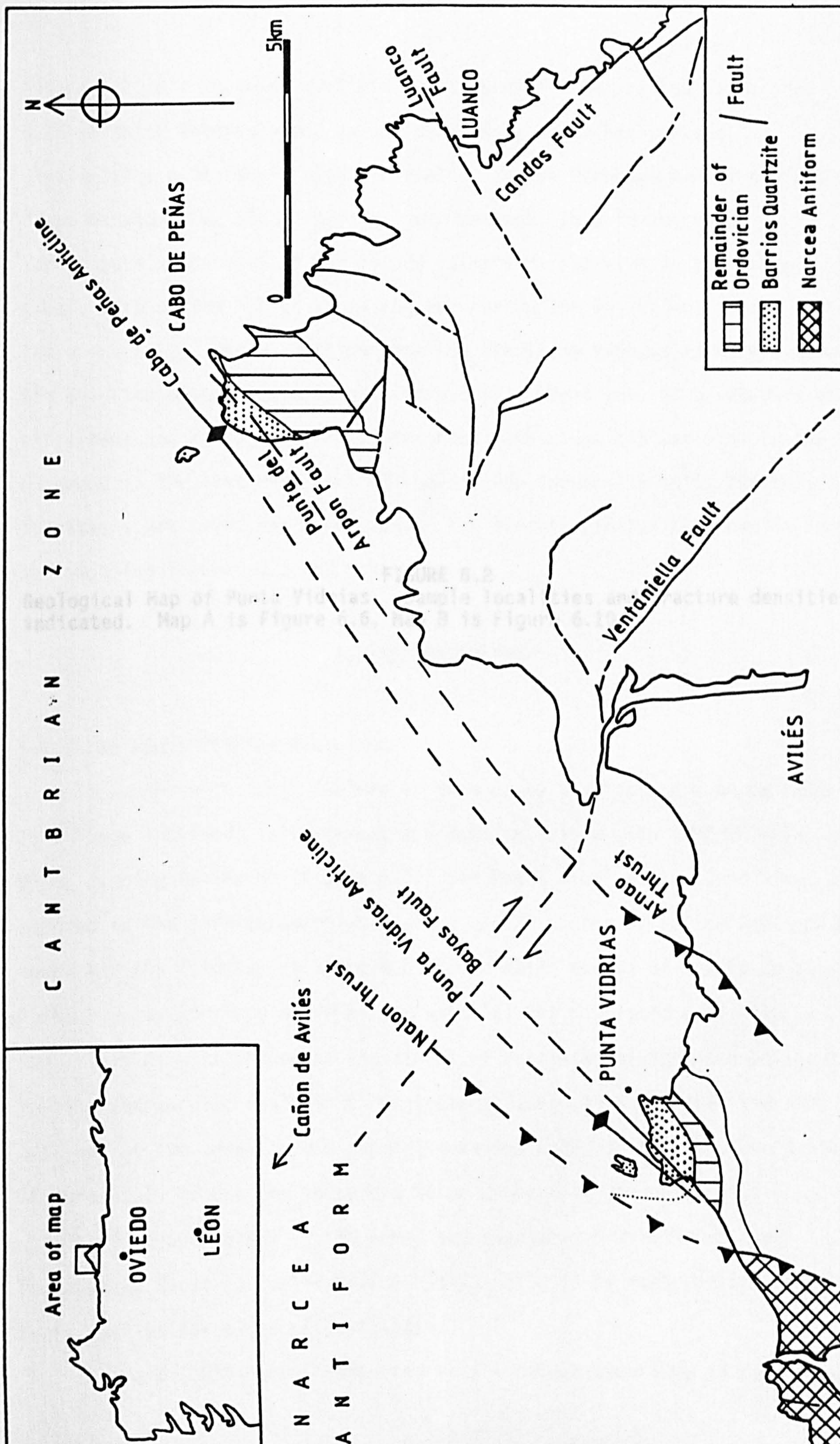

FIGURE 6.1
Major structures and location of Punta Vidrias and Cabo de Peñas.

FIGURE 6.2

Geological Map of Punta Vidrias. Sample localities and fracture densities indicated. Map A is Figure 6.6, Map B is Figure 6.10.

Figure 6.2 is a succession of black shales with fine-grained sandstones 0.25-1m thick intercalated, up to 150m thick, which has obvious similarities with the Formigoso Formation of the Bernesga Valley and can be dated as mid-upper Llandovery to lower Wenlock. This is succeeded by ferruginous sandstones of the Furada Formation (not seen in the study area), with shales and white quartzites, being the equivalent of the San Pedro quartzite, whose junction with the overlying Raneces Formation marks the Silurian-Devonian boundary (Figure 6.3). Above this is a sequence of calcareous and clastic rocks 2,500m thick with close similarities to the sequence in the southwest part of the Somiedo-Correcilla unit, but the formations are given different names: the overall similarities can be seen by comparing figures 5.1 and 6.3.

6.2 MACROSTRUCTURE

6.2.1 The Punta Vidrias Anticline

The major structural feature at both Punta Vidrias and Cabo de Peñas is a large inclined, assymetrical and open anticline with a NE-SW axial plane dipping to the NW (Figure 6.2). At Punta Vidrias, the fold hinge is exposed in the Barrios quartzite, and a gentle plunge of 20^{0} to 218^{0} can be shown for the fold axis (Figure 6.2). The axial traces of the folds at Punta Vidrias and Cabo de Peñas are parallel but displaced dextrally by 3km. This is also the sense and amount of displacement that can be shown for the Ventaniella fault which projects offshore in a NW direction from between the two areas into a submarine valley known as the Canon de Aviles (Figure 6.1). There can therefore be no doubt that the major fold structure of both areas is the same, but displaced dextrally by the Ventaniella fault in post-Variscan times. It will be referred to as the Punta Vidrias anticline (Figure 6.2).

Julivert (1976) has interpreted this inclined structure as formed by

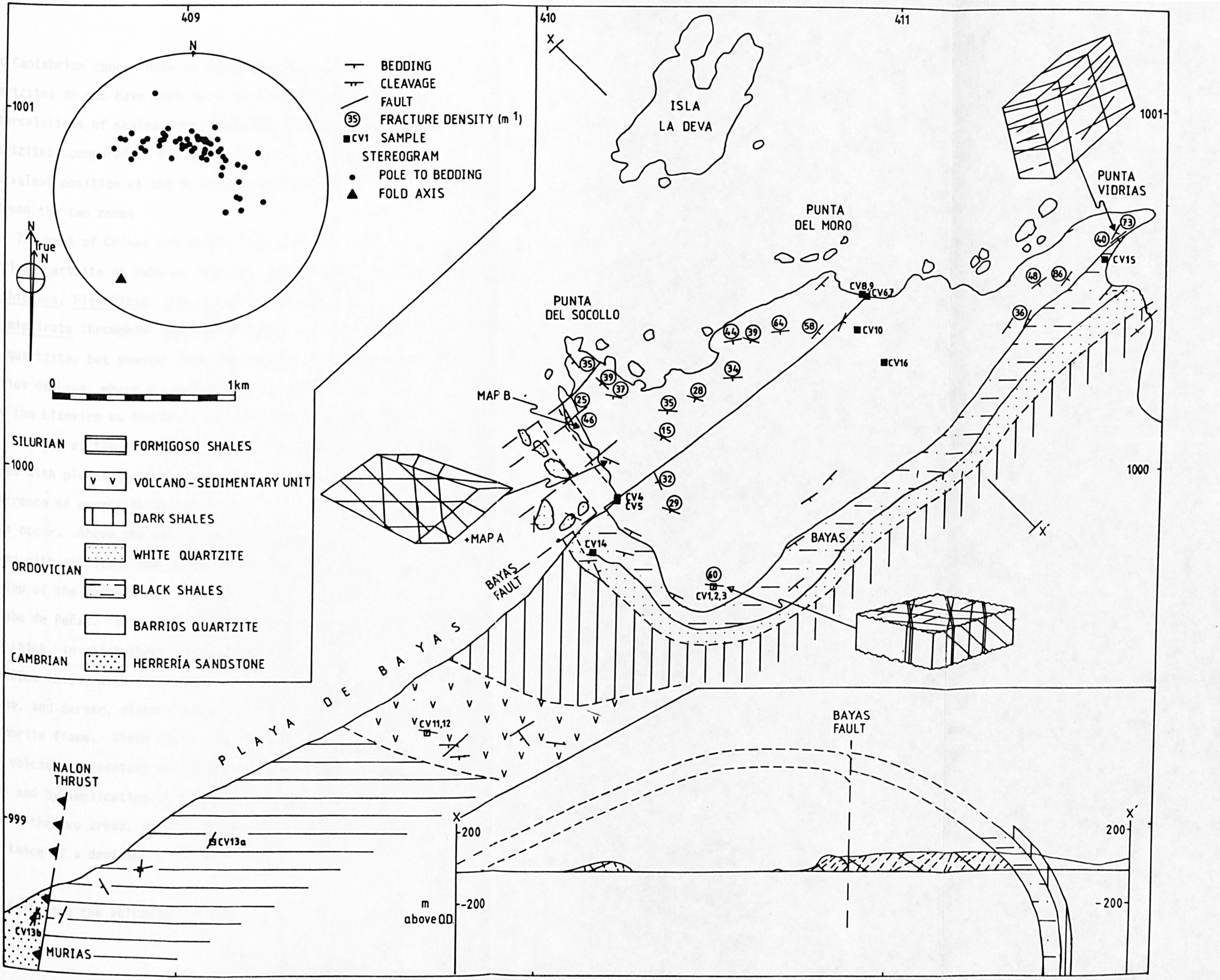
409
410
411
N
1001
1000
999
True
N
0
1km
BEDDING
CLEAVAGE
FAULT
FRACTURE DENSITY (m 1)
CV1 SAMPLE
STEREOGRAM
POLE TO BEDDING
FOLD AXIS
SILURIAN
FORMIGOSO SHALES
VOLCANO-SEDIMENTARY UNIT
DARK SHALES
WHITE QUARTZITE
ORDOVICIAN
BLACK SHALES
BARRIOS QUARTZITE
CAMBRIAN
HERRERÍA SANDSTONE
ISLA
LA DEVA
PUNTA
VIDRIAS
PUNTA
DEL MORO
PUNTA
DEL SOCOLLO
MAP B
+MAP A
BAYAS
FAULT
BAYAS
PLAYA DE BAYAS
NALON
THRUST
MURIAS
CV1,2,3
CV4
CV5
CV6,7
CV8,9
CV10
CV11,12
CV13a
CV13b
CV14
CV15
CV16
X
X'
200
-200
m
above OD
BAYAS
FAULT

the Cantabrian zone. Here at Punta Vidrias and Cabo de Peñas the quartzites do not have such thick or coarse beds, and there are intercalations of shales with increasing frequency towards the top of the quartzites, compared to the massive, thick, pure quartzite in the equivalent position at the Bernesga locality: the situation is intermediate between the two zones.

The work of Crimes and Marcos (1976) on the trace fossils of the Barrios quartzite at Cabo de Peñas has been referred to in 5.1. Scolithos, Teichichnus, Planolites, Cruziana and Rusophycus are found. The absence of C.semiplicata throughout the section implies a Tremadoc age for the base of the quartzite, but younger than the lower part of the Barrios quartzite at Barrios de Luna, where C. semiplicata is present. The quartzite may extend into the Llanvirn on the basis of the range of C.furcifera (Figure 6.3).

The top of the main body of quartzite is followed by 40-50m of dark shales with planar laminated sandstone beds 50-100mm thick before a second occurrence of quartzite 20-30m in thickness, in which 1-3m massively-bedded units occur. Above the second quartzite comes 200-250m of black or grey shales with siltstone and sandstone beds decreasing in abundance towards the top of the succession. A Llandeilo age can be given to this shale unit at Cabo de Peñas. It is succeeded by volcanigenic sediments approximately 180m thick, in which there are planar-bedded, laterally continuous units 50-1000mm thick, with fine sandy intercalations in whispy or lensoid shapes, and darker, discontinuous, flattened, irregular lumps, possibly ignimbrite fiame. Black shales, cherts and sandstones are also found. This volcano-sedimentary unit can be given an upper Ordovian age at Cabo de Peñas and by implication at Punta Vidrias, but there are some differences between the two areas, notably the greater thickness in the former and the importance of a dominantly shale unit near the top of the latter (Figure 6.3).

Following the volcanigenic unit and exposed in the southwest part of

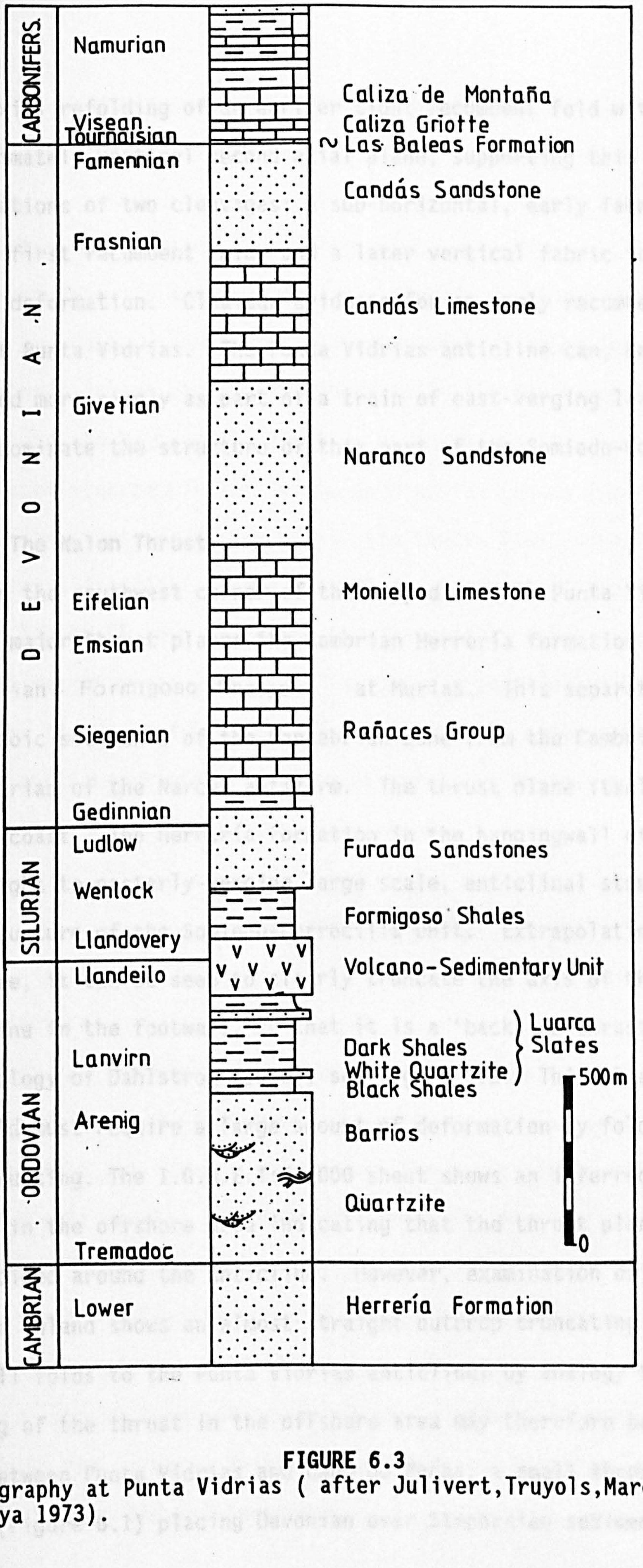

FIGURE 6.3

Stratigraphy at Punta Vidrias (after Julivert, Truyols, Marcos & Arboleya 1973).

homo-axial refolding of an earlier tight recumbent fold with an approximately vertical second axial plane, supporting this with observations of two cleavages: a sub-horizontal, early fabric, axial planar to the first recumbent fold, and a later vertical fabric formed in the second deformation. Cleavage evidence for an early recumbent fold is not seen at Punta Vidrias. The Punta Vidrias anticline can, however, be regarded more simply as part of a train of east-verging large scale folds which dominate the structure of this part of the Somiedo-Correcilla Unit.

6.2.2 The Nalon Thrust

In the southwest corner of the mapped area at Punta Vidrias (Figure 6.2) a major thrust places the Cambrian Herrería formation over the upper Silurian Formigoso Shales at Murias. This separates the palaeozoic sediments of the Cantabrian zone from the Cambrian and Precambrian of the Narcea antiform. The thrust plane itself is not exposed at the coast. The Herrería formation in the hangingwall of the thrust has an upright to easterly-verging large scale, anticlinal structure similar to the structure of the Somiedo-Correcilla Unit. Extrapolating the thrust offshore, it can be seen to clearly truncate the axis of the Punta Vidrias Anticline in the footwall, so that it is a 'backlimb thrust' in the terminology of Dahlstrom (1970); see Figure 5.5. This clear truncation of the fold must require a large amount of deformation by folding to precede the thrusting. The I.G.M.E.I:50,000 sheet shows an inferred position of the thrust in the offshore area indicating that the thrust plane itself has been folded around the anticline. However, examination of the Nalon thrust further inland shows an almost straight outcrop truncating similar major footwall folds to the Punta Vidrias anticline; by analogy the extent of folding of the thrust in the offshore area may therefore be limited.

Between Punta Vidrias and Cabo de Peñas, a small thrust outcrops at Arnao (Figure 6.1) placing Devonian over Stephanian sediments. The Arnao thrust loses displacement to the south and has been reactivated as a strike-slip fault (Julivert et al. 1973).

6.2.3 Other Major Faults

Apart from the Ventaniella fault already described separating Punta Vidrias and Cabo de Penas, there are a number of other major faults in the area between Aviles and Gijon. These fall into two groups: a NW-SE set, parallel to the Ventaniella fault (e.g. Candas Fault) and a NE-SW set, approximately perpendicular to it, such as the Luanco fault and the Verina fault. The Luanco fault may offset the Candas fault sinistrally, while the Verina fault is offset by the dextral displacement of the Ventaniella fault. The NW-SE set, including the Ventaniella fault, have post-Palaeogene movements as well as being displaced by the NE-SW set, which are in turn cut by them. The entire fault system thus appears to have a long-lived history of movement, probably beginning in the Permian and lasting at least until post-Palaeogene.

6.3 MESOSTRUCTURES

6.3.1 Fractures

As in the Bernesga Valley, the Barrios quartzite is everywhere characterised by a dense network of fractures with largely the features described in 5.3.1. There are however three noticeable differences between the two areas: firstly, slickenside lineations are less common at Punta Vidrias, and correspondingly there are fewer fractures on which clear shear displacements are visible. Lastly, there are many more fractures containing a vuggy quartz filling, up to 5mm wide, which has euhedral prismatic crystal terminations on exposed fracture surface (see 6.3.6). Again as in the Bernesga Valley, no clear overprinting relations are observed between the fracture sets.

Orientations of fractures measured at five localities are at Punta Vidrias are shown in Figure 6.4. Each diagram shows at least three well defined concentrations of poles to fractures and in the case of the most southern locality, four sets of fractures. The fracture sets are all within a girdle normal to the pole of bedding, forming a 'necklace' pattern similar to that observed in the Bernesga Valley, which rotates with the bedding around the fold axis. Fracture orientations were also measured at Punta del Arpon, Cabo de Peñas, where two very clearly defined sets lie in the bedding-normal necklace, with the suggestion of a weak third concentration (Figure 6.5).

Fracture densities are shown in Figure 6.2, from which it can be seen that, although there is a considerable range of fracture densities (from 15-73m^{-1}), this is much less than the range observed in the Bernesga Valley. Furthermore, the majority of fracture densities are close to a mean value of 42m^{-1} (the standard deviation of 23 measurements is 16.6m^{-1}). There is no obvious relationship between the distribution of fracture densities and the structure. Fracture density/bed thickness relationships were investigated by measuring densities on one fracture plane from each of the three fracture sets at one locality: no relationship existed over a range of bed thicknesses from 15-600mm.

Some control of fracture characteristics by lithology was noted: fractures tended to be more irregular in bedding plane profile in an area where bed thickness was also quite irregular due to sedimentary structure (large scale waves). The very highest fracture density measured was restricted to a well cemented, medium-grained quartzite.

6.3.2 Deformation and Breccia Zones, Faults

Deformation zones of high density fracturing occur parallel to all fracture sets as seen in Plate 6.1(a). Figure 6.6 is a detailed map of a bedding plane located as Map A on Figure 6.2 which shows deformation zones

FIGURE 6.4

Fracture Orientations at Punta Vidrias. The ‘necklace’ of at least three fracture sets in the great circle of bedding planes is seen in each pattern.

N = Number of measurements

A,B = Method of measurement (see 3.1.2)

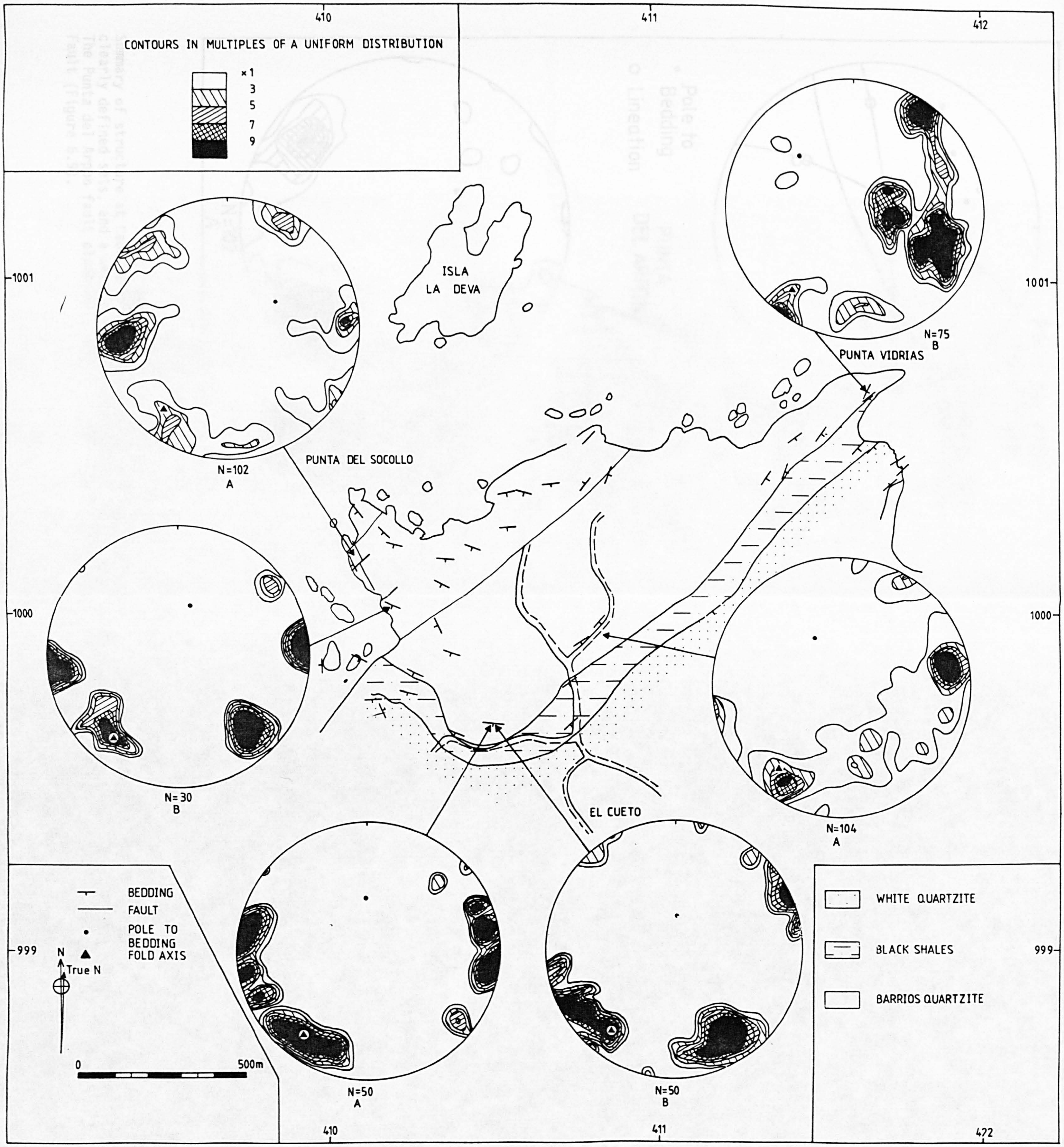

CONTOURS IN MULTIPLES OF A UNIFORM DISTRIBUTION
×1
3
5
7
9
410
411
412
1001
1000
999
ISLA
LA DEVA
PUNTA VIDRIAS
PUNTA DEL SOCOLLO
EL CUETO
N=102
A
N=75
B
N=30
B
N=104
A
N=50
A
N=50
B
BEDDING
FAULT
POLE TO
BEDDING
FOLD AXIS
N
True N
0
500m
WHITE QUARTZITE
BLACK SHALES
BARRIOS QUARTZITE
410
411
472

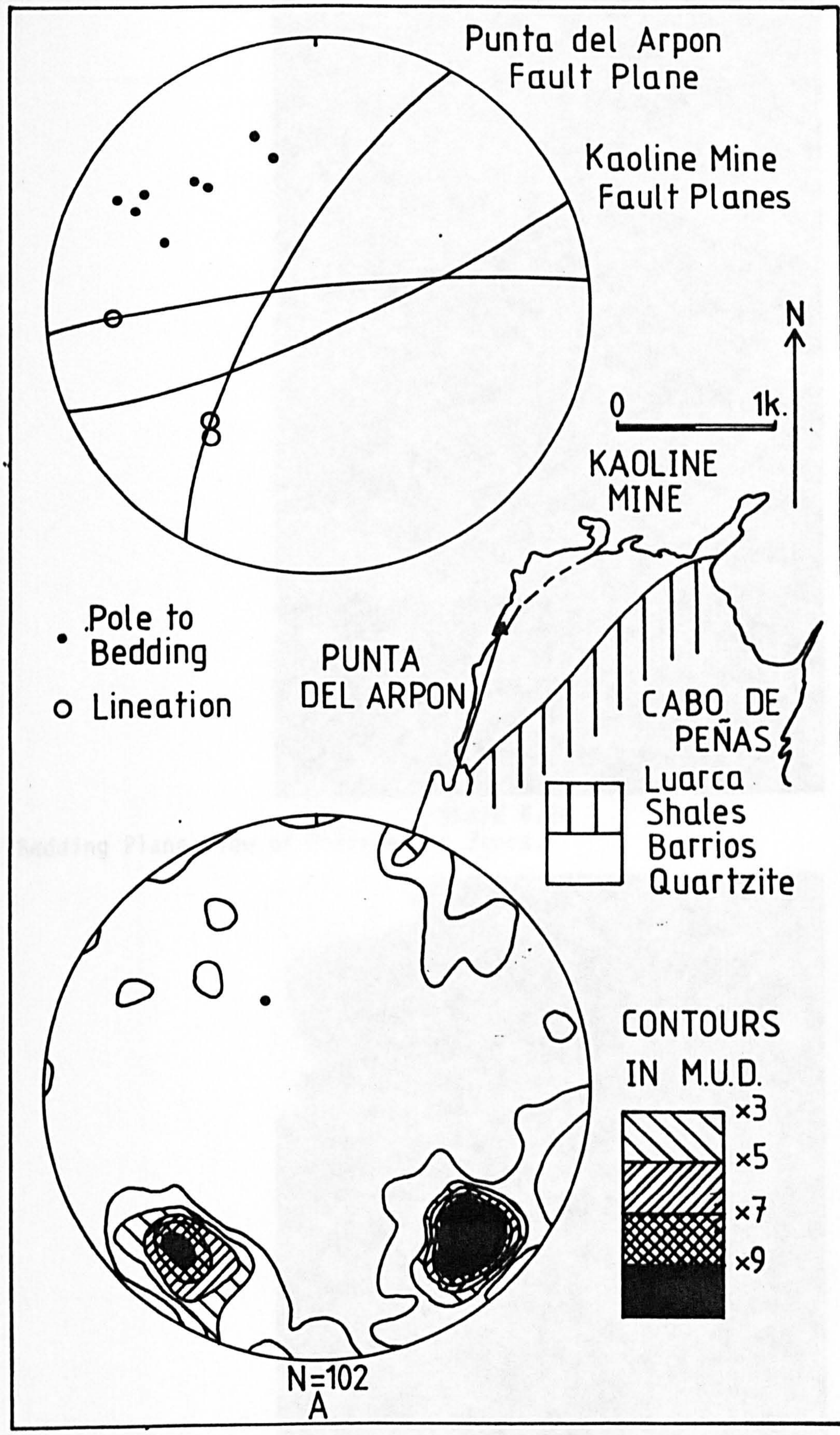

FIGURE 6.5

Summary of structure at Cabo de Peñas. Fracture orientations show two clearly defined sets, and a weak third set, perpendicular to the bedding. The Punta del Arpon fault plane has a similar orientation to the Bayas Fault (Figure 6.9).

PLATE 6.1a

Bedding Plane view of Deformation Zones.

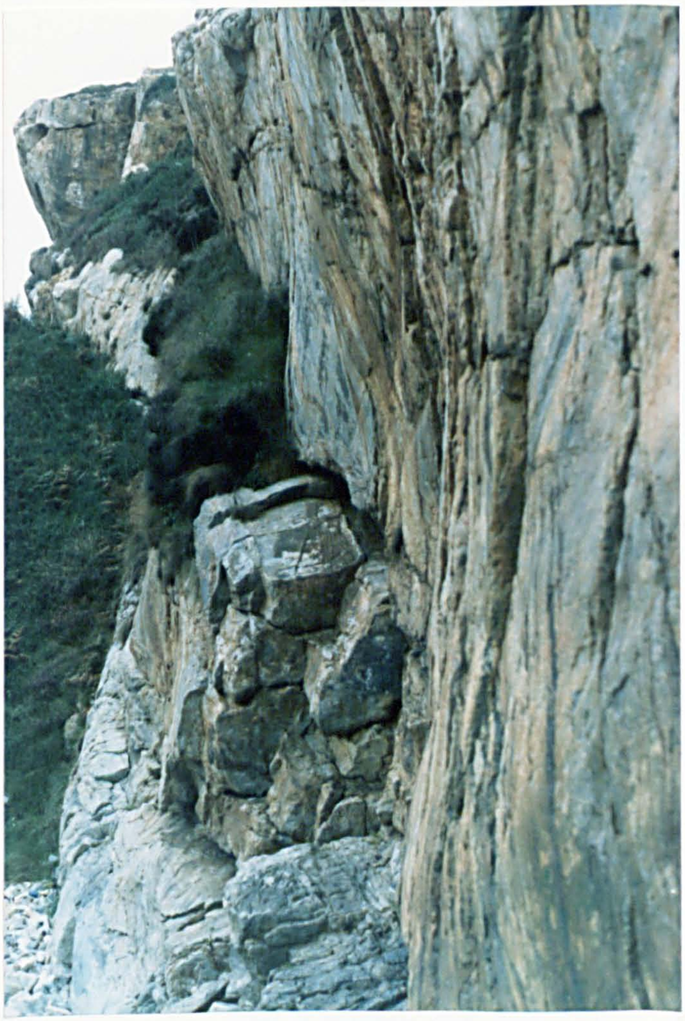

PLATE 6.1b

Bayas Fault Plane showing undulations, lineations, and displacements along both large dilatant fractures and bedding planes.

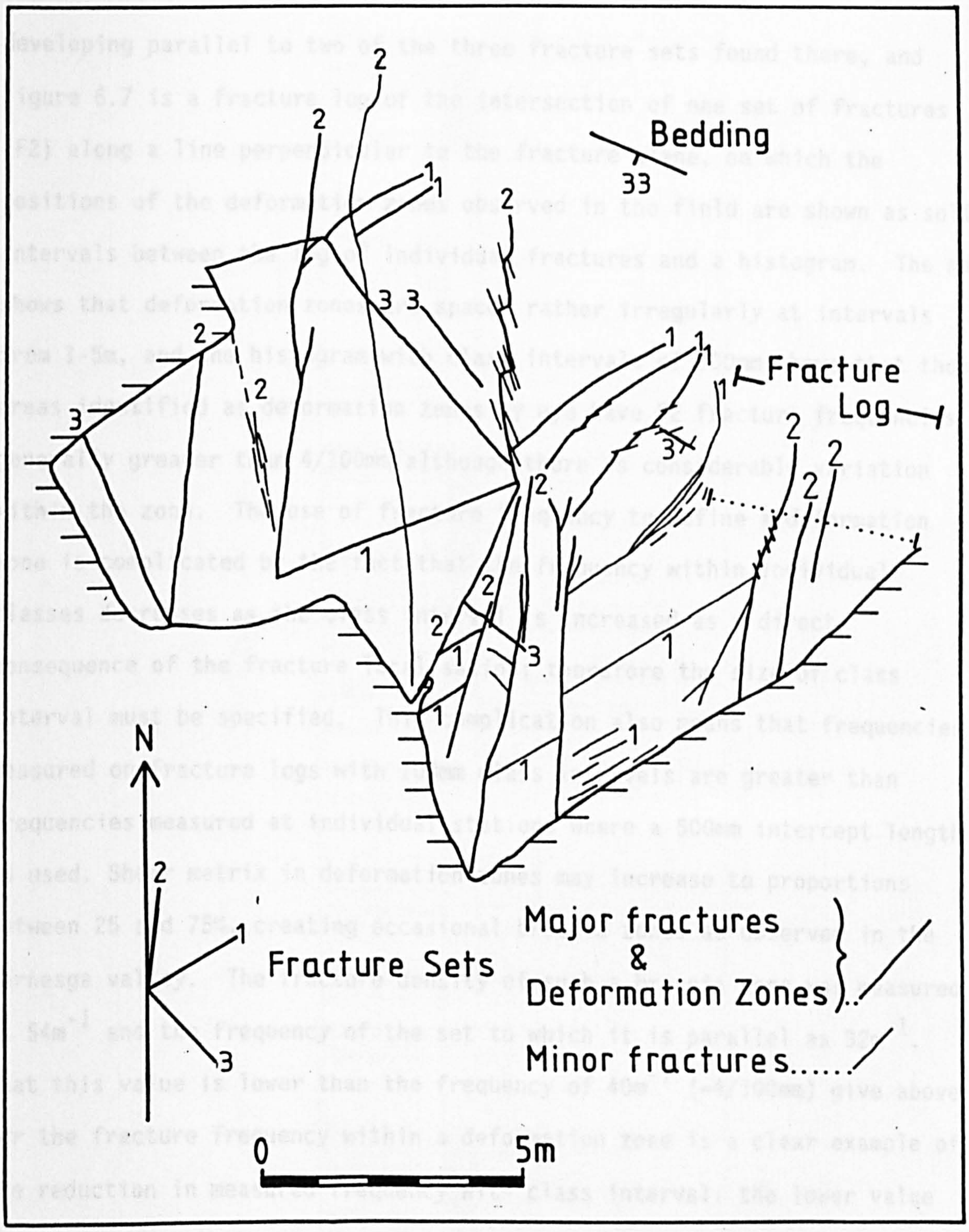

FIGURE 6.6

Detailed Map of Deformation Zones. Area of Map A on Figure 6.2. Deformation Zones form parallel to N-S and NE-SW Fracture sets with spacings of 1-5m. Position of Fracture Log, Figure 6.7, indicated.

developing parallel to two of the three fracture sets found there, and Figure 6.7 is a fracture log of the intersection of one set of fractures (F2) along a line perpendicular to the fracture plane, on which the positions of the deformation zones observed in the field are shown as solid intervals between the log of individual fractures and a histogram. The map shows that deformation zones are spaced rather irregularly at intervals from 1-5m, and the histogram with class intervals of 100mm shows that those areas identified as deformation zones by eye have F2 fracture frequencies generally greater than 4/100mm, although there is considerable variation within the zone. The use of fracture frequency to define a deformation zone is complicated by the fact that the frequency within individual classes decreases as the class interval is increased as a direct consequence of the fracture localisation; therefore the size of class interval must be specified. This complication also means that frequencies measured on fracture logs with 100mm class intervals are greater than frequencies measured at individual stations where a 500mm intercept length is used. Shear matrix in deformation zones may increase to proportions between 25 and 75%, creating occasional breccia zones as observed in the Bernesga valley. The fracture density of such a breccia zone was measured as $54m^{-1}$ and the frequency of the set to which it is parallel as $32m^{-1}$. That this value is lower than the frequency of $40m^{-1}$ (=4/100mm) give above for the fracture frequency within a deformation zone is a clear example of the reduction in measured frequency with class interval: the lower value was obtained with the standard 500mm intercept length compared to the 100mm class interval of the histogram.

A few faults are shown in Figure 6.2 on which horizontal displacements of several hundred millimetres to metres occur on discrete planes.

6.3.3 Bayas Fault

An exposure of one fault plane on the Playa de Bayas merited a more

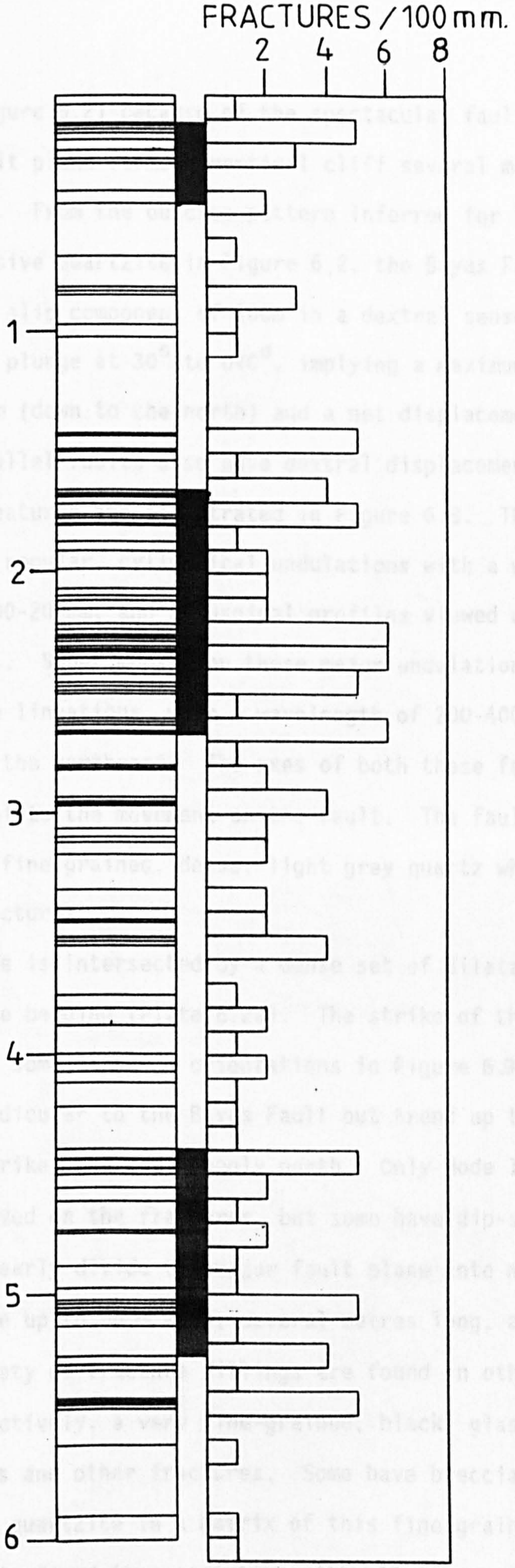

FIGURE 6.7

Fracture Log of NE-SW Fractures only across area indicated on Figure 6.6. Individual fractures represented on left; histogram with 100mm class intervals on right. Solid areas represent deformation zones as observed in the field.

detailed study (Figure 6.2) because of the spectacular fault surface features. The fault plane forms a vertical cliff several metres high trending northeast. From the outcrop pattern inferred for the boundary of the top of the massive quartzite in Figure 6.2, the Bayas Fault has a maximum horizontal slip component of 100m in a dextral sense. Lineations on the fault plane plunge at 30^0 to 040^0, implying a maximum vertical displacement of 58m (down to the north) and a net displacement of 115m. Small adjacent parallel faults also have dextral displacements.

Fault plane features are illustrated in Figure 6.8. The most noticeable are the regular, cylindrical undulations with a wavelength of 2m and amplitude of 100-200mm, and sinusoidal profiles viewed downplunge, shown in Plate 6.1b. Superimposed on these major undulations are much smaller slickenside lineations, with a wavelength of 200-400mm, also plunging at 30^0 to the northeast. The axes of both these features are taken to be parallel to the movement on the fault. The fault plane consists of a very fine-grained, dense, light grey quartz which preserves no sedimentary structures.

The fault plane is intersected by a dense set of dilatant fractures, perpendicular to the bedding (Plate 6.2a). The strike of these fractures is rather variable; some measured orientations in Figure 6.9a show that they are sub-perpendicular to the Bayas Fault but trend up to 20^0 anticlockwise in strike, and dip steeply north. Only Mode I displacements are generally observed on the fractures, but some have dip-slip components of movement that clearly divide the major fault plane into metre-sized blocks. They may be up to 50mm wide, several metres long, and many are quite open. A variety of fracture fillings are found in others: most commonly and distinctively, a very fine-grained, black, glassy quartz which also occurs in veins and other fractures. Some have breccias consisting of fragments of intact quartzite in a matrix of this fine grained, black quartz. Haematite is found in association with all types of filling, and

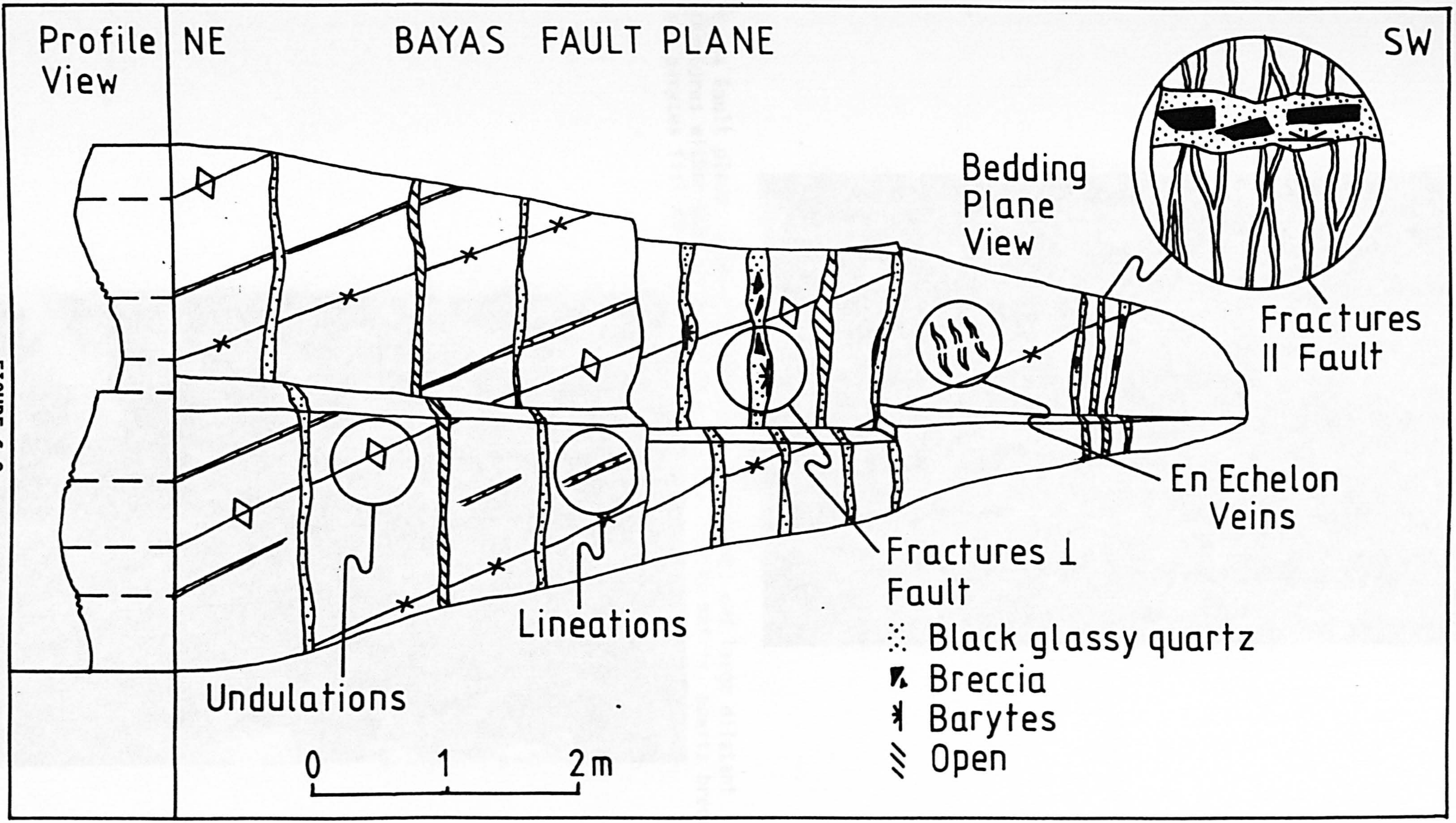

FIGURE 6.8
Fault Plane Features of the Bayas Fault Plane (located in Figure 6.2).

PLATE 6.2a

Bayas Fault plane, showing undulations, lineations and large dilatant fractures either open or with black, glassy, quartz matrix, quartz breccia and barytes fillings.

PLATE 6.2b

Faulting at entrance to kaoline mine, Cabo de Penas. Notice discrete gouge zones with a spacing of 1-2m downthrowing to the east and converging to vertical dips.

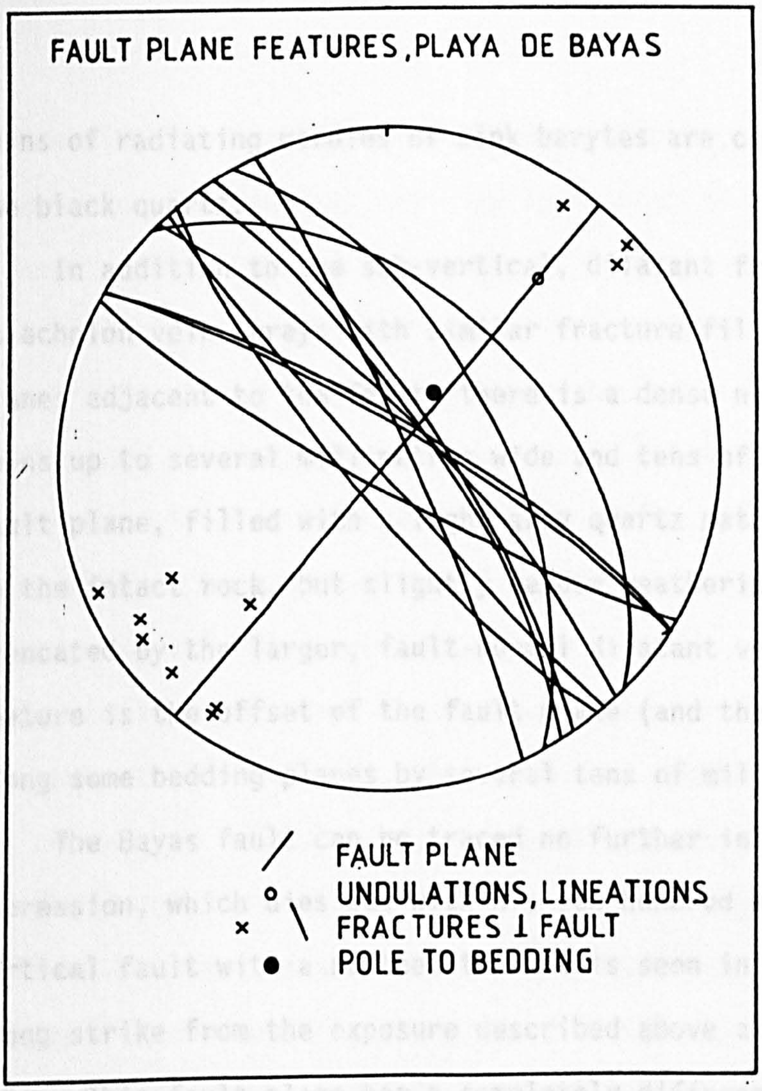

a) At Playa de Bayas

FIGURE 6.9

Structural data of the Bayas Fault Plane.

b) At Punta del Moro

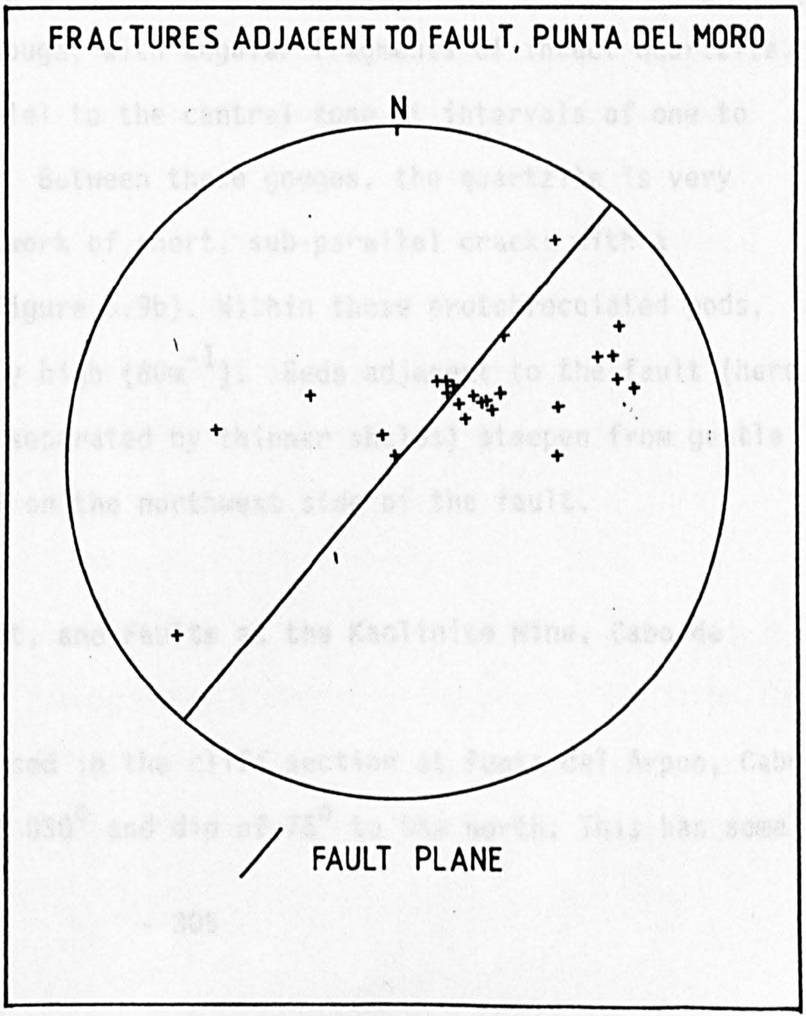

veins of radiating needles of pink barytes are common in association with the black quartz.

In addition to the sub-vertical, dilatant fractures, there are en-echelon vein arrays with similar fracture fillings, and on bedding planes adjacent to the fault, there is a dense network of fine anastomosing veins up to several millimetres wide and tens of mm long parallel to the fault plane, filled with a light grey quartz matrix of similar appearance to the intact rock, but slightly harder weathering. These are clearly truncated by the larger, fault-normal dilatant veins (Figure 6.8). A final feature is the offset of the fault plane (and the large dilatant veins) along some bedding planes by several tens of millimetres.

The Bayas fault can be traced no further inland than its topographical expression, which dies out within a few hundred metres. However, a vertical fault with a northeast trend is seen in the cliff section directly along strike from the exposure described above at Punta del Moro (Figure 6.2). This fault plane has a completely different aspect: it consists of a zone with variable width up to several tens of millimetres, containing incohesive, yellow fault gouge, with angular fragments of intact quartzite. Similar gouges exist parallel to the central zone at intervals of one to two metres on either side. Between these gouges, the quartzite is very heavily fractured by a network of short, sub-parallel cracks with a moderate dip to the WSW (Figure 6.9b). Within these protobrecciated pods, fracture densities are very high ($80m^{-1}$). Beds adjacent to the fault (here quartzite beds of 0.5m-1m separated by thinner shales) steepen from gentle southeast dips to vertical on the northwest side of the fault.

6.3.4 Punta del Arpon Fault, and Faults at the Kaolinite Mine, Cabo de Peñas

A large fault is exposed in the cliff section at Punta del Arpon, Cabo de Peñas, with a strike of 030^{0} and dip of 75^{0} to the north. This has some interesting similarities with the Bayas Fault (Figure 6.5). The sense of movement on the fault is not readily determined, but small parallel adjacent faults downthrow to the east, suggesting approximately equal dextral horizontal and reverse vertical components of movement. The minimum amount of vertical displacement must be of the order of 100m since no beds in the 100m cliff section can be clearly matched across the fault. The fault plane is also corrugated on two scales: major undulations with a wavelength of 5m, and parallel lineations with a wavelength of 50mm, both plunging at 43^{0} to the southwest. The fault plane is heavily kaolinitised at the base, where there are also veins of pyrite.

Like the Bayas fault, this cannot be traced inland, but at the north end of Cabo de Peñas, a large fault is exposed in the cliff along strike of the Punta del Arpon fault. Also like the northern exposure of Punta Vidrias, the fault plane here has a different appearance: rather than a single discrete surface, there are at least five narrow, sub-vertical gouge zones striking between $075-085^{0}$ with a spacing of 1-2m (Plate 6.2b). They converge downwards to become vertical, and have reverse downthrows of several tens of millimetres to the east, with lineations plunging gently to the north and south and thin seams of blue gouge as well as yellow matrix along the fault planes.

The converging geometry of the individual gouges with their reverse sense of movement is an example of a negative flower structure (Woodcock and Fischer 1986). The intervening areas of quartzite are very heavily fractured, and veined by kaolinite, which increases in proportion towards the gouge zones at the expense of quartzite fragments.

6.3.5 Shatter Fracture Pattern

An unusual pattern of fracture was observed along a minor fault on the north side of Playa de Bayas. The vertical, NW-SE fault is well exposed for 150m on a bedding plane which it crosses in a straight line (Figure

6.2). Several major fracture zones are dextrally offset by 50-100mm along the fault, which also displaces bedding, downthrowing to the southwest by the same amount.

At fairly regular intervals of 1-2m, dense clusters of fractures are observed along the fault plane (Plates 6.3a, 6.3b). These are shown in the detailed map of Figure 6.10 located in Figure 6.2 as Map B. At these points, referred to as shatter points, an asymmetric radiating pattern of dense fractures is observed with a concentration of fractures intersecting the fault in a north-south direction. Cracks in this orientation remain linear, while others at more, or less, acute angles to the fault curve with distance from the shatter point to become parallel and eventually return to the fault plane at the site of the adjacent shatter point. These features are illustrated diagrammatically in Figure 6.11. As well as their fairly regular spacing, the shatter points correspond to the intersection of deformation zones of the north-south fracture set with the fault plane (Plate 6.6). Negligible displacements occur on the shatter fractures, and all of them are preferentially developed on the downthrown, southwesterly side of the fault. The main fault offsets fractures of a second NE-SW fracture set, but shear displacements of the N-S fracture set cannot be detected, although this may be due to the dense development of the N-S set at shatter points, making it impossible to trace individual fractures across the fault. To the southeast of the map, the fault continues as a weakly developed vein network. In the opposite direction, it is dextrally offset by 20m along a fault parallel to the Bayas fault, and continues as a strong feature out to sea. At places, a good fabric is defined in a zone 0.5m wide adjacent to the fault by a large number of small subvertical fractures making an acute angle of 10^0 to the fault; they are therefore in a similar orientation to the N-S fracture set, but much shorter and not localised into deformation zones.

PLATE 6.3a

Shatter Fracture Pattern. Two shatter points along the main fault are seen in this view to the southeast.

PLATE 6.3b

Shatter Fracture Pattern. The intersection of two deformation zones of one fracture set at shatter points is clearly seen here.

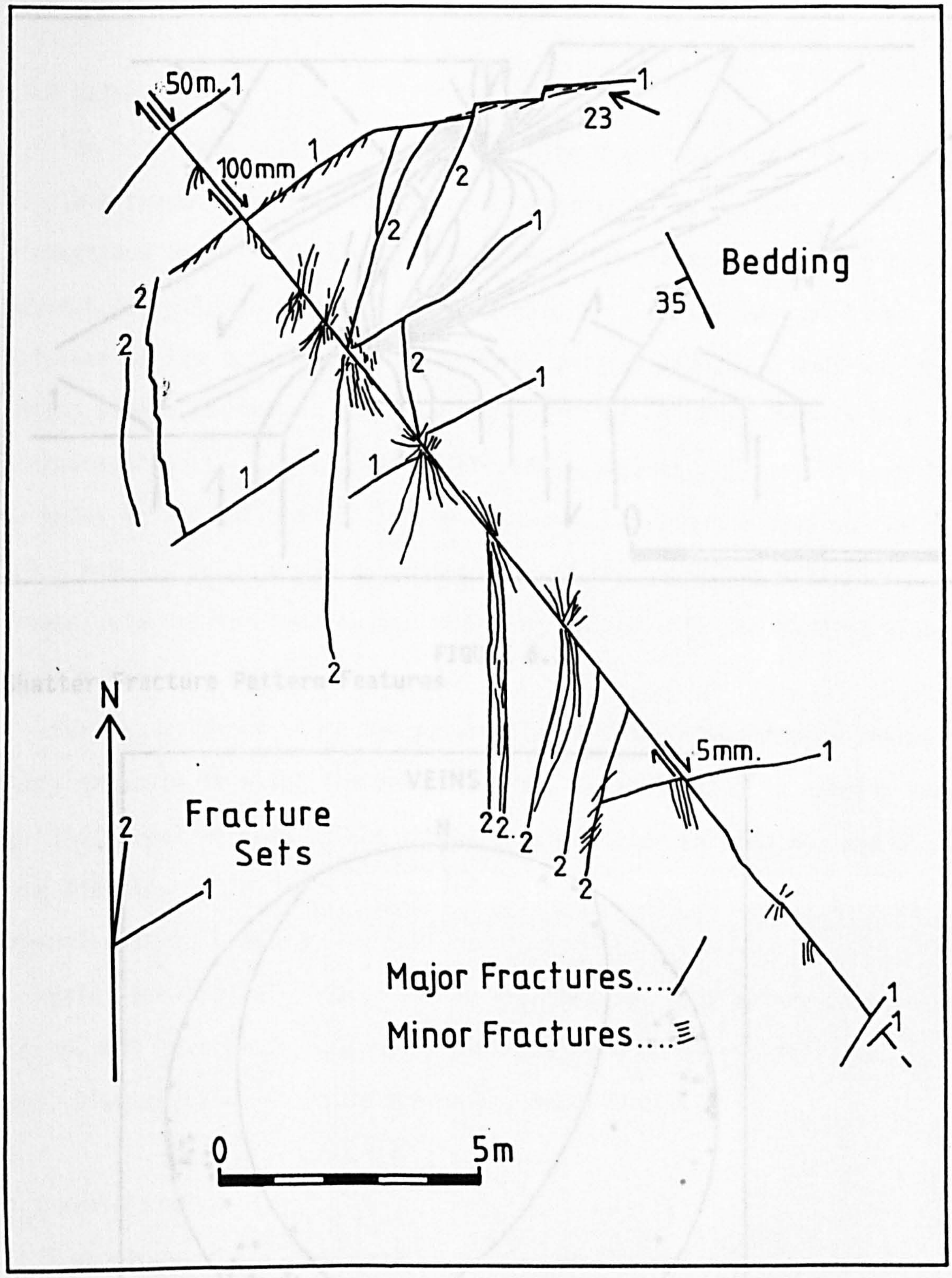

FIGURE 6.10

Detailed Map of Shatter Fracture Pattern. Dense clusters of radiating fractures occur at 1-2m intervals along a dextral strike-slip fault, corresponding to the intersection of deformation zones of the N-S fracture set with the fault. Area of Map B, Figure 6.2.

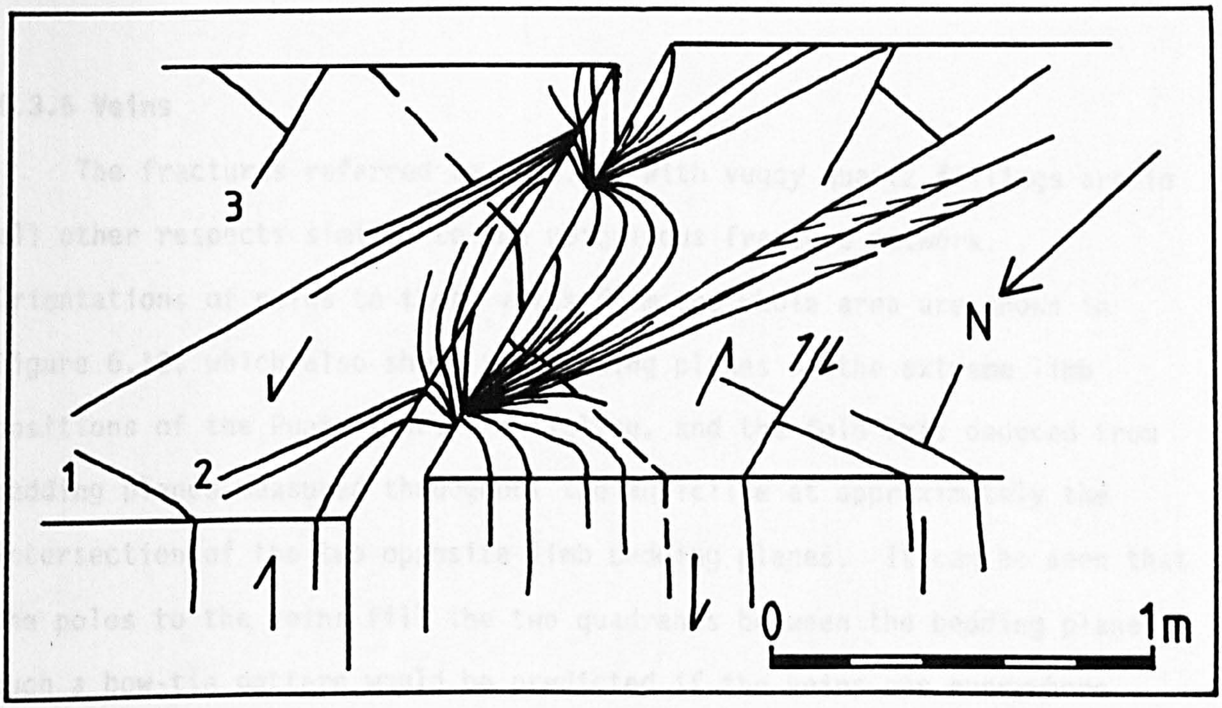

FIGURE 6.11

Shatter Fracture Pattern Features

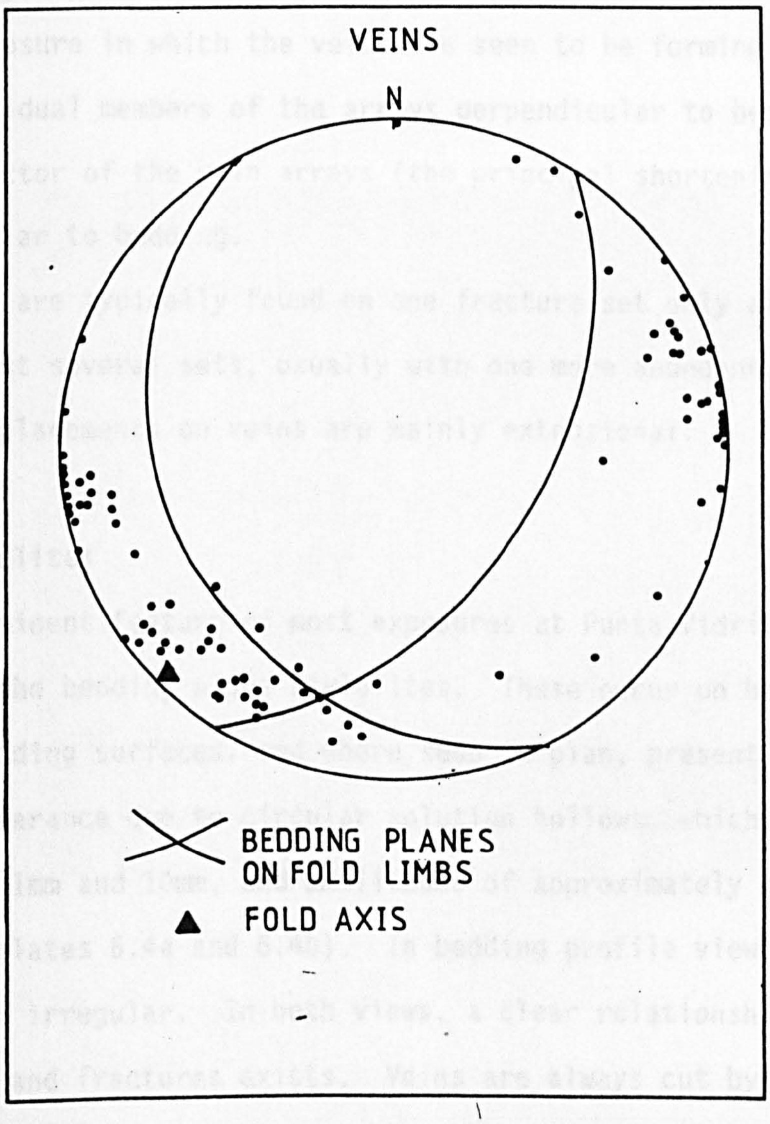

FIGURE 6.12

Vein Orientations. Poles to veins lie within a 'bow-tie' defined by bedding planes on the limbs of the Punta Vidrias Anticline. This implies that they are all approximately normal to bedding.

6.3.6 Veins

The fractures referred to in 6.3.1 with vuggy quartz fillings are in all other respects similar to the ubiquitous fracture network. Orientations of poles to those veins from the whole area are shown in Figure 6.12, which also shows the bedding planes on the extreme limb positions of the Punta Vidrias anticline, and the fold axis deduced from bedding planes measured throughout the anticline at approximately the intersection of the two opposite limb bedding planes. It can be seen that the poles to the veins fill the two quadrants between the bedding planes; such a bow-tie pattern would be predicted if the veins are everywhere perpendicular to the bedding and have been folded with the bedding around the fold axis.

Further evidence about the nature of the veins comes from a small quarry exposure in which the veins are seen to be forming en-echelon arrays with individual members of the arrays perpendicular to bedding, and the acute bisector of the vein arrays (the principal shortening axis) also perpendicular to bedding.

Veins are typically found on one fracture set only at any particular outcrop, but several sets, usually with one more abundant, may also be found. Displacements on veins are mainly extensional.

6.3.7 Stylolites

A prominent feature of most exposures at Punta Vidrias and Cabo de Peñas are the bedding plane stylolites. These occur on both main and foreset bedding surfaces, and where seen in plan, present a distinctive pitted appearance due to circular solution hollows, which are of two diameters: 1mm and 10mm, and amplitudes of approximately one tenth of the diameter (plates 6.4a and 6.4b). In bedding profile view, the stylolites are wavy or irregular. In both views, a clear relationship between veins, stylolites and fractures exists. Veins are always cut by both stylolites

PLATE 6.4a
Stylolites in bedding plane view. Notice fractures cutting solution hollows, which have diameters of 1mm and 10mm.

PLATE 6.4b
Stylolites in profile. Stylolites cut veins but are cut by fractures.

and fractures, while fractures invariably cut but are unaffected by stylolites and veins. No oblique stylolites (slickolites) are seen. A useful observation on sample 102 from Cabo de Peñas is that the solution pits of stylolite are strained to form hemiellipsoids with lengths of 1-2mm and widths of 1mm on the bedding plane.

6.3.8 Intra- and Inter-bed Shear

Slickenside lineations are not observed on bedding planes. However, there is clear evidence for shear parallel to bedding from three sources: firstly, as referred to above, the Bayas fault plane is displaced along a bedding plane. Secondly, a shale horizon adjacent to the Bayas fault at Punta del Moro has vertical sandfilled burrows (skolithos) which have been sheared by intrabed movement and record intrabed shear strains of up to 1. Thirdly, small scale thrusting observed in the same locality produced dramatic cataclasis of a 0.5m bed of quartzite where the thrust ramped from a shale horizon below to one above. The quartzite in the hangingwall is completely fragmented into angular pieces 10mm large and folded into a hangingwall antiform with a total displacement of 1-2m on the thrust. The footwall quartzite is much less heavily fractured, while a few larger fractures accommodate structurally necessary folding in the hangingwall culmination above the ramp.

6.3.9 Cleavage

Cleavage is generally not observed, but traces of a sub-horizontal incipient cleavage were noticed at Punta del Moro, and at Punta Vidrias itself dipping at 70^{0} to the north west, and in the Formigoso Formation near the Nalon thrust, dipping at 50^{0} to the west (Figure 6.2). The latter two orientations are approximately axial planar to the inclined Punta Vidrias anticline. The cleavage at Punta del Moro, in a shale layer between quartzites, is considered to be related to intrabed shear.

Cleavage is also very faintly developed in the Herrería formation in the hangingwall of the Nalon thrust, dipping at 80^{o} to the NNW, and a good pencil cleavage is found in the volcanigenic unit to the east of Punta Vidrias.

6.3.10 Discussion

The earliest mesoscopic strain features observed at Punta de Vidrias are bedding-normal veins with a vuggy quartz filling and stylolites parallel to both foresets and principal bedding planes. Although the former are almost always truncated by stylolites, it is considered likely that both veins and stylolites belong to a common earliest deformation episode in which the solution from stylolites was balanced by deposition within the veins. This is supported by the observation that stylolites are observed exclusively along bedding planes and veins are formed perpendicular to bedding, compatible with a common vertical principal stress axis which suggests that they may simply be a consequence of burial. Sample 102 has evidence of an episode of mesoscopically homogeneous strain that deformed the stylolite surface, but predates several fractures. All veins and stylolites have been folded with bedding and are cut by later fractures.

The necklace pattern of fractures, with at least three contemporary sets of fractures rotating with bedding around the fold axis, shows that the fracture system also predates the folding and that it may have accommodated the imposed strains during folding. It can also be established that many fractures formed after the vein and stylolite episode.

It is therefore suggested that, exactly as in the Bernesga Valley, a multiple fracture network formed in response to imposed strains and continued to be reactivated to allow folding. The majority of fracture orientation diagrams shown in Figure 6.4 show only three sets of fractures;

the fourth shear system required by the Reches theory to accommodate a three-dimensional strain may be provided by bedding parallel displacements; evidence (in 6.3.8) exists for both inter and intra-bed shear. A significant difference between the Bernesga Valley and Punta Vidrias in this respect is the nature of these movements: lineations on bedding planes are not common at Punta Vidrias, where the role of the more abundant shales between quartzites is more important both as detachment horizons for thrusts and for intrabed shear as recorded by the deformation of the pipes. The reason for the lack of lineations on quartzite beds is not hard to understand: the early episode of bedding plane solution produced highly irregular bed-to-bed contacts along interlocking stylolites which would require much higher stresses to shear than movement on adjacent shales. Although the Punta Vidrias anticline has not been studied in such detail at Cabo de Peñas, the bedding-normal necklace can again be identified, so that cataclastic fold accommodation is likely (Figure 6.5).

Fracture densities are dominated again by the formation of deformation zones with spacings of 1-5m. The relatively restricted range of densities recorded may be due to the lack of the very thick quartzites at Punta Vidrias; it is only in these lithologies that the very highest densities are observed at Bernesga Valley. An additional observation was made here about the presence of a fabric of short acute fractures in some deformation zones and along the fault discussed in 6.3.3. These have similarities with feather fractures described by Hancock and others (2.1.4) and could be interpreted as extension fractures formed during shear on the deformation zone or fault.

Mesoscopic evidence from the Bayas Fault can be used to build up a complex tectonic history in which the earliest event was the formation of the fault plane. This, however, postdates both the regional vein and stylolite episode, fracturing, and folding since the fault cuts all these features. Undulations of the polished fault surface suggest that they were formed as part of the original fault plane morphology rather than by wear during movement because of their highly cylindrical nature, which does not terminate in steps. Intrinsic undulations on fault planes are also known on a much smaller scale from Westphalian conglomerate pebbles collected in the Central Coal Basin, where the undulations extend cylindrically across the whole fault plane without steps, and are much longer than the displacement. They can therefore only have formed as initial features in this case. The smaller lineations, however, are shorter and stepped: these could be genuine wear grooves, although consistent stepping directions are difficult to detect.

Subsequently to formation and initial displacement along the fault plane, dilatant fractures opened normal to it and were filled with a variety of products. The orientation of these fractures is not easily reconciled with dextral shear on the fault, and a number of them clearly cut the fault plane. However, some overlap of activity is suggested by the presence of breccias similar to those on the fault plane itself within the dilatant veins. Hancock & Barka (1985) also report dilatant fractures normal to a fault which they have called 'Comb fissures'. Because of their bedding perpendicular character, it is suggested that these fractures are reactivated from the earlier pre-fold fracture system, probably by high fluid pressures existing within the fault. A mechanism of seismic pumping (Sibson et al. 1975) would explain all the observed characters of the dilatant fractures. Dilatancy in the pre-seismic period allows ingress of pore fluid under the hydraulic gradient created. Pore pressure re-equilibriates as dilatancy reduces, and when the failure envelope is first breached for the appropriate pore fluid pressure, sudden crack closure can expel large volumes of fluid. It is possible to view the process as driven either by the remote applied stress or by the pore fluid pressure: in both cases, the result is the transport of large amounts of fluid, but only in the stress-driven model are large hydrostatic pressures created by faulting itself. This model could apply to the reactivation of the pre-existing fracture network and filling of the fractures with the various products, including fault breccia, described here.

The final stage of the fault history is recorded in the displacement of both fault plane and dilatant fractures along a bedding plane, in this case a shale layer.

The contrast between the exposure of the Bayas fault and its southwest and northwest ends is not easily understood. One possible explanation is that early fractures did not exist in appropriate orientations to allow the formation of dilatant veins in the northeast. The sub-horizontal dense protobreccia adjacent to the fault in this locality could be partly an earlier bedding-normal fracture fabric where the beds have been locally steepened to vertical.

The similar orientation, fault plane morphology and strike-slip displacement of the Punta Vidrias and Punta del Arpon faults raises the possibility that they may be linked. Extending both faults along strike, it can be seen (Figure 6.1) that they meet the offshore trace of the Ventaniella fault in a position which require the same amount of dextral strike-slip to match them as the axis of the Punta Vidrias anticline. This would imply a fault approximately 15km long and therefore potentially of considerable regional importance.

An important similarity between the Punta del Moro fault exposure and that at the kaoline mines is the presence of regularly spaced, sub-parallel fault planes with fault gouges 1-2m apart. This localisation suggests the formation and spacing of deformation zones; possibly the faults localise on early-formed deformation zones.

The origin of the shatter fracture pattern is unknown. One geometry that the curving cracks recall is that of failure in a Boussinesq point loading configuration, in which a median tensile fracture is flanked by shear fractures which curve up to the free surface (Figure 2.12). The presence of a large number of fractures at an acute angle is not predicted in this simple analysis, but can be understood if these fractures are simply early deformation zones which intersect a later fault. These intersection points could provide the stress focus that the Boussinesq configuration requires to generate the curved cracks, and would explain the spacing of the shatter points along the fault.

6.4 MICROSTRUCTURES

6.4.1 Grain Size and Shape

The number of grains per square millimetre measured in the S.E.M. is within the range measured for the Bernesga Valley samples (Appendix A4): the grain size of the Barrios quartzite at Punta Vidrias is therefore similar, between 0.1 and 0.2mm.

Grain shape fabrics were easily visible by eye in all of the thin sections, and these were investigated in more detail for samples CV1, CV5 and 102 by determining the three dimensional fabric. Axial ratios from Fryplots of up to 2.8 were obtained.

The weakest fabric, for CV1, was oblate ($k=0.515$, $\nu=0.314$) with a natural strain, Es, of 0.124 (Appendix A5, Figure 9.5). As for the fabric of sample 14, the minimum principal axis of the fabric is sub-perpendicular to the bedding, and the maximum principal axis lies at an angle of 24^{o} to the bedding plane, which also contains the intermediate principal axis. The value of ρ, 1.07, indicates one of the best fits between calculated data and input.

More complex fabrics were revealed by the Fryplots of both the other samples. There were two fabrics in each of two sections for 102; a three dimensional fit was attempted for the most clearly defined fabrics in conjunction, and for the least clear fabrics together, which failed to give a best fit solution. The solution based on the clearly outlined fabrics in each section, gave a weakly prolate fabric ($k=1.179$, $\nu=-0.082$) and natural strain 0.440 (Appendix A5 and Figure 9.5). In this case, although the bedding plane again contained the intermediate principal axis, the maximum and minimum axes were symmetrically disposed in the great circle normal to the bedding. ρ took a value of 1.25, indicating a relatively poor fit. Although no best fit solution was obtained for the less clear fabrics, all trial solutions indicated an oblate fabric with the minimum axis sub-perpendicular to the bedding plane, and the maximum axis slightly oblique. The values of ρ for these trial solutions (1.20-1.21) were better than for the best fit solution to the other fabric.

Sample CV5 yielded three fabrics in one section, and two in another. These were offered to the three-dimensional ellipsoid-fitting procedure in all six possible combinations; the best possible fit could be evaluated by the parameter ρ, which gave very similar results (1.06 and 1.07) for two combinations. These also gave similar magnitude and orientations for the fabric: both were fairly prolate shapes ($k=1.325$, 2.381, $\nu=-0.140$, -0.408 respectively) with the highest values of natural strain in this study (0.760 and 0.838). The maximum principal axes were inclined to 10-15^{0} to bedding, the minimum axes at 60-70^{0}, and the intermediate axes therefore also oblique at smaller angles to the bedding. The other combinations that yielded solutions had much higher values of ρ (1.20, 1.40, 1.42) and gave quite different fabrics.

The fabric of CV1 is considered to be a primary fabric on the basis of associated type 1 grain boundaries (see below), and the orientation of the minimum principal axis sub-perpendicular to bedding with the maximum axis lying at a slightly oblique angle: these characters were also observed for sample 14 from the Bernesga Valley, although any of them could result from a tectonic component. On the other hand, there is positive evidence for an imposed tectonic strain in sample 102: the minimum principal axis is oblique to the bedding plane. The trial solutions for the more hazy fabric in 102 have the characteristics of a possible primary fabric, with the minimum axis sub-perpendicular to the bedding. It is therefore suggested that the two fabrics of 102 may represent tectonic and primary fabrics respectively.

This simple explanation also suggests a possible interpretation for the more complex fabrics of CV5. Two of the best fit solutions both have a possible primary fabric configuration, while the others clearly do not, suggesting again that a primary fabric may be distinguished from one or possibly more tectonic fabrics. In both the above cases, the fabrics interpreted as primary have larger natural strains than the tectonic components, but the better defined fabric is tectonic in 102 compared with primary in CV5. The existence of two distinct fabrics places some constraints on their mechanism of formation: this cannot be due to progressive modification of an early primary fabric (for example by grain rotation) since a complete spread of intermediate orientations would be preserved. The type 1 grain boundaries, and high G.M.A. values (see below) of 102 and vein quartz both suggest that these tectonic fabrics are due to crystal plasticity, and the same may be true for CV5.

6.4.2 Grain Boundaries and Porosity

Generally only type 1 (usually 1b) grain boundaries are seen, although some type 2 were observed in CV2 (Appendix A2). This is taken to indicate a lack of grain boundary solution processes, which is confirmed by the observation from CV1 that good overgrowths are seen in directions parallel to stylolites. Both existing and pre-cataclastic porosities are low for all specimens (less than 4% and 13% respectively), and such porosity as exists is type 1.

6.4.3 Fractures

a) Intragranular Fractures. Intragranular microcracks, visible in

C.L., have similar characteristics to those seen in the Bernesga Valley. The majority have impingement geometries; grain edge cracking was also observed.

b) Transgranular Fractures. Transgranular cracks as described in the previous chapter are of particular importance in the Punta Vidrias samples. When open or filled by oxide, they are visible in the optical microscope, but many more are revealed in C.L. by their non-luminescencing quartz matrix, although this too can occasionally be seen optically as lines of small, slightly misorientated, rounded patches within otherwise homogeneous and unstrained grains. The transgranular fractures may extend the whole length of a section yet may be only 50μ wide. They often occur in pairs with separations of approximately a quarter of a grain diameter, or as arrays of en echelon cracks with each individual crack at a very low angle to the array boundary. The overlaps of such cracks are shown in Plate 6.5a where a good example of the sort of crack interaction described by Kranz (1979b) an 'en passant' can be seen: the crack tips curve very slightly towards each other and then diverge. Bifurcations of the main microcrack may enclose small fragments which recognisably belong to the adjacent grains in the walls of the microcrack. A transgranular microcrack can be observed in Plates 6.6a and 6.6b exploiting in part an earlier shear. In the optical micrograph, the later transgranular is opaque due to its iron oxide, while the matrix of the shear appears as birefringent quartz. The same view in C.L. contrasts the largely non-luminescing, black shear matrix with the brightly-luminescing iron oxide, and shows that the shear and the microcrack are very similar features, with the former differing by having a shear matrix and small shear displacement. A final observation is that multiple generations of microcracks clearly exist.

These observations can be rationalised by considering many transgranular microcracks as parts of low-angle en-echelon vein arrays. Sections through such arrays may give the appearance of paired microcracks.

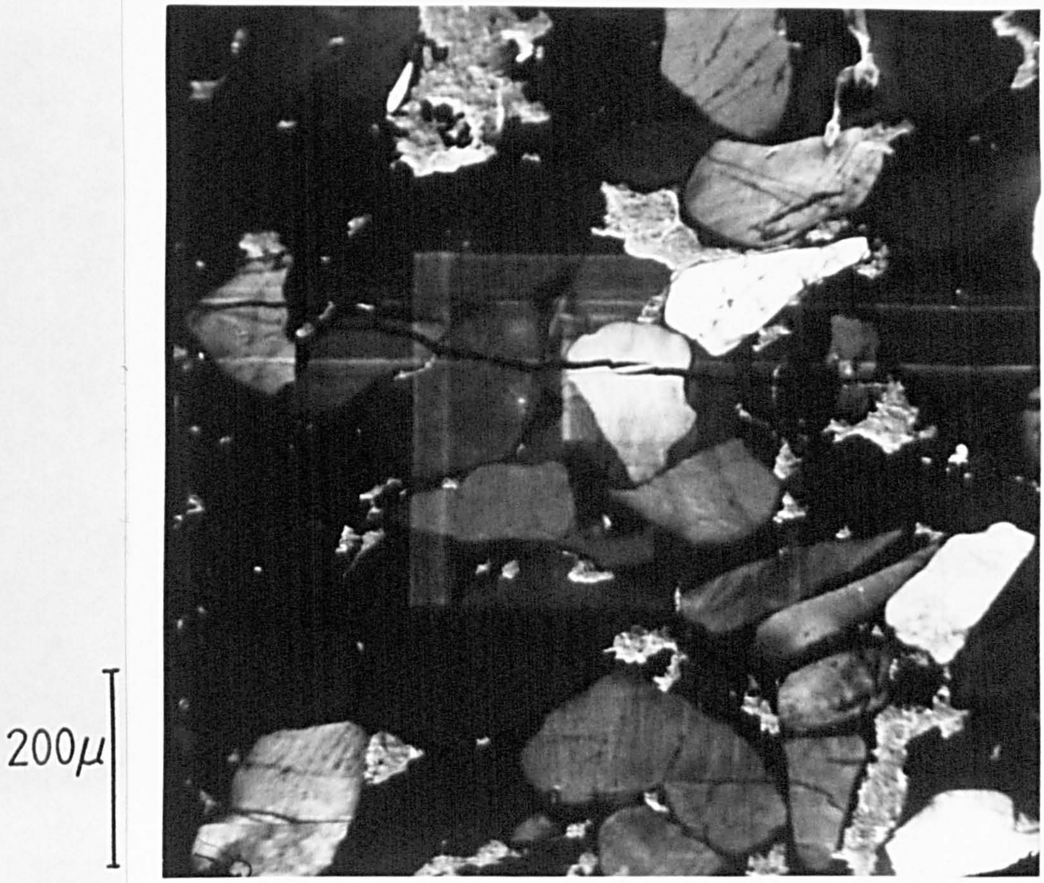

PLATE 6.5a

Transgranular microfracture array overlap, centre of field of view, is an excellent example of 'en passant' geometry sample CV5, C.L.

PLATE 6.5b

A fault visible from the fine grained shear matrix, can be seen narrowing from left to right until it becomes a transgranular microcrack beyond the field of view. A subparallel microcrack, filled by iron oxides, cuts a grain at top right. Sample CV7 X.P.

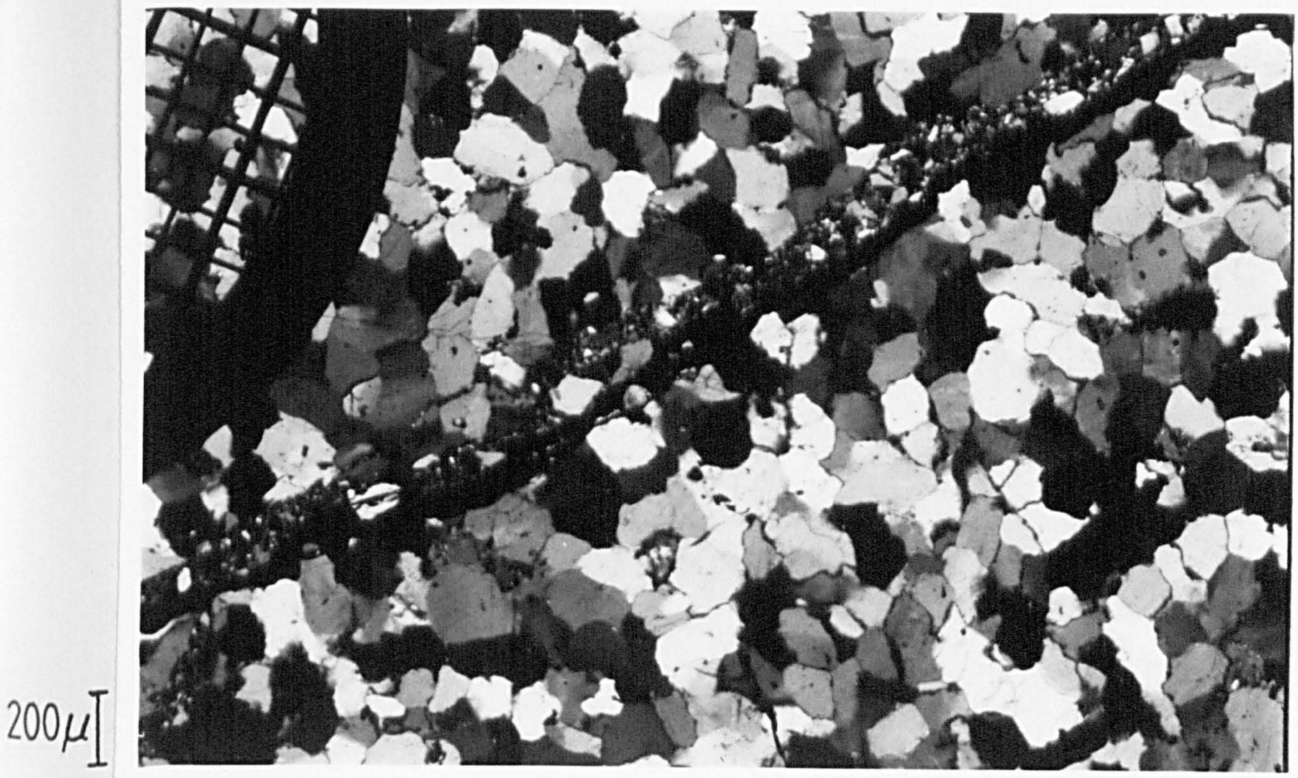

PLATE 6.6a

A transgranular microcrack, visible as an opaque line of iron oxides, exploits the edge of an earlier shear with a fine grained matrix Sample CV7, X.P.

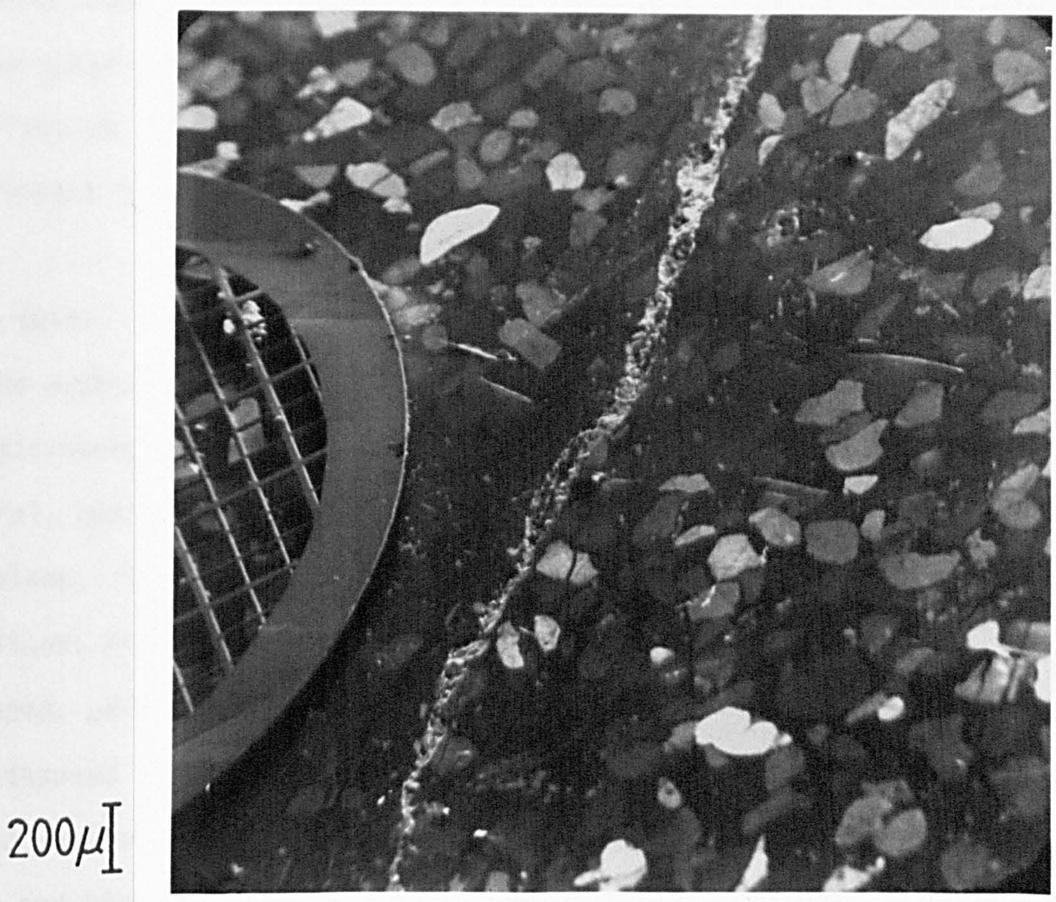

PLATE 6.6b

A transgranular microcrack is seen as brightly luminescing iron oxides exploiting the shear which has a non-luminescing matrix with grain fragments. The crack is the same as Plate 6.6a. Sample CV7, C.L.

Both the observations of the low twist angle and the 'en passant' type of crack interactions can be used to deduce that the arrays formed at a very low angle to the maximum prinicipal stress. Similar considerations apply to the origin of the transgranular cracks as given in 5.3: either an unstable tensile crack growth, or growth by linkage of impingement-induced, intragranular cracks can be envisaged.

c) Microfracture Densities. Microfracture densities (Appendix A3) vary from 8 to 16mm^{-1}, and conform to all the trends noted in 5.3.4. These are shown as crosses on Figures 5.20 to 5.22, in particular confirming the increase of microfracture density with shear matrix up to a maximum of 25%, followed by a decrease with further shear matrix.

d) Faults. Shear faults with widths from 50μ to greater than the thin section are observed. The narrower faults have already been compared in important respects to transgranular microcracks, and this impression is confirmed in Plate 6.5b, showing a shear fault narrowing to become a cemented transgranular crack. The geometrical similarity between the narrow shear faults and the transgranular fractures implies that shear is localised on early transgranular fractures, in the same way as deduced for the compact type of faults in 5.3.7.

6.4.4 Veins

An example of a typical bedding-perpendicular vein (6.3.6) was studied at a microscopic scale in sample CV2. The vein matrix consists of large, euhedral, quartz grains with a strong shape fabric due to shear across the vein plane. The quartz grains have type 1 grain boundaries and are full of inclusions, but do not appear to be microcracked. They also have strongly developed, pervasive, undulatory extinction, for which extinction angles were measured separately from the host-rock, giving values of 21^{o} and 9^{o} on limited samples from two perpendicular sections (Appendix A7). The shape fabric and high G.M.A. values, together with a lack of microcracking, are fairly conclusive evidence for a period of crystal plasticity and vein-parallel shear after the formation of the vein.

6.4.5 Stylolites

The stylolites are readily visible in thin section as highly porous, irregular bands filled by well-crystallised phyllosilicates, oxides and chlorite, with diffuse edges, sometimes sending branches off the main parting at high angles. Both original grains and overgrowths are truncated by the stylolites, which are in turn cross-cut by transgranular and shear fractures.

6.4.6 Optical Strain Features

Samples CV1, CV2, and CV7 have very low G.M.A. values (less than 4^{0}) and also a positively skewed distribution of extinction angles, both features comparable to samples in the Bernesga Valley (Appendices A7, A10). Sample 102 has a G.M.A. of 7.1^{0}, and a less skewed distribution of A. The much higher fracture density of CV7 does not correspond with any significant changes in G.M.A. (Fracture densities of CV2 and 102 were not determined), and the very high values of G.M.A. for the vein also do not appear to be associated with increased microcrack densities. These observations would indicate that, like the vein, the high G.M.A. of sample 102 is not due to microcracking. From the stronger grain shape fabric of 102 compared with CV1 or CV2, and the strong fabric in the vein, it is possible to infer that the higher G.M.A. values are due to the onset of crystal plasticity.

Samples CV4 and CV6 also have higher G.M.A. values: these are discussed below in association with the microstructures of the Bayas fault.

CV5 has a G.M.A. of 4.77^{0}, which is significantly higher than CV1, CV2, or CV7, and a higher microfracture density (Appendix A4). This, combined with the correlation observed between microfracture density and

G.M.A. in 5.3.4. suggests that the high G.M.A. is due to microcracking. However, the tectonic fabric of CV5 points to the operation of intracrystalline plasticity, which may equally be responsible for the higher value. The two possibilities cannot be distinguished.

6.4.7 Microstructures of the Bayas Fault Plane

The spectacular features of the Bayas fault plane were made the subject of an intensive microstructural examination with the aim of deducing a palaeostress estimate in conjunct ion with Transmission Electron Microscopy performed by Dr. M. Drury at the University of Utrecht. This section incorporates these observations which are gratefully acknowledged.

a) Cataclasite Matrix. The matrix of the cataclasite appears as a light grey very fine grained quartz in hand specimen; in this section, the grain size is generally too small to resolve, but some small strain-free grains are seen growing into strained grains, and they may have crystallographically controlled faces. These features suggest fluid-assisted grain boundary migration. There is also a concentration of very fine grained iron oxide in the cataclasite matrix.

More detail is revealed in Cathodoluminescence, where three components can be identified in the matrix: luminescing angular fragments of grains, non-luminescing fine-grained matrix interpreted as cement, and the fine-grained iron oxides.

b) Wall rock and cataclastic wall rock fragments. Fragments of wall rock are not distinguishable from matrix in the cataclasite hand specimen: both appear as fine-graind, light grey quartzite. Optically, however, original grains with type 1 grain boundaries and negligible porosity are easily visible (Plate 6.7a) in which three separate features are observed:

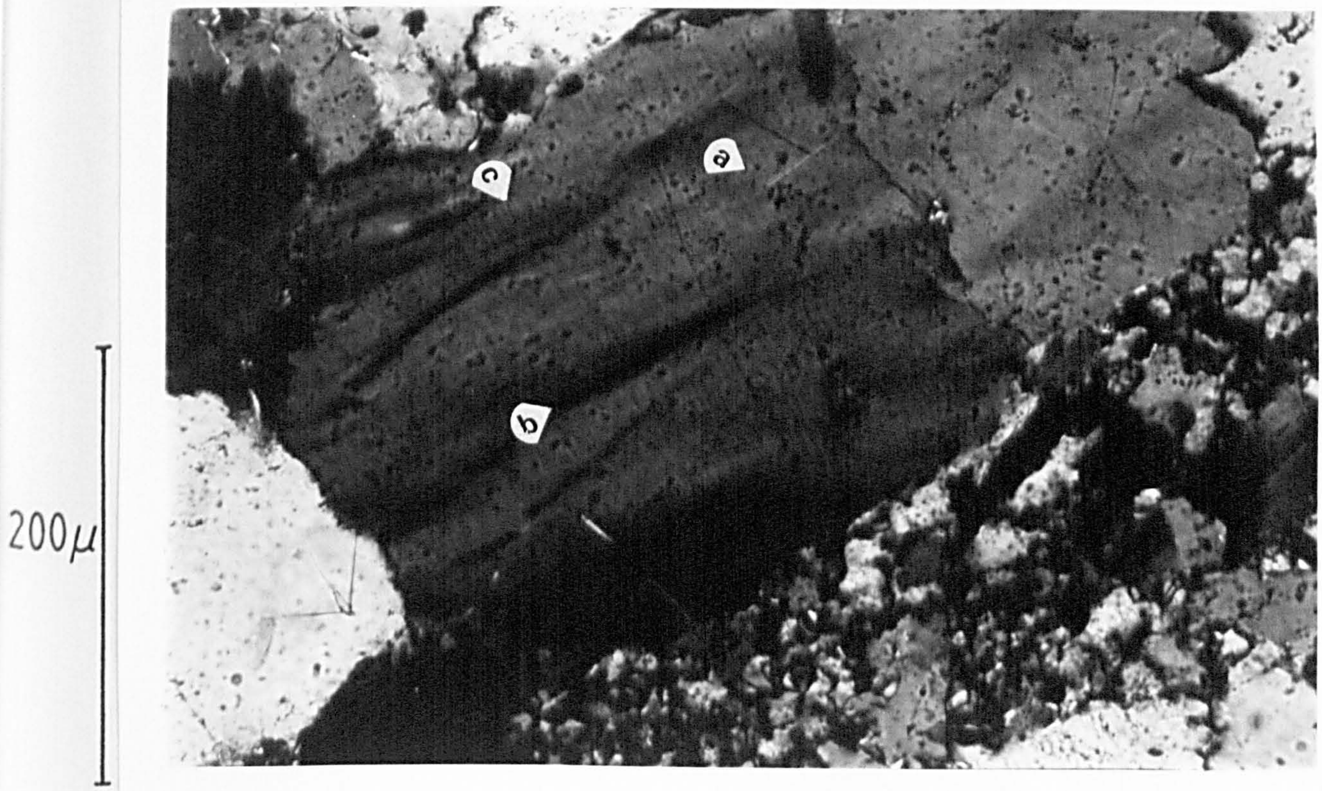

PLATE 6.7a

Fragment of grains in cataclasite from Bayas Fault Plane. Three features can be identified:

a) Microfractures. Curved lines of bubbles or inclusions.

b) Deformation Bands. Triangular shaped bands of extinction contrast with poorly defined edges.

c) Deformation Lamellae. Sharply defined, extremely narrow bands of extinction contrast, perpendicular to deformation bands. Sample CV4, X.P.

i) Microfractures with the same characteristics as described in 6.4.3 are common, usually sub-parallel within single clusters of grains but not between different clusters, and they are often perpendicular to deformation bands (below). Their optical appearance is distinguished by transgranular paths with curved profiles (Plate 6.7a), but they are much more clearly seen in C.L. where they appear as non-luminescing bands up to 100μ wide, and intragranular cracks are also revealed sub-parallel to the transgranular cracks. Some of these cut both clusters of grains and cataclasite matrix. Mode I displacements are dominant; microcrack densities of $15mm^{-2}$ were measured.

The microcracks have also been seen in T.E.M., where they are straight-walled and have a very distinctive dislocation substructure consisting of a low density of straight dislocations and a high density of radiation damage centres. The former feature has been described for pressure-shadow fringes of quartz, and the latter for quartz cement in cataclasites (Stel 1981), suggesting that the T.E.M. features are cemented microcracks.

ii) Deformation Bands. The grains in both wall rock and fragments are unique in this study for the abundance of deformation bands: a majority of grains have several bands which are sub-parallel across single clusters (Plate 6.7a). They are distinguished optically from microfractures by rather diffuse and non-parallel edges, forming triangular shapes of differing extinction position up to 10μ wide. They are not visible in C.L.

iii) Deformation Lamellae (D.L.). These have some optical representation which is seen exceptionally at high magnification as very narrow, sharp-edged lines of contrasting extinction position, only a few microns wide and up to several tens of microns long (Plate 6.7a). In T.E.M. however they are well defined by a banded sub-grain structure of elongate sub-grains 1.5μ wide, mostly parallel to basal and also to rhomb planes. The sub-grain walls are serrated and consist of segments of dense, well-ordered dislocation networks with two or three sets of dislocations. The sub-grain walls are decorated by bubbles.

Dislocation densities vary from $2 \times 10^{13} m^{-2}$ to $4 \times 10^{12} m^{-2}$ with an average of $7.5 \times 10^{12} m^{-2}$ (measured over a total area of $80 \mu^2$ at 11 sample sites in four grains). Within the D.L. subgrains, dislocations are usually arranged in coarse, well-ordered hexagonal to square networks, and many may link bubbles. This type of structure indicates recovery.

Deformation lamellae appear to be more common in the intact wall rock than in clusters of grains in the cataclasite matrix. They are always associated with deformation bands, but the latter may occur without lamellae.

Deformation Lamellae are not visible in C.L.

The optical strain features as assessed by the geometric mean of extinction angles (G.M.A.) give high values for both the gouge sample CV6 and the fault plane sample (CV4): 10.91^{o} and 5.34^{o} respectively. The particularly high value in CV4 is clearly due to the D.L.: measuring of grains with D.L. only gives a G.M.A. of 16.68^{o}, compared to an aggregate value for all grains within fragments of 15.086^{o}, and 3.67^{o} for grains within a late vein (Appendix A7).

c) **Gouge Matrix.** The gouge matrix is a yellow, brown and red powder with a faint fabric defined by colour banding. In thin section it consists of angular grain fragments in a fine-grained quartz matrix with a high concentration of iron oxides both as fine disseminated speckles and larger, amorphous, clast-supporting lumps.

d) **Black Veins.** The black glassy quartz described in 6.3.3. occurs both as a filling for the large dilatant veins perpendicular to the fault and an anastomosing network of very thin veins in the cataclasite on the fault surface. In optical thin section, the reason for their dark colour becomes apparent: they have a very high density of extremely fine-grained iron oxide particles. More useful information can be obtained from C.L.:

the luminescence of these veins contrasts with the luminescence of the cataclasite matrix and with the luminescence of intragranular crack cements within fragments of wall rock. This is seen most readily by windowing luminescence levels using the C.L. image in conjunction with the I.M.A.S. system. In Plate 6.8a, the ordinary C.L. image of several thin black veins can be seen luminescing as a ligher grey than the cataclasite matrix. In Plate 6.8b both black veins and cataclasite matrix are non-luminescing, and it can be seen that no grain fragments are present in the black vein. By manipulating the windowed level of luminescence, an image of the same area in Plate 6.9a shows the cataclasite matrix and black veins as bright in order to show that intragranular cements within a grain adjacent to the black vein have a different luminescence: they are not discriminated from the host grain fragment. The fourth image of the same area (Plate 6.9b) shows the intragranular cracks as bright, distinguishing them from the host grain, cataclasite matrix and black vein. It is therefore possible to establish that host grains, intragranular cement, cataclasite matrix and black veins each have their unique luminescence, pointing towards separate sources.

e) Barytes Veins. Several of the large, fault plane-normal, dilatant veins contain radiating clusters of euhedral barytes. Optically, barytes is colourless and isotropic, but in C.L. two more interesting textures are observed (Plate 6.10). A large part of the central vein is filled by brightly luminescing homogeneous barytes, which also occurs as small euhedral crystals. Exceptionally bright patches can be distinguished as iron oxides. Below the homogeneous barytes, there is a variegated texture referred to as 'speckly-mottled' shown in more detail in Plate 6.7b. This shows that three components are very finely intergrown: barytes, iron oxides, and non-luminescing quartz. Sub-parallel veins appearing light grey are more black veins as described above.

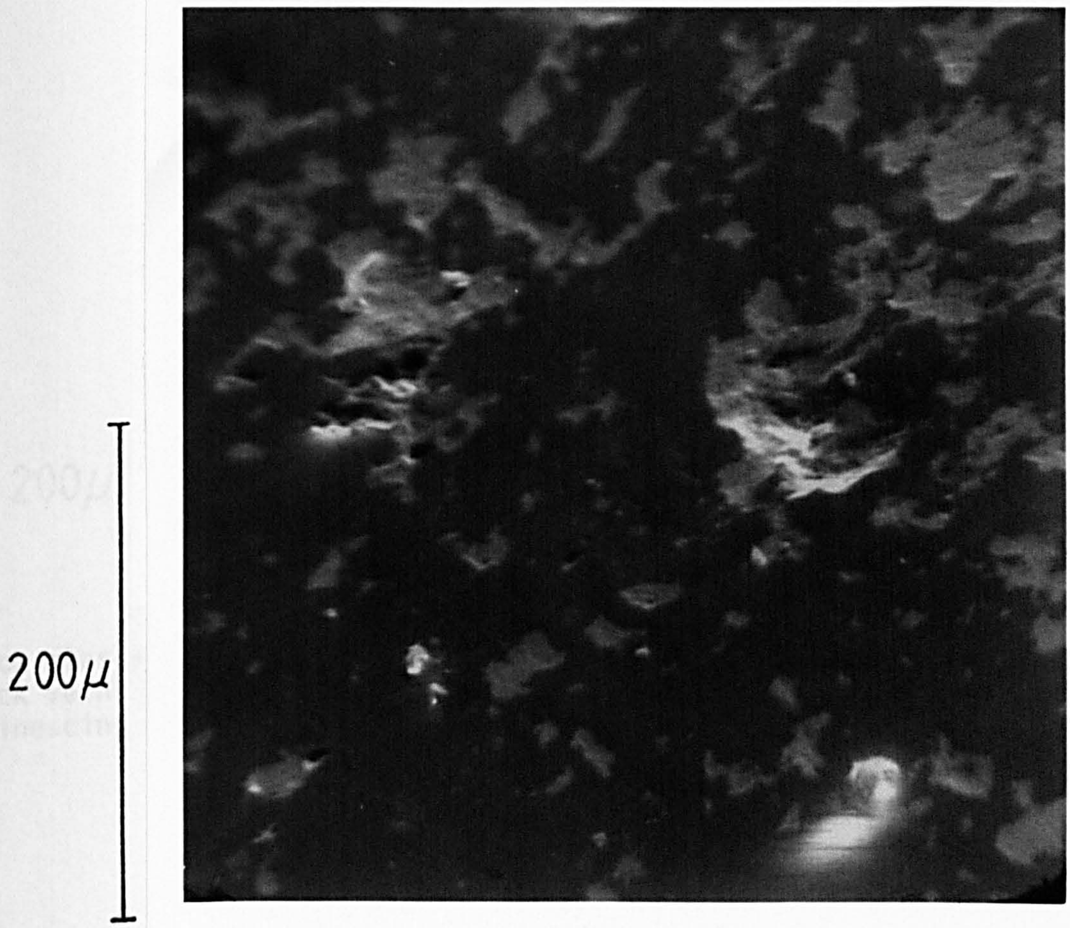

PLATE 6.7b

'Speckly-mottled' texture of dilatant vein matrix, Bayas Fault. There are three components:

a) Brightly luminescing iron oxides.
b) Light luminescing barytes.
c) Non-luminescing quartz.

The texture is due to the fine interspersion of all three components. Sample CV4, C.L.

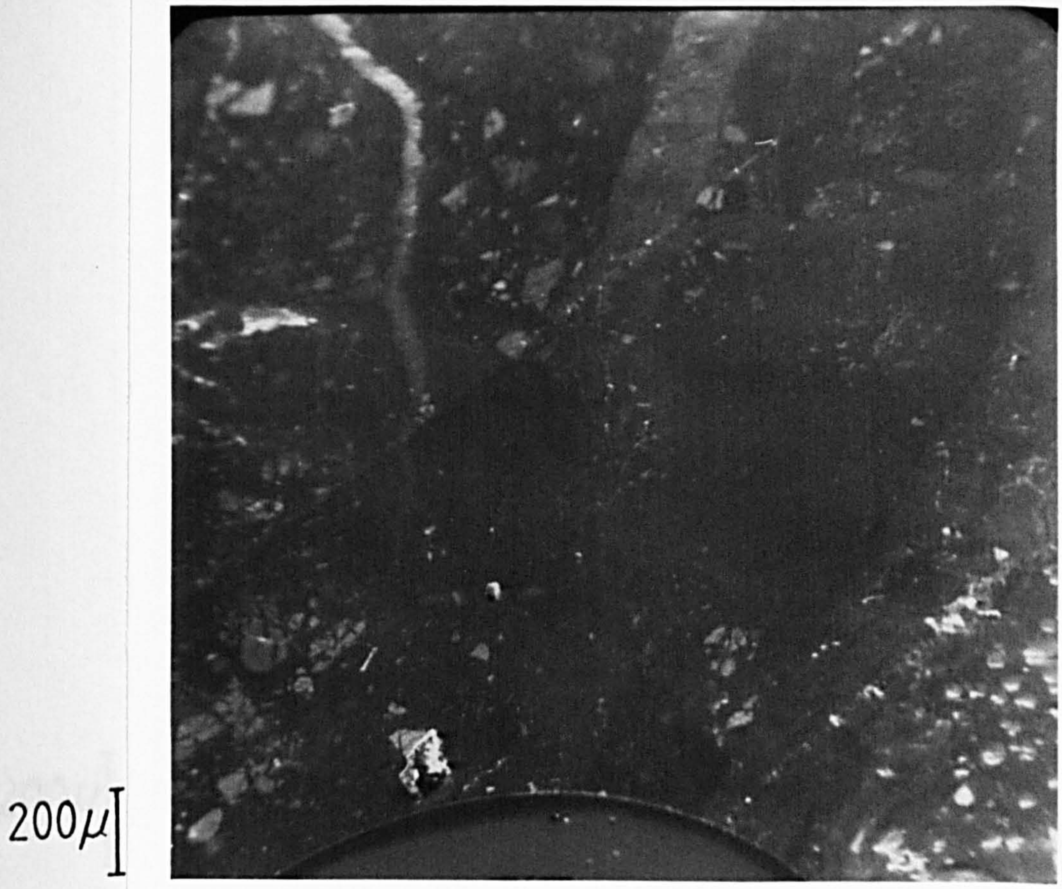

PLATE 6.8a

Black glassy quartz veins, Bayas Fault. This shows a contrast between the black veins (luminescing light grey) and the dark cataclasite matrix with luminescing grain fragments. Sample CV4, C.L.

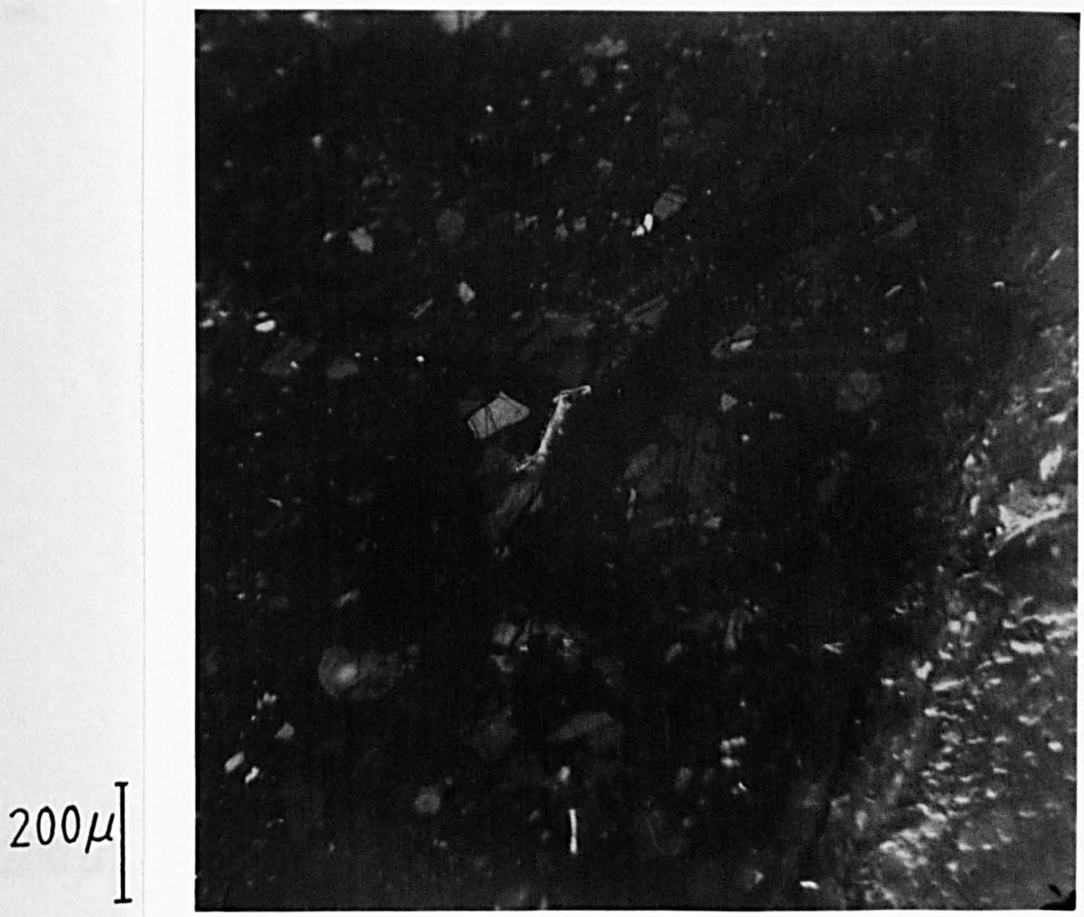

PLATE 6.8b

In this view, both black veins and cataclasite matrix are non-luminescing, and the lack of grain fragments within black veins is apparent. The brightly luminescing feature on the right is a barytes vein. Sample CV4, C.L. Intragranular cracks in a grain fragment to the left of the centre.

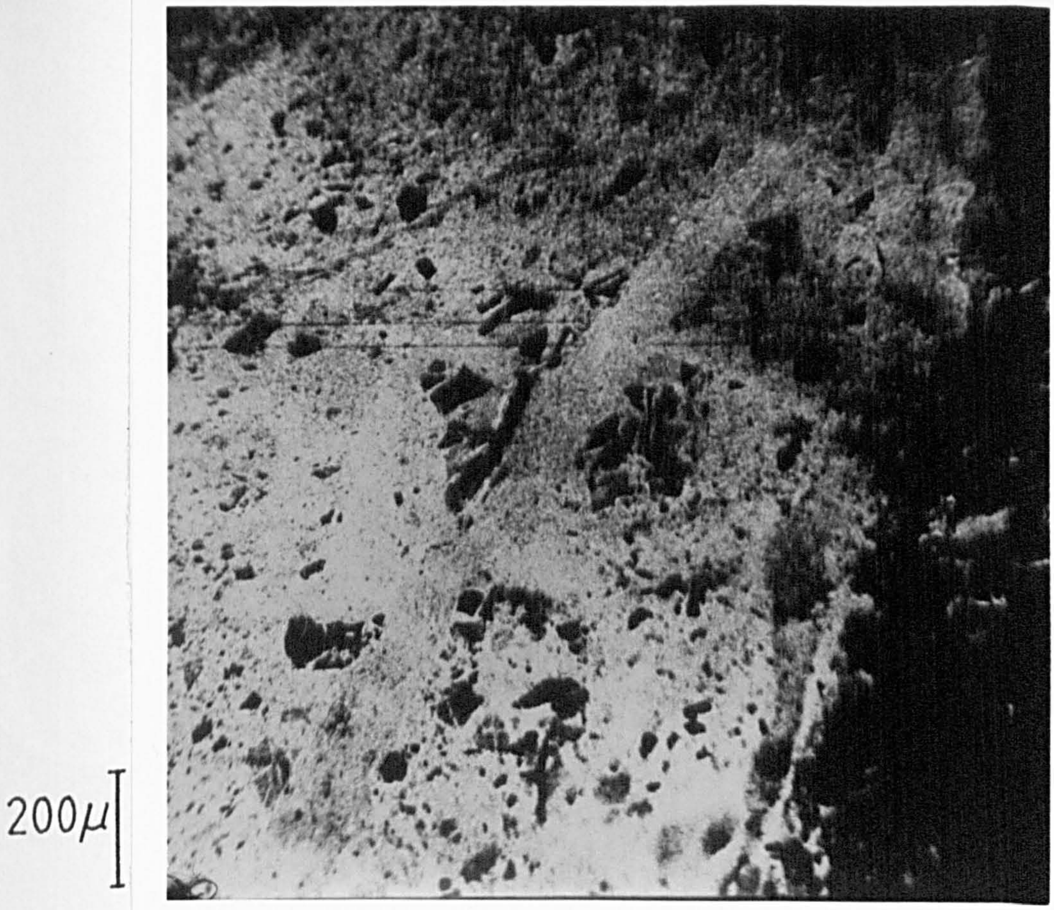

PLATE 6.9a

Black veins and cataclasite matrix are bright, but intragranular cracks in the grain fragment to the left of the central vein, visible in Plate 6.8a, are black. Same area as Plate 6.8b. Sample CV4, C.L. with I.M.A.S. system.

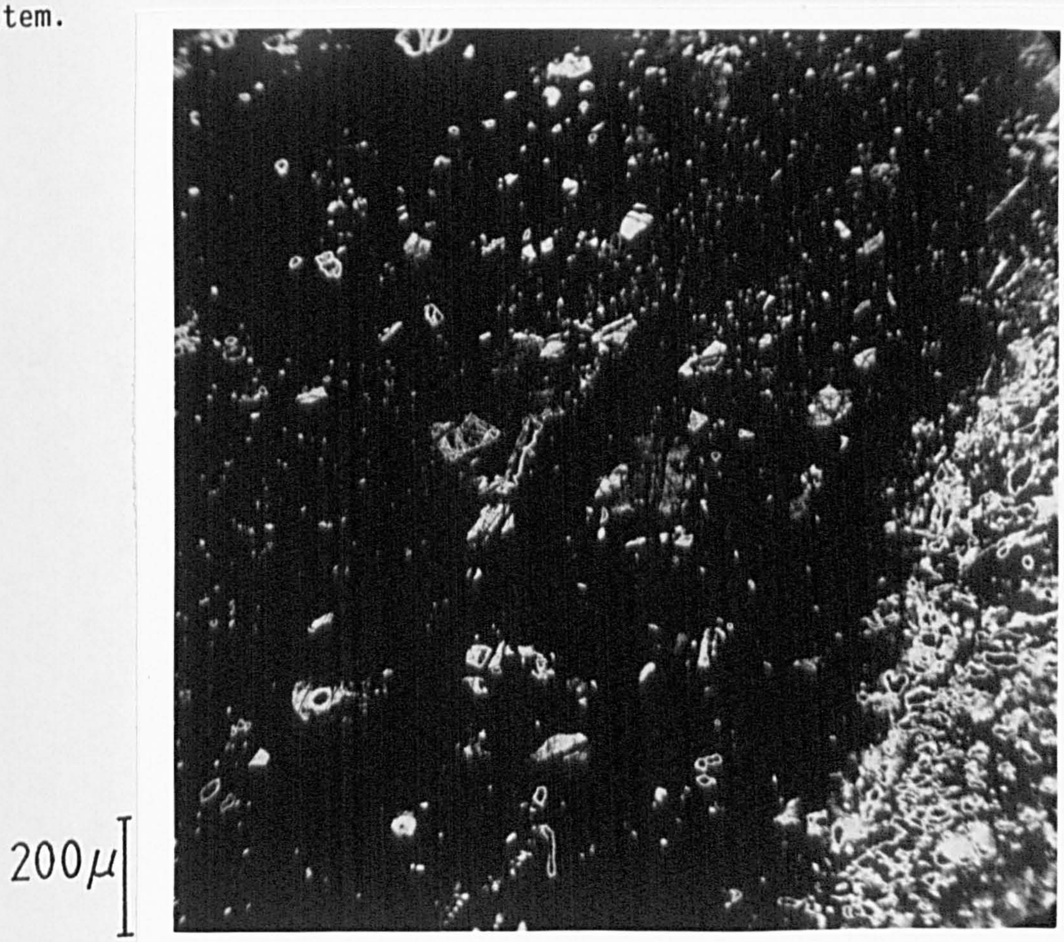

PLATE 6.9b

Black veins and cataclasite matrix are black, but the intragranular cracks referred to in the previous two plates are bright in this view. Several grains also have bright oxide rims, which are seen abundantly with barytes

PLATE 6.10

Photomontage of Barytes Vein. Five components can be identified:

a) Bright luminescence, distributed small patches - iron oxides.
b) Bright luminescence in central vein - barytes.
c) 'Speckly-mottled texture' of central vein - barytes, iron oxides and quartz finely intergrown.
d) Light Grey Veins sub-parallel to central vein - black glassy quartz.
e) Non-luminescing matrix with grain fragments - cataclasite matrix. Sample CV4, C.L.

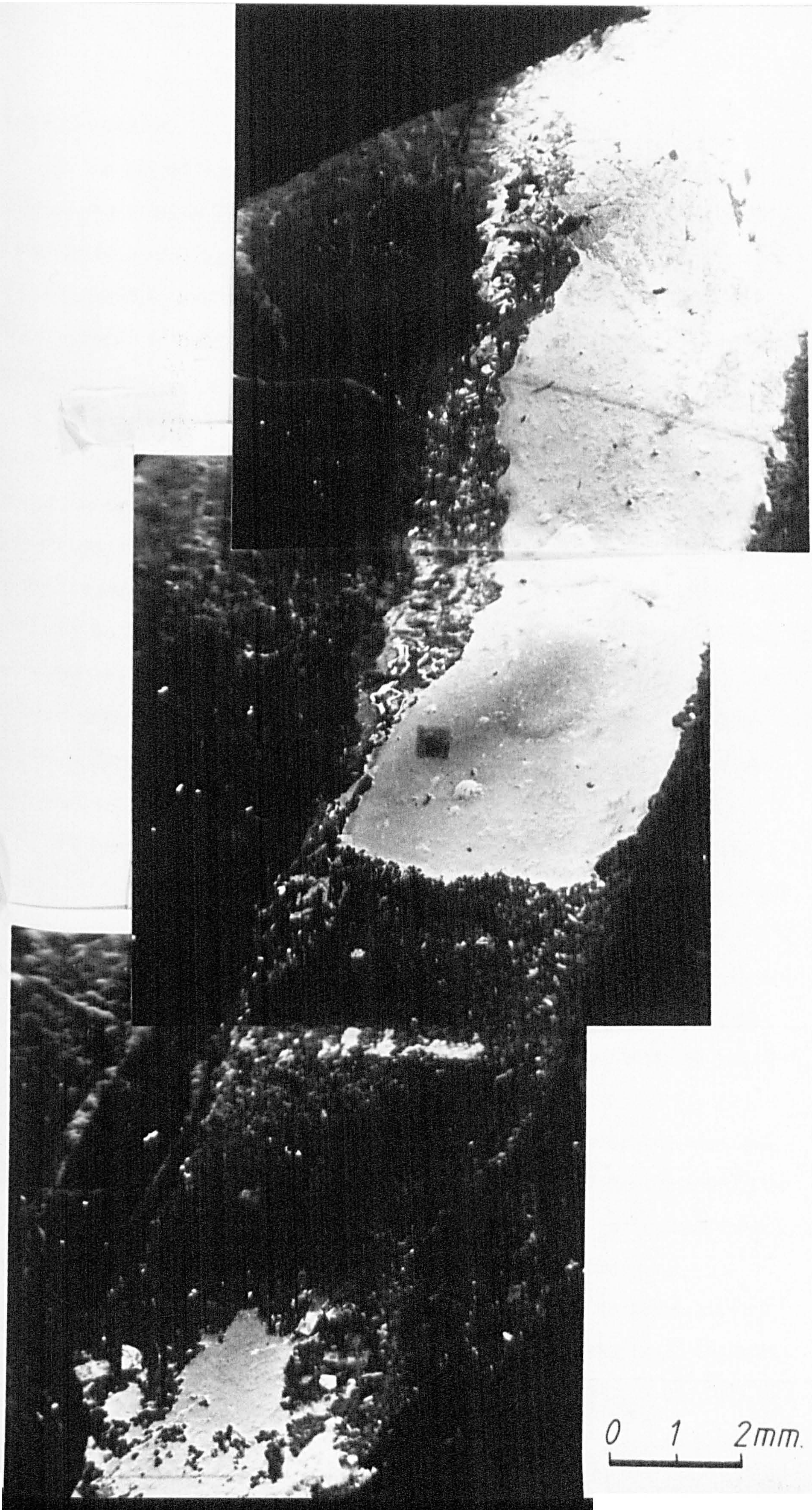
0 1 2mm.

6.4.8 Discussion

In the classification of 5.3.7., the microstructures of the Punta Vidrias and Cabo de Peñas samples are compact by all criteria: relatively large grain size, types 1 and 2 grain boundaries and type 1 porosity, low present and B.C. porosity. The type of shear faulting, dominated by transgranular microcracking, is also characteristic of these well cemented microstructures.

The microstructures of the samples reveal a slightly more complex history than the field evidence alone, in which the first stage was extensive cementation, followed by veining and solution transfer along bedding-parallel stylolites but not extensively on grain boundaries, after initial compaction and the production of a strong primary fabric (the two possible mechanisms of compaction and deposition cannot be distinguished, although the consistent inclination of the maximum principal axis to the bedding plane suggests imbrication by deposition). The microstructural evidence for the early nature of the solution/veining confirms the field observations that fractures invariably cut stylolites.

The high G.M.A. values of the fault plane samples, 102, and veins, have been interpreted as indicating an episode of crystal plasticity which was localised on fault planes and veins. This again complements the field observations of 6.3.8 on the deformed solution pits of sample 102. It was noted that the vein quartz was unusually full of inclusions: this leads naturally to the suggestion that the localisation of plasticity on the vein quartz may be due to hydrolytic weakening.

The ensuing cataclasis by the process of transgranular cracking and shearing evidently involved several phases of movement from the exploiting relationships observed between transgranular cracks and early shears but a chronology of individual fracture sets cannot be established.

The microstructures of the Bayas fault confirm the tectonic history deduced in 6.3.10, but add a large amount of extra information. The most important microstructural contribution is evidence for an early episode of intracrystalline plasticity restricted to the fault plane and shown by the high G.M.A. values of CV4 and CV6.

There is an empirical correlation between the occurrence of deformation lamellae in metals with the transition from creep described by a power law to a regime better described by an exponential law, known as 'Power Law Breakdown' (P.L.B.) creep. The lamellae indicate that the mechanism is a complex mixture of glide and creep because some recovery occurs. The significance of the D.L. is that the onset of P.L.B. occurs at a critical stress (σc) (or critical strain rate + temperature) which can be characterised by differential stress normalised by shear modulus (μ) for various materials:

Material	$\sigma c/\mu$ for P.L.B.
Metals	$10^{-3}\mu$
Halite	$10^{-3}\mu$
Calcite	$4 \times 10^{-3}\mu$
Olivine	$3 \times 10^{-3}\mu$
Quartz	$7\text{-}11\times10^{-3}\mu$

The value appears to increase with bond strength, but the quartz data are not well characterised. Therefore a conservative value for σ_c of $3\text{-}4\times10^{-3}\mu$ has been used to derive a stress estimate of 170 MPa for the deformation lamellae. It is stressed that this is a minimum value since recovery is indicated by the D.L. substructure, and a conservative choice of $\sigma c/\mu$ has been made; the actual quartz data suggests 300-500MPa.

There is some experimental evidence to corroborate these high values. Loose sand was deformed experimentally by Borg and Maxwell (1956) at 270-320^{o}C in various solutions at differential stresses of 100-110MPa. A slight increase of grains with D.L. (from 3 to 10%) was observed, indicating local onset of P.L.B. creep. However, Borg et al. (1960), in similar experiments, failed to produce a significant increase in D.L. even at 190MPa. This, together with the low proportion of D.L. produced in the earlier experiments, suggests that widespread D.L. develop only at still higher stresses.

A second palaeopeizometer may be used on the basis of the dislocation densities: an experimental calibration on synthetic quartz by McCormick (1977) yields a value of 116MPa from the densities reported here. There are three important limitations to consider in this estimate: firstly, there may be large differences between synthetic and natural quartz (e.g. Paterson and Kekulawala 1979, Ord and Christie 1984). Secondly, it may apply only to small strains (1-2%), and lastly, as for the estimate derived from D.L., the dislocation network character, implying recovery, indicates that this stress is a minimum. It is proposed that the restriction of D.L. to the fault plane and the significance of the high stresses can be satisfactorily modelled by considering the stress system predicted by fracture mechanics in front of an advancing shear mode crack given in 2.3.1. The stresses in x, y coordinates of Figure 2.11 are:

$$\sigma_x = K_{II}\ fx(\phi)/2\pi r^{0.5}$$
$$\sigma_y = K_{II}\ fy(\phi)/2\pi r^{0.5}$$
$$\tau_{xy} = K_{II}\ fxy(\phi)/2\pi r^{0.5}$$

where K_{II} is the critical stress intensity factor for Mode II crack propagation, given by $\tau_{xyL}\ (\pi c)^{1/2}$ where τ_{xyL} is the remote applied shear stress and c the crack half length. $fx(\phi)$, $fy(\phi)$ and $fxy(\phi)$ are functions of the angle from the crack plane (ϕ) and r is the distance from the crack tip (Lawn and Wilshaw 1975a). Substituting for these and K_{II}, transforming to principal stresses and taking the difference, it is possible to derive the following expression for differential (σ_1-σ_3) in front of the crack tip:

$$\sigma_1-\sigma_3 = \tau_{xyL}c^{0.5}(fxy(\phi)^2+0.25(fx(\phi)-fy(\phi))^2)^{0.5}/\ \pi^{0.5}r^{0.5} \qquad 6.1$$

where $fx(\phi) = -\sin(\phi/2)(2+\cos(\phi/2)\cos(3\phi/2))$

$fy(\phi) = \sin(\phi/2)\cos(\phi/2)\cos(3\phi/2)$

$fxy(\phi) = \cos(\phi/2)(1-\sin(\phi/2)\sin(3\phi/2))$

The essential feature of Equation 6.1 is that stress rises to infinite values as the crack tip is approached. It has been pointed out that this is one of the strengths of the fracture mechanics approach (2.3.1) since it predicts that there is a 'process zone' in front of the crack tip where the assumptions of elasticity breakdown and other processes operate. It is therefore suggested that the formation of D.L. in the high stress induced in front of the crack is evidence for this process zone, which advances with the propagating crack and relieves the crack tip stresses. A similar model was proposed for the formation of shear zones by Attfield and Kusznir (1985), who used the Mode II crack as an analogy for a plastic shear zone, which was self-propagating due to the crack tip stress field for certain rheologies.

Microstructural evidence shows that cataclasis followed the early P.L.B. plasticity, breaking and rotating grains and clusters of grains into the cataclasite and forming a matrix of crushed fragments and cement. The evidence for grain boundary migration within this matrix might indicate a component of superplasticity. Narrow black veins closely interwoven with the cataclasite fabric were part of this process, indicating that fluids were involved, and also formed later veins with either homogeneous or finely-intergrown barytes and quartz. The episodic nature of intragranular microcracking cementation, cataclasite cement, and black veining is revealed by the different nature of quartz luminescence for each.

6.5 ILLITE CRYSTALLINITY

6.5.1 Results

16 illite crystallinities were determined with the objectives of establishing a regional metamorphic grade, and investigating the effects of burial and deformation, especially with respect to the Nalon thrust. The results (Appendix A8) have a very narrow range of values (Kubler Index from 0.6 and $0.35^{o}2\theta$), almost equally divided between the diagenetic and anchizones. The mean Kubler Index is $0.436^{o}2\theta$. An approximate stratigraphic log for the results is shown in Figure 6.13 constructed in the same way as those of 5.5.1 and distinguishing between quartzite and shales. The crystallinity does not show any trend with either stratigraphic position or lithology, or with structural position with respect to the Nalon thrust, the fold axial trace or the Bayas Fault plane. The mean shale crystallinity, $0.476^{o}2\theta$, is slightly lower than the quartzite ($0.404^{o}2\theta$), entirely due to the two low values recorded in the Black Shales.

6.5.2 Interpretation

It is clear that the small range of crystallinities cannot be related to any of the intrinsic factors that determine crystallinity and that there is no relationship between permeability and crystallinity: shales have no consistent differences from quartzites from the same locality. Yet the total range of crystallinity is greater than the mean diagenetic or anchizone error (+/-0.05 and $0.04^{o}2\theta$ respectively). It is therefore suggested that the small crystallinity differences are a function of lithology through a subtle intrinsic control such as pore fluid chemistry. However, the range of crystallinities is low enough over the two extreme types of sample measured (quartzite and shales) for a meaningful specification of the grade as diagenetic-anchizone boundary (Kubler Index

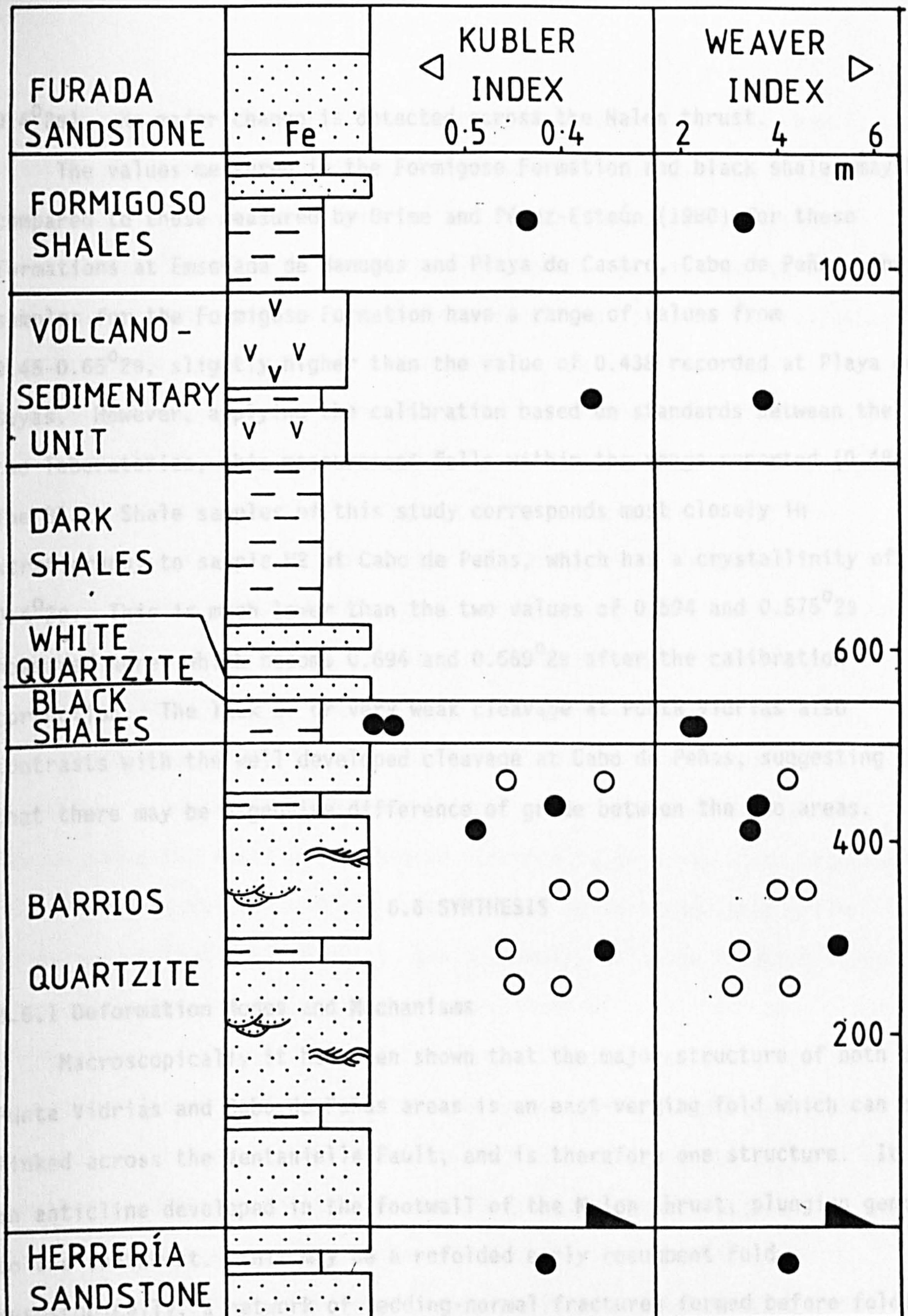

FIGURE 6.13

Stratigraphic log of Illite Crystallinity. There is no relationship to stratigraphy or contrast across the Nalon Thrust, but some variation in crystallinity.

$0.4^{o}2\theta$). No major change is detected across the Nalon thrust.

The values measured in the Formigoso Formation and black shales may be compared to those measured by Brime and Pérez-Estaún (1980) for these formations at Emseñada de Banuges and Playa de Castro, Cabo de Peñas. Their samples for the Formigoso Formation have a range of values from 0.45-$0.65^{o}2\theta$, slightly higher than the value of 0.438 recorded at Playa de Bayas. However, applying the calibration based on standards between the two laboratories, this measurement falls within the range reported (0.484). The Black Shale samples of this study corresponds most closely in stratigraphy to sample M2 at Cabo de Peñas, which has a crystallinity of $0.4^{o}2\theta$. This is much lower than the two values of 0.594 and $0.575^{o}2\theta$ measured here, which become 0.694 and $0.669^{o}2\theta$ after the calibration correction. The lack of or very weak cleavage at Punta Vidrias also contrasts with the well developed cleavage at Cabo de Peñas, suggesting that there may be a genuine difference of grade between the two areas.

6.6 SYNTHESIS

6.6.1 Deformation Modes and Mechanisms

Macroscopically it has been shown that the major structure of both the Punta Vidrias and Cabo de Peñas areas is an east-verging fold which can be linked across the Ventaniella Fault, and is therefore one structure. It is an anticline developed in the footwall of the Nalon thrust, plunging gently to the southwest. This may be a refolded early recumbent fold. Mesoscopically, a network of bedding-normal fractures formed before folding and were rotated with bedding around the fold axis, reactivation of which, together with bedding-parallel shear, allowed the accommodation of folding strains within the quartzite. This process is seen microscopically as the formation of transgranular cracks and then shear faults by movement along them; the cataclasis is controlled by these processes in the well cemented microstructure of the quartzites. Microscopic evidence is also seen for veining, solution along bedding planes, crystal plasticity on veins, and more pervasively at Cabo de Peñas. The distinctive mesostructures (undulations, lineations, normal dilatant veins, vein matrix, parallel veins, gouge zones separating protobrecciated pods at 1-2m intervals) and microstructures (cataclasite, microfractures, deformation bands, deformation lamellae) of the Bayas Fault have been described and used to deduce the fault plane history. This had an initial phase of plasticity before cataclastic shearing during which the evidence for fluid flow suggests a seismic pumping mechanism. The formation of deformation lamellae, limited to the fault plane, can be attributed to the high stress of a crack tip stress field, reaching at least 170MPa in this case.

The necklace fracture pattern and fold accommodation by multiple fracture sets is common to both the Punta Vidrias and Bernesga Valley folds in the Barrios quartzite. However there are two important differences between these two areas of the Somiedo-Correcilla unit. Solution transfer in the Bernesga Valley is never observed on a scale larger than grain boundaries, but at Punta Vidrias, grain boundary solution transfer is not common while bedding plane stylolites are abundant. This can be interpreted to indicate longer diffusion pathways at Punta Vidrias. A second significant difference is that no evidence for crystal plasticity is observed at Bernesga Valley. At Punta Vidrias, the shearing of veins and formation of deformation lamellae and grain shape fabrics adjacent to the Bayas fault plane are two clear instances of the operation of this deformation mechanism, also seen in the sample from Cabo de Peñas. This is reflected in the mean G.M.A. values of the two areas, which are 3.70^{0} and 5.22^{0} respectively.

6.6.2 Deformation Conditions

Using the entire range of crystallinities to infer temperatures from

Figure 45gives a range of 100-320^{o}C, but a better estimate can be obtained from the shale samples within the Barrios quartzite itself. The mean, 0.413^{o}2θ, gives a range of 191-291^{o}c.

The stratigraphic thickness of the Somiedo Correcilla unit can be estimated by summing the individual lithologies from the base of the Barrios quartzite, giving an estimate of 3.23-3.97km (Julivert et al. 1973). The minimum confining pressure was therefore 75-99MPa; with hydraulic pore fluid pressures, this becomes 46-59MPa effective confining pressure.

An increased crystallinity was noted for the Cabo de Peñas area compared to Punta Vidrias. It is suggested that this represents a small temperature difference, which may also be responsible for the crystal plasticity observed in the Cabo de Peñas sample and the better development of cleavage there. A further difference between the two areas is the kaolinisation of the Punta del Arpon and Kaoline mine faults. This has been attributed to an unexposed granite beneath the Cabo de Penas area (Pérez-Estaún pers. comm. 1982). All these observations support the possibility of higher temperatures related to plutonism. A small pluton in the Somiedo-Correcilla unit is exposed in the Belmonte thrust sheet 50km further south.

The crystallinities and inferred temperatures at Punta Vidrias and Cabo de Peñas are also significantly higher than those at Bernesga Valley; a temperature increase of 40^{o}C is likely (compare with 5.6.3). The stratigraphic thickness of the two areas is however identical (3.5km), and their structural features are comparable (large wavelength folds and thrusts) except for the proximity of the Narcea antiform; the evidence of this study is that no major increase in grade occurs across the Nalon thrust. It is therefore concluded that the increased temperatures in this part of the Somiedo-Correcilla unit could be due to local contact metamorphism, which reflects the regional increase in plutonism to the west. This increase in temperature is coincident with two changes in deformation mechanisms: the bedding parallel stylolite solution and limited crystal plasticity. Both of these are thermally activated processes which can be attributed to the temperature rise.

6.6.3 Regional Tectonic History

The earliest deformation observed is the veining and bedding plane solution transfer: it has been suggested that this is a burial phenomenon. Subsequently, some intracrystalline plasticity deformed early veins before cataclastically accommodated folding, which clearly predates thrust movement along the Nalon thrust and displacement on the Bayas fault. The timing of the Bayas fault movement is difficult to establish with more precision: its relationship to the Nalon thrust is not seen. However, if linked to the Punta del Arpon fault, it must have formed before the Permian displacements of the Ventaniella fault. Its kinematic significance as a dextral strike-slip fault is quite consistent with movement on the Nalon thrust towards the southwest: both indicate shortening in the NW-SE direction, which occurred in the final stages of the Variscan orogeny as the Ibero-Armorican arc was tightened. In this context it is significant that further west of this area, in the West Asturian-Leonese zone, there is a well developed set of late dextral strike slip faults with a strike from 107^{o} at Cabo Vidio, becoming 125^{o} at Cabo Busto. These faults have also been interpreted kinematically as late shear movements due to the arc closure (Peréz-Estaún 1985). Observations on the Bayas fault fit into this overall movement picture and extend it further east than hitherto, although there is a considerable swing in strike.

CHAPTER 7

LUARCA

7.1 STRATIGRAPHY AND LITHOLOGY

The oldest formation seen at Luarca is the top of the Los Cabos series. The lowest part of the formation at Portizuelo (Figures 7.1, 7.2) consists of alternate fine-grained, light grey quartzite beds, 0.5-1m thick, and black shale beds less than 0.5m thick. This is followed by a thick, well bedded quartzite unit (54m) with a few thin shale horizons near the top, referred to here as the 'Thick' quartzite, separated by a more prominent black shale 1m thick from a second thick quartzite (10m) referred to as the 'Top' quartzite. Based on mapping of the whole West Asturian-Leonese zone coast, Marcos (1973, Figures 11 and 12) equates the two thick quartzites to the quartzite which commonly marks the top of the Los Cabos series, described in some detail by Baldwin (1976) from this section. He distinguished five major lithofacies:

a) Foreshore. Alternations of sandstone, siltstones and shales with 1-1.5m beds of sandstone. Two sub-facies are identified, depending on whether the sandstones or shales are dominant.

b) Tidal Lagoon. Intercalations of mudstones up to 30m thick, siltstones and rare erosive-based sands 0.1-0.4m thick.

c) Offshore Facies. Sandstones 0.15-3m thick form 60 to 80% of this facies, with regular alternations of thinner-bedded siltstones. A typical sequence of sandstones fining up to siltstones is interbedded with tabular and lenticular cross-bedded sandstones up to 25m thick.

d) Shore-face Facies. Siltstones with occasional sandstones.

e) Muddy Shelf Facies. Mudstones and siltstones with rare sandstones.

These facies are in sequence the parts of a deepening bathymetric profile in which the relative proportions of tidal and wave energy vary. From the facies, Baldwin deduced a sequence of three transgressive-regressive couplets for the Luarca section: the Thick and Top quartzites are presumably the offshore facies of two such

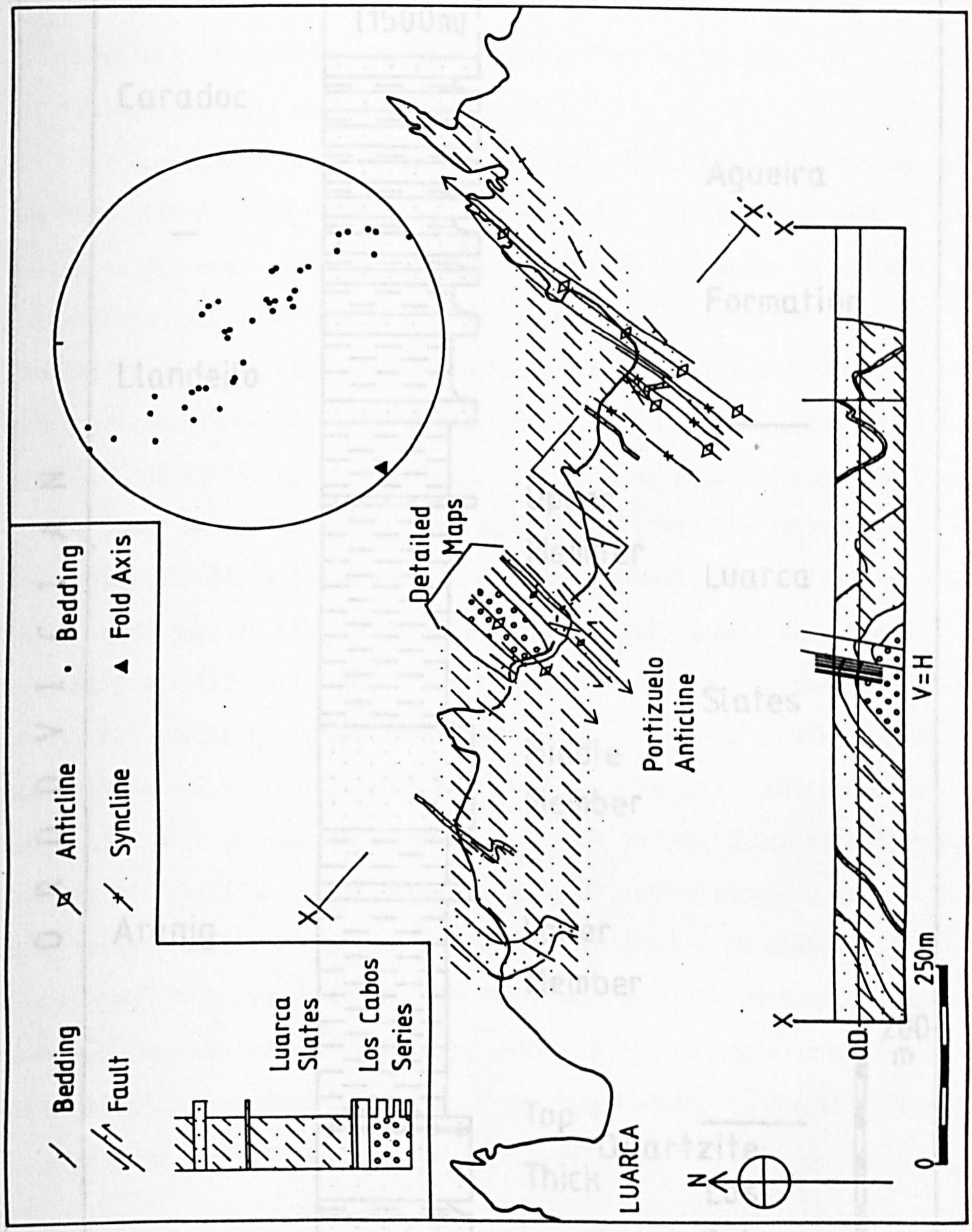

FIGURE 7.1
Geology, structure of stratigraphy and cross-section coast to east of Luarca.

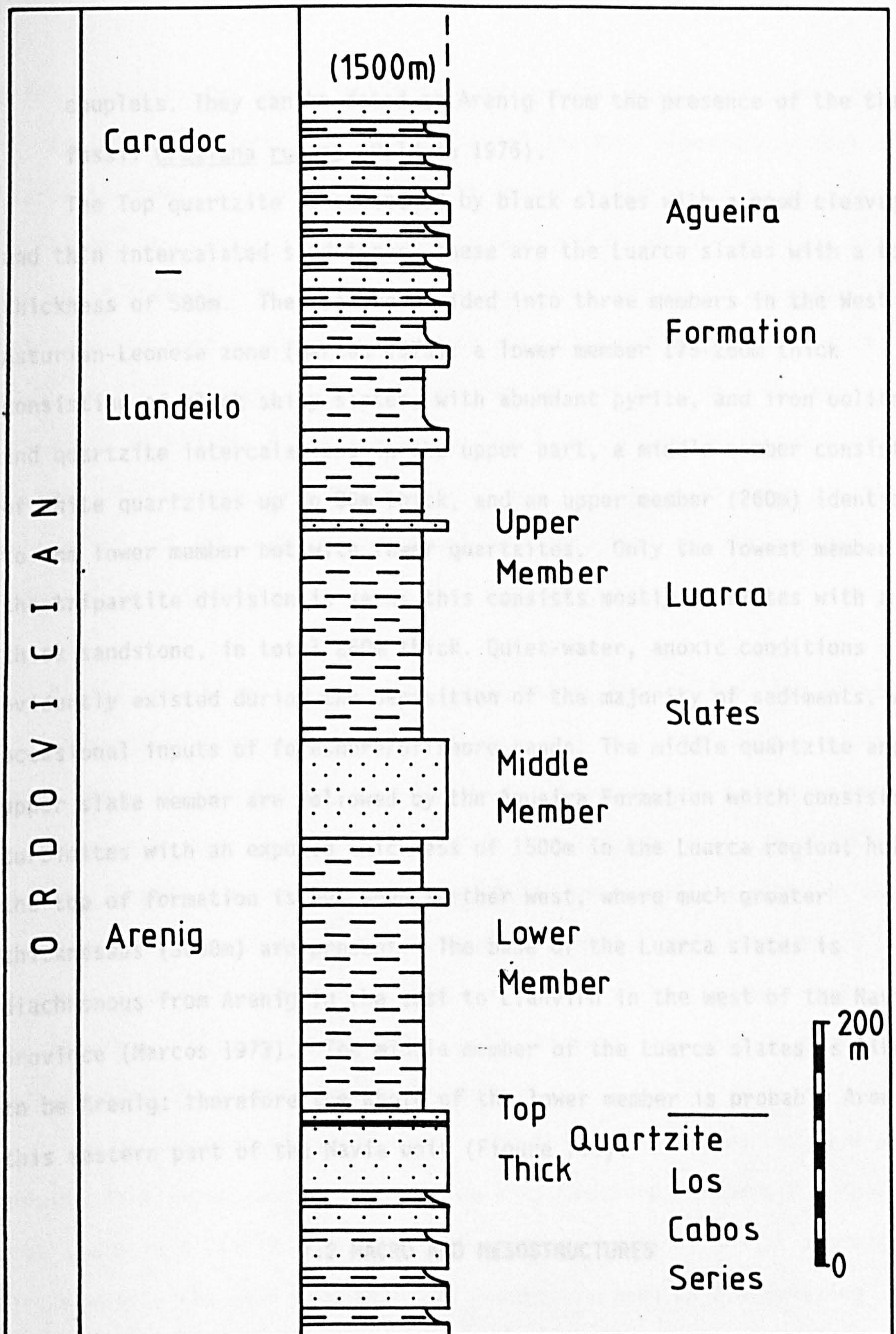

FIGURE 7.2
Stratigraphy of the east Navia Domain; after Marcos (1973) and this study.

couplets. They can be dated as Arenig from the presence of the trace fossil Cruziana rugosa (Baldwin 1976).

The Top quartzite is succeeded by black slates with a good cleavage and thin intercalated sandstones: these are the Luarca slates with a total thickness of 580m. They can be divided into three members in the West Asturian-Leonese zone (Marcos 1973): a lower member 175-260m thick consisting of black shiny slates, with abundant pyrite, and iron oolites and quartzite intercalations in the upper part, a middle member consisting of white quartzites up to 80m thick, and an upper member (260m) identical to the lower member but with fewer quartzites. Only the lowest member of the tripartite division is seen: this consists mostly of slates with a 12m thick sandstone, in total 260m thick. Quiet-water, anoxic conditions evidently existed during the deposition of the majority of sediments, with occasional inputs of foreshore/offshore sands. The middle quartzite and upper slate member are followed by the Agueira Formation which consists of turbidites with an exposed thickness of 1500m in the Luarca region; however the top of formation is not seen further west, where much greater thicknesses (3000m) are present. The base of the Luarca slates is diachronous from Arenig in the east to Llanvirn in the west of the Navia province (Marcos 1973). The middle member of the Luarca slates is likely to be Arenig: therefore the whole of the lower member is probably Arenig in this eastern part of the Navia unit (Figure 7.2).

7.2 MACRO AND MESOSTRUCTURES

7.2.1 The Portizuelo Anticline

The visible structure in the area around Luarca consists of easterly verging upright folds developed on all scales within the Ordovician quartzite, sandstones and slates, between the SE-directed Touran thrust to the west of Luarca and the vertical or E-dipping Allende fault to the east, which separates the Narcea antiform from the West Asturian Leonese zone.

A simplified sketch map and section of the area immediately east of Luarca is shown in Figure 7.1. The structure is dominated by an upright anticline, the Portizuelo anticline in the core of which the basal beds of the Thick quartzite at the top of the Los Cabos series are exposed. The anticline is seen at the surface to be upright, with a fold axis plunging at 5^{o} to 225^{o} (Figure 7.1). A detailed map and cross-section are presented in Figures 7.3 and 7.4. In the limbs of the folds are the Luarca slates, with considerable minor folding and faulting. Good way up criteria in some of the intercalated sandstone beds show that all structures observed face upwards.

7.2.2 Cleavage, Minor Folds, Veins, Kink Bands, Bedding Parallel Shear

Throughout most of the Luarca slates, and in slates between quartzite beds, there are two fairly well-developed cleavages. In some exposures, it can be clearly seen that one cleavage is developed by crenulation of an earlier fabric; however this relationship is not readily visible in many cases, where both cleavages may be equally strong slaty cleavages. Fracture cleavages in sandstone units pass into slaty cleavage with considerable angles of refraction. Both cleavages may develop good bedding-cleavage intersection lineations.

The orientation of the cleavage, and the cleavage vergence, are of considerable importance in determining the structure. Figure 7.5 shows that there is a fairly even spread of cleavage orientations in a great circle around the fold axis with the bedding. Based on overprinting relations where visible, the cleavages can be divided into two groups: the early cleavage, C1, with sub-horizontal or moderately NW-dipping orientations, and a later sub-vertical cleavage C2, striking NE-SW. Figure 7.5 subdivides the cleavage data into SE and NW-dipping beds for each cleavage, and shows the cleavage vergence (as defined by Bell 1981). The

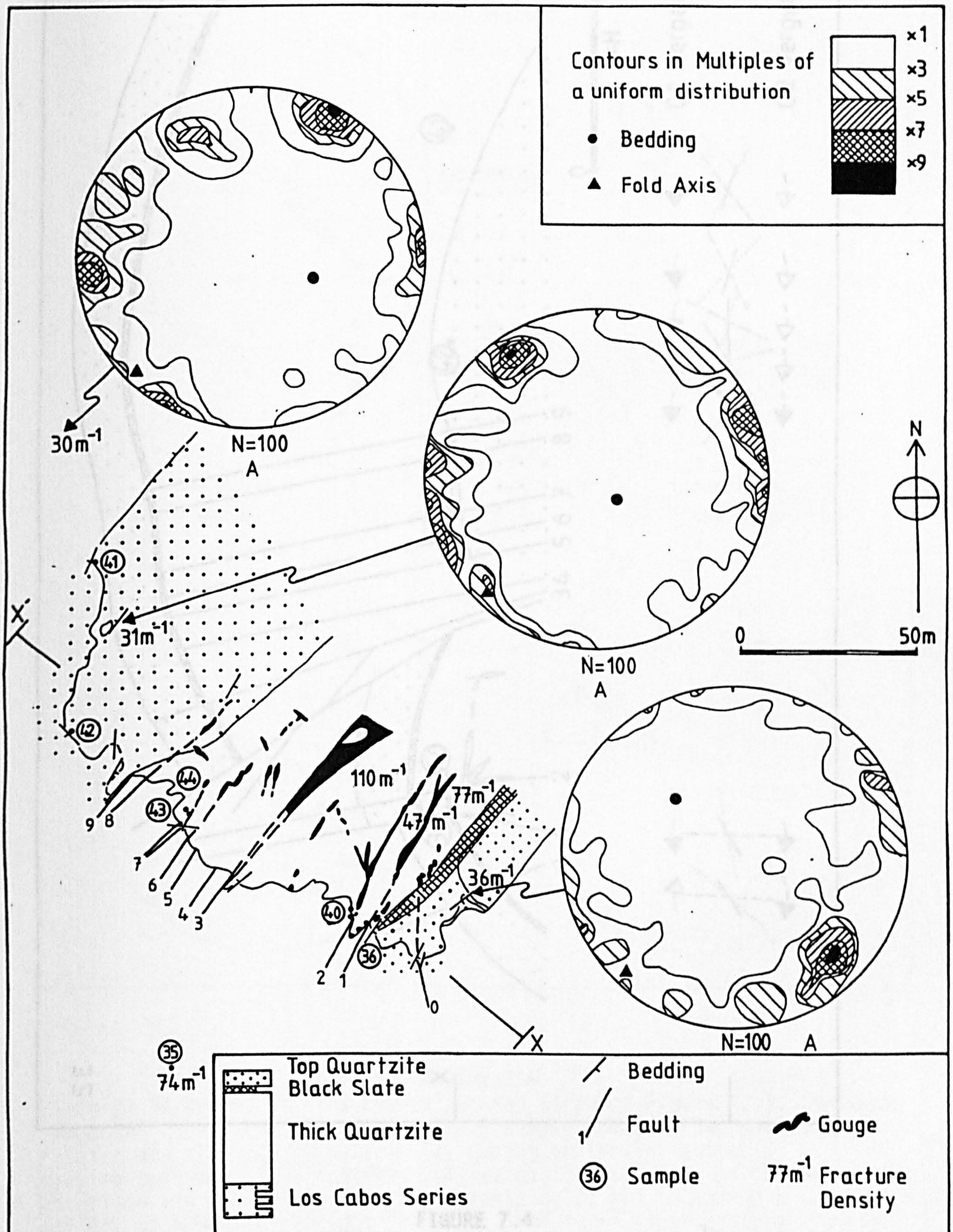

FIGURE 7.3

Detailed Geology, Structure, Fracture Orientations and Densities of the Portizuelo Anticline. Area marked 'Detailed Maps' in Figure 7.1. Fracture Orientations of all sets of fractures are shown in the stereogram. X-X[1] is the cross-section of Figure 7.4.

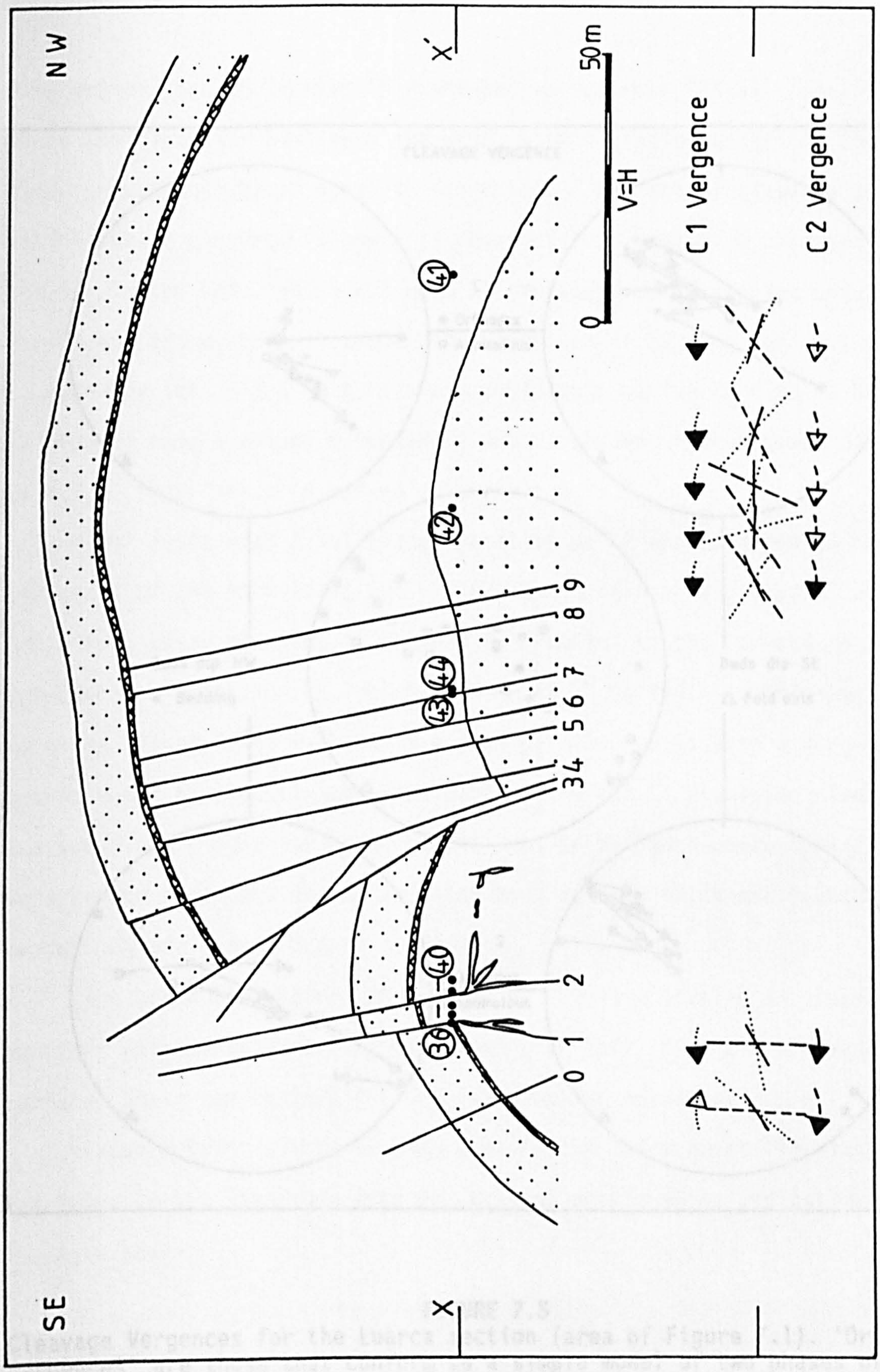

FIGURE 7.4

Cross-section of the Portizuelo Anticline along line X-X' of Figure 7.3, showing the detailed structure of the Top and Thick quartzites in the hinge of the anticline and the effect of sinistral strike-slip faults labelled 0 to 9 displacing the anticline axis. Cleavage vergences are shown for two cleavages identified as C1 and C2. 'Orthodox' vergence is indicated by a solid arrowhead, 'anomalous' vergence by an open arrowhead.

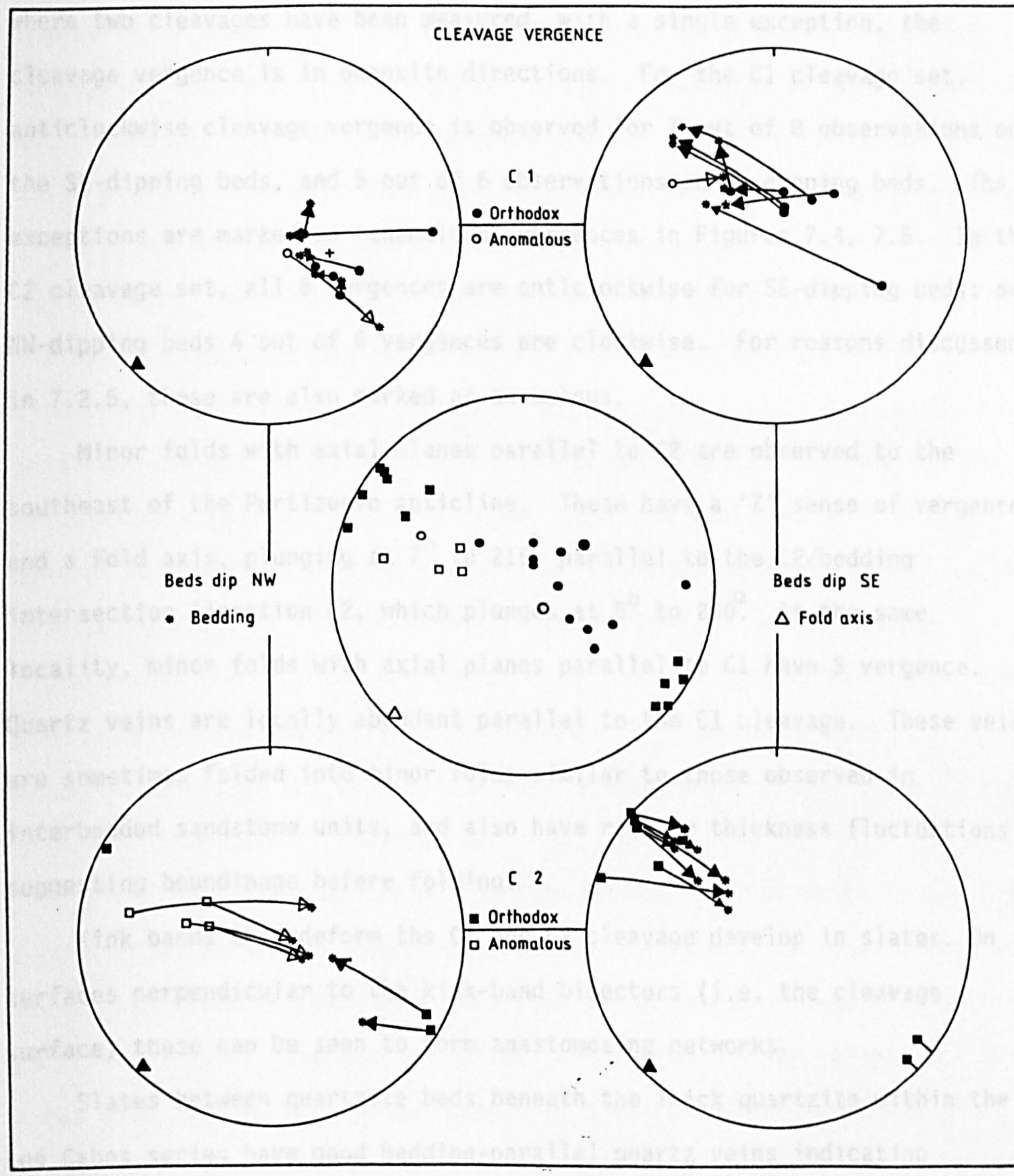

FIGURE 7.5

Cleavage Vergences for the Luarca section (area of Figure 7.1). 'Orthodox vergences' are those that conform to a simple model of two phases of folding and cleavage formation: C1, during an initial easterly verging-recumbent fold episode, indicating that all beds on the Portizuelo Anticline are on normal limbs of an early fold, and C2 during a second episode of homoaxial upright folding. Some later cleavages are clearly incompatible with this simple model; they are designated 'anomalous'.

observations can be succinctly expressed as follows. At all localities where two cleavages have been measured, with a single exception, the cleavage vergence is in opposite directions. For the C1 cleavage set, anticlockwise cleavage vergence is observed for 7 out of 8 observations on the SE-dipping beds, and 5 out of 6 observations on NW-dipping beds. The exceptions are marked as 'anomalous' vergences in Figures 7.4, 7.5. In the C2 cleavage set, all 8 vergences are anticlockwise for SE-dipping beds; on NW-dipping beds 4 out of 6 vergences are clockwise. For reasons discussed in 7.2.5, these are also marked as anomalous.

Minor folds with axial planes parallel to C2 are observed to the southeast of the Portizuelo anticline. These have a 'Z' sense of vergence and a fold axis, plunging at 7^{o} to 216^{o}, parallel to the C2/bedding intersection lineation L2, which plunges at 5^{o} to 230^{o}. At the same locality, minor folds with axial planes parallel to C1 have S vergence. Quartz veins are locally abundant parallel to the C1 cleavage. These veins are sometimes folded into minor folds similar to those observed in interbedded sandstone units, and also have regular thickness fluctuations suggesting boundinage before folding.

Kink bands that deform the C1 and C2 cleavage develop in slates. On surfaces perpendicular to the kink-band bisectors (i.e. the cleavage surface) these can be seen to form anastomosing networks.

Slates between quartzite beds beneath the Thick quartzite within the Los Cabos series have good bedding-parallel quartz veins indicating interbed shear.

7.2.3 Fractures

Fractures similar to those described in the previous chapter are seen throughout the Thick and Top quartzites, and orientations measured at points on the NW-dipping limb, hinge and SW-dipping limb of the Portizuelo anticline are shown in Figure 7.3. This reveals that in these localities all fractures are vertical to sub-vertical, with fractures present in almost all azimuths, but concentrated in two or three directions. The NW-dipping limb and hinge areas have identical patterns of three fracture sets. One (F1) is a NE-SW set dipping steeply to the east, approximately axial planar to the anticline ('ab' fractures). A second (F2) is vertical, striking N-S to NNW-SSE, and a third (F3), also vertical, strikes NW-SE approximately perpendicular to the fold axis and first set ('ac' fractures). By contrast, only two sets are clearly defined on the SE-dipping limb, where a NE-SW set is also visible (F1), but dipping in this case steeply to the west. The second set (F2) has the same NNW-SSE orientation as the set observed at the other two positions on the fold. None of the sets can be clearly dated with respect to one another. In the NW-dipping limb, F1 is more strongly defined than F2, which is more concentrated than F3. In the hinge, F1 and F2 are equally developed, and both more so than F3, while on the SE limb, F1 is stronger than F2. Fracture densities for the three areas are remarkably similar: $30m^{-1}$, $31m^{-1}$ and $26m^{-1}$ respectively (Figure 7.3).

Lithological influences on fracture density were evident: in the Los Cabos series below the Thick quartzite, beds of quartzite intercalated with shales had lower fracture densities than the homogeneous beds of the Thick quartzite itself. The small increase in fracture density between the three areas also correlated with a decrease in average bed thickness and a tendency for the fractures to be shorter and more irregular in the thicker, lower density beds.

A quite distinctive fracture pattern characterises the area between the faults labelled 0 to 9 in Figure 7.3. This is dominated by a single fracture set, with vertical dip and E-W strike, developed extremely densely in the areas between faults where this set has frequencies up to $175m^{-1}$ (Figures 7.6, 7.3). The frequency of this set is not seen to be related to distance from the fault, but does fluctuate over areas of 1 square metre.

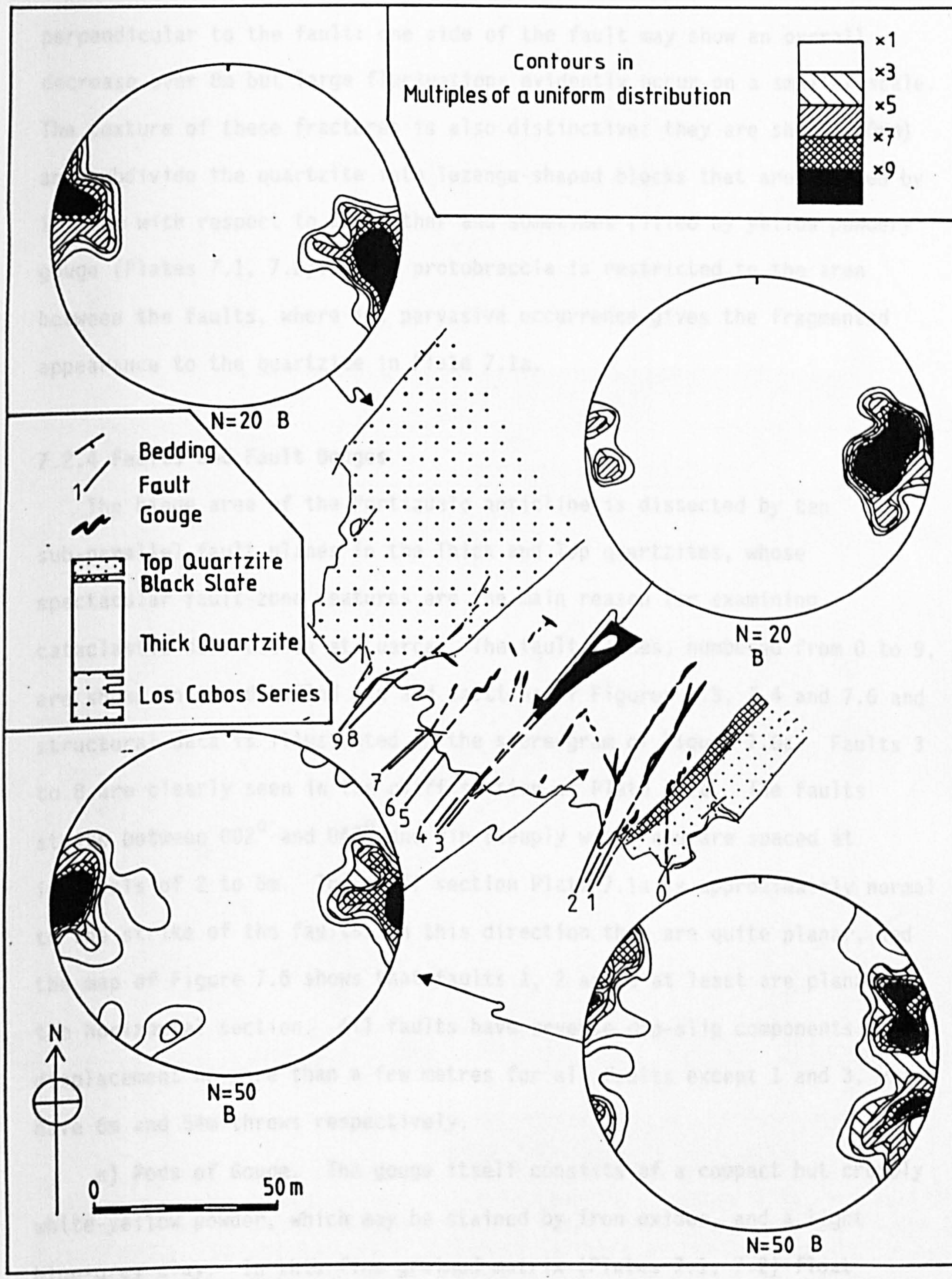

FIGURE 7.6

Fracture orientations of the dense N-S fracture set found in the protobrecciated area between faults 0 to 9. A quite consistent N-S vertical orientation is found at all localities.

Figure 7.7a shows the relationship between frequency and distance perpendicular to the fault: one side of the fault may show an overall decrease over 8m but large fluctuations evidently occur on a smaller scale. The texture of these fractures is also distinctive: they are short (50mm) and subdivide the quartzite into lozenge-shaped blocks that are sheared by 10-20mm with respect to each other and sometimes filled by yellow powdery gouge (Plates 7.1, 7.2). This protobreccia is restricted to the area between the faults, where its pervasive occurrence gives the fragmented appearance to the quartzite in Plate 7.1a.

7.2.4 Faults and Fault Gouges

The hinge area of the Portizuelo anticline is dissected by ten sub-parallel fault planes in the Thick and Top quartzites, whose spectacular fault-zone features are the main reason for examining cataclastic deformation at Luarca. The fault planes, numbered from 0 to 9, are shown in the detailed map and sections of Figures 7.3, 7.4 and 7.6 and structural data is illustrated in the stereogram of Figure 7.8a. Faults 3 to 8 are clearly seen in the cliff section of Plate 7.1a. The faults strike between 002^{o} and 045^{o} and dip steeply west, and are spaced at intervals of 2 to 6m. The cliff section Plate 7.1a is approximately normal to the strike of the faults: in this direction they are quite planar, and the map of Figure 7.6 shows that faults 1, 2 and 3 at least are planar in the horizontal section. All faults have reverse dip-slip components of displacement no more than a few metres for all faults except 1 and 3, which have 6m and 54m throws respectively.

a) Pods of Gouge. The gouge itself consists of a compact but crumbly white-yellow powder, which may be stained by iron oxides, and a light blue-grey clay. In this fine-grained matrix (Plates 7.1, 7.2) float isolated fragments of quartzite up to 5-10mm across with approximately equidimensional shapes. The gouge usually has sharp but irregular

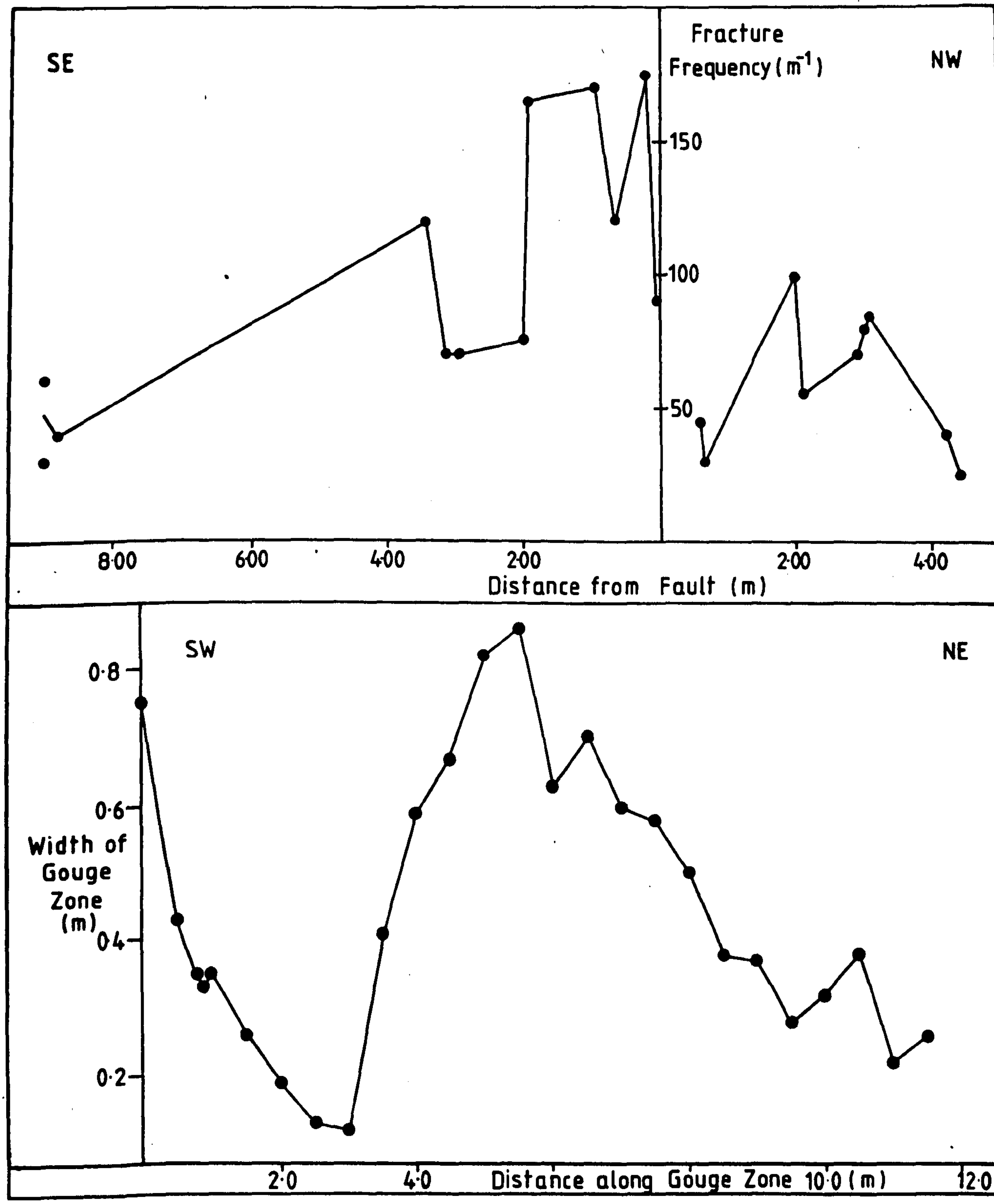

FIGURE 7.7

a) The relationship between fracture frequency and distance from fault plane. The data has been collected from Fault number 2 in Figures 7.3 and 7.6; it shows the generally extremely dense fracturing around the faults, but there is no significant increase in fracture density immediately adjacent to the faults.

b) The relationship between gouge zone width normal to displacement direction and distance along the zone in the displacement direction. The periodic fluctuation is due to the gouge pod shapes. Fault number 2.

PLATE 7.1a

Multiple Faults 3 to 8 of Figures 7.3 and 7.6 are seen cutting the Portizuelo Anticline axis in straight, sub-parallel planes dipping steeply NW along which gouge zones are developed. The intervening areas of quartzite are heavily protobrecciated.

PLATE 7.1b

Edge of Gouge Zone, marked by pencil. The gouge zone has an irregular margin where dense fractures of the vertical N-S set intersect the zone. A Y shear is seen parallel to and below the pencil.

PLATE 7.2a

Gouge Zone Features. The shear sense is SINISTRAL. Note:

a) Irregular boundaries of Gouge Pods.
b) Heavily fractured quartzite (protobreccia) adjacent to fault.
c) Kaoline/quartz veins.
d) Several Reidel Shears (R1) parallel to pencil.
e) A Y shear marked by thin blue clay, horizontal below pencil.
f) Two Late NW-SE faults, to left of pencil and right edge of photograph, heavily impregnated with iron oxides.

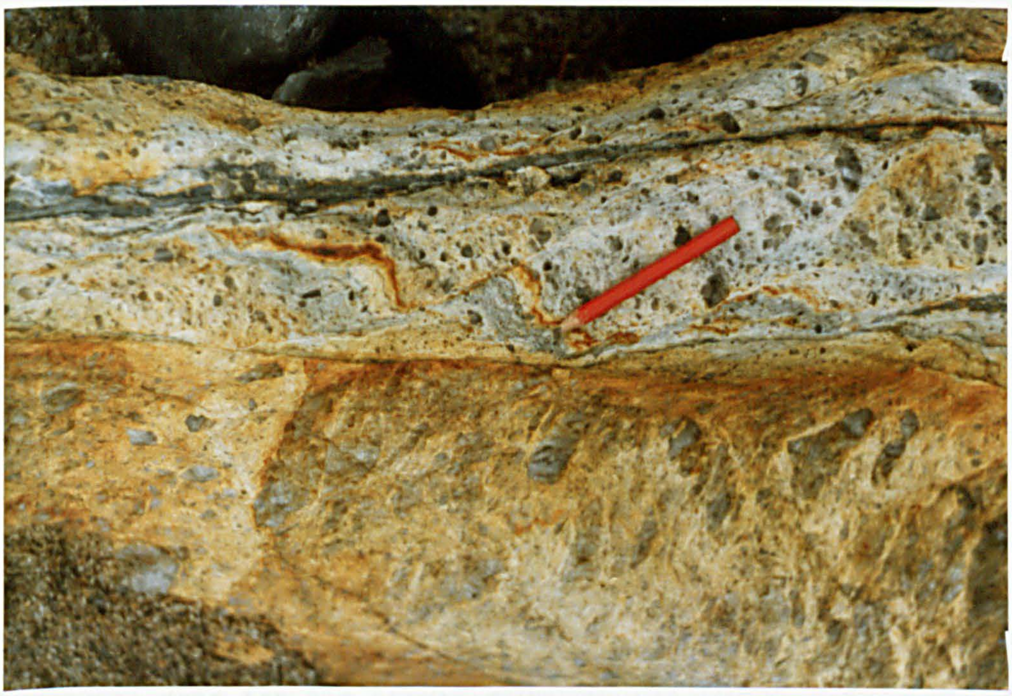

PLATE 7.2b

Detail of Gouge Pod Features. SINISTRAL shear sense. Note:

a) Heavily fractured quartzite (protobreccia) adjacent to fault.
b) Kaoline/Quartz matrix of pods, in which angular-sub rounded fragments of quartz can be seen.
c) P-foliation, defined by bands of iron oxides and clay (e.g. at pencil tip), often crenulated and displaced by
d) Reidel Stress, parallel to pencil, also with sinistral shear.
e) Y-Shears, horizontal across photograph, marked by thin seams of blue clay, cutting Reidel Shears.

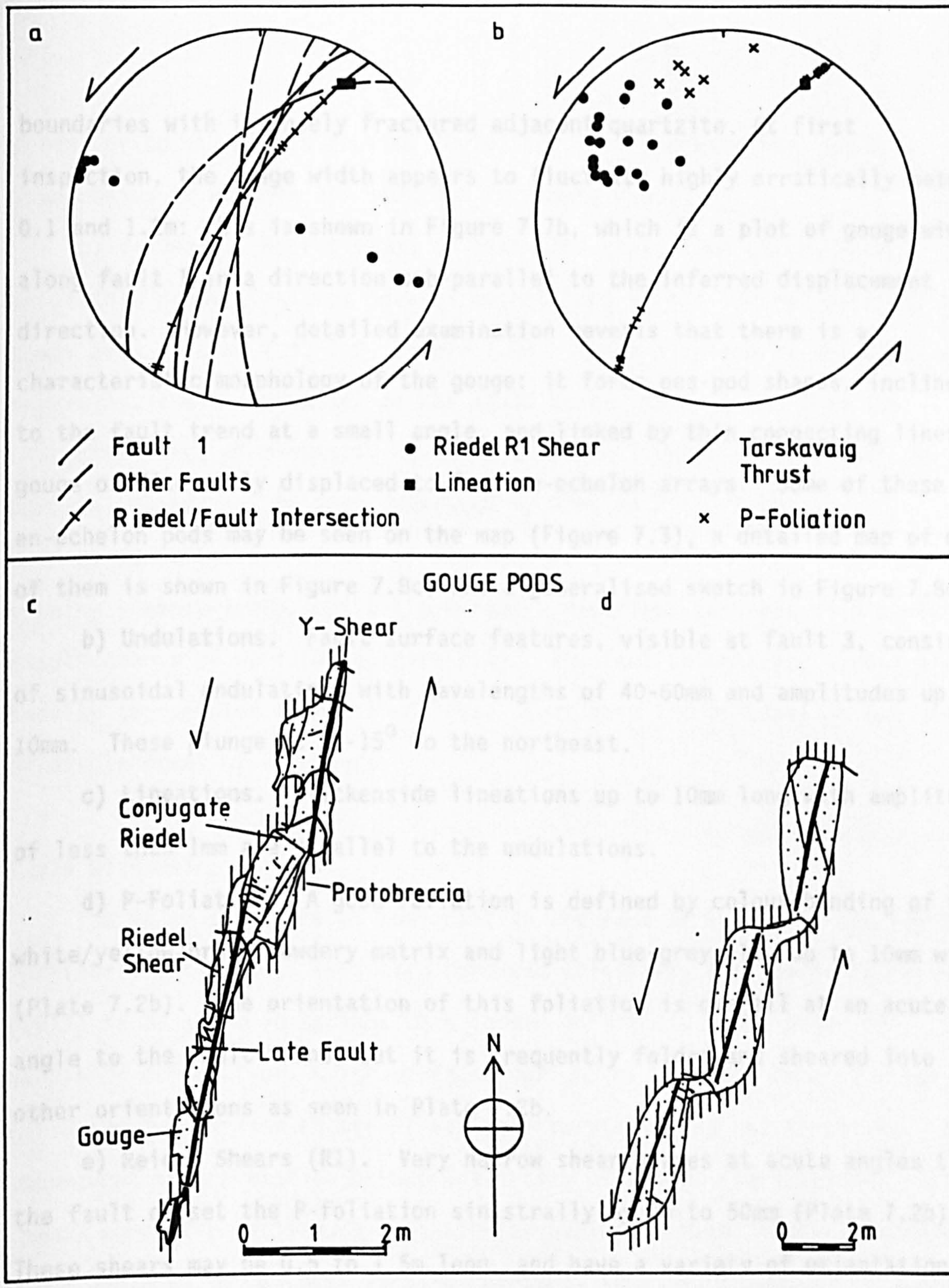

FIGURE 7.8

a) Structural data for multiple fault planes cutting the Portizuelo Anticline.

b) Structural data for the thrust gouge of the Tarskavaig Thrust, Moine thrust zone, Isle of Skye.

Both a and b show a distinctive spread of Reidel shear orientations, such that the Reidel Shear/Fault Plane intersections are dispersed about the normal to the slip direction, which is well constrained by clear lineations in both cases. The data for the Tarskavaig Thrust has been rotated to assume the same orientation as fault 1.

c) Detailed map of Gouge Pod. The characteristic pod shape is clearly seen.

d) Sketch illustrating en echelon Gouge Pod geometry.

boundaries with intensely fractured adjacent quartzite. At first inspection, the gouge width appears to fluctuate highly erratically between 0.1 and 1.2m: this is shown in Figure 7.7b, which is a plot of gouge width along fault 1 in a direction sub-parallel to the inferred displacement direction. However, detailed examination reveals that there is a characteristic morphology of the gouge: it forms pea-pod shapes, inclined to the fault trend at a small angle, and linked by thin connecting lines of gouge or discretely displaced to form en-echelon arrays. Some of these en-echelon pods may be seen on the map (Figure 7.3), a detailed map of one of them is shown in Figure 7.8c, and a generalised sketch in Figure 7.8d.

b) Undulations. Fault surface features, visible at fault 3, consist of sinusoidal undulations with wavelengths of 40-60mm and amplitudes up to 10mm. These plunge at 10-15^{o} to the northeast.

c) Lineations. Slickenside lineations up to 10mm long with amplitudes of less than 1mm are parallel to the undulations.

d) P-Foliation. A good foliation is defined by colour banding of the white/yellow/brown powdery matrix and light blue-grey clay up to 10mm wide (Plate 7.2b). The orientation of this foliation is overall at an acute angle to the fault trend, but it is frequently folded and sheared into other orientations as seen in Plate 7.2b.

e) Reidel Shears (R1). Very narrow shear planes at acute angles to the fault offset the P-foliation sinistrally by up to 50mm (Plate 7.2b). These shears may be 0.5 to 1.5m long, and have a variety of orientations as shown in Figure 7.8a for Reidels measured on Fault 2. The pattern may be summarised as a girdle of Reidel poles around sub-horizontal axis trending towards 020^{o}, 10^{o} anticlockwise from the fault trend. Reidel shears therefore intersect the fault in a fan of lines about the normal to the slickenside lineations. The gouge pods are elongate parallel to the Reidel Shears.

f) Conjugate Reidel Shears (R2). Discrete narrow shears in conjugate

Reidel orientations are shorter (0.5m) and less abundant than Reidels. Some conjugate Reidels are sketched in Figure 7.8a.

g) Y-Shears. Narrow seams of dark blue clay, 10mm thick, form absolutely planar features several metres long in the central parts of the gouge pods (Plates 7.1, 7.2, Figure 7.8). These displace R1 and R2 shears sinistrally, and are parallel to the fault zones, thus giving them the characteristics of Y-shears. Usually a single Y-shear develops but two parallel shears may be seen separated by 50mm in Plate 7.2b.

h) NW-SE Faults. A set of discrete faults in a NW-SE orientation, dipping steeply south, cut all previously described features with sinistral displacements of up to 1m (Figure 7.8). The fault planes are almost always heavily impregnated with iron oxides. They have the orientation and sense of displacement of R2 shears.

7.2.5 Discussion

The major structure of the coast to the east of Luarca is clearly the Portizuelo anticline. This structure was originally considered by Marcos (1973) to be a simple upright fold formed during his third phase of Hercynian deformation, which produced upright or westerly verging folds following the earlier phases of easterly verging folds and thrusting. A subsequent interpretation at the University of Oviedo (Pérez-Estaún pers. comm.) shows the Portizuelo anticline as part of a much larger structure which began as an easterly verging recumbent fold, subsequently refolded by the upright phase; there is evidence further inland for the existence of this recumbent structure (Pérez-Estaún pers.comm.) but the actual coastal exposure admits of either of the interpretations above.

However, both interpretations agree that cleavage evidence at Portizuelo indicates an early episode of cleavage formation subsequently deformed by the folding which generated the visible anticline. Since way up criteria show that beds are everywhere facing upwards, the early cleavage (C1) should have an anticlockwise vergence on both limbs of the Portizuelo anticline. This is shown to be the case with two exceptions ('anomalous') in the top two diagrams of Figure 7.5. Any cleavage produced during the later folding of the anticline, however, should change vergence across the anticline axis from anticlockwise on NW-dipping limbs to clockwise on limbs with a southeast dip. Figure 7.5 shows that all the cleavages identified as C2 do indeed have this orthodox vergence on SE-dipping limbs, but that 4 out of 6 vergences on northwest limbs have anomalous clockwise vergences, also seen in the section on Figure 7.4. This shows that the anomalous vergences appear to be rotated with the bedding and C1 cleavage around the anticline axis, maintaining an approximately constant angular relationship to the bedding. A hypothesis to account for these cleavages is that they formed as an extensional crenulation cleavage of the earlier C1 cleavage due to interbed shear during the final stages of the early recumbent folding, or during the initial stage of the upright folding, for which there is additional evidence from slickenside lineations on bedding planes in slates. This is illustrated in Figure 7.9.

The above hypothesis has an interesting implication for the 'phases' of deformation. Such cleavage formation at an intermediate stage between Marcos' first and third phases of deformation suggests that they were not separated by any significant time interval and may perhaps be viewed more accurately as a continuous tectonism in which cleavage could be continuously produced and subsequently rotated passively. This is confirmed by the even distribution of cleavages within the bedding girdle seen in the centre of Figure 7.5, in which there is no sharp division between the C1 and C2 cleavages.

Four pieces of evidence can be produced in favour of this hypothesis: firstly, the anomalous C2 cleavages crenulate the C1 cleavages; they therefore post-date C1. Secondly, they appear to be folded with bedding

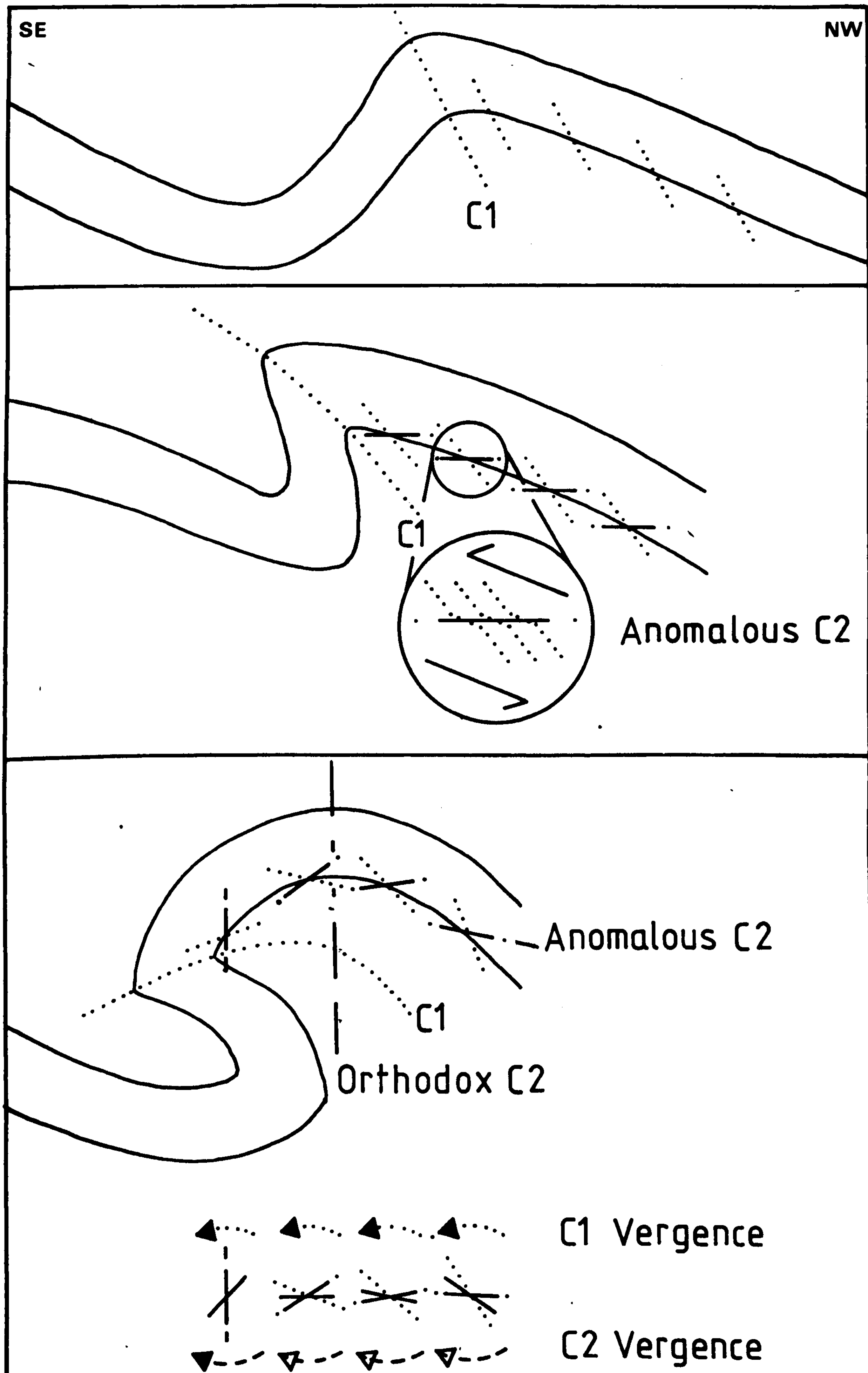

FIGURE 7.9

Origin of cleavages around the Portizuelo Anticline. During early stages of east verging folds, C1 is produced. Later the ‘anomalous’ C2 vergences are formed, perhaps by crenulation of C1, due to interbed shear on the NW-dipping limbs. The final stages of cleavage are due to upright, homoaxial refolding (Orthodox C2).

and C2 about the Portizuelo anticline; they therefore pre-date this deformation. Thirdly, if interpreted as an extensional crenulation cleavage, they are in an appropriate orientation with respect to C1 and bedding to indicate sinistral shear across bedding planes, correct for flexural-slip folding of the Portizuelo anticline. Lastly, the confinement of the anomalous vergence to the northwestern limb is predicted by the model since the earlier C1 fabric is close to a shortening direction of the incremental strain ellipsoid on the SE-dipping limb during flexural-slip shear. Extensional crenulation of this cleavage would not occur. It would, however, be possible to treat all the C2 vergences as orthodox if the Portizuelo anticline had an axial plane dipping to the southeast at 70^0. This would separate the C2 vergences into two quadrants on the stereogram, each with opposite vergence. Such a model is proposed by Marcos (1973), who shows a southeast dip to C2 ('S3' in his terminology) at Portizuelo and at three other localities further west. The more complex model proposed here is preferred for three reasons: firstly, the moderate SE-dipping anomalous C2 cleavage is not observed on the SE-dipping beds of the Portizuelo anticline, where all C2 cleavages are sub-vertical. Its restriction to the northwest limb is a feature in favour of the present model. Secondly, it has been observed that the anomalous C2 vergences preserve an approximately constant angular relationship to bedding: this also suggests that they may have formed before and separately from the orthodox, sub-vertical C2 cleavages. Finally, the geometry of the anticline (Figure 7.4) suggests that it is upright or even E-verging; no clearly W-verging structures are seen.

Furthermore, if such a process of crenulation were active on a small scale around minor folds at any stage, anomalous cleavage vergences would be common. This could be represented, for example, by the two anomalous C1 cleavages shown in Figure 7.5.

The minor folds described in 7.2.2 however, are consistent with a simple model of two fold and cleavage episodes. The Z asymmetry of the minor fold with C2 axial planes indicates an anticline to the west as observed, while the opposite asymmetry for a minor fold with an axial plane parallel to C1 suggests an early antiformal closure to the east.

Possible mechanisms for the formation of quartz veins parallel to C1 include the transfer of quartz by pressure solution to low-stress sites localised on hinges of early-formed buckle folds where a horizontal stress-supporting fabric exists; a large scale analogue of the process of creating Q and P domains by buckling of a pre-existing fabric described by Knipe and White (1977). Taking this to completion could result in pure quartz veins separating phyllosilicate bands. Alternatively, the mechanism of Rutter described in 2.3.1 can be invoked, where tensile failure may occur along planes perpendicular to the greatest principal stress in rocks with high anisotropy in tensile strength within tensile stress fields. West of Luarca there is evidence for the development of metamorphic differentiation by the first mechanism described, utilising buckles in the folded quartz veins described here. Such a mechanism is considered likely for the original formation of the quartz veins.

Two of the fracture sets (F1 and F3) appear to have a consistent relationship to the fold geometry: F1 is approximately axial planar, and F3 is normal to the fold axis. The second set, F2, is most densely developed in the faulted hinge area. The relationships of F1 and F3 fractures to the fold geometry suggest that they are related to the fold, but the field evidence does not provide any indication of the time of their formation: F3, normal to the fold axis, would not show evidence of folding, and F1 may be either folded with bedding or a divergent axial-planar fracture cleavage. Steeply-dipping beds could resolve this question but unfortunately are not exposed in the study area. F2 was certainly most densely developed during faulting, but it is possible that it originated as an earlier fracture set.

Observations reported for the nine faults in 7.2.4 are satisfactorily interpreted as evidence for a system of sinistral, strike-slip reverse faults which formed after folding of the Portizuelo anticline. The sinistral sense of displacement is clearly indicated by

i) The small acute angle between the Reidel (R1) shears and Y shears or fault strike.

ii) Sinistral displacement of P-foliation on R1 shears.

iii) The larger acute angle between R2 shears and the fault.

iv) Sinistral displacements of R2 on Y shears.

v) The inclination of the P-foliation to the fault in the opposite sense.

The slip vector is given by the coincident undulations and lineations, plunging to the northeast. Rutter et al. (1986) have cautioned against the use of lineations to give macroscopic slip directions in fault zones since they may often reflect merely local displacements accommodating movements between independent blocks within fault zones: however, this caveat applies to fault zones of kilometric width in which such divergent movements may be common. In the case of the relatively discrete faults at Portizuelo, the coincidence of all lineation measurements (Figure 7.8) adds confidence to their significance as macroscopic displacement indicators.

The total displacement is calculated simply from the vertical component measured in the section (Figure 7.4) and the displacement vector. For fault 1, 6m dip slip gives 22m strike slip and 23m net slip. On fault 3, the comparable figures at 50m, 137m and 146m. Minor displacements on the other faults are estimated to add 2m, 6m and 6m to these values, so that for the whole fault system, the total dip slip, strike slip and net slip are 58m, 164m and 175m respectively.

Details of the gouge features correspond well with those reported for other natural gouges and with experimental features, as summarised by Rutter et al. (1986). Particularly striking is the coincidence in fault evolution between natural and experimental studies. It is clear from truncating relationships that P-foliations are formed before Reidel shears, which in turn are cut by Y shears. Such an early P-foliation followed by R shears corresponds to the spread of deformation throughout gouges reported in the experimental studies of Rutter et al., and interpreted by them as coincident with observed strain hardening due to mutual interference of the two shear directions. Y shears were not observed in these experiments, but Logan et al. (1981) recorded their development in San Andreas fault gouge deformed experimentally as the latest stage, and such shears were suggested by them to be the locus of stick-slip displacements. The reason for their absence in the experiments of Rutter et al. appears to be because large shear strains are taken up on the gouge-intact rock boundary; when movement at this point is suppressed, Y shears may form in the body of the work-hardened gouge. The irregular nature of the gouge/quartzite boundary observed in the fault planes would certainly create favourable conditions for localising Y shears within the gouge.

There is some uncertainty as to the timing of the conjugate Reidel shears (R2). R2 features in Rutter's experiments consisted of kink bands localised on quartz particles in the gouge, but discontinuous displacements were observed in Logan's experiments. Both authors considered them to be developed with R1 shears in response to the imposed strain. On the other hand, clay cake experiments of Hempton and Neher (1986) showed that R2 shears developed before R1, which gradually superceded them as R2 were passively rotated into sigmoidal traces, giving a final pattern in which R2 were clearly truncated by R1. Figure 7.8 shows that R1 both truncate and are truncated by R2, suggesting that they operated simultaneously and probably accommodated strain as suggested by Logan and Rutter.

The closely comparable natural and experimental gouge microstructures admit at least the possibility that stress-strain relationships for the faults are similar to the experiments. Thus a period of strain hardening may have occurred while deformation spread throughout the gouge by formation of a P-foliation and combined operation of R1 and R2 shears. Localisation on to the Y shears could have accompanied a stress drop and switch to stick-slip oscillation as in the experiments of Logan et al.

A further possible analogy with experimental results may offer an interpretation of the dense N-S fracture set observed adjacent to the faults. In many frictional sliding experiments, microcracking at an acute angle to the sliding surface is observed (2.2.1) and as reviewed in 2.3, all microstructural studies of specimens in triaxial failure confirm the importance of 'axial' microcracks in the formation of the sliding surface. Such microcracks may form in both pre- and post-failure stages, the latter being referred to by Conrad and Friedman as microscopic feather fractures (2.2.1). Of the microcrack mechanisms in 2.2.1, impingement and pre-existing flaws may induce pre-failure axial microcracks, while post-failure cracks form by a shear-induced mechanism. The N-S fracture set is in the appropriate orientation to suggest that it formed as a large scale analogue of axial cracks, for sinistral shear on the faults at Portizuelo.

Dense development of the fractures restricted to the area between faults is clear evidence that the fractures are related to the strike-slip movement on the faults. It is also clear that the fracture set does not have the large scale characteristics of microscopic feather fractures, since they are not restricted to the area immediately adjacent to faults but are pervasively developed throughout the intervening areas. It is therefore possible that they are large-scale analogues of axial, pre-failure microcracks, marking an important stage of protobrecciation prior to the development of the main fault planes.

It was observed that these fractures commonly had shear displacements; this is not a feature of experimental axial cracks. However, once formed they would represent a potential sliding surface along which displacements would inevitably occur when the faults themselves moved. It is however difficult to distinguish this hypothesis from the equally viable suggestion that the entire fracture set represents a conjugate system to the faults. Plate 7.2a shows that some of the fractures displace the gouge dextrally, which is both the correct sense for a conjugate system, and evidence for their shear displacement post-dating gouge formation.

There are two further observations on the fault structure that have not been made before and may be of more general significance. The first is the distribution of gouge in pod shapes parallel to Reidel (R1) shears, and offset along the R2 direction (Figure 7.8). This seems to be an inherent feature of gouge formation since the en-echelon R1 pods are connected by continuous but thinned gouge along R2. The en-echelon pattern is reminiscent of the geometry of the ductile stringers of more ductile minerals in the experiments of Logan et al., or 'trails' in Rutter et al's experiments, with the difference that the en-echelon gouge pods are elongate along R1 and displaced along R2; in the experiments, ductile stringers are generally extended in the P-foliation direction, and displaced along the R1 direction. Both pods and ductile stringers reflect the operation of R1 and R2 shears on deformed material. A very significant aspect of the segmentation of gouge zones is that all shears, including the late Y shears, are capable of accumulating limited shear strain: they must work harden. Such work hardening may explain why deformation spreads to adjacent faults.

The second observation concerns the orientation of Reidel (R1) shears. These are conventionally regarded as co-zonal with the fault plane, and therefore should intersect the fault in a direction perpendicular to the slip vector. However, when three-dimensional orientations of R1 shears are measured, they show that the R1/Fault intersection has a range of orientations from close to the slip vector in either direction towards the normal to the slip vector (Figure 7.8). This observation has also been made for a thrust gouge below the Tarskavaig thrust in the Moine thrust zone, N.W. Scotland (Blenkinsop 1982), and the measurements reported in Rutter et al. (1986) show a similar spread in both Reidel and P-shear orientations. Although not referred to as Reidel shears, the macrofactures reported by Brock and Engelder (1977) below the Muddy Mountain overthrust also show a variety of orientations, with poles to the macrofractures lying in a girle normal to the thrust plane. The variable orientations of the Reidel Shears can be easily understood as accommodation of shear in directions other than the net slip vector.

The fact that such a variation has not been reported is probably due to the restriction of measurements and observations to sections perpendicular to the fault plane and parallel to the slip direction.

There is a particularly striking correspondence between three observations of a the faulting here at Luarca and at Punta Vidrias. Firstly, the occurrence of parallel multiple faults separated by several metres is similar to the northern exposures of the Bayas and Punta Vidrias. Secondly, the intervening areas between both faults have a dense development of protobreccia, dominated by a single fracture set that has similar densities of 80-100m^{-1}. Finally, the fault planes described are all characterised by bimodal corrugations; large undulations, with wavelengths of 50mm-1m and amplitudes of 10mm, and smaller lineations.

7.3 MICROSTRUCTURES

7.3.1 Grain Size and Shape

The grain size of the Thick quartzite samples from Portizuelo is typical of the Barrios quartzite and the equivalent quartzites at the top of the Los Cabos series in the West Asturian-Leonese zones: 100-200μ. All the quartzite samples have strong grain-shape fabrics with axial ratios of up to 1.9, seen for example in Plates 7.3a and 7.5b. Four samples were chosen for a complete determination of the three-dimensional fabric: 38,

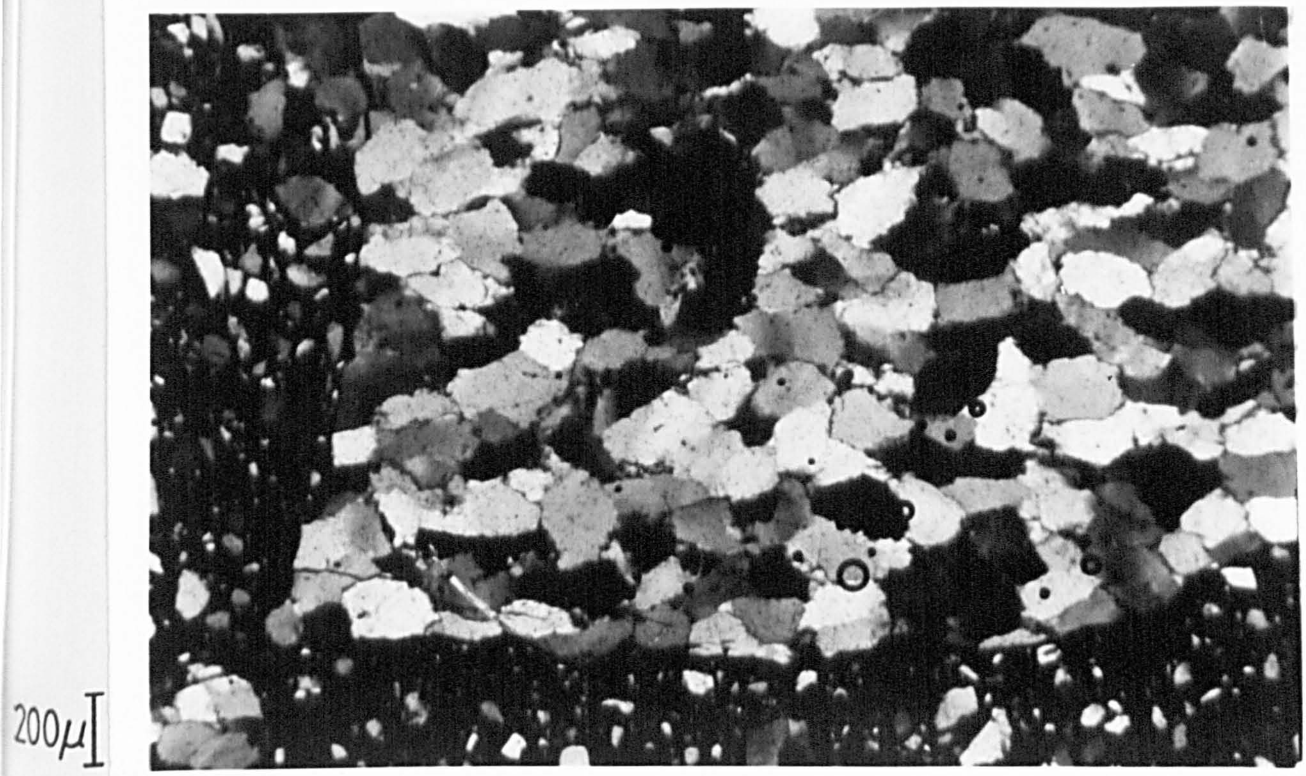

PLATE 7.3a

Cluster of grains within gouge. The grains have a good shape fabric within the cluster. The matrix of fine grained quartz and oxides, contains poorly sorted angular grain fragments. Sample 36, X.P.

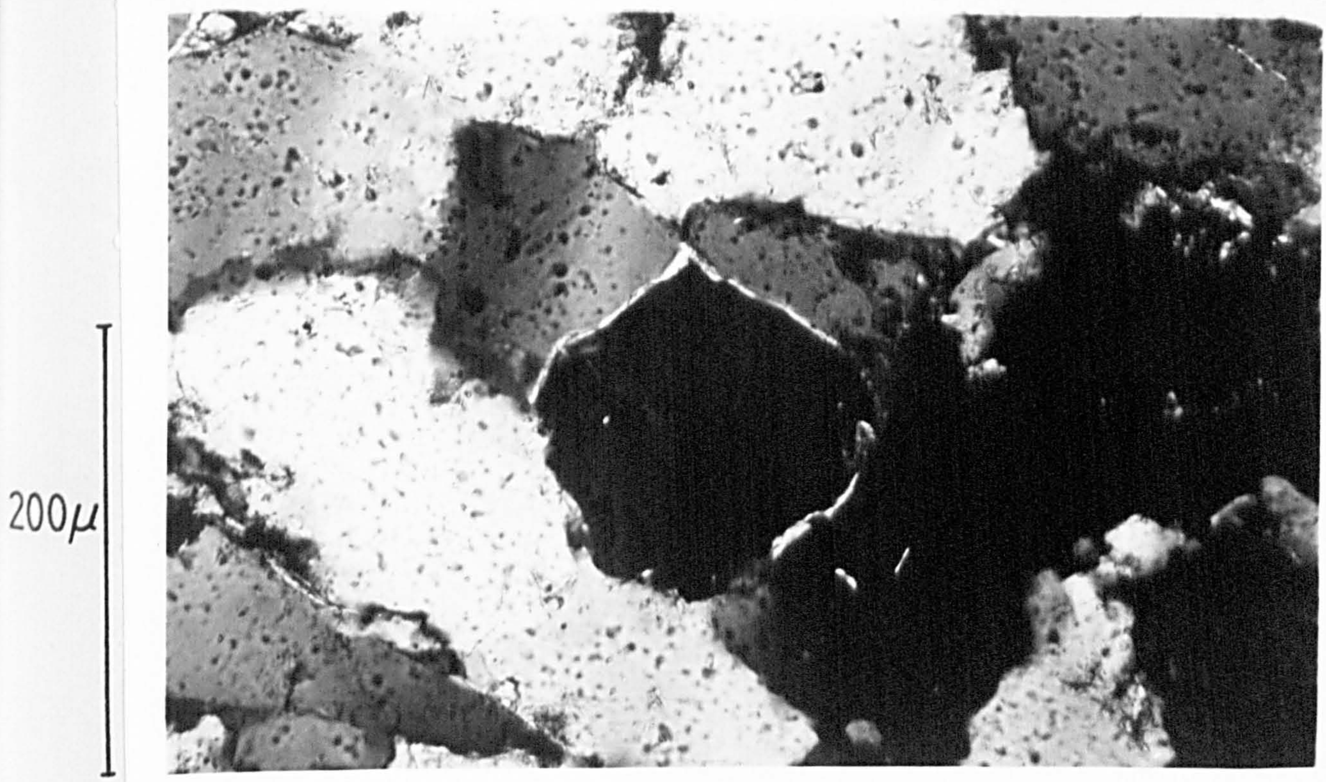

PLATE 7.3b

Type 5 grain boundary: well crystallised phyllosilicates mark the grain boundary. Sample 38, X.P.

39, 40 and 41. The values of the fabric ellipsoid parameters are given in Appendix A5, and these and the orientations are shown in Figure 7.10. All four examples have similar natural octahedral unit shears and natural strains of approximately 0.5 and 0.45 respectively. Samples 38 and 39 have markedly oblate fabrics (Lode's parameter (ν) 0.4 and logarithmic Flinn parameter (k) also 0.4), sample 40 has an almost uniaxial fabric and 41 is strongly prolate (ν=-0.72, k=6.088). The goodness-of-fit parameter ρ for all samples but 39 is less than 1.05, indicating relatively good results, but 39 has a poor value of 1.23.

Figure 7.10 shows that 38, 39 and 40 have fabrics with a minimum axis close to the pole to bedding, with the other two axes at low angles to the bedding plane. In 41, however, the fabric axes do not show any relationship to bedding: the maximum axis plunges gently to the southwest, parallel to the anticline axis, while the minimum axis plunges at 50^{o} to the northwest.

Figure 7.10 also shows the relationships between the fabric axes, the fold axis, and the nearest cleavage measurements from the field. There is quite clearly no relationship between the minimum fabric axis and the 'orthodox' C2 pole in any sample. In 38, 39, and 40, the minimum axis is closer to the bedding pole than the C1 pole, although this is not very remote. In 41, the 'anomalous' C2 pole is closest to the minimum axis, and the maximum axis is nearly parallel to the fold axis.

The characteristics of the shape fabrics in 38, 39 and 40 are similar to those described for the primary fabrics of the Bernesga Valley and at Punta Vidrias. Natural octahedral unit shears and Lode's parameters can be compared for these samples (38, 39, 40, 41) and those of the Bernesga Valley (14, 28) and Punta Vidrias (CV1, 102) in Figure 7.10. Nevertheless, there is evidence of considerable deformation by crystal plasticity (discussed below). They could be interpreted as essentially primary depositional/compactional fabrics, which may have been accentuated by

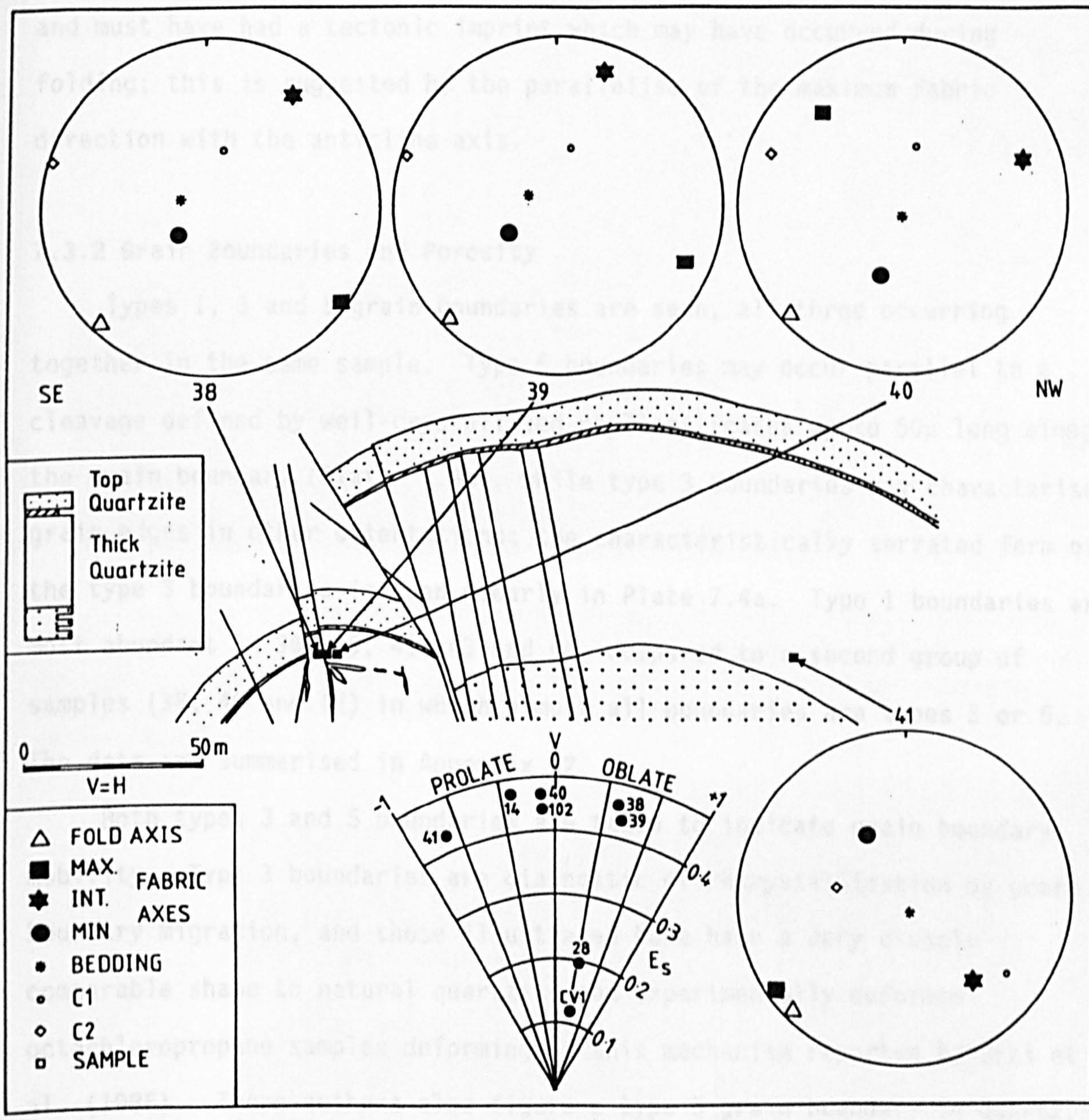

FIGURE 7.10

Shape Fabric data, samples 38, 39, 40, 41. The minimum fabric axis for the first three cases is close to the bedding normal, but sample 41 contrasts with the hinge samples (38, 39, and 40) in not showing such a relationship between the minimum axis and bedding, and by the SW plunge of the maximum axis. These features can be interpreted as evidence of a primary fabric modified by tectonic strain during folding. The samples are compared with those from Punta Vidrias (CV1, 102) and the Bernesga Valley (14, 18) in the Hsu plot of Natural Octahedral Shear stress and Lode's parameter.

plasticity. On the other hand, the fabric of 41 cannot be purely primary, and must have had a tectonic imprint,which may have occurred during folding; this is suggested by the parallelism of the maximum fabric direction with the anticline axis.

7.3.2 Grain Boundaries and Porosity

Types 1, 3 and 5 grain boundaries are seen, all three occurring together in the same sample. Type 5 boundaries may occur parallel to a cleavage defined by well-crystallised phyllosilicates up to 50μ long along the grain boundary (Plate 7.3b), while type 3 boundaries may characterise grain edges in other orientations; the characteristically serrated form of the type 3 boundaries is seen clearly in Plate 7.4a. Type 1 boundaries are most abundant in 36, 39, 41, 43 and 44, compared to a second group of samples (38, 40 and 42) in which almost all boundaries are types 3 or 5. The data are summarised in Appendix A2.

Both types 3 and 5 boundaries are taken to indicate grain boundary mobility. Type 3 boundaries are diagnostic of recrystallisation by grain boundary migration, and those illustrated here have a very closely comparable shape to natural quartzite and experimentally deformed octachloropropane samples deforming by this mechanism reported by Urai et al. (1986). These authors also figure a type 5 grain boundary in quartz, produced by the interaction of a migrating grain boundary with a mica grain: the grain boundary simply becomes planar along the interface with the mica grain. This impurity pinning of grain boundaries is a well known metamorphic process (e.g. Vernon, 1976).

Porosity in these samples is entirely confined to bedding planes and stylolites; in the remainder of the rock there is negligible porosity.

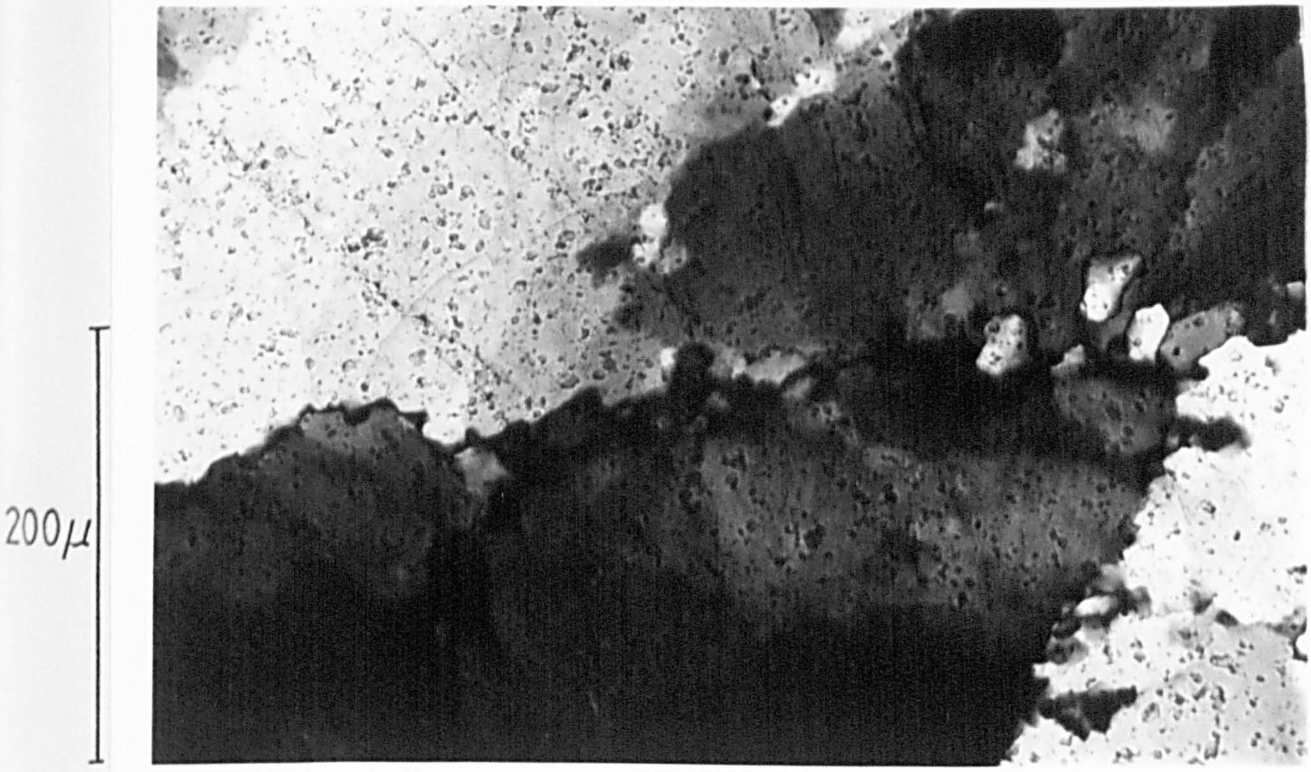

PLATE 7.4a

Type 3 grain boundary: serrated grain boundary giving excellent evidence for grain boundary mobility. Some new grains are formed by subgrain rotation. Inclusion trails marking transgranular microfracture can also be seen. Sample 40, X.P.

PLATE 7.4b

Transgranular microfracture. The poor definition and lack of luminescence contrast is typical of the Luarca samples. Sample 40, C.L.

7.3.3 Fractures

Observations in hand specimen, optical thin section and C.L. identify transgranular microfractures several tens of millimetres long as an important microstructural feature (Plates 7.4, 7.5). They have both mode I and shear displacements, may be open or have fillings of clay minerals or oxides, and consist of en-echelon arrays with overlap distances of several grains between adjacent fractures: 'en passant' interactions in which crack tips curve slightly away from each other are observed. These features cut and displace all other microstructures described. Plate 7.5a shows an array of such fractures as dark, oxide-filled lines displacing a stylolite in plane polarised light; the same view in crossed polars (Plate 7.5b) shows the fractures also cutting a vein. C.L. images obtained from the Luarca samples showed a poor contrast between grains and lack of definition (hence no attempt was made to determine microcrack densities); however, one of the best pictures (Plate 7.4b) shows the transgranular cracks as non-luminescing lines, as well as some intragranular cracking.

7.4.3 Veins

In hand specimen, a network of veins up to 5mm wide can be identified on cut surfaces where they are seen as bands of clear quartz, contrasting slightly in translucence from the opaque host matrix. Shear displacements of up to 10mm affect bedding planes, marked by small patches of iron oxide. In thin section, the clear quartz is seen to consist of larger crystals 1mm across with prismatic shapes and long axes perpendicular to vein walls. They are entirely free of iron oxide inclusions. Grain boundaries are predominantly type 5, but may show a banded structure of large crystals in the central part of the vein flanked by a narrower zone of much smaller grains on either one or both sides. In some cases, stylolites follow one vein boundary, and the opposite boundary is marked by a band of small grains. Transgranular microfractures may follow parts of vein boundaries

200μ

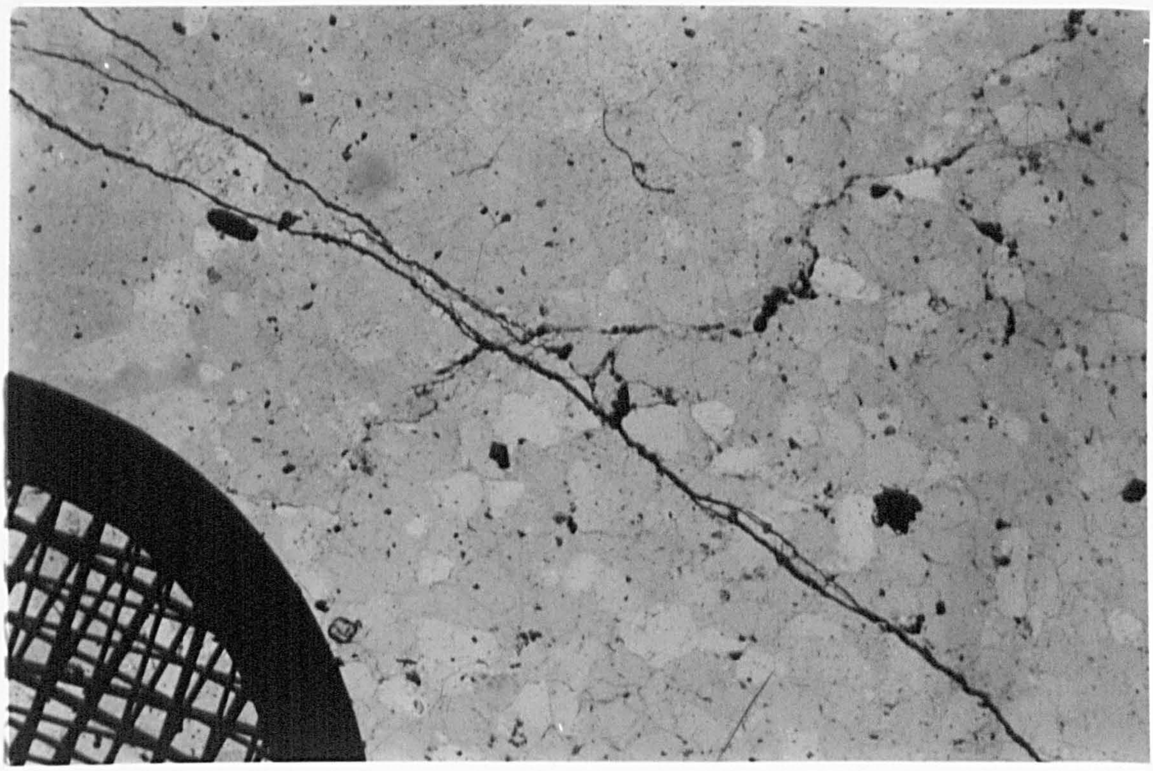

PLATE 7.5a

Transgranular microfracture array. The microfractures, visible from their oxide filling, overlap for several tens of grains and clearly cut and displace a styolite running diagonally in the opposite direction. Sample 40, P.P.L.

500μ

PLATE 7.5b

Vein, stylolite and transgranular microfractures. The vein has one extensively recrystallised margin; on the opposite side, it is bound by the stylolite, more clearly visible in this view of Plate 7.5a in plain polarised light. Transgranular microfractures clearly cut both vein and stylolite. Sample 40, X.P.

or their median lines as well as cross-cutting them. The relationships described above can be seen in Plates 7.5a and b, in which a vein (large crystals visible under crossed polars, 7.5b) is bounded on one side by a stylolite (7.5a), and a band of fine grains on the other. This whole structure is cut by an oxide-filled transgranular.

7.3.5 Stylolites

Stylolites may occur in several directions, oblique to bedding planes, but are seen clearly in thin section, where they are wavy lines of pores up to 0.5mm long often filled by iron oxides (Plate 7.5a). As mentioned above, stylolites may form vein boundaries, but in other cases, stylolites terminate at veins or are cross-cut by them.

7.3.6 Optical Strain Features

G.M.A. values of all samples from Luarca are among the highest measured, from 7 to 15^{0} (Appendix A7) with an average of 9.82^{0}. Not only is there a large range in G.M.A. between the samples, but there is also a considerable variation between different sections of an individual sample (up to 2.5^{0}, Appendix A7). The inter-sample variation cannot be related to position around the fold axis or distance from fault planes: samples 36 to 40 are a sequence taken at 0.15 to 0.25m intervals away from fault 3, but the G.M.A. does not change systematically. However, it may be significant that both of the two measurements made of fragments within a gouge zone (36 and 44) had relatively low G.M.A. values (7.32 and 8.85^{0} respectively). Another pertinent observation is that samples with type 3 or 5 grain boundaries (38, 40 and 42) had much higher G.M.A. values than the other samples in which type 1 grain boundaries were dominant.

A few thin deformation bands were seen, with a consistent preferred orientation, giving a grainy appearance to quartz in extinction.

C-axis orientations were measured for 302 grains in sample 43. A very weak preferred orientation is seen (Figure 8.13) consisting of two concentrations in the plane normal to the axial plane, separated by 30^0 and bisected by the axial plane.

7.3.7 Gouge Microstructure

The gouge matrix is seen to consist of very fine-grained quartz with dense concentrations of small oxide patches: variation in amounts of oxide are responsible for the contrasts between white and dark brown colours seen in hand specimen. Due to the difficulty of obtaining C.L. images, the proportion of cement to fragmented quartz cannot be estimated. Fragments of quartzite within the matrix are extremely poorly sorted, ranging in size from fractions of a grain to clusters of grains several millimetres long. The grain clusters exhibit typical features of the relatively intact quartzite, shown for one large fragment in Plate 7.3a: a good grain-shape fabric in random directions between fragments, and types 1, 3 and 5 grain boundaries, with type 1 most common. An important additional observation is that transgranular fractures, filled by oxides, which do not pass into the adjacent gouge matrix, may be seen within the clusters.

7.3.8 Discussion

The microstructures described add considerably more information to the deformation mechanism history than can be deduced from macro- and mesostructures alone; most importantly, two mechanisms previously unidentified are solution transfer and veining, and crystal plasticity.

The earliest deformation recorded is an episode of solution along stylolites. Unlike the samples described at Punta Vidrias, these are not exclusively bedding-parallel and may occur in several directions. They may have contributed an unquantifiable but significant amount of strain. Although there is clear evidence for some veining which post-dates stylolites, it is considered likely that much was synchronous, as for the example at Punta Vidrias.

The type 3 and 5 grain boundaries and high G.M.A. values are clear evidence for deformation by crystal plasticity, which followed the solution transfer and veining, since the large vein crystals are equally affected. Grain boundary migration was the dominant process, well demonstrated by the grain boundaries, but an important aspect was also the penetrative strain recorded by undulose extinction giving the high G.M.A. values. Whether the grain boundary migration was of the 'fast' or 'slow' types recognised by Urai et al. (1986) cannot be determined since diagnostic microstructures for each have not been identified. Although the measured strain magnitudes overlap with those previously deduced to be primary fabrics, the good fabrics of these samples may have a tectonic component due to crystal plasticity: this is suggested by the parallel grain shape fabrics and type 5 grain boundaries. The correlation observed between the samples with high G.M.A.'s and types 3 or 5 grain boundaries suggests that the intersample G.M.A. variation is due to variable amounts of crystal plasticity, but the controlling factor here is not evident.

The fact that the high G.M.A. values are not reflected in the natural shear strains (Appendix A5) may mean that only a very small increment of strain will promote widespread grain boundary mobility; the strain measurements are insufficiently precise to detect the difference.

Interpretation of the grain shape fabric is particularly difficult following the above observations on the role of crystal plasticity; and the restricted range of positions sampled around the anticline. Neither simple models of tangential longitudinal strain or strain due to flexural folding alone can account for the observed fabric orientations. A flattening sub-parallel to bedding, as observed in all four samples, could belong to the limb position in an early, tight fold, from flattening parallel to the axial plane: this is suggested by the proximity of the C1 cleavage pole to the shortening direction, but the minimum fabric axis does not rotate in the correct sense for subsequent folding in sample 41.

However, a simple model invoking tangential longitudinal strains during refolding, superimposed on primary fabrics, can successfully predict the difference between the pattern of strain in the hinge area (38, 39 and 40) compared to the limb (41). The hinge fabrics, with minimum axes perpendicular to bedding, follow from their positions on the outer arc of the quartzite (see section in Figure 7.10), while the shortening direction in 41, oblique to bedding, is predicted by the addition of a layer parallel tectonic compression on the inner arc to a primary, bedding-sub-parellel fabric. The hinge fabrics preserve some evidence of primary features, as seen from their different maximum axis orientations. Although there is clear evidence for flexural slip approximately normal to the fold axis, from bedding plane slickenside lineations within the interbedded shales and quartzites of the Los Cabos series, the obliquity of the grain shape fabric to the bedding is in the incorrect sense for flexural slip or flow on the W-dipping beds of the Portizuelo anticline.

It is concluded that the grain shapes represent tectonic strains superimposed on primary fabrics, and that they can be simply predicted by states of strain within a layer with tangential longitudinal strains produced during the later, upright folding. However, the data is insufficient to draw firm conclusions, except that the fabrics are not related to faulting since they are rotated within clusters of grains in the gouge zones, and the G.M.A. value decreases in such clusters.

An interesting feature of the veins is the band of fine grains along vein edges. This can be observed to form by convolution of both vein crystals and host grains, and is clearly due to intense recrystallisation by grain boundary migration. Localisation of shear and plasticity along veins is common to these samples and to those from Punta Vidrias (see 6.4.4), and suggests that the vein quartz may be inherently weaker, possibly due to enhanced hydrolitic weakening.

The weak c-axis fabric of sample 43 is difficult to interpret given that recrystallisation in the remainder of the quartzite is limited to the formation of small grains along boundaries. It may therefore be a primary fabric of the sort detected by Borg et al. (1960) and Prior and Sims (1986), but the similarity of the fabric to the stronger fabrics observed in the recrystallised samples V8 and V12 also suggest that a tectonic component may be important.

Crystal plastic features are clearly cross-cut by transgranular fractures from both the faulted and unfaulted areas. Cataclasis therefore evidently followed the crystal plasticity with some transgranular fracturing before the development of faults with gouges, as seen by the presence of transgranulars within quartzite fragments. The random orientations of fabrics between fragments shows clearly that they were deformed plastically before faulting, and rotated within the gouge. During the faulting, no further plasticity operated: this can be deduced from the fact that G.M.A. values of fragments within the gouge are no higher than adjacent quartzite. The observation that G.M.A. values are lower within the two gouges could indicate that grains with high G.M.A. values are preferentially destroyed during gouge formation: this would be a consequence of higher unrelieved internal strain energies following earlier crystal plasticity, favouring microcracking in these grains.

7.4 ILLITE CRYSTALLINITY

7.4.1 Results

Nine crystallinity determinations were made for samples of the Thick quartzite. In the 0.45-2μ fraction, these had a fairly restricted range of results (0.175 to 0.294 $^{o}2\theta$) distributed between the anchi- and epi-zone, with one quite anomalous diagenetic zone value (0.550 $^{o}2\theta$) which is influenced by the presence of mixed layers (Appendix A8). The average value of the eight consistent results ($0.233^{o}2\theta$) is very similar to the value obtained from an adjacent sample of Luarca slates ($0.244^{o}2\theta$).

Illite crystallinity was also determined for a sample of the gouge matrix. This value, $0.369^{o}2\theta$, is significantly higher than the quartzites or slates.

The results of determinations for the 0.45-20μ fraction made on all the above samples follows these patterns, but the crystallinities of the larger size fraction are generally higher by $0.04^{o}2\theta$. One large discrepancy between the two size fractions occurs for the anomalous diagenetic zone value: the crystallinity of this sample in the larger size fractions is closely similar to the remaining quartzite samples.

Bulk rock X-ray diffraction analyses of one quartzite sample showed that it consisted only of quartz and illite. In the shale and gouge samples, chlorite +/- kaolinite was also present, in larger quantities in the gouge.

7.4.2 Discussion

The range of crystallinities for the Luarca quartzite samples, although restricted, is nevertheless slightly greater than the anchizone error ($+/-0.04^{o}2\theta$). This cannot be attributed to stratigraphic changes (negligible variation over the sample area) or structural factors, nor does it appear to relate simply to lithology, since the quartzites have the same crystallinity as the slates. This small variation is similar to the variation noted for the samples at Punta Vidrias, and like the interpretation given in 6.5.2, it is suggested that lithology exerts some control on crystallinity through a cryptic intrinsic parameter such as pore fluid chemistry. The mean value of the quartzite crystallinities, which is effectively identical to the slate crystallinity, can characterise the grade as upper anchizone. The gouge crystallinity, however, is lower anchizone and it is suggested that this represents a genuine retrogression from the higher grade conditions of the quartzite.

The increase in crystallinity with size fraction is interpreted as evidence of a prograde reaction rather than either the influence of detrital micas, which are not seen, or retrogression, since the gouge crystallinity shows a similar increase to all the other samples: the effects of retrogression seem to be independent of size fraction.

7.5 SYNTHESIS

7.5.1 Deformation Modes and Mechanisms

The Portizuelo anticline has been interpreted as the apex of a larger recumbent fold structure. This is broadly supported by the observations of two cleavages reported here, but important exceptions to the predicted cleavage vergences, and the wide variation in cleavage dip, suggest that cleavage formation and folding were continuous; both crenulation of existing cleavage, and formation of new cleavage at intermediate stages of folding, may account for anomalous cleavage vergences.

Microstructural evidence establishes the importance of crystal plasticity from high G.M.A. values, grain boundaries and shape fabrics, mainly by grain boundary migration, and especially concentrated along veins. Stylolites and veins also establish the importance of diffusive mass transfer of quartz, not only in response to a vertical principal stress. Finally, cataclastic deformation mechanisms operated both pervasively with the development of the F1 and F3 fracture sets, and in a localised fashion leading to the formation of multiple, spaced, sinistral strike-slip faults, which have gouge structures very similar to those reported on a much smaller scale from experiments.

In comparison with Punta Vidrias, there are two important changes in deformation mechanisms. The first is the operation of solution transfer along planes other than bedding: this cannot be a simple response to burial as deduced for the former case, but must be an important aspect of the tectonic deformation. Secondly, while crystal plasticity was limited to veins and fault planes at Punta Vidrias, much more extensive plasticity is evident at Luarca: this is most succinctly expressed by comparing the average G.M.A. value at Punta Vidrias, 3.70^{o}, to that at Luarca: 9.819^{o}.

7.5.2 Deformation Conditions

The upper anchizone crystallinity for the Luarca shale sample indicates a temperature range of 283-383°C. Unfortunately, it is not possible to make a realistic estimate of the stratigraphic depth of burial at Luarca; the top of the Agueira Formation is nowhere exposed. The total exposed stratigraphy from the base of the Thick quartzite is approximately 2,150m, but this includes only an unknown proportion of the Ordovician (Agueira Formation) and none of the Silurian, which is known to outcrop in the Navia Unit of the West-Asturian Leonese zone; there may also have been any thickness of Devonian sediments above this, although the fact that they are not seen anywhere in the Navia unit, or throughout the West Asturian-Leonese or Gal ician zones could imply that there was a complete absence of Devonian at the time of deformation. Marcos (1973) suggests that the pre-Devonian thickness from the base of the Luarca slates may be about 2000m; this is the minimum possible depth of burial, corresponding to a pressure of 50MPa; or 30MPa effective confining pressure (hydrostatic pore fluid pressure).

The lower anchizone crystallinity of the gouge gives a temperature range of 215-315°C, 60°C lower than the quartzite samples. Again, no reasonable estimate of confining pressures can be made.

7.5.3 Regional Tectonic History

The macro and mesostructural information can be tentatively correlated with the microstructural deformation mechanisms to produce a synthesis for the regional tectonic sequence. The earliest deformation for which there is evidence is diffusive mass transfer. The lack of evidence for any cataclasis associated with this process suggests a relatively low strain rate at a sufficiently low temperature to suppress crystal plasticity i.e. less than 200^{o}C (Rutter 1976, White 1976). Subsequently, the rise in temperature to 275-375^{o}C allowed crystal plasticity to operate, and it is suggested that this was the major fold accommodating mechanism in the quartzites for the E-verging recumbent folds, while cleavage formation and interbed shear occurred in slates. The increase in temperature is interpreted as the effect of a regional metamorphism rather than burial, which would require a minimum 3km of additional, post-Silurian sediments to achieve such temperatures (assuming a high geothermal gradient of 50^{o}C/km).

The formation of the fracture network probably occurred as this metamorphism waned but while the Navia unit was still under radial compression during the closure of the Ibero-Armorican arc: thus the fractures are related to the fold geometry. However, there must have been a quite significantly different strain field to cause sinistral displacement on the Portizuelo faults. Lower temperatures from the fault gouge suggest a reason for the change in deformation mode to faulting. The regional significance, and the timing of the faulting, are quite unclear: in particular, there is no constraint on the latter within the entire period from the Variscan orogeny to the Quaternary.

CHAPTER 8

PUNTA DEL SOL

8.1 STRATIGRAPHY AND LITHOLOGY

The lowest stratigraphic sequences are exposed on the southeast side of Playa de Vega (Figure 8.1). Here a variable sequence, approximately 60m thick, consists of orange sandstones followed by black or grey shales with siltstones, culminating in a medium-grained, massive quartzite, which is in faulted contact with a major quartzite approximately 300m thick (Figures 8.1, 8.2). The quartzite can be divided into at least two repeated cycles, consisting of a medium-grained, thickly bedded lower part with trough cross-bedding, becoming planar-bedded with low-angle cross-bedding and passing up into shales with thinly interbedded sandstones or quartzites.

The major quartzite and the variable beds immediately below can be ascribed to the top of the Los Cabos series (Marcos 1973) and therefore probably dated as Arenig (see Figure 8.2). By analogy with the Luarca section, the two fining-upwards sequences within the quartzite probably represent another pair of transgressive-regressive couplets, with the thickly bedded quartzites corresponding to the 'offshore' facies of Baldwin (1976).

The three members of the Luarca slates (Figure 8.2) can be distinguished from the Playa de Sabugo eastwards. The lower member (200m) is composed for the most part of black shales but there is a transitional passage from the top of the underlying quartzite with sandstone interbeds. The middle member consists of a quartzite identical to those of the Los Cabos series, including two similar fining-upwards sequences into shales and siltstones. The latter contain cross-laminated ripples, and abundant burrows and load casts at the base of siltstone beds, which have planar tops. This member is approximately 100m thick, including the two fining-upward sequences, the lower of which has 6m of finer beds. The quartzites themselves have planar and tabular cross-bedding, and hummocky cross-stratification. There is a magnificent exposure of <u>Cruziana</u>

FIGURE 8.1
Geology and Structure of Punta del Sol

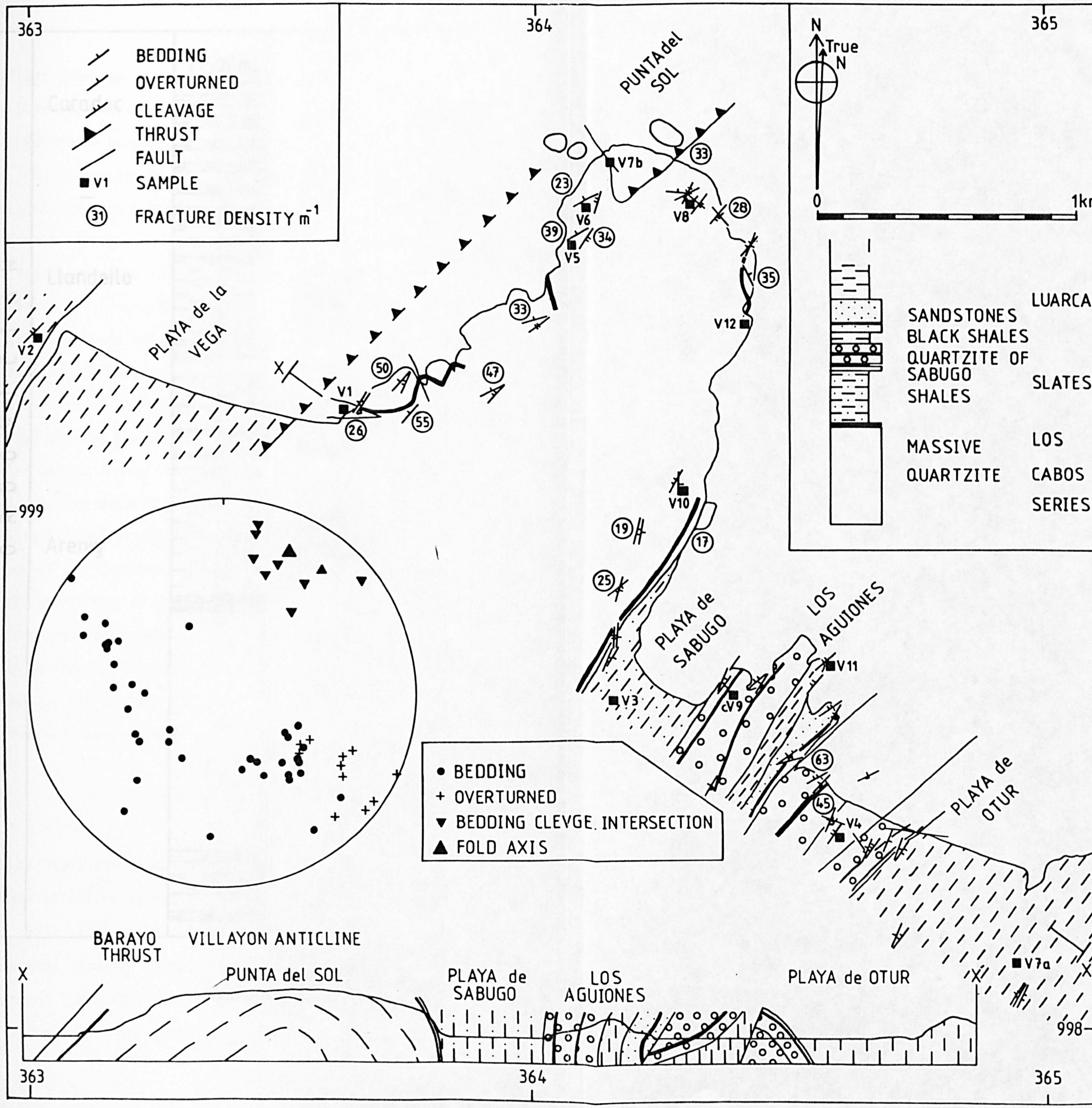

363
364
365
BEDDING
OVERTURNED
CLEAVAGE
THRUST
FAULT
V1 SAMPLE
31 FRACTURE DENSITY m-1
PUNTA del SOL
True N
0
1km
PLAYA de la VEGA
V1
V2
V3
V4
V5
V6
V7b
V7a
V8
V9
V10
V11
V12
33
23
28
39
34
35
50
47
26
55
19
17
25
63
45
SANDSTONES
BLACK SHALES
QUARTZITE OF SABUGO
SHALES
MASSIVE QUARTZITE
LUARCA SLATES
LOS CABOS SERIES
999
998
PLAYA de SABUGO
LOS AGUIONES
PLAYA de OTUR
BEDDING
OVERTURNED
BEDDING CLEVGE. INTERSECTION
FOLD AXIS
BARAYO THRUST
VILLAYON ANTICLINE
X
PUNTA del SOL
PLAYA de SABUGO
LOS AGUIONES
PLAYA de OTUR
X'

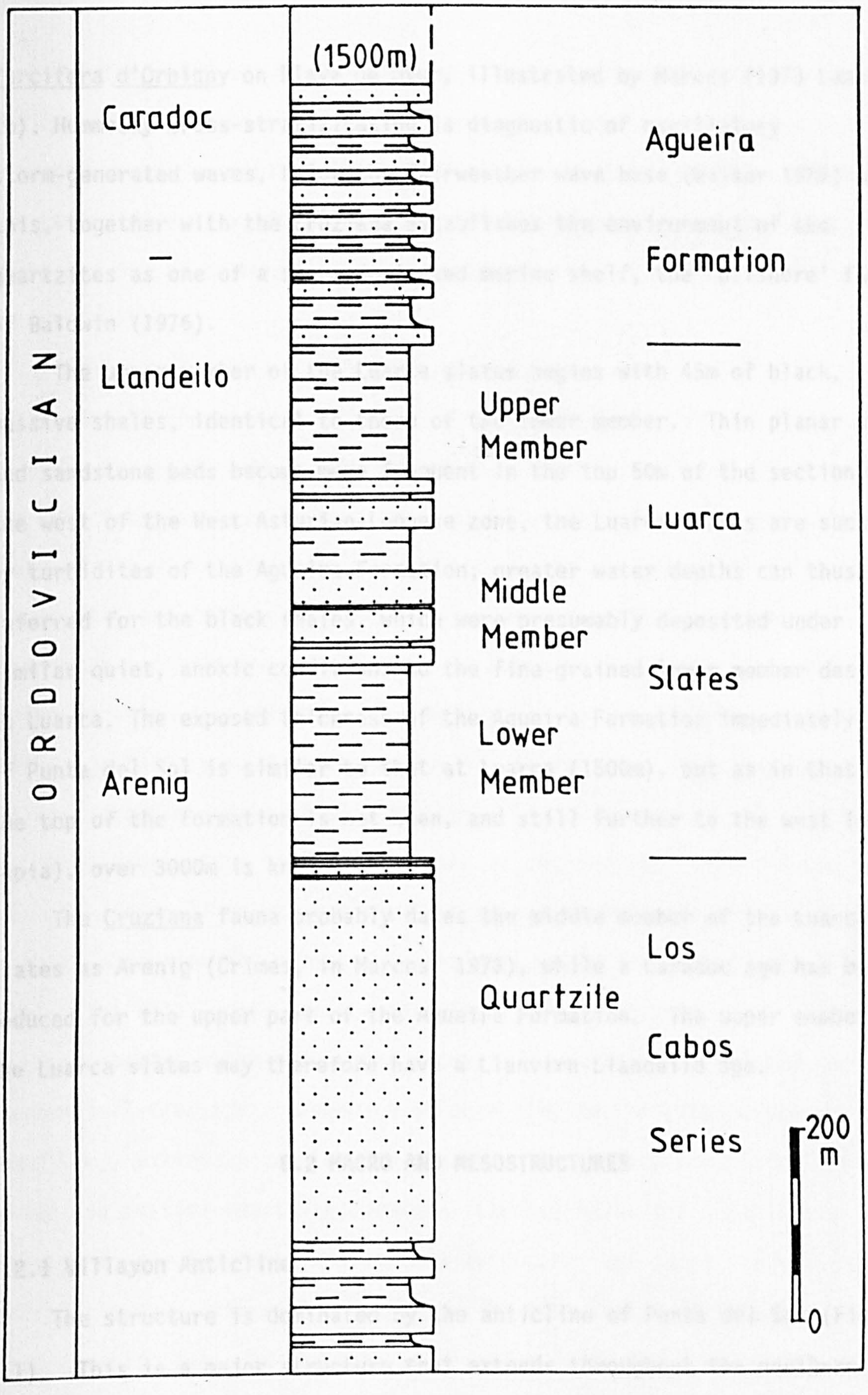

FIGURE 8.2
Stratigraphy at Punta del Sol.

furcifera d'Orbigny on Playa de Otur, illustrated by Marcos (1973 Lamina Ib). Hummocky cross-stratification is diagnostic of oscillatory storm-generated waves, below the fairweather wave base (Walker 1979) and this, together with the Cruziana establishes the environment of the quartzites as one of a storm-dominated marine shelf, the 'offshore' facies of Baldwin (1976).

The upper member of the Luarca slates begins with 45m of black, massive shales, identical to those of the lower member. Thin planar silt and sandstone beds become more frequent in the top 50m of the section. In the west of the West Asturian-Leonese zone, the Luarca slates are succeeded by turbidites of the Agueira Formation; greater water depths can thus be inferred for the black shales, which were presumably deposited under similar quiet, anoxic conditions to the fine-grained lower member described at Luarca. The exposed thickness of the Agueira Formation immediately west of Punta del Sol is similar to that at Luarca (1500m), but as in that case, the top of the formation is not seen, and still further to the west (near Tapia), over 3000m is known.

The Cruziana fauna probably dates the middle member of the Luarca slates as Arenig (Crimes, in Marcos, 1973), while a Caradoc age has been deduced for the upper part of the Agueira Formation. The upper member of the Luarca slates may therefore have a Llanvirn-Llandeilo age.

8.2 MACRO AND MESOSTRUCTURES

8.2.1 Villayon Anticline

The structure is dominated by the anticline of Punta del Sol (Figure 8.1). This is a major structure that extends throughout the northern part of the West Asturian Leonese zone, as the Villayon anticline. It is an overturned tight fold plunging at 20^{0} to 025^{0} (Figure 8.1). The massive quartzites of the Los Cabos series are seen only in the normal and vertical parts of the fold, but to the southwest, cross-bedding, burrows, ripples and loads provide unambiguous evidence that all the Luarca slates are inverted, reaching dips as low as 20^{0} (Figure 8.1) on the Playa de Otur. The facing direction therefore changes from upwards for all the beds on Punta del Sol to downwards on the overturned beds of Los Aguiones and further east.

8.2.2. Barayo Thrust

The Barayo Thrust, another major structure in the Navia province of the West Asturian-Leonese zone, runs parallel to and west of the axial plane of the Villayon anticline. In the south, anticlines in both the hangingwall and footwall of the thrust give indisputable evidence of considerable displacement. However, at Punta del Sol, the younger Luarca slates occur in a synform in the hangingwall against the older quartzites of the Los Cabos series in the footwall. There is no clear map evidence for the amount or sense of displacement.

The thrust plane itself is exposed at the northern tip of Punta del Sol. The footwall quartzites form a spectacular cataclasite along a sheet 1m thick approximately parallel to the northwesterly dipping beds (Plate 8.1a). The cataclasite has a knife-sharp contact with the fine-medium quartzite below, which shows good planar and trough cross-bedding and a sub-vertical cleavage. Fragments of quartzite in the cataclasite are up to 500mm long, extremely angular and poorly sorted. They consist of cleaved, bedded and massive quartzite identical to that below the cataclasite. The cleavage in the fragments is randomly orientated and shows various bedding/cleavage intersection angles. The cataclasite has a high proportion of clasts in contact: it is clast-supported. The matrix consists of very fine-grained white silica, with blackened areas and red-stained veins due to iron oxides. The only homogeneous fabric in the quartzites is a set of large fractures several metres long, which are often irregular in profile and stained by oxides. Some are also open. They have a very consistent NW-SE vertical orientation, also seen in a fracture set in the beds below and over the whole study area (Figure 8.3). However there is a noticeable reduction in fracture density and planarity passing from the intact quartzite to the cataclasite: many fractures terminate at the boundary.

300mm immediately below the thrust plane is a zone of fine, white, grey or pink, powdery gouge, containing some small angular fragments of quartzite and shale (Plate 8.4b). A faint foliation with a similar strike but steeper dip to the thrust plane is developed, particularly immediately below the thrust. It contains isoclinal folds, and may anastomose around the quartzite/shale fragments.

The gouge and thrust are exposed on one of the NW-SE vertical fractures that cut both hanging- and foot-wall, which shows slickensides plunging at 30^{o} to the southeast.

The hangingwall consists of a massive fine-grained white ultracataclasite (Plate 8.1b) in which partially rounded fragments of this material up to 100mm diameter occur. Numerous short and highly irregular fractures penetrate throughout this rock in all directions.

8.2.3 Other Major Faults

At least two other major faults can be inferred from the double repetition of the middle member quartzite of the Luarca slates on Playa de Otur (Figure 8.1). The detailed geometry of these cannot be deduced from the coastal sector alone, but the way-up criteria and bedding/cleavage relationships show clearly from which parts of a large recumbent fold structure each exposure of the quartzite must have been derived. Figure 8.4 presents three possible interpretations of the structure, made with the following simplifying assumptions:

a) All models start from the same refolded, east-verging recumbent

FIGURE 8.3

Fracture Orientations at Punta del Sol. A, B: method of measurement (see 3.1.2). N, Number of Measurements.

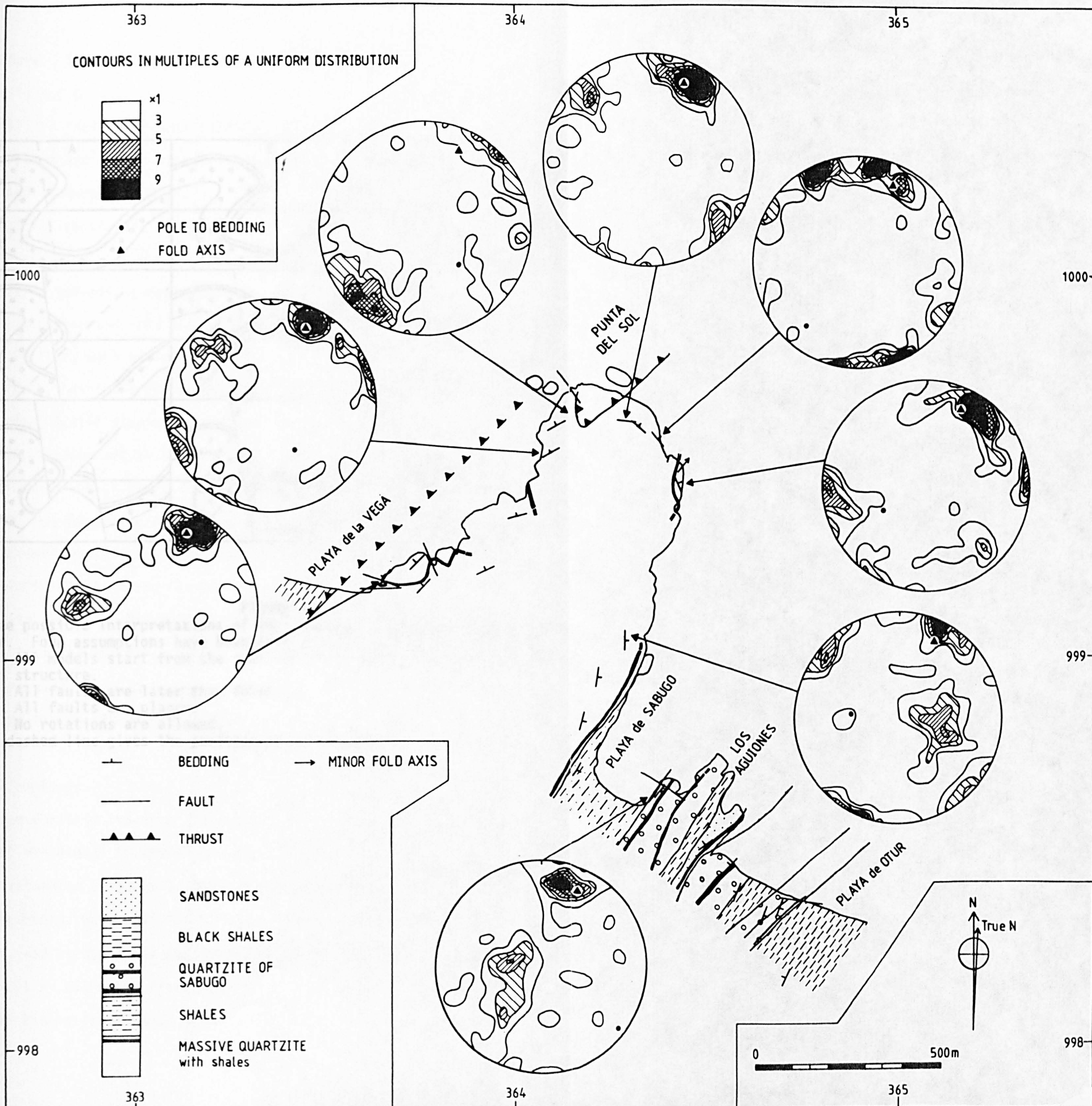

363
364
365
CONTOURS IN MULTIPLES OF A UNIFORM DISTRIBUTION
×1
3
5
7
9
POLE TO BEDDING
FOLD AXIS
1000
999
998
PUNTA DEL SOL
PLAYA de la VEGA
PLAYA de SABUGO
LOS AGUIONES
PLAYA de OTUR
BEDDING
MINOR FOLD AXIS
FAULT
THRUST
SANDSTONES
BLACK SHALES
QUARTZITE OF SABUGO
SHALES
MASSIVE QUARTZITE with shales
N
True N
0
500m

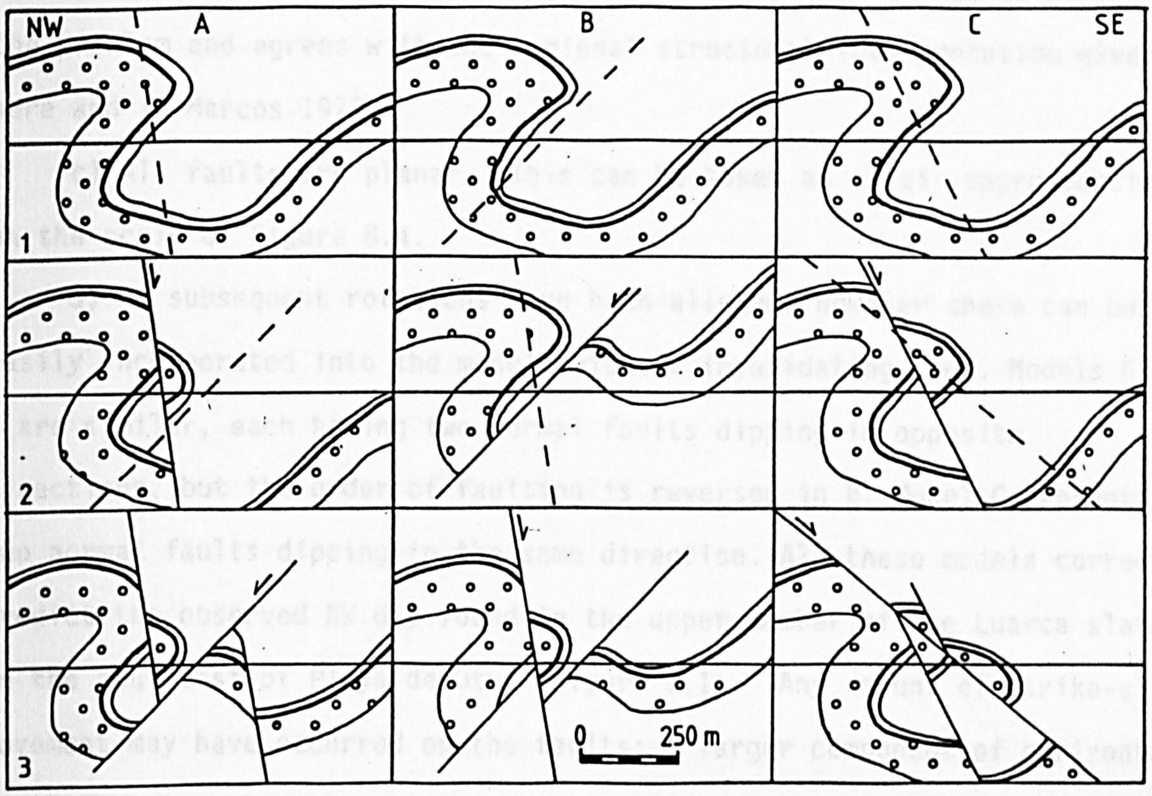

FIGURE 8.4

Three possible interpretations of the structure on Playas de Sabugo and Otur. Four assumptions have been made in constructing the models:

a) All models start from the same refolded, east-verging recumbent structure.

b) All faults are later than folding.

c) All faults are planar.

d) No rotations are allowed.

The dashed line gives the position of incipient faults.

structure. The cleavage evidence for the existence of this structure is given in 8.2.8.

b) All faults are post-folding. This assumption is made to simplify the problem and agrees with the regional structural interpretation given here and in Marcos 1973.

c) All faults are planar. This can be taken as a fair approximation on the scale of Figure 8.4.

d) No subsequent rotations have been allowed; however these can be easily incorporated into the models without invalidating them. Models A and B are similar, each having two normal faults dipping in opposite directions, but the order of faulting is reversed in B. Model C presents two normal faults dipping in the same direction. All these models correctly predict the observed NW dip found in the upper member of the Luarca slates on the southeast of Playa de Otur (Figure 8.1). Any amount of strike-slip movement may have occurred on the faults; a larger component of horizontal displacement could account for the steeper dip of one of the normal faults in A and B. Models A and C predict a considerable thickness of Luarca slates to the SE of Playa de Otur; and Model A predicts a sub-vertical orientation for the first fault. Both these features are observed, and for these reasons, Model A is preferred. It is similar to the interpretation given by Marcos (1973), but this showed only one normal fault.

8.2.4 Fractures

Two sorts of fracture are seen at outcrop:

a) **Non-Planar Fractures.** Irregular narrow fractures, which do not form systematic sets, up to 500mm long with no clearly visible displacements, have a lining of opaque, white, fine-grained matrix of iron oxides, and occur at low densities throughout the quartzite. They are cross-cut by all other fractures.

b) **Planar Fractures.** By contrast, these may be planar over several metres although in one area of minor folds, near the fold area, they are shorter and more irregular. They have no shear displacements, they are narrow (1mm), with a fine-grained opaque white matrix with or without oxide staining. There are at least two planar fracture sets and usually three. One set is always perpendicular to the fold axis (ESE-WNW strike, dipping vertically or steeply south). This set is always the most dense, with fracture densities typically of $20m^{-1}$, compared to $5m^{-1}$ for any other set. The low-density fracture sets have no consistent orientation around the fold other than a tendency for one set to be subparallel to the cleavage (Figure 8.3). All sets show some concentration into deformation zones, but this is much more prominent for the high density set (see below). They occur ubiquitously, cutting all non-planar fractures, and the majority of the high density set cuts the minor sets, although there are frequent exceptions.

Punta del Sol was the only locality where any fracture surface features other than lineations were observed in the quartzite at the top of Los Cabos series. In a railway cutting 0.5km south of Figure 8.1, excellent plume structure, en-echelon fractures and cross joints are all observed on discrete fractures up to several tens of metres long confined to single beds within the quartzite (Plate 8.2b). The relationship of the en-echelon and cross fractures to the plumes, which is exceptionally well displayed, consists of the replacement of faint plumes by en-echelon and cross-joints with increasing amplitude away from the plume axis. Initially closely spaced en-echelon fractures coalesce in this direction to form a river pattern with the 'upstream current' directed away from the axis, usually intersecting it at an acute angle, which may be either in the plume propagation direction or against it. The en-echelon fractures are commonly asymmetrically developed or exclusively along one edge of the bedding plane, usually the lower. The plume axis is always parallel to the bedding (in the relationship illustrated in Figure 2.3). All these features can be

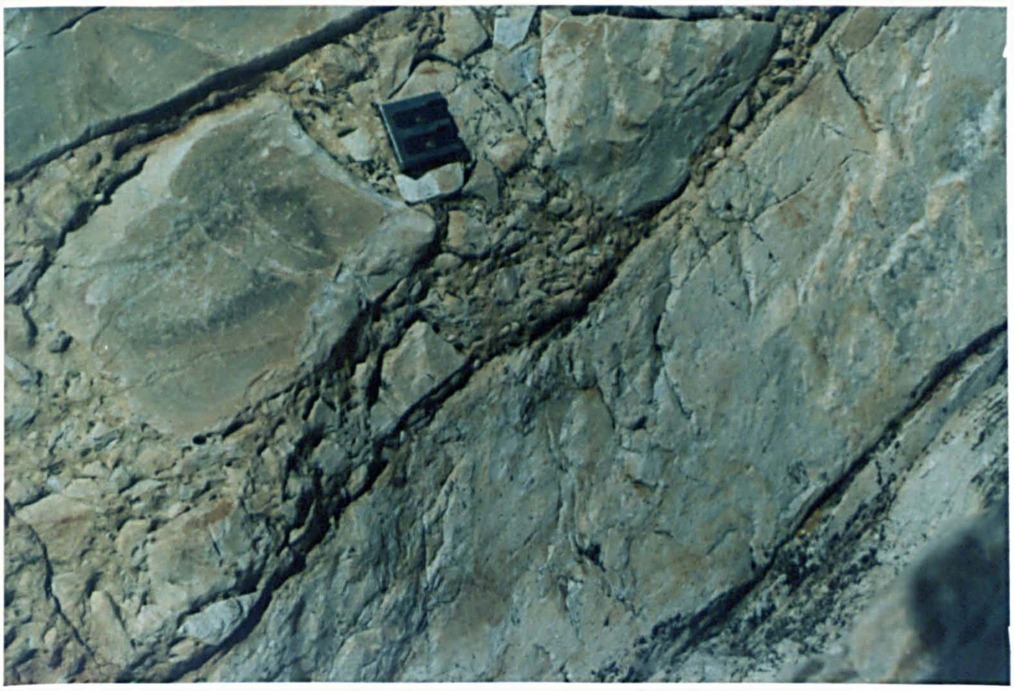

PLATE 8.1a

Cataclasite in footwall of Barayo Thrust. The cataclasite has a knife sharp contact with the quartzite below, in which cleavage can be seen, defined by a quartz grain shape fabric and phyllosilicates. Fragments of quartzite in the cataclasite are extremely poorly sorted, up to 500mm long, and have variable bedding cleavage intersections, showing that they have been derived from a variety of positions around the fold. It is clast-supported. The matrix consists of fine grained quartz cement.

PLATE 8.1b

Gouge along thrust plane of Barayo Thrust. A weak P-foliation dips more steeply than the thrust plane, Reidel (R1) shears can be seen displacing the foliation. The hangingwall consists of a massive, fine grained ultracataclasite with small fragments in a quartz matrix. Here the section of the hangingwall, thrust plane, gouge and footwall are provided by a NW-SE vertical fracture.

PLATE 8.2a

Fractures, Deformation Zones and Faults, Playa de Vega. The dominant set of fractures dipping steeply to the right is perpendicular to the fold axis, and can be observed forming a prominent deformation zone in this orientation at the centre of the photograph. This is cut by a later fault in the same orientation.

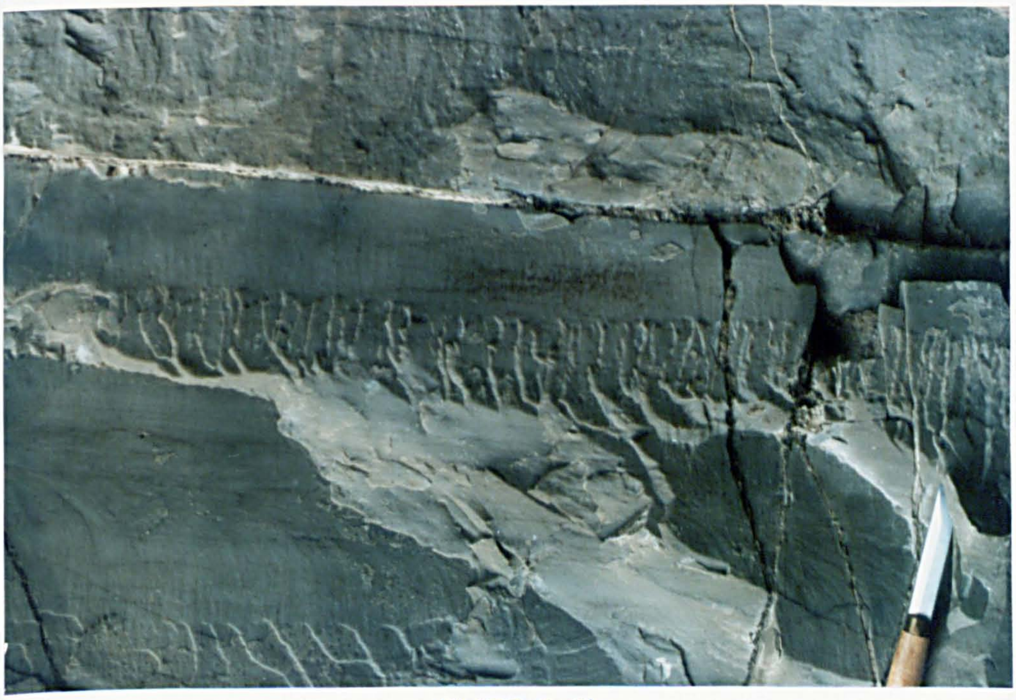

PLATE 8.2b

Fracture surface features, Railway cutting 0.5km south of Figure 8.5. The following features are clearly visible:

i) Plume Structure, axis in centre of bed, propagation direction from left to right.

ii) En echelon and cross-joints, developing from plume structure and coalescing downwards to form river pattern, with the upstream direction intersecting the plume axis in an acute angle in the direction of plume propagation.

seen in Plate 8.2b.

8.2.5 Master Fractures, Deformation and Breccia Zones

All these features are quite planar and several tens of metres long: they completely dominate the fabric of the quartzite when viewed from a distance, as seen in Plate 8.2a. Figure 8.5 shows detailed maps of master fractures, deformation zones and faults on Playas de Vega and Sabugo. They show that the master fractures and many deformation zones have a single consistent orientation perpendicular to the fold axis, which is shown in Figure 8.3, where the concentration of fractures around the fold axis is due to both one set of the smaller fractures described in the previous section, and to the master fractures and fractures of this set within these deformation zones.

Deformation zones consist of densely developed planar fractures in zones up to 500mm wide, where the frequency of the planar fractures parallel to the zone is greater than $30m^{-1}$. The densities of all planar fractures in the deformation zone increases: the total fracture density is greater than $45m^{-1}$. Figures 8.6 and 8.7 show fracture logs of all fractures across or adjacent to deformation zones in the positions indicated in Figure 8.5. They show the characteristic tendency for fractures to cluster, although for the reasons given in 6.3.2, the fracture log frequencies do not correspond with the fracture densities; those corresponding to observed deformation zones are greater than 4/100mm in log P.S.1. Deformation zones occur parallel to all sets of fractures; those parallel to the prominent NW-SE fracture set are particularly prominent and may accumulate 2-300mm of strike displacement, usually in a dextral sense. Breccia zones, comparable to those of Punta Vidrias and the Bernesga Valley are not identified, but this may be because the red colour of the shear matrix, allowing ready assessment of its proportion, is absent from these deformation zones.

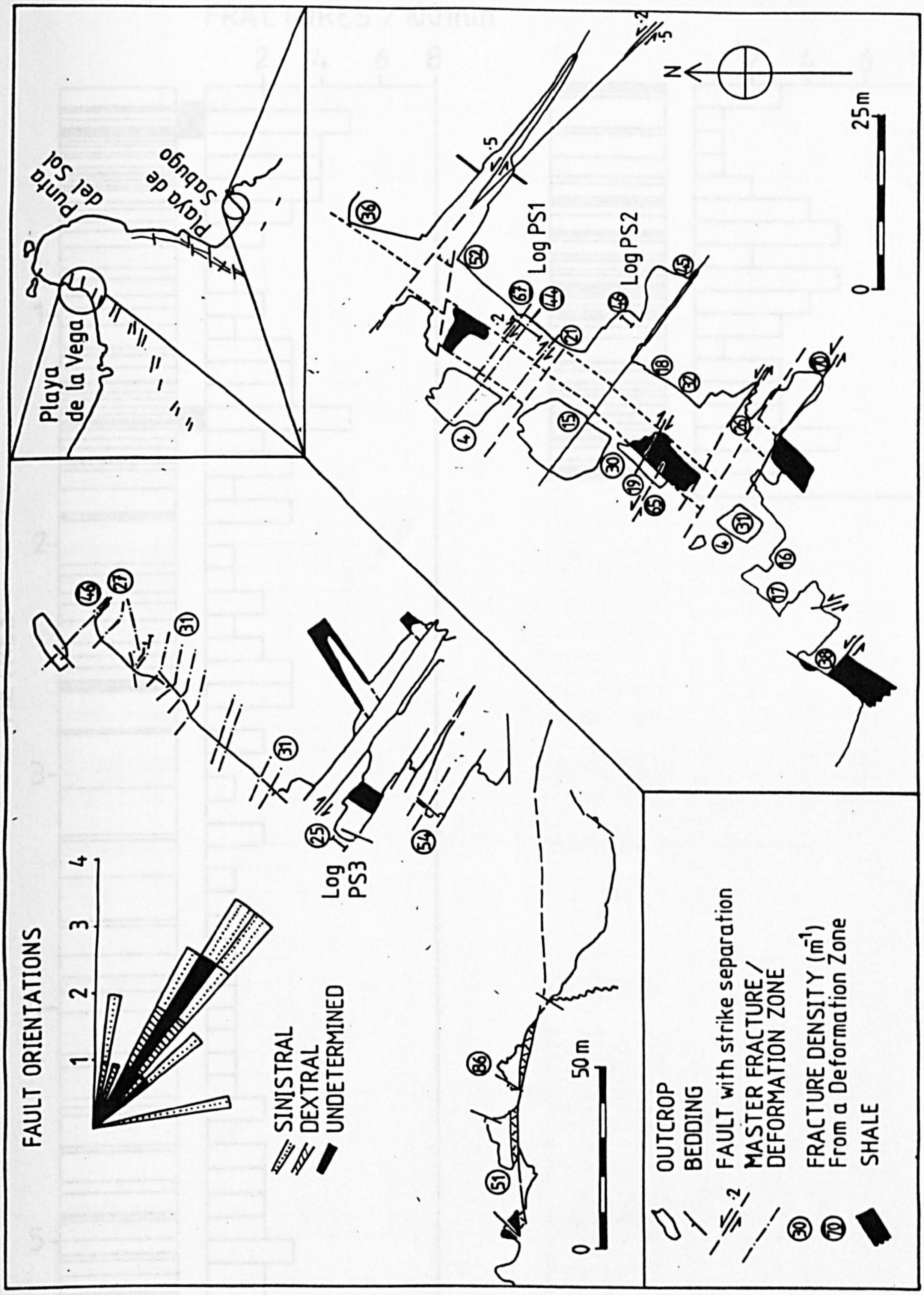

FIGURE 8.5

Deformation Zones, Master Fractures, and Faults. The two detailed maps are from Playa de Vega and Playa de Sabugo (Figure 8.1) and show the position of the Fracture Logs measured in Figures 8.6 and 8.7. The inset shows lineaments traced from an aerial photograph.

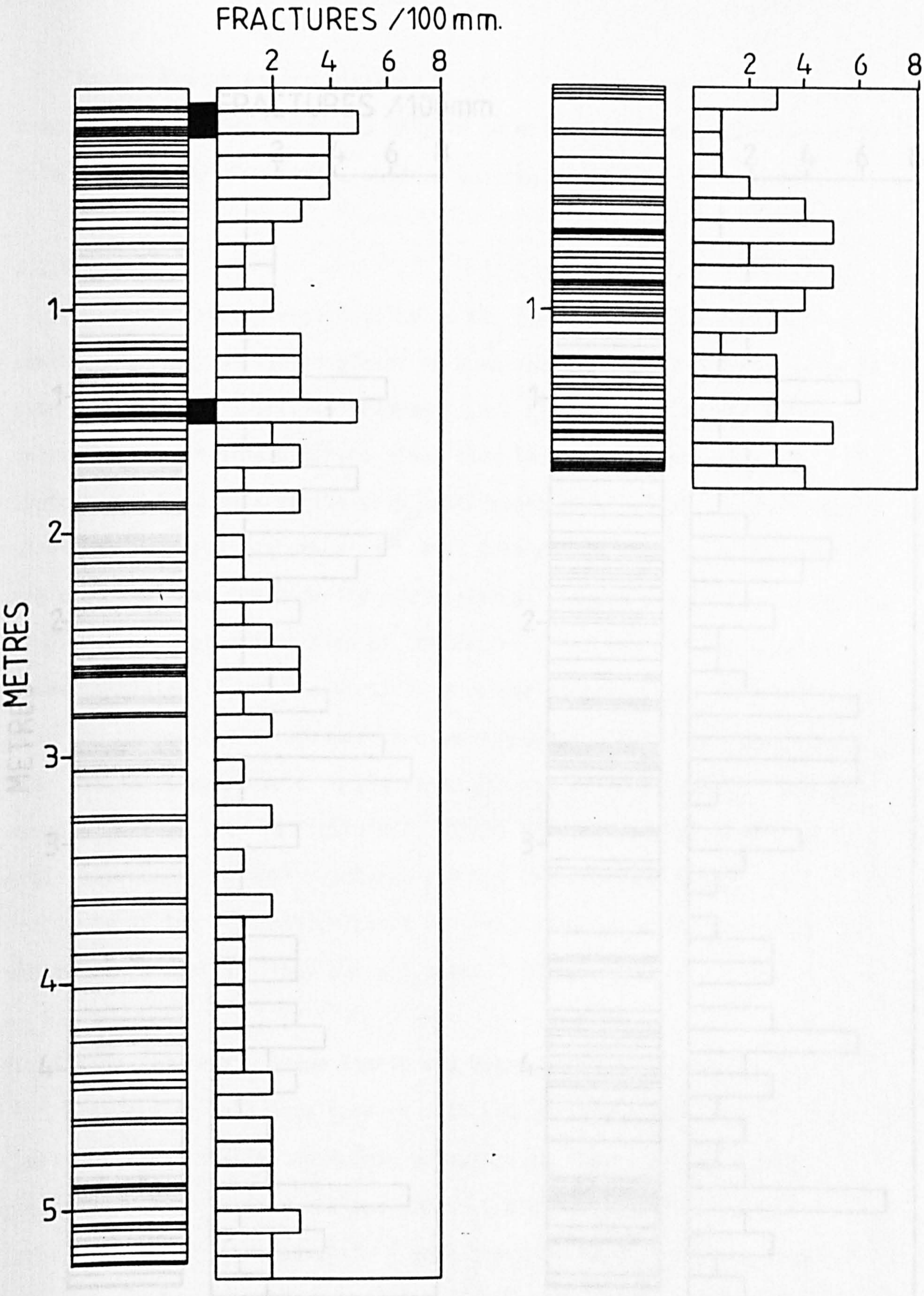

FIGURE 8.6

Fracture Logs 1 and 2, Playa de Sabugo. For locations of Logs, see Figure 8.5. The left column of each log gives the position of individual fractures on the log, and the histogram gives the number of fractures/100mm. Two deformation zones shown in Figure 8.5 are marked on Log 1 by the solid part of the column, where the log fracture density is greater than 4/100mm. The tendency for fractures to cluster is evident on both logs.

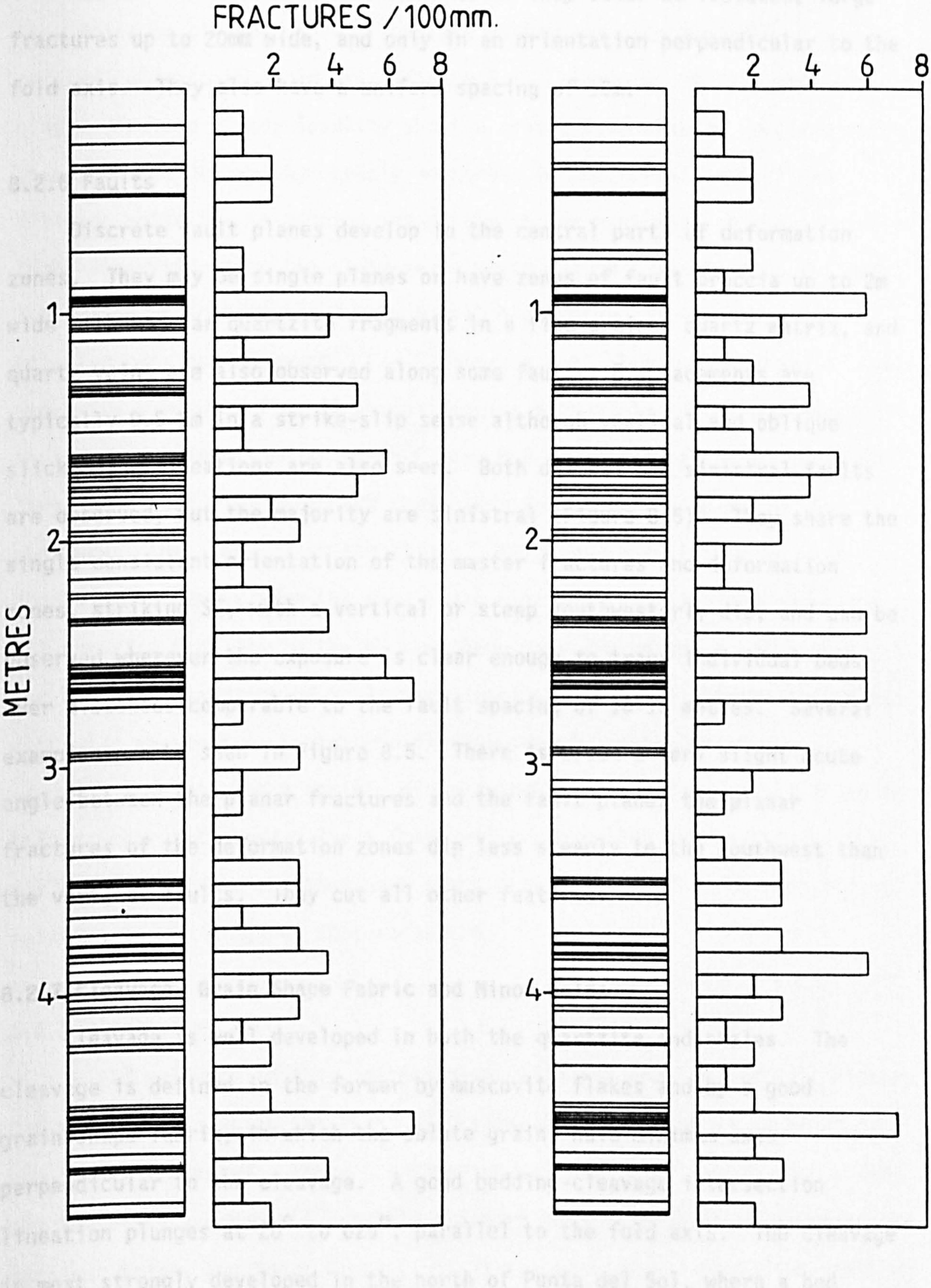

FIGURE 8.7
Fracture Logs 3 and 3R Playa de Vega. The Log is located on Figure 8.5, and the format is as in Figure 8.6. 3R is a repeated measurement of 3 to determine the error: the logs are almost identical. The clustering of fractures is again observed.

Master fractures are distinct because they occur as isolated, large fractures up to 20mm wide, and only in an orientation perpendicular to the fold axis. They also have a uniform spacing of 10m.

8.2.6 Faults

Discrete fault planes develop in the central parts of deformation zones. They may be single planes or have zones of fault breccia up to 2m wide with angular quartzite fragments in a fine grained quartz matrix, and quartz veins are also observed along some faults. Displacements are typically 0.5-5m in a strike-slip sense although vertical and oblique slickenside lineations are also seen. Both dextral and sinistral faults are observed, but the majority are sinistral (Figure 8.5). They share the single consistent orientation of the master fractures and deformation zones, striking SE, with a vertical or steep southwesterly dip, and can be observed wherever the exposure is clear enough to trace individual beds over distances comparable to the fault spacing of 10-15 metres. Several examples can be seen in Figure 8.5. There is often a very slight acute angle between the planar fractures and the fault plane; the planar fractures of the deformation zones dip less steeply to the southwest than the vertical faults. They cut all other features.

8.2.7 Cleavage, Grain Shape Fabric and Minor Folds

Cleavage is well developed in both the quartzite and shales. The cleavage is defined in the former by muscovite flakes and by a good grain-shape fabric, in which the oblate grains have minimum axes perpendicular to the cleavage. A good bedding-cleavage intersection lineation plunges at 20^{o} to 025^{o}, parallel to the fold axis. The cleavage is most strongly developed in the north of Punta del Sol, where a bed containing numerous horizontal burrows is exposed. These tubular traces are clearly flattened perpendicular to the cleavage. The cleavage in the shale is a penetrative slaty type, which may be crenulated.

Poles to cleavage show a complete dispersion over a girdle perpendicular to the fold axis (Figure 8.8). There is usually only a single cleavage at any locality and the orientation changes progressively from vertical or dipping steeply northwest in the normal limb of the Villayon anticline to dipping moderately to the northwest on the overturned limb. Observations on the cleavage vergence can be summarised as follows, and are shown in Figure 8.8. On normal beds three cleavage vergence relationships are observed. For SE-dipping beds, there is a group of small clockwise vergences from cleavages dipping moderately to the southeast: these are distinguished as C1 on Figure 8.8. There is a second group of large anti-clockwise vergences from cleavages steeply dipping to the northwest: these are C2 in the figure. Thirdly, beds dipping NW have clockwise vergences from the same steep cleavage (C2) with one exception. All inverted beds dip to the NW and these have two vergence relations: anticlockwise vergence of a cleavage dipping moderately northwest (C1) and clockwise vergence of a cleavage dipping steeply northwest (C2).

Minor folds with a variety of wavelengths and amplitudes are found in thinner quartzite beds. Their fold axes are parallel to the axis of the Villayon anticline, and they have correct asymmetries for their positions relative to the hinge of that structure.

8.2.8 Discussion

Field evidence in this section gives a fairly complex tectonic history for the area, in which the first identifiable deformation is recorded by non-planar fractures. These are clearly deformed by all later events and may therefore represent a pre-fold fracture network such as observed in the Bernesga Valley and Punta Vidrias; it is not possible to establish whether a bedding-perpendicular necklace exists due to subsequent deformation. The folding of the Villayon anticline followed; the parallelism of the

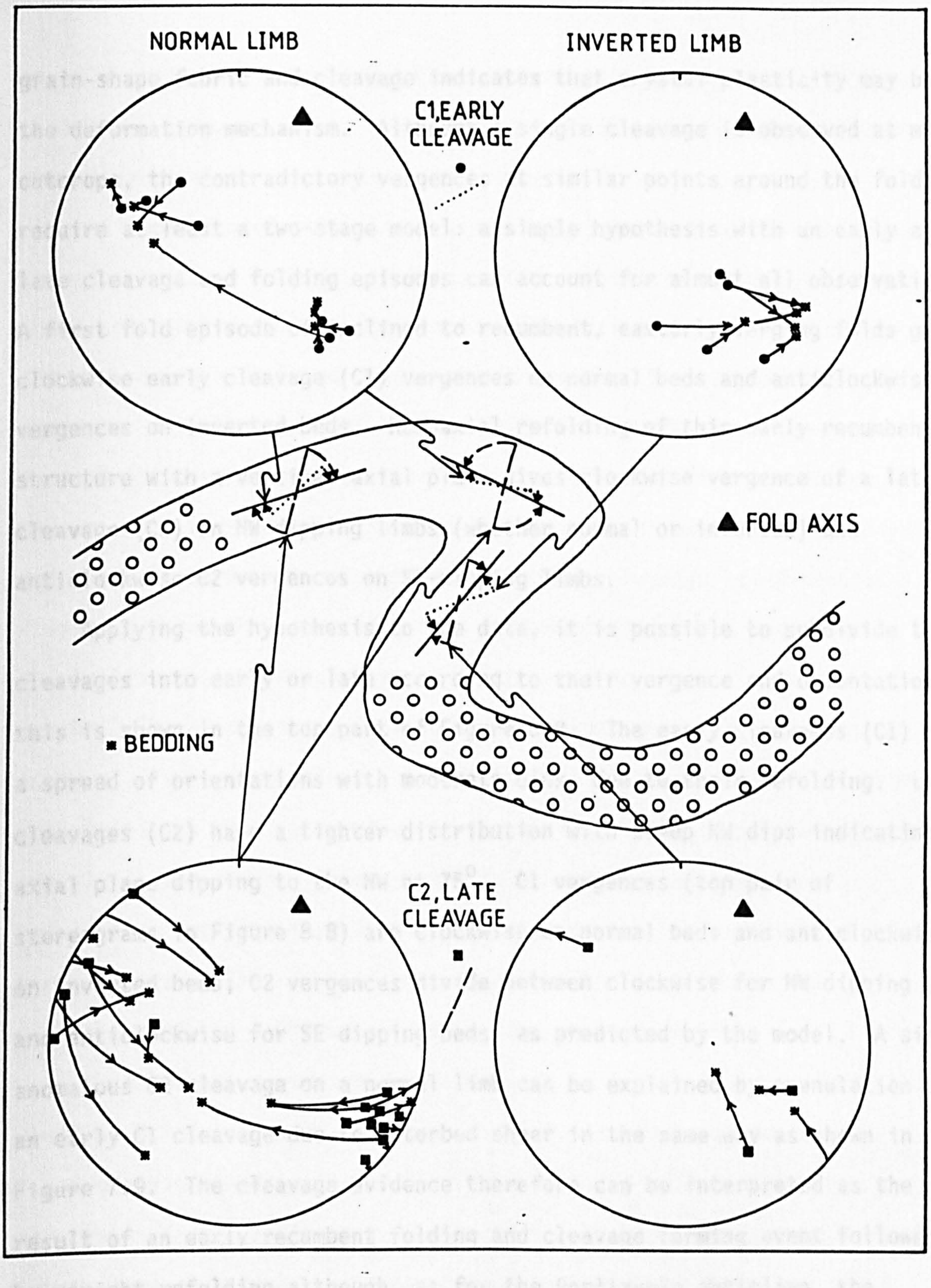

FIGURE 8.8

Cleavage Vergence at Punta del Sol. Cleavages can be subdivided into C1, early cleavage, showing small clockwise vergence on normal limbs and small anticlockwise vergence on inverted limbs, and C2, late cleavage, dipping steeply west, divided into clockwise vergences on NW dipping beds (normal and inverted) and anticlockwise vergences on SE dipping beds.

grain-shape fabric and cleavage indicates that crystal plasticity may be the deformation mechanism. Although a single cleavage is observed at most outcrops, the contradictory vergences at similar points around the fold require at least a two-stage model: a simple hypothesis with an early and late cleavage and folding episodes can account for almost all observations. A first fold episode of inclined to recumbent, easterly verging folds gives clockwise early cleavage (C1) vergences on normal beds and anticlockwise C1 vergences on inverted beds. Homoaxial refolding of this early recumbent structure with a vertical axial plane gives clockwise vergence of a later cleavage (C2) on NW-dipping limbs (whether normal or inverted) and anticlockwise C2 vergences on SE-dipping limbs.

Applying the hypothesis to the data, it is possible to subdivide the cleavages into early or late according to their vergence and orientation; this is shown in the top part of Figure 8.8. The early cleavages (C1) have a spread of orientations with moderate dips, due to their refolding. Late cleavages (C2) have a tighter distribution with steep NW dips indicating an axial plane dipping to the NW at 75^{o}. C1 vergences (top pair of stereograms in Figure 8.8) are clockwise on normal beds and anticlockwise on inverted beds; C2 vergences divide between clockwise for NW dipping beds and anticlockwise for SE dipping beds, as predicted by the model. A single anomalous C2 cleavage on a normal limb can be explained by crenulation of an early C1 cleavage due to interbed shear in the same way as shown in Figure 7.9. The cleavage evidence therefore can be interpreted as the result of an early recumbent folding and cleavage forming event followed by upright refolding although, as for the Portizuelo anticline, the 'events' are not necessarily separated by any time interval, and both folding and cleavage formation may be continuous.

The planar fractures follow the folding and have the same pattern as observed at Luarca: two sets are clearly defined, one perpendicular to the fold axis, and the other approximately axial planar. The former set dips steeply south, corresponding to the gentle north plunge of the Villayon anticline, compared to the reverse situation at Luarca. Deformation zones formed parallel to both sets at this time.

At approximately this time, displacement occurred along the Barayo thrust. A thrust breccia was formed in a discrete zone, with a thrust gouge beneath the thrust plane, and a cataclasite above. The discrete thrust breccia with large angular fragments is 'clast supported'. This suggests very strongly that high pore-fluid pressures were involved. The incorporation of cleaved quartzite fragments in random orientations within the breccia shows clearly that the thrust movement post-dated the folding and cleavage formation. The variable bedding/cleavage relationships in the fragments shows that they have been derived from several areas of the fold and implies minimum displacements of the order of half the fold wavelength, or 2km. There is nothing to suggest the amount and little clue to the sense of displacement along the thrust; the strongest evidence is from the weak foliation that is parallel to the strike of the thrust but dips more steeply to the south. This appears to be primary and therefore a P-foliation implying thrust movement perpendicular to strike, i.e. towards the southwest. This is the same sense that can be deduced from the repetition of the Villayon anticline 30km further south.

Observations on the unique occurrence of the fracture surface features given in 8.2.4 have some important similarities to experimental fractographic features in 2.2.3. The coalescing river pattern of en-echelon fractures is very similar to the hackle of glass surfaces; the faint plume structure can be considered analogous to the mist. It is therefore suggested that the appearance of en-echelon fractures either marks a threshold across which the developing crack acquires sufficient energy to divide into four new surfaces (the Johnson and Holloway criterion) or the point at which reflected elastic waves interact with the crack to produce branching. Although these two mechanisms cannot be distinguished, the importance of either is the implication that crack growth was dynamic. The en-echelon fractures are also taken to imply that there must be a shear component of stress along the main fracture surface from the arguments of Nicholson and Pollard (1985) and the similar deduction of Ramsay (2.2.3) (1986).

These observations are useful because they indicate that fractography is potentially important in studies of naturally deformed quartzites, and demand an answer to the question of why they are restricted to this single outcrop. If they represent natural fracture surfaces, all other surfaces are either too weathered or reactivated to obscure these features. They may, however, have been induced by the extensive blasting necessary to form the cutting, but the fact that such markings on natural surfaces have been observed further west in quartzites lower in the Los Cabos series suggests that they may be naturally formed, but late features.

The exact relationship between the timing of the planar fractures and the thrusting is problematic since no exactly comparable lithologies can be traced across the thrust plane. The fracture density drops from $30m^{-1}$ to $10m^{-1}$ in the thrust breccia, in which only a single set of fractures is developed. However, these contrasts may be due in part to the contrast between the homogeneous quartzite below the breccia and the extremely inhomogeneous texture of the breccia itself.

Two further phases of cataclastic deformation certainly post-date the thrusting. The master fractures, and further localisation on deformation zones, with a spacing of 10m in the former and a consistent orientation perpendicular to the fold hinge, are developed in quartzites throughout the area. Both these features, which can be related by their orientation, have negligible shear displacements and imply a minimum horizontal stress parallel to the fold axis. This could indicate that they may be related to the same stress system that produced the fold and thrust. They are considered to have formed shortly after the thrusting.

The final deformation at Punta del Sol is the development of a set of shear faults. These are vertical or dip at 80-90^{o} to the south, and have a very consistent orientation of 120^{o} (Figure 8.5). It is quite clear that these faults develop through the centres of deformation zones or along master fractures. This association explains why they have such a constant orientation, and do not form conjugate sets. Either deformation zones and master fractures have been reactivated during later faulting or the faults may represent the final stages of localisation during the development of deformation zones. The observed features are similar to those in the Navajo and Entrada sandstones reported by Aydin (1978), Aydin and Johnson (1978), Aydin and Reches (1982) and Aydin and Johnson (1983), where slip surfaces are found in deformation zones. The latter authors have used the Rudniki and Rice (1975) model for the development of localisation in pressure-sensitive dilatant materials to give conditions under which both deformation bands and slip surfaces may form. Slip surfaces may form due to runaway instability of an inclusion, when large elastic stresses accumulating in the matrix are relieved by large strains at a critical contrast between stress in the matrix and inclusion, and a critical length of inclusion. Here the deformation zones are considered to behave as stiff inclusions.

However, it is not possible to constrain the timing of the faulting relative to the development of the deformation zones, and thus to distinguish whether the faults have a genetic relationship to the zones or merely exploit the anisotropy.

8.3 MICROSTRUCTURES

8.3.1 Bedding

Bedding is defined in hand specimen by dark bands of iron oxides and large grains of mica, often separating beds of slightly different colour due to variable oxide concentration. The bands have variable widths from 1-2mm up to 10mm and may be discontinuous. In thin section, bedding is often harder to observe, but can be seen from increased oxide concentrations often occurring as amorphous patches, and larger grains of muscovite parallel to the bedding surface, which is inevitably a zone of high porosity. Clear bedding is seen in Samples V1 and V9. In V8 and V10, bedding is just visible as discontinuous lines of oxides, while in V5 it is marked only by stylolites. Only a weathered bedding surface can be identified in V12 on the hand specimen.

8.3.2 Grain Size

Linear intercept measurements of grain size are given in Appendix A1 and histograms with a geometric grouping (logarithmic class intervals) are shown in Figure 8.9. The geometric mean of linear intercepts (G.M.L.) varies from 0.05 to 0.09mm with anisotropy in individual slides up to 1.3. In general the difference in G.M.L. between different sections of the same specimen is far less, with the (D) section parallel to cleavage consistently slightly larger than the F section (perpendicular to cleavage and fold axis).

Figure 8.9 shows that some distributions of intercepts are bimodal. This confirms an initial optical impression that there are two sizes of grains in most samples: the small fraction intercepts of 0.02mm and a large fraction with intercepts of 0.1mm.

Based on the cleavage sections, the samples ranked by G.M.L. are V9, V1, V10, V8, V5, V12. On the F section perpendicular to cleavage and fold axis, the ranking is the same except that V8 and V12 are interchanged.

8.3.3 Grain Shape

The two grain sizes referred to above can also be identified by their distinctive two-dimensional grain shapes. The smaller grains are polygonal

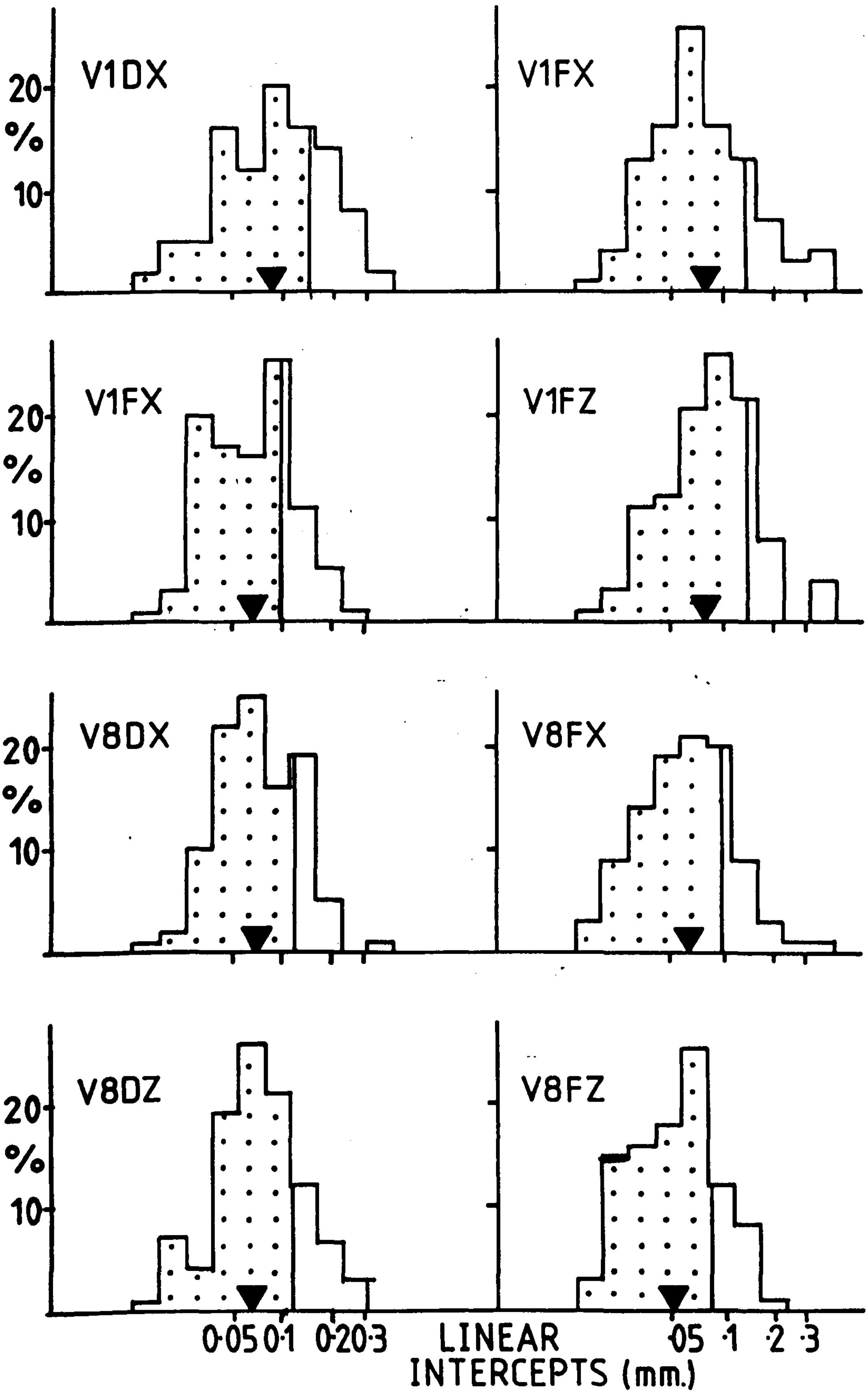

FIGURE 8.9
Histograms of Linear Intercept Measurements of grain size with a geometric grouping. The Geometric Mean of Linear Intercepts (G.M.L.) is indicated by the triangle, and the percentage recrystallisation, determined by point counting, is shown by the dotted area. The greater proportion of recrystallisation in V8 is reflected in the lower G.M.L. and the unimodal grain size distribution. Bimodal distributions are due to the existence of two populations of grains: small, recrystallised grains (0.05mm) and larger, original grains (0.1mm).

and equant, the larger becoming irregular in shape, with intermediate sizes taking on a moderate grain-shape fabric, generally with a rectangular section.

Figure 8.10 shows the orientation of the grain shape fabrics and other microstructural features of the quartzite samples plotted in true geographical orientations. The results on a Hsü diagram are also shown with natural octahedral unit shear, natural principal strains, Lodes parameter and K value, in Appendix A5.

All the best-fit solutions record a consistent oblate strain (k=0.1 to 0.879), with minimum values of E_3=-0.419 or λ_3=0.433. All show that the shortening direction, E_3, is perpendicular to the cleavage. The direction of maximum extension is parallel to the fold axis in samples V5, V8 and V12, but is exchanged with the intermediate principal axis in V5. In V1 the E_1 and E_2 also lie on a great circle in the axial plane, with E_2 closest to, but displaced from the fold axis. No best-fit result is available for V10, but all the trial solutions have an orientation of principal strain axes similar to the pattern of V1 but with E_2 closer to the fold axis.

8.3.4 Grain Boundaries

The majority of grain boundaries are of types 3 and 6. The same two-fold division made for grain size and shape applies to grain boundaries: large, irregularly shaped grains have type 3 (or 5) boundaries, while the small, equant, polygonal grains have exclusively type 6 boundaries that are often oblique to the plane of section, giving them a broad appearance. The grain boundary types observed in order of abundance are listed in Appendix A2. Type 3 grain boundaries on a larger grain are seen in Plate 8.3a, and typical type 6 boundaries on smaller grains in Plate 8.3b. V9 has only type 3 and some type 5 boundaries, with any planar boundaries possibly belonging to type 1. In V1, V5, V8 and V10, most

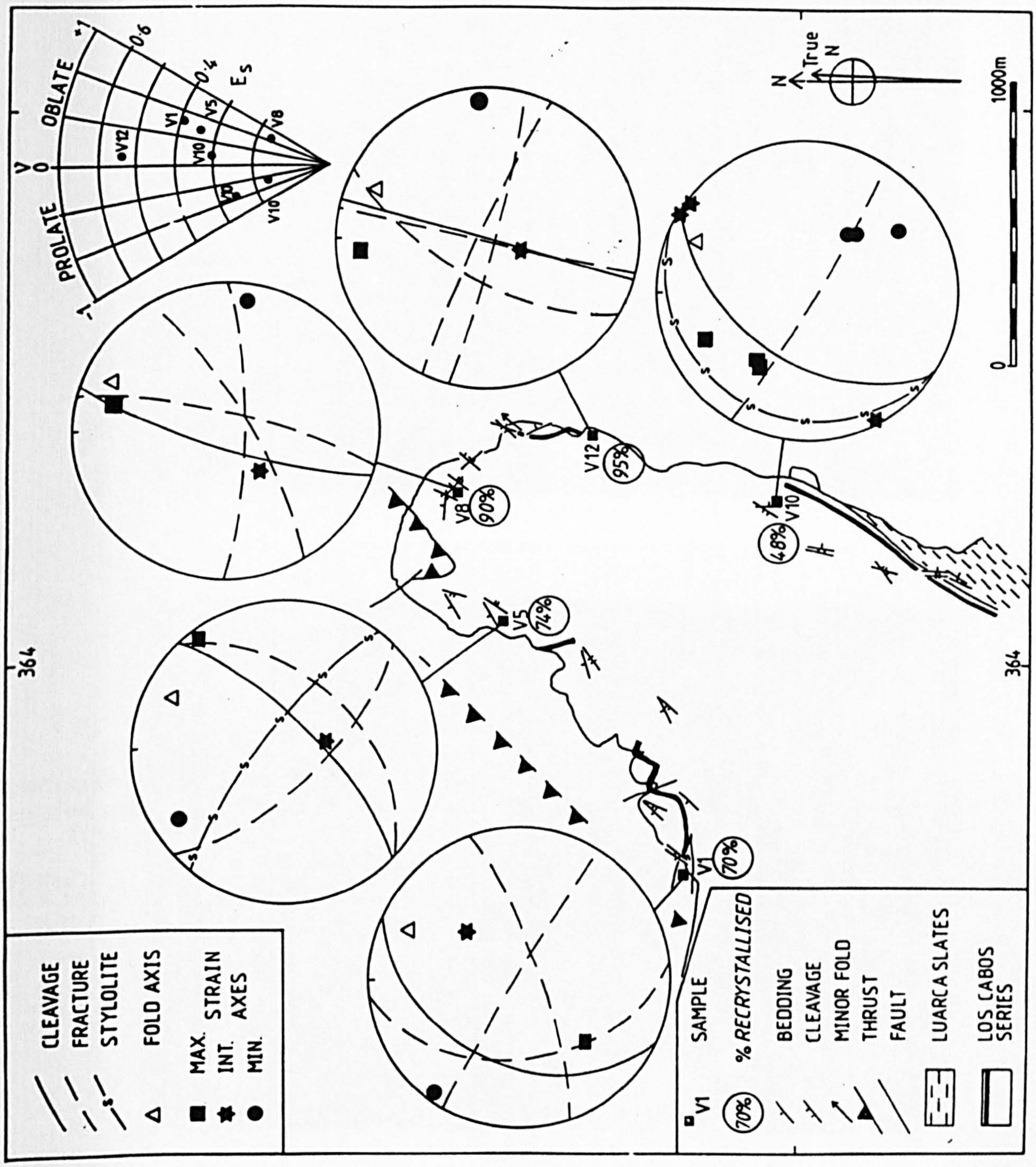

FIGURE 8.10

Shape Fabric and microstructural data. All show a shortening direction perpendicular to the late, C2, cleavage, and all best fit results give an oblate fabric. Although no best fits were obtained for sample V10, the three trial solutions plotted give similar results.

PLATE 8.3a

Type 3 grain boundaries. Sample V10, X.P.

PLATE 8.3b

Type 6 grain boundaries between smaller grains. Recrystallisation by both subgrain rotation (centre) and grain boundary migration below centre) can be seen. Some grain boundaries are flat along well crystallised phyllosilicates (Type 5). Sample V8, X.P.

PLATE 8.3c

Large elliptical pore with irregular margins and patchy quartz filling, on section perpendicular to late cleavage. Sample V12, P.P.L.

200μ

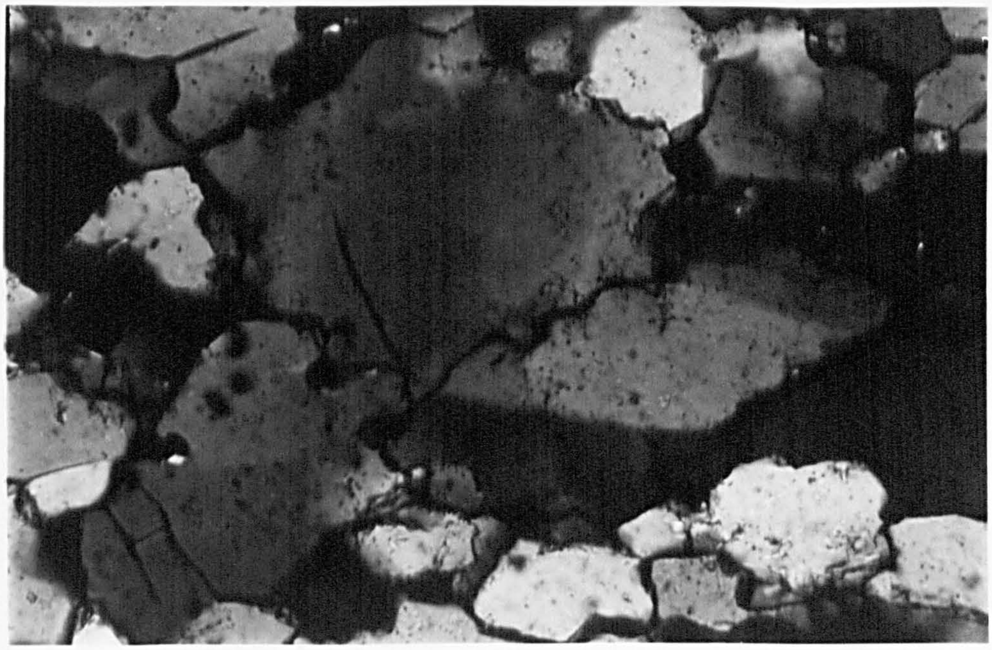

200μ

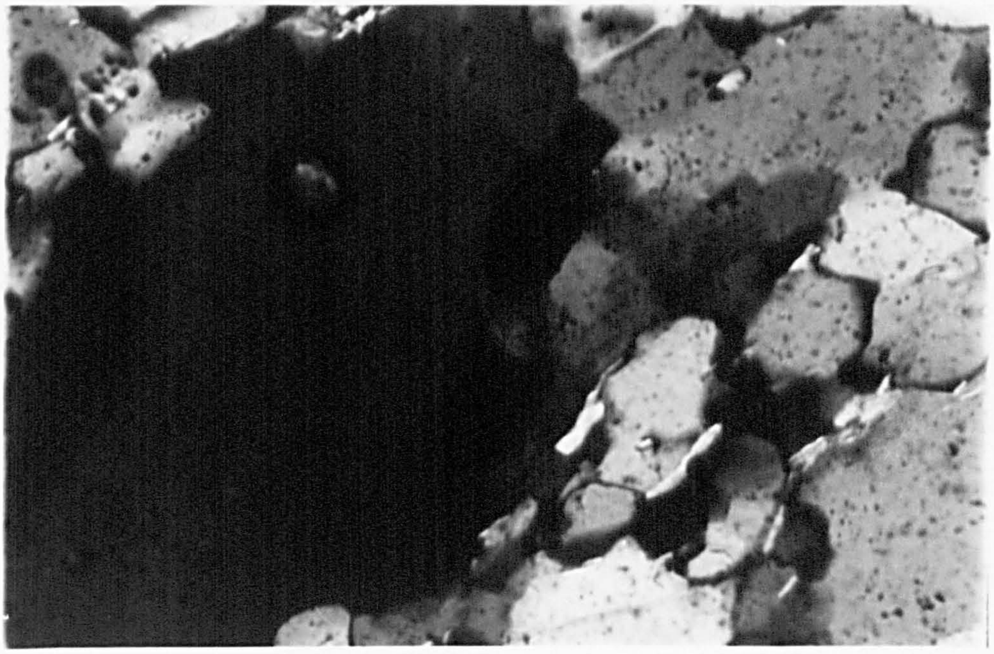

500μ

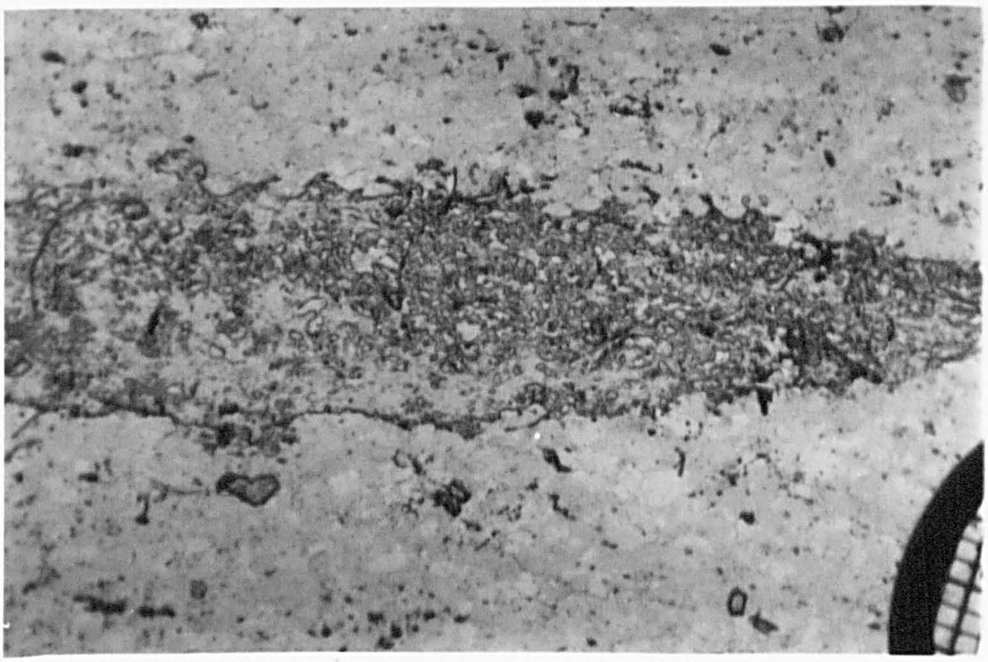

boundaries are of type 6; type 3 boundaries are subordinate and type 5 boundaries still less common in V5 and V8. V12 consists almost entirely of type 6 boundaries, but they are thin and faint compared to the type 6 boundaries in the other samples.

8.3.5 Porosity

Present porosity (sensu strictu) in the quartzites is uniformly very low (0-6%) (Appendix A3). Even when iron oxide and muscovite, which occur as pore fillings, are added to give a figure comparable to the 'precataclastic (B.C.)' porosities of samples from the Cantabrian zone, the range of values is from 5-10%, among the lowest measured (column 8 of Appendix A3). The porosity classification employed earlier is not readily applicable to these samples; rather, some unusual types of porosity are observed.

a) Grain boundary porosity. All samples have a varying number of small pores along grain boundaries and at grain junctions, best described as a combination of types 3 and 1 ("3+1").

b) Type 2 porosity - circular/elliptical grain-sized pores up to 0.2mm diameter are seen in V1, V9 and V10.

c) Bedding planes and stylolites have highly porous traces in thin section ("B+S").

d) Very large elliptical pores 2mmx10mm are observed in V12 and figured in Plate 8.3c ("E"). Considerable fracture porosity (type 4) is also observed in V9.

The distribution of porosity types, referred to by the above classification, is given in Appendix A2.

Both shape and amount of porosity, however, depends very considerably on section orientation. This is shown in Appendix A3, in which the point-count measurements are given, in these samples, for individual slides. The 'D' sections, parallel to cleavage, are all more porous (with the exception of V9) than the E sections perpendicular to the cleavage and bedding/cleavage intersection by up to six times, with the F sections intermediate.

The shape of both the grain-sized pores and the large elliptical pores reflect this section dependence. On the D sections, the pores are approximately circular: on both of the two sections perpendicular to cleavage, the pores are elliptical and take on the fabric of the grains, parallel to cleavage. This does not apply to the localised porosity along stylolites or open fractures; in the latter case, porosity is confined between the margins of the fractures and has a rectangular shape with a length parallel to the crack.

8.3.6 Fractures

In most samples, there is a clear distinction in both hand specimen and thin section between two types of fracture.

a) Non-Planar Fractures. These fractures have curved or kinked paths, occasionally resembling stylolites. They are generally thin (up to 0.08mm wide) and consist of short segments that link to form lengths of up to 100mm. They may be open or lined by oxides, but more commonly are filled with fine-grained, opaque, white quartz which is seen in thin section to have a cryptocrystalline nature, occasionally full of small oxide inclusions. A cleavage mica can be seen growing across a non-planar fracture from the intact rock. The surface topography of these fractures exhibits a distinctive roughness, reflecting their non-planar morphology. Cleavage can be clearly seen on fresh faces. The majority of non-planar fractures are sub-parallel but definitely oblique to the cleavage, but they also define an axial-planar fracture cleavage in V5 and V9 (Figure 8.10). They terminate at, or cut, stylolites.

b) Planar Fractures. These are up to 0.4mm wide, are longer than the non-planar fractures (up to and greater than 200mm), and most often have only extensional displacement, though some have a shear component (Plate 8.4a). They may also be filled by oxides or quartz and may be porous. The quartz cement is, however, well crystallised, occasionally forming very large strained crystals that are distinct from the grains of the host rock because they have inclusion-free type 1 grain boundaries, or may themselves be either inclusion free or highly inclusion-rich. The cement usually shows much lower G.M.A. values than the host quartzite: the value from a planar fracture cement in V12 is 4.34^{0} compared to 8.87^{0} for the quartzite itself. Grains on the walls of shear fractures are highly microfractured, have many inclusions, and high G.M.A. values. The microfractures cut and displace kink bands in original grains.

Planar fractures have a much smoother surface topography than non-planar fractures. They cut both stylolites and the non-planar fractures as well as the patches of irregularly distributed oxides and epidote crystals. A bleached band 5mm wide surrounds one example in V5. The planar fractures have a consistent orientation perpendicular to the cleavage and the bedding/cleavage intersection. They are thus perpendicular to the fold axis and parallel to the F sections (Figure 8.10).

Both types of crack are transgranular cracks. They occur mostly singly, though occasionally en-echelon with a short overlap length.

8.3.7 Stylolites

Stylolites are seen across the whole of several hand specimens. They have amplitudes of 1 to 2mm and wavelengths of 2-3mm, and can be classified as the 'composite' form of Guzetta (1984). Drawings of stylolites in perpendicular sections are shown in Figure 8.11 and a good example is seen in Plate 8.4c, which has a well-developed morphology of interlocking teeth with a square waveform. Teeth crowns themselves may be indented on a smaller scale. Traces of the stylolites may bifurcate around intact rock. The stylolite surfaces are marked by pores, oxides and large muscovite

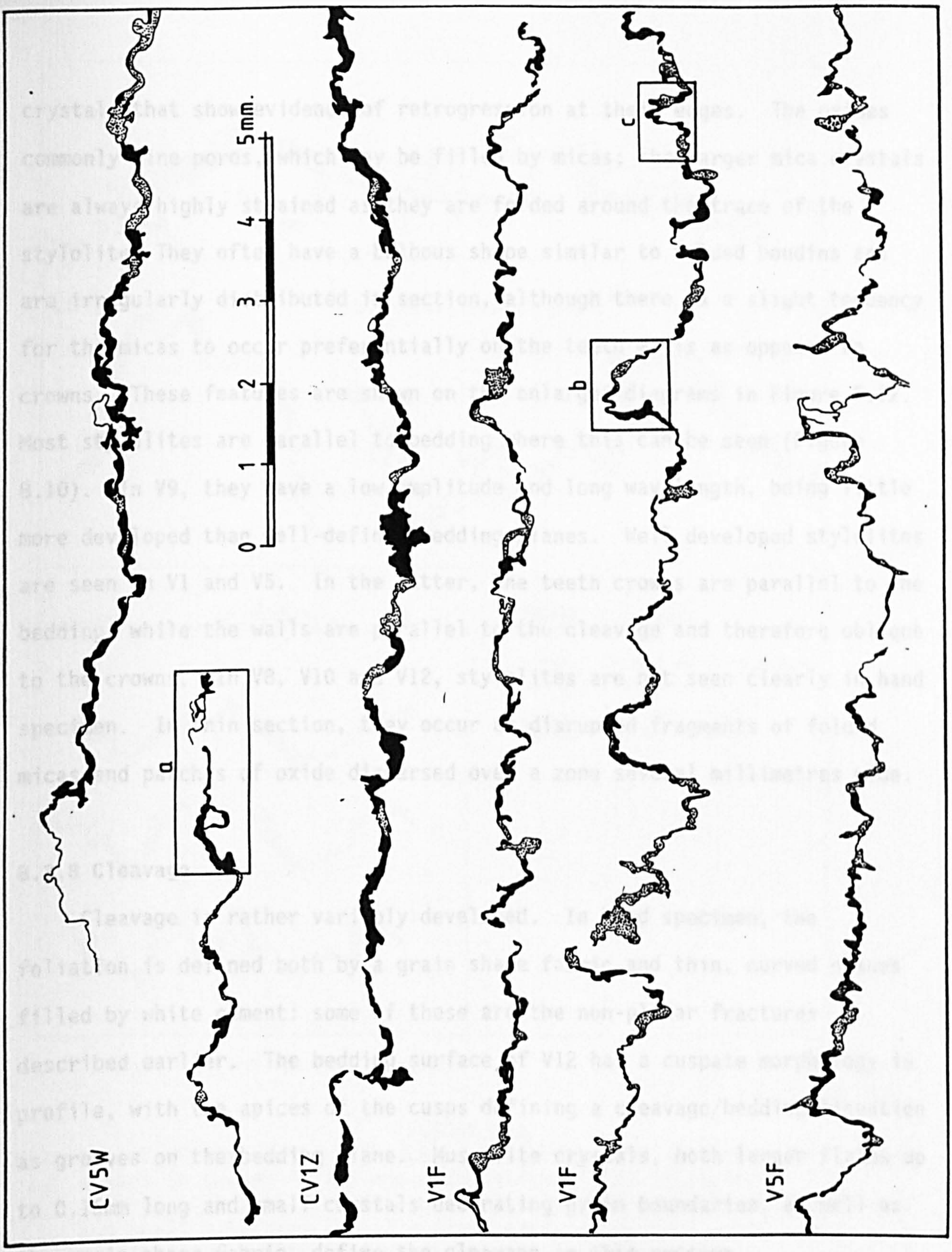

FIGURE 8.11

Tracings of stylolites from samples at Punta Vidrias (CV5, CV1) and Punta del Sol (V1, V5). Solid filling represents iron oxides, dotted symbol for clays or phyllosilicates. The tracings are arranged in order of increasing maturity and de formation from top to bottom. In this sequence, the following changes can be observed:

i) Linking of existing porosity, grain boundaries and phyllosilicates to form a continuous feature.
ii) Amplification of teeth structure.
iii) Narrowing of filling.
iv) Rotation of phyllosilicates to form walls of teeth.
v) Finally, disarticulation of stylolite.

Sub areas a, b, and c are shown in detail in Figure 8.12.

crystals that show evidence of retrogression at their edges. The oxides commonly line pores, which may be filled by micas; the larger mica crystals are always highly strained as they are folded around the trace of the stylolite. They often have a bulbous shape similar to folded boudins and are irregularly distributed in section, although there is a slight tendency for the micas to occur preferentially on the teeth walls as opposed to crowns. These features are shown on the enlarged diagrams in Figure 8.12. Most stylolites are parallel to bedding where this can be seen (Figure 8.10). In V9, they have a low amplitude and long wavelength, being little more developed than well-defined bedding planes. Well developed stylolites are seen in V1 and V5. In the latter, the teeth crowns are parallel to the bedding, while the walls are parallel to the cleavage and therefore oblique to the crowns. In V8, V10 and V12, stylolites are not seen clearly in hand specimen. In thin section, they occur as disrupted fragments of folded micas and patches of oxide dispersed over a zone several millimetres wide.

8.3.8 Cleavage

Cleavage is rather variably developed. In hand specimen, the foliation is defined both by a grain shape fabric and thin, curved planes filled by white cement: some of these are the non-planar fractures described earlier. The bedding surface of V12 has a cuspate morphology in profile, with the apices of the cusps defining a cleavage/bedding lineation as grooves on the bedding plane. Muscovite crystals, both larger flakes up to 0.15mm long and small crystals decorating grain boundaries, as well as the grain-shape fabric, define the cleavage in thin section.

8.3.9 Optical Strain Features

A clear contrast can be made between very low G.M.A. values of the small, equant grains and larger, irregular or elliptical grains with much higher values. This is seen in Appendices A7 and A10, where measurements

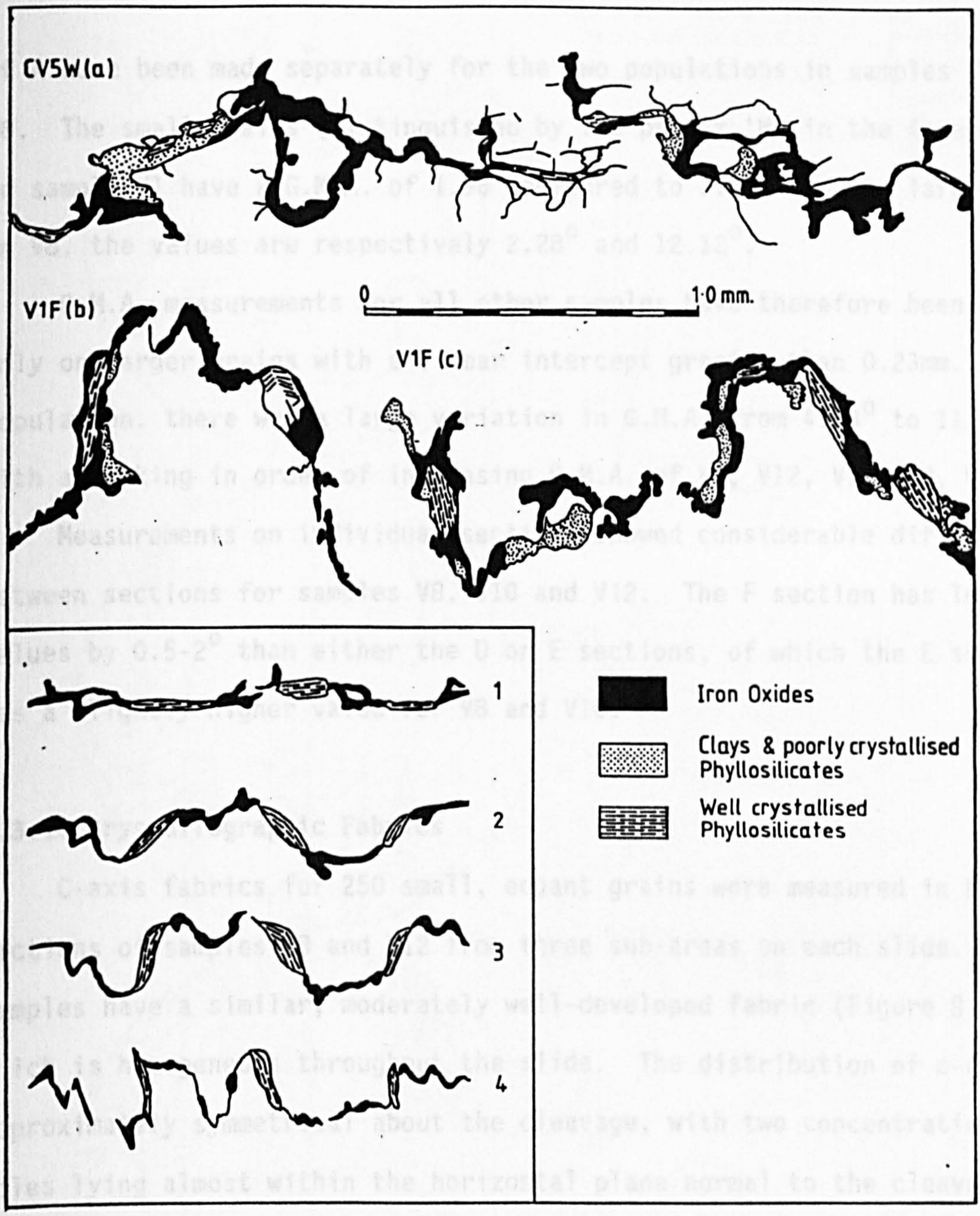

FIGURE 8.12

Enlargement of stylolites in Figure 8.11 (areas a, b, c) and model to show four stages in the evolution and deformation of the stylolites.

1. Initial stylolite formed largely by existing pores, grains boundaries and phyllosilicates (usually along bedding surface).
2. Linking of porosity to form a continuous feature.
3. Amplification of stylolite teeth, narrowing of filling, and rotation of phyllosilicates to form walls of teeth, with characteristic 'folded boudin' shapes.
4. Strain causes disarticulation of stylolite.

Enlargement of area a corresponds to a juvenile stylolite in stage 1; b and c are mature stylolites in stage 3.

of A have been made separately for the two populations in samples V1 and V8. The small grains (distinguished by the prefix 'N' in the Appendices), in sample V1 have a G.M.A. of 1.96° compared to 7.53° for the large grains: in V8, the values are respectively 2.28° and 12.12°.

G.M.A. measurements for all other samples have therefore been made only on larger grains with a linear intercept greater than 0.23mm. In this population, there was a large variation in G.M.A. from 4.83° to 11.43°, with a ranking in order of increasing G.M.A. of V9, V12, V1, V10, V5, V8.

Measurements on individual sections showed considerable difference between sections for samples V8, V10 and V12. The F section has lower values by 0.5-2° than either the D or E sections, of which the E section has a slightly higher value for V8 and V10.

8.3.10 Crystallographic Fabrics

C-axis fabrics for 250 small, equant grains were measured in F sections of samples V8 and V12 from three sub-areas on each slide. Both samples have a similar, moderately well-developed fabric (Figure 8.13), which is homogeneous throughout the slide. The distribution of c-axes is approximately symmetrical about the cleavage, with two concentrations of poles lying almost within the horizontal plane normal to the cleavage, at right angles to each other.

The strength of the preferred orientation, determined by the cumulative percentage of the stereogram within contours of multiples of a uniform distribution is given below for these two samples and for the sample measured from Luarca:

Concentration greater than	Cumulative % Area		
	43	V8	V12
4 x Uniform Distribution	0	1.0	1.0
3 x Uniform Distribution	0.7	3.3	5.0
2 x Uniform Distribution	7.0	14.3	11.7
1 x Uniform Distribution	33.3	40.6	47.4
0.5 x Uniform Distribution	67.6	57.9	79.1

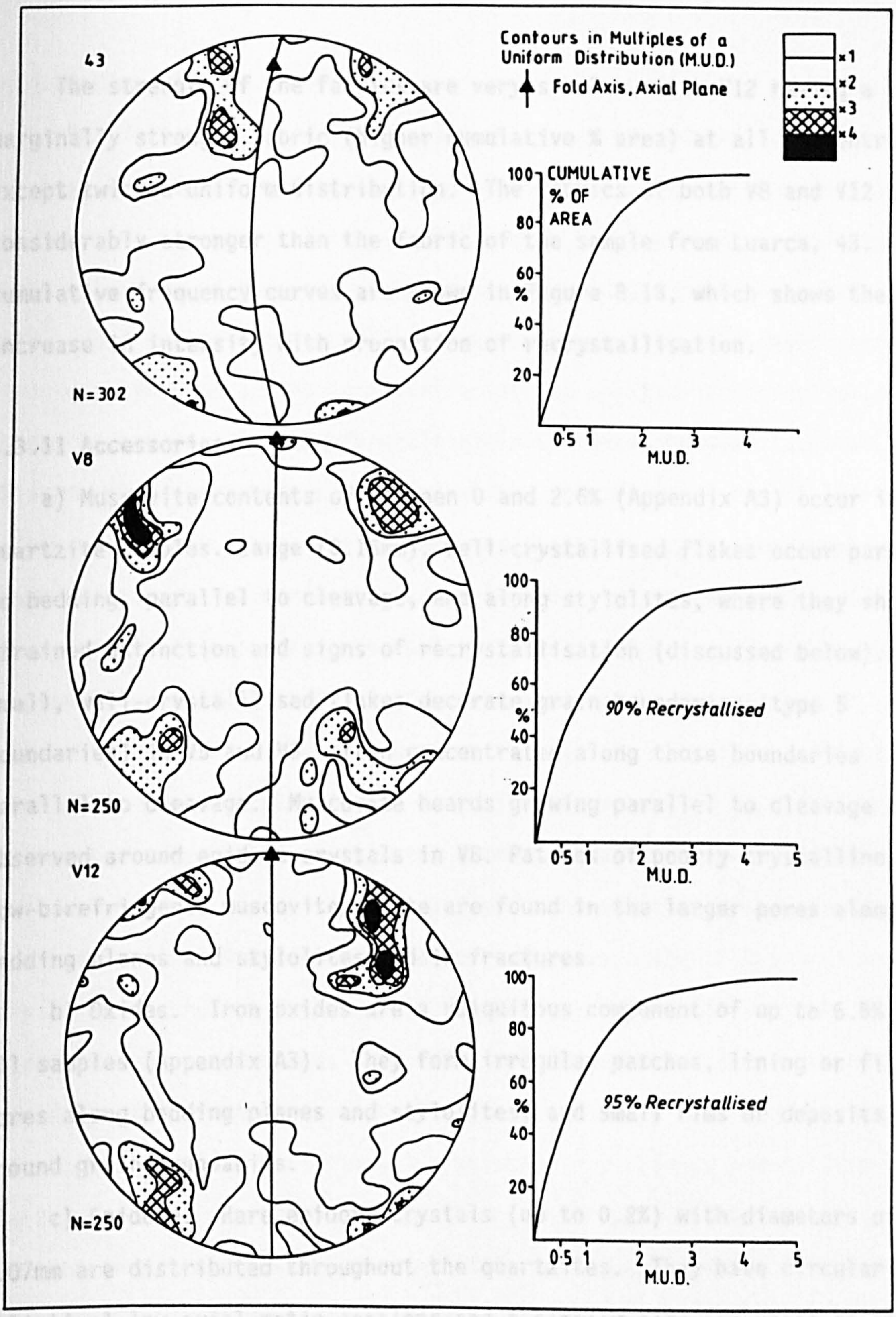

FIGURE 8.13

Quartz c-axes fabrics from U-stage measurements. Equal Area, lower hemisphere projection; contouring by Kalsbeck net. N - number of grains. Cumulative frequency curves show the cumulative area percentage of the stereogram as a function of distribution density measured in multiples of a uniform distribution. All three fabrics show a similar pattern and symmetry with respect to the fold geometry: the c-axes are concentrated in the horizontal plane normal to the axial plane, in two mutually perpendicular directions bisected by the axial plane. The fabric intensity increases with the proportion of recrystallised grains.

The strength of the fabrics are very similar, with V12 having a marginally stronger fabric (higher cumulative % area) at all concentrations except twice a uniform distribution. The fabrics of both V8 and V12 are considerably stronger than the fabric of the sample from Luarca, 43. The cumulative frequency curves are shown in Figure 8.13, which shows the increase in intensity with proportion of recrystallisation.

8.3.11 Accessories

a) Muscovite contents of between 0 and 2.6% (Appendix A3) occur in the quartzite samples. Large (0.15mm), well-crystallised flakes occur parallel to bedding, parallel to cleavage, and along stylolites, where they show strained extinction and signs of recrystallisation (discussed below). Small, well-crysta llised flakes decorate grain boundaries (type 5 boundaries) in V5 and V9, often concentrated along those boundaries parallel to cleavage. Muscovite beards growing parallel to cleavage can be observed around epidote crystals in V8. Patches of poorly crystalline, low-birefringence muscovite/illite are found in the larger pores along bedding planes and stylolites and in fractures.

b) Oxides. Iron oxides are a ubiquitous component of up to 6.5% in all samples (Appendix A3). They form irregular patches, lining or filling pores along bedding planes and stylolites, and small rims or deposits around grain boundaries.

c) Epidote. Rare epidote crystals (up to 0.2%) with diameters of 0.07mm are distributed throughout the quartzites. They have circular or elliptical low-axial-ratio sections and a similar size and shape to the larger quartzite grains, but they do not assume any shape fabric. They are unzoned but may have a margin of small mica crystals. Epidote can also be found along stylolites.

8.3.12 Discussion

The following microstructural history can be deduced for all samples.

a) Solution transfer. All samples show evidence for an initial period of solution transfer. This was confined to bedding surfaces and stylolites only: there is no evidence of any pressure solution contacts between individual grains within bedding planes. The sedimentary fabric exerted a further control over the localisation of the solution transfer: solution seems to have occurred preferentially in the sites between large mica flakes, which have been passively rotated and folded as the stylolites developed. This process is illustrated in figure 8.12. The model suggests that solution may be concentrated in the intervals between mica flakes as these rotate into positions normal to the stylolite and become stress supports, relieving stress on the teeth walls and concentrating it on the crowns. The role of mica flakes as stress guides in this model is thus similar to that accepted in the model for the formation of differentiated layering during buckling, in which flakes on buckle hinges support stress. The amplitude of the stylolites (1-2mm) suggests that little strain was achieved during this period: given an average spacing of 0.5-1m, the stylolites represent less than 1% flattening. Where fabrics have been unaffected by later events (e.g. V9 - see below) , it appears that the porosity at this stage was low: 5.2%. It is likely that the dissolved quartz was reprecipitated locally, reducing any primary porosity to this value.

b) Early cataclasis. The next deformation episode was the production of the non-planar fractures by mode 1, transgranular cracking. These fractures are not associated with intragranular cracking, which may have been suppressed in the pre-shear failure stage by low porosity. Further evidence for the lack of grain-grain impingement is the absence of pressure-solution contacts between grains. The non-planar fractures generally cut stylolites and therefore post-date them. They are transitional between the solution transfer and the major deformation by crystal plasticity.

c) Crystal plasticity, cleavage formation and dynamic recrystallisation. The main penetrative features of the fabric at Punta del Sol are interpreted to be due to an episode of crystal plasticity with dynamic recrystallisation. The clearest evidence for this is the observation of small, equant strain-free grains (White 1976). Their formation by both sub-grain rotation and grain boundary migration from larger, old grains can be seen in Plate 8.3b. Once formed, they grow to assume a moderate grain-shape fabric before recrystallising again, due to accumulation of strain. This process is recorded in the difference in G.M.A. values measured between the small grains and large grains in Samples V1 and V8, and in the moderate crystal fabrics shown in Figure 8.12 from the small, recrystallised grains in V8 and V12. The existence of the crystal fabric can also explain the variation between G.M.A. measured in different sections. The E sections would be expected to show the largest values of G.M.A. since the c-axes are approximately within the plane of the section in two directions. On the other hand, c-axes lie in a plane perpendicular to the F section, which would therefore not record any variation in angle between them. The D sections are intermediate between these two extremes.

The production of a grain-shape fabric is clearly coeval with the formation of the cleavage, to which the fabric is parallel. The plasticity also affected existing porosity, firstly by reducing it on sections perpendicular to the cleavage, and secondly by imparting a shape fabric to the pores themselves on these sections; all these relationships are consistent with a conventional view of cleavage as the principal plane of strain normal to the shortening direction. It post-dates the stylolites because they are deformed by the cleavage to give the obliquity between the teeth crowns and walls noted in V5, and the fragmented appearance of stylolites and bedding planes in V8, V10, and V12. It post-dates the non-planar fractures, deforming them to give their non-planar morphology and surface roughness. Two further proofs of this relationship are the fact that cleavage can be seen on the surfaces of the non-planar fractures, and in thin section, a cleavage mica can be seen growing across a fracture plane from the intact rock. The interpretation of the shape fabrics as strain ellipsoids imposes some constraints on the fold mechanism. The existence of the most intense fabrics in the hinge zone precludes a purely flexural-flow or shear-fold mechanism, and the position of the samples on the outer arc of the quartzite, where tangential longitudinal shortening would be normal to the fold surface, is evidence that tangential longitudinal strains alone were not experienced. The simplest strain distribution that matches the observed pattern would be produced by a pure shear flattening normal to the fold axial plane following earlier folding by any of the mechanisms above. Additional evidence for this is the flattened trace fossils described in 8.3.4, and the anisotropy in porosity described above.

d) Late cataclasis. The final tectonic episode is a later stage of cataclasis which produced the planar fractures. These are, like the non-planar fractures, mode 1, transgranular fractures unaccompanied by any intragranular fracturing, except where they have shear components (V9). In this case, grains adjacent to the shear are highly microfractured, suggesting that the microfractures are due to shear. They may have formed as ‘microscopic feather fractures’ by the mechanism proposed by Friedman and Logan (1970): during shear, local sticking of the fracture walls creates a tensile stress around the sticking point, relieved by extension microcrack formation. The planar fractures cut and therefore post-date all the earlier features. These fractures were also cemented; the strained features of the cement reveal that a limited amount of crystal plasticity occurred subsequently (see low G.M.A. value of planar fracture cement in

V12, Appendix A7).

While the general microstructural history outlined above applies to all the samples at Punta del Sol, significant variations in the microstructures have been referred to. These are summarised below:

1. Loss of Bedding. Clear bedding is seen in V1 and V9. In V8, V10 and V5, the bedding is discontinuous and only just visible, while in V12, it is represented only by the surface of the hand specimen.

2. Grain Size. The G.M.L. decreases from 0.08mm in V9 to 0.06mm in the order V9-V1-V10-V8-V5-V12 (on D Sections).

3. Grain Boundaries. V9 consists of type 3 and 5 boundaries, V1, V5, VC8 and V10 have mostly type 6 with some type 3 boundaries, and V12 has only type 6 boundaries.

4. G.M.A. The G.M.A. of the samples increases from 4.83° in V9 to 11.43° in V8 in the order V9-V12-V1-V10-V5-V8.

5. Stylolites. Stylolites are weakly developed along bedding in V9; in V1 and V5 they are clearly developed, but they are disrupted in V8, V10 and V12.

6. Cleavage. Cleavage is visible in thin sections only of V9, V1 and V10, but well developed in hand specimen and thin section in V5, V8 and V12.

All these features suggest that the amount of recrystallisation during the episode of crystal plasticity increases from V9 to V12 with intermediate stages V1-V10-V5-V8. The percentage of recrystallisation was measured by two methods to test this interpretation. Initially, the G.M.L. of 20 old (non-recrystallised) grains was measured in the visually estimated X and Z directions. The average of these was used to specify a minimum linear intercept for old grains. The percentage of recrystallised grains was calculated from linear intercept measurements of the whole sample by:

$$\% \text{ Recrystallised Grains} = N-N_0/N \times 100\%$$

where N is the total number of linear intercepts and N_o is the number greater than the minimum specified to define an old grain. The results are given as column 12 in Appendix A3. This shows that estimates of the proportion of recrystallised grains have a large inaccuracy; for example, there is a typical variation of 10% in the estimate from the X and Z directions of a single sample.

The proportion of recrystallised grains was therefore re-measured by point count, relying on the combination of the following visual criteria to identify recrystallised grains:

1. Small grain size.
2. Equant grain shape.
3. Straight, polygonal grain boundaries.
4. Narrow grain boundaries.
5. Low G.M.A. and absence of optical strain features. The results of the point counting are given in column 8 of Appendix A3, showing an increase in proportion of recrystallisation from 0.8% in V9 through V1-V10-V5-V8 to 95% in V12. The discrepancy between the estimate in columns 9 and 12, and the inaccuracy of the size criterion alone, are due to the fact that the latter method classes as recrystallised grains those old grains with a linear intercept smaller than the geometic mean of old grains, and it classes as old grains some recrystallised grains with large linear intercepts. The relative effects of these two factors depends on the proportion of recrystallised grains. When the proportion of recrystallised grains is less than 80% the size criterion method gives an estimate of percentage recrystallisation which is too high: old grains with linear intercepts less than the G.M.L. of old grains are not counted, thus reducing the measured number of old grains and correspondingly increasing the number of recrystallised grains. However, above 80% recrystallisation, an underestimate is obtained. These are two possible reasons for this: firstly a significant proportion of new grains may have intercepts greater

than the average G.M.L. of the old grains, these are therefore incorrectly counted as old grains, decreasing the estimate of recrystallised grains. Secondly, the measured value of the average G.M.L. of old grains may be too low due to the limited sample (20 grains). Some indication that this may be responsible for the underestimate in V5 is given by a comparison of the average G.M.L. of old grains with that of the whole population. For samples V1, V10 and V8, this ratio is consistent at 1.6-1.7. However, it is significantly lower (1.2) for V5. The underestimates of percentage recrystallisation in V1 and V10 are probably due to the former reason.

The variation in proportion of recrystallised grains is nevertheless reflected in the inverse relationship between G.M.L. and percentage recrystallisation (Figure 8.14). This relationship is clearly not due to variable initial grain sizes since the smaller grains have been interpreted as being recrystallised on the basis of several criteria as well as grain size. Confidence in the interpretation of recrystallisation as a deformation mechanism and in the measurements of proportion of recrystallised grains is strengthened by the distribution of grain boundary types. The prevalence of type 3 boundaries in V9 is expected since there is almost no recrystallisation. The observation that most boundaries are of type 6 in V1, V5, V8, and V10 is due to the greater than 50% recrystallisation measured for these sections, with V12 (94.4% recrystallisation) being observed to have almost exclusively type 6 boundaries.

The relation between G.M.A. and proportion of recrystallised grains is shown in Figure 8.14. There is an overall increase in G.M.A. from the lowest value of 4.83° with no recrystallisation (V9) to a value of 11.43° at 90% recrystallisation (V8). V12 is almost totally recrystallised (95%) and has a low G.M.A. (7.159°). These G.M.A. values were measured on only the larger grains (greater than 0.23mm) in each section; these are generally the grains interpreted as old grains, although a size criterion

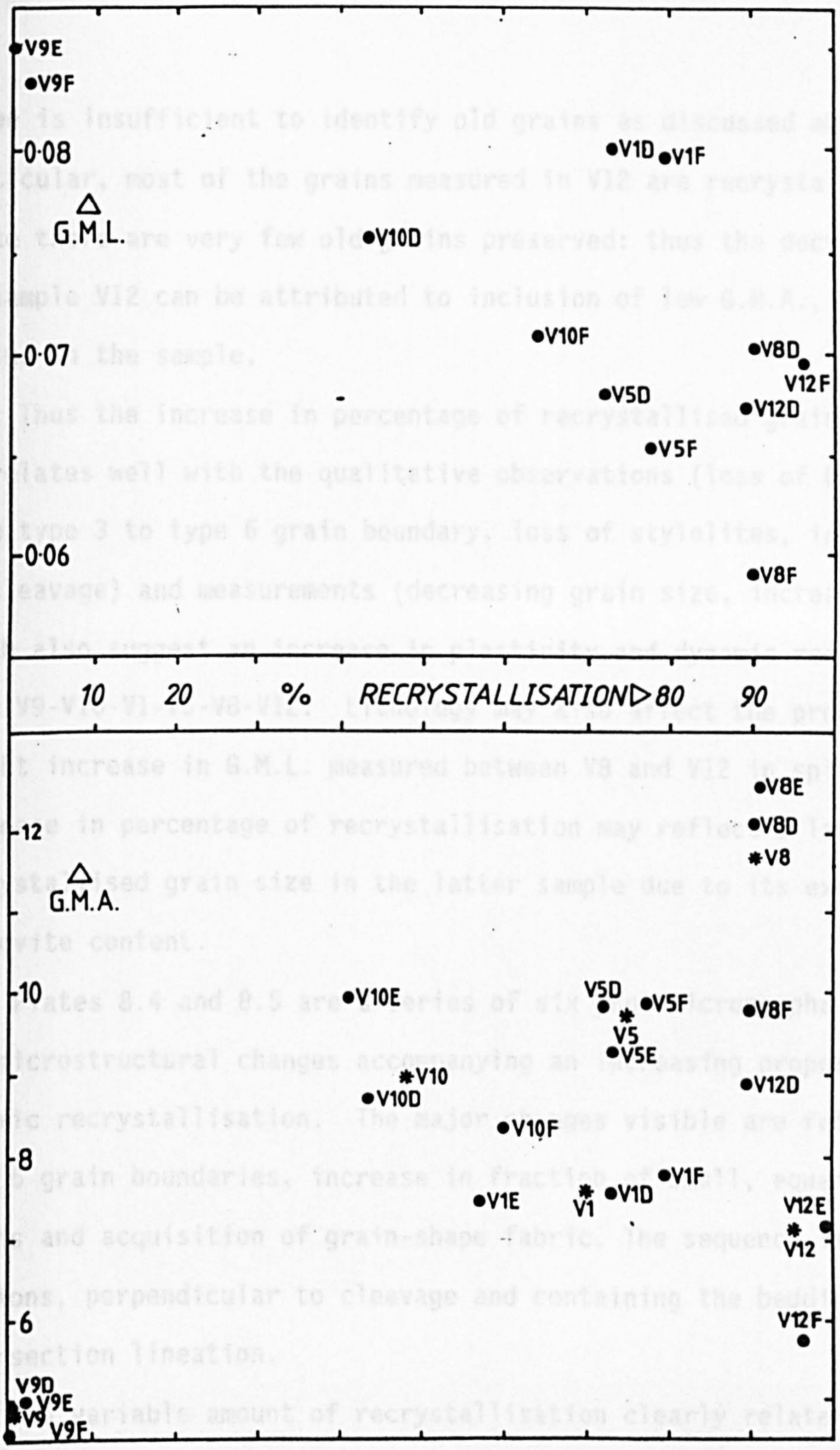

FIGURE 8.14

The relationships between Geometric Mean of Linear Intercepts (G.M.L. (upper diagram), and Geometric Mean of Extinction Angles (G.M.A.) (lower diagram), and proportion of recrystallised grains. There is clearly an inverse relationship in the former case, due to the increasing proportion of small, recrystallised grains. In the latter case, the G.M.A. appears to increase with proportion of recrystallisation as more plastic strain is accommodated in original grains. However, in the case of V12, almost total recrystallisation lowers the G.M.A. value because most of the grains measured are probably relatively strain-free, recrystallised grains. The results in both diagrams are shown for individual section measurements (given by the suffix D, E, F), and the average sample results are indicated in the lower diagram by stars.

alone is insufficient to identify old grains as discussed above. In particular, most of the grains measured in V12 are recrystallised grains since there are very few old grains preserved: thus the decrease in G.M.A. in sample V12 can be attributed to inclusion of low G.M.A., recrystallised grains in the sample.

Thus the increase in percentage of recrystallised grains (Appendix A3) correlates well with the qualitative observations (loss of bedding, change from type 3 to type 6 grain boundary, loss of stylolites, intensification of cleavage) and measurements (decreasing grain size, increasing G.M.A.) which also suggest an increase in plasticity and dynamic recrystallisation from V9-V10-V1-V5-V8-V12. Lithology may also affect the process: the slight increase in G.M.L. measured between V8 and V12 in spite of the increase in percentage of recrystallisation may reflect a larger recrystallised grain size in the latter sample due to its exceptionally low muscovite content.

Plates 8.4 and 8.5 are a series of six photomicrographs illustrating the microstructural changes accompanying an increasing proportion of dynamic recrystallisation. The major changes visible are from type 3 to type 6 grain boundaries, increase in fraction of small, equant, strain-free grains and acquisition of grain-shape fabric. The sequence is shown on E sections, perpendicular to cleavage and containing the bedding/cleavage intersection lineation.

The variable amount of recrystallisation clearly relates to structural position around the hinge of the Punta del Sol anticline. The largest values are in the hinge areas (V5, V8) and on the minor fold V12 with lower values on the limbs (V1, V5 and V9; Figure 8.1).

PLATE 8.4a

Microstructure showing negligible recrystallisation (0.2%). Grain boundaries of types 3, 5 and porosity of types 3+1, 2 and 4 (see 8.3.5).

PLATE 8.4b

41% Recrystallisation. Grain boundary types 3 and 6, porosity 3+1, 2. Sample V10E, X.P.

PLATE 8.4c

57% recrystallisation. Grain boundary types 6 and 3, porosity 2 and B. A mature stylolite can be seen as an opaque, castellated trace across the field of view. Sample V1E, X.P.

200μ

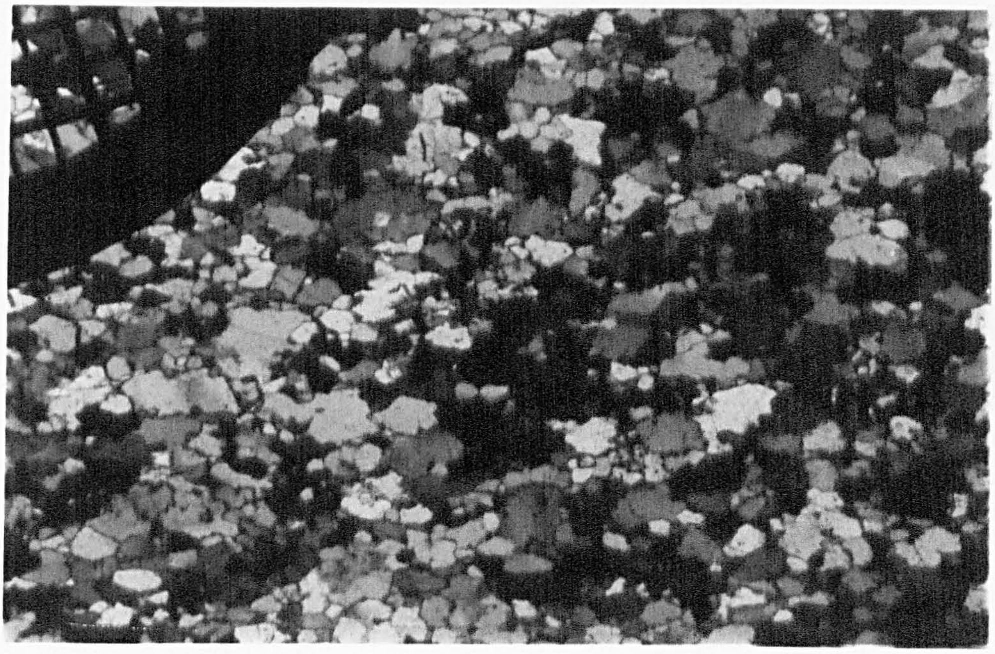

200μ

200μ

PLATE 8.5a

73% recrystallisation. Grain boundary types 6 and 3, porosity 2 and B. A few larger original grains with type 3 grain boundaries may be seen. Sample V5E, X.P.

PLATE 8.5b

91% recrystallisation. Grain boundaries almost entirely type 6, porosity 3+1. Sample V8E, X.P.

PLATE 8.5c

95% recrystallisation. Grain boundaries type 6. Virtually all grains are recrystallised (though to a larger grain size than 8.5b), negligible porosity. Sample V12E, X.P.

200μ
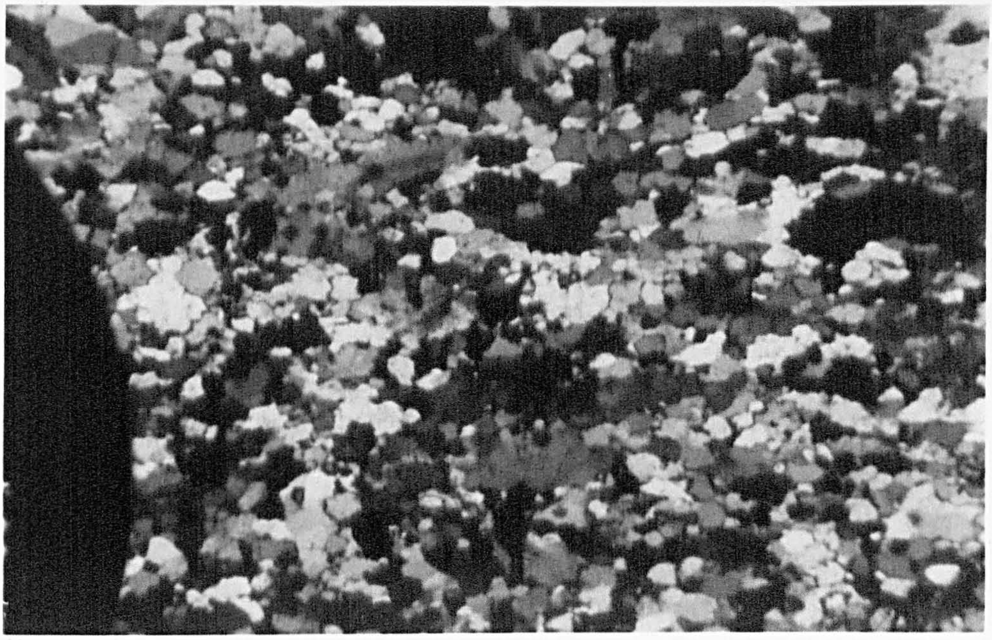

200μ
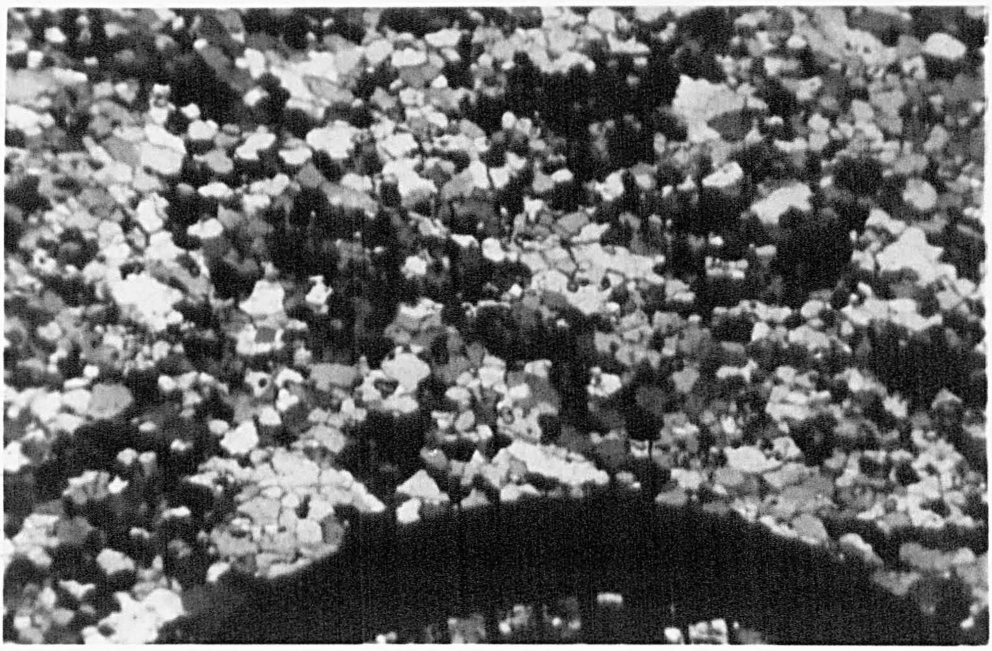

200μ
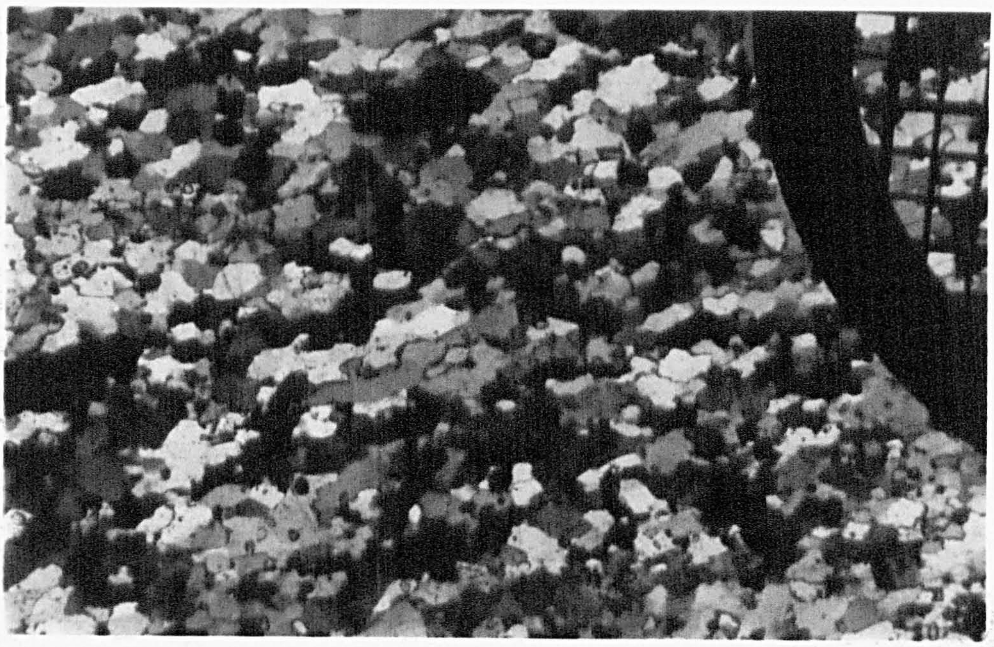

8.4 ILLITE CRYSTALLINITY

8.4.1 Results

Illite crystallinities vary from $0.31^{o}2\theta$ to $0.481^{o}2\theta$, thus spanning the entire range from epizone to upper diagenetic zone (Appendix A8) The variation is illustrated in Figure 8.15. No stratigraphic or structural control is evident. Crystallinities from the pelite samples (V2, V3, V4, V7a and V11) have very consistent epizone values (mean Kubler Index $0.184^{o}2\theta$) but the quartzite crystallinities are much more variable, with a lower mid-anchizone mean crystallinity of $0.295^{o}2\theta$. The gouge (V7b) from the Barayo thrust has a similar lower crystallinity, $0.300^{o}2\theta$. Within the quartzites, there is a good correlation between crystallinity and proportion of muscovite from point counting measurements (Figure 8.15), but no relationship to porosity.

8.4.2 Discussion

There is clear evidence above for the importance of either or both permeability and lithology as extrinsic factors in the determination of crystallinities at Punta del Sol. The distinction that can be drawn between pelites and quartzites initially suggests that permeability may be important; however, this is questioned to some extent by the lack of relation between porosity and crystallinity in the quartzites, and furthermore, an alternative explanation is suggested by the crystallinity/muscovite correlation. Both the higher and consistent pelite crystallinities, and the variation in quartzite crystallinity, can be more economically explained as a lithological control on crystallinity, perhaps by pore-fluid chemistry.

It is possible to deduce a broad outline of the metamorphic history from some of the microstructural observations in conjunction with crystallinity measurements. Large micas along stylolites are often highly

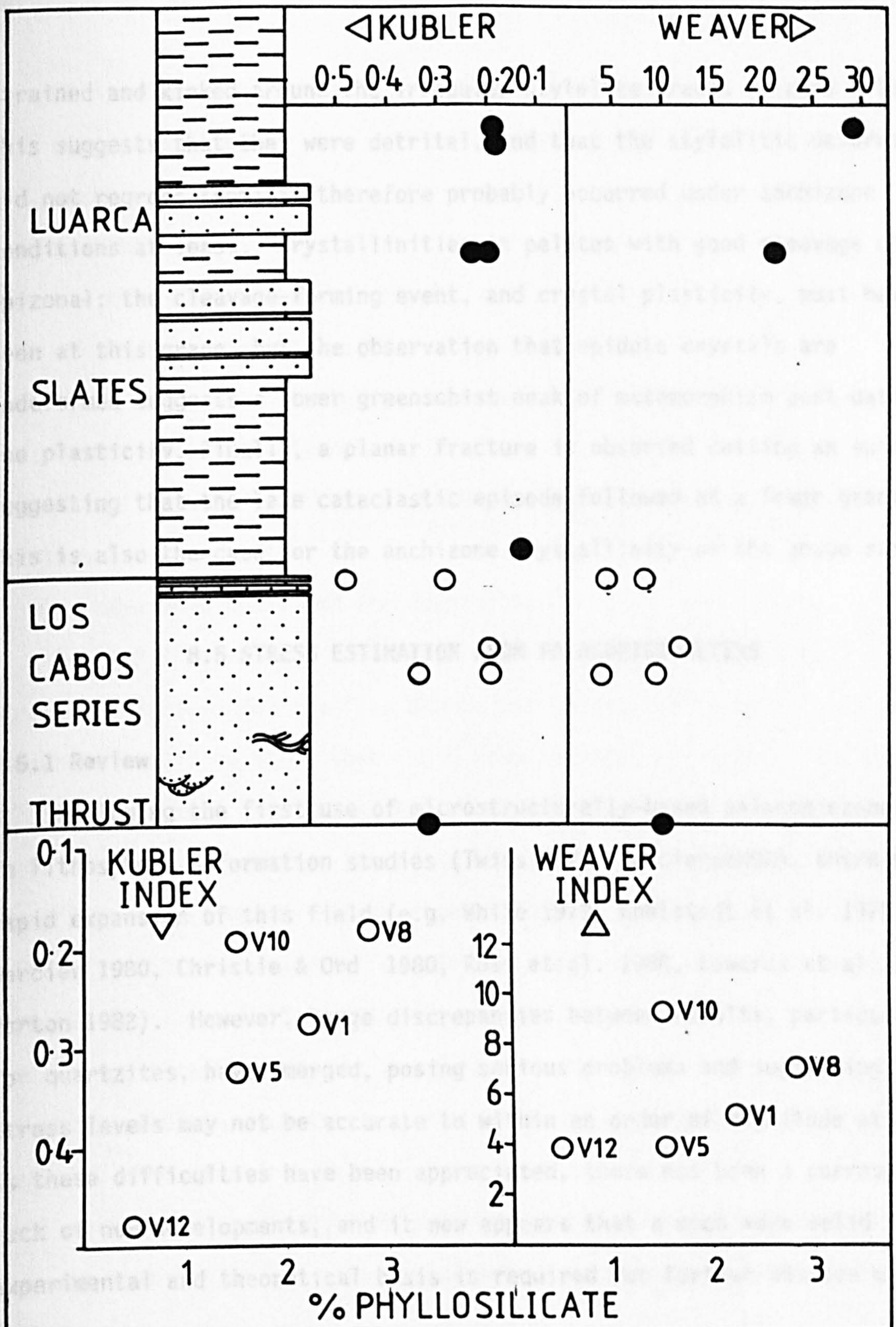

FIGURE 8.15

Illite Crystallinity as a function of stratigraphic position and lithology (upper diagram) and phyllosilicate content (lower diagram). The top diagram shows that there is no stratigraphic control on crystallinity. Pelite determinations (in solid circles) are very consistently epizone (<0.215°2θ), but quartzite samples (open circles) are more variable, including one diagenetic zone result. There is a clear positive correlation between crystallinity and phyllosilicate proportion in the quartzite samples. This indicates that crystallinity variations are due to an extrinsic lithological effect.

strained and kinked around the irregular stylolite traces (Figure 8.13). This suggests that they were detrital, and that the stylolitic deformation did not regress them; it therefore probably occurred under anchizone conditions at least. Crystallinities in pelites with good cleavage are epizonal: the cleavage-forming event, and crystal plasticity, must have been at this grade, but the observation that epidote crystals are undeformed suggests a lower greenschist peak of metamorphism post-dating the plasticity. Finally, a planar fracture is observed cutting an epidote, suggesting that the late cataclastic episode followed at a lower grade. This is also the case for the anchizone crystallinity of the gouge sample.

8.5 STRESS ESTIMATION FROM PALAEOPIEZOMETERS

8.5.1 Review

Following the first use of microstructurally-based palaeopiezometers in lithosphere deformation studies (Twiss 1977, Mercier et al 1977), there was a rapid expansion of this field (e.g. White 1979, Kohlstedt et al. 1979, Mercier 1980, Christie & Ord 1980, Ross et al. 1980, Edwards et al. 1982, Norton 1982). However, large discrepancies between results, particularly for quartzites, have emerged, posing serious problems and suggesting that stress levels may not be accurate to within an order of magnitude at best. As these difficulties have been appreciated, there has been a corresponding lack of new developments, and it now appears that a much more solid experimental and theoretical basis is required for further advance of the technique.

Six microstructural palaeopiezometers have been introduced based on recrystallised grain size, subgrain size, dislocation density, twinning, exsolution lamellae and deformation lamellae. The first three are potentially applicable to the quartzites of this chapter. They have the following stress dependencies (after White 1979)

Dislocation density, ρ. $\sigma = k\mu b\rho^{u}$

Sub-grain size, d. $\sigma = l\mu bd^{-v}$

Recrystallised grain size, D. $\sigma = mD^{-w}$

μ = Shear modulus

b = Most common Burgers vector

σ = Differential Stress,MPa

k, l, m, u, v, w = material constants, theoretically or experimentally derived.

Attention will be focussed on the recrystallised grain size relationship, since it is the most applicable. Five sets of the parameters m and w have been published for quartzites.

Table 8.1 below is a summary of the experimental conditions and parameters derived for the five quartz palaeopiezometers so far published, though it should be noted that those from Arkansas novaculite samples (Christie and Koch 1982) were derived from transposing a regression of grain size against stress; therefore the parameters derived from correctly regressing stress against grain size are likely to be considerably different. This is suggested by the statement by Christie and Koch (1982) that "In the lower half of the stress range the novaculite data do not differ significantly from our previous data for 'wet' Simpson quartzite... but the novaculite data are larger than for wet quartzite at higher stresses". The data from Table 8.1 are plotted in Figure 8.16 which shows the novaculite data giving much smaller recrystallised grain sizes at all stresses than any of the other palaeopiezometers: this relationship is clearly very suspect.

The table below gives the flow stresses calculated by each of the flow laws for a recrystallised grain size of 7.945×10^{-5}mm. This is the mean value of the arithmetic means of linear intercepts (A.M.L.) measured for V12 (Appendix A1) and this is used as the most accurate value of grain size, allowing for both sampling and truncation effects, following the

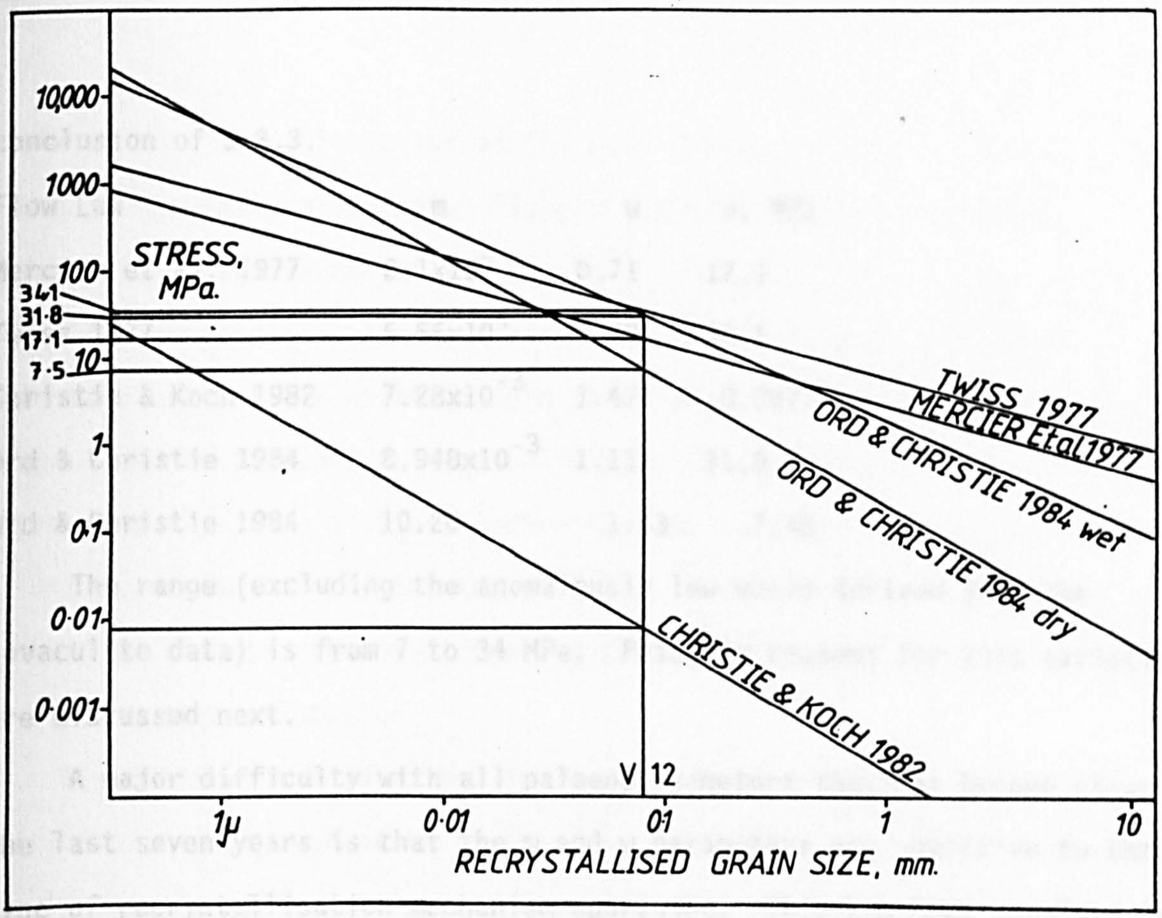

FIGURE 8.16

The Relationship between log Differential stress (MPa) and log Recrystallised Grain Size (mm). The palaeopiezometers are based on the relationship given in Table 9.1 and show that the data for Arkansas Novaculite (Christie and Koch 1982) yield stresses lower by 1-2 orders of magnitude than other palaeopiezometers. The lines indicate the stress estimate derived from the grain size of 0.079mm measured in sample V12.

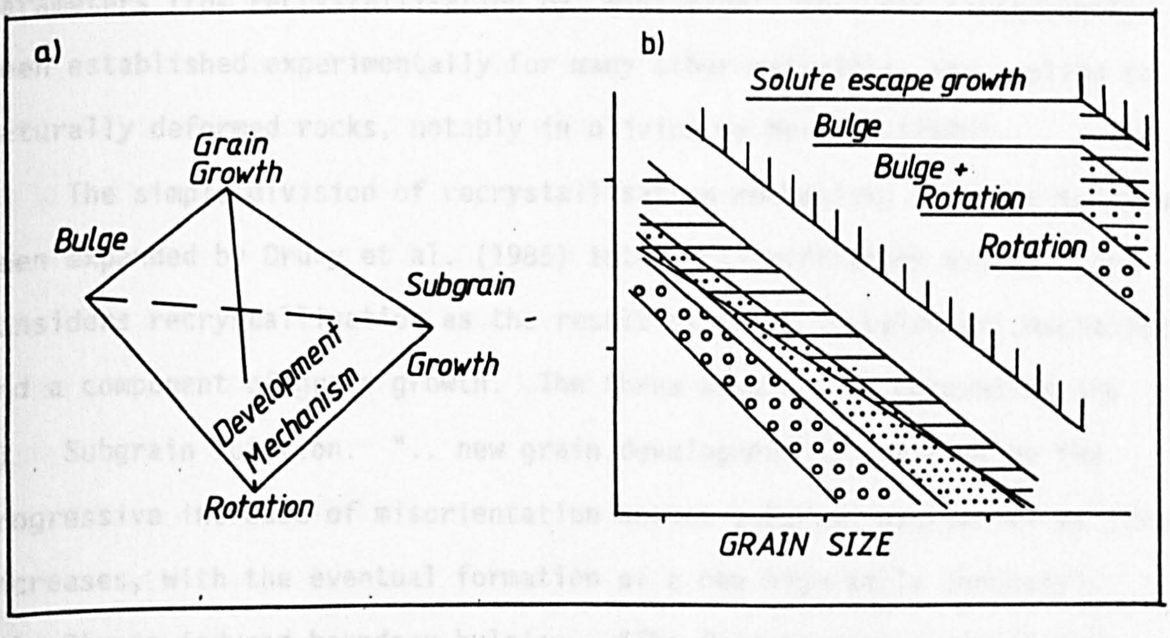

FIGURE 8.17

a) The Recrystallisation Mechanism Tetrahedron, after Drury et al. (1985). A mechanism involves components of three 'development mechanisms' on the base of the tetrahedron, and a component of grain growth.

b) The Relationship between normalised stress and grain size for different recrystallisation mechanisms.

conclusion of 3.3.3.

Flow Law	m	w	σ, MPa
Mercier et al. 1977	$2.1x10^4$	0.71	17.1
Twiss 1977	$5.56x10^4$	0.68	34.1
Christie & Koch 1982	$7.28x10^{-3}$	1.471	0.00774
Ord & Christie 1984	$8.948x10^{-3}$	1.11	31.8
Ord & Christie 1984	10.26	1.43	7.48

The range (excluding the anomalously low value derived from the novaculite data) is from 7 to 34 MPa. Possible reasons for this variation are discussed next.

A major difficulty with all palaeopiezometers that has become clear in the last seven years is that the m and w parameters are sensitive to the type of recrystallisation mechanism operating. This has been examined in detail by Drury et al. (1985). It was first appreciated from experimental studies in halite (Poirier and Guillope 1979), who found that recrystallisation due to subgrain rotation gave different m and w parameters from recrystallisation by 'migration'. This has subsequently been established experimentally for many other materials, and applied to naturally deformed rocks, notably in olivine by Mercier (1980).

The simple division of recrystallisation mechanisms into two types has been expanded by Drury et al. (1985) into a classification scheme which considers recrystallisation as the result of three 'development mechanisms' and a component of grain growth. The three development mechanisms are

i) Subgrain rotation. ".. new grain development is achieved by the progressive increase of misorientation across subgrain boundaries as strain increases, with the eventual formation of a new high angle boundary".

ii) Strain-induced boundary bulging. "The formation of a strain-free bulge along a high-angle boundary due to the occurrence of local grain boundary migration". The authors point out that this in itself will not produce separate grains unless the bulge is subsequently isolated and rotated from the orientation of the host grain.

iii) Sub-boundary migration. "Subgrain growth in areas with large gradients of strain and orientation".

The recrystallisation mechanism can be plotted on a tetrahedral diagram, the base of which has the three development mechanisms at the corners while the apex consists of the extra component of grain growth (Figure 8.17). Two distinct mechanisms are identified for quartz; both plotting on the base of the tetrahedron (i.e. no further component of grain growth accompanies the development mechanism).

A - Subgrain Rotation

B - 50% Subgrain rotation, 50% Grain boundary bulging.

Drury et al. were able to show the important effect of mechanism on grain size by plotting stress/grain-size relationships of all experimental results, normalising the stress by

$\Gamma = \mu/(1-\nu)$

μ = Shear Modulus ν = Poisson's Ratio

and grain size by b, the Burgers Vector. Each recrystallisation mechanism defined a distinct stress/grain-size relationship with, at any given stress, rotation having the smallest grain size, followed by rotation and bulge, then bulge and the largest grain size given by the solute escape growth mechanism (Figure 8.17b). It therefore becomes essential to identify both the recrystallisation mechanism on which the palaeopiezometer is based, and that operating in the rock, before one can be applied to the other.

Drury et al. identify the recrystallisation mechanism of quartz in Mercier et al's (1977) experiments, as subgrain rotation (A), and that in Christie et al. (1980) as rotation and bulge (B). These two palaeopiezometers confirm the general trend that, for a grain size, mechanism B yields a higher stress than A; for example, the Mercier palaeopiezometer gives 17.1MPa for a grain size of 7.9×10^{-4}mm, compared to

31.8MPa from the wet law of Ord and Christie (1984). Unfortunately, the published literature accompanying the other palaeopiezometers does not allow identification of the recrystallisation mechanisms to establish whether they too fit the general observation of Drury et al. However, the position of the Christie and Koch (1982) and Ord and Christie 'dry' (1984) laws on figure 8.17b strongly suggests that these experiments lie within the rotation mechanism field.

The second difficulty in the formation of the palaeopiezometers is whether a temperature dependence should be included, in the form of an Arrhenius term:

$$\sigma = mD^{-w} \exp. (-A/RT)$$

where A is the enthalpy of the temperature dependence, R the gas constant, and T the temperature. Temperature effects were not observed in the Christie and Koch palaeopiezometer, nor are they predicted by the Twiss theoretical relationship. However, they are observed for other materials including olivine (e.g. Mercier et al. 1977) and predicted by theory developed by Mercier (1980). Norton (pers.comm.) has investigated the possibility of a temperature dependence in some detail for a range of materials, and shown that the exponent w changes for these materials depending on whether the tests were at constant strain rate or at constant temperature. This is interpreted as indicating a temperature-dependence of the palaeopiezometer, and a simple numerical example for olivine illustrates that a temperature increase of 500^{0}c causes an order-of-magnitude increase in recrystallised grain size based on the data for the temperature dependence of grain-size from Ross et al. (1980). It is therefore considered probable that quartz, too, should have a temperature term in the palaeopiezometer. The qualitative effect of this would be that the recrystallised grain size would reduce with temperature for a give stress. In order to investigate the situation in more detail, the recrystallisation mechanism would also have to be constrained; the two effects are probably interrelated.

Linked to the question of a temperature effect is that of the quartz phase. Some experiments have shown that the α-β transition causes significant changes in the pre-exponential term, the activation energy and the stress dependence of the flow law (e.g. Linker and Kirby 1981 for synthetic quartz crystals). Kronenberg and Tullis (1984) found a small phase dependence for activation energy but not stress exponent. It is therefore quite possible that a stress/grain-size relationship would be phase-dependent, and therefore palaeopiezometers should be calibrated and applied in the same phase field.

It is well known that the presence of impurities affects recrystallisation considerably whether they are present as discrete second phases or not. The presence of an impurity increases the activation energy, and thus retards the process of recrystallisation, while second phases retard grain boundary movement. Such effects can be observed in quartzites with mica present, which commonly have smaller grain sizes that adjacent pure quartzites: the mica is interpreted as 'pinning' the quartz grain boundaries, yielding a smaller grain size than the equilibrium value for pure quartz (e.g. Vernon 1976, Hobbs et al. 1976, Evans and White 1984).

A further uncertainty in all palaeopiezometers derives from the effect of water. The dramatic importance of hydrolitic weakening in flow laws for quartzites has been appreciated since the early work of Griggs (e.g. Griggs and Blacic 1965). Although the role of water in the recrystallisation process is quite unknown, it is equally certain to have a large effect: this is clear from the contrast between the 'wet' and 'dry' palaeopiezometers of Ord and Christie (1984). A major experimental problem is to distinguish between the kinetic effects due to diffusivity of water and the intrinsic effects of the water itself.

Finally, even if all these difficulties can be overcome, the interpretation of the stress levels obtained is likely to be problematic. They can be taken to indicate the flow or steady state stress if there is evidence that the recrystallisation was dynamic (i.e. there is no evidence of annealing) and that it was accommodating the observed structure. Otherwise, the stresses may represent a decaying stress field at the end of deformation or a completely unrelated stress field, such as that due to uplift. This possibility was raised by Etheridge and Wilkie (1981), but discounted by them on the basis that it predicts that all grains will equilibriate to similar low-stress sizes: however, many mylonite zones show a clear decrease of grain size, interpreted as representing a stress gradient, from the margins to the centre. This can be preserved because of the high stress sensitivity of strain rate in the flow law.

Norton (pers.comm.) suggests that dislocation densities and subgrain sizes were more easily reset by subsequent events than grain sizes, and showed how the relationship between dislocation density and either grain size or subgrain size, could be used to deduce whether the two parameters were set at the same stress by suggesting the position of a line of equilibrium values. Departures of points from this equilibrium on a plot of dislocation density against either subgrain or recrystallised grain size could be satisfactorily interpreted in terms of the uplift history anticipated for kimberlite nodules.

Twiss (1977) introduced two further potential difficulties of interpretation: firstly, that kinetic problems may exist for the establishment of equilibrium-recrystallised grain size at low stress and secondly that the minimum critical strain necessary for recrystallisation may not be achieved.

8.5.2 Application of a Recrystallised-Grain-Size Palaeopiezometer

The textural evidence of a grain-shape fabric with a z-axis perpendicular to cleavage, a good crystal preferred orientation, and the formation of new grains by grain-boundary migration and subgrain rotation suggests that the samples at Punta del Sol could be used in a recrystallised grain-size palaeopiezometer. The choice and justification of a palaeopiezometer is next given in the context of the problems mentioned in the previous section.

A palaeopiezometer based on recrystallised grain size is preferred to either dislocation density or subgrain size since the recrystallisation can be related to the major fold structure (see above), this parameter is least likely to have been affected subsequently, and it is the quickest and most reliably determined.

Of the alternatives the most appropriate to the Punta del Sol quartzites is probably that of Ord and Christie (1984). The Twiss palaeopiezometer is not suitable for two reasons: the theoretical approach derives from a model considering only recrystallisation by subgrain rotation; Twiss shows that the model parameters agree with a wide range of materials, but most of these do not show hydrolitic weakening. The Ord and Christie palaeopiezometer is preferred to that of Mercier since the inferred recrystallisation mechanism ('B': grain boundary migration and subgrain rotation) is the same for both experiment and natural sample. A further important similarity is between the original grain size of the Simpson quartzite (200μ) and that of the Punta del Sol quartzites (100-200μ). This discriminates between the Ord and Christie palaeopiezometers and that of Christie and Koch which is based on Arkansas novaculite with an original grain size of 7μ. The presence of well-crystallised muscovite suggests that the anhydrous conditions of the Ord and Christie 'dry' palaeopiezometer were not attained: therefore the 'wet' law is used. Both this palaeopiezometer and the natural samples were deformed in the α quartz field.

However, many other conditions applied in the calibration of the former stress-grain size relationship are significantly different from the deformation conditions at Punta del Sol. Perhaps the most significant is temperature: the experimental temperatures (750-900^{o}c) are probably twice those of the natural samples, and no temperature correction can be applied to the palaeopiezometer. The confining pressures are probably greater by a factor of twenty and the strain rates several orders of magnitude greater. For these reasons, the stress estimate (32MPa) must be treated with considerable caution. It is interpreted as the steady-state flow stress during the main folding episode that produced the Villayon anticline in the massive quartzite at the top of the Los Cabos series, since the crystalline plasticity can be geometrically related to the fold by the grain-shape fabric.

8.6 SYNTHESIS

8.6.1 Deformation Modes and Mechanisms

Combining the microstructural and field observations gives a more complex tectonic history than the other localities studied. Early bedding-parallel solution transfer may be related to burial; though oblique stylolites are also seen, suggesting tectonic deformation by diffusive mass transfer. It is suggested that the non-planar fractures represent a prefold fracture network. However, the major fold accommodating mechanism was crystal plasticity at least in the later stages. This can be established from the grain-shape fabric and dynamic recrystallisation, which can be related to folding by the orientation of the minimum fabric axis perpendicular to cleavage, the symmetry of the c-axis fabric about the axial plane and the greater intensity of recrystallisation in the hinge region. A return to cataclastic deformation, represented by the planar fractures, has different characteristics to the prefold fracture networks of the Bernesga valley and Punta Vidrias: the fracture orientations remain approximately constant around the fold. The cataclasis continued with movement on the Barayo thrust, intensification of deformation zones perpendicular to the fold axis and establishment of similarly orientated master fractures, and finally strike-slip faulting. It is likely that the dissection of the major fold structure by the large faults on Playas de Otur and Sabugo occurred at the same time as movement on the Villayon thrust.

Several important differences can be noted between the deformation modes and mechanisms here and at Luarca. Firstly, the early cataclastic episode is not seen at Luarca but this may be due to the limited exposure of the Portizuelo anticline. More significantly, the extent of crystal plasticity is far greater, with thorough dynamic recrystallisation producing strong grain-shape and crystallographic preferred orientations. In both areas there is a similar post-fold fracture network, with two sets of fractures, one perpendicular to the fold axis and one approximately axial planar, similar fracture densities ($30m^{-1}$), and the same clustering of fractures into deformation zones, but no evidence of major sinistral strike-slip faulting is seen at Punta Del Sol.

8.6.2 Deformation Conditions

Approximate temperatures can be assigned to each of the deformation stages on the basis of observations in 8.5.2. Anchizone conditions during the stylolite solution transfer suggest temperatures of 250-350^{o}c, rising to 315-415^{o}c at the peak of metamorphism from the pelite crystallinities. This postdates the early cataclasis and folding, which therefore may have occurred at intermediate temperatures. The maximum temperature for the peak of metamorphism is constrained also by the lack of biotite within the pelites: this means that the low-pressure biotite isograd, at 400^{o}c, was probably not reached. A reduction in temperature to 250-350^{o}c for movement on the Villayon thrust can be inferred from the gouge anchizone crystallinity, and still lower temperatures for all the late cataclastic features.

A minimum value for the confining pressure can be estimated from the stratigraphic thickness of known Ordovician and Silurian sediments above the Cabos series. These comprise 800m of Ordovician Luarca slates and a minimum of 1400m for the Agueiras Formation. A limited amount of Silurian deposition over the east part of the W.A.L.Z. is inferred by Marcos (1973) because Monograptus faunas have been reported from the south in the Léon province although no Silurian is known from the north part of the Navia unit. A thickness of 500m is implied by Marcos. The complete lack of post-Silurian sediments throughout the W.A.L.Z. and Galician-Castellian zone could suggest that they were never present as mentioned in 7.5.2. Therefore the total thickness can be estimated as 2700m for a lithostatic overburden, this gives a confining pressure of 67.5MPa or 41MPa effective confining pressure assuming hydrostatic pore fluid pressure. However, this is likely to be an underestimate for the depth at which the deformation occurred, since tectonic thickening accompanied folding, although the amount is impossible to estimate. It is, however, possible to say that the thickness was not due to the Barayo thrust since this moved later than the folding.

8.6.3 Regional Implications

The tectonic history deduced for the Punta Del Sol region has two important differences from the three-phase sequence of early east-verging recumbent folding, thrusting and late west-verging folding given by Marcos (1973). Evidence for east-verging recumbent folds is seen from cleavage, but the refolding at this locality also has an east-vergence. A second major difference concerns the timing of thrust movement on the Villayon thrust: incorporation of cleaved quartzite fragments in the thrust breccia, and the lack of cleavage in the breccia make it plain that the thrust movement postdates any later refolding and cleavage events.

Marcos (1973) dismisses cataclastic deformation following his third phase as not substantially modifying the major structure previously established. However, this cataclasis may be of greater significance: it may be the deformation mechanism by which a substantial part of the closure of the Ibero-Armorican arc occurred. Palaeomagnetic evidence suggests that a primary arc of 60-80^{0} existed, but was subsequently tectonically tightened to the present value of 170^{0}. A fracture network distributed throughout the arc would require individually small displacements to accommodate the necessary strain over the whole arc. It is therefore suggested that the late cataclasis, firstly in the form of the planar fracture network, and latterly by shear faults localising in deformation zones accommodated much of this strain.

This interpretation is supported by the extensional nature of the strains parallel to the strike of the arc, on both the mode 1 fractures perpendicular to the fold axis, and the sinistral and dextral strike-slip shear faults, which would generate a net extension in this direction, and shortening normal to the strike of the arc. These late fractures are therefore kinematically similar to the role suggested for the Bayas fault and sub-parallel faults noted at Punta Vidrias (6.6.3).

The deformation mechanism history presented for the quartzites shows that repeated switches occurred in both deformation mode (localised stylolites and fractures, penetrative grain shape fabrics and cleavage) and deformation mechanism (cataclasis, solution transfer and crystal plasticity). This interchange of deformation mechanisms is due to small changes in conditions around the critical values for the cataclasis-crystal plasticity transition inferred to take place at 200-250^{0}c under confining pressures of 50-100MPa and differential stresses of 250MPa or greater. These are likely to have been part of the same continuous episode of deformation, occurring between the late Westphalian.

CHAPTER 9

CONCLUSIONS

9.1 DEFORMATION MECHANISMS

9.2 INITIAL MICROSTRUCTURES

9.3 DEFORMATION CONDITIONS

9.4 DEFORMATION FACIES AND PATHS

9.5 THE CENTRAL CONCLUSIONS

9.6 RECOMMENDATIONS FOR FUTURE RESEARCH

9.1 DEFORMATION MECHANISMS

This concluding chapter abstracts the most significant findings of this study by describing four basic deformation mechanisms identified in the Ordovician quartzite from the Cantabrian and West Asturian-Leonese zones of NW Spain. Diagnostic microstructures of each mechanism are detailed and the mechanisms are sub-divided mainly on the basis of their meso and macroscale features, leading to a statement of the deformation mode. Scale definitions (2.4.1) are macro: >10m, meso: 10mm-10m, micro: <10mm. Initial microstructures and deformation conditions across the study area are summarised, and in the final section, the deformation modes and conditions are linked to define nine 'deformation facies'. The sequence of deformation facies describes a deformation path for any sample, and it is shown that the study area can be divided into four sub-areas, each characterised by different deformation paths.

9.1.1 Cataclasis

The diagnostic microstructural feature of cataclasis is the microfracture, which has been most effectively studied by cathodoluminescence revealing the two typical features: non-luminescencing quartz cement and dominant mode I displacements. **Intragranular microfractures** may have quite irregular paths and variable widths, form principally due to impingement, but flaw- and cleavage-induced microcracking and pre-existing flaws have also been deduced as significant mechanisms. An important instance of the latter is grain-edge cracking, partially controlled by original grain/overgrowth boundaries. **Transgranular microfractures** have, by contrast, more regular paths, but often link points of impingement between adjacent grains, where they may change direction and width in preference to crossing intervening cement, although they do also cut cement. A model for the development of transgranular microfractures by sequential linking of intragranulars has been proposed. **Circumgranular microfractures** are also observed, but are difficult to detect. Shear faults are distinguished by their three-component shear matrix, consisting of grains and grain fragments, cement and iron oxides, and shear displacements. Two end-member types of shear faults are recognised: **compact faults**, dominated by transgranular microfractures, with high proportions of matrix to fragments, small fragments, and low porosity; and **porous faults**, which are the opposite of compact faults in these respects. During shear fault evolution, microfracture densities appear to increase to a maximum value of $33mm^{-2}$ in compact faults as the proportion of shear matrix rises to 30%: thereafter, the microfracture density decreases. In porous faults, microfracture densities reach only $8mm^{-2}$. This may be interpreted as continuous work hardening until a threshold volume of shear matrix is reached, followed by progressive destruction of remaining fragments. Other microstructural features of exclusively cataclastic deformation are type 1 or 4 grain boundaries and geometric mean extinction angles (G.M.A. values) values of less than 6^{0}.

In the field, there are four main cataclastic features. The **fracture** has a variety of sizes and degrees of planarity, may have slickenside lineations, linings of iron oxides or vuggy quartz, and can usually be ascribed to a set of sub-parallel fractures. Without exception, all fractures form concentrations known as **deformation zones** where the frequency of the set parallel to the zone increases to greater than $30\text{-}40m^{-1}$, and frequencies of all sets increase within deformation zones, where minimum densities of $45m^{-1}$ are measured. Very high fracture densities ($>100m^{-1}$) are also observed in wider areas adjacent to major faults. These fractures are short and have a strong preferred orientation at an acute angle to the shear direction on the fault plane; they usually form areas of protobreccia. When shear matrix inside a deformation zone reaches a proportion greater than 25%, a breccia zone forms, usually heavily impregnated by iron oxides. Finally large fault planes may occur within deformation or breccia zones, or cutting across all other features; they have slickenside lineations and are distinguished from fractures by size.

The formation of an individual fracture representing an instability (strain-rate discontinuity) is predicted under certain conditions by theory based on elastic-plastic or non-linear material properties; it may occur during either strain hardening or strain softening. It is suggested here that the formation of deformation zones can be viewed as a similar localisation phenomenon on a much larger scale when a set of fractures begins to accommodate bulk strain. It is thus an intrinsic feature of cataclasis and the fundamental control of fracture density. Although localisation has been reported before (Stearns 1968b Jamison and Stearns 1982, Aydin and Johnson 1983), its importance has only been emphasised by the Aydin and Johnson study, and it has not hitherto been given a mechanical interpretation. It is suggested that the phenomenon may be widespread, and potentially capable of describing many other fracture density variations. Fault plane formation may be understood also in terms of instability theory, which allows the development of 'runaway instabilities' or zones of infinite strain rate. Lithological controls of fracture density are also evident: highest densities are confined to the most massive, compact beds at the top of the Barrios quartzite; densities are lower in sandstones, and in very coarse facies, in which fractures become less planar. No consistent fracture density/bed thickness relationships were observed.

Where there is a significant proportion of clay on a fault plane, fault gouges may develop with the characteristic features of gouge pods, p-foliation, Reidel (R1) and conjugate Reidel (R2) shears and Y shears. The development of good fault gouges depends on the availability of a local source of phyllosilicates. These features have experimental analogues from which a strain-hardening gouge-forming period is deduced before failure along Y surfaces, which may correspond to the stable-sliding to stick-slip transition. Four new observations on fault planes and gouges are made: firstly, fault planes may often have a surface morpholgy of sinusoidal, cylinders referred to as undulations with metre-scale wavelengths and amplitudes of several tens of millimetres, parallel to but quite distinct from associated smaller slickenside lineations; both features have axes in the inferred slip direction of the fault. Evidence has been given that undulations are primary features of the fault surface. Secondly, Reidel (R1) shears intersect the fault plane with a real distribution of orientations around the normal to the slip direction; this distribution does not merely reflect measurement error but can be understood as the accommodation of local shear strains oblique to the main shear direction. Thirdly, gouge forms en-echelon gouge pods along Reidel (R1) shears divided up by R2 shears, each pod containing one or several Y shears. This must imply that even Y shears can accumulate only limited amounts of shear. Related to this is the fourth observation that large faults also occur as sub-parallel multiple planes, several metres apart. This spread of deformation may be seen as the response to the restricted shear of segmented gouge zones leading to strain hardening. The spacing of multiple planes could be controlled by former deformation zones. On a meso- and macro-scale, cataclasis occurs in two deformation modes.

a) Macroscopically pervasive cataclasis. A distinctive fracture orientation pattern, consisting of a necklace of poles to at least three fracture sets in the girdle around the pole to bedding, which is rotated with bedding, is characteristic of this deformation mode when it occurs before folding. Fracture sets operated simultaneously and have slickensides in many orientations, even on the scale of a hand specimen. Evidence has been given that such early fracture networks, together with bedding-plane shears can be activated as slip systems to provide the bulk strain required for folding, and may even have formed initially in response to a three-dimensional strain. Post-folding cataclasis may also be macroscopically pervasive; in this instance, two to three fracture sets of approximately constant orientation, one axial planar and the other normal to the fold axis, are observed.

b) Macroscopically localised cataclasis. Faults, including thrusts, and all the gouge-zone features described above, are localised on the macroscopic scale. They may form in multiple planes.

9.1.2 Grain Boundary Sliding

Grain boundary sliding can be identified as a separate deformation mechanism in samples with low microfracture densities by the distortion of mica grains between unfractured quartz grains. Additional features are the wide, type four grain boundaries and G.M.A. values less than 6^{o}; these are useful diagnostics of this process, which is otherwise difficult to detect because some cataclasis always accompanies grain boundary sliding, also an integral part of cataclasis during fault formation. On a meso-scale, minor angular chevron folds are formed, with wavelengths of one to several metres. The deformation mode is localised and discontinuous grain boundary sliding on a microscopic scale, but pervasive on larger scales.

9.1.3 Solution Transfer

Two types are distinguished:

a) Grain boundary (short diffusion-path) solution transfer. This is readily appreciated from the type 2 grain boundaries. Type 2a boundaries between grains of similar radius or curvature (planar or gently convex) become type 2b (highly indented, convex towards the grain with a larger curvature) continuously, with all intermediate stages seen. The shape of the boundary has been shown to behave in accordance with the modelled and experimental stress distributions between an indenter and a plate, the higher normal stress and greater solution occurring within the plate. The deformation mode is solution transfer localised and discontinuous on the microscopic scale, but pervasive on the meso- and macro-scale.

b) Stylolitic (long diffusion path) solution transfer. The excellent stylolites described here within quartz are an unusual feature. They are irregular traces of pores with 'composite' profiles, of variable width in section, that truncate both original grains and overgrowths, and are lined by iron oxides, clay minerals or micas, which are bent around stylolite teeth. The micas are more common along the side of teeth than on their crowns; a model suggesting that solution is localised adjacent to micas is presented. Stylolite surfaces have circular pits with diameters of both 1-2mm and 10mm and amplitudes one tenth of these amounts respectively; they are most commonly bedding or foreset surfaces. The deformation mode is distinct from (a) because it is localised and discontinuous at both micro- and meso-scales.

9.1.4 Crystal Plasticity

Crystal Plasticity is subdivided into four states:

i) **Deformation lamellae.** These are probably not visible directly optically, but some representation is seen at high power where they are revealed as micron-sized parallel, straight lines of slightly contrasting extinction. However, they are associated with obvious dense development of deformation bands several microns wide. Transmission Electron Microscopy shows the lamellae structure to consist of elongate subgrains, with highly variable densities of curved dislocations and walls consisting of well-ordered arrays of two to three sets of dislocations, indicating recovery. The lamellae have a dominantly sub-basal orientation. Deformation lamellae probably form before deformation bands at a critical stress. Grain boundaries are of type 1; G.M.A. values of 17^{o} are measured in grains in the deformation lamellae or 15^0 in all grains. This stage is observed only on samples from a fault plane.

ii) The second stage has good tectonic shape fabrics with axial ratios up to 2.0, type 1 grain boundaries, G.M.A. values of $6\text{-}7^0$ and localised intense recrystallisation to a fine grain size along veins. These features are taken as evidence of the initiation of widespread crystal plasticity by intracrystalline deformation with limited recovery.

iii) The third stage also develops good shape fabrics, but here type 3 and 5 grain boundaries are common, and G.M.A. values range from 7 to 14^0. Complete recrystallisation may occur along veins, and very weak crystallographic preferred orientations may develop. Ubiquitous plasticity now extends to appreciable grain boundary migration in which boundaries may be pinned along mica grains, or develop a structure of subgrains in grain mantles. Locally there is thorough dynamic recrystallisation.

iv) In the final stage, tectonic shape fabrics persist; mean grain sizes are reduced by a factor of two due to the appearance of a population of small, equant, strain-free grains with type 6 grain boundaries. G.M.A. values of these grains are $1\text{-}2^0$ compared to $7\text{-}11^0$ for the larger grains, which have type 3 boundaries. Moderate crystallographic preferred orientations occur. These observations are interpreted as the result of variable extents of pervasive dynamic recrystallisation, by both grain boundary migration and subgrain rotation, to give a population of initially small but growing new grains, and a population of old, recrystallising grains.

The strain distribution of all crystal-plastic mechanisms is pervasive on all scales, down to the microscopic as defined above but becomes pervasive on a smaller scale from stages (i) to (iv) as localised vein shear ceases and the proportion of dynamic recrystallisation increases.

9.2 INITIAL MICROSTRUCTURE

Microstructural measurements indicate that all the samples of Ordovician quartzite in this study can be regarded as having a similar pre-deformation microstructure. The grain size is remarkably constant, from 0.1-0.2mm, and the total content of clay minerals with phyllosilicates generally less than 5%. The measured proportions of iron oxides are more variable (from less than 1% to 22%), but much of this can be attributed to secondary deposition. Quartz cement is universal, although to differing degrees in the pre-cataclastic samples. These characteristics would be expected from the very similar sedimentary facies and diagenetic conditions deduced across the whole Cantabrian and West Asturian-Leonese zones.

However, an important distinction has been made between two extreme types of microstructure in samples from the Bernesga Valley. The **compact (C) microstructure** has medium grain size, types 1 and 2 grain boundaries, 1 and 2 porosity, low pre-cataclastic and present porosities (less than 15 and 7% respectively), shear matrix up to 70% and microfracture densities of 2 to $33mm^{-2}$. This contrasts with **porous microstructure (P)**, with a fine grain size, type 4 grain boundaries, types 3 and 1b porosity, high pre-cataclastic and present porosities (greater than 15 and 7 %), high clay contents, less than 10% shear matric and maximum microfracture densities of $8mm^{-2}$.

This distinction is also seen in the deformation mechanisms: compact samples show compact faulting dominated by transgranular microfracture, porous samples have porous faulting and an important element of grain boundary sliding. The contrast is also observed in deformation modes, with pervasive cataclasis accommodating large-scale folding in the compact microstructure, and small-scale kinking and chevron folds forming in the porous microstructure. The contrast can be attributed entirely to variation in an initial microstructure, which was well-cemented in the compact samples but poorly-cemented in the porous cases.

Instability theory predicts a change from faulting to kinking with increasing intrinsic anisotropy. It is apparent that the high intrinsic anisotropies of the kinked materials can be well explained by their initial microstructure, leading both to the grain boundary sliding deformation mechanism and to strain accommodation by kinking. The cemented microstructures with low anisotropies form pervasive fracture networks by comparison. The microstructures then offer a strong physical interpretation of the theory.

Apart from this distinction, the detailed microstructural study has therefore been made on effectively a single, uniform lithology.

9.3 DEFORMATION CONDITIONS

9.3.1 Temperature

The several factors other than temperature that influence illite crystallinity means that only a range of possible temperatures should be given from this method, and that the range should be no less than 100^{o}C. Other variables have been eliminated as far as possible by comparing untreated crystallinities for shales or pelites in the 0.45-2μ fraction having no other recognisable 10A phases. For the case of Bernesga Valley and Punta Vidrias, the shales sampled are confined to those within the quartzites to avoid any possible stratigraphic control. On this basis, temperatures obtained for the four areas are 148-248^{o}c, 191-291^{o}c, 283-383^{o}c, and 311-411^{o}c. These temperatures can be confirmed both at the lower end by the small proportion of mixed layers and at the highest values by the lower-greenschist mineralogy and lack of biotite, implying temperatures of 350-400^{o}c. The progressive temperature increase of 160^{o}c from east to west across the Cantabrian West Asturian Leonese zones is not related to a known increase in stratigraphic depth, but does follow the trend of regional metamorphism, increasing through all the greenschist facies to andalusite grade in the westernmost West Asturian-Leonese zone, the Mondoñedo nappe. The illite crystallinity data have therefore enabled the regional metamorphic gradient to be followed east from the conventional mineralogical low-grade zones, summarised in Figure 9.1. The figure includes some crystallinities measured further west than the four areas mentioned above. In the Cantabrian zone, there is evidence for the preservation of burial diagenetic gradients in the Bernesga Valley crystallinities, but there is also a small increase in temperature from these to Punta Vidrias and again to Cabo de Peñas. This suggests a local source, but may be related to a more regional increase to the north of the Cantabrian zone. The Narcea antiform does not therefore mark a sharp increase in grade.

9.3.2 Confining Pressure

Stratigraphic depths of burial of the base of the Ordovician quartzite at the time of deformation can be reliably estimated in the Bernesga Valley (and Cremenes and Luna Lake) at 2.2-4.6km, and 3.23-3.97km at Punta Vidrias. Only minimum values of 2km and 2.7km can be deduced from Luarca and Punta del Sol respectively. These figures can be used to give minimum confining pressures of 63-114MPa, 77-99MPa, 50MPa and 68MPa for the four areas. Abundant evidence of the importance of fluid flow during cataclasis (crack cementation, redistribution of iron oxides from intact rock to shear matrix) requires pore fluid pressures to be at least hydrostatic. Minimum effective confining pressures can therefore be estimated as 19-68MPa, 46-59MPa, 30MPa and 41MPa. These values will be increased by the amount of tectonic overburden, which can only be estimated from detailed geometrical models, and decreased by excess pore-fluid pressures. Evidence for the establishment of a pre-fold fracture network at Bernesga Valley and Punta Vidrias, and an early phase of cataclasis at Punta del Sol, implies that excess pore-fluid pressures must be local and transitory at least in these

FIGURE 9.1

Illite Crystallinity and Greenschist facies isograds in the Cantabrian and West Asturian-Leonese Zones. Crystallinities are for the 0.45-2μ fraction, and have been grouped into quartzites with sandstones, and shales. There is a clear overall westwards increase in crystallinity, parallel to the regional metamorphic gradient defined by the greenschist isograds. There is also an increase in crystallinity northwards within the Cantabrian zone.

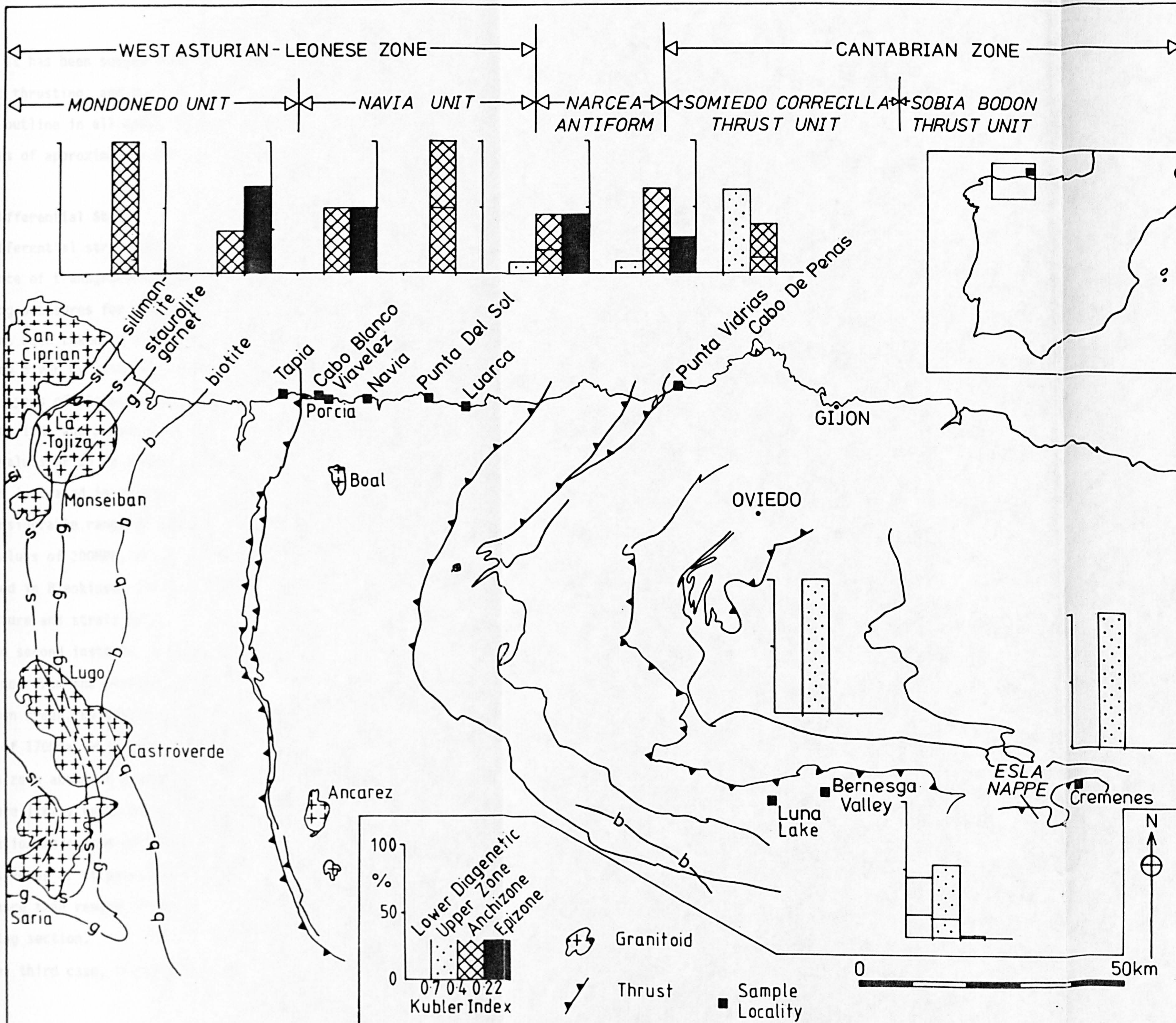

WEST ASTURIAN-LEONESE ZONE
CANTABRIAN ZONE
MONDONEDO UNIT
NAVIA UNIT
NARCEA ANTIFORM
SOMIEDO CORRECILLA THRUST UNIT
SOBIA BODON THRUST UNIT
sillimanite
staurolite
garnet
biotite
San Ciprian
La Tojiza
Monseiban
Lugo
Castroverde
Saria
Boal
Ancarez
Tapia
Porcia
Cabo Blanco
Viavelez
Navia
Punta Del Sol
Luarca
Punta Vidrias
Cabo De Penas
GIJON
OVIEDO
Bernesga Valley
Luna Lake
ESLA NAPPE
Cremenes
N
0
50km
100
%
50
0
Lower Diagenetic
Upper Zone
Anchizone
Epizone
0·7 0·4 0·22
Kubler Index
Granitoid
Thrust
Sample Locality

areas. It has been suggested that a substantial component of folding preceded thrusting, and that the geometry of deformation may have a broadly similar outline in all cases, leading to similar effective confining pressures of approximately 50MPa, 50MPa, 30MPa and 41MPa respectively.

9.3.3 Differential Stress

Differential stress has been estimated in three instances. The importance of transgranular microfracturing suggests low effective confining pressures for cataclasis of the quartzite in the Bernesga Valley: 50MPa has been taken as a maximum (9.3.2). Minimum stresses for failure have been given by uniaxial compressive strengths, considered for the two extreme types of microstructure: compact (pre-cataclastic porosities of less than 10%) and porous (pre-cataclastic porosities greater than 15%), giving values of up to 300MPa and 50MPa respectively. The range of stresses indicated is primarily a function of microstructure, which implies this considerable range of values for the samples. The quartzite samples imply values of 300MPa, while the sandstones may have failed at 50MPa: as discussed in Blenkinsop and Rutter (1986), these are quite independent of temperature and strain rate.

The second instance, from the samples of Bayas fault plane, was determined from the presence of deformation lamellae indicating power-law breakdown creep, by analogy with metals. This gives a minimum differential stress of 170MPa, which has been interpreted as a crack-tip stress within a process zone ahead of a growing crack. The remote applied stress is therefore likely to be much less than this value. In the description of deformation modes and conditions, localised stresses such as those in process zones or at points of impingement between grains, are of less importance than remote stresses. Only the latter will be considered in the following section.

The third case, from the recrystallised samples at Punta del Sol, used a recrystallised grain size palaeopiezometer to indicate a stress of 32MPa, considered to represent the steady-state flow stress during dynamic recrystallisation and folding of the Villayon anticline.

9.4 DEFORMATION FACIES AND PATHS

A **Deformation facies** is defined as a description of the associated deformation modes and conditions at a single time or stage of deformation. Based on the deformation modes and conditions described in chapters 5-8, table 9.1 has been constructed in which the postulated conditions have been linked to the inferred mechanisms and deformation continuity to define nine deformation facies. The continuity is specified by a scale length above which the deformation appears continuous. However, the complete description of deformation also requires a consideration of the change of deformation facies with time at any point. This is defined as the **Deformation path**, the history of deformation facies at a single point. Deformation mechanism paths have been proposed by Knipe (1985) as the sequence of deformation mechanisms and conditions. The deformation paths proposed here are distinct because they include some description of strain distribution as well as deformation mechanism; they are descriptive of deformation modes and conditions.

The microstructural histories allow identification of five separate deformation paths within the quartzite. These are shown by plotting the deformation mode in the coordinates of the deformation conditions stress, effective confining pressure, and temperature in Figure 9.2. From Table 9.1 and basic rock mechanics data, it is possible to subdivide deformation condition space into volumes which define the nine deformation facies. The paths within these volumes cannot be precisely constrained, but their likely positions have been indicated. It is important to emphasise that the stress (and effective stress) referred to is the remote stress considered

DEFORMATION FACIES = DEFOMATION MODE + DEFORMATION CONDITIONS

	Mechanism	Continuity	Temperature c°	Effective Confining Pressure MPa	Differential Stress
1	Solution Transfer (Grain Boundaries)	1m	0-250	0-75	
2	Solution Transfer (Stylolites	10m	191-291	46-59	
3	Cataclasis (Pervasive)	10^{2}m	0-250	19-75	50-300
4	Cataclasis (Localised)	10^{7}m	0-250		>50
5	Grain Boundary Sliding	1m	0-250	19-75	50
	Crystal Plasticity				
6	Stage (i)	10^{-5}m	191-291	46-59	>170
7	Stage (ii)	1m	191-291	46-59	
8	Stage (iii)	10^{-1}m	283-383	>30	
9	Stage (iv)	10^{-2}m	311-411	>41	32

TABLE 9.1

Deformation facies, modes and conditions. The deformation conditions are the range of values estimated for the facies during the deformation described in this study.

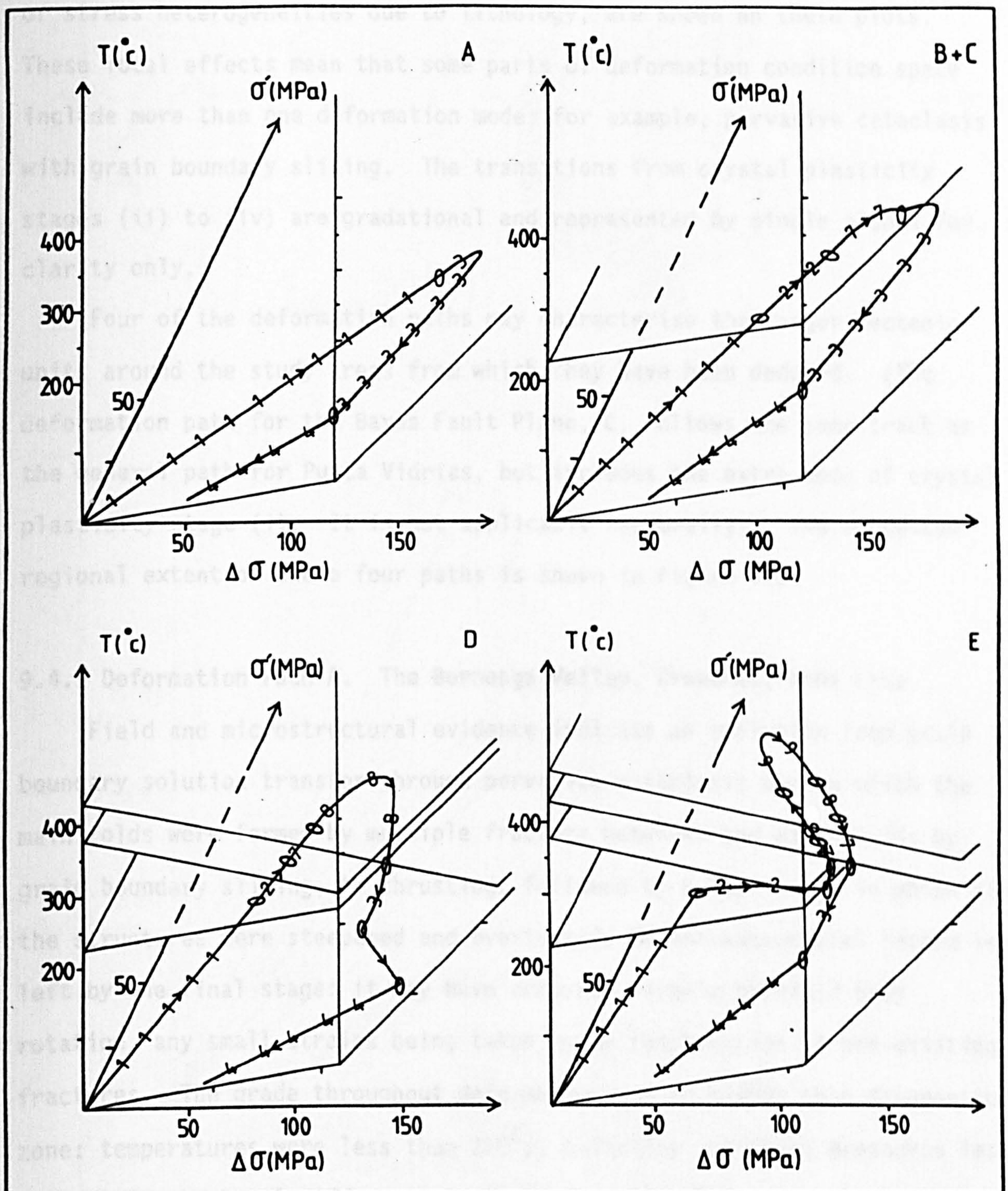

FIGURE 9.2

The four main deformation paths in quartzites of the Cantabrian and West Asturian Leonese Zones. The coordinates of deformation conditions are Differential Stress (Δσ, MPa), Effective Stress (σ, MPa) and Temperature (T, ^{o}c). Each deformation path shows the deformation facies (1 to 9) on the relevant part of the path. The volumes defining the deformation facies are outlined by planes. Transitions in facies along the paths are shown by ellipses which represent the points at which the deformation paths cross the bounding planes.

on a macroscopic scale, sufficiently large that neither crack-tip stresses, or stress heterogeneities due to lithology, are shown on these plots. These local effects mean that some parts of deformation condition space include more than one deformation mode: for example, pervasive cataclasis with grain boundary sliding. The transitions from crystal plasticity stages (ii) to (iv) are gradational and represented by single planes for clarity only.

Four of the deformation paths may characterise the larger tectonic units around the study areas from which they have been deduced. (The deformation path for the Bayas Fault Plane, C, follows the same track as the general path for Punta Vidrias, but includes the extra mode of crystal plasticity stage (i). It is not applicable regionally). The suggested regional extent of these four paths is shown in Figure 9.3.

9.4.1 Deformation Path A. The Bernesga Valley, Cremenes, Luna Lake

Field and microstructural evidence indicate an evolution from grain boundary solution transfer through pervasive cataclasis during which the main folds were formed by multiple fracture networks and minor folds by grain boundary sliding, to thrusting, followed by a late stage in which all the structures were steepened and overturned. No microstructural record is left by the final stage: it may have occurred largely by rigid-body rotation, any small strains being taken up by reactivation of pre-existing fractures. The grade throughout deformation was no higher than diagenetic zone: temperatures were less than 250^{0}c, effective confining pressures less than 75MPa and local differential stress for cataclasis from 50 to 300MPa depending on lithology. A remote stress of greater than 100MPa was likely. This deformation path may characterise the whole southern part of the Somiedo-Correcilla nappe unit.

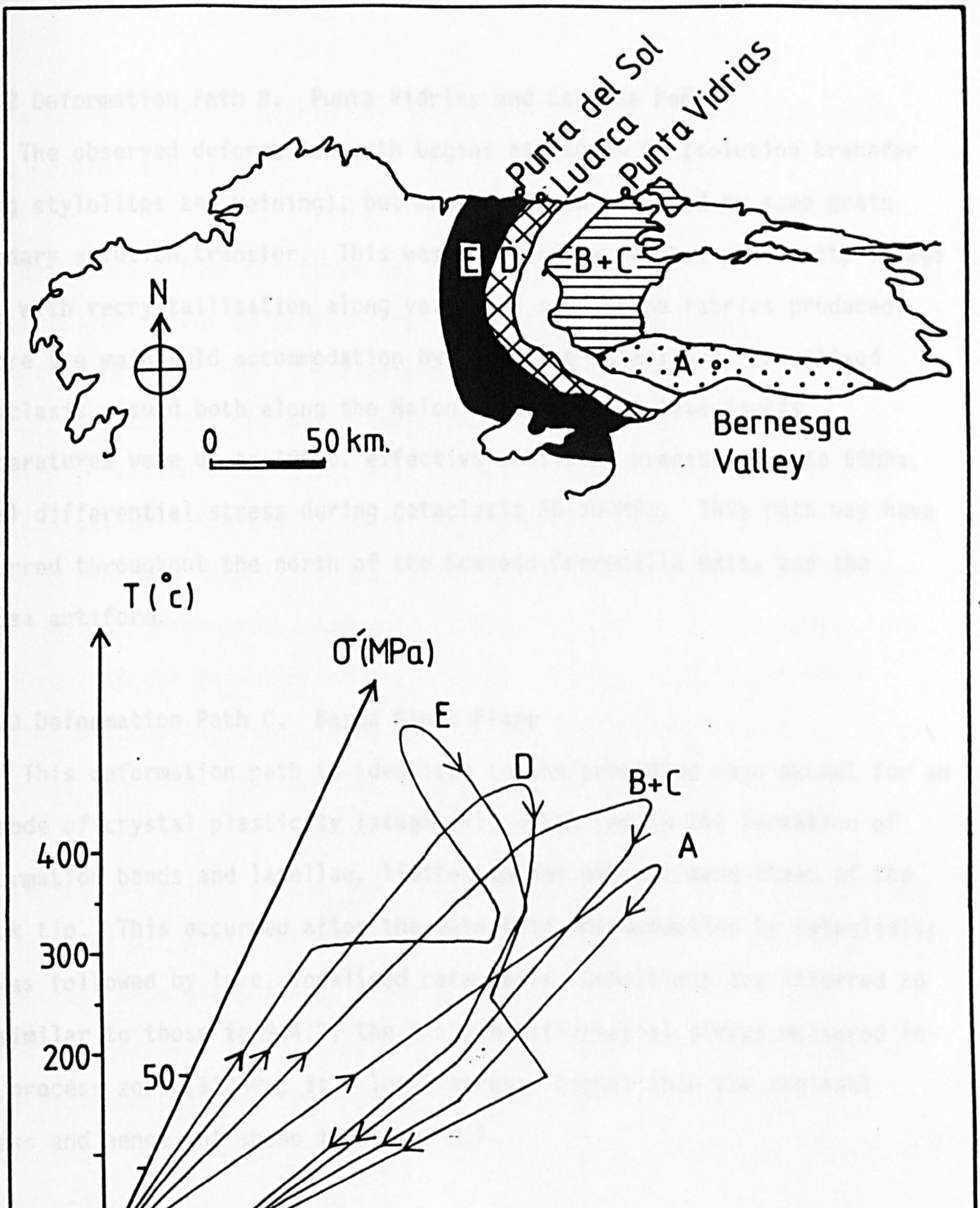

FIGURE 9.3

The suggested regional extent of the four main deformation paths

A - South part of the Somiedo-Correcilla Unit
B+C - North part of the Somiedo-Correcilla Unit.
D - East Navia Domain
E - West Navia Domain

9.4.2 Deformation Path B. Punta Vidrias and Cabo de Peñas

The observed deformation path begins at facies 2, (solution transfer along stylolites and veining), but may have been preceded by some grain boundary solution transfer. This was followed by crystal plasticity (stage ii), with recrystallisation along veins and some shape fabrics produced, before the main fold accommodation by pervasive cataclasis. Localised cataclasis ensued both along the Nalon Thrust and on late faults. Temperatures were up to 190^{o}c, effective confining pressures up to 59MPa, local differential stress during cataclasis 50-300MPa. This path may have occurred throughout the north of the Somiedo-Correcilla unit, and the Narcea antiform.

9.4.3 Deformation Path C. Bayas Fault Plane

This deformation path is identical to the preceding case except for an episode of crystal plasticity (stage (i)) which led to the formation of deformation bands and lamellae, limited to the process zone ahead of the crack tip. This occurred after the main fold accommodation by cataclasis; it was followed by late, localised cataclasis. Conditions are inferred to be similar to those in 9.4.2; the minimum differential stress measured in the process zone (170MPa) is a local stress, higher than the regional stress and hence not shown in Figure 9.2.

9.4.4 Deformation Path D. Luarca

Stylolitic solution transfer and veining is observed to have preceded crystal plasticity (stages (ii) and (iii)), which were the main fold accommodating mechanisms evident for both early and late stages of folding of the Portizuelo anticline. There is a characteristic late-fold fracture network, but the latest deformation facies was localised cataclasis, when the Portizuelo faults formed in multiple planes. Maximum temperatures rose to 383^{o}c, and effective confining pressures were greater than 30Mpa. The eastern Navia Province, within the West Asturian-Leonese zone, may have had such a deformation path.

9.4.5 Deformation Path E. Punta Del Sol

Stylolitic solution transfer was again the earliest visible deformation mode but may have been preceded by grain boundary solution as in paths B, C and D. The early non-planar fractures may represent a pre-fold, pervasive cataclasis, but the main folding of the Villayon anticline was coincident with crystal plasticity, stages (ii)-(iv). A late-fold fracture network formed, before thrust movement on the Villayon thrust, which represented deformation facies 4, localised cataclasis. This continued with the formation of master fractures and late faults which exploited deformation zones formed during the late-fold fracturing. This deformation path may have applied to the west of the Navia Province.

Individual points within the areas given above all progress along the same deformation paths, but different points within these areas may be at various positions along the deformation paths simultaneously as the deformation spreads. It is important therefore to realise that stages on the deformation paths do not represent deformation phases in the conventional sense, and they most probably are not separated by significant time intervals.

From the accounts in 9.4.1 and 9.4.5 it can be seen that the major differences in deformation paths during the Variscan orogeny are the changes from grain boundary solution transfer to stylolite solution transfer, and the progressive addition of stages (i) to (iv) of crystal plasticity to pervasive cataclasis. These were coincident with a rise in temperature. The four main deformation paths are therefore rather clearly distinguished on the composite plot of G.M.A. against illite crystallinity in Figure 9.4, since the G.M.A. value records the effects of crystal

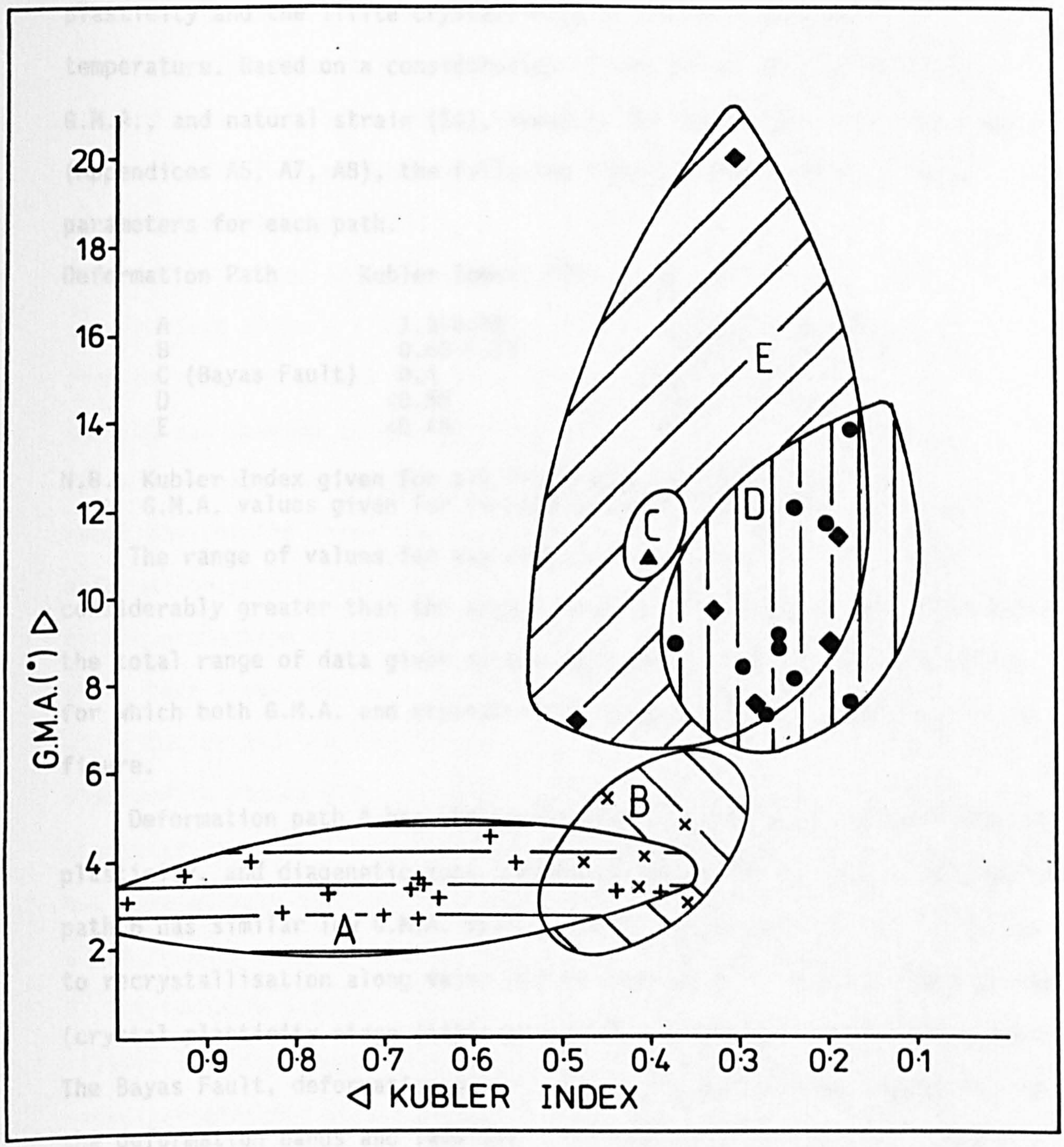

FIGURE 9.4

The relationship between G.M.A. and Illite Crystallinity. The five deformation paths can be discriminated by their fields on the diagram.

+ - Deformation Path A
× - Deformation Path B
▲ - Deformation Path C
● - Deformation Path D
◆ - Deformation Path E

plasticity and the illite crystallinity is mostly a function of temperature. Based on a consideration of the values of crystallinity, G.M.A., and natural strain (Es), shown by the entire data set from each (Appendices A5, A7, A8), the following limits can be placed on these parameters for each path.

Deformation Path	Kubler Index, $^{o}2\theta$	G.M.A.^{o}	Es
A	1.2-0.39	2.5-6.1	0.1-0.5
B	0.60-0.35	3.0-7.6	0.1-0.5
C (Bayas Fault)	0.4	11.0	
D	<0.55	7.0-14.0	>0.35
E	<0.48	>4.8	0.1-0.6

N.B. Kubler Index given for all lithologies, 0.45-2μ fraction.
G.M.A. values given for average of three perpendicular sections.

The range of values for any deformation path given in the table is considerably greater than the areas shown in Figure 9.4 since it considers the total range of data given in the Appendices, not merely those points for which both G.M.A. and crystallinity values coexist, as plotted in the figure.

Deformation path A has the lowest G.M.A. values and crystallinity: no plasticity, and diagenetic-zone conditions have been inferred. Deformation path B has similar low G.M.A. values, since crystal plasticity is limited to recrystallisation along veins and to production of a grain shape fabric (crystal plasticity stage (ii)); crystallinity results are slightly higher. The Bayas Fault, deformation path C, has much higher G.M.A. values due to the deformation bands and lamellae. The inception of recrystallisation (crystal plasticity stage (iii)) raises the G.M.A. value fxrom a maximum of 7.6^{o} for deformation paths A and B to 7.0-14.0^{o} in deformation path D, with a concurrent increase in crystallinity. Finally, extensive recrystallisation is associated with a still higher G.M.A. value and higher (anchizone-epizone) crystallinities in deformation path E. Progressively greater amounts of crystal plasticity (from stages (ii) to (iv)) thus correlate with increasing G.M.A. values. This is expected from the method of measurement, in which only larger, old, non-recrystallised grains are measured, preserving and accumulating crystal plastic strains.

A similar discrimination of deformation paths was sought in Figures 9.5 and 9.6, which show Lodes parameter plotted against natural shear strain, and G.M.A. versus natural shear strain respectively, with samples distinguished by deformation path. However there is evidently no discrimination possible based on shape (Lodes Parameter) and natural shear strain alone (Figure 9.5). This is due to two factors. Samples 28 and 14 from deformation path A show that variable and quite large strains (E_s up to 0.5) can develop in deformation paths without any crystal plasticity: these have been interpreted as primary fabrics. Apart from this complication, the large spread of natural strains in samples with deformation path E, including extensive recrystallisation, can be explained by the production of recrystallised equant grains as outlined in 8.3.12: these have a variable effect probably because of their heterogeneous distribution and the limited sampling area. However, some trends can be observed in Figure 9.6. The deformation paths excluding crystal plasticity stages (iii) or (iv) have G.M.A. values less than 4^o. Deformation Path D has a relatively high and well-constrained natural strain (0.3-0.45) and G.M.A. greater than 6^o. Deformation Path E has G.M.A. values greater than 7^o but variable natural strains. G.M.A. values again prove useful in illustrating the progressive increase in crystallinity; the non-discriminatory strain measurements, including recrystallised equant grains, do not reveal the change in deformation paths, except for the very similar values of E_s in deformation path D where recrystallisation is not widespread.

The regional distribution of the deformation paths can also be shown clearly by the parameters of Illite Crystallinity and G.M.A. Figure 9.7 shows the regional distribution of illite crystallinity ranges and means of all samples for which the 0.45-2μ size fraction was measured. The clear overall increase westwards in crystallinity has previously been interpreted

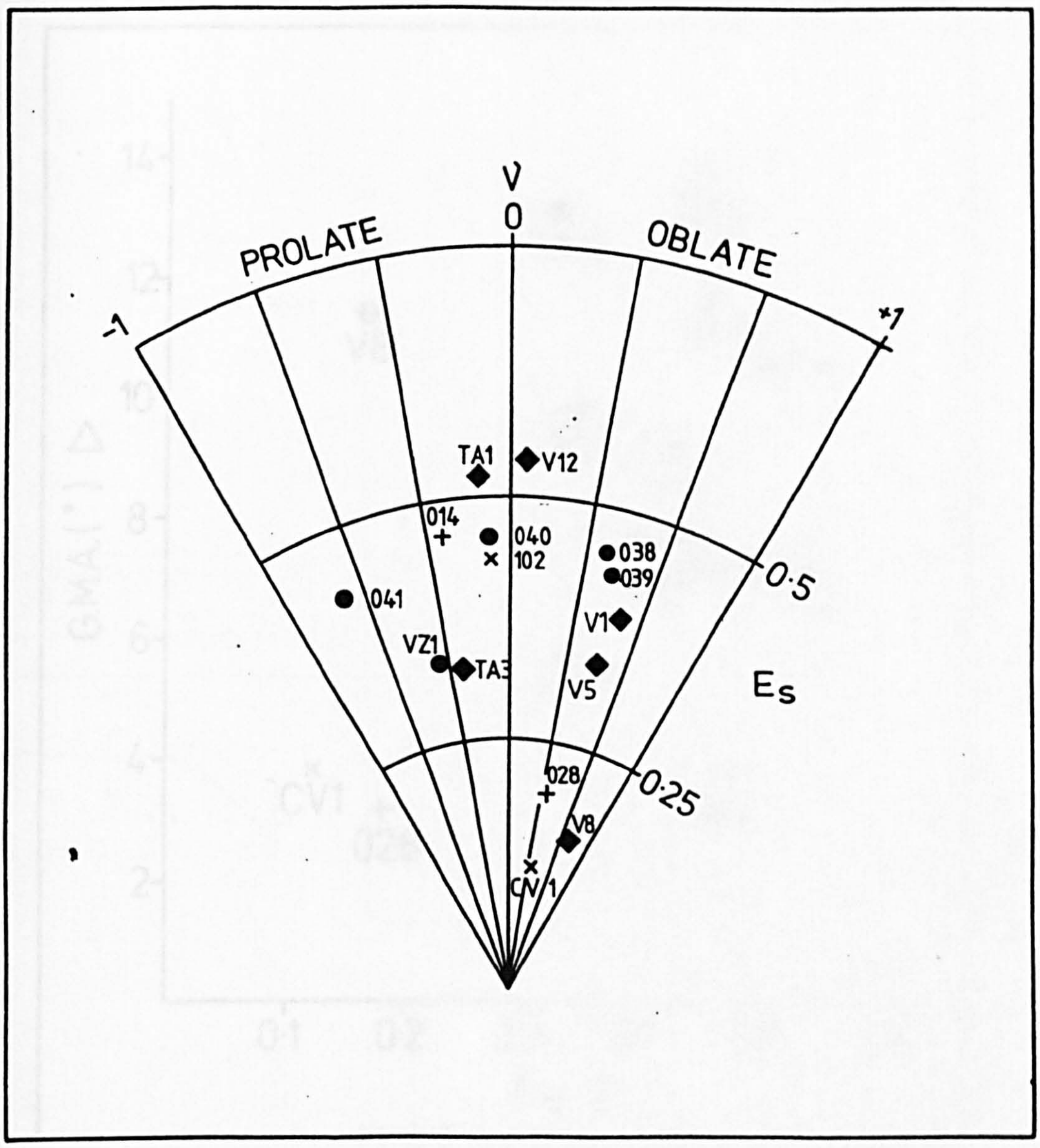

FIGURE 9.5

Hsu plot of Lode's Parameter, ν, against natural shear strain, E_s. Symbols represent samples from various deformation paths as indicated in Figure 9.4, but these do not fall into recognisable fields.

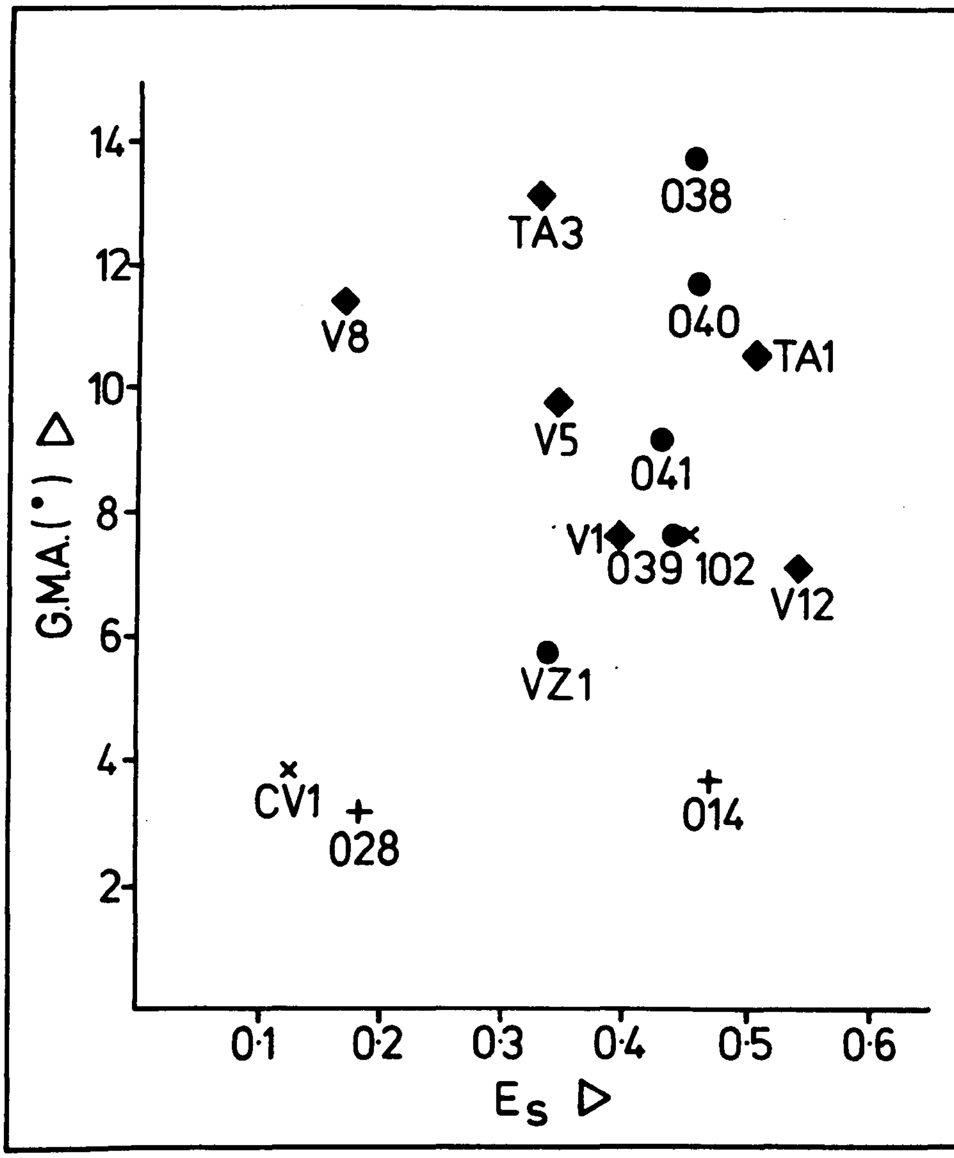

FIGURE 9.6

The relationship between Geometrical Mean of Extinction Angles, G.M.A., and natural shear stain, E_s. Deformation path represented by the same symbols as Figure 9.4. Deformation paths A and B, exluding crystal plasticity (ii) and (iv), have G.M.A. values less than 4^o; Deformation path D has high and restricted values of E_s (0.3-0.45), and G.M.A. greater than 6^o. Deformation path E has G.M.A. values greater than 7^o but variable E_s.

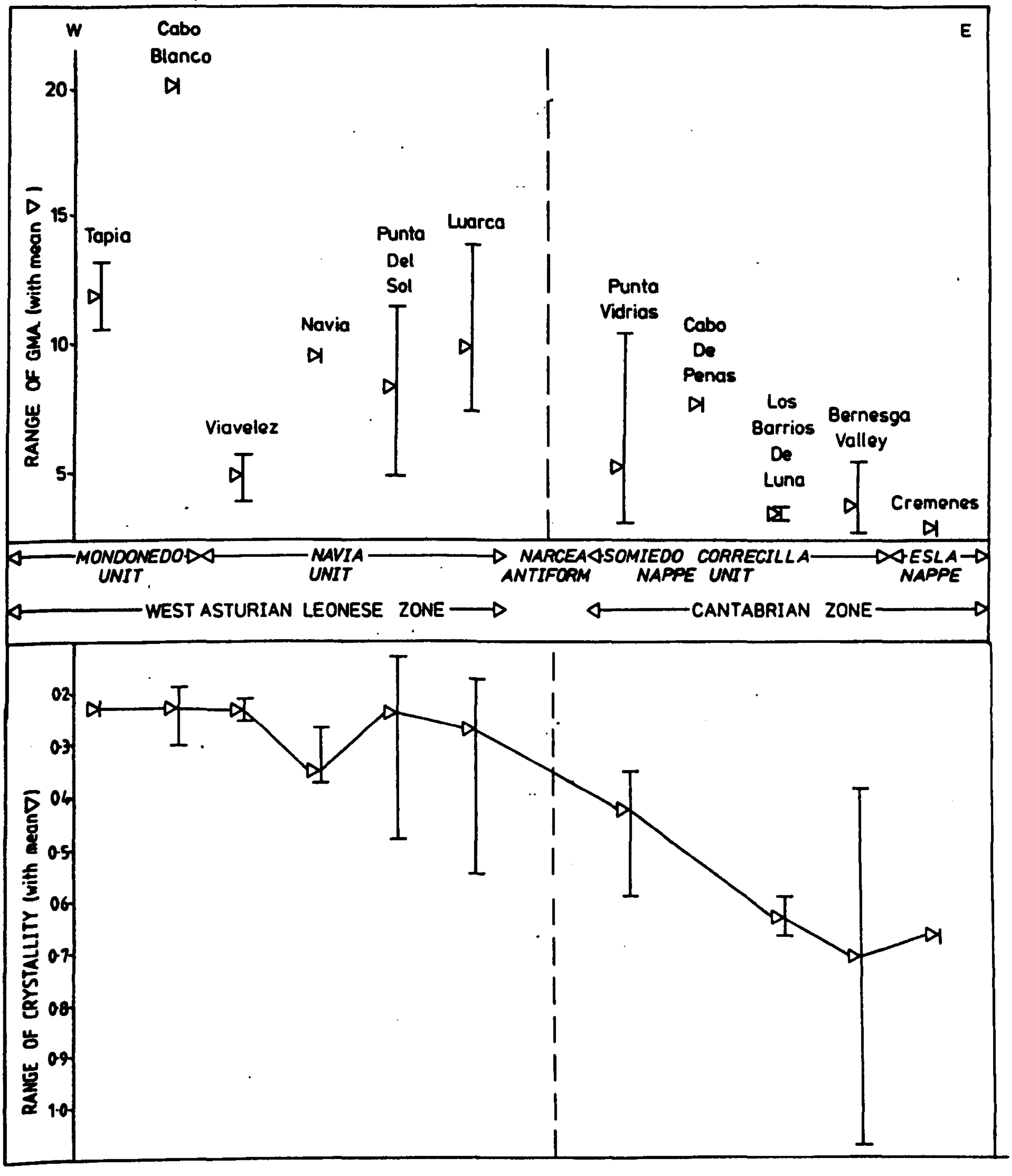

FIGURE 9.7

The Regional distribution of Illite Crystallinity and G.M.A. G.M.A. values and Kubler Indices (°2θ) are shown as ranges with means indicated by the triangle, for all samples on which the 0.45-2.0μ fraction has been measured. The sample localities are shown in their correct relative east-west positions, but not to scale. A clear overall westwards increase in crystallinity (decrease in Kubler Index) is evident; this is also the direction of regional metamorphism established by conventional greenschist facies isograds in Figure 9.1

(9.3.1) as the regional metamorphic gradient. There is an anomalously low crystallinity at Navia; it is possible that the regional gradient was heterogeneous on a small scale due to plutonism. The G.M.A. data are shown on the same figure. The rise in G.M.A. to the west corresponds closely with the illite crystallinity, confirming that the change in deformation paths is controlled mostly by the regional metamorphic gradient. Cabo de Peñas has a significantly higher G.M.A. than Punta Vidrias but the representativeness of this result, based on a single sample, is uncertain. The low G.M.A. at Viavellez may be due to a change in lithology reducing the component of plasticity at the expense of grain boundary sliding, while the extremely high value at Cabo Blanco is from an intensely deformed area of isoclinal folding in which strains are much higher than other samples.

9.5 THE CENTRAL CONCLUSIONS

9.5.1 Nine low-grade deformation modes have been identified in Ordovician quartzites and sandstones deformed during the Variscan orogeny in the Cantabrian and West Asturian-Leonese zones of North West Spain. These are:

1. Grain Boundary Solution Transfer
2. Stylolitic Solution Transfer
3. Pervasive Cataclasis
4. Localised Cataclasis
5. Grain Boundary Sliding
6. Crystal Plasticity: formation of Deformation Lamellae
7. Crystal Plasticity: no recrystallisation
8. Crystal Plasticity: inception of grain boundary migration
9. Crystal Plasticity: widespread recrystallisation

9.5.2 Some of the conditions under which these mechanisms operate have been deduced; together with the mechanisms above, they define nine

Deformation Facies given in Table 9.1.

9.5.3 New insights into the mechanisms of cataclasis in quartzites include:

a) **Transgranular microfracture** formation, by linkage of impingement microfractures, is an important deformation mechanism.

b) The formation and reactivation of **several fracture sets** in a **necklace** pattern around the pole to the bedding plane is the fold accommodation mechanism. This fracture pattern is understood as a response to an imposed bulk strain.

c) Fractures under all conditions studied cluster together to form **deformation zones** as an inherent part of the evolution of fracture networks.

d) Fault planes characteristically show corrugations at two scales: **undulations**, which have wavelengths from 0.5 to several metres, and are primary features of the fault surface, and **lineations** with wavelengths of millimetres, which are wear grooves.

e) Faults form in parallel **multiple planes**.

f) Newly observed gouge features are en-echelon **gouge pods**, which give large variations in gouge width along the fault and the real distribution of **Reidel (R1)** shear orientations within the fault zone.

9.5.4 Deformation modes in quartzites (large scale folds accommodated by multiple fracture sets) contrast with sandstones (minor angular folds). A difference is also seen in deformation mechanisms (compact shear controlled by transgranular microfractures in quartzites compared to grain boundary sliding leading to porous shear in sandstones). These changes are due to a lower initial porosity in the quartzite (compact microstructure) compared to a loose, porous initial microstructure in the sandstones.

9.5.5 Illite crystallinities have shown that a prograde, burial diagenetic gradient was passively deformed by folding and thrusting, and established a regional metamorphic gradient from lower diagenetic zone in the east and south of the Somiedo-Correcilla Nappe unit to the diagenetic-anchizone boundary in the north of this unit of the Cantabrian zone. There is a further and progressive increase through anchizone to epizone conditions from east to west within the Navia u nit of the West Asturian-Leonese zone, which extends the regional metamorphic gradient defined by conventional greenschist facies isograde eastwards.

9.5.6 At diagenetic grade, the major influence on illite crystallinity is from lithology. Even at anchi- and epi-zone grades, lithology exerts a cryptic influence on crystallinity.

9.5.7 Deformation paths (evolution of deformation facies) in quartzites change across the Cantabrian and West Asturian Leonese zones in concert with the regional metamorphic gradient. The main changes in the direction of increasing grade are the transition from boundary to stylolitic solution transfer, and the addition of progressively greater amounts of crystal plasticity to pervasive cataclasis, firstly by production of a grain shape fabric with localised recrystallisation, followed by the initiation of grain boundary migration leading eventually to thorough dynamic recrystallisation.

9.5.8 The technique of measuring intracrystalline extinction angles to assess deformation mechanism has been developed, and its use and reliability demonstrated. The geometric mean of extinction angles increases with intracrystalline plasticity and has the following advantages as a microstructural parameter:

a) It can detect the earliest appearance of crystal plasticity quantitatively when this is not apparent from other features such as fabrics (shape or crystallographic) or recrystallisation.

b) It can distinguish relict from recrystallised grains, and give relative deformation chronologies.

c) Data can be acquired in a relatively short time.

d) No specialised equipment nor preparation technique is necessary.

9.5.9 It has been demonstrated that the arithmetic mean of linear intercepts is good measurement of the true grain size, accounting for both sampling and truncation effects.

RECOMMENDATIONS FOR FURTHER RESEARCH

One of the most significant conclusions of this study is that all fractures in quartzites inherently cluster together to form deformation zones, which have been described in their essential nature. However, research is required to characterise deformation zones more quantitatively - for example, critical fracture frequencies and densities defining deformation zones should be established, and these characteristics should be investigated as a function of deformation conditions, lithology and microstructure. This needs to be complemented by, and form the basis of, a theoretical understanding of the reason for the formation of deformation zones, and the mechanism in terms of their stress-strain behaviour, since it is unlikely that features of this scale can benefit from an experimental approach. The identification of deformation zones is almost certainly possible in a wide variety of environments outside those of this study.

Deformation paths have been deduced for quartzites and sandstones in a range of conditions that are particularly relevant to mathematical models for the crust requiring simplified strength criteria. It would be useful to extend this study to several other lithologies so that direct comparisons could be made under the known deformation conditions. A variety of different lithologies share a widespread outcrop with the Ordovician quartzite across the Cantabrian and West Asturian-Leonese zones including siltstones, shales and limestones; deformation mechanisms and paths could be deduced for these formations. This work would be usefully concluded with an evaluation of the likely properties of the lower Palaeozoic, pre-orogenic wedge as a whole unit, which would have widespread application in modelling work because of its similarity to many other 'foreland' lithological sequences.

Important aspects of regional geology have been covered within the study. Two particular areas can be identified as meriting further work: the extension of the use of illite crystallinity to define low-grade conditions on a regional extent over the whole Cantabrian and West Asturian-Leonese zones. One especial problem that requires clarification is the apparent increase in grade in the north of the Somiedo-Correcilla Unit; the significance of the Narcea antiform in other areas also needs evaluation. Secondly, some doubt has been cast on two aspects of the conventional three-phase deformation sequence in the West Asturian-Leonese zone: the identification of two distinct cleavages (vide the 'anomalous' cleavages at Luarca), and the timing of thrust movement relative to the third phase of folding at Punta del Sol. Detailed measurements of cleavage orientation and mechanism of formation could be studied along the whole northern coast from the inception of cleavage at Cabo de Peñas westwards; and mapping of the Barayo thrust in greater detail is required to clarify the second point.

The new observations on fault-plane and gouge-zone features need to be investigated in more detail. The identification of undulations as an inherent fault-plane feature may be of considerable importance in faulting mechanisms, and the observation of multiple, spaced, fault planes likewise. Observations on natural fault gouges have proved to be useful because of their similarity to experimental features. The Reidel (R1) shear orientations and fault gouge pods reported here should be compared to experimental features: as experimental programme of ‘clay cake’-type simple shear, and of shear to large strains of simulated and natural fault gouge, is proposed to investigate these aspects. Finally, a microstructure of interest is the well developed stylolite in the quartzites. There are several quantitative measurements that could usefully be made on these features, leading to the determination of strains accommodated and the mechanism of formation.

REFERENCES

ALLER, J. & BRIME, C. 1981 Deformacion y metamorfismo en la parte sur de la Cuenca Carbonifera central (NO. de Espana). *Proceedings 10th International Congress of Carboniferous Stratigraphy and Geology, Madrid*, 541-548.

ALONSO, J.L. 1987 Sequences of thrusts and displacement transfer in the superposed duplexes of the Esla Nappe region (Cantabrian zone, NW Spain). Submitted to *J.Struct.Geol.*

ANDERSON, O.L. & GREW, P.C. 1977 Stress Corrosion Theory of Crack Propagation with application to geophysics. *Rev.geophys. & Space Phys.* **15**, 77-104.

APRAHAMIAN, J. 1974 La cristallinité de l'illite et les minéraux argileux en bordure des massifs cristallins externes de Belledonne et du Pelvoux. *Geol.Alpine* 50, 5-15.

ATKINSON, B.K. 1979 A fracture mechanics study of Subcritical Tensile cracking of Quartz in wet environments. *Pure appl. Geophys.* **117**, 1011-24.

ATKINSON, B.K. 1982 Subcritical crack propagation in rocks: theory, experimental results and applications. *J.Struct.Geol.* **4**, 41-56.

ATKINSON, B.K. 1980 Stress Corrosion and the rate-dependent tensile failure of a fine-grained quartz rock. *Tectonophysics* **65**, 281-90.

ATKINSON, B.K. & MEREDITH, P.G. 1981 Stress corrosion cracking of Quartz: A note on the influence of chemical environment. *Tectonophysics* **77**, T1-T11.

ATTFIELD, P. & KUSZNIR, N.J. 1985. A crack tip analogy model for the propagation of a plastic shear zone. *Abstract, Tectonic Studies Group Annual General Meeting*, University of Southampton.

AYDIN, A. 1978. Small faults formed as deformation bands in sandstones. *Pure appl. Geophys.* **116**, 931-942.

AYDIN, A. & JOHNSON, A.M. 1978. Development of faults as zones of deformation bands and as slip surfaces in sandstones. *Pure appl. Geophys.* **116**, 931-942.

AYDIN, A. & JOHNSON, A.M. 1983. Analysis of Faulting in porous sandstones. *J.Struct.Geol.* **5**, 19-31.

AYDIN, A. & RECHES, Z. 1982. Number and orientation of fault sets in the field and in experiments. *Geology* 10, 107-112.

BADHAM, J.P.N. 1982. Strike-slip orogens - an explanation for the Hercynides. *J.geol.Soc.Lond.* 139, 495 - 507.

BAHAT, D. 1979. Theoretical considerations on mechanical parameters of joint surfaces based on studies in ceramics. *Geol.Mag.* **116**, 81 - 92.

BAHAT, D. 1986. Joints and en echelon cracks in Middle Eocene chalks near Beer Sheva, Israel. *J.Struct.Geol.* 8, 2 181-190.

BAHAT, D. & ENGELDER, T. 1984. Surface morphology on joints of the Appalachian Plateau, New York and Pennsylvania. *Tectonophysics* 104, 299-313.

BALDWIN, C.T. 1976. The trace fossil stratigraphy of some shallow marine Cambro-Ordovician rocks from Brittany, N.W. Spain, and the United Kingdom. Unpubl. Ph.D. Thesis, Univ. of Liverpool.

BALDWIN, C.T. 1977. The stratigraphy and facies associations of trace fossils in some Cambrian and Ordovician rocks of North Western Spain. *Trace Fossils 2*, 9-40.

BANSAL, G.K. 1977. On fracture mirror formation in glass and polycrystalline ceramics. *Philos.Mag.* 35, 935-44.

BARLIER, J. 1974. Recherches paleothermometriques dans le domaine des Terres Noires Subalpines méridionales. Thèse 3eme cycle, Univ. Paris-Sud, Orsay, 98pp.

BASTIDA, F. 1981. Medida de la deformacion a partir de plieques paralelos aplastados. *Trab.Geol.University of Oviedo* 11, 15-33.

BASTIDA, F. & MARTINEZ-CATALIAN, J.R. & PULGAR, J.A. 1986. Structural metamorphic and magmatic history of the Mondonedo nappe (Hercynian belt, NW Spain). *J.Struct.Geol.* 8, 415-430.

BASTIDA, F. & PULGAR, J.A. 1978. La estructura del manto de Mondonedo entre Burela y Tapia de Casaiego (Costa Cantabria, NW de Espana). *Trab.Geol.University of Oviedo* 10, 75-124.

BAYER,R, & MATTE,Ph. 1979. Is the mafic/ultramafic massif of the Cabo-Ortegal (N.W.Spain) a nappe emplaced during a Variscan obduction A new gravity interpretation. *Tectonophysics* 57, T9 - T18.

BELL, A.M. 1981. Vergence: an evaluation. *J.Struct.Geol.* 3, 197-202.

BEVAN, T.G. & HANCOCK, P.L. 1986. A late Cenozoic regional mesofracture system in Southern England and Northern France. *J.geol.Soc.Lond.* 143 Pt.2, 355-362.

BILBY, B.A., ESHELBY, J.D. & KUNDU, A.K. 1975. The change of shape of a viscous ellipsoidal region embedded in a slowly deforming matrix having a different viscosity. *Tectonophysics* 28, 265-274.

BIOT, M.A. 1965. *Mechanics of Incremental Deformations*. New York: Wiley, 504pp.

BLENKINSOP, T.G. 1982. Cataclasis and the thrust tectonics of SW Sleat, Isle of Skye. Unpubl. M.Sc. Thesis, Univ. of London.

BLENKINSOP, T.G., LONG, R.E., KUSZNIR, N.J. & SMITH, M.J. 1986. Seismicity and Tectonics in Wales. *J.geol.Soc.Lond.* 143, 327-334.

BLENKINSOP, T.G. & RUTTER, E.H. 1986. Cataclastic deformation of quartzite in the Moine thrust zone. *J.Struc.Geol.* 8, 669-681.

BLOSS, F.D. 1957. Anisotropy of Fracture in Quartz. *Am.J.Sci.* 256, 214-225.

BOLES, J.R. 1984. Diagenetic studies in active burial settings of Texas and California. *Abstract, Conf. on Diagenesis & Low Temperature Metamorphism*, University of Bristol.

BONHOMMET, N., COBBOLD, P., PERROUD, H. & RICHARDSON, A. 1981. Palaeomagnetism and cross-folding in a key area of the Asturian arc

(Spain). *J.geophys.Res.* 86, 1873-1887.

BORG, I., FRIEDMAN, M., HANDIN, J. & HIGGS, D. 1960. Experimental Deformation of St. Peter Sand: A Study of Cataclastic Flow. In: *Rock Deformation*. (Edited by Griggs, D. & Handin, J.) *Geol.Soc.Am. Memoir* 78, 193-226. 79, 133-191.

BORG, I. & MAXWELL, J.C. 1956. Interpretation of Fabrics of Experimentally Deformed Sands. *Am.J.Si.* 254, 71-81.

BOYER, S.E. 1986. Styles of folding within thrust sheets: examples from the Appalachian and Rocky Mountains of the U.S.A. and Canada. *J.Struct.Geol.* 8, 325-339.

BOYER, S.E. & ELLIOTT, D. 1982. Thrust systems. *Bull.Am.Ass.Petrol.Geol.* 66, 1196-1230.

BRACE, W.E. & BOMBOLAKIS, E.G. 1963. A Note on Brittle Crack Growth in Compression. *J.geophys.Res.* 68, 3709-13.

BRACE, W.F., PAULDING, D.W.Jr. & SCHOLZ, C.H. 1986. Dilatancy in the fracture of crystalline rocks. *J.geophys.Res.* 71, 3939-3953.

BRACE, W.F. & WALSH, J.B. 1962. Some direct measurements of the surface energy of quartz and orthoclase. *Am.Min.* 47, 1111-1122.

BRAZIER, S., ROBINSON, D. & MATTHEWS, S.C. 1979. Studies of illite crystallinity in Southwest England. Some preliminary results and their geological setting. *Neues.Jahrb.Geol.Palaont.Mh.* 11, 641-662.

BRIME, C. 1981. Post-depositional transformation of clays in palaeozoic rocks of northwest Spain. *Clay Minerals* 16, 421-424.

BRIME, C. 1985. A diagenesis to metamorphism transition in the Hercynian of north-west Spain. *Min.Mag.* 49, 481-484.

BRIME,C. 1986. Personnal Communication.

BRIME, C. & PEREZ-ESTAUN, A. 1980. La transicion diagenesis-metamorfismo en la region del Cabo Penas. *Cuad.Lab.Xeol. de Laxe* 1, 85-97.

BROCK, W.G. & ENGELDER, T. 1977. Deformation associated with the movement of Muddy Mountain overthrust in the Buffington Window, Southeastern Nevada. *Bull.geol.Soc.Am.* 88, 1667-77.

BROWN, G. & FARROW, R. 1956. Introduction of Glycerol into flakes aggregates by vapour pressure. *Bull.Clay Min.* 3, 44-45.

BROWN, S.D. 1979. Multibarrier kinetics of brittle fracture: I. Stress dependence of the subcritical crack velocity. *J.Am.Ceram.Soc.* 62, 515-524.

BROWN, S.P. & SPANG, J.H. 1978. Geometry and mechanical relationship of folds to thrust fault propagation using a minor thrust in the Front Ranges of the Canadian Rocky Mountains. *Bull.Can.Pet.Geol.* 26, 551-571.

BRUHN, R.L.L & PAVLIS, T.L. 1981. Late Cenozoic deformation in the Forearc region: Matanuska Valley, Alaska: three dimensional strain in a forearc region. *Bull.geol.Soc.Am.* 92, 282-293.

BURG, J.P. & LAURENT, Ph. 1978. Strain analysis of a shear zone in a granodiotite. *Tectonophysics* 47, 15-42.

BURST, J.F. 1969. Diagenesis of Gulf Coast Clayey sediments and its possible relation to petroleum migration. *Bull.Am.Assoc.Pet.Geol.* 53, 73-93.

BUTLER, R.W.H. 1982. The terminology of structures in thrust belts. *J.Struct.Geol.* 4, 239-245.

BUTLER, R.W.H. 1982. Hangingwall strain: a function of duplex shape and footwall topography. *Tectonophysics* 88, 235-246.

BYERLEE, J.D. 1968. Brittle-ductile transition in rocks. *J.geophys.Res.* 73, 4741-4750.

CARRERAS, J., ESTRADA, A. & WHITE, S.H. 1977. The Effects of Folding on the c-axis fabrics of a Quartz Mylonite. *Tectonophysics* 39

CARTER, N.L., ANDERSON, D.A., HANSEN, F.D. & KRANZ, R.L. 1981. Creep and Creep rupture of granitic rocks. In: *The Mechanical Behaviour of Crustal Rocks*, 61-82. Geophysical Monograph 24 (edited by Carter, N.L., Friedman, M., Logan, J.M. & Stearns, D.W.) American Geophysical Union, Washington.

CARTER, N.L. & KIRBY, S.H. 1978. Transient Creep and Semibrittle behaviour of Crystalline Rocks. *Pure appl. Geophys.* 116, 807-839.

CASEY, M. 1982. An alternative model for ramping. *Abstract, Tectonic Studies Group Annual General Meeting, Univ. Cardiff*, 13.

CHAPMAN, J.J., MILTON, N.J. & WILLIAMS, G.D. 1979. Shape fabric variations in deformed conglomerates at the base of the Laksefjord Nappe, Norway. *J.geol.Soc.Lond.* 136, 683-691.

CHARLES, R.J. 1958. Static fatigue of glass. *J.appl.Phys.* 29, 1549-1560.

CHRISTIE, J.M. & KOCH, P.S. 1982. Grain size-flow stress relations for novaculite deformed in hydrous assemblies. *Abstract, Trans.Am. geophys. Union (EOS)* 63, 1095.

CHRISTIE, J.M. & ORD, A. 1980. Flow stress from microstructure of mylonites: example and current assessment. *J.geophys.Res.* 85, 6253-6262.

CHRISTIE, J.M., ORD, A. & KOCH, P.S. 1980. Relationship between recrystallized grain size and flow stress in experimentally deformed quartzite. *Abstract, Trans. Am. geophys. Un. (EOS)* 61, 377.

CLOOS, E. 1947. Oolite deformation in the South Mountain Fold, Maryland. *Bull.geol.Soc.Am.* 58, 843-913.

COBBOLD, P.R. & GAPAIS, D. 1983. Pure shear and simple shear of particle/matrix systems with viscosity contrasts. *Terra Cognita* 3, 247.

COOK, A.C. & JOHNSON, K.R. 1970. Early joint formation in sediments. *Geol.Mag.* 107, 361-368.

COOK, N.G.W., HOOD, M. & TSAI, F. 1984. Observations of Crack growth in hard rock loaded by an indenter. *Int.J.Rock Mech.Min.Sci. & Geomech.* 21, 97-107.

CONRAD, R.E. & FREIDMAN, M. 1976. Microscopic Feather Fractures in the Faulting Process. *Tectonophysics* 33, 187-198.

COOMBS, D.S., ELLIS, A.J., FYFE, W.S. & TAYLOR, A.M. 1959. The zeolite facies, with comments on the interpretation of hydrothermal syntheses. *Geochim.Cosmochim.Acta* 17, 53-107.

COOMBS, D.S., HORODYSKI, R.J. & NAYLOR, R.S. 1970. Occurrence of prehnite-pumpellyite facies in northern Maine. *Am.J.Sci.* 268, 142-156.

COOPER, M.A. & TRAYNER, P.M. 1986. Thrust surface geometry: implications for thrust-belt evolution and section-balancing techniques. *J.Struct.Geol.* 8, 305-312.

COSTIN, L.S. 1983. A Microcrack Model for the Deformation and Failure of Brittle Rock. *J.geophys.Res.* 88, 9485-9492.

COWARD, M.P. & POTTS, G.J. 1983. Complex strain patterns developed at the frontal and lateral tips to shear zones and thrust zones. *J.Struct.Geol.* 5, 383-399.

COX, S.J.D. & ATKINSON, B.K. 1983. Fracture Mechanics and acoustic emission of anti-plane Shear Cracks in rocks. *Earthquake Prediction & Res.* 2, 1-24.

CRIMES, T.P. & MARCOS, A. 1976. Trilobite traces and the age of the lowest part of the Ordovician reference section for NW Spain. *Geol.Mag.* 113, 349-356.

CRONSHAW, D. 1984. Aspects of Low-Grade Metamorphism in Northern Snowdonia, Wales. Unpublished Ph.D. Thesis, University of Keele.

CRUDEN, D.M. 1971. The form of the creep law for rock under uniaxial compression. *Int.J.Rock Mech.Min.Sci.* 8, 105-126.

CRUDEN, D.M. 1974. The static fatigue of brittle rock under uniaxial compression. *Int. J. Rock Mech. Min. Sci. & Geomech. Abstr.* 11, 67-73.

DAHLSTROM, C. 1970. Structural Geology in the Eastern Margin of the Canadian Rock Mountains. *Bull.Can.Pet.Geol.* 18, 332-406.

DAS, S. & SCHOLZ, C.H. 1981. Theory of Time-Dependent Rupture in the Earth. *J.geophys.Res.* 86 6039-6051.

DAVIES, G.R. 1929. The Analysis of Frequency Distributions. *J.Am. Stat.Assoc.* 349-366.

DE SITTER, L.V. 1960. Crossfolding in non-metamorphic of the Cantabrian Mountains and in the Pyrenees. *Geologie Mijnb.* 22, 189-194.

DE SITTER, L.U. 1962. The Structure of the southern slope of the Cantabrian Mountains. *Leidse.Geol.Meded.* 26, 255-264.

DIEGEL, F.A. 1986. Topological constraints on imbricate thrust networks, examples from the Mountain City window, Tennessee, U.S.A. *J.Struct.Geol.* 8, 269-279.

DIETRICH, J.A. 1981. Constitutive Properties of faults with simulated gouge. In: *Mechanical Behaviour of Crustal Rocks*, 103-120 Geophysical Monograph 24 (edited by Carter, N.L., Friedman, M., Logan, J.M. & Steans, D.W.). American Geophysical Union, Washington.

DIETRICH, D. & GRANT, P.R. 1986. Cathodoluminescence petrography of syntectonic quartz fibres. *J.Struct.Geol.* 7, 541-568.

DOUGLAS, R.J.W. 1950. Callum creek, Langford creek and Gap map-areas, Alberta. *Mem.geol.Surv.Can.* 255

DRURY, M.R., HUMPHREYS, P.J. & WHITE, S.H. 1985. Large strain deformation studies using polycrystalline magnesium as a rock analogue. Part II: dynamic recrystallisation mechanisms at high temperatures. *Phys.Earth Plan.Int.* 40, 208-222.

DUNN, D.E., La FOUNTAIN, L.J. & JACKSON, R.E. 1973. Porosity dependence and mechanism of brittle fracture in sandstones. *J.geophys.Res.* 78, 2403-2417.

DUNOYER DE SEGONZAC, G. 1969. Les Minéraux argileux dans las diagenèse pasage au métamorphisme. *Mem.Serv.Carte Geol.Alsace Lorraine, (Strasbourg)* 29, 320

DUNOYER DE SEGONZAC, G. 1970. The transformation of clay minerals during diagenesis and low grade metamorphism: a review. *Sedimentology*, 15 281-346.

EDWARD, G.H., ETHERIDGE, M.A. & HOBBS, B.E. 1982. On the stress dependence of subgrain size. *Text. & Microstructures* 5, 127-152.

ELLIOT, D. 1972. Deformation paths in structural geology. *Bull.geol. Soc.Am.* 83, 2621-2638.

ELLIOT, D. 1976. The Energy Balance and Deformation Mechanisms of Thrust Sheets. *Phil.Trans.R.Soc.* A283, 289-312.

ELLIOT, D. & JOHNSON, M.R.W. 1980. Structural evolution in the northern part of the Moine Thrust Zone. *Geol.Trans.R.Soc. Edinburgh (Earth Sci.)* 71, 69-96.

ENGELDER, T. 1974. Cataclasis and the generation of fault gouge. *Bull.geol.Soc.Am.* 85, 1515-1522.

ENGELDER, T. 1985. Loading paths to joint propagation during a tectonic cycle: an example from the Appalachian Plateau, U.S.A. *J.Struct.Geol.* 7, 459-476.

ESQUEVIN, J. 1969. Influence de la composition chimique des illites sur leur crystallinity. *Bull. Centre Rech.Pau-S.N.P.A.* 3, 147-154.

ETCHECOPAR, A., VASSEUR, G. & DAIGNIERES, M. 1981. An inverse problem in microtectonics for determination of stress tensores from fault striation analysis. *J.Struct.Geol.* 3, 51-65.

ETHERIDGE, M.A. & WIKIE, J.C. 1981. An assessment of dynamically recrystallised grain size as a paleopiezometer in quartz-bearing mylonite zones. *Tectonophysics* 78, 475-508.

EVANS, D.J. & WHITE, S.H. 1984. Microstructural and fabric studies from the rocks of the Moine Nappe, Eriboll, N.W. Scotland. *J.Struct.Geol.* 6, 369-389.

EXNER, H.E. 1972. Analysis of Grain- and Particle-Size Distributions in Metallic Materials. *Int.Met.Rev.* 159 [17], 25-42.

FAIRHURST, C. 1964. On the validity of the 'Brazilian' test for brittle materials. *Int.J.Rock Mech.Min.Sci.* 1, 535-546.

FITCHES, W.R., CAVE, R., CRAIG, J. & MALTMAN, A.J. 1986. Early veins as evidence of detachment in the Lower Palaeozoic rocks of the Welsh Basin. *J.Struct.Geol.* 8, 607-620.

FREY, M. 1970. The step from diagenesis to metamorphism in pelitic rocks during Alpine orogenesis. *Sedimentology*, 15, 261-279.

FREY, M., TEICHMULLER, M., TEICHMULLER, R., MULLIS, J., KUNZI, B., BREITSCHMID, A., GRUNER, U. & SCHWIZER B. 1980. Very low grade metamorphism in external parts of the Central Alps: Illite Crystallinity, coal rank and fluid inclusion data. *Eclog.geol.Helv.* 73, 173-203.

FREY, M. 1984. The transition from diagenesis to low temperature metamorphism in the Alps - a review. *Abstract, Conf. on Diagenesis and Low Temperature Metamorphism*, University of Bristol.

FRIEDMAN, M. & LOGAN, J.M. 1970. Microscopic Feather Fractures. *Bull.geol.Soc.Am.* 81, 3417-3420.

FRY, N. 1979. Random point distributions and strain measurement in rocks. *Tectonophysics* 60, 89-105.

GALLAGHER, J.J. 1981. Tectonics of China: Continental Scale Cataclastic Flow. In *Mechanical Behaviour of Crustal Rock*, 259-273. Geophysical Monograph 24, (edited by Carter, N.L., Friedman, M., Logan, J.M. and Stearns, D.W.) American Geophysical Union, Washington.

GALLAGHER, J.J., FRIEDMAN, M., HANDIN, J. & SOWERS, G.M. 1974. Experimental studies relating to microfractures in sandstone. *Tectonophysics* 21, 203-247.

GAY, N.C. 1968. Pure shear and simple shear deformation of inhomogeneous viscous fluids - I. Theory. *Tectonophysics* 5, 211-234.

GENDZWILL, D.J. & STAUFFER, M.R. 1981. Analysis of triaxial ellipsoids: their shapes, plane sections and plane projections. *Math.Geol.* 13, 135-152.

GILL, W.D., KHALAF, F.I. & MASSOUD, M.S. 1977. Clay Minerals as an index of the degree of metamorphism of the carbonate and terrigenous rocks in the South Wales coalfield. *Sedimentology* 24, 675-691.

GRIFFITH, A.A. 1924. The theory of rupture. In: Proc. 1st Int. Congr. Appl. Mech. Biezeno, C.B., Burgers, J.M. (eds.). Delft: Tech. Boekhandel en Drukkerij J. Waltman Jr., 54-63.

GRIGGS, D.T. & HANDIN, J. 1960. Observations on fracture and a hypothesis of earthquakes. In: *Rock Deformation*. Griggs, D., Handin, J. (eds.), *Geol.Soc.Am.Memoir* 79, 347-364.

GRIGGS,D.T. & BLACIC, J.D. 1965. Quartz; Anomalous weakness of synthetic crystals. *Science* 147, 292 - 295.

GRINFELDS,A.U., ABOTTYN, D.E. & PLEKHANOV,V.G. 1984. Luminescence of autolocalised electrons in SiO_2. *Sov.Phys.Solid State* 26, 1075 - 1077.

GUZZETTA, G. 1984. Kinematics of stylolite formation and physics of pressure solution process. *Tectonophysics* 101, 383-394.

HADIZADEH, J. 1980. An experimental study of cataclastic deformation in a quartzite. Unpublished Ph.D. thesis, Imperial College, University of London.

HADIZADEH, J. & RUTTER, E.H. 1982. Experimental study of cataclastic deformation of a quartzite. *Proc. 23rd Symp. Rock Mech., University California, Berkeley*. Edited Goodman, R.E. & Heuze, F.E.

HADLEY, K. 1976. Comparison of calculated and observed crack densities and seismic velocities in Westerly granite. *J.Geophys.Res.* 81, 3484-3494.

HALLBAUER, D.K., WAGNER, H. & COOK, N.G.W. 1973. Some observations concerning the microscopic and mechanical behaviour of quartzite specimens in stiff, triaxial compression tests. *Int.J.Rock Mech. & Min.Sci.* 10, 713-726.

HANCOCK, P.L. 1964. The relations between fold and late formed joints in South Pembrokeshire. *Geol.Mag.* 101, 174-184.

HANCOCK, P.L. 1985. Brittle microtectonics: principles and practice. *J.Struct.Geol.* 7, 437-451.

HANCOCK, P.L. & BARKA, A.A. 1985. Kinematic indicators on freshly exposed active normal faults. *Abstract, Tectonic Studies Group Meeting, Shear Criteria*, Imperial College, London.

HANCOCK, P.L., DUNNE, W.M. & TRINGHAM, M.E. 1982. Variscan Deformation in South-West Wales. In: *The Variscan Fold Belt in the British Isles* (ed. Hancock, P.L.) Adam Hilger, Bristol, 47-73.

HANDIN,J.W. & HEGER, R.V. 1957. Experimental deformation of sedimentary rocks under confining pressure : pore pressure tests. *Bull.Am.Assoc.Petrol.Geol.* 44, 1853 - 1873.

HANUSIAK, W.M. & WHITE, E.W. 1975. SEM Cathodoluminescence for characterisation of damaged and undamaged alpha quartz in respirable dusts. *Proc. 8th Annual S.E.M. Symposium, IITRI*, Chicago, 125-131.

HARRASOWITZ, H. 1927. Anchimetamorphose, das Gebiet zwischen Oberflachenund Tiefenumwandlung der Erdrinde. *Ber.Oberhess.Ges.Nat.Heilk, Giessen, Naturwiss.Abt.* 12, 9-15.

HARRIS, L.D. 1976. Thin-skinned tectonics and potential hydrocarbon traps - illustrated by a seismic profile in the Valley and Ridge province of Tennesse. *J.Res. U.S. geol.Surv.* 4, 379-386.

HARRIS, L.D. & MILICI, R.C. 1977. Characteristics of thin-skinned style of deformation in the southern Appalachians, and potential hydrocarbon traps. *Prof.Pap. U.S. geol.Surv.* 1018 40.

HARRIS, J.E., TAYLOR, G.L. & WALPER, J.L. 1960. Relation of deformation fractures in sedimentary rocks to regional and local structure. *Bull.Am.Assoc.Pet.Geol.* 44, 1853-1873.

HARTLEY, N.E.W. & WILSHAW, T.R. 1973. Deformation and fracture of synthetic alpha-quartz. *J.Mater.Sci.* 8, 265-278.

HATHAWAY, J.C. 1956. Procedure for clay mineral analysis used in the Sedimentary Petrology Laboratory of the U.S. Geological Survey. *Clay Min.Bull.* 3, 8-13.

HAWORTH, R.T. & LEFORT, J.P. 1979. Geophysical Eviddnce for the extent of the Avalon zone in Atlantic Canada. *Can.J.Earth Sci.* 16, 552-567.

HAYES, W., KANE, M.K., SALMINEN, O., WOOD, R.L. & DOHERTY, S.P. 1984. ODMR of recombination centres in crystalline quartz. *J.Phys.(c): Solid State Phys.* 17, 2943-2951.

HEARD, H.C. 1960. Transition from brittle fracture to ductile flow in Solenhofen limestone as a function of temperature, confining pressure, and interstitial fludi pressure. In: *Rock Deformation.* (Edited by Griggs, D. & Handin, J. *Geol.Soc.Am.Memoir* 79, 193-226.

HELM, D.G. & SIDDANS, A.W.B. 1971. Deformation of a slaty, lapillar tuff in the English Lake District: discussion. *Bull.geol.Soc.Am.* 82, 523-531.

HEMPTON, M.R. & NEHER, K. 1986. Experimental fracture, strain and subsidence patterns over en-echelon strike-slip faults: implications for the structural evolution of pull-apart basins. *J.Struct.Geol.* 8, 597-605.

HESSE, R. 1984. The step from diagenesis to low grade metamorphism in the Taconic Belt of the Northern Appalachians in Quebec. *Abstract, Conf. on Diagenesis and Low Temperature Metamorphism,* University of Bristol.

HIGGINS, A.C. & WAGNER-GENTIS, C.H.T. 1982. Connodonts, goniatites and the biostratigraphy of the earlier Carboniferous from the Cantabrian Mountains, Spain. *Palaeontology* 25, 313-350.

HIGGS, W.G., STIMPSON, I.G. & WILLIAMS, G.D. 1986. Fault-Related Folds. Abstract, Tectonic Studies Group Annal General Meeting, University of Hull.

HOBBS, B.E., MEANS, W.D. & WILLIAMS, P.F. 1976. *An Outline of Structural Geology.* John Wiley & Sons.

HODGSON, R.A. 1961. Classification of structures on joint surfaces. *Am.J.Sci.* 259, 439-502.

HORI, H. & NEMAT NASSER, S. 1985. Compression-Induced Microcrack Growth in Brittle Solids: Axial Splitting and Shear Failure. *J.geophys.Res.* 90, 3105-3125.

HOSSACK, J.R. 1968. Pebble deformation and thrusting in the Bygdin Area (Southern Norway). *Tectonophysics* 5, 315-339.

HOSSACK, J.R. 1983. A cross-section through the Scandanavian Caledonides constructed with the aid of branch line maps. *J.Struct.Geol.* 5, 103-111.

HOUSE, W.M. & GRAY, D.R. 1982. Cataclasites along the Salteville thrust U.S.A., and their implications for thrust sheet emplacement. *J.Struct.Geol.* 4, 257-269.

HOWER, J., ESLINGER, E.V., HOWER, M.E. & PERRY, E.A. 1976. Mechanism of burial metamorphism of argillaceous sediment: 1. Mineralogical and chemical evidence. *Bull.Geol.Soc.Am.* 87, 725-737.

HOWER, J.H. & MOFFAT, T.C. 1966. The mineralogy of illites and mixed layer illite-montmorillonites. *Am.Min.* 51, 63-74.

HUDSON, J.A. & PRIEST, S.D. 1983. Discontinuity Frequency in Rock Masses. *Int.J.Rock Mech.Min.Sci. & Geomech.Abstr.* 30, 73-89.

INGLIS, C.E. 1913. Stresses in a plate due to the presence of cracks and sharp corners. *Trans.Inst.Nav.Archit., London* 55, 219-241.

JACKSON, R.E. & DUNN, D.E. 1974. Experimental sliding friction and cataclasis of foliated rocks. *Int.J.Rock Mech.Min.Sic.* 11, 235-249.

JAEGER, J.C. & COOK, N.G.W. 1979. *Fundamentals of Rock Mechanics*. 3rd ed. London: Chapman and Hall, 585pp.

JAMISON, W.R. 1978. Fracture generation in a porous sandstone: inferences from tectonically deformed material. *Trans.Am.geophys.Union (EOS)* 59, 1191-1192.

JAMISON,W.R. 1987. Geometric analysis of fold development in overthrust terranes. *J.Struc.Geol.* 7, 207 - 219.

JAMISON, W.R. & STEARNS, D.W. 1982. Tectonic Deformation of Wingate Sandstone, Colorado National Monument. *Bull.Am.Ass.Pet.Geol.* 66, 2584-2608.

JOHNSON, H.D. 1978. Shallow Siliclastic Seas. *Sedimental Environments and Facies* (edited Reading, H.G.) Blackwell Scientific Publications, 207-257.

JOHNSON, J.W. & HOLLOWAY, D.G. 1966. On the size and shape of the fracture zones of glass fracture surfaces. *Philos.Mag.* 14, 731-743.

JOHNSON, M.R.W., KELLEY, S.P., OLIVER, G.J.H. & WINTER, D.A. 1985. Thermal effects and timing of thrusting in the Moine thrust zone. *J.Geol.Soc.Lond.* 142, 863-873.

JONES, M.E. & ADDIS, M.A. 1986. The application of stress path and critical slate analysis to sediment deformation. *J.Struct.Geol.* 8, 575-580.

JULIVERT, M. 1971. Decollement tectonics in the Hercynian Cordillera of N.W. Spain. *Am.J.Sci.* 270, 1-29.

JULIVERT, M. 1976. La Estructura de la region del Cabo-Peñas. *Trab.Geol.University of Oviedo* 8, 203-309.

JULIVERT, M. & ARBOLEYA, M.L. 1984. A geometrical and kinematical approach to the nappe structure in an arcuate fold belt: the Cantabrian Nappes (Hercynian chain, N.W. Spain). *J.Struct.Geol.* 6, 499-519.

JULIVERT, M. & ARBOLEYA, M.L. 1986. Areal balancing and estimate of areal reduction in thin-skinned fold-and-thrust belt (Cantabrian zone, N.W. Spain): constraints on its emplacement mechanism. *J.Struct.Geol.* 8, 407-414.

JULIVERT, M. & MARCOS, A. 1973. Superimposed folding under flexural conditions in the Cantabrian Zone (Hercynian Cordillera, N.W. Spain).

Am.J.Sci. 273, 353-375.

JULIVERT, M., TRUYOLS, J. & GARCIA-ALCALDE, J. 1981. Mapa Geologico de España. E.1:200,000 I.G.M.E., Madrid.

JULIVERT, M., TRUYOLS. J., MARCOS, A. & ARBOLEYA, M.L. 1973. Mapa Geologico de España. E.1:50,000. I.G.M.E., Madrid.

KEMP, A.E.S., OLIVER, G.J.H. & BALDWIN, J.R. 1985. Low-grade metamorphism and accretion tectonics: Southern Uplands terrain, Scotland. *Miner.Mag.* 49, 335-344.

KIRBY, S.H. 1980. Tectonic Stresses in the lithosphere: constraints provided by the experimental deformation of rocks. *J.geophys.Res.* 85, 6353-6363.

KIRBY, S.H. & KRONENBERG, A.K. 1984. Deformation of Clinopyroxenite: Evidence for a transition in Flow Mechanisms and Semibrittle behaviour. *J.geophys.Res.* 89, 3177-3192.

KISCH, H.J. 1980. Incipient metamorphism of Cambro-Silurian clastic rocks from the Jamtland Supergroup, Central Scandanavian Caledonides, Western Sweden: illite crystallinity and 'vitrinite' reflectance. *J.geol.Soc.Lond.* 137, 271-288.

KISCH, H.J. 1983. Mineralogy and petrology of burial diagenesis (burial metamorphism) and incipient metamorphism is clastic rocks. In: *Diagenesis in Sediments and Sedimentary Rocks, 2.* (edited by Larsen, G. & Chillinger, G.V.) *Developments in Sedimentology, 25B.* Elsevier, Amsterdam, 289-493.

KISCH, H.J. 1984. Correlation between the parameters of burial diagenesis and incipient metamorphism: causes of divergency. *Abstract, Conf. on Diagenesis and Low Temperature Metamorphism,* University of Bristol.

KNIPE, R.J. 1981. The Interaction of Deformation and Metamorphism in Slates. *Tectonophysics*, 78, 249-272.

KNIPE, R.J. 1985. Deformation Mechanism path diagrams and the assessment of faulting mechanisms. *Abstract, Tectonic Studies Group Annual General Meeting,* University of Southampton.

KNIPE, R.J. & WHITE, S.H. 1977. Microstructural Variation of An axial planar Cleavage around a Fold - a H.V.E.N. Study. *Tectonophysics* 39, 355-380.

KNIPE, R.J. & WHITE, S.H. 1979. Deformation in Low grade Shear zones in the Old Red Sandstone, S.W. Wales. *J.Struct.Geol.* 1, 53-66.

KOHLSTEDT, D.L., COOPER, R.F., WEATHERS, M.S. & BIRD, J.M. 1979. Paleostress analysis of deformation-induced microstructures: Moine Thrust Zone and Ikertoq shear zone. Analysis of Actual Fault Zones in Bedrock, 394-425, Open File Report 79-1239, U.S. Geol.Surv. Mento Park, California.

KOSSOVSKAYA, A.G. & SHUTOV, V.D. 1963. Facies of regional epigenesis and metagenesis. *Int.Geol.Rev.* 7, 1157-1167.

KRANZ, R.L. 1979a. Crack growth and development during creep and Barre Granite. *Int.J.Rock Mech.Min.Sci. & Geomech.Abstr.* 16, 23-35.

KRANZ, R.L. 1979b. Crack-crack and crack-pore interactions in stressed granite. *Int.J.Rock Mech.Min.Sci. & Geomech.Abstr.* 16 37-47.

KRANZ, R.L. 1983. Review of microcracks. *Tectonophysics* 100, 449-480.

KRONENBERG, A.K. & TULLIS, J. 1984. Flow strengths of Quartz Aggregates: Grain Size and Pressure Effects due to Hydrolitic Weakening. *J.geophys.Res.* 89, 4281-4297.

KUBLER, B. 1964. Les argiles, indicateurs de métamorphisme. *Rev.Inst.France Petrol.* 19, 1093-1112.

KUBLER, B. 1967a. La cristallinité de l'illite et les zones tout a fait supérieurs du métamorphisme. Colloque sur les "Étages tectoniques", Neuchatel, Festschrift, 105-122.

KUBLER, B. 1967b. Anchimétamorphisme et schistosité. *Bull.Cent.Rech. Pau.-S.N.P.A.* 1, 259-278.

KUBLER, B. 1968. Evaluation quantitative du métamorphisme par la cristallinité de l'illite. *Bull.Cent.Rech.Pau.-S.N.P.A.* 2, 385-397.

KULLMAN,J. & SCHONBERG, R. 1979. Facies differentiation caused by wrench deformation along a deep seated fault system (Leon line, Cantabrian Mountains, North Spain - Reply.

KUSZNIR, N.J. & PARK, R.G. 1982. Intraplate lithosphere strength and heat flow. *Nature, Lond.* 299, 540-542.

KUSZNIR, N.J. & PARK, R.G. 1984. Intraplate lithosphere deformation and the strength of the lithosphere. *Geophys.J.R.astr.Soc.* 79, 513-538.

LACASSIN, R. & VAN DEN DRIESSCHE, J. 1983. Finite strain determination of gneiss: application of Fry's method to porphyroid in the southern Masif Central (France). *J.Struct.Geol.* 5, 245-253.

LADEIRA F.L. & PRICE, N.J. 1981. Fracture Spacing and Bed Thickness. *J.Struct.Geol.* 3, 179-183

LAJTAI, E.Z. 1972. Effect of tensile stress gradient on brittle fracture initiation. *Int.J.Rock Mech.Min.Sci. & Geomech.Abstr.* 9, 569-578.

LANGLEY, R. 1971. *Practical Statistics.* David & Charles (Publishers) Ltd., Newton Abbot, Devon.

LATHAM, J.P. 1985a. A numerical investigation and geological discussion of the relationship between folding, kinking and faulting. *J.Struct.Geol.* 7, 237-249.

LATHAM, J.P. 1985b. The influence of non-linear material properties and resistance to bending on the development of internal structures. *J.Struct.Geol.* 7, 225-236.

LAW, R.D. 1986. Relationship between strain and quartz crystallographic fabrics in the Roche Maurie quartzites of Plougastel, Western Brittany. *J.Struct.Geol.* 8, 493-515.

LAW, R.D., KNIPE, R.J. & DAYAN, H. 1984. Strain path partitioning within thrust sheets: microstructural and petrofabric evidence from the Moine Thrust Zone at Loch Eriboll, northwest Scotland. *J.Struct.Geol.* 6, 477-497.

LAWN, B.R. & WILSHAW, T.R. 1975a. *Fracture of Brittle Solids*. Cambridge University Press, Cambridge.

LAWN, B. & WILSHAW, R. 1975b. Review Indentation Fracture: principles and applications. *J.Mater.Sci*. 10, 1049-1081.

LEE, J.H., PEACOR, D.R., LEWIS, D.D. & WINSTON, R.P. 1986. Evidence for syntectonic crystallisation for the mudstone to slate transition at Lehigh Gap, Pennsylvania, U.S.A. *J.Struct.Geol*. 8, 767-780.

LE FORT, P. 1979. Ibero-Armorican Arc and Hercynian Orogeny in Western Europe. *Geology* 7, 384-388.

LESPINASSE, M. & PECHER, A. 1986. Microfracturing and regional stress field: a study of the preferred orientations of fluid-inclusion planes in a granite from the Massif Central, France. *J.Struct.Geol*. 8, 2 169-180.

LINDQVIST, P.A., LAI, H.H. & ALM, O. 1984. Indentation Fracture Development in rock continuously observed with a Scanning Electron Microscope. *Int.J.Rock Mech.Min.Sci. & Geomech.Abstr*. 21, 165-184.

LINKER, H.F. & KIRBY, S.H. 1981. Anisotropy in the rheology of hydrolitically weakened synthetic quartz crystals. In: *Mechanical Behaviour of Crustal Rocks*, Geophysical Monograph 24 (edited by Carter, N.L., Friedman, M., Logan, J.M. & Stearns, D.W.) American Geophysical Union, Washington.

LISLE, R.J. 1977a. Estimation of the tectonic strain ratio from the mean shape of deformed elliptical markers. *Geologie Mijnb*. 56, 140-144.

LISLE, R.J. 1977b. Clastic grain shape and orientation in relation to cleavage from the Aberystwyth Grits, Wales. *Tectonophysics* 39, 381-395.

LISLE, R.J. 1979. Strain analysis using deformed pebbles: the influence of initial pebble shape. *Tectonophysics* 60, 263-277.

LISLE, R.J. 1985. *Geological strain Analysis: A Manual for the Rf/O Technique*. Pergamon Press, Oxford.

LISLE, R.J. & FREEMAN, B. 1985. The Nature of Bias involved in strain estimation from competent inclusions. *Abstract, Tectonic Studies Group Annual General Meeting*, Southampton.

LISLE, R.J., RONDEEL, H.E., DOORN, D., BRUGGE, J. & VAN de GAAG, P. 1983. Estimation of viscosity contrast and finite strain from deformed elliptical inclusions. *J.Struct.Geol*. 5, 603-609.

LISTER, G.S. & WILLIAMS, P.F. 1979. Fabric development in Shear Zones: Theoretical Controls and Observed Phenomena. *J.Struct.Geol*. 1, 283-298.

LLOYD, G.E. & WHALLEY, J.S. 1986. The modification of chevron folds by simple shear: examples from north Cornwall and Devon. *J.geol.Soc.Lond*. 143, 89-94.

LOGAN, J.M. 1979. Brittle Phenomena. *Rev.geophys. & Space Phys*. 17, 1121-1132.

LOGAN, J.M., HIGGS, N.G. & FRIEDMAN, M. 1981. Laboratory Studies on Natural Gouge from U.S. Geological Survey Dry Lake Valley No.1 Well, San Andreas Fault Zone. In: *Mechanical Behaviour of Crustal Rocks* Geophysical Monograph 24 (edited by Carter, N.L., Friedman, M., Logan, J.M. & Stearns, D.W.) American Geophysical Union, Washington.

LORENZ, V. & NICHOLLS, I.A. 1984. Plate and intraplate processes of Hercynian Europe during the late Palaeozoic. *Tectonophysics* 107, 25-56.

LUDWIG, V. 1972. Die Paragenese Chlorit, Muscovit, Paragonit und Margarit im 'Griffelschieffer' des Ordoviziums in NE-Bayern (mit einem Beitrag zum Problem der Illit-Kristallinitat). *Neues Jb.Geol.Palaont.Mon.* 9, 546-560.

MARCOS, A. 1973. Las Series de Paleozoico Inferior y la estructura Hercinian del occidente de Asturias (N.W. de Espana). *Trab. Geol. University of Oviedo* 6, 1-113.

MARCOS, A. 1979. Facies differentiation caused by wrench deformation along a deep seated fault system (Leon line, Cantabrian Mountains, North Spain) - Discussion. *Tectonophysics* 60, 303-309.

MARCOS, A. & PULGAR, J.A. 1982 An approach to the tectonostratigraphic evolution of the Cantabrian foreland thrust and fold belt, Hercynian Cordillera of N.W. Spain. *Neues Jb.Geol.Palaont.Abh.* 163, 256 - 260.

MARTIN, R.J. & DURHAM, W.B. 1975. Mechanisms of Crack Growth in Quartz. *J.geophys.Res.* 80, 4837-4843.

MATTE, Ph. & BURG, J.P. 1981. Sutures, thrusts and nappes in the Variscan Arc of western Europe: plate tectonic implications. In: *Thrust and Nappe Tectonics* (edited by McClay, K.R. & Price, N.J.) *Spec.Publs.geol.Soc.Lond.* 9, 353-358.

MATTHEWS, P.E., BOND, R.A.G. & VAN DEN BERG, J.J. 1984. An algebraic method of strain analysis. *Tectonophysics* 24, 31-67.

MAXWELL, J.C. 1960. Experiments on compaction and cementation of sand. In: *Rock Deformation* (edited by Griggs, D. & Handin, J.), *Geol.Soc.Am.Memoir* 79, 105-132.

MERCIER, J-C.C. 1980. Magnitude of Continental Lithospheric Stresses inferred from Rheomorphic Petrology. *J.geophys.Res.* 85, 6293-6303.

MERCIER, J-C.C., ANDERSON, D.A. & CARTER, N.L. 1977. Stress in lithosphere: Inferences from steady state flow of rocks. *Pure appl.geophys.* 115, 199-226.

MEREDITH, P.L. A fracture mechanics study of experimentally deformed crustal rocks. Unpublished Ph.D. Thesis, University of London.

MERRIMAN, R.J. & ROBERTS, B. 1985. A survey of white mica crystallinity and polytypes in pelitic rocks of Snowdonia and Llyn, North Wales. *Min.Mag.* 49, 305-319.

MICHALSKE, T.A. & FRECHETTE, V.D. 1980. Dynamic Effects of Liquids on crack growth leading to catastrophic failure. *J.Am.Ceram.Soc.* 63, 603-609.

MILTON, N.J. 1980. Determination of the strain ellipsoid from measurements on any three sections. *Tectonophysics* 64 T19-T27.

MITRA, G. & BOYER, S.E. 1986. Energy balance and deformation mechanisms of duplexes. *J.Struct.Geol.* 8, 291-304.

MOGI, K. 1972a. Fracture and Flow of Rocks. *Tectonophysics* 13, 541-568.

MOGI, K. 1972b. Effect of the triaxial stress system on fracture and flow of rocks. *Phys. Earth Planet Int.* 5, 318-324.

MOGI, K. 1974. On the pressure dependence of strength in rocks and the Coulomb fracture criterion. *Tectonophysics* 21, 273-285.

MURRELL, S.A.F. 1963. A criterion for brittle fracture of rocks and concrete under triaxial stress, and the effect of pore pressure on dthe criterion. In: *Rock Mechanics*. Fairhurst, C. (ed.). Proc. 5th Symp. Rock Mech. New York: Pergamon Press, 563-577.

MURRELL, S.A.F., DIGBY, P.J. 1970 The theory of brittle fracture initiation under triaxial stress conditions. *Geophys.J.R. Astron.Soc.* 19, 309-334.

McCORMICK, J.W. 1977. Transmission electron microscope investigation of some naturally deformed quartzites. Unpublished Ph.D. Thesis, University of California, Los Angeles.

McDOWELL, S.O. 1984. Geothermal metamorphism of sedimentary rock in the Salton Trough/Imperial Valley, U.S.A. and Mexico. *Abstract, Conf. on Diagenesis and Low Temperature Metamorphism*, University of Bristol.

McDOWELL,S.D. & ELDERS,W.A. 1980. Authigenic layer silicate minerals in borehole Elmore 1, Salton Sea Geothermal Field, California U.S.A. *Cont.Min.Pet.* 74, 293 - 310.

McEWEN, T.J. 1981. Brittle deformation in pitted pebble conglomerates. *J.Struct.Geol.* 3 25-37.

McCLINTOCK, F.A. & WALSH, J.B. 1962. Friction on Griffith cracks in rocks under pressure. In: *Proc. 4th U.S. Nat. Congr. Appl. Mech., Vol.II. New York: Am. Soc. Mech. Eng.* 1015-1021.

McQUILLAN, H. 1973. Small scale fracture density in Asmari formation of S.W. Iran and its relation to bed thickness and structural setting. *Bull.Am.Ass.Pet.Geol.* 57, 2367-2385.

NADEAU, P.H., WILSON, M.J., McHARDY, W.J. & TAIT, J.M. 1985. The conversion of smectite to illite during diagenesis: evidence of some illitic clays from bentonites and sandstones. *Min.Mag.* 49, 393-400.

NARAHARA, D.K. & WILTSCHKO, D.V. 1986. Deformation in the hinge region of a chevron fold, Valley and Ridge Province, central Pennsylvania. *J.Struct.Geol.* 8, 157-168.

NIAMATULLAH, M. 1983. The Laxfordian Structure of the Kenmore Inlier, Loch Torridon, Ross Shire. Unpublished Ph.D. Thesis, University of Keele.

NICHOLSON, R. & POLLARD, D. 1985. Dilation and linkage of echelon cracks. *J.Struct.Geol.* 7, 583-590.

NICOLAS, A. & POIRIER, J.P. 1976. *Crystalline Plasticity and Sold State Flow in Metamorphic Rocks*. London: Wiley-Interscience.

NORTON, M.G. 1982. The kinematic and microstructural development of some shear zones. Unpublished Ph.D. Thesis, University of London.

NORTON, M.G. & ATKINSON, B.K. 1981. Stress dependent morphological features on fracture surfaces of quartz and glass. *Tectonophysics* 77, 283-295.

O'CONNELL, R.J. & BUDIANSKY, B. 1974. Seismic velocities in dry and saturated cracked solids. *J.geophys.Res.* 79, 5412-5426.

ODE, H. 1960. Faulting as a velocity discontinuity in plastic deformation. In: *Rock Deformation.* (edited by Griggs, D. & Handin, J.) *Geol.Soc.Am.Memoir* 79, 293-321.

OFFLER, R. & PRENDERGAST, E. 1984. Significance of illite crystallinity and b_0 values of K-white mica in low grade metamorphic rocks, North Hill End Synclinorium, N.S.W., Australia. *Abstract, Conf. on Diagenesis and Low Temperature Metamorphism,* University of Bristol.

OERTEL, G. 1965. The mechanism of faulting in clay experiments. *Tectonophysics*, 2, 343-393.

OERTEL, G. 1978. Strain determination from the measurement of pebble shapes. *Tectonophysics* 50, T1-T7.

OLSSON,W.A. & PENG,S.S. 1976. Microcrack nucleation in marble. *Int.J.Rock Mech. Min. Sci.* 13, 53 - 59.

ORD, A. & CHRISTIE, J.M. 1984. Flow stresses from microstructures in mylonitic quartzites of the Moine Thrust zone, Assynt area, Scotland. *J.Struct.Geol.* 6, 639-654.

OROWAN, E. 1960. Mechanism of seismic faulting. In: *Rock Deformation.* (edited by Griggs, D. & Handin, J.) *Geol.Soc.Am.Memoir* 79, 323-345.

ORTEGA, E. 1977. La Estructura de la Unidad de Somiedo-Correcilla en el valle del Rio Bernesga (N.W. de Espana). *Brev.Geol.Astur.* 21 (1), 12-16.

OWENS, W.H. 1974. Representation of finite strain by three axis planar diagrams. *Bull.geol.Soc.Am.* 85 307-310.

OWENS, W.H. 1984. The calculation of a best fit ellipsoid from elliptical sections on arbitrarily orientated planes. *J.Struct.Geol.* 6, 571-578.

PARKER, J.M. 1942. Regional systematic jointing in slightly deformed sedimentary rocks. *Bull.Geol.Soc.Am.* 53 381-408.

PATERSON, M.S. 1978. *Experimental Rock Deformation - The Brittle Field.* Springer Verlag, Berlin.

PATERSON, MN.S. & KEKULAWALA, K.R.S.S. 1979. The role of water in quartz deformation. *Bull.Mineral.* 102, 92-98.

PATERSON, S.R. 1983. A comparison of methods used in measuring finite strain from ellipsoidal objects. *J.Struct.Geol.* 5, 611-618.

PECK, L. 1983. Stress corrosion and crack propagation in Sioux Quartzite. *J.geophys.Res.* 88, 5037-5046.

PENG, S. & JOHNSON, A.M. 1972. Crack growth and faulting in a cylindrical sample of Chelmsford Granite. *Int.J.Rock Mech.Min.Sci.* 9, 37-86.

PÉREZ-ESTAÚN, A. 1973. Datos sobre la sucesion estratigrafica del Precambrico y la estructura del extremo sur del antiforme de Narcea. *Brev.Geol.Astur.* 1, 5-16.

PERROUD, H. & BONHOMMET, N. 1981. Palaeomagnetism of the Ibero-Armorican Arc and the Hercynian orogeny in Western Europe. *Nature, Lond.* 292, 445-448.

PERROUD, H., VAN DER VOO, R. & BONHOMMET, N. 1984. Palaeozoic evolution of the Armorica Plate on the basis of palaeomagnetic data. *Geology* 12, 579-582.

PERRY, E. & HOWER, J. 1970. Burial diagenesis in Gulf Coast peletic sediments. *Clays and Clay Minerals* 18 165-177.

PITTMAN, E.D. 1981. Effect of fault-related granulation on porosity and permeability of quartz sandstones, Simpson Group (Ordovician), Oklahoma. *Bull.Am.Ass.Pet.Geol.* 65, 2381-2387.

PLATT, J.P. & BEHRMANN, 1986. Structures and fabrics in a crustal scale shear zone, Betic Cordillera, S.E. Spain. *J.Struct.Geol.* 8, 15-33.

POHN, H.A. 1981. Joint Spacing as a method of locating faults. *Geology* 9, 258-261.

POIRIER, J.P. & GUILLOPE, M. 1979. Deformation induced recrystallisation of minerals. *Bull.Mineral* 102, 67-71.

POLLARD, D.D., SEGALL, P. & DELANEY, P.T. 1982. Formation and interpretation of dilatant echelon cracks. *Bull.Geol.Soc.Am.* 93, 1291-1303.

PRICE, N.J. 1966. *Fault and Joint Development in Brittle and Semi-Brittle Rock*. Pergamon Press, Oxford.

PRIMMER, T.J. 1983. Low-grade regional metamorphism across the Perranporth-Pentavan Line, Cornwall. *Proc.Ussher Soc.* 5, 421-427.

PRIMMER, T.J. 1985. A transition from diagenesis to greenschist facies within a major Variscan fold/thrust complex in southwest England. *Min.Mag.* 49, 365-374.

PRIOR, D.J. & SIMS, A. 1986. Quartz crystallographic fabrics of undeformed sandstones. Abstract, Tectonic Studies Group Annual General Meeting, University of Hull.

QUAKENBUSH, C.L. & FRECHETTE, V.D. 1978. Crack front curvature and Glass Slow Fracture. *J.Am.Ceram.Soc.* 61, 402-406.

RAMSAY, J.G. 1967. *Folding and Fracturing of Rocks*. McGraw-Hill, New York.

RAMSAY, J.G. 1980. The crack-seal mechanism of rock deformation. *Nature, Lond.* 284, 135-139.

RAMSAY, J.G. 1986. The surface fractures of joints in the Jura Mountains, Switzerland. *Abstract, Tectonic Studies Group Annual General Meeting,* University of Hull.

RAMSAY, J.G. & HUBER, M.I. 1984. *The Techniques of Modern Structural Geology, Volume 1: Strain Analysis*. Academic Press, London.

READING, H.G. 1980. Characteristic and recognition of strike slip systems. In: *Sedimentation in Oblique-Slip Mobile Zones* (ed. Ballance, P.F. and Reading H.G.) Int.Assoc.Sedimentologists, Oxford, 7-26.

RECHES, Z. 1978. Analysis of faulting in a three dimensional strainfield. *Tectonophysics* 47, 109-129.

RECHES, Z. 1983. Faulting of rocks in three dimensional strain fields. II. Theoretical Analysis. *Tectonophysics* 15, 133-156.

RECHES, Z. & DIETRICH, J.H. 1983. Faulting of rocks in three dimensional strain fields. I. Failure of rocks in polyaxial, servocontrolled experiments. *Tectonophysics* 95, 111-132.

RETTKE, R.C. 1981. Probable burial diagenetic and provenance effects on Dakota Group clay mineralogy. *J.Sediment.Petrol.* 51, 541-551.

REYNOLDS, R.C. & HOWER, J. 1970. The nature of interlayering in mixed-layer illite-montmorillonites. *Clays and Clay Minerals* 18, 25-36.

RICE, J.R. 1968. Mathematical Analysis in the mechanics of freacture. In: *Fracture* (edited H. Leibowitz) Academic Press, New York.

RICH, J.L. 1934. Mechanics of low-angle overthrust faulting illustrated by Cumberland thrust block, Virginia, Kentucky and Tennessee. *Bull.geol.Soc.Am.* 18, 1584-1596.

RIES, A.C., RICHARDSON, A. & SHACKLETON, R.M. 1980. Rotation of the Iberian Arc; palaeomagnetic results from North Spain. *Earth Planet Sci. Lett.* 70, 301-310.

ROBERTS, J.C. 1961. Feather fractures and the mechanics of rock jointing. *Am.J.Sci.* 259, 481-492.

ROBERTS,B. & MERRIMAN,R.J. 1985. The distinction between Caledonian burial and regional metamorphism in metapelites from North Wales : an anaylsis of isocryst patterns. *J.Geol.Soc.Lond.* 142, 615 - 624.

ROBERTSON, E.C. 1982. Continuous formation of gouge and breccia during fault displacement. *Proc. 23rd Symp. Rock Mech. University California, Berkely* (edited by Goodman, R.E. & Heuze, F.E.) 397-404.

ROBERTSON, E.C. 1983. Relationship of fault displacement to gouge and breccia thickness. *Min.Engng.* 35, 1426-1432.

ROBIN, P-Y.F. 1977. Determination of geologic strain using randomly orientated strain markers of any shape. *Tectonophysics* 42, T7-16.

ROBINSON, D. & BEVINS, R.E. 1986. Incipient metamorphism in the Lower Palaeozoic marginal basin of Wales. *J.geol.Soc.Lond.* 4, 101-113.

ROSS, J.V., AVE LALLEMANT, H.G. & CARTER, N.L. 1980. Stress dependence of recrystallized-grain and subgrain size in olivine. *Tectonophysics* 70, 39-61.

RUDNICKI, J.W. 1980. Fracture Mechanics Applied to the Earth's Crust. *Ann.Rev.Earth Plan.Sci.* 8, 489-525.

RUDNICKI, J.W. & RICE, J.R. 1975. Conditions for the localization of deformation in pressure-sensitive dilatant materials. *J.Mech.Phys.Solids*

23, 371-394.

RUPKE,J. 1965. The Esla Nappe, Cantabrian Mountains (Spain). *Leidse. Geol. Meded.* 32, 1 - 74.

RUTTER, E.H. 1976. The Kinetics of rock deformation by Pressure Solution. *Phil.Trans.R.Soc.* A283, 203-219.

RUTTER, E.H. 1979. The mechanical properties of kaolinite fault 'gouge' at moderate confining pressure, 20^{o}C. *Int.J.Rock Mech.Min.Sci. & Geomech.Abstr.* 16 407-410.

RUTTER, E.H. 1986. On the nomenclature of mode of failure transitions in rocks. *Tectonophysics* 122, 381-387.

RUTTER, E.H., MADDOCK, R.H., HALL, S.H. & WHITE, S.H. 1986. Comparative Microstructures of Natural and Experimentally Produced Clay-Bearing Fault Gouges. *Pure appl.Geophys.* 124, 1-30.

RUTTER, E.H. & MAINPRICE, D.H. 1978. The effect of water on stress relaxation of faulted and unfaulted sandstone. *Pure appl.Geophys.* 116, 634-654.

RUTTER, E.H. & WHITE, S.H. 1979. The effects of water, temperature and time on the microstructural and mechanical properties of experimentally produced fault gouge. *Bull.Mineral* 102, 93-101.

SAGON, J.P. & DUNOYER de SEGONZAC, C. 1972. La cristallinite des micas dans les schistes Paleozoiques et brioveriens du Bassin de Chateaulin (Massif Armoricain). *C.r.hebd.Seances Acad.Sci. Paris, Ser D.* 275, 1023-1026.

SAHA, D. 1983. Intensity of Quartz c-axis fabric and its correlation with strain. *Abstract, Tectonic Studies Group Annual General Meeting*, University of Glasgow.

SASSI, F.P. & SCOLARI, A. 1974. The b_o value of potassic white micas as a Barometric Indicator in Low-Grade Metamorphism of Pelitic Schists. *Contr.Min.Petrol.* 45, 143-152.

SCHEIDDEGGER, A.E. 1983. Interpretation of fracture and physiographic patterns in Alberta, Canada. *J.Struct.Geol.* 5, 1, 53-59.

SCHOLZ, C.H. 1968. Mechanism of Creep in Brittle Rock. *J.geophys.Res.* 73, 3295-3302.

SCHOLZ, C.H. 1972. Static Fatigue of Quartz. *J.geophys.Res.* 77, 2104-2114.

SHIMAMOTO, T. & IKEDA, Y. 1976. A simple algebraic method for strain estimation from deformed ellipsoidal objects. 1. Basic Theory. *Tectonophysics* 36, 315-337.

SIBSON, R.H. 1977. Fault Rocks and Fault Mechanisms. *J.geol.Soc.Lond.* 133, 191-213.

SIBSON, R.H. 1983. Continental fault structure and the shallow earthquake source. *J.geol.Soc.Lond.* 140, 741-767.

SIBSON, R.H. 1985. Stopping of earthquake ruptures at dilational fault jogs. *Nature, Lond.* 316, 248-251.

SIBSON, R.H. 1986. Earthquakes and lineament infrastructure. *Phil.Trans.R.Soc.Lond.* A317, 63-79.

SIBSON, R.H., MOORE J.McM. & RANKIN, A.H. 1975. Seismic pumping - a hydrothermal fluid transport mechanism. *J.geol.Soc.Lond.* 131, 653.

SIDDANS, A.W.B. 1980a. Elliptical markers and non-coaxial strain increments. *Tectonophysics*, 67, T21-25.

SIDDANS, A.W.B. 1980b. Analysis of three-dimensional homogeneous finite strain using ellipsoidal objects. *Tectonophysics* 64, 1-16.

SIMMONS, G. & RICHTER, D. 1976. *Microcracks in Rocks*. Wiley-Interscience, New York.

SIMPSON, C. 1980. Oblique Girdle Orientation Patterns of Quartz c-axes from a Shear Zone in the basement core of the maggia Nappe, Ticino, Switzerland. *J.Struct.Geol.* 1 Note 2.

SIMPSON, C. 1982. Strain and shape variations associated with ductile shear zone. *J.Struct.Geol.* 5, 61-72.

SMITH, D.L. & EVANS, B. 1984. Diffusional Crack healing in quartz. *J.geophys.Res.* 89, 4125-4135.

SPRUNT, E.S. & BRACE, W.F. 1974. Direct observation of microcavities in crystalline rocks. *Int.J.Rock Mech.Min.Sci.* 11, 139-150.

SPRUNT, E.S., DENGLER, L.A. & SLOAN, D. 1978. Effects of metamorphism on quartz cathodoluminescence. *Geology* 6, 305-308.

SPRUNT, E.S. & NUR, A. 1979. Microcracking and Healing in granites: New evidence from Cathodoluminescence. *Science* 205, 495-497.

STADLER, P.J. 1979. Organic and Inorganic Metamorphism in the Tavajannaz Sandstone of the Swiss Alps and equivalent sandstones in France and Italy. *J.Sedim.Pet.* 49, 463-482.

STEARNS, D.W. 1964. Macrofracture Patterns on the Teton Anticline, northwestern Montana. *Trans.Am.geophys.Union (EOS)* 45, 107-108.

STEARNS, D.W. 1968a. Fracture as a mechanism of flow in naturally deformed layered rocks. *Proc. Conf. on Research in Tectonics, Kink Bands and Brittle Deformation*, Ottawa (edited Baer, A.J. and Norris, D.K.).

STEARNS, D.W. 1968b. Certain aspects of fracture in naturally deformed rocks. *N.S.F. Advanced Science Seminars in Rock Mechanics* (edited Riecker, R.E.) Laboratories, Air Force Cambridge research labs., Bedford, Massachusetts, U.S.A.

STEL, M. 1981. Crystal growth in cataclasites: diagnostic microstructures and implications. *Tectonophysics* 78, 585.

SUMMERS, R. & BYERLEE, J. 1977. A note on the effect of fault gouge composition on the stability of frictional sliding. *Int.J.Rock Mech.Min.Sci. & Geomech.Abstr.* 14, 155-160.

SUPPE, J. & MEDWEDEFF, D.A. 1984. Fault propagation folding. *Abs. with Programs geol.Soc.Am.* 16, 670.

SWANSON, P.L. 1980. Stress corrosion cracking in Westerly granite: an investigation by the double torsion technique. Unpublished M.Sc. Thesis, University of Colorado, Boulder.

SWANSON, P.L. 1981. Sub-critical crack propagation in Westerly Granite: An investigation into the Double Torsion Method. *Int.J.Rock Mech.Min.Sci. & Geomech.Abstr.* **18**, 445-449.

SYME GASH, P.J. 1971. A study of surface features relating to brittle and semibrittle fractures. *Tectonophysics* **12**, 349-391.

TAPPONIER, P. & BRACE, W.F. 1976. Development of stress induced microcracks in Westerly granite. *Int.J.Rock Mech.Min.Sci. & Geomech.Abstr.* **13**, 103-112.

TAYLOR, G.I. 1938. Plastic strain in metals. *J.Inst.Met.* **62**, 307-324.

TCHALENKO, J.S. 1970. Similarities between shear zones of different magnitudes. *Bull.geol.Soc.Am.* **81**, 1625-1640.

TEUFEL, L.W. 1981. Pore volume changes during frictional sliding of simulated faults. In: *Mechanical Behaviour of Crustal Rocks.* (edited by Carter, N.L., Friedman, M., Logan, J.M. & Stearns, D.W.), *Am.Geophys.Un. Monogr.* **24**, 135-145.

THOMPSON,, R. 1980. Theory of chemical assisted fracture. *J.Mater.Sci.* **15**, 1014-1026.

TREAGUS, S.H. 1986. Some applications of the Mohr Diagram for three-dimensional strain. *J.Struct.Geol.* **8**, 819-830.

TULLIS, J. & YUND, R.A. 1977. Experimental Deformation of Dry Westerly Granite. *J.geophys.Res.* **82**, 5105-5118.

TURNER, J. 1986. Mesofracture domains controlled by thrust front location in the SW Pyrenean foreland basin. *Abstract, Tectonic Studies Group Annual General Meeting*, University of Hull.

TWISS, R.J. 1977. Theory and applicability of a recrystallised grain size palaeopiezometer. *Pure appl.Geophys.* **115**, 227-244.

UNDERHILL, J. & WOODCOCK, N. 1985. Faulting mechanisms in high porosity sandstones, Permo-Triassic, Arran, Scotland. *Abstract, Tectonic Studies Group Meeting*, University of London.

URAI, J.L., MEANS, W.D. & LISTER, G.S. 1986. Dynamic recrystallisation of minerals. In: *Mineral and Rock Deformation: Laboratory Studies* Geophysical Monograph 26, American Geophysical Union, Washington, 36, 161-199.

VARNER, J.R. & FRECHETTE, V.D. 1971. Fracture marks associated with Transition-region behaviour of Slow cracks in glass. *J.appl.Phys.* **42**, 1983-1984.

VELDE, B. 1965. Phengitic micas: synthesis, stability and natural occurrence. *Am.J.Sci.* **263**, 886-913.

VELDE, B. 1977. Clays and Clay Minerals in natural and synthetic systems. Elsevier, Amsterdam.

VERNON, R.H. 1976. *Metamorphic processes: reactions and microstructure development*. Allen & Unwin, London.

WALKER, G. 1979. *Facies Models*. Geoscience Canada Reprint series 1.

WALLACE, P. 1972. The Geology of the Palaeozoic Rocks of the S.W. part of the Cantabrian Cordillera, North Spain. *Proc.Geol.Assoc.* **83**, 57-73.

WAWERSIK, W.R. & BRACE, W.F. 1971. Post-failure behaviour of a granite and a diabase. *Rock Mech.* 3, 61-85.

WEAVER, C.E. 1960. Possible uses of clay minerals in search for oil. *Bull.Am.Assoc.Petrol.Geol.* **44**, 1505-1518.

WEBER, K. 1972a. Note on the determination of illite crystallinity. *Neues.Jahrb.Mineral Monatshefte* 6, 267-276.

WEBER, K. 1972b. Kristallinitat des Illites in Tonschiefern und undere Kr Kriterion Schwacher metamorphose im nordostlichen Rheinischen Schiefergebirge. *Neues Jb.Geol.Palaont.Abh.* **141**, 333-363.

WHEELER, J. 1984. A new plot to display the srain of elliptical markers. *J.Struct.Geol.* **6**, 417-423.

WHEELER, R.L. 1980. Cross-strike structural discontinuities: possible exploration tool for natural gas in Appalachian overthrust belt. *Bull.Am.Ass.Pet.Geol.* **154**, 2166-2177.

WHEELER, R.L. & DIXON, J.M. 1980. Intensity of Joints: Methods and Applications. *Geology* 8, 230-231.

WHITE, S.H. 1976. The effects of strain on the microstructures, fabrics, and deformation mechanisms in quartzites. *Phil.Trans.R.Soc.* **A283**, 69-86.

WHITE, S.H. 1979. Difficulties associated with palaeostress estimates. *Bull.Mineral.* **102**, 210-215.

WIEDERHORN, S.M. & BOLZ, L.H. 1970. Stress corrosion and static fatigue of glass. *J.Am.Ceram.Soc.* **53**, 543-548.

WILLIAMS, G.D. & CHAPMAN, T.J. 1986. The Bristol-Mendip foreland thrust belt. *J.geol.Soc.Lond.* **143**, 63-73.

WINKLER, H.G.F. 1970. Abolition of metamorphic facies, introduction of the four divisions of metamorphic stage, and of a classification based on isograds in common rocks. *Neues Jahrb.Mineral Monatsh* 5, 189-248.

WINSOR, C.N. 1985. Interpretation of a set of faults across the hinge and limb of a large scale flexure in the Mount Isa district, Queensland, Australia, in terms of fractures relating to the folding process. *J.Struct.Geol.* **7**, 719-725.

WONG, T.F. & BIEGEL, R. 1985. Effects of pressure on the micromechanics of faulting in San Marcos gabbro. *J.Struct.Geol.* **7**, 737-749.

WOODCOCK, N. & FISCHER, M. 1986. Strike-slip duplexes. *J.Struct.Geol.* **8**, 725-735.

ZINKERNAGEL, V. 1978. Cathodoluminescence of quartz and its application to sandstone petrology. *Contr.Sediment* 8, 1-6.

APPENDIX A1

Grain Size and Fabric Measurements

G.M.L.	= Geometric Mean of Linear Intercepts
A.M.L.	= Arithmetic Mean of Linear Intercepts
A.M.D.	= Arithmetic Mean of equivalent Sphere Diameters
C	= Class Interval, mm.
N	= Number of Intercepts
F	= Fabric (G.M.L.X / G.M.L.Y)

SLIDE	G.M.L.	A.M.L. C = 0.1	A.M.D. C = 0.1	A.M.L. C = 0.025	A.M.D. C = 0.025	N	FABRIC

a) Bernesga Valley

SLIDE	G.M.L.	A.M.L.	A.M.D.	A.M.L.	A.M.D.	N	FABRIC
0007BX0	0.1730	0.2130	0.2082	0.2105	0.1728	088	
0007BZ0	0.1469	0.1803	0.1739	0.1786	0.1693	165	1.1787
0007CX0	0.1716	0.2044	0.1997	0.2075	0.1261	114	
0007CZ0	0.1642	0.1964	0.2392	0.1945	0.1277	118	1.0451
0008BX0	0.1337	0.1614	0.1609	0.1622	0.1376	184	
0008BZ0	0.1280	0.1491	0.1775	0.1497	0.1738	227	1.0445
0008CX0	0.1460	0.1699	0.1958	0.1703	0.1606	176	
0008CZ0	0.1315	0.1536	0.1695	0.1527	0.1705	197	1.1103
0011AX0	0.2487	0.3074	0.2840	0.3030	0.1907	108	
0011AZ0	0.1934	0.2332	0.2008	0.2356	0.2000	107	1.2869
0011BX0	0.1980	0.2492	0.2029	0.2456	0.2001	123	
0011BZ0	0.1762	0.2147	0.1962	0.2164	0.1219	136	1.1237
0011CX0	0.1820	0.2278	0.1860	0.2287	0.2147	108	
0011CX2	0.1831	0.2278	0.1864	0.2285	0.1832	108	
0011CZ0	0.1472	0.1883	0.1768	0.1870	0.1326	162	1.2405
0012AX0	0.1383	0.1705	0.1642	0.1703	0.1211	190	1.1104
0012BX0	0.1672					197	
0012BZ0	0.1096	0.1244	0.1332	0.1302	0.1291	223	1.5255
0012CX0	0.1275	0.1573	0.1508	0.1555	0.1116	165	
0012CZ0	0.1040	0.1266	0.1412	0.1238	0.1151	214	1.2260
J012AX0	0.1589	0.1912	0.1965	0.1911	0.1711	119	
J012AZ0	0.1256	0.1529	0.1685	0.1513	0.0938	168	
K012AX0	0.1257	0.1633	0.1539	0.1602	0.0912	150	
K012AZ0	0.1283	0.1494	0.1678	0.1493	0.1206	169	
0016AX0	0.1068	0.1299	0.1497	0.1268	0.1284	163	
0016AX2	0.1597	0.1754	0.2125	0.1796	0.1433	063	
0016AZ2	0.1432	0.1718	0.2127	0.1711	0.1306	087	1.0747
0016BX0	0.1166	0.1355	0.1432	0.1389	0.1178	159	
0016BZ0	0.1047	0.1226	0.1442	0.1241	0.1357	168	1.1137
0016CX0	0.1110	0.1348	0.1460	0.1335	0.0959	099	
0016CZ0	0.0879	0.1036	0.1272	0.1062	0.0927	140	1.2628
0103AX0	0.1494	0.1776	0.1945	0.1773	0.1439	123	
0103AZ0	0.1209	0.1493	0.1567	0.1468	0.1199	140	1.2357
0103BX0	0.1675	0.1990	0.2059	0.2002	0.1832	100	
0103BZ0	0.1194	0.1500	0.1547	0.1497	0.1156	183	1.4028
0103CX0	0.1481	0.1814	0.1706	0.1811	0.1314	153	
0103CZ0	0.1227	0.1452	0.1693	0.1435	0.1417	186	1.2070
0104AX0	0.1598	0.1864	0.2002	0.1815	0.1568	118	
0104AZ0	0.1654	0.1955	0.2621	0.1897	0.1386	112	1.0351
0104BX0	0.1701	0.2015	0.2442	0.2001	0.1627	097	
0104BZ0	0.1695	0.1971	0.2308	0.1942	0.1708	119	1.0035
0104CX0	0.1484	0.1848	0.1905	0.1806	0.1699	115	
0104CZ0	0.1576	0.1796	0.2359	0.1806	0.1699	108	1.0620
0105AX0	0.1375	0.1610	0.1720	0.1641	0.1444	091	
0105AZ0	0.1381	0.1640	0.2108	0.1622	0.1162	108	1.0620
0105BX0	0.1280					121	
0105BZ0	0.1150	0.1359	0.1516	0.1352	0.1595	200	1.1130
0105CX0	0.1120	0.1371	0.1527	0.1383	0.1306	150	
0105CZ0	0.1170	0.1396	0.1476	0.1341	0.1399	166	1.0447
0106AX0	0.1272	0.1462	0.1871	0.1452	0.1452	133	
0106AZ0	0.0938	0.1109	0.1331	0.1097	0.1183	198	1.3561
0106BX0	0.1263	0.1407	0.1787	0.1414	0.1730	097	
0106BZ0	0.1051	0.1221	0.1572	0.1179	0.1422	129	1.2017
0106CX0	0.1077	0.1271	0.1361	0.1297	0.1189	179	
0106CZ0	0.0728	0.0846	0.1141	0.0875	0.0941	162	1.4794

0107CX0	0.1809	0.2212	0.1986	0.2228	0.1461	073	
0107CZ0	0.1615	0.1755	0.1856	0.1795	0.1595	047	1.1201
0109AX0	0.1463	0.1784	0.1733	0.1723	0.1781	158	
0109AZ0	0.1400	0.1678	0.1680	0.1660	0.1453	154	1.0450
0109BX0	0.1421	0.1768	0.1716	0.1782	0.1551	067	
0109BZ0	0.1507	0.1767	0.2315	0.1735	0.1714	086	1.0606
0109CX0	0.1652	0.2004	0.1865	0.2017	0.1801	123	
0109CZ0	0.1490	0.1771	0.2120	0.1743	0.1626	129	1.1087
0110AX0	0.1354	0.1594	0.1672	0.1610	0.1544	149	
0110AZ0	0.1195					142	1.1331
0110BX0	0.1316	0.1642	0.1750	0.1595	0.1368	134	
0110BZ0	0.1099	0.1305	0.1475	0.1312	0.1257	159	1.1975
0110CX0	0.1297	0.1488	0.1574	0.1554	0.1386	162	
0110CZ0	0.1273	0.1482	0.1563	0.1498	0.1468	163	1.0189
0111XX0	0.1238	0.1389	0.1645	0.1412	0.1510	162	
0111XZ0	0.1087	0.1186	0.1469	0.1215	0.1351	194	1.1389
0111YX0	0.1591	0.1849	0.2043	0.1848	0.1754	129	
0111YZ0	0.1397	0.1589	0.1756	0.1608	0.1526	146	1.1389
0111ZX0	0.1196	0.1348	0.1522	0.1374	0.1446	191	
0111ZZ0	0.1184	0.1361	0.1693	0.1341	0.1189	198	1.0101

b) Punta Del Sol

00V1DX0	0.0905	0.1094	0.1241	0.1100	0.0945	192	
00V1DZ0	0.0696	0.0803	0.1111	0.0779	0.1111	244	1.3000
00V1FX0	0.0786	0.0969	0.1181	0.0971	0.0874	177	
00V1FZ0	0.0805	0.0969	0.1187	0.0972	0.0838	177	1.0242
00V5DX0	0.0709	0.0866	0.1139	0.0853	0.0823	161	
00V5DZ0	0.0653	0.0725	0.1093	0.0745	0.0840	187	1.0856
00V5FX0	0.0768	0.0897	0.1130	0.0939	0.0941	199	
00V5FZ0	0.0559	0.0665	0.1057	0.0663	0.0746	206	1.374
00V8DX0	0.0726	0.0814	0.1125	0.0833	0.0896	210	
00V8DZ0	0.0701	0.0844	0.1127	0.0848	0.0829	224	1.0360
00V8FX0	0.0656	0.0784	0.1100	0.0774	0.0837	222	
00V8FZ0	0.0522	0.0624	0.1047	0.0604	0.0656	290	1.2567
00V9DX0	0.0858	0.0951	0.1231	0.0975	0.0990	175	
00V9DZ0	0.0806	0.0920	0.1201	0.0919	0.1014	200	1.0645
00V9EX0	0.0901	0.1038	0.1254	0.1049	0.1067	184	
00V9EZ0	0.0802	0.0900	0.1192	0.0936	0.1064	220	1.1230
0V10DX0	0.0817	0.0962	0.1195	0.0976	0.0895	158	
0V10DZ0	0.0697	0.0846	0.1135	0.0829	0.0796	153	1.1722
0V10FX0	0.0765	0.0908	0.1163	0.0922	0.0864	191	
0V10FZ0	0.0650	0.0730	0.1088	0.0757	0.0836	191	1.1769
0V12DX0	0.0699	0.0809	0.1113	0.0827	0.0895	181	
0V12DZ0	0.0647	0.0795	0.1107	0.0795	0.0795	200	1.0803
0V12FX0	0.0739	0.0849	0.1124	0.0890	0.0930	212	
0V12FZ0	0.0651	0.0725	0.1087	0.0744	0.0809	236	1.1352

APPENDIX A2

Summary of Microstructural Observations

G.M.L.	= Sample Geometric Mean of Linear Intercepts
A.M.L.	= Sample Arithmetic Mean of Linear Intercepts
G.Boundaries	= Types defined in 3.4 for a) - c) and 8.3 for d).
Pores	= Types defined in 3.4
G.M.A.	= Sample Geometric Mean of Extinction Angles
D(mm^{-2})	= Microfracture Density per square millimetre
C/P	= Compact/Porous Microstructure

SAMPLE	G.M.L.	A.M.L.	G.BOUNDARIES	PORES	G.M.A.	D(mm^{-2})	C/P
a) Bernesga Valley,Cremenes,Luna Lake							
1			2a,b,1a,b,4b	1	4.501	2.69	C
2			1a,b,2b	1,2,3	3.026		C
3			2a,b,1a	1,2		5.10	C
5			1a	1a	3.288	17.3	C
6			1a,b	1,2	2.831	13.1	C
7	0.1640	0.1985	1a,2	2	3.660		C
8	0.1309	0.1585	4b,2b,1a	1b,3	3.357	2.84	C
9			1,2,4	1	2.667	8.29	C
10			1a,1b,2a,2b	1	3.886	7.11	C
11	0.1910	0.2055	1	1	5.926	18.8	C
12	0.1308	0.1469	1a,2b	1,2	3.671		C
13			1a,4	2,3	2.635		C
14			4,1	3	3.693	6.16	P
15			1a,4	3,2			P
16	0.1161	0.1368	1a,4	3,4	3.693	7.53	P
17			4,1	3,4	4.151	6.59	P
18			1b,1a,2a	1a			C
19			4b,1	1b,4	3.465		C
20			2a,4b,1	1a,b	3.521		C
23			4,1a	3	2.787	5.91	P
26			1a,4	1b			C
27			1a,1b,4	1a,2,3			C
28			1	1a,2,3	3.125		C
31			1	4	3.684		C
33			1a	4	3.293		C
103	0.1380	0.1671	1b,2a,b	1a	4.242		C
104	0.1618	0.1908	1a	2	4.081		C
105	0.1246	0.1475	1	1b	3.235		C
106	0.1055	0.1219	1a	2	3.313	18.2	C
107	0.1712	0.1984	1b	2	4.698	33.2	C
109	0.1489	0.1795	1,2b	1a	2.725	7.58	C
110	0.1282	0.1502	1,2a	3,2	3.216		C
111	0.1282	0.1454	1,2a	1,2	3.670	20.8	C
b) Punta Vidrias							
CV1			1		3.922		C
CV2			1,2		3.002	8.2	C
CV4			1		10.906	14.8	C
CV5			1,5		4.772	16.3	C
CV6			1		5.339	8.8	C
CV7			1b		3.382	13.1	C
c) Luarca							
36			1,3		7.316		C
37					8.942		C
38			5,3,1b		13.860		C
39			1,5,3		7.499		C
40			3,5		11.704		C
41			1,5,3		9.183		C
42			3,5		12.718		C
43			1,3		8.154		C
44			1,5,3		8.852		C

d) Punta Del Sol

V1	6,3	2,B	7.592
V5	6,3,5	2,B	9.729
V8	6,3,5	3+1,B	11.427
V9	3,5	3+1,2,4	4.830
V10	3,6	3+1,2,B	8.967
V12	6	E	7.159

APPENDIX A3

Point Count Measurements by Sample

For a) to c):

1+2 = % Unsheared Quartzite
3 = % Shear Matrix
4 = % Iron Oxides in Shear Matrix
5 = % Iron Oxides in Unsheared Quartzite
6 = % Clay Minerals
7 = % Present Porosity
8 = % Porosity before cataclasis
9 = Microfracture Density (D mm^{-2})
10 = Illite Crystallinity, Kubler Index ($^{o}2\theta$)
11 = Sample Geometric Mean of Extinction Angle
12 = Iron Oxide enrichment in Shear Matrix

For d)

1+2 = % Old Grains
3 = % New Grains
4 = % Epidote
5 = % Iron Oxides
6 = % Muscovite
7 = % Present Porosity
8 = % 4 + 5 + 6
9 = % Recrystallisation from point count (2/(1+2) x 100%)
10 = Illite Crystallinity, Kubler Index ($^{o}2\theta$)
11 = Sample Geometric Mean of Extinction Angles
12 = % Recrystallisation from linear intercept measurements

SAMPLE	1+2	3	4	5	6	7	8	9	10	11	12
a) Bernesga Valley											
1	92.4	0.0	0.0	5.3	0.1	2.1	7.5	2.69	0.581	4.501	
2	80.8	5.5	2.3	4.7	0.2	6.5	12.3		0.606	3.026	8.2
3	26.1	62.5	8.1	2.3	0.0	6.5	25.2	5.10			2.0
5	89.9	4.8	0.5	3.6	0.0	1.2	5.1	17.3		3.288	2.7
6	80.8	11.5	0.7	4.7	0.1	2.3	8.1	13.1		2.831	1.2
7	69.6	22.6	2.4	4.1	0.2	1.1	7.8			3.660	1.9
8	87.6	1.3	0.0	3.3	1.1	5.8	10.5	2.84	0.625	3.357	0.0
9	78.6	12.0	3.5	4.9	0.3	0.7	7.0	8.29	0.556	2.667	1.8
10	84.7	8.9	1.4	4.5	0.0	0.6	3.7	7.11		3.886	3.1
11	60.7	35.8	1.2	1.2	0.0	1.1	8.4	18.8		5.926	1.8
12	78.3	7.6	3.5	6.5	0.1	0.6	8.6			3.671	6.1
13	78.6	0.3	0.1	15.5	2.0	3.5	21.1		0.663	2.635	2.1
14	77.6	0.0	0.0	7.2	7.3	7.9	15.7	6.16	0.925	3.693	
15	73.4	1.0	0.2	19.2	1.0	5.2	21.6		0.919		1.0
16	72.5	3.8	2.4	10.3	2.2	11.7	17.6	7.53	0.850	3.693	5.9
17	67.8	4.1	0.7	10.9	5.5	11.3	19.5	6.59	0.950	4.151	1.5
18	80.7	9.8	1.4	4.6	0.0	3.5	5.4		0.650		2.8
19	53.4	19.3	8.5	13.9	0.6	3.4	21.4		0.563	3.465	2.3
20	88.1	0.0	0.0	10.6	0.1	1.1	11.8		0.663	3.521	
23	72.8	0.0	0.0	22.4	2.6	2.2	27.2	5.91	0.816	2.787	
26	73.9	10.0	1.1	12.9	0.1	1.9	16.8		0.600		0.8
27	73.0	9.4	1.0	12.9	0.2	3.4	17.3		0.619		0.8
28	87.7	1.2	0.0	5.8	0.0	5.2	11.1		0.640	3.125	0.0
31	29.1	58.3	7.5	1.2	0.0	4.3	4.0			3.684	3.7
33	86.5	1.5	0.4	6.9	0.1	5.9	7.5		0.699	3.293	3.9
104	90.2	0.0	0.0	8.5	0.1	1.1	8.7		0.406	4.081	
105	84.7	0.0	0.0	15.2	0.1	0.0	15.3		0.388	3.235	
106	69.3	2.2	1.1	13.3	8.6	5.5	24.0	18.2	0.438	3.313	3.6
107	58.1	27.3	4.0	7.9	0.7	1.8	12.9	33.2		4.698	1.3
109	53.4	34.6	7.5	3.3	0.1	0.8	7.3	7.58	0.700	2.725	3.8
110	88.1	0.5	0.1	11.1	0.1	0.2	11.5		0.762	3.216	1.8
111	86.0	7.7	0.9	4.4	0.1	0.6	5.6	20.8		3.670	2.4
b) Punta Vidrias											
CV1	86.0	0.0	0.0	10.2	0.8	1.1	12.1		0.475	3.922	
CV2	88.2	0.6	0.3	7.0	0.4	3.5	11.0	8.2	0.356	3.002	4.7
CV4	42.1	52.1	2.3	1.7	0.0	0.3	4.5	14.8	0.400	10.906	1.1
CV5	86.3	1.3	0.0	9.6	2.7	0.1	12.6	16.3	0.361	4.772	0.0
CV6	46.0	39.4	12.7	1.2	0.1	0.6	4.0	8.83	0.444	5.339	2.5
CV7	94.9	1.1	0.2	3.3	0.1	0.3	3.8	13.1	0.412	3.382	4.6
c) Punta Del Sol											
V1D	22.6	62.8	0.0	1.0	4.4	9.2	14.6	73.0		7.560	86.0
V1E	40.4	53.8	0.0	1.6	1.4	2.8	5.8	57.1		7.464	
V1F	18.6	72.0	0.0	2.6	0.8	6.0	9.4	79.5		7.781	83.0
V1	27.2	62.9	0.0	1.7	2.2	6.0	9.9	69.9	0.281	7.592	
V5D	25.0	64.8	0.0	7.6	0.8	1.8	10.2	72.1		9.810	91.6
V5E	25.6	70.0	0.2	2.2	2.0	0.0	4.2	73.2		9.268	
V5F	20.6	70.4	0.0	5.4	2.0	1.4	8.8	77.4		9.857	81.5
V5	23.7	68.4	0.1	5.1	1.5	1.7	8.3	74.2	0.339	9.729	
V8D	9.2	84.8	0.2	4.2	0.6	1.0	5.8	90.2		12.12	81.2
V8E	8.4	87.0	0.4	0.2	4.2	0.2	4.6	91.0		12.57	
V8F	9.6	85.8	0.2	0.6	3.6	0.2	4.4	89.9		9.756	85.0
V8	9.1	85.9	0.3	1.7	2.8	0.5	5.0	90.4	0.188	11.43	

V9D	87.4	2.0	0.2	0.6	5.6	4.2	10.4	2.2		4.957	
V9E	88.8	0.2	0.0	3.4	4.2	2.8	10.4	0.2		4.943	
V9F	92.4	0.4	0.0	1.2	2.4	0.2	3.8	0.0		4.598	
V9	89.0	0.1	0.1	2.1	4.9	3.1	10.1	0.8		4.830	
V10D	48.0	37.0	0.0	3.6	1.8	9.6	15.0	43.5		8.699	62.4
V10E	49.0	48.6	0.0	0.2	1.4	0.8	2.4	41.0		9.926	
V10F	35.6	54.4	0.0	1.0	1.2	7.8	10.0	60.0		8.347	66.0
V10	44.2	46.7	0.0	1.6	1.5	6.1	9.2	48.2	0.197	8.967	
V12D	9.8	82.6	0.2	5.8	1.4	1.4	8.6	89.4		8.872	
V12E	3.6	89.2	0.0	3.0	0.0	2.8	5.8	99.4		7.187	
V12F	0.6	92.4	0.0	1.6	5.6	5.4	12.6	96.1		5.754	
V12	4.7	88.1	0.1	3.5	0.5	3.2	7.2	95.0	0.481	7.159	

d) Tarskavaig, Isle of Skye

T6	51.6	46.7	0.0	0.1	0.9	0.5	2.8	23.6		3.364	
T7	22.4	71.8	5.6	0.3	0.0	0.1	1.8	28.9		3.857	5.5
T11	84.2	11.8	0.2	0.3	1.2	2.2	5.3	20.7			4.9
T12	69.0	26.0	0.2	0.2	3.6	1.2	7.2	20.9			3.1
T32	94.9	0.0	0.0	0.6	4.2	0.3	5.1	14.3		4.365	

APPENDIX A4

Point Count and Microfracture Density Measurements by slide

1+2 = % Unsheared Quartzite

3 = % Shear Matrix

4 = % Iron Oxides In Shear Matrix

5 = % Iron Oxides In Unsheared Quartzite

6 = % Clay Minerals

7 = % Present Porosity

8 = % Porosity before cataclasis

9 = Microfracture Density per square millimetre (Dmm^{-2})

10 = Geometric Mean of Extinction Angles (G.M.A.)

11 = Number of Grains per square millimetre (Gmm^{-2})

12 = Microfracture Density per grain (DG^{-1})

SAMPLE	1+2	3	4	5	6	7	8	9	10	11	12
a) Bernesga Valley,Cremenes,Luna Lake											
1A	92.8	0.0	0.0	2.2	0.4	4.6	7.2	2.69	4.412	12.5	0.214
3A	36.9	49.8	7.4	3.8	0.0	2.4	14.4	5.10		20.7	0.254
5A	85.2	8.8	0.8	3.2	0.0	1.8	11.6	17.3	3.173	15.8	1.11
6A	80.8	8.2	0.4	6.0	0.2	4.4	5.5	13.1	3.389	13.9	0.936
8B	91.0	0.0	0.0	5.2	0.4	3.4	9.0	2.84	3.389	15.9	0.187
9A	67.6	18.6	3.2	7.4	0.2	1.0	8.9	8.29	2.839	25.5	0.360
10A	78.0	14.4	2.6	2.4	0.0	1.6	4.9	7.11	4.064	11.4	0.604
11A	63.6	29.4	2.2	2.2	0.0	0.2	3.6	18.8	5.485	7.3	2.55
14A	76.0	0.0	0.0	4.4	12.8	6.6	18.6	6.16	3.325	16.8	0.351
16A	54.6	9.2	6.8	15.6	1.0	12.8	23.5	7.53	4.232	24.2	0.389
17A	76.2	0.0	0.0	5.4	5.8	11.2	12.8	6.59	4.137	24.7	0.284
23	71.6	0.0	0.0	22.4	2.6	2.2	27.2	5.91	2.787	40.9	0.147
106A	62.6	4.5	2.7	10.1	9.0	1.6	23.4	18.2	3.455	29.8	0.610
107A	72.1	26.4	1.5	4.4	2.1	2.5	8.3	33.2	5.303	14.5	2.410
109A	73.0	21.4	0.4	2.6	0.2	2.0	6.2	7.85	2.160	10.9	0.723
111Y	91.0	4.8	0.0	3.8	0.2	0.0	4.2	20.8	3.193	16.1	1.300
b) Punta Vidrias											
CV2X	90.4	0.0	0.0	2.6	1.0	6.0	9.6	8.23	3.102	16.1	0.512
CV4U	36.4	59.2	1.8	2.0	0.0	0.4	6.2	14.8	14.85	9.4	1.500
CV5U	84.5	4.0	0.0	8.1	3.4	0.0	11.9	16.3	3.921	22.4	0.725
CV6X	57.0	29.0	9.8	2.7	0.0	1.3	6.6	10.8	5.699	32.8	0.427
CV7U	93.6	2.4	0.4	3.4	0.2	0.0	3.7	13.1	3.682	18.4	0.706

APPENDIX A5

Summary of 3 Dimensional Strain Data

E_1 - E_3 = Maximum, intermediate and minimum natural strain

γ_o = Natural Octahedral Unit Shear, $2/3((E_1-E_2)^2+(E_2-E_3)^2+(E_3-E_1)^2)^{1/2}$

E_s = Natural Shear Strain, $(3/2)^{1/2}\gamma_o$

ν = Lode's Parameter, $2E_2-E_1-E_3/(E_1-E_3)$

θ = Arctan (ν)

k = Logarithmic Flinn Parameter, $E_1-E_2/(E_2-E_3)$

ρ = Owen's goodness of fit parameter

SAMPLE	E_1	E_2	E_3	γ_0	E_s	ν	θ	k	ρ
a) Bernesga Valley									
14	0.335	-0.051	-0.284	0.538	0.466	-0.247	-8.12	1.65	1.24
28	0.111	0.029	-0.140	0.209	0.181	0.347	11.33	0.481	1.11
b) Punta Vidrias and Cabo de Peñas									
CV1	0.077	0.018	-0.095	0.143	0.124	0.314	10.28	0.515	1.07
ACV5	0.395	0.219	-0.613	0.879	0.761	0.651	20.60	0.212	1.26
BCV5	0.655	-0.157	-0.498	0.967	0.838	-0.408	-13.25	2.381	1.07
CCV5	0.561	-0.050	-0.511	0.878	0.760	-0.140	-4.621	1.325	1.06
DCV5	0.219	-0.009	-0.211	0.351	0.304	-0.060	-1.98	1.129	1.20
ECV5	0.292	0.076	-0.368	0.550	0.476	0.345	11.27	0.486	1.40
102	0.319	-0.017	-0.302	0.508	0.440	-0.082	-2.715	1.179	1.25
A102	0.417	0.193	-0.610	0.881	0.763	0.564	18.03	0.279	1.20
c) Luarca									
38	0.274	0.080	-0.353	0.524	0.453	0.381	12.41	0.448	1.05
39	0.258	0.086	-0.344	0.506	0.433	0.429	13.91	0.384	1.23
40	0.330	-0.015	-0.315	0.527	0.456	-0.070	-2.31	1.151	1.01
41	0.347	-0.134	-0.213	0.495	0.429	-0.718	-22.51	6.088	1.01
d) Punta Del Sol									
V1	0.222	0.092	-0.313	0.456	0.395	0.514	16.53	0.321	1.21
V5	0.199	0.073	-0.272	0.398	0.345	0.465	15.03	0.365	1.10
V8	0.082	0.052	-0.135	0.192	0.166	0.724	22.67	0.160	1.03
33V10	0.206	-0.065	-0.140	0.297	0.257	-0.566	-18.10	3.61	1.30
22V10	0.205	0.019	-0.224	0.351	0.304	0.133	4.390	0.765	1.30
11V10	0.097	0.032	-0.129	0.190	0.165	-0.425	-13.78	0.404	1.30
V12	0.373	0.016	-0.390	0.623	0.539	0.064	2.120	0.879	1.04
e) Viavellez, Tapia									
VZ1	0.261	-0.057	-0.204	0.388	0.336	-0.368	-11.99	2.160	1.03
TA1	0.367	-0.026	-0.342	0.580	0.502	-0.109	-3.590	1.244	1.15
TA3	0.249	-0.039	-0.210	0.379	0.328	-0.255	-8.370	1.684	1.42

APPENDIX A6

Microfracture Density Measurements in Cathodoluminescence

D (mm^{-2}) = Microfracture Density per square millimetre

D (G^{-1}) = Microfracture Density per grain

F_x(mm^{-1}) = Microfracture Frequency in arbitrary direction

F_z(mm^{-1}) = Microfracture Frequency perpendicular to x

D (mm^{-1}) = Microfracture Density calculated from F_x and F_z

SAMPLE	$D(mm^{-2})$ Initial	$D(mm^{-2})$ Final	$D(G^{-1})$ Initial	$D(G^{-1})$ Final	$F_x(mm^{-1})$	$F_z(mm^{-1})$	$D(mm^{-1})$
a) Bernesga Valley							
5A		17.3		1.11	2.211	1.263	2.546
6A		13.1		0.936	2.199	1.941	2.932
8B		2.84		0.187	2.038	0.691	2.152
9A		8.39		0.360	2.712	1.829	3.271
14	2.124	6.16	0.149	0.351			
106A	3.476	18.2	0.424	0.610			
107A	10.430	33.2	3.094	2.410	6.805	3.362	7.590
109A		7.85	0.613	0.723			
109B		1.12					
109C	3.360		0.528				
R109C	3.310		0.577				
111Y		20.8		1.300	4.268	2.673	5.035
b) Punta Vidrias							
CV4U	5.883	14.8	1.435	1.50			
CV5U		16.3	0.486	0.725			
CV5V	6.605		0.324				
CV5W	6.083		0.353				

APPENDIX A7

Geometric Means of Extinction Angles

A,D,L,R,U,X
B,E,M,S,V,Y   Index of slide (see 3.2)
C,F,N,T,W,Z

R = Repeated measurement

V = Crystals in Vein

D.L. = Grains with Deformation Bands

G = Grains in shear matrix

N = New grains

AVERAGE = Average Geometric Mean of Extinction Angles from 3 perpendicular sections

N = Number of Measurements

SAMPLE	SLIDE ADLRUX	SLIDE BEMSVY	SLIDE CFNTWZ	AVERAGE	N
a) Bernesga Valley,Cremenes,Luna Lake					
1	4.412	4.734	4.027	4.424	150
2	3.026			3.026	100
5	3.173	3.636	3.087	3.288	150
6	3.389	2.477	2.686	2.831	150
7	4.135	3.294	3.578	3.660	150
8	3.641	3.389	3.141	3.357	150
9	2.830	2.607	2.641	2.667	150
10	4.064	3.225	4.480	3.887	150
11	5.797	6.505	6.023	6.101	150
R11	5.485	5.812	5.733	5.751	150
12	3.174	3.956	3.939	3.671	150
14	3.325	3.572	4.241	3.693	150
16	4.232	3.868	3.803	3.963	150
17	4.137	4.197	4.120	4.151	150
19				3.465	150
20	3.860	3.326	3.401	3.521	150
23				2.787	50
28	2.731	3.287	3.400	2.622	150
31	3.620	3.559	3.840	3.684	150
33	3.552	3.122	3.220	3.293	150
103	4.471	3.890	3.528	3.901	150
104	4.211	4.091	3.923	4.081	150
105	3.223	3.109	3.377	3.235	150
106	3.455	3.415	3.288	3.313	150
107	5.303	4.632	4.427	4.698	150
109	2.610	2.621	2.815	2.725	150
110	3.525	3.151	2.996	3.216	150
111	3.708	3.193	4.175	3.670	150
R111	2.225	2.461	2.912	2.496	153
b) Punta Vidrias and Cabo de Peñas					
CV1	4.957	3.178	4.159	3.922	150
CV2	3.102	2.981	2.925	3.002	150
VCV2	21.475	9.228			18
CV4	14.847	9.574	8.988	10.906	150
VCV4	3.668				45
DLCV4	16.676				45
CV5	3.921	5.734	5.315	4.772	150
CV6	5.699	5.399	5.315	5.339	150
GCV6	5.399				50
CV7	3.682	3.250	3.321	3.382	150
102	7.125	7.389	8.265	7.613	150
c) Luarca					
36	8.095	7.335	6.595	7.316	150
37				8.942	159
38	14.846	14.07	12.760	13.860	150
39	7.890	7.804	7.404	7.645	159
R39	7.112	6.976	7.773	7.352	150
40	12.048	11.533	11.533	11.704	150
41	9.017	10.200	8.133	9.183	150
42	12.073	11.694	14.230	12.718	150
43	7.952	9.093	6.826	8.154	205
44				8.852	111

d) Punta Del Sol

V1	7.526	7.464	7.787	7.592	151
NV1	1.963				53
RV1	8.520				50
V5	9.810	9.268	9.857	9.729	157
V8	12.118	12.569	9.796	11.427	150
NV8	2.281				53
V9	4.957	4.943	4.598	4.830	150
V10	8.699	9.926	8.967	8.967	304
V12	8.872	7.187	5.754	7.159	301
VV12	4.336				38

e) West Asturian - Leonese Zone

N1	10.049	8.716	8.279	8.990	301
VZ1	5.924	5.218	6.096	5.722	312
VZ3	4.108	3.977	3.556	3.897	308
CB1	19.327	21.012	20.294	20.195	305
TA1	12.904	12.974	10.585	12.194	302
TA3	15.990	13.276	11.017	13.181	316

APPENDIX A8

Illite Crystallinity Measurements with Absolute and % Errors

R = Repeated Measurement

Size Fraction in micrometres (μ) from 0.45 μ to value given.

Lithology:

Q = Quartzite
S = Shale
G = Gouge
V = Volcaniclasite

SAMPLE	SIZE FRACTION	KUBLER INDEX ($^{o}2\theta$)	+/-	+/-%	WEAVER INDEX	+/-	+/-%	LITHOLOGY
a) Bernesga Valley								
1	2.0	0.581	0.031	5.38	2.753			Q
2	1.6	0.996	0.070	7.11	1.492	0.016	1.099	Q
2	2.0	0.606	0.006	1.04	2.675	0.133	4.972	Q
8	1.6	0.625			2.290	0.029	1.230	Q
9	2.0	0.556	0.031	5.63	2.478			Q
13	2.0	0.663	0.013	1.89	1.939			Q
R13	2.0				1.933			Q
13	20.0	0.575	0.013	2.17	2.223			Q
14	1.6	0.866			1.555	0.090	5.79	Q
14	2.0	0.925	0.013	1.35	1.620	0.119	7.32	Q
R14	2.0				1.647			Q
14	20.0	0.894	0.019	2.10	1.451	0.012	0.80	Q
15	1.6	0.913			1.439	0.003	0.20	Q
15	2.0	0.919	0.006	0.68	1.924	0.175	9.10	Q
15	20.0	0.875	0.013	1.43	1.756			Q
16	1.6	0.931			1.539	0.009	0.60	Q
R16	1.6				1.364			Q
16	2.0	0.850	0.013	1.47	1.877	0.054	0.29	Q
16	20.0	0.931	0.019	2.01	1.760	0.021	1.21	Q
17	1.6	0.894			1.955	0.004	0.21	Q
17	2.0				1.930			Q
R17	2.0	0.950	0.000	0.00	1.682	0.009	0.51	Q
17	20.0	0.938	0.000	0.00	1.533	0.093	5.71	Q
18	2.0	0.650	0.025	3.85	1.949	0.213	10.90	Q
18	20.0	0.650	0.000	0.00	2.341			Q
19	2.0	0.663	0.013	1.88	2.032	0.228	11.22	Q
19	20.0	0.563	0.163	29.0	2.618			Q
20	2.0	0.663	0.025	3.77	3.146			Q
20	20.0	0.581	0.019	3.20	2.483	0.151	6.06	Q
22	2.0	0.667	0.417	6.25	2.045			Q
22	20.0	0.638	0.038	5.88	2.863			Q
23	20.0	0.816	0.008	1.00	1.433	0.366	25.51	Q
26	2.0	0.600	0.050	8.30	2.069	0.279	13.44	Q
26	20.0	0.556	0.019	3.37	1.550	0.358	22.95	Q
27	2.0	0.606	0.006	1.00	2.100	0.051	2.43	Q
R27	2.0	0.631	0.006	0.99				Q
27	20.0	0.544	0.006	1.15	1.504	0.167	11.10	Q
28	2.0	0.655	0.018	2.67	2.105			Q
R28	2.0	0.625	0.025	4.00				Q
28	20.0	0.638	0.013	1.96	2.340			Q
32	2.0	0.588	0.038	6.38	2.510			Q
32	20.0	0.663	0.000	0.00	2.758			Q
33	2.0	0.669	0.034	5.04	1.996			Q
33	20.0	0.513	0.025	4.80	2.120			Q
104	2.0	0.406	0.019	4.60	7.757	1.788	23.00	Q
104	20.0	0.369	0.006	1.69				Q
105	2.0	0.388	0.013	3.20	4.678	0.131	2.80	Q
105	20.0	0.354	0.013	3.53				Q
106	2.0	0.438	0.000	0.00	3.510	0.367	10.40	Q
109	2.0	0.700	0.100	14.30	1.763	0.107	6.00	Q
R109	2.0	0.700	0.100	14.30				Q
110	2.0	0.856	0.069	8.00	1.441	0.038	2.60	Q
R110	2.0	0.669	0.031	4.67				Q
112	2.0	0.801	0.038	4.70	1.727	0.016	0.90	S

112	20.0	0.694	0.044	6.30				S
113a	2.0	0.481	0.019	3.90	2.481	0.053	2.12	Q
113a	20.0	0.458	0.043	9.28				Q
113b	2.0	0.931	0.076	8.16	1.484	0.024	1.58	S
113b	20.0	0.788	0.000	0.00				S
114	2.0	0.806	0.013	1.60	1.650	0.039	2.36	S
114	20.0	0.700	0.025	3.57				S
115	2.0	0.644	0.019	2.91	2.168	0.140	6.46	Q
115	20.0	0.644	0.019	2.91				Q
116	2.0	0.719	0.082	11.00	2.123	0.234	11.00	S
116	20.0	0.563	0.025	4.44				S
117	20.0	0.419	0.006	1.49				S
119	2.0	0.644	0.006	0.90	2.087	0.015	0.69	Q
119	20.0	0.606	0.006	1.03				Q
120	2.0	0.663	0.013	1.89	2.035	0.004	0.19	S
120	20.0	0.538	0.025	4.65				S
121	2.0	0.744	0.019	2.50	1.821	0.005	0.25	S
121	20.0	0.513	0.025	4.87				S
136	2.0	0.563	0.050	8.80	2.373	0.142	5.96	Q
R136	2.0	0.628	0.010	1.50				Q
137	2.0	0.500	0.000	0.00	2.316	0.049	2.12	S
137	20.0	0.381	0.006	1.64				S
138	2.0	0.844	0.031	3.70	1.606	0.890	0.55	S
138	20.0	0.763	0.100	13.11				S
139	2.0	0.863	0.013	1.45	1.626	0.014	0.86	S
139	20.0	0.731	0.019	2.56				S
140	2.0	0.663	0.013	1.89	2.035	0.004	0.19	S
140	20.0	0.819	0.044	5.34				S
141	2.0	0.881	0.056	6.82	1.466	0.062	4.23	S
141	20.0	0.788	0.025	3.17				S
142	2.0	0.825	0.013	1.50	1.608	0.026	1.62	S
142	20.0	0.731	0.019	2.56				S
143	2.0	0.906	0.056	6.20	1.453	0.024	1.65	S
143	20.0	0.719	0.006	0.87				S
144	2.0	0.863	0.025	2.90	1.476	0.013	0.88	S
144	20.0	0.794	0.031	3.94				S
145	20.0	1.150	0.038	3.26				S
146	20.0	0.913	0.050	5.50				S
147	2.0	1.056	0.094	3.88	1.573	0.069	4.39	S
147	20.0	0.781	0.169	21.61				S
148	2.0	0.481	0.189	3.90	2.856	0.002	0.07	S
148	20.0	0.381	0.006	1.64				S
150	2.0	0.625	0.013	2.00	2.025	0.007	0.35	S
150	20.0	0.475	0.013	2.63				S
151	2.0	0.900	0.000	0.00	1.212	0.010	0.79	Q
151	20.0	0.750	0.013	1.67				Q
152	2.0	0.543	0.018	3.20	2.271	0.026	1.17	S
152	20.0	0.475	0.013	2.63				S
153	2.0	0.906	0.006	0.69	1.620	0.018	1.11	G
153	20.0	0.825	0.013	1.52				G

b) Punta Vidrias and Cabo de Peñas

CV1	2.0	0.475	0.000	0.00	4.129	0.284	6.88	Q
CV2	2.0	0.356	0.094	26.00				Q
CV3	2.0	0.406	0.063	1.54	3.552	0.371	10.45	S
RCV3	2.0	0.400	0.073	3.00				S
CV4	2.0	0.400	0.038	9.38	4.620	0.337	7.29	Q
CV5	2.0	0.361	0.024	6.57	7.486	0.070	0.90	Q
RCV5	2.0	0.356	0.001	0.18				Q

CV6	2.0	0.413	0.025	6.06	3.036	0.726	23.90	G
RCV6	2.0	0.475	0.013	2.60				G
CV7	2.0	0.400	0.013	3.13	4.225	0.001	0.10	G
RCV7	2.0	0.425	0.012	2.90				G
CV8	2.0	0.356	0.006	1.75	5.253	0.099	1.90	S
RCV8	2.0	0.356	0.006	1.75				S
CV9	2.0	0.456	0.007	1.38	3.216	0.077	2.40	Q
CV10	2.0	0.450	0.013	2.78	3.668	0.014	0.38	G
CV11	2.0	0.369	0.018	5.08	5.025	0.621	12.36	V
CV13a	2.0	0.438	0.000	0.00	3.276	0.062	1.89	S
CV13b	2.0	0.413	0.025	6.10	3.392	0.103	3.02	Q
CV14	2.0	0.594	0.006	1.05	2.206	0.085	3.87	S
CV15	2.0	0.575	0.000	0.00	2.183	0.021	0.97	S
CV16	2.0	0.488	0.013	2.56	3.419	0.032	0.93	S
102	20.0	0.331	0.006	1.89				Q

c) Luarca

35	2.0	0.200	0.013	6.25	14.659	1.170	8.00	Q
35	20.0	0.188	0.000	0.00	28.810	6.335	22.70	Q
36	2.0	0.269	0.038	14.00	13.530	1.685	12.45	Q
36	20.0	0.225	0.000	0.00	14.050	1.799	12.80	Q
37	2.0	0.294	0.006	2.00	14.300	0.240	0.29	Q
37	20.0	0.225	0.025	11.00	24.114	1.214	5.03	Q
38	2.0	0.175	0.013	7.84	12.760	2.500	6.60	Q
38	20.0	0.231	0.033	14.10	23.651	2.261	9.56	Q
39	2.0	0.175	0.013	7.84	37.950	2.500	6.60	Q
39	20.0	0.200	0.013	6.25	33.475	1.641	4.90	Q
40	2.0	0.550	0.075	13.60	2.188	0.002	0.09	Q
40	20.0	0.201	0.014	6.80	29.437	6.740	22.90	Q
41	2.0	0.256	0.031	12.20	12.400	3.930	31.60	Q
41	20.0	0.188	0.013	6.67	11.967	3.013	25.17	Q
43	2.0	0.238	0.063	26.30				Q
43	20.0	0.194	0.006	3.20	26.210	5.690	21.70	Q
44	2.0	0.256	0.019	7.30	11.000	0.628	5.40	Q
44	20.0	0.175	0.013	7.14	28.245	3.569	12.60	Q
45a	2.0	0.369	0.006	1.64	5.353	0.112	2.09	G
45a	20.0	0.313	0.000	0.00	7.351	0.139	1.88	G
45b	2.0	0.244	0.019	7.70	13.127	0.203	1.54	S
45b	20.0	0.250	0.013	5.00	14.641	0.170	1.16	S

d) Punta Del Sol

V1	2.0	0.281	0.006	2.22	6.427	0.229	3.68	Q
V2	2.0	0.181	0.019	10.30				S
V3	2.0	0.131	0.006	4.76	121.870	10.935	8.97	S
V4	2.0	0.225	0.013	5.56	20.141	2.070	10.28	S
RV4	2.0	0.219	0.019	8.57				S
V5	2.0	0.329	0.004	1.14	4.799	0.127	2.65	Q
V7a	2.0	0.188	0.013	6.67	29.164	1.234	4.22	S
RV7a	2.0	0.200	0.025	12.50				S
V7b	2.0	0.300	0.013	4.17	10.570	0.205	0.19	G
RV7b	2.0	0.313	0.000	0.00				G
V8	2.0	0.188	0.013	6.67	8.743	1.028	11.76	Q
V10	2.0	0.219	0.006	2.85	11.730			Q
RV10	2.0	0.175	0.013	7.14				Q
V11	2.0	0.194	0.019	9.6				S
V12	2.0	0.481	0.006	1.30	4.803	0.308	6.4	Q

e) West Asturian - Leonese Zone

N1	2.0	0.369	0.019	5.08	2.680	0.154	5.70	Q
RN1	2.0	0.375	0.000	0.00				Q
N2	2.0	0.369	0.563	15.25	2.46	0.143	5.89	Q
N3	2.0	0.269	0.019	6.98	6.247	0.855	1.36	S
RN3	2.0				11.358	1.078	9.49	S
N4	2.0	0.363	0.000	0.00	4.790	0.083	1.70	S
RN4	2.0	0.375	0.013	3.30				S
VZ2	2.0	0.256	0.019	7.32	8.918	0.175	1.96	S
VZ4	2.0	0.213	0.025	11.76	19.550	0.457	2.34	S
CB1	2.0	0.301	0.014	4.56	4.514	0.118	2.60	Q
CB2	2.0	0.200	0.038	18.75	18.561	2.157	11.62	Q
CB3	2.0	0.188	0.012	6.67	23.145	1.439	5.70	S
TA4	2.0	0.238	0.000	0.00	9.345	1.879	20.10	S

f) Samples from Dr.Brime for interlaboratory correlation

C89	2.0	0.303	0.035	11.39	10.430	0.051	0.49
C12	2.0	0.393	0.045	11.45	3.530	0.059	1.69
C93	2.0	0.668	0.058	8.61	1.892	0.22	1.14
C55	2.0	0.881	0.182	20.66	1.509	0.092	6.06

APPENDIX A9

Listings of Main Programs

A9.1 FRACTLOG

A9.2 LINCEP

A9.3 RLTONDC (+A,B,G,F)

A9.4 FRY26 (+50,FRYCOL)

A9.5 FRYCIC

A9.6 RSAVPHI (+RSPHI)

All programs use Fortran 77, the Gino graphics packet, and N1051 Calcomp plotter.

A9.1 FRACTLOG

```
C     PROGRAMME SORTS FRACTURE LOGS INTO HISTOGRAMS WITH VARIABLE
C     CLASS INTERVAL CLINT.
      DIMENSION DIST(500)
      INTEGER LEN (500),UCL(500),LCL(500),FREQ(500),CLINT
      CLINT=100
      DO 10 I=1,500
      READ (5,*,END=20) LEN(I)
      DIST(I)=FLOAT(LEN(I))
      N=N+1
   10 CONTINUE
   20 CONTINUE
      NCLASS=LEN(N)/CLINT+1
      UCL(0)=0
      DO 40 J=1,NCLASS
      LCL(J)=UCL(J-1)
      UCL(J)=LCL(J)+CLINT
      IFREQ=0
      DO 30 K=1,N
      IF(LEN(K).LT.UCL(J).AND.LEN(K).GE.LCL(J)) IFREQ=IFREQ+1
   30 CONTINUE
      FREQ(J)=IFREQ
      WRITE (2,*) LCL(J),UCL(J),FREQ(J)
   40 CONTINUE
C     PROGRAMME DRAWS BAR DIAGRAMS FROM FRACTURE LOGS
      SCALE=0.04
      CALL N1051
      CALL PICCLE
C     SET OUT BAR OUTLINE
      HEIGHT=DIST(N)*SCALE
      CALL SHIFT2(150.0,300.0)
      CALL MOVTO2(0.0,0.0)
      CALL LINTO2(0.0,-HEIGHT)
      CALL LINTO2(20.0,-HEIGHT)
      CALL LINTO2(20.0,0.0)
      CALL LINTO2(0.0,0.0)
C     PROGRAMME DRAWS FRACTURE LOG
      DO 50 J=1,N
      Y=DIST(J)*SCALE
      CALL MOVTO2(0.0,-Y)
      CALL LINTO2(20.0,-Y)
      CALL MOVTO2(0.0,-Y)
   50 CONTINUE
C     PROGRAMME SETS OUT HISTOGRAM OUTLINE
      DEPTH=FLOAT(NCLASS*CLINT)*SCALE
      CALL MOVTO2(25.0,0.0)
      CALL LINTO2(65.0,0.0)
      CALL LINTO2(65.0,-DEPTH)
      CALL LINTO2(25.0,-DEPTH)
      CALL LINTO2(25.0,0.0)
C     PROGRAMME DRAWS HISTOGRAM
      DO 60 J=1,NCLASS
      RLCL=FLOAT(LCL(J))*SCALE
      RUCL=FLOAT(UCL(J))*SCALE
      RFREQ=FLOAT(FREQ(J))*5.0+25.0
      CALL MOVTO2(25.0,-RLCL)
      CALL LINTO2(RFREQ,-RLCL)
      CALL LINTO2(RFREQ,-RUCL)
      CALL LINTO2(25.0,-RUCL)
   60 CONTINUE
      CALL DEVEND
      STOP
      END
```

A9.2 LINCEP

```
C     PROGRAM CALCULATES LINEAR INTERCEPTS (=INCEP) AND SCALES
C     (=INCEPT) FROM INTERCEPT COORDINATES. THE G.M.L.,G.S.D.L., & N
C     ARE ALSO GIVEN.
      REAL INCEPT, INCEP, LGMEAN
      REAL COORD(2,1000)
      DIMENSION TITLE(6)
      N=-1
      READ (5,20) (TITLE(I),I=1,6)
      WRITE (2,20) (TITLE(I),I=1,6)
   20 FORMAT (6A2)
      DO 1 J=1,1000
      READ (5,*,END=2) (COORD(I,J),I=1,2)
      IF (COORD(1,J).EQ.000000) GOTO 2
      N=N+1
    1 CONTINUE
    2 CONTINUE
C     CALCULATE INCEP
      M=0
  100 DO 400 J=1,N
      X1=COORD(1,J)
      X2=COORD(1,J+1)
      Y1=COORD(2,J)
      Y2=COORD(2,J+1)
      INCEP=SQRT(ABS((X1-X2)**2-(Y1-Y2)**2))
C     CALCULATE INCEPT BY SCALING INCEP
      IF (COORD(1,J).GT.4000.0) GOTO 400
      IF (COORD(1,J+1).GT.4000.0) GOTO 400
      IF (INCEP.GT.1000.0) GOTO 400
      INCEPT=INCEP*0.0010145
      INCEPT=ABS (INCEPT)
      M=M+1
      SUM=SUM+ALOG10 (INCEPT)
      SUMSQ=SUMSQ+(ALOG10(INCEPT))*(ALOG10(INCEPT))
      WRITE(4,*) INCEPT
  400 CONTINUE
      TOAT=FLOAT(M)
      LGMEAN=SUM/TOAT
      GSUMSQ=SUMSQ/TOAT
      GV=GSUMSQ-(LGMEAN*LGMEAN)
      GSD=10.0**SQRT(GV)
      GMEAN=10.0**LGMEAN
      WRITE(2,500)
      WRITE(6,500)
  500 FORMAT (42H SLIDE GEOMETRIC MEAN GEOMETRIC SD  NUMBER)
      WRITE(6,600) (TITLE(I),I=1,6),GMEAN,GSD,M
      WRITE(2,600) (TITLE(I),I=1,6),GMEAN,GSD,M
  600 FORMAT (6A2,E15.7,E15.7,I5)
      STOP
      END
```

A9.3 RLTONDC

```
C     PROGRAM CALCULATES R(L), THE DISTRIBUTION OF LINCEPTS ON AN
C     ARITHMETIC GROUPING CLASS INTERVAL(C) = 0.1,FROM SCALED LINEAR
C     INTERCEPTS (INCEPT) WITH A.M.L.,A.S.D.L., THEN N(D), THE
C     DISTRIBUTION OF EQUIVALENT SPHERES OF DIAMETER D IS CALCULATED
C     FROM BOCKSTEIGEL'S FORMULA, WITH A.M.D. & A.S.D.D.
      REAL INCEPT (500),RL (5,10),ND,LCL,LCLD,NRL
      DIMENSION TITLE(6)
      READ (1,20) (TITLE(I),I=1,6),N
      WRITE (4,20) (TITLE(I),I=1,6),N
      WRITE (6,20) (TITLE(I),I=1,6),N
   20 FORMAT (6A1,1X,I3)
      DO 30 I=1,N
      READ (5,*) INCEPT(I)
      TOTL=TOTL+INCEPT(I)
   30 CONTINUE
      UCL=0.0
      SFXL=0.0
      SFXLSQ=0.0
      DO 300 J=1,10
      LCL=UCL
      UCL=UCL+0.1
      CMD=UCL-0.05
      NL=0
      DO 200 I=1,N
      IF (INCEPT(I).GE.LCL.AND.INCEPT(I).LT.UCL) NL=NL+1
  200 CONTINUE
      NRL=NL/TOTL
      RL(1,J)=J
      RL(2,J)=LCL
      RL(3,J)=CMD
      RL(4,J)=UCL
      RL(5,J)=NRL
      WRITE (4,*) J,LCL,CMD,UCL,NL
      WRITE (6,*) J,LCL,CMD,UCL,NL
      FXL=0.0
      FXLSQ=0.0
      FXL=CMD*NL
      FXLSQ=FXL*CMD
      SFXL=SFXL+FXL
      SFXLSQ=SFXLSQ+FXLSQ
  300 CONTINUE
      T=FLOAT(N)
      AML=SFXL/T
      ASDL=SQRT(SFXLSQ/T-AML**2.0)
      WRITE (4,340) AML,ASDL
      WRITE (6,340) AML,ASDL
340   FORMAT ( 7H AML = ,E15.7,8H ASDD = ,E15.7)
C     PROGRAM NOW CALCULATES ND,THE DISTRIBUTION OF SPHERES OF
C     DIAMETER D CORRESPONDING TO LINEAR INTERCEPTS L.
      WRITE (4,350)
      WRITE (6,350)
      UCLD=RL(3,1)
      AMD=0.0
      ASD=0.0
      SN=0.0
      SFX=0.0
      FX=0.0
      SFXSQ=0.0
      ND=0.0
```

```
      DO 400 J=1,9
      LCLD=UCLD
      UCLD=RL(3,J+1)
      Q=FLOAT(J)
      ND=63.6619*((RL(5,J)/(2.0*Q-1.0))-(RL(5,J+1)/(2.0*Q+1.0)))
      IF (ND.LT.0.0) ND=0.0
      CMD=UCLD-0.05
      FX=CMD*ND
      FXSQ=FX*CMD
      SFX=FX+SFX
      SFXSQ=SFXSQ+FXSQ
      SN=SN+ND
 350  FORMAT (53H     J       LCLD              CMD              UCLD
ND)
      WRITE (4,*) J,LCLD,CMD,UCLD,ND
      WRITE (6,*) J,LCLD,CMD,UCLD,ND
 400  CONTINUE
      AMD=SFX/SN
      ASD=SQRT(SFXSQ/SN-AMD**2.0)
      WRITE (4,500) AMD, ASD
      WRITE (6,500) AMD, ASD
 500  FORMAT ( 7H AMD = ,E15.7,8H ASDD = ,E15.7)
      STOP
      END
```

```
 RLTONDA     C = 0.025
 RLTONDB     C = 0.01
 RLTONDF,G   R(L) & N(D) ARE CALCULATED ON A GEOMETRIC GROUPING,
             MODULE ROOT 2, WITH LOWER LIMIT OF SMALLEST CLASS, L.C.
 RLTONDF     L.C. = 0.00003
 RLTONDG     L.C. = 0.005
```

A9.4 FRY26

```
      PROGRAM FRYPLOT CALCULATES FRYCOORDINATES FROM COORDS. OF GRAIN
C     CENTERS, THEN CALCULATES AND PLOTS A 26 X 26 GRID OF THE
C     FRYPLOT,PRINTING THE NUMBER OF FRYCOORDINATES WITHIN EACH
C     SQUARE.
C     THE VALUES OF L,M, AND N ARE ALSO PRINTED.
      DIMENSION X(1000),Y(1000),XFRY(2000),YFRY(2000)
      DIMENSION XFRYP(2000),YFRYP(2000),TITLE(7)
      DIMENSION NFRY(26,26)
      REAL LFRY
      RESCAL=4.0
      READ (5,5) (TITLE(I),I=1,7)
  5   FORMAT(7A1)
      DO 10 I=1,1000
      READ (5,*,END=20) X(I),Y(I)
      N=N+1
 10   CONTINUE
 20   CONTINUE
      LFRY=+00250
      DO 50 I=1,N
      IF (X(I).GT.03750-LFRY/2.0) GOTO 50
      IF (Y(I).GT.03000-3.0*LFRY/2.0) GOTO 50
      IF (Y(I).LT.LFRY/2.0) GOTO50
      XPLOT=X(I)
      YPLOT=Y(I)
      L=L+1
      DO 40 J=1,N
      IF (X(J).LT.XPLOT) GOTO 40
      XFRY(J)=(X(J)-XPLOT)
      YFRY(J)=(Y(J)-YPLOT)
      IF (XFRY(J).GT.LFRY.OR.XFRY(J).EQ.LFRY) GOTO 40
      IF (YFRY(J).GT.LFRY.OR.YFRY(J).EQ.LFRY) GOTO 40
      IF (YFRY(J).LT.-LFRY.OR.YFRY(J).EQ.-LFRY) GOTO 40
      IF (XFRY(J).LT.2.0.AND.YFRY(J).GT.-2.0.AND.YFRY(J).LT.2.0)
     1GOTO 40
      M=M+1
      XFRYP(M)=XFRY(J)
      YFRYP(M)=YFRY(J)
      KX=INT(XFRYP(M)/20.0)+14
      IF (YFRYP(M).LT.0.0) GOTO 35
      KY=INT(YFRYP(M)/20.0)+14
      GOTO 38
 35   KY=13-INT(-YFRYP(M)/20.0)
 38   CONTINUE
      LX=14-(KX-13)
      LY=13-(KY-14)
      NFRY(KX,KY)=NFRY(KX,KY)+1
      NFRY(LX,LY)=NFRY(KX,KY)
 40   CONTINUE
 50   CONTINUE
      WRITE (2,80) (TITLE(I),I=1,7),L,M,N
 80   FORMAT (7A1,4X,"L = ",I4,3X,"M = ",I4,3X,"N = ",I4)
      DO 85 J=1,26
      K=14-(J-13)
      WRITE (2,70) (NFRY(I,K),I=1,26)
 70   FORMAT (26I2)
 85   CONTINUE
      CALL N1051
      CALL SCALE(RESCAL)
      CALL MOVTO2(0.0,28.0)
```

```
      CALL CHAA1(TITLE,7)
      CALL MOVTO2(10.0,28.0)
      CALL CHAINT(L,4)
      CALL MOVTO2(15.0,28.0)
      CALL CHAINT(M,4)
      CALL MOVTO2(20.0,28.0)
      CALL CHAINT(N,4)
      CALL MOVTO2(14.0,14.0)
      CALL SYMBOL(4)
      DO 60 I=1,26
      DO 60 J=1,26
      MFRY=NFRY(I,J)
      IF (MFRY.EQ.0) GOTO 60
      RX=FLOAT(I)
      RY=FLOAT(J)
      CALL MOVTO2(RX,RY)
      CALL CHAINT(MFRY,2)
 60   CONTINUE
      CALL DEVEND
      STOP
      END
```

FRY50 THE SAME PROCEEDURE IS FOLLOWED FOR A 50 X 50 GRID.
FRYCOL THE GRID SQUARES ARE COLOURED BY THE NUMBER WITHIN
       THE SQUARE.

A9.5 FRYCIC

```
      PROGRAM FRYPLOT
      DIMENSION X(10000),Y(10000),XFRY(11000),YFRY(11000)
      DIMENSION XFRYP(11000),YFRYP(11000),TITLE(7)
      DIMENSION NFRY(26,26)
      REAL LFRY
      RESCAL=0.5
      OLAP=0.3
      READ (5,5) (TITLE(I),I=1,7)
  5   FORMAT(7A1)
      DO 10 I=1,10000
      READ (5,*,END=20) X(I),Y(I)
      IF (X(I).GT.XMAX) XMAX=X(I)
      IF (Y(I).GT.YMAX) YMAX=Y(I)
      N=N+1
 10   CONTINUE
 20   CONTINUE
      LFRY=+00150
      WRITE (2,*) XMAX,YMAX,N
      DO 50 I=1,N
      IF (X(I).GT.XMAX-LFRY/2.0) GOTO 50
      IF (Y(I).GT.YMAX-3.0*LFRY/2.0) GOTO 50
      IF (Y(I).LT.LFRY/2.0) GOTO50
      XPLOT=X(I)
      YPLOT=Y(I)
      L=L+1
      DO 40 J=1,N
      IF (X(J).LT.XPLOT) GOTO 40
      XFRY(J)=(X(J)-XPLOT)
      YFRY(J)=(Y(J)-YPLOT)
      IF (XFRY(J).GT.LFRY.OR.XFRY(J).EQ.LFRY) GOTO 40
      IF (YFRY(J).GT.LFRY.OR.YFRY(J).EQ.LFRY) GOTO 40
      IF (YFRY(J).LT.-LFRY.OR.YFRY(J).EQ.-LFRY) GOTO 40
      IF (XFRY(J).LT.2.0.AND.YFRY(J).GT.-2.0.AND.YFRY(J).LT.2.0) GOTO
40
      M=M+1
      XFRYP(M)=XFRY(J)
      YFRYP(M)=YFRY(J)
 40   CONTINUE
 50   CONTINUE
      WRITE (2,80) (TITLE(I),I=1,7),L,M,N
 80   FORMAT (7A1,4X,"L = ",I4,3X,"M = ",I4,3X,"N = ",I4)
      RR=OLAP*2.0/FLOAT(M)*(LFRY*RESCAL)**2.0
      RADIUS=RR/RESCAL
      WRITE (2,*) RR,RADIUS
      HEAD=LFRY+10.0/RESCAL
      CALL N1051
      CALL SHIFT2(150.0,150.0)
      CALL SCALE(RESCAL)
      CALL MOVTO2(-250.0,HEAD)
      CALL CHAA1(TITLE,7)
      CALL MOVTO2(-125.0,HEAD)
      CALL CHAINT(L,4)
      CALL MOVTO2(0.0,HEAD)
      CALL CHAINT(M,4)
      CALL MOVTO2(125.0,HEAD)
      CALL CHAINT(N,4)
      CALL MOVTO2(0.0,0.0)
      CALL SYMBOL(4)
      DO 60 I=1,M
```

```
      XA=XFRYP(I)+RADIUS
      XB=XFRYP(I)+(RADIUS/2.0)
      CALL MOVTO2(XA,YFRYP(I))
      CALL ARCTO2(XFRYP(I),YFRYP(I),XA,YFRYP(I),0)
      CALL MOVTO2(XB,YFRYP(I))
      CALL ARCTO2(XFRYP(I),YFRYP(I),XB,YFRYP(I),0)
      CALL MOVTO2(-XA,-YFRYP(I))
      CALL ARCTO2(-XFRYP(I),-YFRYP(I),-XA,-YFRYP(I),0)
      CALL MOVTO2(-XB,-YFRYP(I))
      CALL ARCTO2(-XFRYP(I),-YFRYP(I),-XB,-YFRYP(I),0)
   60 CONTINUE
      WRITE (2,*) I
      CALL DEVEND
      STOP
      END
```

A9.6 RSAVPHI

```
C     PROGRAM CALCULATES RS AND PHI BY THE ALGEBRAIC
C     METHOD OF SHIMAMOTO AND IKEDA (1976) FROM COORDINATES
C     OF LONG AND SHORT AXES OF GRAINS. 2 PAIRS OF COORDINATES
C     FOR EACH AXIS MAY BE INPUT IN ANY ORDER.
      DIMENSION X (2000), Y (2000)
      DO 10 I=1,2000
      READ(5,*,END=20) X(I),Y(I)
      N=N+1
   10 CONTINUE
   20 WRITE (2,*) N
      DO 40 I=1,N-3,4
      DY1=Y(I)-Y(I+1)
      DX1=X(I)-X(I+1)
      AXIS1=SQRT(DY1*DY1+DX1*DX1)
      DY2=Y(I+2)-Y(I+3)
      DX2=X(I+2)-X(I+3)
      AXIS2=SQRT(DY2*DY2+DX2*DX2)
      IF (AXIS1.GT.AXIS2) GOTO 30
C      EXCHANGE AXES
      DUMMY=AXIS1
      AXIS1=AXIS2
      AXIS2=DUMMY
      DUMMY=DY1
      DY1=DY2
      DY2=DUMMY
      DUMMY=DX1
      DX1=DX2
      DX2=DUMMY
   30 RF=AXIS1/AXIS2
      PHI=ATAN(DY1/DX1)
C     CHANGE TO SHIMAMOTO & IKEDO COORDINATES
      IF (PHI.LT.0.0) PHI=3.142+PHI
      CSQ=COS(PHI)*COS(PHI)
      SSQ=SIN(PHI)*SIN(PHI)
      F=1.0/RF*CSQ+RF*SSQ
      SF=F+SF
      G=1.0/RF*SSQ+RF*CSQ
      SG=G+SG
      H=(1.0/RF-RF)*SIN(PHI)*COS(PHI)
      SH=H+SH
      SUM=SUM+1.0/RF
   40 CONTINUE
      HA=FLOAT(N)/4.0/SUM
      WRITE(2,50) HA
   50 FORMAT("HARMONIC MEAN = ",E15.6)
      AVF=SF/FLOAT(N)*0.25
      AVG=SG/FLOAT(N)*0.25
      AVH=SH/FLOAT(N)*0.25
      WRITE (2,*) AVF,AVG,AVH
      B=SQRT((AVG+AVF)**2.0-4.0*(AVG*AVF-AVH*AVH))
      RS=SQRT((AVG+AVF+B)/2.0)/SQRT((AVG+AVF-B)/2.0)
      AVPHI=(ATAN(2.0*AVH/(AVF-AVG)))/2.0*180.0/3.142
      WRITE (2,*) RS,AVPHI
      STOP
      END
```

RSPHI THE SAME CALCULATION IS EXECUTED ON PHI/RF DATA INPUT DIRECTLY.

APPENDIX A10

Histograms of Intracrystalline Extinction Angles

Bernesga Valley.	1,2,5,6,7,8,9,10,11,11R,12,13,14,16,17 19,20,103,104,105,106,107,109,111
Cremenes.	23
Luna Lake.	28,31,33
Punta Vidrias.	CV1,CV2,CV4,CV5,CV6,CV7
Cabo de Peñas.	102
Luarca.	36,38,39,40,41,42
Punta del Sol.	V1,V5,V10,V12,V8DX,V12DC
Navia.	N1
Viavelez.	VZ1,VZ3
Cabo Blanco.	CB1
Tapia.	TA1,TA3
Tarskavaig, Isle of Skye.	T6,T7,T29,T32,T35

R = Repeat Measurement
DX = Recrystallised Grains
DC = Vein Grains

▼ = Geometric Mean (G.M.A.)

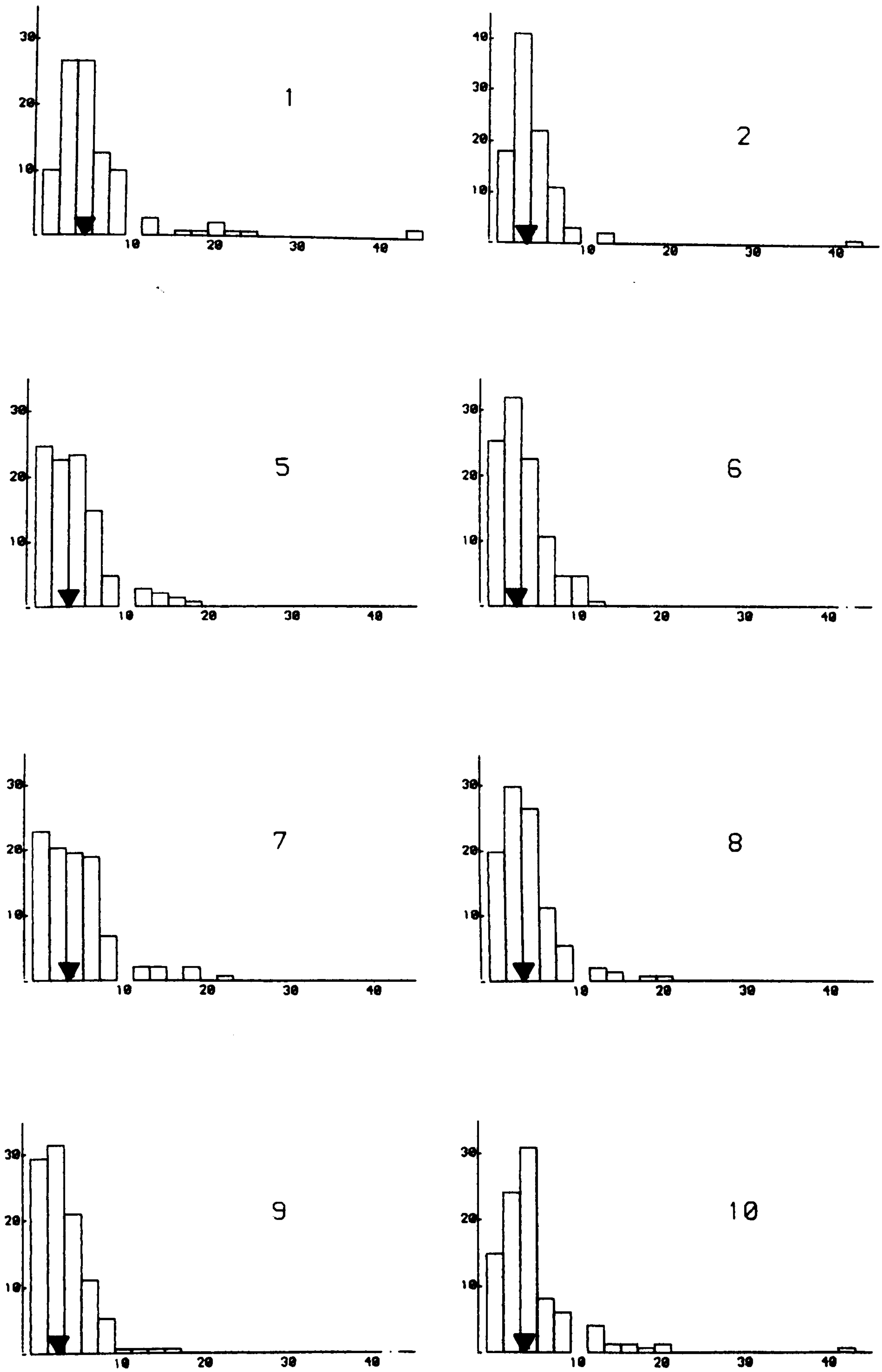
1
2
5
6
7
8
9
10
10
20
30
40

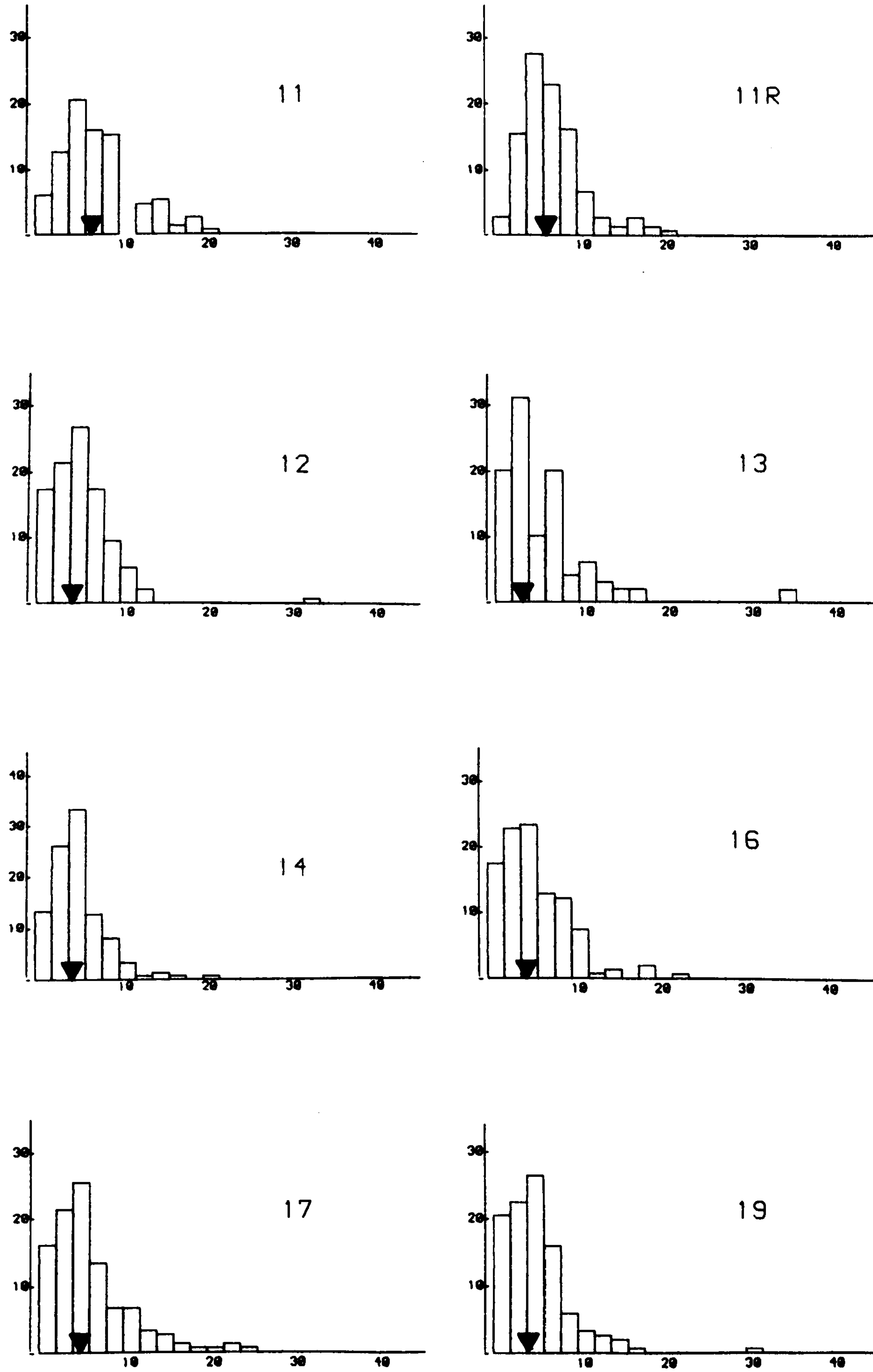

11
11R
12
13
14
16
17
19
10
20
30
40

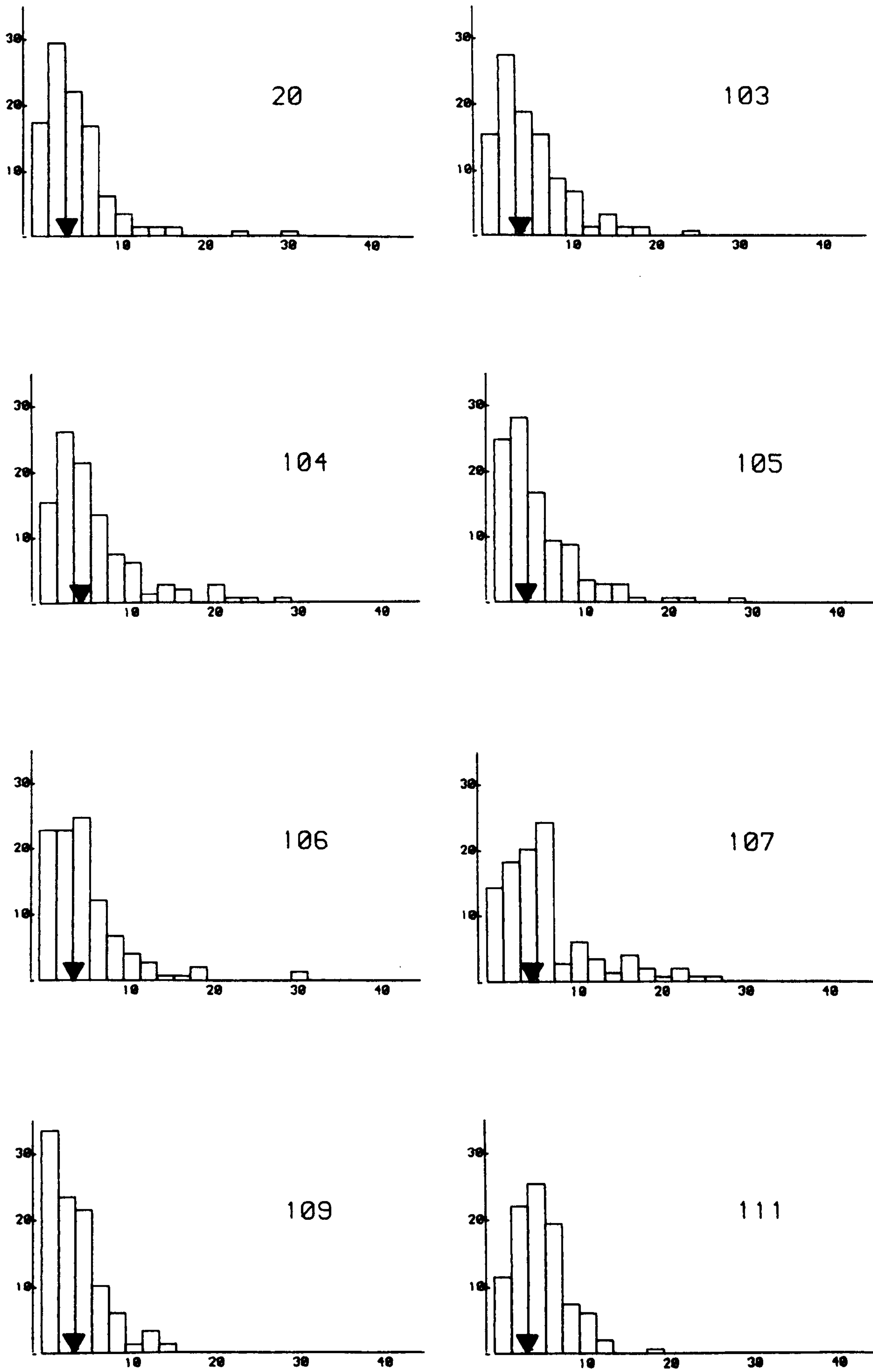
20
103
104
105
106
107
109
111
10
20
30
40

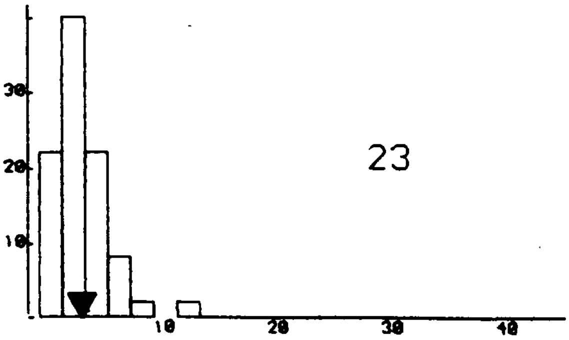
23
10
20
30
10
20
30
40

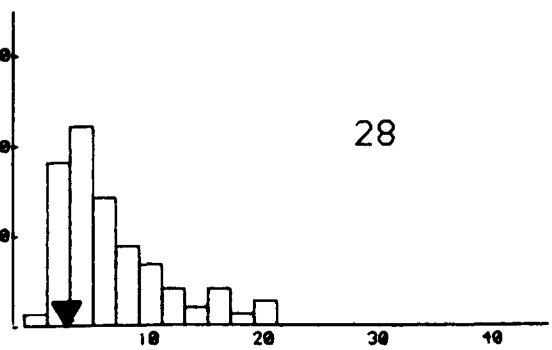
28
10
20
30
10
20
30
40

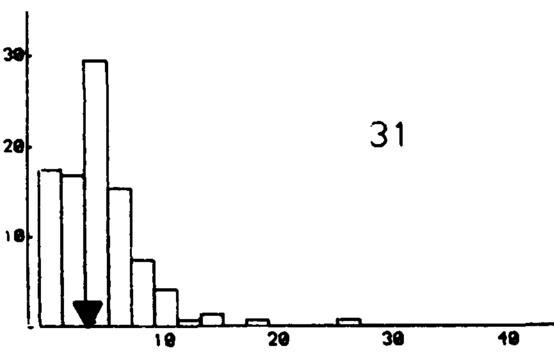
31
10
20
30
10
20
30
40

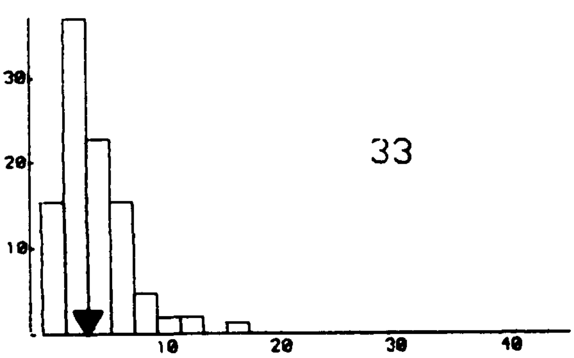
33
10
20
30
10
20
30
40

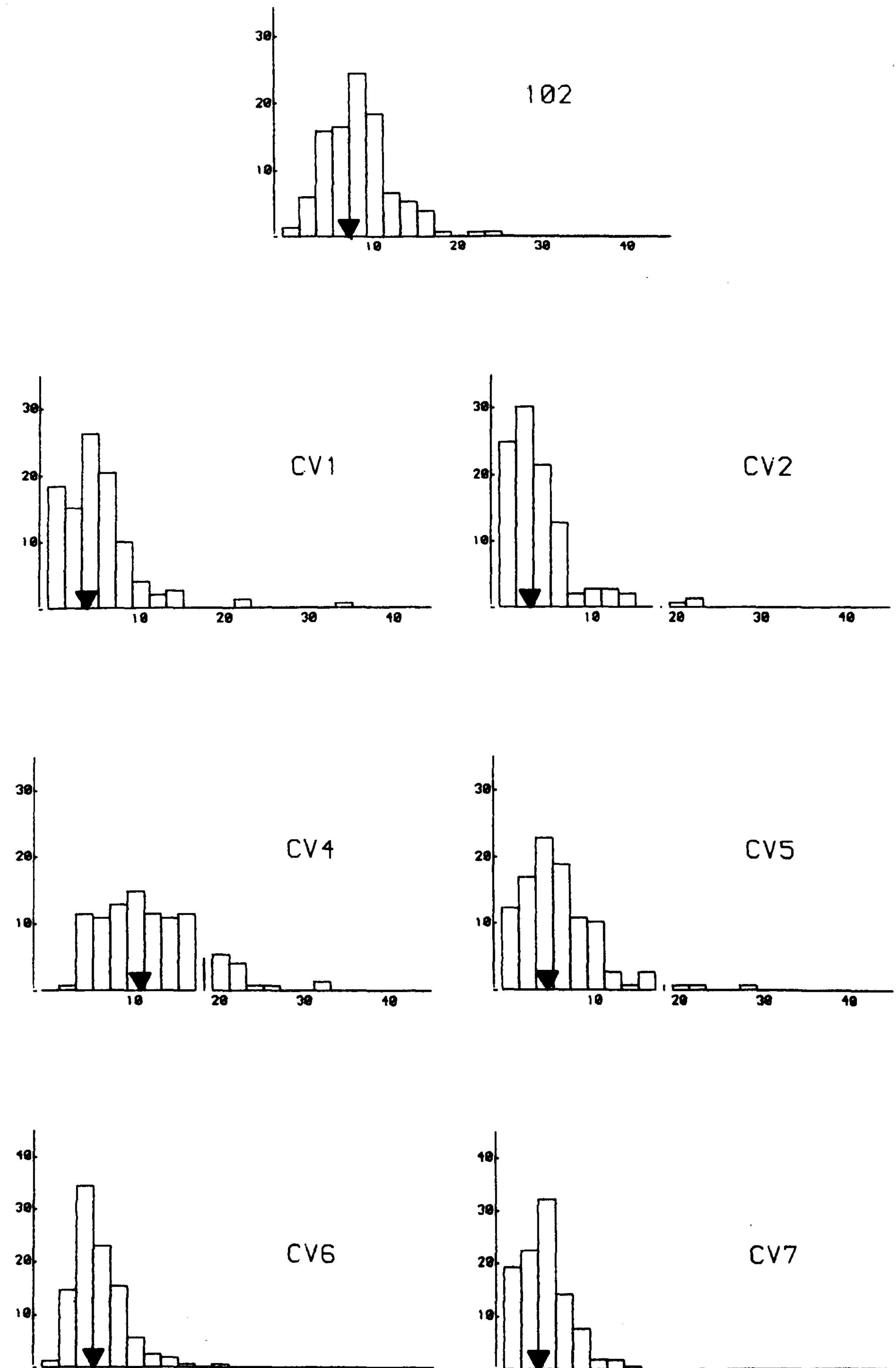
102
CV1
CV2
CV4
CV5
CV6
CV7
10
20
30
40

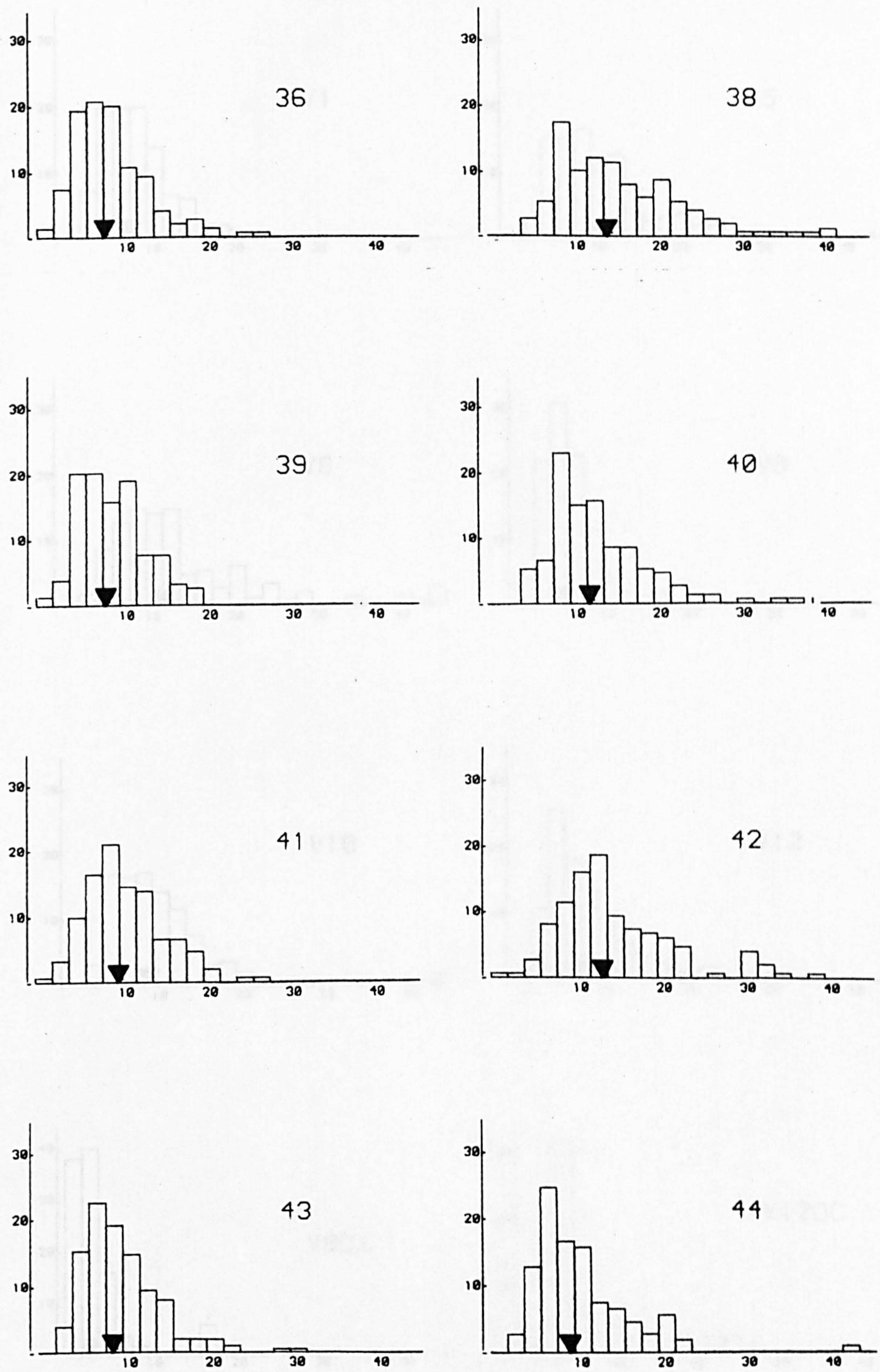
36
38
39
40
41
42
43
44
10
20
30
40

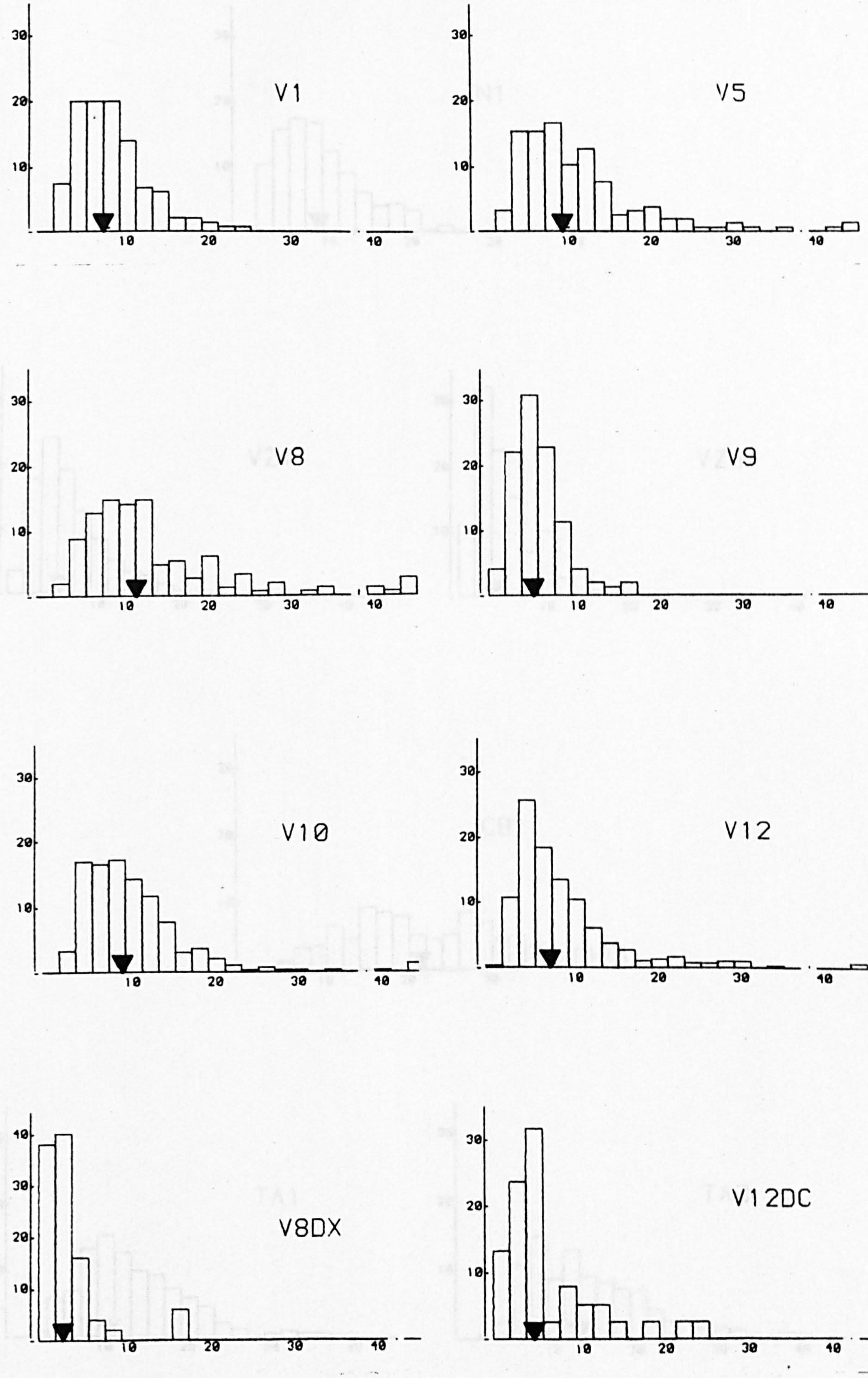
V1
V5
V8
V9
V10
V12
V8DX
V12DC

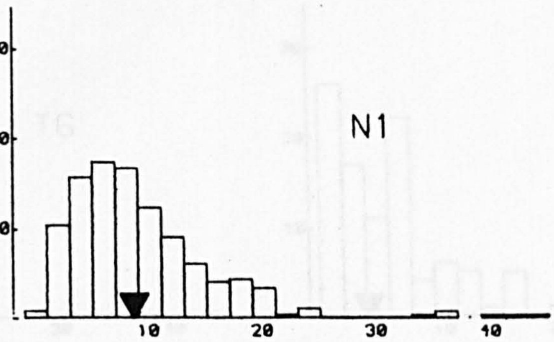
N1
30
20
10
10
20
30
40

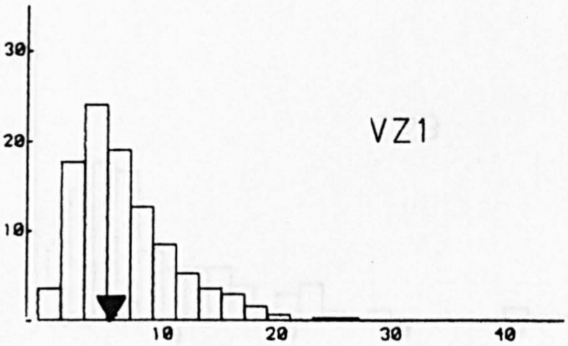
VZ1
30
20
10
10
20
30
40

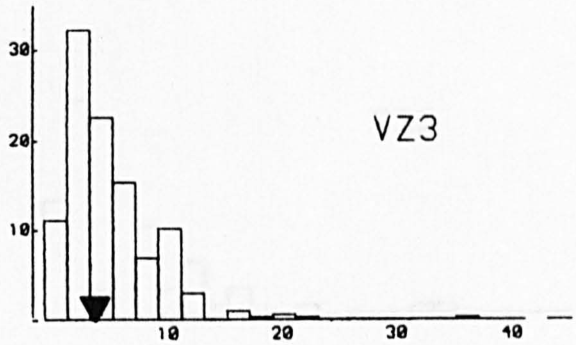
VZ3
30
20
10
10
20
30
40

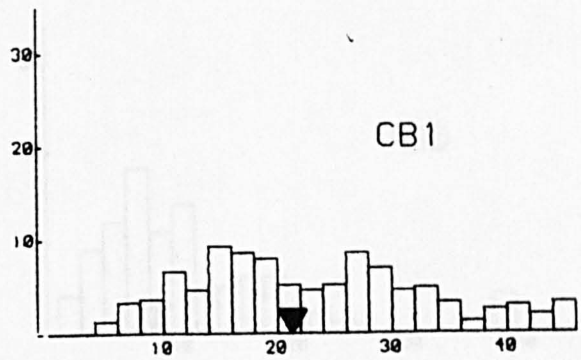
CB1
30
20
10
10
20
30
40

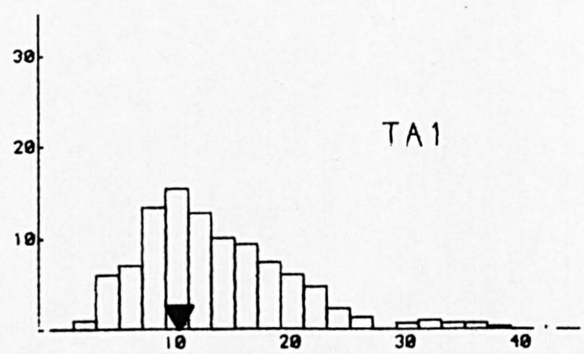
TA1
30
20
10
10
20
30
40

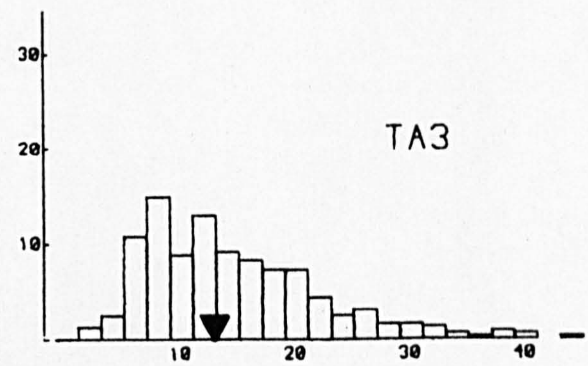
TA3
30
20
10
10
20
30
40

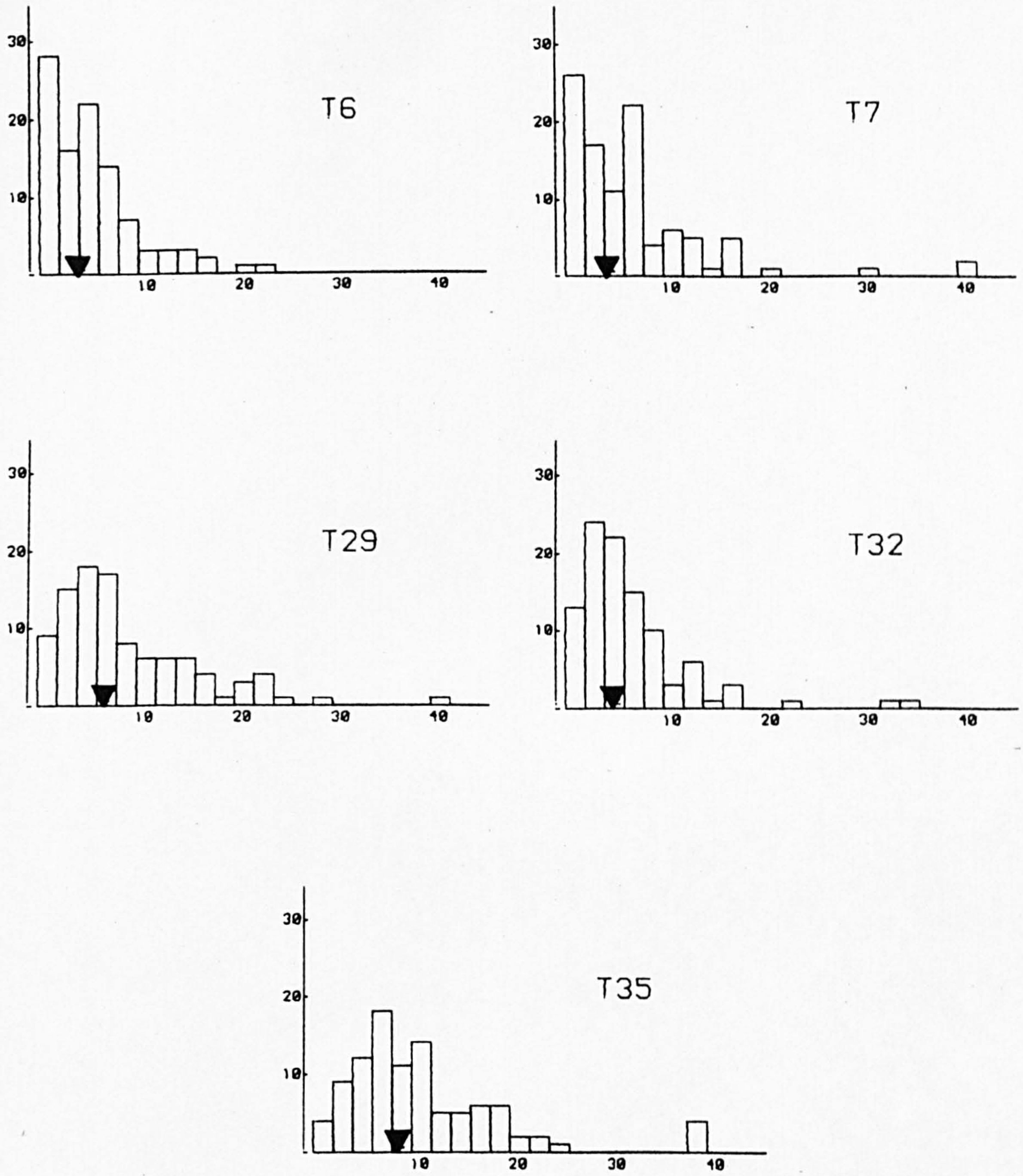
T6
T7
T29
T32
T35
10
20
30
40